

# A history-matching analysis of Antarctic Ice Sheet evolution since the last interglacial

by

© Benoit S. Lecavalier

A Thesis submitted to the  
School of Graduate Studies  
in partial fulfillment of the  
requirements for the degree of  
Doctor of Philosophy

Department of Physics and Physical Oceanography  
Memorial University of Newfoundland



September 2024

St. John's

Newfoundland

# Abstract

One technique to explicitly quantify uncertainties of glacial systems is a history-matching analysis (HMA) of a model against a large observational database. This is achieved by ruling out simulations that are inconsistent with an observational constraint database. A comprehensive database (“AntICE2”) was compiled for state-space estimation of past Antarctic Ice Sheet (AIS) changes and to evaluate model reconstructions. This research applies a HMA on a 3D glacial systems model (GSM) for Antarctica against the AntICE2 observational constraint database. A HMA represents a crucial steppingstone towards a comprehensive Bayesian calibration. A HMA consists of identifying model reconstructions that are consistent with observations given uncertainties in the model and data. Our HMA extensively samples model uncertainties against fits to observational data through Markov Chain Monte Carlo methods using Bayesian artificial neural network emulators of the full GSM. This methodology produced several large ensembles exceeding 40,000 simulations that were evaluated against observational constraints. The terminal large ensemble consisting of 9,293 members represents the culmination of this research.

The GSM simulation output is scored against the AntICE2 database to evaluate the model reconstruction. The HMA rules simulations as being broadly inconsistent with the AntICE2 database based on being within a  $3\sigma$  or  $4\sigma$  threshold of each various observational data type. The simulations from the full ensemble that are tentatively not inconsistent with the observational constraint database are classified as the not-ruled-out-yet (NROY) sub-ensemble.

The HMA of the AIS since the last interglacial and the resulting NROY sub-ensemble addresses several outstanding research questions. Considering the extent to which uncertainties across the glacial system and data were incorporated in the HMA, the NROY sub-ensemble should approximately bracket the past evolution of the actual ice sheet. The NROY simulations have excess Last Glacial Maximum (LGM) volumes ranging between 9.2 to 26.5 meters equivalent sea level. This range has upper limits that are considerably higher than past studies and this addresses in large part inferential deficits in the LGM sea-level budget. Moreover, the NROY sub-ensemble represents an envelop of chronologies which can be used as input boundary conditions for general circulation models and glacial isostatic adjustment models to better understand past atmospheric and oceanic circulation, and sea-level change.

# Acknowledgements

I would like to start by thanking my supervisor Lev Tarasov who has been an exceptional and inspiring role model throughout my studies. I thank you for providing me a chance to prove myself along with the opportunity to establish myself in an active, dynamic, and fascinating field of research. Even with your busy schedule you have made time to guide me through my research and have always been available to discuss my research and pet projects. I am looking forward to continuing our work together in the future. I wish the best for you and your family. Furthermore, I would like to thank my numerous collaborators. You have provided encouragement, feedback, code, data, and inspiring discussions. You have received me in your countries and exercised patience with my questions, for which I am thankful for.

To my friends and colleagues, thanks for keeping me grounded through it all and for the company. I would like to thank my parents, Pierre and Julie for the continuous support. You have always been there to discuss everything and anything from science, philosophy, economics, and politics. You have instilled my scientific curiosity for which I will be forever grateful for. Finally, to my partner Eve Tunney, you have supported and believed in me, thanks to you I managed to get through this journey.

Financial support for this work was provided through a NSERC PGS Doctoral scholarship and Lev Tarasov's NSERC Discovery Grant. Computational resources were provided by the Canadian Foundation for Innovation and ACEnet.

# Co-Authorship Statement

The research project described in this thesis was initially formulated by the thesis supervisor, Professor Lev Tarasov, and subsequently revised by Benoit Lecavalier. Benoit Lecavalier wrote the thesis abstract, introduction, and conclusion with editorial input by Lev Tarasov.

The research paper presented in Chapter 2 is a one-to-one copy of Lecavalier et al. (2023). Chapter 2 is a large international study that was initially conceptualized by Benoit Lecavalier and Lev Tarasov. Benoit Lecavalier compiled and received disparate datasets, processed, standardized, evaluated, sieved, and recalibrated the data under the supervision of Lev Tarasov. All other co-authors contributed datasets, feedback on the manuscript, and evaluation of the quality criteria for curation of the resulting database.

The research paper presented in Chapter 3 is a one-to-one copy of the Lecavalier and Tarasov (2024) preprint and Chapter 4 is a manuscript intended for publication. The two main authors of both studies are Benoit Lecavalier and Lev Tarasov. Lev Tarasov originally developed the GSM. The GSM Antarctic configuration was developed jointly by both Benoit Lecavalier and Lev Tarasov. The Penn State University ice sheet model was provided by Dave Pollard, of which only the ice dynamical core was extracted and implemented in the GSM. The data-model evaluation and statistical methodology was developed by Lev Tarasov (paleoExt, paleoH, and paleoRSL data) while Benoit Lecavalier developed the evaluation to the ice core borehole temperature profiles and PD scores. The model-data analysis was conducted by Benoit Lecavalier and Lev Tarasov. The

manuscripts were written and assembled by Benoit Lecavalier with contributions from Lev Tarasov.

## Table of Contents

Abstract .....	ii
Acknowledgements .....	iv
Co-Authorship Statement.....	v
Table of Contents .....	vii
List of Tables .....	xii
List of Figures .....	xiii
Abbreviations .....	xxx
Chapter 1: Introduction .....	1
1.1 Motivation .....	1
1.2 Present day Antarctic ice sheet.....	3
1.3 Antarctic ice sheet evolution .....	8
1.3.1 Ice sheet formation .....	9
1.3.2 Ice dynamics .....	11
1.3.3 Ice shelves.....	13
1.3.4 Sub-ice-shelf mass balance.....	15
1.3.5 Marine ice sheet instability.....	16
1.3.6 Marine ice cliff instabilities .....	19
1.3.7 Antarctic mass loss, GIA and sea-level change.....	20
1.3.8 Future Antarctic ice sheet changes .....	24
1.4 Key periods in the paleorecord.....	25
1.4.1 Climate history.....	25

1.4.2 Last interglacial sea level.....	29
1.4.3 Last Glacial Maximum .....	31
1.4.4 Deglacial sea level and melt water pulses .....	34
1.5 Primary Research Questions .....	38
1.6 Previous Antarctic Modelling Studies.....	39
1.7 Glacial Systems Model.....	48
1.7.1 Ice sheet component .....	48
1.7.2 Atmospheric climate component .....	61
1.7.3 Solid Earth component .....	62
1.7.4 Model configuration and parameters .....	63
1.8 History-Matching Analysis .....	64
1.9 Objective and thesis overview.....	70
1.10 References .....	71
Preface to Chapter 2, 3, and 4 .....	99
Chapter 2: Antarctic Ice Sheet paleo-constraint database.....	100
Abstract .....	100
2.1 Introduction .....	101
2.2 AntICE2 constraints .....	103
2.2.1 Paleo-ice-sheet thickness .....	107
2.2.2 Paleo-ice-sheet extent .....	113
2.2.3 Paleo relative sea level.....	117

2.2.4 Ice core borehole temperatures .....	121
2.2.5 Present-day uplift vertical land motion.....	123
2.2.6 Present-day geometry and surface ice velocity .....	124
2.2.7 Data uncertainty structure.....	127
2.3 Discussion .....	127
2.3.1 Data curation and tiered data quality assessment .....	131
2.3.2 Potential future and rejected data types .....	141
2.4 Data availability .....	145
2.5 Summary .....	145
2.6 Author contributions. ....	146
2.7 References .....	147
Chapter 3: A history-matching analysis of the Antarctic Ice Sheet since the last	
interglacial – Part 1: Ice sheet evolution.....	165
Abstract .....	165
3.1 Introduction .....	166
3.2 Observational constraints – AntICEdat 2.0.....	177
3.3 Model description.....	178
3.4 Methodology .....	189
3.4.1 Scoring a reconstruction .....	189
3.4.2 History-matching analysis .....	191
3.4.3 Ensembles and not-ruled-out-yet (NROY) sub-ensembles .....	195

3.5 NROY fits to data constraints .....	198
3.5.1 Ice core borehole temperature profiles .....	201
3.5.2 Past ice extent .....	205
3.5.3 Past ice thickness .....	212
3.5.4 Present day geometry.....	215
3.5.5 Present day surface velocities.....	217
3.6 Results .....	219
3.6.1 Last interglacial .....	219
3.6.2 Last Glacial Maximum .....	225
3.6.3 Deglaciation.....	228
3.6.4 Present-day AIS.....	231
3.7 Conclusion.....	233
3.8 Author Contributions.....	234
3.9 References .....	235
Chapter 4: A history-matching analysis of the Antarctic Ice Sheet since the last interglacial – Part 2: Glacial isostatic adjustment.....	254
Abstract .....	254
4.1 Introduction .....	256
4.2 Model description.....	259
4.3 Methodology .....	261
4.4 Results and Discussion.....	269

4.4.1 Data-model comparisons .....	269
4.4.2 Glacial isostatic adjustment model predictions .....	276
4.5 Conclusion.....	284
4.6 Author Contributions.....	286
4.7 References .....	286
Chapter 5: Conclusion.....	294
5.1 Antarctic Ice Sheet constraints .....	294
5.2 Antarctic Ice Sheet evolution .....	295
5.3 Antarctic glacial isostatic adjustment.....	296
5.4 Future work .....	297
Supplement for Chapter 1 .....	300
Supplement for Chapter 2 .....	309
Supplement for Chapter 3 .....	326
Supplement for Chapter 4 .....	339

# List of Tables

Table 2.1: Summary of Antarctic Ice Sheet Evolution database version 2 (AntICE2) and quality tier subsets.....	138
Table 3.1: Ensemble parameters in the Antarctic configuration of the Glacial Systems Model. ....	182
Table 3.2: The full ensemble and sub-ensemble descriptions. ....	192
Table 3.3: The contribution of the AIS to the LIG (deficit relative to present) and LGM (excess relative to present) for the full ensemble, AN4sig sub-ensemble, and not-ruled-out-yet (NROY) AN3sig sub-ensembles. ....	223
Table S3.1: The thresholds imposed on the AntICE2 data-model scores in the history-matching analysis. The thresholds to define the AN4sig and AN3sig sub-ensembles are based on internal/external discrepancy bias corrections plus 4 or 3 multiples of the standard deviations, respectively.....	334

# List of Figures

Figure 1.1: Antarctica and named places in the document. The Dark blue contour denotes the position of the present-day grounding line. The Antarctic basemap was generated using Quantarctica (Matsuoka et al., 2021). .....	4
Figure 1.2: Present day Antarctic ice sheet boundary conditions – Antarctic BedMachine Version 2 a) Surface, b) Basal topography, c) ice thickness (Morlighem et al., 2020), and d) MEaSURES surface velocity (Mouginot et al., 2019). .....	6
Figure 1.3: Boundary conditions for the a-c) PD monthly climatologies (RACMO 2.3p2; Melchior Van Wessem et al., 2018). Basal boundary conditions such as the d) basal till fraction beneath the Antarctic ice sheet and the geothermal heat flux field based on e) magnetic data (Martos et al., 2017) and f) seismic data (An et al., 2015). ...	10
Figure 1.4: An illustration depicting key principles of marine ice sheet instability (MISI) where a marine-based ice sheet is grounded on a reverse-bed slope. a) The grounding line (GL) is in a stable position when the GL is located on a prograde bed slope. b) An incursion of warm circumpolar deep water below the ice shelf leads to increase melt at the GL causing it to retreat into a retrograde bed slope where it undergoes an unstable GL retreat. As the GL retreats into deeper water, the height of the ice column at the GL ( $H_{GL}$ ) increases and in turn, ice flux through the GL increases ( $Q_{GL}$ ). .....	16
Figure 1.5: An illustration depicting key principles of marine ice cliff instability (MICI) where a) a crevassed ice shelf experiences surface/basal melt or rainfall. The ice shelf undergoes hydrofracturing that propagates crevasses and enhances ice calving	

culminating in an ice cliff. b) The ice cliff becomes unstable if it exceeds a threshold height which can no longer support the yield strength of the ice, at which point the cliff fails. .... 19

Figure 1.6: An illustration depicting ice sheet unloading and the resulting glacial isostatic adjustment (GIA). a) During peak glaciation, an ice sheet depresses the lithosphere which displaces mantle material. Proximal to the ice load, a peripheral forebulge forms and the gravitational field is deflected upwards due to the mass of the large ice load. b) Throughout the deglaciation the grounded ice sheet retreats which contributes to regional sea-level change by shifting the ocean from one equipotential surface of the gravitational field to a higher one. The newly deglaciated regions rebound, the forebulge collapses and the near-field gravitational field relaxes. The redistribution of ice to the ocean leads to hydro isostasy due to ocean loading. In the near-field RSL decreases while in the far-field RSL increases. .... 21

Figure 1.7: An Antarctic sea-level fingerprint demonstrates a normalize sea-level contribution from Antarctic due to the immediate elastic response of the solid Earth from ice mass loss from grounded ice..... 23

Figure 1.8: The EPICA Dome C deuterium record spanning a) 800 kyr, b) the last interglacial and glacial cycle, and c) the deglaciation. Key periods of interest are labelled which include the last interglacial (LIG), Last Glacial Maximum (LGM), and Meltwater Pulse 1a (MWP1a). The EPICA Dome C data is also shown in Chapter 3 (Lecavalier and Tarasov, 2024). .... 27

Figure 1.9: Far-field relative sea-level records demonstrating the LGM sea-level minima and deglacial sea-level history, include meltwater pulse 1a and 1b (MWP-1a/1b). The sea-level proxy data was collected across a variety of sites minimally impacted by isostasy induced by previously glaciated regions (Fairbanks et al., 2005; Yokoyama et al., 2000; Hanebuth et al., 2009 Deschamps et al., 2012). .....32

Figure 2.1: Antarctic Ice Sheet Evolution database version 2 (AntICE2) summary plot. The Antarctic basemap was generated using Quantarctica (Matsuoka et al., 2021)... 103

Figure 2.2: (a) Clustered IMBIE2 ice drainage basins (boundaries between clusters marked by red lines), key cross-section profiles (orange lines), and place names mentioned in the text; (b–f) are the sites with past ice thickness data (paleoH), past ice extent data (paleoExt), ice core borehole temperature profiles (boreTemp), present-day uplift rates (rdotGPS), and past relative sea level data (paleoRSL), respectively. The basemap shown in (a) was generated using Quantarctica (Matsuoka et al., 2021). The surface elevation shown in (b–f) is based on the BedMachine Antarctica version 2 dataset (Morlighem et al., 2020). ..... 105

Figure 2.3: Sample past ice thickness (paleoH) data to illustrate the data quality and tier assignment. The elevation data are converted to ice thickness data using the BedMachine basal topography data. The grey band illustrates the expert-assessed  $2\sigma$  bounds on history at the given site. The blue and red transparent bands represent other C-14 and Be-10 data not assigned to a quality tier. .... 108

Figure 2.4: Sample past ice extent (paleoExt – proximal to the grounding line, PGL; sub-ice-shelf, SIS; open-marine conditions, OMC) data from a marine sediment core to illustrate the data quality and tier assignment. .... 115

Figure 2.5: Sample past relative sea level (paleoRSL) data to illustrate the data quality and tier assignment. The grey band illustrates the expert-assessed  $2\sigma$  bounds on history at the given site. The transparent blue and red bands represent other limiting ages not assigned to a quality tier..... 118

Figure 2.6: Ice core borehole temperature (boreTemp) data to illustrate the data quality and tier assignment. The dashed lines represent the sites in the Siple Coast which are tier-2 data, and the dotted lines represent the most limited borehole temperature data which do not cover the majority of the ice column (tier-3 data)..... 122

Figure 2.7: (a–d) Present-day Antarctic Ice Sheet geometry based on the BedMachine version 2 PD data (Morlighem et al., 2020) and (e–f) MEaSURES ice surface velocity over 2005–2017 and its associated uncertainties (Mouginot et al., 2019). ..... 126

Figure 2.8: Age distribution of AntICE2 paleo-data (paleoExt, paleoH, paleoRSL), with the vertical solid line, dashed lines, and dotted lines representing the mean,  $\pm 1\sigma$ , and  $\pm 2\sigma$  ranges, respectively. The  $1\sigma$  and  $2\sigma$  bounds correspond to the nominal 68% and 95% confidence intervals. The skewed distribution has a median value of 7.4 ka. .... 128

Figure 3.1: a) Antarctic continent and names of locations mentioned in the study are shown alongside the Antarctic Ice sheet Evolution database version 2 (AntICE2) database (symbols), the main Antarctic sectors delineated by the dark red outlines, and key cross section profiles (orange lines). The data ID numbers and ice core names are labelled in Figure S3.1. The Antarctic basemap was generated using Quantarctica (Matsuoka et al., 2021)..... 168

Figure 3.2: The EPICA Dome C deuterium record spanning (a) the time since the last interglacial (LIG), and b) the Last Glacial Maximum (LGM), post-LGM deglaciation (including Meltwater Pulse 1a, MWP1a) and the Holocene. ....171

Figure 3.3: Ice core borehole temperature profile data-model comparison where the grey shading are the full ensemble statistics. The solid and dashed black lines are the mean and min/max ranges for the not-ruled-out-yet (NROY) best fitting AN3sig sub-ensemble. Simulations consisting of a high variance subset (HVSS) of the NROY AN3sig sub-ensemble are shown in red. Site a-h) and n-p) are high quality tier-1 temperature profiles; i-k) are tier-2 profiles since they correlate significantly with the Siple Dome profile; and l-m) are lower quality tier-3 profiles which only partially span the ice column. The  $2\sigma$  and  $1\sigma$  ranges are the nominal 95% and 68% ensemble intervals based on the equivalent Gaussian quantiles, respectively.....200

Figure 3.4: Past ice extent data-model comparison scores for the highest quality tier-1 data in AntICE2. The grey shading represents the min/max,  $1\sigma$  and  $2\sigma$  ranges of the full ensemble. The solid black circles and lines are the mean and min/max ranges for the not-ruled-out-yet (NROY) AN3sig sub-ensemble. Simulations consisting of a high variance subset (HVSS) of the NROY AN3sig sub-ensemble are shown as red circles. The  $2\sigma$  and  $1\sigma$  ranges are the nominal 95% and 68% ensemble intervals based on the equivalent Gaussian quantiles, respectively. The AntICE2 paleoExt data ID are shown in Figure S3.1.....206

Figure 3.5: The mean and  $2\sigma$  range grounded ice extent for the not-ruled-out-yet (NROY) AN3sig sub-ensemble is shown by the black and dashed black line, respectively. It is compared against the RAISED consortium scenario A and B measured and

inferred contours at a) 20 ka, b) 15 ka, c) 10 ka, and d) 5 ka. The  $2\sigma$  ranges are the nominal 95% ensemble intervals based on the equivalent Gaussian quantiles....208

Figure 3.6: Past ice thickness data-model comparison for the highest quality tier-1 exposure data in AntICE2 at its respective elevation. The grey shading represents the min/max, 1 and  $2\sigma$  ranges of the full ensemble. The solid black circles and lines are the mean and min/max ranges for the not-ruled-out-yet (NROY) AN3sig sub-ensemble. Simulations consisting of a high variance subset (HVSS) of the NROY AN3sig sub-ensemble are shown as red circles. The  $2\sigma$  and  $1\sigma$  ranges are the nominal 95% and 68% ensemble intervals based on the equivalent Gaussian quantiles, respectively. The AntICE2 paleoH data ID are shown in Figure S3.1.  
 .....211

Figure 3.7: Present-day ice thickness data-model comparison for the not-ruled-out-yet (NROY) AN3sig sub-ensemble a) mean, b-c) minus and plus  $2\sigma$ , d-e) minus and plus  $2\sigma$ . Three glaciology self-consistent simulations chosen from a NROY high variance subset (HVSS): d) RefSim1; e) RefSim2; f) RefSim3. The  $2\sigma$  ranges are the nominal 95% ensemble intervals based on the equivalent Gaussian quantiles.  
 .....214

Figure 3.8: Present-day surface velocity model-data comparison for the not-ruled-out-yet (NROY) AN3sig sub-ensemble a) mean, b-c) minus and plus  $2\sigma$ , d-e) minus and plus  $2\sigma$ . Three glaciology self-consistent simulations chosen from a NROY high variance subset (HVSS): d) RefSim1; e) RefSim2; f) RefSim3. The  $2\sigma$  ranges are the nominal 95% ensemble intervals based on the equivalent Gaussian quantiles.  
 .....218

Figure 3.9: Antarctic grounded ice volume anomaly through time for the a) full ensemble AN; b) AN4sig sub-ensemble; and c) not-ruled-out-yet (NROY) AN3sig sub-ensemble. A high variance subset (HVSS) of the NROY AN3sig sub-ensemble is shown in grey which also includes three reference simulations (RefSim1, RefSim2, RefSim3) to illustrate glaciologically self-consistent simulation results. The  $2\sigma$  and  $1\sigma$  ranges are the nominal 95% and 68% ensemble intervals based on the equivalent Gaussian quantiles, respectively. ....221

Figure 3.10: The histograms of key metrics are shown for the full ensemble (leftmost column), AN4sig sub-ensemble (middle column), and not-ruled-out-yet (NROY) AN3sig sub-ensemble (rightmost column). The key metrics of interest being a-c) the LIG Antarctic Ice Sheet (AIS) grounded ice volume deficit relative to present day (PD); d-f) the timing of the LIG grounded volume minimum; g-i) the LGM grounded volume excess relative to PD; and j-l) the AIS contribution to MWP-1a. The  $2\sigma$  and  $1\sigma$  ranges are the nominal 95% and 68% ensemble intervals based on the equivalent Gaussian quantiles, respectively. ....222

Figure 3.11: The not-ruled-out-yet (NROY) AN3sig sub-ensemble a) mean and b-c)  $2\sigma$  range are shown during the LIG. Three glaciology self-consistent simulations chosen from a NROY high variance subset (HVSS) are showcased: d) RefSim1; e) RefSim2; f) RefSim3. The  $2\sigma$  ranges are the nominal 95% ensemble intervals based on the equivalent Gaussian quantiles. ....225

Figure 3.12: The not-ruled-out-yet (NROY) AN3sig sub-ensemble a) mean and b-c)  $2\sigma$  range are shown during the LGM. Three glaciology self-consistent simulations chosen from a NROY high variance subset (HVSS) are showcased: d) RefSim1; e)

RefSim2; f) RefSim3. The  $2\sigma$  ranges are the nominal 95% ensemble intervals based on the equivalent Gaussian quantiles. ....227

Figure 3.13: AIS grounded ice volume equivalent sea-level contributions since the LGM for the Weddell Sea (WS), Antarctic Peninsula (AP), Amundsen Sea (AS), Ross Sea (RS), Wilkes – Victoria Land (WVL), Lambert – Amery (LA), Dronning Maud-Enderby Land (DMEL) as defined in Fig. 3.1 during the deglaciation based on the NROY AN3sig sub-ensemble mean. ....230

Figure 4.1: Antarctic continent and sector names mentioned in the study are shown alongside the Antarctic ICe sheet Evolution database version 2 (AntICE2) database (symbols). The data ID numbers for the paleoRSL and GPS data are shown. The remaining data ID information can be found in Figure 2 of Lecavalier et al. (2023). The Antarctic basemap was generated using Quantarctica (Matsuoka et al., 2021). ....263

Figure 4.2: Paleo relative sea level data-model comparison where the grey shading are the full ensemble statistics. The solid and dashed black lines are the mean and min/max ranges for the not-ruled-out-yet (NROY) best fitting sub-ensemble. Simulations consisting of a high variance subset (HVSS) of the NROY sub-ensemble are shown in red. The  $2\sigma$  and  $1\sigma$  ranges are the nominal 95% and 68% ensemble intervals based on the equivalent Gaussian quantiles, respectively. ....268

Figure 4.3: Global Positioning System elastic-corrected rate of bedrock displacement data-model comparison for tier-1/2/3 data in AntICE2. The grey shading represents the min/max,  $1\sigma$  and  $2\sigma$  ranges of the full ensemble. The solid black circles and lines are the mean and min/max ranges for the not-ruled-out-yet (NROY) sub-ensemble.

Simulations consisting of a high variance subset (HVSS) of the NROY sub-ensemble are shown as red circles. The  $2\sigma$  and  $1\sigma$  ranges are the nominal 95% and 68% ensemble intervals based on the equivalent Gaussian quantiles, respectively.  
 .....273

Figure 4.4: The not-ruled-out-yet (NROY) sub-ensemble mean (left), minus  $2\sigma$  (middle), and plus  $2\sigma$  (right) regional Antarctic RSL during the deglaciation at 15 ka (top), 10 ka (middle), and 5 ka (lower). The  $2\sigma$  ranges are the nominal 95% ensemble intervals based on the equivalent Gaussian quantiles. ....278

Figure 4.5: Present-day rate of bedrock displacement for the not-ruled-out-yet (NROY) sub-ensemble a) mean, b-c) minus and plus  $2\sigma$ . Three glaciology self-consistent simulations chosen from a NROY high variance subset (HVSS): d) RefSim1 (NROY member with minimum score across all the data types in AntICE2); e) RefSim4 (NROY member with minimum GPS score); f) RefSim5 (NROY member with joint minimum score across all the paleo data types in AntICE2). The  $2\sigma$  ranges are the nominal 95% ensemble intervals based on the equivalent Gaussian quantiles.  
 .....281

Figure 4.6: Present-day Antarctic rate of geoid displacement for the not-ruled-out-yet (NROY) sub-ensemble a) mean, b-c) minus and plus  $2\sigma$ . The geoid trend presented above only includes the Antarctic contribution to geoid perturbations and does not include global eustatic contributions. Three glaciology self-consistent simulations chosen from a NROY high variance subset (HVSS): d) RefSim1 (NROY member with minimum score across all the data types in AntICE2); e) RefSim4 (NROY member with minimum GPS score); f) RefSim5 (NROY member with joint

minimum score across all the paleo data types in AntICE2). The  $2\sigma$  ranges are the nominal 95% ensemble intervals based on the equivalent Gaussian quantiles....283

Figure 4.7: The (a) minimum and (b) maximum bounds for the PD rate of bedrock displacement for the three reference Antarctic GIA models (IJ05\_R2 - Ivins and James, 2005; W12a - Whitehouse et al., 2012; ICE-6G\_D - Peltier et al., 2015). These three GIA models represent nominal  $2\sigma$  bounds on the PD GIA corrections applied in the IMBIE studies to infer contemporary mass balance of the AIS. (Shepherd et al., 2018; Otosaka et al., 2023). The not-ruled-out-yet (NROY) sub-ensemble  $2\sigma$  (c) lower and (d) upper bounds minus the respective bounds of the three reference GIA models. The differences shown in (c) and (d) demonstrate regions where the three reference GIA models underestimate PD GIA uncertainties or where the NROY sub-ensemble better constrain the regional GIA response relative to the three reference GIA models. ....284

Figure S1.1: Verification & Validation EISMINT experiments conducted after integrating the hybrid ice physics into the GSM. Experiment G consists basal slip throughout the base of the ice. The top row illustrates the ice thickness (left) and basal temperature (right), the grey horizontal line depicts the cross section for the middle frames. The middle row shows the velocity, basal temperature, and elevation profile across the centre of the dome. The bottom row shows the volume (left) and basal melt fraction (right) of the GSM (red) compared to reference ice sheet models (blue) (Payne et al., 2000).....300

Figure S1.2: Verification & Validation EISMINT experiments conducted after integrating the hybrid ice physics into the GSM. Experiment H consists basal slip only where

basal ice reaches the melting point. The top row illustrates the ice thickness (left) and basal temperature (right), the grey horizontal line depicts the cross section for the middle frames. The middle row shows the velocity, basal temperature, and elevation profile across the centre of the dome. The bottom row shows the volume (left) and basal melt fraction (right) of the GSM (red) compared to reference ice sheet models (blue) (Payne et al., 2000). .....301

Figure S1.3: Verification & Validation HEINO experiments conducted after integrating the hybrid ice physics into the GSM. The HEINO experiment shown here consists of an idealized North America domain with a square Hudson Bay (Calov et al., 2010) with basal sliding always on. The top row illustrates the ice thickness (left) and basal temperature (right), the grey horizontal line depicts the cross section for the bottom frames. The middle row shows the surface velocity (left) and basal drag coefficient (right) in the u-direction. The bottom row shows the average velocity, basal temperature, and elevation profile across the centre of the domain.....302

Figure S1.4: Verification & Validation HEINO experiments conducted after integrating the hybrid ice physics into the GSM. The HEINO experiment shown here consists of an idealized North America domain with a square Hudson Bay (Calov et al., 2010) with basal sliding always on. The top row illustrates the basal temperature (left) and basal melt (right). The middle row shows the temperature-dependent flow coefficient (left) and Arrhenius coefficient (right). The bottom row shows the shallow ice approximation heating term (left) and basal shear stress heating term (right).....303

Figure S1.5: Verification & Validation HEINO experiments conducted after integrating the hybrid ice physics into the GSM. The HEINO experiment shown here consists of an idealized North America domain with a square Hudson Bay (Calov et al., 2010) with basal sliding occurring wherever the base reaches the pressure melting point. The top row illustrates the ice thickness (left) and basal temperature (right), the grey horizontal line depicts the cross section for the bottom frames. The middle row shows the surface velocity (left) and basal drag coefficient (right) in the u-direction. The bottom row shows the average velocity, basal temperature, and elevation profile across the centre of the domain. ....304

Figure S1.6: Verification & Validation HEINO experiments conducted after integrating the hybrid ice physics into the GSM. The HEINO experiment shown here consists of an idealized North America domain with a square Hudson Bay (Calov et al., 2010) with basal sliding occurring wherever the base reaches the pressure melting point. The top row illustrates the basal temperature (left) and basal melt (right). The middle row shows the temperature-dependent flow coefficient (left) and Arrhenius coefficient (right). The bottom row shows the shallow ice approximation heating term (left) and basal shear stress heating term (right).....306

Figure S1.7: The fully unloaded glacial isostatic equilibrium sea-level thresholds range between -300 to -100 m due to significant uncertainties in dynamic topography on timescales of ~35 Myr. These elevation thresholds are regional chosen to delineate deep subglacial troughs and regions where PD surface ice moves at >400 m/yr since this indicates loose basal till.....306

Figure S1.8: Ice rises (orange) and ice rumples (green) across the present-day Antarctic ice sheet. Ice rises and rumples are frequently below the model grid resolution and can buttress back ice. Therefore, it is important to resolve these key features that can have a significant impact on ice dynamics. The Antarctic basemap was generated using Quantarctica (Matsuoka et al., 2021). .....307

Figure S1.9: The method by which the raw basal topography is upscaled to the model grid resolution can emphasize or de-emphasize certain subgrid pinning points. This is due to the pinning point scale, geometry, relative position and orientation of the model grid. Subgrid pinning points have persisted throughout several glaciations and therefore should be represented by hard bedrock basal features. This is achieved by using a subgrid enhancement exponent ranging between 1 to 12 that is regionally varied to enhance specific key PD subgrid hard bedrock features which would otherwise be neglected by the upscaling procedure. ....308

Figure S2.1: Past ice thickness (paleoH) entire tier-2/3 dataset. ....316

Figure S2.2: Past ice extent (paleoExt) summary tier-1/2 dataset. ....317

Figure S2.3: Past ice extent (paleoExt) entire tier-1/2 dataset. ....323

Figure S2.4: Past sea level (paleoRSL) entire tier-1/2 dataset. ....324

Figure S2.5: Present-day GPS uplift rate (rdotGPS) of the tier-1 (orange circle) and tier-2 (blue circles) data. ....325

Figure S3.1: AntICE2 observational constraint database used to history match the Glacial Systems Model. a - f) are the site locations and identification numbers for past ice thickness data (paleoH), past ice extent data (paleoExt), ice core borehole

temperature profiles (ICbore) and names, present-day uplift rates (rdotGPS), and past relative sea level data (paleoRSL) respectively.....326

Figure S3.2: Diagram summarizing major components of the Glacial Systems Model (GSM). .....327

Figure S3.3: Distribution of output scores and metrics for the full ensemble (blue), not-ruled-out-yet (NROY) AN3sig sub-ensemble (orange), and NROY sub-ensemble high variance subset (red). The individual model scores are defined in Table S1. The present-day (PD) metrics shown are the PD grounded ice volume (volg0), PD floating ice volume (volf0), PD West AIS grounded ice volume (volgWAIS), and PD East AIS grounded ice volume (volgEAIS). .....328

Figure S3.4: Distribution of output metrics, scores, and ensemble parameters (detailed in Table 3.1) for the full ensemble (blue), not-ruled-out-yet (NROY) AN3sig sub-ensemble (orange), and NROY sub-ensemble high variance subset (red). The present-day (PD) metrics shown are PD grounded ice area (arg0), PD floating ice area (arf0), PD West AIS grounded ice area (argWAIS), and PD East AIS grounded ice area (argEAIS). The LGM metrics shown are the 20 ka grounded ice volume (volg20), 20 ka grounded ice volume excess relative to present (volg20diff), 20 ka grounded ice area (arg20), 20 ka grounded ice area excess relative to present (arg20diff). The Meltwater Pulse 1a (MWP1a) metric is the grounded ice volume change over the MWP1 interval (volgMWP1a). The last interglacial (LIG) metrics are the timing of the LIG AIS minimum (timeLIGmin), LIG grounded ice volume deficit relative to present (volgLIGdiff/v121dfG), and LIG grounded ice area deficit relative to present (argLIGdiff). .....329

Figure S3.5: Distribution of ensemble parameters (detailed in Table 3.1) for the full ensemble (blue), not-ruled-out-yet (NROY) AN3sig sub-ensemble (orange), and NROY sub-ensemble high variance subset (red). .....331

Figure S3.6: Distribution of ensemble parameters (detailed in Table 3.1) for the full ensemble (blue), not-ruled-out-yet (NROY) AN3sig sub-ensemble (orange), and NROY sub-ensemble high variance subset (red). .....332

Figure S3.7: Distribution of ensemble parameters (detailed in Table 3.1) for the full ensemble (blue), not-ruled-out-yet (NROY) AN3sig sub-ensemble (orange), and NROY sub-ensemble high variance subset (red). .....332

Figure S3.8: Diagram illustrating the history-matching analysis methodology. ....333

Figure S3.9: High variance subset (HVSS; N=18) of simulations in the not-ruled-out-yet (NROY) AN3sig sub-ensemble. ....335

Figure S3.10: Metric/score-parameter correlation heat map of not-ruled-out-yet (NROY) AN3sig sub-ensemble. The ensemble parameters are defined in Table 3.1, the individual model scores are defined in Table S3.1. The present-day (PD) metrics shown are the PD grounded ice volume (volg0), PD floating ice volume (volf0), PD West AIS grounded ice volume (volgWAIS), PD East AIS grounded ice volume (volgEAIS), PD grounded ice area (arg0), PD floating ice area (arf0), PD West AIS grounded ice area (argWAIS), and PD East AIS grounded ice area (argEAIS). The LGM metrics shown are the 20 ka grounded ice volume (volg20), 20 ka grounded ice volume excess relative to present (volg20diff), 20 ka grounded ice area (arg20), 20 ka grounded ice area excess relative to present (arg20diff). The Meltwater Pulse 1a (MWP1a) metric is the grounded ice volume change over the MWP1 interval

(volgMWP1a). The last interglacial (LIG) metrics are the timing of the LIG AIS minimum (timeLIGmin), LIG grounded ice volume deficit relative to present (volgLIGdiff), and LIG grounded ice area deficit relative to present (argLIGdiff).  
 .....336

Figure S3.11: NROY AN3sig sub-ensemble deglacial ice thickness difference for the interval of a-c) 16-14 ka d-f) 14-12 ka g-i) 12-10 ka j-l) 10-8 ka and their respective grounding lines for the ensemble mean (leftmost column),  $-2\sigma$  bound (center column), and  $+2\sigma$  bound (rightmost column). .....337

Figure S3.12: NROY AN3sig sub-ensemble deglacial ice thickness difference for the interval of a-c) 8-6 ka d-f) 6-4 ka g-i) 4-2 ka j-l) 2-0 ka and their respective grounding lines for the ensemble mean (leftmost column),  $-2\sigma$  bound (center column), and  $+2\sigma$  bound (rightmost column). .....338

Figure S4.1: Paleo relative sea level data-model comparison of the not-ruled-out-yet (NROY) sub-ensemble high variance subset. A sensitivity analysis was performed on the NROY HVSS based on their respective reference Earth (RefEarth) model with a progressively lower upper mantle viscosity (UMV) and thinner lithospheric thickness (LT) to investigate the impact of lateral Earth structure. The LT and UMV experiments range from 146 to 46 km and  $5 \cdot 10^{21}$  to  $0.005 \cdot 10^{21}$  Pa·s, respectively.  
 .....339

Figure S4.2: Global Positioning System elastic-corrected rate of bedrock displacement data-model comparison of the not-ruled-out-yet (NROY) sub-ensemble high variance subset. A sensitivity analysis was performed on the NROY HVSS based on their respective reference Earth (RefEarth) model with a progressively lower

upper mantle viscosity (UMV) and thinner lithospheric thickness (LT) to investigate the impact of lateral Earth structure. The LT and UMV experiments range from 146 to 46 km and  $5 \cdot 10^{21}$  to  $0.005 \cdot 10^{21}$  Pa·s, respectively. ....346

Figure S4.3: The not-ruled-out-yet (NROY) sub-ensemble mean (left), min (middle), and max (right) regional Antarctic RSL during the deglaciation at 15 ka (top), 10 ka (middle), and 5 ka (lower).....341

Figure S4.4: Present-day rate of bedrock displacement for the not-ruled-out-yet (NROY) sub-ensemble a) mean, b-c) minimum and maximum. ....342

Figure S4.5: Present-day Antarctic rate of geoid displacement for the not-ruled-out-yet (NROY) sub-ensemble a) mean, b-c) minimum and maximum. ....342

Figure S4.6: The (a) minimum and (b) maximum bounds for the PD rate of bedrock displacement for the three reference Antarctic GIA models (IJ05\_R2 - Ivins and James, 2005; W12a - Whitehouse et al., 2012; ICE-6G\_D - Peltier et al., 2015). These three GIA models represent nominal  $2\sigma$  bounds on the PD GIA corrections applied in the IMBIE studies to infer contemporary mass balance of the AIS. (Shepherd et al., 2018; Otosaka et al., 2023). The not-ruled-out-yet (NROY) sub-ensemble (c) minimum and (d) maximum minus the respective bounds of the three reference GIA models. The differences shown in (c) and (d) demonstrate regions where the three reference GIA models underestimate PD GIA uncertainties or where the NROY sub-ensemble better constrain the regional GIA response relative to the three reference GIA models. ....343

# Abbreviations

## Ice sheets

- AIS Antarctic ice sheet  
EAIS East Antarctic ice sheet  
EIC Eurasian ice complex  
GrIS Greenland ice sheet  
NAIC North American ice complex  
WAIS West Antarctic ice sheet

## Ice sheet related

- GL Grounding line  
SSM Sub-ice-shelf melt

## Sea level

- GIA glacial isostatic adjustment  
GMSL global mean sea level  
mESL metres equivalent sea level  
MWP melt water pulse  
RSL relative sea level

## Temporal

- BP before present

ka thousand years before present

kyr thousand years

LIG last interglacial

LGM Last Glacial Maximum

PD present-day

yr years

### Mechanisms

MICI Marine Ice Cliff Instability

MISI Marine Ice Sheet Instability

### Other

AntICEdat Antarctic ICE sheet Evolution database

AntICE2 Antarctic ICE sheet database version 2

BANNs Bayesian Artificial Neural Networks

DATED Digital Atlas of the Eurasian Deglaciation

ECCO Estimating the Circulation and Climate of the Ocean

GSM Glacial Systems Model

HMA History-Matching Analysis

IPCC Intergovernmental Panel on Climate Change

MCMC Markov Chain Monte Carlo

NROY Not-ruled-out-yet

PMIP Paleoclimate Modelling Intercomparison Project

PREM      preliminary reference Earth model  
RAISED    Reconstruction of AIS Deglaciation

# Chapter 1: Introduction

## 1.1 Motivation

The Antarctic Ice Sheet (AIS) is an important component of the global climate system and has been identified as a major source of uncertainty to future sea level change (Meredith et al., 2019; Masson-Delmotte et al., 2021). Studying the past evolution of the Antarctic ice sheet allows us to better understand the role Antarctica plays in the global climate system, to better interpret observed contemporaneous ice sheet changes, and to better predict its future behaviour. This is primarily achieved using model simulations that reconstruct the past evolution of the Antarctic ice sheet. To interpret model reconstructions with any degree of confidence, meaningful uncertainty estimates should be attributed to properly assess the sensitivity of the ice sheet. This remains ever relevant in an age where ice sheet instabilities could potentially contribute metres to global sea level change over the next couple of centuries (Rignot et al., 2014; DeConto and Pollard, 2016; Pattyn and Morlighem, 2020).

Glaciological modelling is an effective tool to generate continental-scale reconstructions over glacial cycles. The caveat inherent to all computer models is that they represent an imperfect surrogate of reality. The modelled system includes approximations for physical processes, missing physics, poorly represented sub-grid processes, uncertain initial and boundary conditions, and resolution limitations. Parameterizations are typically used to partially address these considerable model limitations, some of these

parameterizations include tunable parameters. Each set of parameter values corresponds to an ice sheet simulation. Past studies that modelled the AIS have relied upon a limited exploration of the ensemble parameter space (Denton and Hughes, 2002; Huybrechts, 2002; Pollard and DeConto, 2009a; Golledge et al., 2014; Pollard et al., 2016; DeConto and Pollard, 2016); moreover, even fewer studies leverage the available observations to constrain their reconstructions (Whitehouse et al., 2012; Albrecht et al., 2020a, b; Pittard et al., 2022). Large ensemble analysis techniques to explore the parameter-space of models configured for the AIS have been conducted to a limited capacity with outstanding and persistent data-model discrepancies (Briggs et al., 2014; Albrecht et al., 2020b) and this study aims to rectify this.

This research aims to provide a data-driven state-space estimation of past AIS changes by compiling, calibrating, and standardizing a comprehensive observational constraint database. Moreover, using said database, the goal is to constrain a large ensemble of model simulations on the past evolution of the AIS, with a comparatively high degree of confidence that simulations consistent with the observations capture reality. I aim to answer several outstanding questions about the AIS during key periods of interest: the past warm climate of the last interglacial (LIG); peak glaciation of the Last Glacial Maximum (LGM); the deglacial meltwater pulses (MWP); and the influence of past uncertainties on the interpretation of the present-day (PD) AIS. This is achieved by completing a history-matching (HM) analysis of the AIS since the LIG.

To provide context on this study for past ice sheet evolution, the introduction has the following structure: Section 1.2 details the current state of the AIS; Section 1.3 covers how an ice sheet changes; Section 1.4 provides an overview of the period of study; Section

1.5 formalizes the key research questions of this thesis; Section 1.6 discusses past studies that have explored the subject; Section 1.7 summarizes the numerical model applied in this research; and Section 1.8 includes a primer on the history-matching analysis methodology. The introduction provides necessary background for the manuscript-based Chapter 2, 3, and 4 that detail the observational constraint database and history-matching analysis of the AIS.

## 1.2 Present day Antarctic ice sheet

The community's understanding of the AIS is based on observations collected during the past three decades through remote sensing and field-based campaigns (e.g. Bentley et al., 2014; Mouginot et al., 2019). Therefore, our overall knowledge of the system is founded on the PD state of the ice sheet. Considerable research is motivated by the apparent relevance of processes responsible for PD ice sheet changes. Paleo-constraints of the ice sheet are spatially and temporally sparse, while the PD ice sheet geometry and velocities effectively provide complete 2D spatial coverage for only a single period. Model simulations use initial and boundary conditions based on a variety of PD inferences. Additionally, many PD metrics and inferences are directly used to constrain the model reconstructions. This section highlights our current understanding of the PD AIS: its role in the climate system; Antarctic metrics; the influence of the past towards our assessment of contemporary mass balance; the challenges in defining crucial boundary conditions; and delineating the processes responsible for ice sheet evolution and instabilities. For reference, a map of Antarctic and named places found in the text are shown in Figure 1.1.

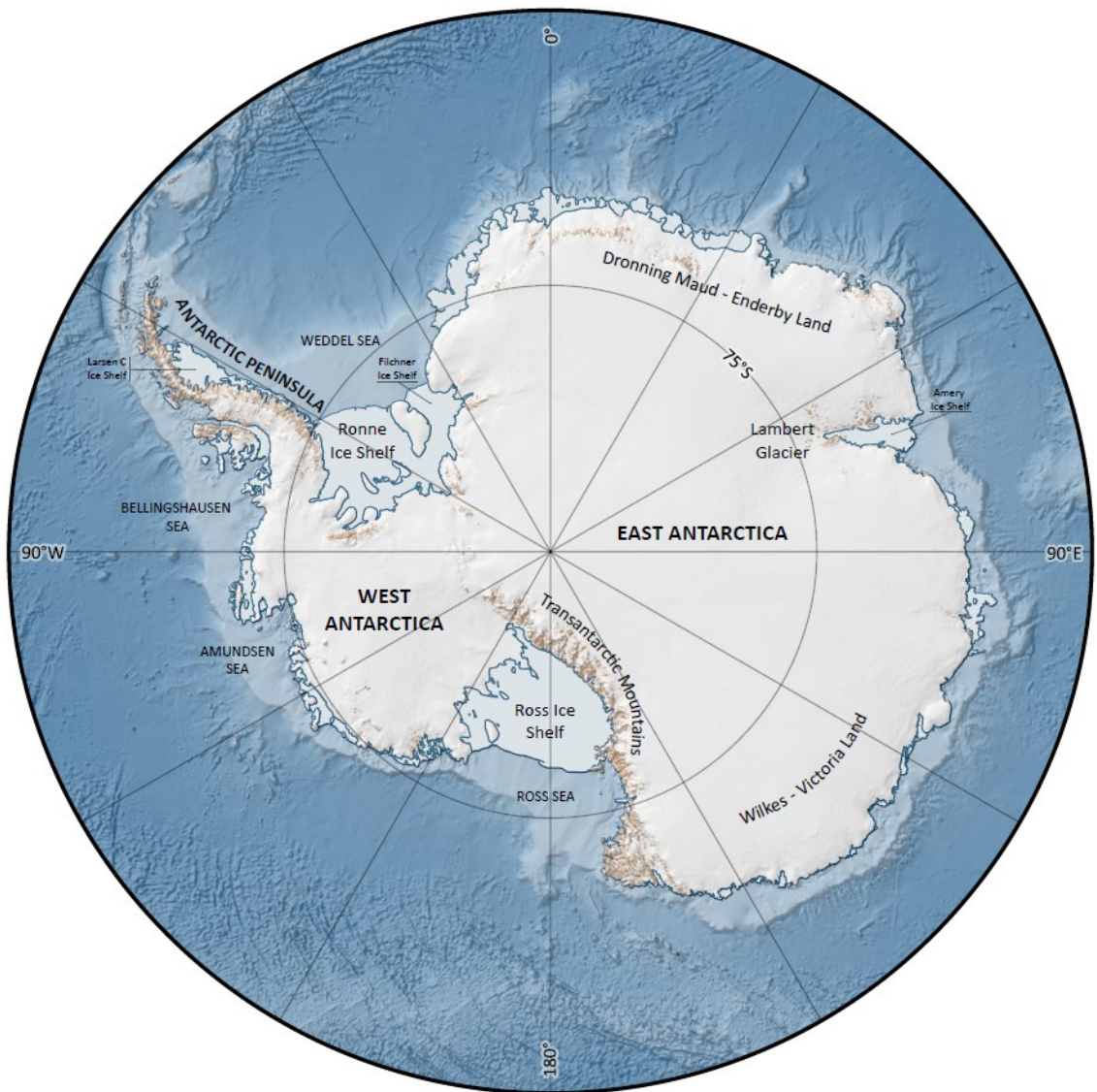


Figure 1.1: Antarctica and named places in the document. The dark blue contour denotes the position of the present-day grounding line and ice shelf extent. The Antarctic basemap was generated using Quantarctica (Matsuoka et al., 2021).

The AIS is interwoven with the climate system through several processes (Vaughan et al., 2013): (1) planetary surface energy budget through the contrast in albedo between snow/ice and water/land; (2) atmosphere/ocean circulation considering the AIS is a major topographical feature; (3) ocean-atmosphere gas exchange given the AIS is surrounded by the southern ocean which is a major source for CO<sub>2</sub> outgassing; (4) the role of the AIS in

Antarctic bottom water formation; and (5) sea level change from the redistribution of grounded-ice to the oceans. The processes and feedbacks between the AIS and the broader Earth system operate on a broad range of timescales with the slowest response time of the AIS on the order of 100 kyr. This implies that the PD ice sheet is actively responding to past changes.

At present, the AIS covers 8.3% of the global land surface ( $12.25 \times 10^6 \text{ km}^2$ ) with a volume of  $57.9 \pm 0.9$  meters of ice-equivalent sea level (mESL) (Morlighem et al., 2020). Satellite, airborne and in situ observations provide a method of quantifying the state of the PD AIS (e.g. transition from grounded to floating ice - grounding line position). To infer a total grounded ice volume, the ice thickness of the ice sheet is derived using the differential between the surface and the basal topography wherever ice is grounded on land (Figure 1.2). The land beneath the ice is most effectively inferred using ground penetrating radar observations interpolated via a mass conservation scheme (Morlighem et al., 2020).

The internal thermal structure of the AIS remains poorly constrained with only a few borehole temperature records available (see Chapter 2). The temperature of the ice has an long memory due to the properties of ice and the various thermodynamic forcings from the atmosphere, ocean, and solid Earth (Ackert, 2003). Moreover, the viscosity of ice depends on temperature, meaning uncertainties on the thermal structure of the ice sheet impacts past, present and future ice dynamics. The method by which ice sheet models initialize and spin up their internal thermal structure can manifest in drastically different model behaviour and future predictions (Seroussi et al., 2019).

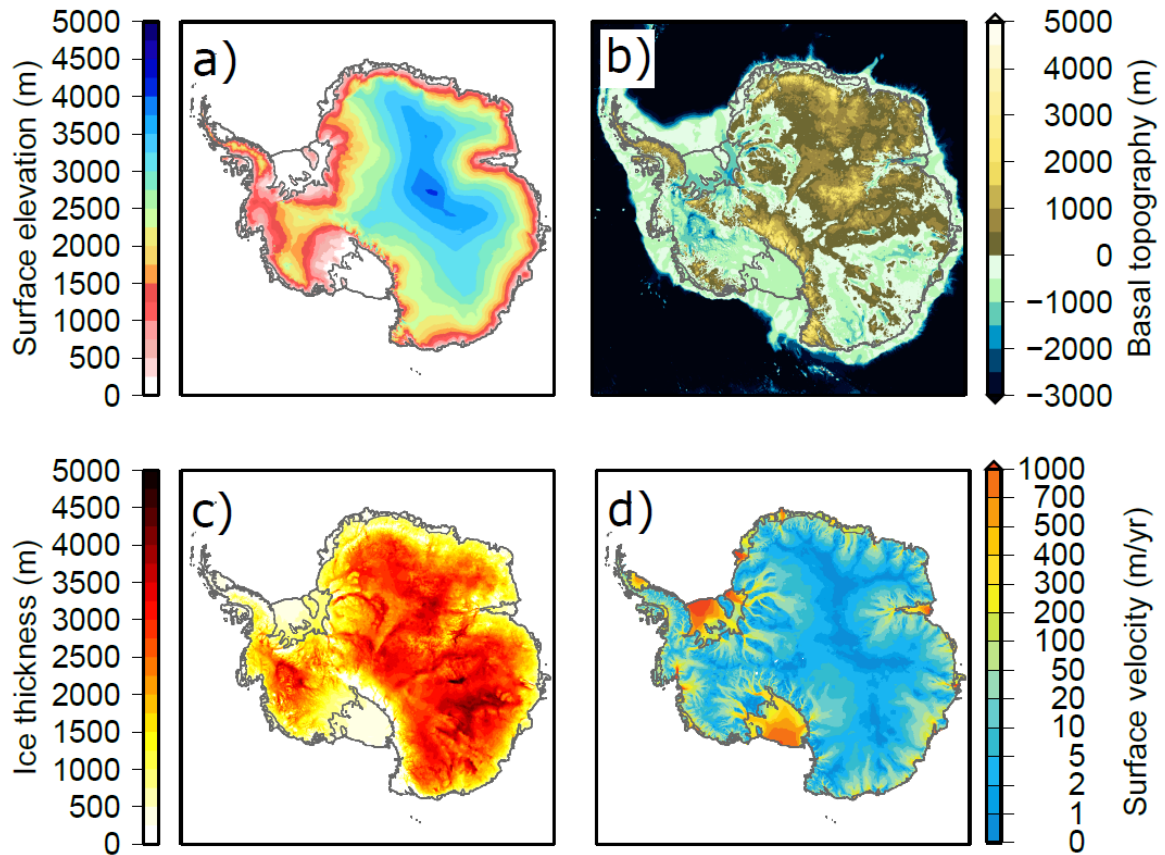


Figure 1.2: Present day Antarctic ice sheet boundary conditions – Antarctic BedMachine Version 2 a) Surface, b) Basal topography, c) ice thickness (Morlighem et al., 2020), and d) MEaSUREs surface velocity (Mouginot et al., 2019).

The mass balance of the PD ice sheet is inferred using a variety of methods (Shepherd et al., 2018; Otosaka et al., 2023). Repeated satellite altimetry measurements (e.g. ICESat) track temporal changes in the surface of the ice sheet (Helm, Humbert and Miller, 2014). However, converting a change of volume to that of mass requires several assumptions on the superficial snow and firn density structure across Antarctica. An alternate method involves satellite measurements of the Earth’s gravitational field over time (GRACE), which directly measures changes in mass across the Antarctic region (King et al., 2012; Shepherd et al., 2018). Unfortunately, measuring the total mass change over a region implies that many signals such as continental hydrology and ocean circulation are

integrated over the region. Another method is to isolate the elastic response of crustal deformation by performing repeated GPS measurements to acquire uplift rates and thereby rates of ice loss (Sasgen et al., 2017; Martín-Español et al., 2016). This comes with its own series of assumptions, specifically the tectonic setting and Earth rheology. Finally, also commonly used is an input-output mass budget method which determines the net surface balance over Antarctica minus the discharge at the perimeter of the grounded ice sheet (Rignot et al., 2019). Uncertainties in the basal topography/ice thickness/velocity data propagate directly to the mass balance estimates. All these methods infer PD mass balance estimates of the ice sheet using independent methodologies with their respective assumptions/limitations. Given the uncertainties in each mass balance assessment method, a major community goal of the IMBIE team was to find consensus across the various inferences (Shepherd et al., 2018).

A common requirement towards inferring continental ice sheet mass balance is the background glacial isostatic adjustment (GIA) signal – the displacement of the crust due to past changes in ice load over centennial to millennial timescales. The geodetic and GRACE remote sensing data must correct for processes that affect the displacement of the solid Earth (basal topography) due to GIA (Shepherd et al., 2012; Velicogna, Sutterley and Broeke, 2014). The GIA signal accounts for the viscoelastic relaxation of the solid Earth due to a redistribution of mass (e.g. ice, water, mantle material) (Whitehouse et al., 2019; Whitehouse, 2018). In the case of Antarctica, previous studies have found that the GIA signal is similar in magnitude to the mass balance signal (Riva et al., 2009; Velicogna, 2009). Considering the viscous response of the solid Earth due to a changing ice sheet is on the time scale of thousands of years, estimates of contemporary mass balance of the AIS

is directly dependent on our ability to accurately simulate past ice sheet evolution and infer the Earth rheology with robust confidence intervals. For more information on GIA the reader is directed to Whitehouse 2018) and Whitehouse et al. (2019) and a discussion on the uncertainties in estimating GIA is found in Chapter 4.

The AIS mass balance as inferred from the aforementioned methodologies are  $-109 \pm 56$  Gt/yr from 1992 to 2020, totalling  $21.0 \pm 1.9$  mm of sea level rise (Otosaka et al., 2023). Nevertheless, these estimates inadequately address uncertainties in past ice sheet changes and earth structure when correcting for GIA (Otosaka et al., 2023). The WAIS is losing mass at an increasing rate while EAIS is gaining mass or near equilibrium. Therefore, quantifying uncertainties on past ice sheet changes will increase confidence in our estimates of contemporary mass balance since it remains a primary source of uncertainty in the analysis (Pattyn and Morlighem, 2020; Otosaka et al., 2023). Ice sheet evolution is driven by the climate, therefore, past ice sheet growth and decay in response to climate change contextualizes PD ice sheet changes. The present-day state of the ice sheet is the primary initial condition used, along side climate scenarios, when forecasting future ice sheet changes and sea-level contributions. Therefore, getting the past right in terms of defining clear confidence intervals is key to better predicting future ice sheet changes.

### 1.3 Antarctic ice sheet evolution

To predict past, present or future ice sheet changes, it is important to understand: how ice sheets persist on the Earth's surface; what forcings and processes drive ice sheet changes; how thermomechanical ice characteristics manifest in distinct ice sheet features

and flow regimes; and which processes and feedbacks can regionally stabilize or destabilize an ice sheet. The following section aims to provide necessary context to understand how an ice sheet responds to change through interactions with the atmosphere, ocean, and solid Earth and which aspects need to be adequately represented in an ice sheet model to study millennial-scale changes.

### 1.3.1 Ice sheet formation

The Earth surface temperature fluctuates across the triple point of water – the point where the liquid, solid, and gaseous state of water molecules can exist together in thermodynamic equilibrium at 273.16 K for atmospheric pressure. Over a given year, half of the Earth’s land surface experiences temperatures below the triple point of water. In areas where snow accumulates and persists year after year, ice forms and given favourable climatic conditions can eventually nucleate a glacier, ice cap, or ice sheet over millennia. Hence an ice sheet is often referred to as “frozen atmosphere” and is the product of the thermodynamic properties of water and ice with its high specific enthalpy and heat capacity.

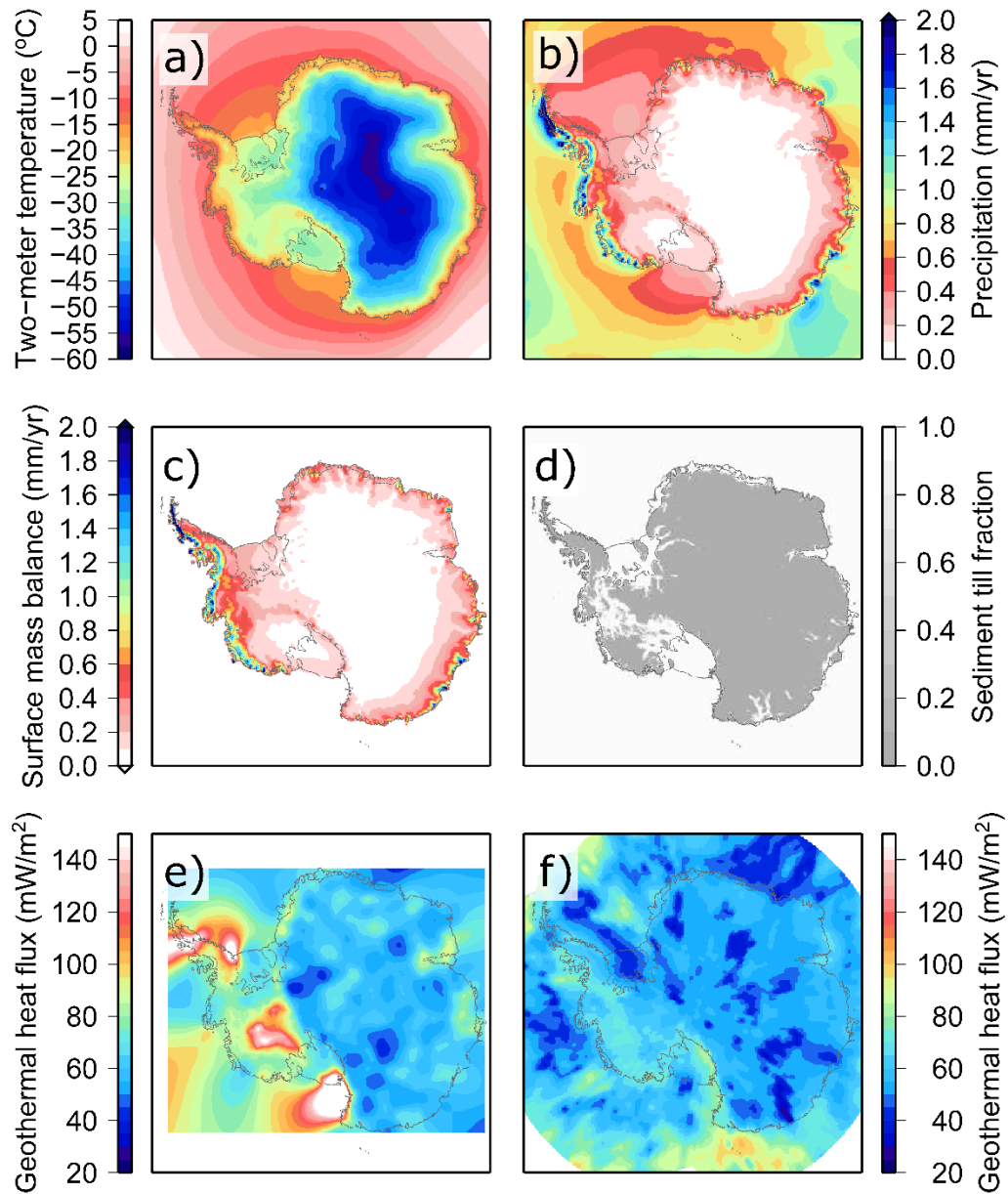


Figure 1.3: Boundary conditions for the a-c) PD monthly climatologies (RACMO 2.3p2; Melchior Van Wessem et al., 2018). Basal boundary conditions such as the d) basal till fraction beneath the Antarctic ice sheet and the geothermal heat flux field based on e) magnetic data (Martos et al., 2017) and f) seismic data (An et al., 2015).

An ice sheet is the manifestation of favourable climatic conditions where ice accumulates, thereby owing its existence to external forcings. In terms of climate forcing,

there are atmospheric, oceanic, and radiative forcings. The former primarily consists of surface temperatures and precipitation (Melchior Van Wessem et al., 2018), where an increase in temperature will increase surface melt and the moisture bearing capacity of air, thus accumulation (Figure 1.3). Radiative forcing is the radiant energy balance at the surface which can impact surface temperatures. Oceanic forcing is predominantly ocean temperatures, where warm waters directly melt marine-terminating glacier fronts (Jacobs et al., 2011), propagate into ice shelf cavities leading to sub-shelf melt (SSM), and melt at the GL (Holland et al., 2008; Pritchard et al., 2012). In the ice shelf cavity, salinity changes from SSM or subglacial discharge can produce buoyancy driven convection which can in turn impact SSM. On longer time-scales, there is sea-level forcing from the growth and retreat of major continental ice sheets (Lambeck et al., 2014). At the base of the ice sheet, the geothermal heat flux (GHF) warms the basal ice with some regions reaching the ice pressure melting point with major consequences on ice dynamics. The GHF beneath the ice sheet is reconstructed using seismic (An et al., 2015) and magnetic (Martos et al., 2017) data inference methodologies (Figure 1.3). The methods by which the climate forcing is reconstructed back in time is discussed in Section 1.4.1, Section 1.7.2, and Chapter 3.

## 1.3.2 Ice dynamics

As the ice sheet is climatically forced, the resulting stress imbalance leads to a dynamic ice sheet response. As the ice undergoes gravitationally driven deformation, it can slide over the underlying bedrock and/or sediment. If basal ice is at the pressure melting point, melt water can lubricate the ice-bed interface and allow for faster flowing ice through the interplay of basal water pressure and basal friction (Zwally et al., 2002; Cuffey and

Paterson, 2013). Therefore, basal meltwater is critical in modulating flow (Schoof, 2010; Sundal et al., 2011; Shannon et al., 2013). Delineating the regions at the bed where ice rests atop sediment or hard bedrock can be physically constrained and inferred based on a variety of methods (Studinger et al., 2001; Pollard and Deconto, 2012a; Yu et al., 2017; Albrecht et al., 2020a). In this research we opt for the following criteria: 1) a fully rebounded bedrock and dynamic topography sea-level threshold, 2) flow regime thresholds, and 3) the persistence of pinning points and subglacial features surviving recurrent glacial cycles (Figure 1.3; Section 1.7.1.6). Additional information pertaining to the till fraction sediment distribution can be found in Chapter 3. Unfortunately, conditions at the bed are poorly characterized across Antarctica with limited direct observations, resulting in a significant source of uncertainty in any modelling study.

Ice dynamics is physically represented by the Stokes equation with ice flow classified in three main regimes. Large parts of the ice sheet interior experience sheet flow represented by the zeroth-order shallow-ice approximation (SIA) where the driving stress is balanced by basal drag. Assuming horizontal length scales are much greater than the height scale, many terms in the Stokes equation become negligibly small. Therefore, the ice flow is dominated by vertical shear stress. The second and third flow regime, stream and shelf flow, are represented by the shallow shelf approximation (SSA) where the driving stress is balanced by horizontal shear stress gradients, compressional and tensile stress gradients. There are many similarities between stream flow and shelf flow; the exceptions are the presence of basal drag and topographical boundary conditions for stream flow. The hybrid implementation of these approximations (SIA-SSA equations) is a common and

computationally efficient scheme for representing warm and cold-based ice, ice streams, and ice shelves (Winkelmann et al., 2011; Pollard and Deconto, 2012b; Pattyn, 2017).

The constitutive equation for ice is Glen's flow law, which relates stresses of the ice to their strain rates (i.e. velocities). This represents the non-linear viscous flow of ice. The viscosity of ice strongly depends on the temperature of the ice through the Arrhenius equation (Cuffey and Paterson, 2013). The thermodynamics of the ice are generally characterized by boundary forcings, vertical heat diffusion through the ice, horizontal ice advection, internal and basal frictional heating. The frictional heating depends on ice dynamics (i.e. strain rates) and the viscosity depends on temperature, hence an ice sheet is a fully coupled thermo-mechanical system.

### 1.3.3 Ice shelves

Ice shelves can buttress and restrain flow of grounded ice and of surrounding outlet glaciers (Scambos et al., 2004; Hulbe et al., 2008; Shepherd et al., 2010; Fricker and Padman, 2012). A reduction of ice-shelves in the Antarctic Peninsula have been followed by increase rates of ice loss and thinning of surrounding outlet glaciers and ice streams (Pritchard et al., 2012). Therefore, it is crucial that the long-term evolution of ice shelves is adequately represented in model simulations.

On decadal time scales, over 90% of recent mass loss across the ice sheet has been driven by ice dynamics where ice is discharged through the GL into ice shelves and floating ice tongues which subsequently undergo negative mass balance (Bindschadler, Vaughan and Vornberger, 2011). For ice shelves, the rate of submarine melting varies greatly and is proportional to ocean thermal forcing and water flow speed at the ice-ocean boundary

(Holland and Jenkins, 1999; Motyka et al., 2003). Conversely, ice calving from ice shelves and marine terminating glaciers is important to simulate mass balance, though a broad range of spatial scales and processes initiate calving from tides, seasonal processes, ocean swells, or the gradual propagation of stress fractures (Scambos et al., 2000; Benn, Warren and Mottram, 2007; Brunt, Okal and Macayeal, 2011). With the latter of these processes being directly coupled to atmospheric forcing such as through the drainage of surface melt into crevasses leading to hydrofracturing, culminating in calving (Nick et al., 2010; Pollard et al., 2015b). Notably, unrestrained floating ice which does not contribute to buttressing has no impact on upstream ice dynamics when calved (Fürst et al., 2016).

Rapid ice sheet changes are driven by rapid dynamic processes on decadal time scales. A number of observations suggest that rapid ice sheet changes in ice shelves and glaciers on the Antarctic Peninsula that are often classified as irreversible. A prime example of rapid ice sheet changes is the collapse of the Larsen B Ice Shelf which resulted in a dynamic acceleration of tributary glaciers by up to 800% (Rignot et al., 2004; Scambos et al., 2004; Rott et al., 2011). The Larsen B ice shelf collapsed in response to a number of forcings and processes: (1) longitudinal stresses gradients across the ice shelf opened up a number of surface and basal crevasse; (2) warm waters gradually thinned the ice shelf through SSM; (3) atmospheric temperatures were sufficiently high for surface melt ponds to form and drain into crevasses, adding to the total longitudinal stress gradient, propagating the crevasses deeper through hydrofracturing until calving/disintegration of the ice shelf (Scambos et al., 2004; Nick et al., 2010).

### 1.3.4 Sub-ice-shelf mass balance

Studies on ice sheets grounded below sea level propose regions of marine-based ice are susceptible to rapid ice mass loss (Schoof, 2007; Holland et al., 2008; Joughin and Alley, 2011; Ross et al., 2012; Rignot et al., 2014; Joughin et al., 2014; Li et al., 2015). The ocean interacts with the ice sheet by delivering water with its high heat capacity to the ice sheet margins (cavities beneath ice shelves, calving front) (Jenkins and Doake, 1991; Jacobs et al., 2011; Pritchard et al., 2012; Paolo et al., 2015). At the ice-ocean interface warm waters melt and undercut the ice front, increasing calving rates, loss of pinning points thereby causing retreat, speed-up and thinning (Benn et al., 2007; Paolo et al., 2015). The heat delivered by the ocean depends on the water temperature and salinity, the bathymetry, and ocean circulation. Unfortunately, in most instances little is known about these conditions around Antarctica in the past, particular beneath the ice shelves. This is further complicated by uncertainties in the geometry of the ice shelf base, water properties and circulation in the ice shelf cavity, and the mixing of water masses inside and outside the cavity (Colloni et al., 2018). Considering that SSM can lead to rapid retreat of marine based ice, it remains a significant source of uncertainty when modelling the AIS.

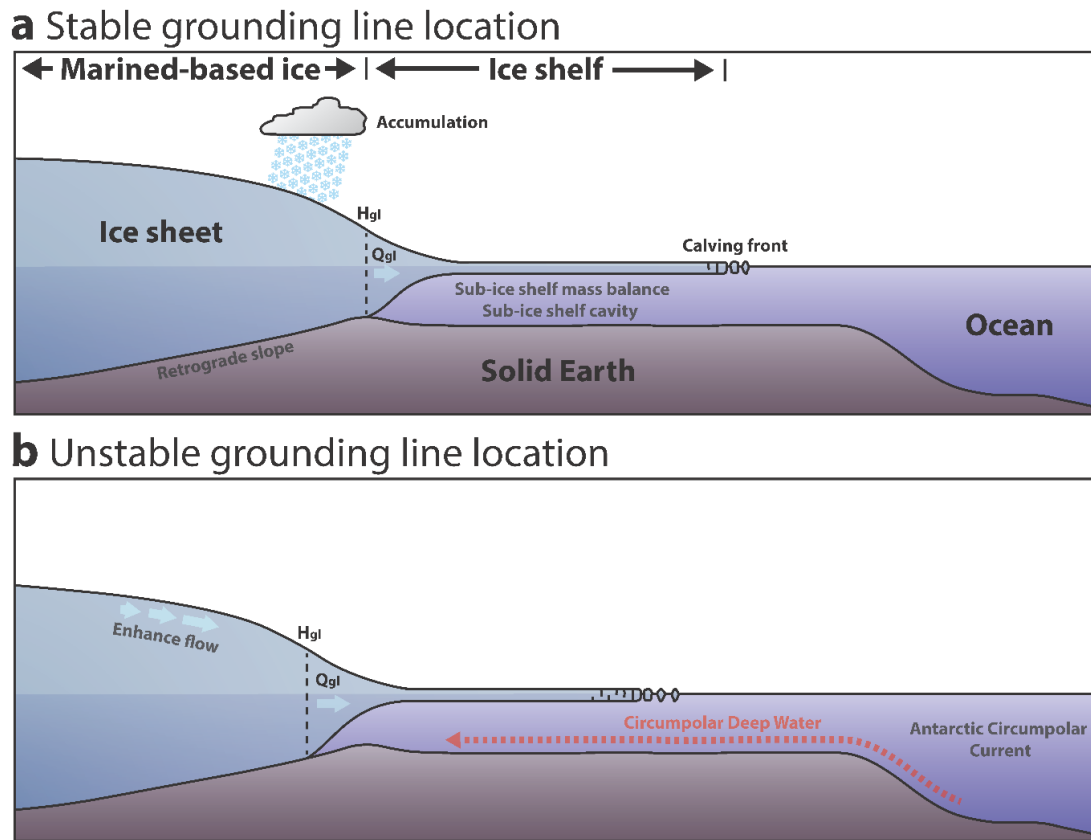


Figure 1.4: An illustration depicting key principles of marine ice sheet instability (MISI) where a marine-based ice sheet is grounded on a reverse-bed slope. a) The grounding line (GL) is in a stable position when the GL is located on a prograde bed slope. b) An incursion of warm circumpolar deep water below the ice shelf leads to increase melt at the GL causing it to retreat into a retrograde bed slope where it undergoes an unstable GL retreat. As the GL retreats into deeper water, the height of the ice column at the GL ( $H_{GL}$ ) increases and in turn, ice flux through the GL increases ( $Q_{GL}$ ).

### 1.3.5 Marine ice sheet instability

The present-day Antarctic ice sheet experiences ice velocities as high as 4 km/yr which demonstrates the ice sheet's rapid dynamic behaviour. The paleo far-field relative sea-level record points to specific events which suggest periods of rapid sea-level rise (see Section 1.4.4) and past warm periods where sea-level exceeded 20 meters above modern

levels (Rowley et al., 2013; Rovere et al., 2014). Therefore, it is important to identify and incorporate mechanisms which lead to major ice sheet instabilities to better understand them and catch early warning signs that the system is about to abruptly change. The two main ice sheet instabilities are the marine ice sheet instability (MISI) and marine ice cliff instability (MICI) as illustrated in Figure 1.4 and Figure 1.5. Marine ice sheet instability (MISI) emerges in the context of grounded ice on a reverse bed-slope where a deepening occurs towards the interior of the ice sheet (Weertman, 1974; Schoof, 2007; Tsai et al., 2015). Ice discharge across the GL is proportional to ice thickness at the GL. Ice retreating on a reversed slope enters deeper water with thicker ice at the GL which in turn increases the flux of ice through the GL (Figure 1.4). As the GL ice thickness increases and the ice approaches the flotation threshold, the ice-ocean interface area also increases, which in turn increases basal melt at the GL. These processes result in a retreat of the GL into even deeper water, leading to a strong positive feedback mechanism (Schoof, 2007).

This MISI mechanism is pertinent considering large parts of the WAIS are below sea level on a reverse bed-slope. The marine-based ice of the WAIS consists of ~3.4 mESL (Bamber et al., 2013; Fretwell et al., 2013; Rignot et al., 2014; Joughin et al., 2014) and potential unstable marine ice exists in the EAIS with an additional ~9 mESL (Young et al., 2011; Li et al., 2015). Rapid ice dynamics through MISI render these areas susceptible to significant ice mass loss and they remain areas of intense research given we are observing rapid GL retreat in accordance with MISI (Rignot et al., 2014; Larter et al., 2014). Rapid ice sheet changes at the margins appear to propagate towards the interior (Pritchard et al., 2009; Joughin et al., 2010a). The Amundsen Sea sector of the WAIS is predominantly grounded below sea level, with the Pine Island Glacier speeding up and thinning in response

to GL retreat into deeper water from the intrusion of warm circumpolar deep waters across the continental shelf (Rignot, 2008; Wingham et al., 2009; Jenkins et al., 2010; Jacobs et al., 2011; Steig et al., 2012; Graham et al., 2022). Other glaciers in the Amundsen Sea sector (Thwaites, Smith, Kohler) are speeding up and thinning in a similar fashion with present-day rates an order of magnitude above millennial-scale rates (Johnson et al., 2008). Mass loss in the Amundsen Sea sector represents a significant portion of the total negative mass balance of the AIS (Otosaka et al., 2023) and is consistent with the development of a MISI due to ocean forcing (Rignot et al., 2014). By looking at the past, we can investigate the response of marine-based ice to past climate forcing and identify whether there are sectors of the contemporary ice sheet that are at a particular high risk of destabilization. Through the comparison between data and models, we can better assess the susceptibility and sensitivity of marine-based ice and whether MISI mechanisms were responsible for the collapse of past marine-based ice.

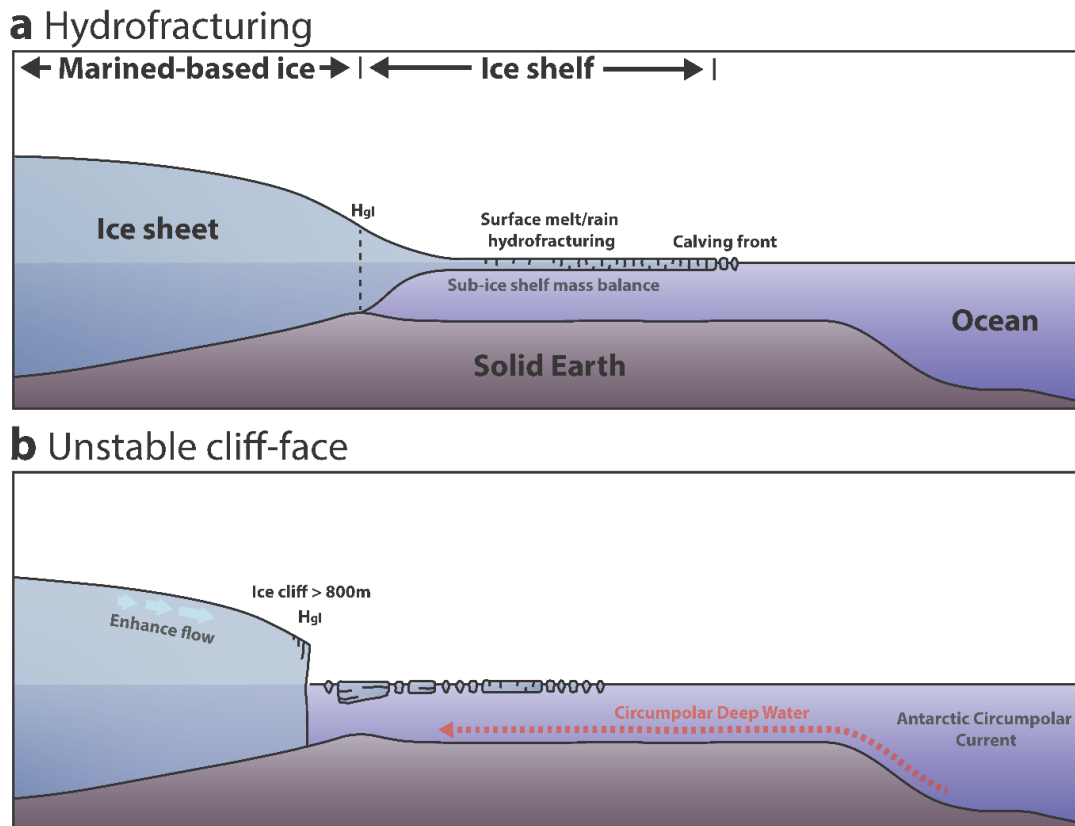


Figure 1.5: An illustration depicting key principles of marine ice cliff instability (MICI) where a) a crevassed ice shelf experiences surface/basal melt or rainfall. The ice shelf undergoes hydrofracturing that propagates crevasses and enhances ice calving culminating in an ice cliff. b) The ice cliff becomes unstable if it exceeds a threshold height which can no longer support the yield strength of the ice, at which point the cliff fails.

### 1.3.6 Marine ice cliff instabilities

An alternate mechanism capable of rapid ice sheet retreat is the marine ice cliff instability (MICI). It consists of two mechanisms operating in sequence. The first being ice shelf collapse through hydrofracture, brought on by surface melt and/or rain draining into surface crevasses, which contributes to horizontal stress gradients enabling widespread calving and ice shelf disintegration (Nick et al., 2010). This non-linear increase in ice shelf calving has been observed in the disintegration of the Larsen B ice shelf (Scambos et al.,

2000). Upon removal of the ice shelf, a tall unstable vertical ice cliff can remain with an unbalanced horizontal stress gradient. If the vertical ice cliff surpasses a critical height (~800 m), the overburden weight exceeds the yield strength of the ice leading to a catastrophic collapse of the ice cliff (Figure 1.5) (Pollard et al., 2015b; Bassis and Walker, 2012; Bassis and Jacobs, 2013). Given the MICI mechanisms remove the unstable ice cliff, it is not surprising there are no present-day instances of these cliffs. The tallest PD subaerial ice cliffs are ~100 m and located in Greenland (Nick et al., 2013; James et al., 2014). The main motivation for invoking MICI was a means of explaining the mid-Pliocene sea-level high stand (Pollard et al., 2015c). However, MICI mechanisms were shown to be unnecessary to achieve an Antarctic sea-level contribution large enough to reach the relatively uncertain mid-Pliocene sea-level high stand (Edwards et al., 2019). The theoretical formulism for MICI is robust, however, the ambiguity of MICI during past warm periods represents an outstanding source of uncertainty on past and future ice sheet evolution.

### 1.3.7 Antarctic mass loss, glacial isostatic adjustment and sea-level change

Ice sheets contribute to sea-level rise whenever grounded ice crosses the GL and begins to float. Alternatively, sea-level rise occurs when grounded ice calves or melts and drains into the ocean. When ice sheets contribute to sea-level rise, it does not simply translate to a uniform increase in the height of the sea surface. There are many processes and feedbacks that lead to spatial and temporal variability in sea-level change.

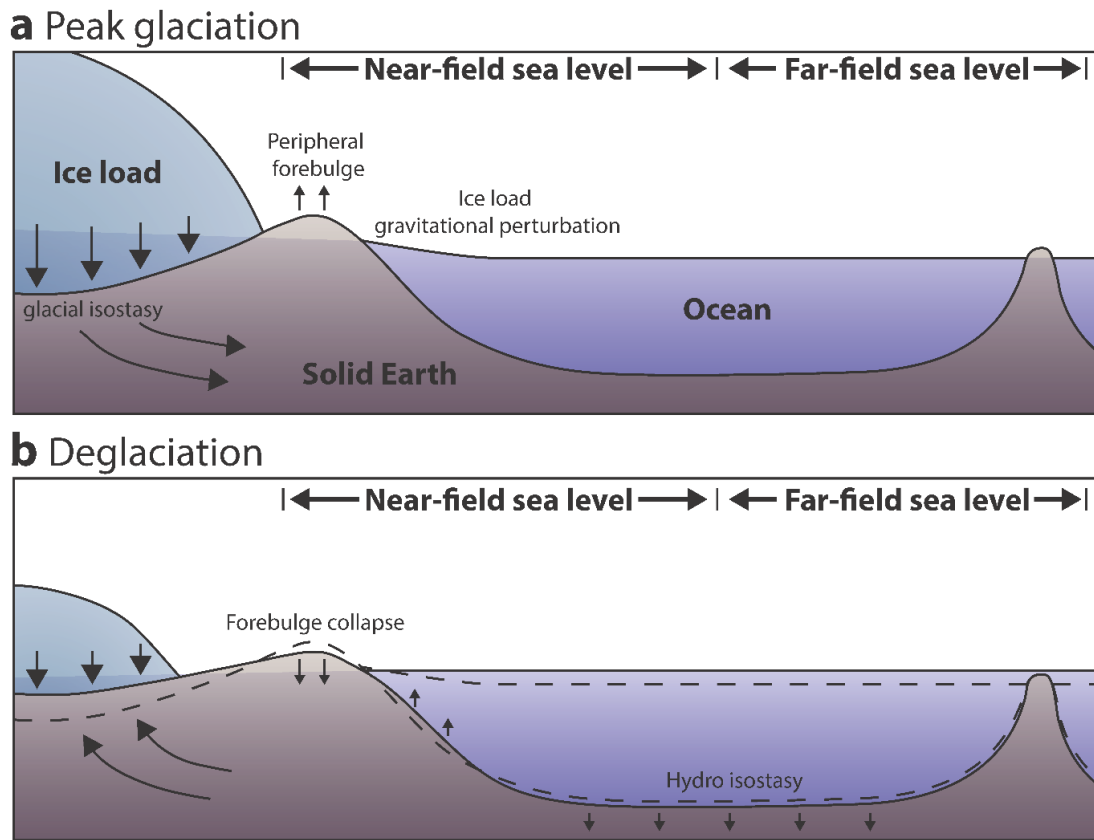


Figure 1.6: An illustration depicting ice sheet unloading and the resulting glacial isostatic adjustment (GIA). a) During peak glaciation, an ice sheet depresses the lithosphere which displaces mantle material. Proximal to the ice load, a peripheral forebulge forms and the gravitational field is deflected upwards due to the mass of the large ice load. b) Throughout the deglaciation the grounded ice sheet retreats which contributes to regional sea-level change by shifting the ocean from one equipotential surface of the gravitational field to a higher one. The newly deglaciated regions rebound, the forebulge collapses and the near-field gravitational field relaxes. The redistribution of ice to the ocean leads to hydro isostasy due to ocean loading. In the near-field RSL decreases while in the far-field RSL increases.

The formal definition of relative sea level (RSL) is defined as the height of the ocean surface relative to that of the solid Earth. Processes that perturb either the ocean surface or the solid Earth can contribute to sea-level change. Processes that affect sea level operate on a wide range of time-scales, from days (e.g. tides, storm surges, ocean circulation), to millennia (e.g. solid earth deformation due to the redistribution of grounded ice), to millions

of years (e.g. dynamic topography due to mantle convection). Those processes that are most relevant over a glacial cycle are GIA induced sea-level change (Figure 1.6).

Depending on the time-scale of the forcing, the solid Earth deforms both elastically and viscously. An instantaneous linear strain response occurs when an elastic rheology is put under stress. An elastic model can simulate a seismic event from an earthquake or the relative impact of recent ice loss on local GPS measurements. Beneath the lithosphere, the solid mantle extends to a depth of 2800 km with a viscosity of approximately  $10^{22}$  Pas. Therefore, if a large mass is placed on the Earth's surface, after the immediate elastic response, pressure gradient stresses in the mantle will accommodate the redistribution of mass via a viscous response. A viscous rheology relates the shear stress (e.g. due to a surface load) to a strain rate response inversely proportional to the viscosity of the material. A viscoelastic rheology, termed a Maxwellian rheology, is applied to simulate GIA of the Earth in response to the redistribution of mass from millennial-scale glacial advance/retreat (Figure 1.6).

The ocean surface lies on an equipotential surface of the Earth's gravitational field termed the geoid. Therefore, any process that perturbs the Earth's gravitational field will affect the ocean surface. As an ice sheet grows, the geoid shifts from one equipotential surface to a lower surface. The now larger ice mass increases the local gravitational field, deflecting the equipotential surface higher near the ice sheet (Figure 1.6). The deeper water column in the vicinity of the ice sheet contributes to the redistribution of mass and introduces additional loading on the surface. Solid Earth deformation related to ice loading is termed glacioisostasy and deformation related to ocean loading is termed hydroisostasy (Milne and Shennan, 2007; Whitehouse et al., 2019). The loading and GIA feedbacks

manifest into prominent features such as: peripheral forebulge near ice sheets, near-field gravitational perturbations, continental levering from far-field ocean loading, and perturbations to the Earth's rotational inertia tensor. Excluding high frequency temporal variations in the ocean surface, the aforementioned processes operating together culminate in the spatio-temporal evolution of global RSL change.

## West Antarctic sea-level fingerprint

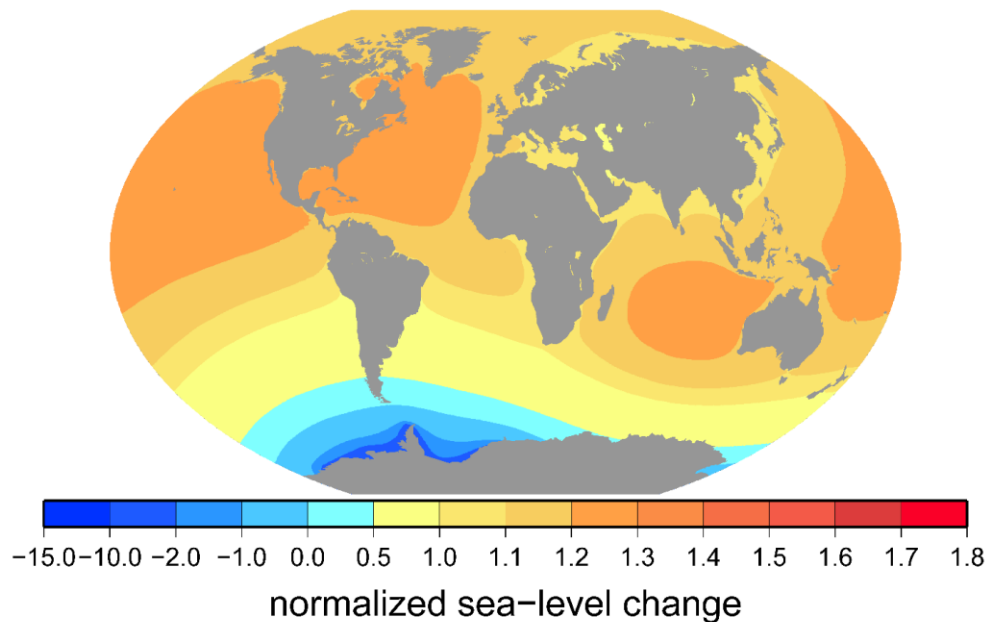


Figure 1.7: An Antarctic sea-level fingerprint demonstrates a normalized sea-level contribution from Antarctica due to the immediate elastic response of the solid Earth to ice mass loss from grounded ice.

To illustrate the spatial variability in global RSL change, Figure 1.7 shows a normalized sea-level fingerprint (Mitrovica et al., 2009). The sea-level fingerprint demonstrates the instantaneous elastic response and gravitational perturbation due to a redistribution of mass loss originally sourced in the WAIS. For a hypothetical nearly instantaneous WAIS sea-level contribution of 1 cm equivalent sea-level, one simply scales the normalized sea-level fingerprint to evaluate how the 1 cm redistributes itself globally

(Figure 1.7). Far-fields regions relative to Antarctica (e.g. North America, Africa, Oceania) would experience a RSL rise exceeding 1 cm, while near-field regions experience a RSL fall due to bedrock uplift and gravitational relaxation. The sea-level fingerprint's simplicity is not appropriate when considering longer time-scales where the viscous GIA response becomes dominant. However, the general trends persist, given an ice mass unloading event there is a sea-level fall in the near-field and sea-level rise in the far-field.

### 1.3.8 Future Antarctic ice sheet changes

The Projected Antarctic sea-level contributions by the end of the century vary broadly (Ritz et al., 2015; Ruckert et al., 2017; Golledge et al., 2015; DeConto and Pollard, 2016; Bamber et al., 2019). The studies suggesting an Antarctic ice sheet highly sensitive to climate change include both MISI and MICI processes (Pollard et al., 2015; DeConto and Pollard, 2016). Under the “business as usual” climate scenario (RCP8.5), DeConto and Pollard (2016) found a sea-level contribution from the Antarctic ice sheet between 0.15 to 1.35 metres by the end of 2100. The projected Antarctic sea-level contributions and accompanying 1-sigma uncertainties from DeConto and Pollard (2016) are based on a limited 64-member ensemble by varying four parameters controlling sub-shelf melt, ice-shelf calving, the maximum rate of ice-cliff retreat, and the ocean bias correction. Other than filtering out runs that are loosely inconsistent with Pliocene and last interglacial far-field sea-level estimates, the model parameters are not constrained by near-field observations of the most recent deglaciation which limits their predictive power. Furthermore, the narrow ensemble heavily sampled upper bound sea-level contributions, thereby producing non-parametric uncertainties that are not representative of a true

probabilistic likelihood of future Antarctic mass loss (Edwards et al., 2019). Upon further evaluation by Edwards et al. (2019), the DeConto and Pollard (2016) results were found to be relatively consistent with previous studies (Little et al., 2013; Levermann et al., 2014; Ritz et al., 2015; Ruckert et al., 2017). A formal calibration of Antarctic projections which makes use of the available paleo and PD data to generate consistent bounds of AIS evolution in the past, present, and future is still lacking. The work detailed in this thesis represents a significant steppingstone to this future research.

## 1.4 Key periods in the paleorecord

There remain many outstanding scientific questions regarding the past evolution of the AIS. By studying the past, we can better understand contemporary and future ice sheet changes. There are many periods of interest which can inform us on the climate sensitivity of the ice sheet by studying past warm and cold periods. Therefore, we study the last two glacial cycles to model the response of the AIS during the last interglacial, glaciation, and subsequent deglaciation. This period includes instances where the AIS was likely smaller and larger than present. This provides an opportunity to study how the ice sheet responded to past climate change, contributed to sea-level change, and culminated in the PD ice sheet. The following section provides context on the research period of interest of this thesis.

### 1.4.1 Climate history

An area of active research is the study of past climate change, particularly research surrounding the Antarctic. This motivates the need to better understand the AIS over the past glacial cycles, particularly as a set of crucial boundary conditions for general

circulation models. Such implementations will improve the delineation of the processes responsible for glacial-interglacial climate change and in turn on the climate forcing necessary for ice sheet model. A better constrained freshwater flux and AIS geometry will affect our understanding of atmosphere-ocean circulation and CO<sub>2</sub> outgassing. Additionally, more robust confidence intervals of the AIS will help better understand sea-level change throughout the last interglacial, LGM and during the melt water pulses. These open scientific questions can provide great insight on the susceptibility and sensitivity of the AIS to future changes.

Ice cores provide a high-resolution and continuous record of past atmospheric conditions (O<sub>2</sub>, N<sub>2</sub>, Ar, CO<sub>2</sub>, CH<sub>4</sub>) (Petit et al., 1999). Melt layers in the ice relate to summer temperatures, while dissolved ions and particles in the ice provide data on volcanic activity, wind strength and sea salt content. Moreover, the ice itself consists of water molecules with varying isotopic compositions, these isotopic ratios are dependent on fractionation processes which are to first order temperature dependent ( $\delta^{18}\text{O}$  and  $\delta^2\text{H}$  (Johnsen et al., 2001)). For these reasons, ice cores are the most valuable records of climate change spanning several glacial cycles (Figure 1.8) (Petit et al., 1999; EPICA, 2004; Mulvaney et al., 2012). Ice cores are the primary proxy records that define the climate of the last several glacial cycles. The past climate, reconstructed from the EPICA Dome C ice core, is one of the components of the external atmospheric forcing driving the evolution of the AIS during this research (Figure 1.8). Key periods of interest often referred to are labeled adjacent to the ice core record shown in Figure 1.8.

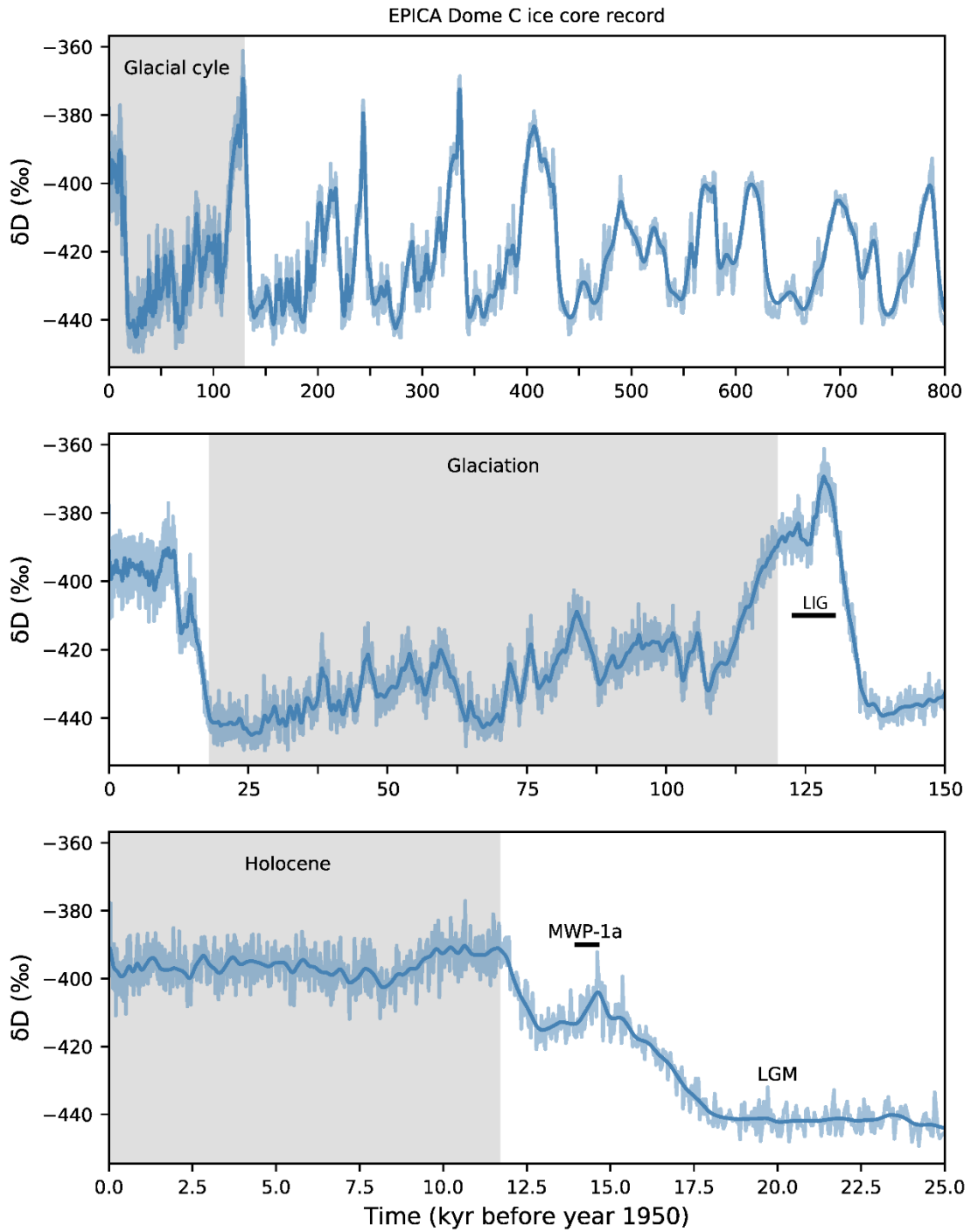


Figure 1.8: The EPICA Dome C deuterium record spanning a) 800 kyr, b) the last interglacial and glacial cycle, and c) the deglaciation. Key periods of interest are labelled including the last interglacial (LIG), Last Glacial Maximum (LGM), and Meltwater Pulse 1a (MWP1a). The EPICA Dome C data is also shown in Chapter 3 (Lecavalier and Tarasov, 2024).

There are several ice cores across Antarctica that span over multiple glacial cycles. The Vostok ice core from East Antarctica is a record of CO<sub>2</sub>, CH<sub>4</sub>, air temperature ( $\delta^2\text{H}$ ) over four glacial cycles (420 ka) (Petit et al., 1999). While the EPICA ice core, taken from Dome C, spans 740 ka consisting of 8 glacial cycles, including the super interglacial marine isotope stage 11 (EPICA, 2004). The different ice cores are highly correlated across greenhouse gases (CO<sub>2</sub>, CH<sub>4</sub>), and climate ( $\delta^2\text{H}$ ) data (Fischer, 1999; Petit et al., 1999; Watanabe et al., 2003). The average amplitude of inferred glacial-interglacial surface temperature change is 8 to 12 °C (Petit et al., 1999). The last 5 Glacial periods appear to reach minimum temperatures of -8 to -9 °C relative to present (Petit et al., 1999; EPICA, 2004). The largest natural changes in greenhouse gases are associated with glacial-interglacial transitions with CO<sub>2</sub> concentrations shifting from ~180 up to 290 ppmv and CH<sub>4</sub> concentrations going from ~335 up to 710 ppbv (Petit et al., 1999). The present-day CO<sub>2</sub> and CH<sub>4</sub> levels are at 400 ppmv and 1700 ppbv, that is unprecedented during the span of the ice core records, with preindustrial levels of 280 ppmv and 650 ppbv, respectively.

Transient Earth System Models do not dynamically reproduce the glacial-interglacial temperature and carbon cycle changes proposed by proxy records (Denton et al., 2010; Menviel et al., 2015). Outgassing from the Southern Ocean is expected to impact CO<sub>2</sub> variations (Völker and Köhler, 2013; Lauderdale et al., 2013); this emphasizes the requirement for a better constrained AIS chronology given its role in Antarctic bottom water formation.

The proxy records have vast utility, they can force paleo ice sheet and climate simulations and constrain the potential triggers, causes, and processes for past climate change (Lemieux-Dudon et al., 2010; Shakun et al., 2012; Rasmussen et al., 2014). The

Greenland ice cores reflect North Atlantic temperature changes and show signs of mild deglacial warming early on (~20-18 ka). Antarctic temperatures rose following those in Greenland, Greenland subsequently cooled into the Oldest Dryas (18-15 ka). Antarctica continued to warm gradually all the way into the Bølling-Allerød (14.6-12.9 ka), while Greenland abruptly and rapidly warmed during this period. The North Atlantic remained warm during the Bølling-Allerød, Antarctica experienced the Antarctic cold reversal where slow gradual cooling persisted until Greenland temperatures abruptly plummeted into the Younger Dryas (YD) cold event (12.9 - 11.7 ka). The Antarctic temperatures gradually approached pre-industrial temperatures by the Holocene (11.7 ka) and marginally overshoot them before cooling to pre-industrial values. These climatic fluctuations as inferred by ice core records generally integrate seasonal changes which complicates their interpretation. Regardless, Greenland surface temperatures remained cold until they abruptly transitioned into interglacial temperatures, marking the transition into the Holocene. When considering all ice core records, they provide both a regional and global climate inference over the last two glacial cycles.

## 1.4.2 Last interglacial sea level

The last interglacial (LIG) is a warm period (129-116 ka; MIS5e), often touted as being partly analogous to present-day. However, the LIG reflects a period that can more appropriately highlight the sensitivity of the ice sheets to a past warm climate. Studying this period can improve our understanding of contemporary climate and ice sheet changes and constrains simulations of future projections. With respect to today, the LIG had a different orbital forcing and lower atmospheric CO<sub>2</sub> concentrations comparable to pre-

industrial values. Global mean air temperatures during the LIG were inferred to be 0.5 to 1°C warmer than preindustrial values (Otto-Bliesner et al., 2013; Fischer et al., 2018; Turney et al., 2020). Based on inferences from ice cores records, the Antarctic interior air temperatures were ~2 °C warmer than preindustrial values (Jouzel et al., 2007; Capron et al., 2014; 2017). Global mean ocean temperatures were  $1.1 \pm 0.3$  °C greater than in the preindustrial period leading up to the LIG, however during the LIG they were effectively identical to preindustrial values (Shackleton et al., 2020). LIG sea surface temperatures during the LIG were between 0.5 to 1.5 °C warmer than preindustrial values (Hoffman et al., 2017). This period of warmer climate is affiliated with global mean sea level (GMSL) estimates of 6 to 9 m above present (Dutton and Lambeck, 2012; Dutton et al., 2015; Kopp et al., 2009).

LIG RSL sites have various interpretations of their respective LIG highstands with some suggesting a stable sea level, two highstands separated by a fall in sea level, stable sea level followed by rapid sea-level rise, and others proposing sea-level oscillations with up to 4 peaks (Stirling et al., 1998; Hearty et al., 2007; Blanchon et al., 2009; Thompson et al., 2011; Dutton et al., 2015). This indicates a potential dynamic response from the polar ice sheets, and it remains unclear whether this implies asynchronous Greenland ice sheet (GrIS) and AIS responses to LIG climate (Dutton et al., 2015). However, there lack high quality constraints on the state of the LIG AIS. Thus, it remains unclear how much the AIS contributed to sea-level change during this period.

### 1.4.3 Last Glacial Maximum

The LGM is described as the period with maximum global ice volume from ~26 to 19 ka (Clark et al., 2009), however, it may refer to a local LGM since not all ice sheets reached a synchronous maximum volume. In the case of the North American Ice Complex (NAIC) the local LGM could have occurred between 26 to 20 ka (Tarasov et al., 2012) while the GrIS reached a maximum volume much later at ~16.5 ka (Lecavalier et al., 2014). The timing of the AIS local LGM is poorly constrained as suggested by the available observations (Bentley et al., 2014; Lecavalier et al., 2023), model reconstructions propose a range of values. Past studies generally assume LGM extent was maintained around ~20 ka (Livingstone et al., 2012; Bentley et al., 2014).

The LGM was a period of global sea level minima on the order of 120 - 134 metres below GMSL (Figure 1.9) (Milne, Mitrovica and Schrag, 2002; Peltier and Fairbanks, 2006; Clark et al., 2012; Austermann et al., 2013; Lambeck et al., 2014). Sea-level change over the last deglaciation was first reported in the landmark Fairbanks (1989) study based on cores taken from submerged coral reefs near Barbados (Fairbanks, 1989; Bard et al., 1990, 2010). More recently, on the tectonically stable continental shelf of Bonaparte Gulf near Australia, sediment cores obtained infer RSL change over the deglaciation based on microfaunal assemblages (Yokoyama et al., 2000, 2001). A RSL record from Sunda Shelf in southeastern Asia based on organic matter in sedimentary cores was interpreted as recording nearshore and shallow water environment during the deglaciation (Hanebuth et al., 2009). A deglacial RSL record was reconstructed from corals drilled offshore from Tahiti based on coralgall assemblages (Deschamps et al., 2012). Finally, a fossil coral record

from the edge of the Great Barrier Reef documents deglacial sea-level change from corals and coralline algae assemblages (Yokoyama et al., 2018). The RSL records of the last deglaciation provides information on the size of past continental ice sheets and their response to climate change. To interpret the RSL proxy records to infer a global sea-level history, many processes must be considered given the regional variability in sea-level change.

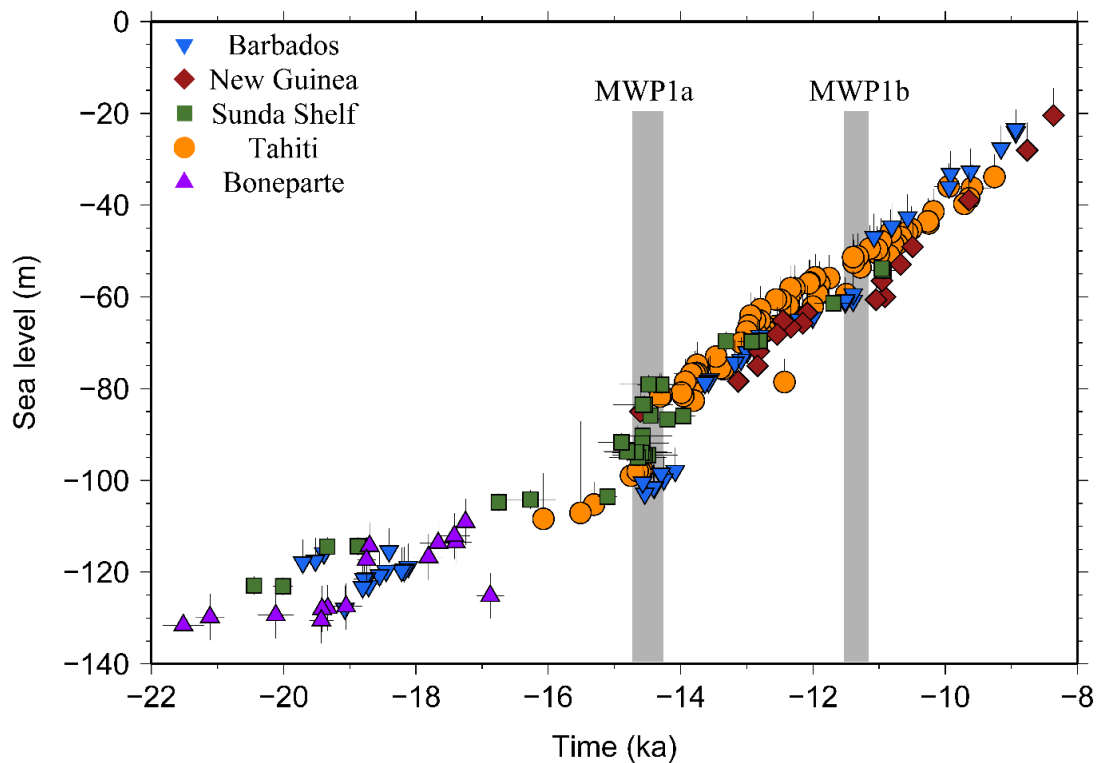


Figure 1.9: Far-field relative sea-level records demonstrating the LGM sea-level minima and deglacial sea-level history, include meltwater pulse 1a and 1b (MWP-1a/1b). The sea-level proxy data was collected across a variety of sites minimally impacted by isostasy induced by previously glaciated regions (Fairbanks et al., 2005; Yokoyama et al., 2000; Hanebuth et al., 2009 Deschamps et al., 2012).

GMSL is an abstraction which reflects spatially averaged sea level across the globe, since on millennial time-scales sea-level change has significant spatial deviations from the

mean due to various processes. The largest influence on spatial variations in sea level over thousands of years arises from GIA caused by the redistribution of mass (Figure 1.6) (i.e. ice sheets, ocean water, mantle material) (Clark et al., 1978; Lambeck and Chappell, 2001; Milne and Mitrovica, 2008). Considering that most of the world's sea-level deviates from the global mean, RSL records must be corrected for GIA prior to extracting GMSL estimates and comparing different sea-level reconstructions. The RSL records from Barbados, Bonaparte, Sunda, Tahiti and Great Barrier Reef were corrected for GIA to assess global sea-level change over the deglaciation (Figure 1.9). These records are all classified as far-field RSL records, meaning these records are located far away from currently and/or previously glaciated regions experiencing the most significant GIA induced sea level change.

Missing ice is an unresolved issue raised by an ongoing discrepancy between far-field RSL records of the deglaciation with estimates of global ice volume at the LGM (Clark and Tarasov, 2014; Simms et al., 2019). By combining the North American ice complex ( $76.0 \pm 6.7$  mESL), Eurasian ice sheets ( $18.4 \pm 4.9$  mESL), Greenland ice sheet ( $4.1 \pm 1.0$  mESL), Antarctic ice sheet ( $9.9 \pm 1.7$  mESL), glaciers and ice caps ( $5.5 \pm 0.5$  mESL), and considering ground water storage and ocean thermosteric effects ( $3.8 \pm 0.3$  mESL), the global sea-level budget remains underestimated by  $15.6 \pm 9.6$  mESL) (Simms et al., 2019). Near-field geological and geomorphological constraints are in direct conflict with the far-field observations given they are thought to favour smaller ice sheet volumes. The Antarctic region has the least number of observational constraints on its deglacial chronology of any Quaternary ice sheet; therefore, a model calibration of the AIS since the last interglacial can potentially help address the LGM volume budget deficit from far-field RSL records by

properly accounting for uncertainties. The remaining discrepancies with the far-field RSL budget have been attributed to various alternate issues, in particular the assumption of present-day living depth ranges for the interpretation of sea-level proxies from ancient corals. Additionally, uncertainties in GIA due to lateral Earth structure and dynamic topography can impact the interpretation of the sea-level proxy data (Austermann et al., 2013; Pan et al., 2022). To close the LGM sea-level budget and resolve the missing ice problem, confidence on the indicative meaning of the far-field RSL data is required; the far-field proxy data must be corrected for GIA and tectonics effects with meaningful uncertainties; additional constraints are needed to robustly determine the extent and timing of the paleo ice sheets; and data-constrained model simulations have to adequately explore uncertainties in the glacial system.

#### 1.4.4 Deglacial sea level and melt water pulses

The global LGM sea-level lowstand is believed to terminate at 19.5-19 ka when sea-level quickly rose due to the predominant northern hemisphere ice sheet retreat from high northern latitude insolation forcing (Clark et al., 2009). The RSL records from 19 - 14.5 ka marked a period of 8.3 - 20.8 m sea level rise (Fairbanks et al., 2005; Yokoyama et al., 2000; Hanebuth et al., 2009). This sea-level change was sourced from the significant retreat of the Laurentide and Eurasian ice sheets (Dyke, 2004; Fairbanks et al., 2005) with limited parts of the AIS retreating as well (Heroy and Anderson, 2007; Weber et al., 2011). It remains unclear as to why some sectors of Antarctica retreated. Ice sheet simulations propose a range of ~14 to 17.5 mESL from the NAIC (Tarasov et al., 2012). A northern hemisphere ice sheet contribution between 19 - 14.6 ka that exceeds that observed in the

far field RSL records implies a net positive mass gain on the AIS. This would require increased accumulation as reported in (Lemieux-Dudon et al., 2010) from ~18 - 14.6 ka. It remains an open question as to why the northern hemisphere ice sheets retreated while the AIS grew, especially given the climate during this period was characterized by cool northern hemisphere conditions (Oldest Dryas) and a warmer southern hemisphere. It is possible that a warming Antarctic is associated with an inferred precipitation increase and a cooling north hemisphere could primarily reflect a change of seasonality (Denton et al., 2022).

During the deglaciation there were abrupt accelerations in sea-level rise termed the melt water pulses (MWP), MWP-1a at ~14.6 ka and later MWP-1b at ~11.3 ka (Figure 1.9) (Bard et al., 1990). The combined RSL records suggest a range of about 12 to 19 m over ~340 years for MWP-1a (Deschamps et al., 2012; Carlson and Clark, 2012). These values are substantially less than the originally estimated 24 metres over a 500-year period (Fairbanks, 1989). The timing and magnitude of MWP-1a is best constrained by the Tahiti record and remains relatively consistent with the other far-field RSL records (Deschamps et al., 2012; Hanebuth et al., 2009). Specifically, Tahiti suggests that MWP-1a began at 14.6 ka and terminated at 14.3 ka (300 yr period) with a more likely amplitude of 14 to 18 m (Deschamps et al., 2012). The source regions responsible for such an abrupt sea-level change remains contested, particularly the AIS contribution.

Initially based on size, the NAIC was assumed the sole contributor of MPW-1a (Fairbanks, 1989; Peltier, 1994). Observational evidence of margin retreat and RSL change constrained NAIC simulations and supported the premise of a significant NAIC contribution to MWP-1a (Peltier, 2004, 2005; Tarasov and Peltier, 2005; Tarasov et al.,

2012; Gregoire et al., 2012). A Bayesian calibration of the NAIC estimates a  $11.6 \pm 2.2$  mESL contribution to MWP-1a, although this is over a 500-year period (Tarasov et al., 2012). The Eurasian ice complex (EIC) extent during the last deglaciation is reported by the Digital Atlas of the Eurasian Deglaciation (DATED) project and suggests margin retreat during MWP-1a. However, the area loss during this period is not anomalous relative to earlier/later periods and when the area is scaled to volume empirically (Cuffey and Paterson, 2013), it yields a sea-level contribution of  $4.9 \pm 0.8$  mESL between 15 to 14 ka (DATED).

Glaciological estimates on the MWP-1a contribution tend to use a duration of 500 years rather than 300 years (Deschamps et al., 2012), therefore, the model predictions are likely overestimations. As of now it appears that the northern hemisphere ice sheets contributed the majority of the ice ESL for the MWP-1a sea-level budget (Lin et al., 2021). A number of studies suggested a likely AIS contribution to address the budget shortfall to MWP-1a (Clark et al., 1996; Heroy and Anderson, 2007; Conway et al., 2007; Carlson and Clark, 2012). This was supported by the geophysical modelling of far-field RSL records which concluded that the dominant geographic source of the MWP was sourced in Antarctica (Bassett et al., 2005; Clark et al., 2002). More recently, sea-level fingerprinting studies propose a marginal AIS MWP contribution (Lin et al., 2021; Liu et al., 2016). Robustly quantifying the AIS contribution given near-field observations would improve our ability to interpret the far-field RSL records.

The far-field RSL observations seem to be in direct conflict with the near-field observations of the AIS chronology. Terrestrial and marine records on the AIS deglaciation consistently conclude a modest MWP-1a contribution, with the majority of ice loss

occurring later (Ackert et al., 1999, 2007; Conway et al., 1999; Harris and Beaman, 2003; Baroni and Hall, 2004; Licht, 2004; Mackintosh et al., 2011; Smith et al., 2011; Bentley et al., 2014). However, well-dated marine sediment cores from the central Scotia Sea in the Southern Ocean contain an increased concentration of ice rafted debris deposition during the MWP-1a (Weber et al., 2014). Data-constrained large-ensemble model simulations of Antarctica supported a small MWP-1a contribution from 0.1 to 1.4 mESL (Briggs et al., 2014). Relative to the NAIC, EIC, and GrIS, the AIS deglaciation is poorly constrained and remains the largest source of uncertainty in the MWP-1a sea-level budget (Tarasov et al., 2012; Bentley et al., 2014; Briggs, Pollard and Tarasov, 2014; Lecavalier et al., 2014). With few high-resolution records to constrain the MWP-1a contribution of the AIS, it is difficult to confidently assess and quantify the vulnerability of the ice sheet to rapid dynamic changes without properly addressing data and model uncertainties.

Following MWP-1a was the Allerød warm period from 14 to 13 ka. This period in the RSL records suggests a sea-level change of 7-10 mESL (Edwards et al., 1993; Bard et al., 1996; Peltier and Fairbanks, 2006) thought to have been sourced from the NAIC and EIC based on data-constrained ice sheet simulations (Tarasov et al., 2012) and DATED estimates. During the Holocene (11.7 ka to present; Rasmussen et al., 2006) sea-level rose another ~60 m (Fairbanks, 1989; Bard et al., 1990). Model simulations of the NAIC and EIC proposes 28 – 30 mESL and 3 - 5 mESL, respectively (Boulton et al., 2001; Carlson et al., 2008; Licciardi et al., 1998; Peltier, 2004; Siegert and Dowdeswell, 2004; Tarasov et al., 2012). This period was punctuated by MWP-1b at ~11.3 ka with a duration of less than 500 years (Fairbanks, 1989; Bard et al., 1990), however, the existence of MWP-1b is contentious since other RSL records do not exhibit anomalous RSL rates during this period

(Lambeck et al., 2014; Stanford et al., 2011). The potential source of MWP-1b appears to be the Laurentide ice sheet and EIC as suggested by the geologic record (DATED) and model simulations (Tarasov et al., 2012). Two additional periods of increase RSL rates are identified at ~9-8.5 ka (Cronin et al., 2007) and ~7.6 ka (Bird et al., 2007; Cronin et al., 2007; Horton et al., 2005; Yu et al., 2007) which suggests anomalously rapid ice sheet changes.

## 1.5 Primary Research Questions

The key research questions this thesis aims to address are the following: what is the sea-level contribution from the Antarctic ice sheet during the 1) last interglacial, 2) Last Glacial Maximum, and 3) Meltwater pulse 1a; 4) Antarctic glacial isostatic adjustment and sea-level change; and 5) present-day thermal structure of the ice sheet? By compiling and incorporating the available data to constrain the system and properly exploring model uncertainties, the model output provides bounds that represent our current knowledge with respect to these research questions.

The ensemble of the AIS simulations since the last interglacial not-ruled-out-yet (NROY) by the data provides necessary products to help quantify Antarctica's role in the climate system. The AIS model output with their NROY sub-ensemble bounds constitutes important boundary conditions in general circulation models such as: topographic boundary conditions which provide orographic forcing on the atmosphere; ice sheet mass balance which prescribes freshwater forcing to the ocean, and grounded ice volume changes which impact GIA and global sea-level change.

Our ability to tightly constrain answers to these questions is entirely limited by the available observational data. The Antarctic continent is data-poor in paleo observations relative to other currently or previously glaciated regions. In this thesis a comprehensive observational constraint database is compiled for the region to data-constrain GSM Antarctic configuration. Any one model simulation will never be an accurate representation of reality. Previous studies have predominantly failed to adequately incorporate and bracket observational constraints and explore parametric uncertainties to address the aforementioned research questions. The research presented below aims to rectify these issues and provide data-driven robust predictions.

## 1.6 Previous Antarctic Modelling Studies

Many Antarctic studies that modelled the evolution of the ice sheet over the last glacial cycle aimed to infer past AIS evolution, while others were not necessarily interested in reconstructing the most accurate ice sheet chronology, but aimed to assess the role and impact of feedbacks/processes in the glaciological system (Denton and Hughes, 2002; Huybrechts, 2002; Philippon et al., 2006; Pollard and DeConto, 2009; Golledge et al., 2012; Gomez et al., 2013; Golledge et al., 2014; Gomez et al., 2020). These process studies often say more about model behaviour and sensitivity rather than actual past changes. Studies often insufficiently explored parametric uncertainties and/or applied limited observational constraints. This severely limits the utility of the model predictions given they lack meaningful uncertainties on model results. To distinguish and contextualize the HMA involved in this thesis, below is a summary of prominent recent AIS modelling studies aiming at reconstructing an accurate chronology.

Previous studies have employed some of the following methodologies at reconstructing the AIS over the last glacial cycle. Ice sheet chronologies have been generated using geophysical inversion techniques (Peltier, 2004; Fleming and Lambeck, 2004; Lambeck et al., 2010; Argus et al., 2014). Even though this method is constrained by geophysical and/or geomorphological observations consisting of RSL, ice elevation and extent data, they lack complete glaciological self-consistency in the ice sheet reconstruction. The reliance on insufficient spatial and temporal coverage of the data limits the ability to constrain the timing of the glacial/deglacial history. The paucity of data is highly problematic, particularly given the heterogeneous distribution and scarcity of older data (Bentley et al., 2014; Lecavalier et al., 2023). Additionally, geophysical inverse methods cannot rigorously distinguish between the timing and magnitude of load removal. This arises due to the similar geophysical response of the system to a recent minor mass change compared to a much larger mass change which occurred much earlier in time (Tarasov and Peltier, 2004). Finally, considering the geophysical reconstructions are hand-tuned, there is no way to quantify uncertainties on the chronologies, therefore, geophysical inverse reconstructions lack robust uncertainty estimates, limiting the usefulness of their predictions.

In contrast to the geophysical inverse method, ice sheet model reconstructions are physically consistent. This approach applies a set of discretized approximations to the governing physical laws of thermodynamics and ice dynamics. Moreover, glaciological models are consistent with inferences of past climate and can formally integrate their uncertainties. The theoretical formulation that describes the thermo-mechanical evolution of ice is sophisticated and invariably approximations are used to solve them numerically.

The first generation of ice sheet models did not represent the key physical processes of ice stream and GL migration (Huybrechts, 2002), while most state-of-the-art ice sheet models incorporate these essential processes to study the AIS (Philippon et al., 2006; Pollard and DeConto, 2009; Pattyn, 2017; Quiquet et al., 2018). On the other hand, the many necessary remaining approximations parameterize processes which are not properly resolved or represented. Empirical parameterizations depend on poorly constrained parameters which have no correct values; they are simply tuned to achieve “reasonable” results. The models only approximate reality, thus, their predictions are neither 'correct' nor 'incorrect' solutions (Hauser et al., 2012), they simply represent a range of solutions which can be compared to observations. The observational constraints then reject possible solutions rather than highlight an optimal solution (Tarantola, 2006; Tarasov et al., 2012; Tarasov and Goldstein, 2021). Moreover, glaciological models can integrate observational constraints from geomorphological evidence, ice temperature and age structure. Generally, AIS model simulations quantitatively compare their output with the observed present day ice sheet geometry and/or surface ice velocity (Huybrechts, 2002; Philippon et al., 2006; Quiquet et al., 2018; Seroussi et al., 2019). Previous glaciologically self-consistent modelling studies have used data-model comparisons in identifying best fitting reconstructions (Denton and Hughes, 2002; Huybrechts, 2002; Philippon et al., 2006; Pollard and DeConto, 2009; Whitehouse et al., 2012; Golledge et al., 2014), rather than a best-fitting ensemble of reconstructions, which limits the level of confidence in predicting ice sheet evolution and gets around the challenges in interpreting model output (Briggs et al., 2014; Chang et al., 2019).

Past studies have proposed a wide range of LGM (~26 to 19 ka) volumes for the Antarctic ice sheet (7.5 to 27.9 mESL; Simms et al., 2019). In the Pollard and DeConto (2009) study, a glaciological model based on hybrid physics (SIA-SSA) and Schoof GL migration scheme (Schoof, 2007) reconstructed the AIS with a horizontal resolution of 40 km. The focus was on West Antarctic ice sheet collapse over the past several glacial cycles. Their model was tuned to fit the PD ice sheet configuration; the last glacial cycle was simulated, and they concluded an excess LGM volume of 12.5 mESL. However, the study did not integrate additional observational data in assessing the ice sheet evolution which results in a weakly constrained chronology.

The AIS deglacial study by (Whitehouse et al., 2012) produced a loading history for a GIA model. The data-constrained deglaciation chronology was generated using the community ice sheet model Glimmer (Rutt et al., 2009) to generate time-slices at 5 ka intervals, starting at 20 ka. The model resolution had a 40 km horizontal resolution and was prescribed a fixed GL extent based on marine geophysical and geological data for each respective interval. Climate inputs, basal sliding coefficients, Earth rheology, geothermal heat fluxes were adjusted to generate a suit of chronologies which were compared to observational constraints and scored. The study compiled a database of observational constraints to assess the quality of a model reconstruction consisting of RSL and ice extent observations, in addition to present-day ice sheet geometry. Based on their ensemble study, it was determined that the AIS had an excess volume of  $9 \pm 1.5$  mESL at the LGM. The glaciological model applied did not contain GL migration. Considering how poorly the AIS is constrained during the deglaciation and the misrepresentation of physical processes (e.g. GL) could lead to a wide variety of alternate and viable Antarctic chronologies.

Additionally, a limited assessment of parametric uncertainty was conducted and only a partial exploration of the parameter phase-space was performed. This suggests that their proposed confidence intervals are too narrow.

Using the parallel ice sheet model (PISM), Golledge et al. (2014) conducted a series of model simulations with a horizontal resolution of 15 km. The study resulted in 250 model reconstructions which were constrained by the PD geometry and the partially constrained LGM extent (Livingstone et al., 2012). The chronologies were assessed qualitatively against past elevations inferred from ice cores and determined the AIS had an excess volume of 14.5 mESL during the LGM. The computational time of running simulations at this resolution restricted the analysis to a small ensemble study with minimum exploration of uncertainties in boundary conditions and ensemble parameters. Furthermore, observational constraints were not integrated to score model reconstructions, which impose a level of subjectivity in assessing their “best-fitting” reconstruction.

Several studies using the Penn State University ice sheet model (PSU-ISM) have conducted ensemble data-constrained analyses to evaluate the WAIS (Pollard et al., 2015; Chang et al., 2016, 2019). They aim to establish a robust statistical methodology towards a Bayesian calibration focused on scoring against the PD ice sheet geometry (Chang et al., 2016, 2019) and AntICEdat (Pollard et al., 2015). Their goal was to generate a probabilistic envelope on the past and future evolution of the AIS, however, they only considered four model parameters for the parametric uncertainties of the entire Antarctic glacial system. The ensemble consisted of 625 simulations (Pollard et al., 2015) and 499 simulations (Chang et al., 2016). These studies did not consider uncertainties in boundary conditions. Their results are more likely the product of the prescribed transient climate forcing, which

remains the same through all their experiments. Past oceanic and atmospheric climate is the largest source of uncertainty for ice sheet evolution, yet they make no allowances for degrees of freedom in the climate forcing, which presumes the prescribed past climate forcing to be accurate (e.g. temperature, precipitation). For these reasons, these studies likely underestimate the ranges of viable AIS responses to past climate change, although the studies do represent progress towards formal statistical methods in ice sheet reconstruction evaluation (Chang et al., 2016, 2019).

The approximate Bayesian calibration of an idealized Antarctic geometry was performed on a simple ice sheet model (Ruckert et al., 2017). Their ice sheet model uses an idealized parabolic geometry (basal topography and ice thickness), lacks key processes (e.g. MICI), and spatially variable forcings. The study performs a Bayesian calibration via a Markov Chain Monte Carlo method across the 13 model parameters. The model is data-constrained against model-produced past grounded ice volumes estimates, to reproduce the temporal evolution of a state-of-the-art model using a simple fast model. They concluded that given the lack of regional characteristics and certain processes, their idealized Antarctic calibration is particularly low-biased during warm periods.

Glacial cycles simulations of the AIS were conducted using the Parallel Ice Sheet Model (Albrecht et al., 2020a, b). A total of 256 model simulations were conducted at a 16x16 km horizontal resolution in which they factorially explored four model parameters (ice enhancement, basal power law exponent, precipitation scaling factor, mantle viscosity). They scored their model simulations against the PD ice sheet geometry, and paleo extent and ice thickness data from AntICEdat. Using four simulations spun up from 210 ka, they began their ensemble simulations at 125 ka. This produced a 5 kyr adjustment

period into the LIG, where the Antarctic sea-level contribution was simulated to be  $1.0 \pm 2.7$  mESL. These LIG Antarctic estimates are likely a product of their four initializations (Albrecht et al., 2020b). They conclude there was a LGM AIS excess of  $9.4 \pm 4.1$  mESL with a consistent deglaciation after 12 ka. Similar to other studies discussed in this section, uncertainties in the climate forcing are inadequately explored. They presume the same prescribed past climate forcing in all their simulations, which could explain why their deglacial timing is consistently after 12 ka.

An ensemble with 632 members of ice sheet simulation using PISM was conducted to study the deglaciation (Pittard et al., 2022). The model considered four distinct climate scenarios and explored four ensemble parameters. They scored their model reconstructions against observations of past ice extent and thickness compiled in the Reconstruction of AIS Deglaciation (RAISED) consortium (Bentley et al., 2014), supplemented by ice thinning rates (Small et al., 2019), and the PD ice sheet geometry (Fretwell et al., 2013). Pittard et al. (2022) presents their 10 best-scoring simulations relative to which parameter combination was used. A narrow range of chronologies over the deglaciation is produced using their distinct climate scenarios ranging from 10.9 to 14.1 mESL. These chronologies exhibit similar behaviours and trends with respect to the timing of the deglaciation and LGM ice extent and maximum ice volume. Given their best-scoring simulations all exhibit similar characteristics, it highlights the limited degrees of freedom in their climate forcing and parameterizations in the analysis.

The research in this thesis partially builds on the previous work initiated by (Briggs and Tarasov, 2013; Briggs et al., 2014). They developed upon and configured the PSU-ISM (Pollard and DeConto, 2009), termed the Pollard Higher Order Model (PHOM) for a

large-ensemble data-constrained analysis of the AIS (Briggs et al., 2013). PHOM consists of many model parameters (31 ensemble parameters) with the intended purpose of fully exploring uncertainties which are inherent in the Antarctic ice sheet system. A subsequent study focused on the methodology involved in evaluating model-derived chronologies using paleo observational constraints (Briggs and Tarasov, 2013). An observational database termed AntICEdat was compiled to constrain the past AIS evolution. The database consists of the present-day ice sheet geometry, past ice thickness, ice extent, and RSL observations. Briggs and Tarasov (2013) use observational error models and data-weighting to evaluate model reconstructions with respect to a heterogeneous observational dataset. The model output is scored by calculating the data-weighting adjusted data-model misfits using a Gaussian error model. A large-ensemble data-constrained analysis of the AIS was then conducted (Briggs et al., 2014). A total of 31 ensemble parameters were used to capture uncertainties in the climate forcing, ice dynamics, and ice-ocean interactions. The aforementioned methodology to evaluate data-model misfits was implemented to score each respective model reconstruction. They performed 3344 model simulations and sieved them by misfit score to extract a best-fitting sub-ensemble. A comparison of the best-fitting sub-ensemble to the constraint database illustrated several outstanding discrepancies unresolvable by parametric sampling. This suggested that the preliminary ensemble is likely not bounding reality even given its 31 ensemble parameters of the PHOM. These notable misfits motivated the development of the GSM such that a large ensemble would adequately encapsulate the paleo and present-day observations. A data-model comparison to present-day observations from Briggs, Pollard and Tarasov (2014) demonstrated a number of discrepancies where ice thickness was over or underestimated in topographically

complex regions. The reconstructed grounding line were mostly within 1 grid cell except for the Ronne shelves and Lambert-Amery ice shelf considering they were coarsely resolved by the 40 by 40 km grid. The present-day surface velocity misfits were large in the tributaries and ice streams and attributed to the coarse model resolution with respect to these features.

For the paleo-data model comparison, there were relative few misfits to the RSL observations which were not encapsulated by the ensemble, except for the South Shetland Islands, where the sea-level high-stand around 8 ka is consistently under-predicted. Past elevation data show large data-model misfits, which are often in areas where present-day misfits are greatest. Even the full ensemble has significant misfits in the Ross Sea Sector. Finally, past extent data demonstrate large data-model discrepancies along the Antarctic Peninsula and Wilkes-Victoria Land sector and these have been affiliated with a sticky grounding line (Briggs et al., 2014). The large-ensemble analysis has shown that PHOM likely had inadequate range of grounding line migration in certain sectors as well as persistent ice thickness biases in topographically complex regions.

The majority of past reconstructions of the AIS deglaciation have relied on the hand-tuning of glaciological models (Denton and Hughes, 2002; Huybrechts, 2002; Philippon et al., 2006; Pollard and DeConto, 2009; Golledge et al., 2012; Gomez et al., 2013; Golledge et al., 2014; Gomez et al., 2020). Other studies explore an extremely limited parameter space with a rigid climate forcing (Pollard et al., 2015; Chang et al., 2016, 2019; Albrecht et al., 2020a, b; Pittard et al., 2022). We build on the initial work of Briggs et al. (2014), switch to the GSM, conduct extensive model development, expand the observational

constraint database and push towards a HMA to provide robust bounds on Antarctic evolution.

## 1.7 Glacial Systems Model

This section consists of a summary of the Glacial Systems Model (GSM). A complete detailed description of the GSM is found in Tarasov et al. (submitted). A series of major developments were implemented in the GSM to simulate the AIS. The necessary developments, verifications, and validations for the GSM to be suited for the Antarctic domain are found in the Supplementary Section for Chapter 1.

The following model developments were conducted: 1) hybrid ice physics; 2) subgrid GL parameterization; 3) dual power basal drag; 4) hydrofracturing and cliff failure; 4) sub shelf melt parameterization that depends on regional ocean temperature; 5) subgrid pinning point scheme; 6) expanded degrees of freedom in the climate forcing; 7) sampling of alternate Earth rheology models for the glacial isostatic adjustment component; and 8) updated initial and boundary conditions.

### 1.7.1 Ice sheet component

#### 1.7.1.1 Hybrid physics

The ice mechanical dynamical core from the PSU-ISM (Pollard and DeConto, 2007, 2009, 2012) was extracted, converted to Fortran 90 standard, rendered modular and fully coupled in the GSM. The PSU-ISM dynamics involve hybrid ice physics, allowing cold/warm-based ice, ice streams, and ice shelves using both shallow ice and shallow shelf/stream regimes (SIA-SSA equations). The physics of hybrid SIA-SSA ice flow are

rigorously described in Pollard and Deconto (2012). Glen's flow law relates stresses of the ice to their strain rates (i.e. velocities), which represents the non-linear viscous flow of ice. The viscosity of ice depends on the temperature of the ice through the Arrhenius coefficient (Cuffey and Paterson, 2013). The thermodynamics of the ice are solved using the finite volume solver of the GSM (Tarasov and Peltier, 1999) given vertical diffusion, 3D advection, internal frictional heating, and boundary fluxes. All these terms depend on ice dynamics, which exhibits the iterative methodology required in solving this system of equations using a coupled thermo-mechanical solver. The model efficiency is increased significantly by limiting the shallow shelf flow to regions with low basal drag, above a certain threshold the regime is purely that of the shallow ice approximation (SIA) (Pollard and DeConto, 2007, 2009; Pollard and Deconto, 2012). This arises due to the high cost of calculating shallow shelf approximation (SSA) flow which requires iteratively solving for non-linear strain-softening terms. The GSM spends most of its time solving sparse matrices, such as those defined by the discretized non-linear strain-softening terms of the SSA equations. To improve performance a sparse matrix solver module (nspcg) was incorporated in the dynamic core by Lev Tarasov who also carried out extensive subsequent optimization.

#### 1.7.1.2 Grounding line scheme

At the GL and ice streams a combination of flow regimes exists (Pollard and DeConto, 2007, 2009, 2012). In the case of the GL, a parameterization based on boundary layer theory is applied (Schoof, 2007; Tsai et al., 2015). It was shown that capturing GL migration involves either highly resolving the grounding zone or placing an analytical

constraint on the flux across the GL. Furthermore, the Marine Ice Sheet Model Intercomparison Project demonstrated the relative validity between the two schemes for steady state and transient responses of the GL given a perturbation (Pattyn et al., 2012a; Drouet et al., 2012). The GSM applies the latter, where the flux depends on longitudinal stress, ice thickness, and sliding coefficient at the GL (Schoof, 2007; Tsai et al., 2015). The analytically determined ice flux at the GL is obtained at the GL using a subgrid interpolation scheme, which yields a depth-averaged velocity at the GL which is subsequently imposed in the shelf flow equations. The power law derived subgrid GL flux parameterization implementation was taken from the PHOM. The GSM has the ability to switch between two different subgrid GL flux parameterizations, a Weertman basal deformation power law derivation (Schoof, 2007) and a coulomb basal deformation-based parameterization (Tsai et al., 2015). There are some limitations in using a subgrid GL flux scheme as compared to an AIS model that highly resolves the GL, particularly with regards to a buttressing ice shelf and its impact on the GL (Reese et al., 2018). The latest version of the GSM uses a revised GL treatment which rectifies this issue (Pollard and DeConto, 2020).

#### 1.7.1.3 Dual power law drag scheme

The community consensus regarding subglacial sediment deformation for glaciers is leaning towards Coulomb plastic rheologies (Cuffey and Paterson, 2013), although it might not apply for continental scale ice sheets (Tulaczyk, 2006). The grounding line flux parameterization previously implemented in the model was only defined for power law basal rheologies (Schoof, 2007). For this reason, the model uses a warm-based basal drag

power law parameterization (Pollard and DeConto, 2007, 2009, 2012). The basal drag beneath floating ice shelves is negligible. For cold-based ice, when basal temperatures are below the pressure melting point, the basal drag is large to simulate ice frozen at the bed. For temperate warm-based ice, slip conditions emerge. When the ice is flowing over hard bedrock, basal stresses are described using a power-law friction scheme (Weertman, 1957):

$$v_b = C' |\tau_b|^{m-1} \tau_b \quad (1)$$

The basal drag coefficient  $C$  encapsulates the underlying physics of the interface. The basal stress is represented by  $\tau_b$  and the basal power-law exponent is shown as  $m$ . The basal drag coefficient is dependent on the temperature, hydrology, basal roughness, and whether the ice is floating or rests atop glacial till or bedrock. Our chosen basal drag coefficient scheme is generally based on Pollard et al. (2015). The temperature dependency is expressed as a transition from no-slip frozen to warm-based basal conditions:

$$C' = (1 - r)C_f + rC \quad (2)$$

$$C = \begin{cases} C_s, & \text{for sediment regions} \\ C_h, & \text{for hardbed regions} \end{cases} \quad (3)$$

$$r = \frac{T + T_{sd}}{T_{sd}}, \text{ for } 0 < r < 1 \quad (4)$$

The no-slip frozen bed basal drag coefficient  $C_f$  is quite small but non-zero for numerical reasons and where  $T$  is the pressure-corrected temperature. The ‘effective basal roughness’ dependence is represented by  $T_{sd}$ . Basal roughness indices are proportional to the basal topographic subgrid standard deviation ( $h_{bsd}$ ) and so  $T_{sd} = \max(3, 0.02 * h_{bsd})$ .

The basal environment is poorly accessible, and the basal drag coefficient incorporates various missing underlying physics that are uncertain, ill defined, and/or

unresolved. Therefore, the coefficient is commonly inverted from present-day surface velocity or surface elevation (inverse linear basal methods: Larour et al., 2012; Schafer et al., 2013; Gladstone et al., 2014). The basal drag coefficients in the GSM are not inferred using an inversion technique to avoid biasing the model to present-day ice dynamics and opt for a first principle approach described in Chapter 3.

For hard bedrock conditions, the basal exponent was historically chosen to be quartic to represent regelation and enhanced creep flow over an impermeable rough bedrock where the prevailing controlling obstacles are cubical bumps - where regelation and enhanced creep flow are jointly inefficient and maximize resistance to sliding. ( $m=3$ ; Schoof, 2007; Gudmundsson et al., 2012; Pattyn et al., 2012b; Weertman, 1974; Pattyn et al., 2013). Conversely for basal sediment environments, the basal power law exponent is chosen to account for basal till deformation. In the literature various basal till models have been developed (Weertman, 1974; Budd et al., 1979; Schoof, 2005; Gagliardini et al., 2007; Tsai et al., 2015). Traditionally, modelling studies have used linear ( $m=1$ ) till basal drag models (Joughin et al., 2010b; Gillet-Chaulet et al., 2016; Larour et al., 2012; Gladstone et al., 2014). A consensus is beginning to emerge that on small scales deformable saturated till undergoes Coulomb plastic till deformation (Truffer et al., 2000; Tulaczyk et al., 2000; Schoof, 2006; Gagliardini et al., 2007; Bueler and Brown, 2009; Winkelmann et al., 2011). To accommodate both basal rugosity and deformation of the soft till, a basal friction scheme is chosen to characterize either regime (Schoof, 2005; Gagliardini et al., 2007; Tsai et al., 2015; Brondex et al., 2017, 2019). Coulomb-plastic deformation can be effectively represented by a power-law with sufficiently high basal drag exponent (Tulaczyk et al., 2000; Nowicki et al., 2013; Gillet-Chaulet et al., 2016; Joughin et al., 2019). To achieve an

approximately continuous transition between basal regimes the till basal drag exponent is represented by an ensemble parameter ranging between one and seven. The chosen range of till basal drag exponent is supported by more recent Antarctic surface velocity assimilation studies which found better agreement with observations for  $m \geq 5$  (Gillet-Chaulet et al., 2016; Nias et al., 2018; Brondex et al., 2019; Joughin et al., 2019).

#### 1.7.1.4 Ice calving

At present approximately half of Antarctic mass balance is due to iceberg calving (Depoorter et al., 2013). The GSM includes several terms that impact ice calving. The first mechanism is based on the large-scale stress field of the ice where the horizontal strain rate divergence represents surface and basal crevasse propagation at depth and manifests as an iceberg calving rate at the margin (Winkelmann et al., 2011; Levermann et al., 2012; Pollard and Deconto, 2012b; Pattyn, 2017).

Another calving term is based on hydrofracturing of ice (Nick et al., 2010, 2013; Pollard et al., 2015). Hydrofracturing occurs where surface meltwater or rain drains into crevasses and contributes to the strain rate divergence of the ice. This further propagates the crevasses which promotes iceberg calving. Another calving term arises from ice cliff failure (Pollard et al., 2015). A tall unstable vertical ice cliff will undergo calving if there remains an unbalanced horizontal stress gradient. When the overburden weight exceeds the yield strength of the ice, the ice cliff collapses/calves (Bassis and Walker, 2012; Bassis and Jacobs, 2013; Pollard et al., 2015). The GSM includes a threshold ice shelf thickness term of 200 m to prevent thin sprawling ice shelves. This produces PD ice shelves which are

similar to those found across the PD AIS. Moreover, ice shelves that extend beyond the continental shelf break undergo total calving.

#### 1.7.1.5 Sub ice shelf mass balance and sea level forcing

The Antarctic ice sheet predominantly loses mass from the ice shelves, either by calving at the ice margin or sub-ice-shelf melting (Rignot et al., 2013; Depoorter et al., 2013; Liu et al., 2015). The GSM calculates sub-ice-shelf mass balance via an ocean temperature dependent parameterization at the ice-ocean interface (Lazeroms et al., 2019). There are three aspects to sub-ice-shelf mass balance: there can be mass loss at the ice front surface, there can be sub-ice-shelf melt (SSM) or refreezing beneath the ice shelves and/or at the grounding line. The SSM calculations are based on a buoyant plume model as a function of basal ice slope, ice depth, and ocean temperature near the GL (Tarasov et al., submitted). The ocean temperature forcing in the GSM is based on transient TRACE-21ka simulations (He, 2011) which are PD bias corrected by Estimating the Circulation and Climate of the Ocean (ECCO) reanalysis ocean temperatures (Fukumori et al., 2017). The ocean surrounding Antarctica is divided in six distinct marine sectors from which ocean temperature profiles are extracted for the Ross Sea sector, Amundsen Sea sector, Antarctic Peninsula, Weddell Sea sector, Amery ice shelf basin, and East Antarctic coast (Dronning Maud Land, Wilkes-Victoria coast). The ocean temperature profiles are extrapolated beneath the ice shelves with a cut off defined by the minimum sill height when dealing with deeper marine basins. This defines the ocean temperatures that are propagated to the ice-ocean interface. Additional ensemble parameters are present in this scheme to account for

the lack of horizontal advection water beneath ice shelves and the limited range in ocean temperature forcing.

The marine benthic foraminifera stack represents a proxy for deep ocean temperatures and global grounded ice volume (Lisiecki and Raymo, 2005). Within the GSM, the benthic stack and RSL observations drive the far-field global sea-level forcing (Lambeck et al., 2014).

#### 1.7.1.6 Sediment distribution

Grounded Antarctic ice rests atop either hard bedrock and/or a till sediment layer which has significant consequences on ice dynamics. The largest glaciers and ice streams on Earth are currently located in Antarctica where warm-based ice is flowing over and deforming a till substrate (Studiver et al., 2001; Cuffey and Paterson, 2010). Therefore, designating the basal fraction of a given model grid cell covered in till, the till fraction, is critical in producing various ice sheet features in the past, present, and future.

The two most common techniques for designating the till fraction beneath an ice sheet are elevation based (Studiver et al., 2001; Pollard and DeConto, 2009; Martin et al., 2011) and inversion schemes (Pollard and DeConto, 2012; Larour et al., 2012; Cornford et al., 2013; Gladstone et al., 2014; Yu et al., 2017; Albrecht et al., 2020a). The former generally postulates that marine basins and ice stream fjords below sea level consists of loose till material and above continental bedrock. This has been progressively expanded, prior to large-scale glaciation across Antarctica (>35Ma), the topography was in glacial isostatic equilibrium, areas below sea-level then encompass the most probable paleo marine sediment sectors (e.g. Studiver et al., 2001). Originally submarine basins were likely soft

limestone as opposed to hard igneous/metamorphic continental bedrock, meaning these sectors were more likely to produce soft sediment when glacially eroded. Over the course of many Quaternary glaciations, the growth and decay of the ice sheet has transported sediments from elevated continental bedrock to marine sectors. Pronounced PD features underpinning the ice sheet have survived the erosion from successive glaciations and are thereby predominantly hard bedrock features.

Inversion schemes involve using PD surface velocity or ice thickness data then inverting for basal drag coefficients or till friction angles (Pollard and Deconto, 2012; Larour et al., 2012; Cornford et al., 2013; Gladstone et al., 2014; Yu et al., 2017; Albrecht et al., 2020a). The basal drag effectively integrates the basal stresses for a given grid cell produced by ice flowing over hard bedrock and/or till. This depends on the extent to which the basal ice is warm and/or cold-based, the fractional area of a grid cell that is pinned by subgrid features, and basal hydrology (Cuffey and Paterson, 2010). The inversion schemes extract individual basal drag coefficients or till friction angles for each grid cell to represent all these poorly constrained PD basal conditions. This method unsurprisingly achieves the strongest model fits to present day geometries given PD boundary conditions are assimilated to initialize key model components/parameters (Seroussi et al., 2019). If specific considerations are not made to account for this PD bias on the state of the basal environment, the model runs the risk of overfitting to the PD ice sheet hampering its ability to hindcast/forecast change.

This research involves transient simulations over two glacial cycles with the goal of bracketing past and present changes. Therefore, to maximize the model's retrodictive capabilities we opt for a first principle approach of a fully unloaded glacial isostatic

equilibrium sea-level threshold scheme. The overlaying ice or water column is removed and an isostatic equilibrated topography is calculated using the density ratio between ice or sea water ( $\rho_o = 910 \text{ kg/m}^3$ ;  $\rho_o = 1028 \text{ kg/m}^3$ ) to mantle material ( $\rho_o = 3300 \text{ kg/m}^3$ ). This leads to bedrock being elevated by  $\sim 700$  m in the interior of the ice sheet while the margins experience a shift of  $\sim 300$  m. In addition to GIA, dynamic topography from mantle dynamics and tectonics produces topographic changes that are spatially variable and of considerable magnitudes (Austermann et al., 2015, 2017). When allowing for uncertainties in dynamic topography on timescales of  $\sim 35$  Myr, it cumulatively impacts the range of viable sea-level elevation thresholds for determining likely subglacial sediment distributions. The spatial variability in dynamic topography motivates the use of regional elevation thresholds ranging between  $-300$  to  $-100$  m (Figure S7). The regional thresholds are chosen to clearly delineate deep subglacial troughs/basins and regions of PD fast-moving ice (e.g. surface velocity exceeding  $400$  m/yr) that are expected to have loose till subglacial material based on first principles. The thresholds are further constrained by PD pinning points and local topographic maxima which are properly classified as hard bedrock and compact/denser sediment. Further details are found in the Supplementary Section for Chapter 1 (Figure S1.7) and Chapter 3.

Upon conducting an ensemble of simulations, outstanding ensemble-wide misfits with the PD ice thickness may reflect the misattribution of the basal till fraction. By identifying regions that are consistently too thick with respect to PD as compared to a full ensemble, this could be due to the bed being till rather than hard bedrock. Conversely, regions that are too thin across the full ensemble can be attributed to till grid cells that should potentially be hard bedrock. Based on an ensemble-wide PD misfit map, an updated

till fraction field can be inferred which acts as a first-order correction to the basal till fraction field to improve fits to PD ice thickness data. Using both the original till fraction map inferred on first principles and the first-order correction, an ensemble parameter can blend between the two fields to allow a variety of till fraction maps to explore uncertainties in the till fraction beneath the AIS.

#### 1.7.1.7 Subgrid pinning

Ice rises and ice rumples, henceforth referred to as pinning points, affect ice dynamics of the GL and of the upstream catchment area (Favier et al., 2012, 2016; Berger et al., 2016). The freely-floating ice shelves are buttressed across numerous topographical features, some of which are inadequately resolved by the coarse resolution of millennial-scale ice sheet models. Studies investigating the influence of ice shelf pinning points have found that transient ice dynamics and grounding line behaviour are significantly influenced by even small pinning points (Favier et al., 2012, 2016). In the study by Berger et al. (2016), they simulated the impact of an uncharted  $8.6 \text{ km}^2$  pinning point in Dronning Maud Land, East Antarctica. Their updated higher resolution surface velocity map identified a decrease of  $-5.2 \pm 4.5 \text{ m yr}^{-1}$  due to the pinning point. Berger et al. (2016) went on to use BISICLES to invert for basal friction coefficients near the pinning point using the updated velocity field and found an increase of  $2250 \text{ Pa m}^{-1}\text{yr}$ . Omitting the pinning point in subsequent ice sheet simulations using inverse methods found a sea-level contribution difference in the catchment of 10% (Favier et al., 2016). Additionally, a full Stokes ice sheet model evaluating the effect of a pinning point on GL dynamics demonstrated a

buttressing of -0.3 MPa upon pinning (Favier et al., 2012). Here we discuss our subgrid pinning point scheme based on a subgrid statistical parametrization.

The pinning points are important in controlling key ice sheet features across the PD grounding line and ice shelves (Figure S1.8). Pinning points that stabilize a particular GL or ice shelf are often smaller than the model resolution – termed unresolved subgrid features. Furthermore, these subgrid pinning points have been persistent over consecutive glaciations, suggesting they are hard bedrock points of contact with the ice. Therefore, to enhance the subgrid pinning points and identify their hard bed geomorphology, the till sediment fraction (1 = 100% till, 0 = 100% hard bed) is exponentiated. Originally, the till fraction is upscaled from the Antarctic BedMachine native resolution of 500x500 m to 40x40 km and 20x20 km. The upscaling averages, thereby it emphasizes and de-emphasizes certain subgrid pinning point features depending on their scale, geometry, and how they are distributed against the model grid. The subgrid enhancement exponent is varied regionally between 1 to 12 to enhance subgrid features that are currently pinning ice across the present-day ice sheet (Figure S1.8 and S1.9).

To consider the impact of subgrid pinning points, one must first calculate the viable subgrid land area that is able to pin against ice. The raw BedMachine data is upscaled from its native resolution ( $dx_{bm} \cdot dy_{bm}$ ) to the GSM horizontal resolution (40 by 40 km =  $dx_{GSM} \cdot dy_{GSM}$ ). Therefore, the BedMachine basal topography is regridded to the coarser GSM resolution, where each GSM grid cell consists of  $n_{dx \cdot dy}$  BedMachine grid cells.

$$n_{dx \cdot dy} = \frac{dx_{GSM} \cdot dy_{GSM}}{dx_{bm} \cdot dy_{bm}}; n_{40 \cdot 40} = 6400 \quad (5)$$

For each GSM grid cell, a mean ( $hb$ ) and standard deviation ( $hb_{sd}$ ) basal topography is obtained from the  $n_{40 \times 40}$  BedMachine grid cells. Given that the BedMachine data is nominally Gaussian when projected on the GSM grid, a z-score is obtained by considering the height of the water column ( $hw$ ) between the bottom of the ice shelf and the ocean floor.

$$z_{score} = \frac{hw - \frac{\rho_{ice}}{\rho_{sea}} h - hb}{hb_{sd}} \quad (6)$$

$$z_{score} \rightarrow P \quad (7)$$

In this instance the  $z_{score}$  is simply converted to the percentile ( $P$ ) of subgrid topography which protrudes up to the base of the ice. The subgrid area ( $A_{fpin}$ ) in  $\text{km}^2$  which protrudes into the ice is then expressed as such:

$$A_{fpin} = (1 - P) \cdot n_{dx \cdot dy} \cdot dx_{bm} \cdot dy_{bm} \quad (8)$$

This subgrid area does not distinguish between multiple smaller pinning points versus one larger pinning point, nor on the geometry of the pinning points themselves. A fractional pinning point ( $f_{pin}$ ) is then expressed in terms of the subgrid pinning area ( $A_{fpin}$ ) relative to the ensemble parameter  $A_{crit}$ , the critical area at which the ice shelf is fully pinned to the topographical feature.

$$f_{pin} = \min \left\{ \max \left\{ \left( \frac{A_{fpin}}{A_{crit}} \right)^{m_{pin}} \right. \right. \quad (9)$$

$$\left. \left. \begin{matrix} 0 \\ 1 \end{matrix} \right. \right.$$

The exponent  $m_{pin}$  is the attenuation power law exponent parameter of the relative impact of subgrid pinning. For a given critical area  $A_{crit}$ , a large power law exponent implies it takes a significantly larger relative subgrid pinning area to pin the ice shelf. Based on the

right-hand-side (RHS) of equation 2a from Pollard and Deconto, (2012), the attenuation of the SSA horizontal stretching term due to subgrid pinning is shown as:

$$RHS = \rho_i g h \frac{\partial h_s}{\partial x} + \frac{f_{pin}}{C^m} |u_b^2 + v_b^2|^{\frac{1-m}{2m}} u_b \quad (10)$$

#### 1.7.1.8 Subgrid topography

Regions that are topographically complex are often not adequately resolved and the resulting ice dynamics due to high roughness features such as deep valleys yielding thicker subgrid warm-based ice with high basal ice stresses and velocities are misrepresented. This manifests in topographically complex basal regions developing excess ice due to the persistence of slow moving cold-based ice in model simulations. This was an apparently issue in the Transantarctic Mountains and Antarctic Peninsula where the modelled mountain chain failed to resolve the countless glaciers flowing across the region. To explore and partly address this issue, the BedMachine version 2 basal topography was upscaled to the GSM grid. Then by leveraging the subgrid standard deviation basal topography ( $hb_{sd}$ ), the width of the basal-temperature ramp is accordingly modified to enable an earlier transition to warm-based ice in topographically complex region, as expressed in equation 12a of Pollard and DeConto (2012).

## 1.7.2 Atmospheric climate component

The climate forcing over glacial cycles is one of the most poorly constrained components of the system (atmospheric temperatures and precipitation, ocean temperatures). For a large-ensemble analysis, the coupling of a regional climate model with the general circulation model is too computationally expensive. Therefore, a climate

forcing parameterization is implemented based on three temperature and precipitation fields merged through ensemble weighing which yields a blended climate field. The various climate fields use a glacial index scheme based on the isotope ratios from the EPICA ice core time series (Figure 1.8).

The first climate scheme uses a fully parameterized approach derived from PD monthly climatologies (RACMO 2.3p2; Melchior Van Wessem et al., 2018) which leverages the relationship between latitude, longitude, and elevation to modify the climatologies. The precipitation field is further modified by elevation controls to prevent significant precipitation at high elevations. Another climate scheme is based on PD monthly climatologies across Antarctica (RACMO 2.3p2; Melchior Van Wessem et al., 2018) and LGM Paleo-Modelling Intercomparison Project III climatologies (PMIP3; Braconnot et al., 2012). The climate forcing is reconstructed back in time based on the PD and LGM climatologies using the EPICA glacial index. The final atmospheric climate scheme is based on a coupled energy balance model using top of atmosphere insolation constrained by glacial-interglacial temperature change inferred by Antarctic ice cores. The blended climatologies through time are subsequently passed to a positive degree day mass balance scheme. This approach is conducted to avoid a heavy reliance on a single atmospheric climate forcing parameterization and to better account for uncertainties in past climate.

### 1.7.3 Solid Earth component

GIA estimates are typically evaluated using a spherically symmetric Earth density and viscosity structure. This remains an efficient means of simulating GIA, yet it is significantly more sophisticated than the commonly applied elastic lithosphere relaxed

asthenosphere GIA component often found in ice sheet models (Albrecht et al., 2020a). However, the lack of lateral Earth structure, specifically heterogeneity in viscosity, impacts the GIA response and the resulting sea-level predictions (Milne et al., 2018). It is unfeasible to couple GIA model with lateral Earth structure to an ice sheet model for large ensemble analysis (Gomez et al., 2018). The GSM deals with bedrock elevation changes due to the redistribution of surface loads using a GIA component based on a spherically symmetric viscoelastic gravitationally self-consistent Earth model (Tarasov and Peltier, 2004). The earth rheology is based on a three-shell viscosity structure and the density structure is based on preliminary reference Earth model (PREM; Dziewonski and Anderson, 1981). The GSM is a synchronously coupled to the GIA component where the bedrock displacement is calculated every 100 years.

The geothermal heat flux acts as a crucial basal boundary condition. It can be directly measured from basal temperature measurements in ice cores (Pattyn, 2010), which are sparse. Therefore, to broaden the uncertainties on the geothermal heat flux fields, a linear combination of two fields are blended together with an ensemble parameter (weight). One of the geothermal heat flux fields is based on a seismic model of the crust and upper mantle to extrapolate between observations (An et al., 2015) while the other is estimated using satellite-measured magnetic data (Martos et al., 2017).

## 1.7.4 Model configuration and parameters

In its current state the GSM configured for the Antarctic domain consists of 38 ensemble parameters to capture uncertainties in the glacial cycle climate, ice mass-balance processes, ice dynamics, and glacial isostatic adjustment. The ensemble parameters and

their ranges are determined by investigating their sensitivities with respect to key metrics, past studies, or stress testing. The model uses a finite-difference Arakawa-C grid scheme with a horizontal resolution of 40 by 40 km, while the vertical consists of 10 unevenly spaced layers for ice dynamic calculations and 65 vertical layers for thermodynamic calculations. The model has adaptive time steps in the event of numerical instabilities which allow the GSM to revert to a previous state with a refined time-step.

Considering we aim to constrain the GSM over the last glacial cycles, a simulation start time at 205 ka was found to be adequate given it is a period when sea level and AIS volume were comparatively close to present-day. Additional experiments evaluating initialization at 391 ka showed minimal impact on simulation results over the last glacial cycle. The GSM is initialized with self-consistent boundary conditions (basal topography, ice thickness, internal ice velocity and temperature fields, geothermal heat flux). The Antarctic ice sheet is located at the south pole, therefore, the GSM was updated to cope with a polar stereographic projection. This involves establishing a polar stereographic grid and domain with polar stereographic to/from latitudinal longitudinal transformations for coupled GIA calculations.

## 1.8 History-Matching Analysis

To understand the evolution of a complex system, it is important to understand that we are dealing with imperfect models and data. The common practice of explicitly focussing solely on a narrow set of best-fitting model simulations that disregard structural uncertainties can lead to completely wrong inferences of past ice sheet changes. Moreover, researchers have implicit biases and motivations meaning it is important to minimize

subjective hand-tuning of models and ambiguous uncertainty estimates. The research in this thesis consists of combining a model with data to bound the evolution of the system using a history-matching methodology. A comprehensive description of a HMA can be found in Tarasov and Goldstein (2021) and an overview is provided below.

The primary aim of this research is to infer and bound the paleo history of the Antarctic ice sheet by performing a HMA. Moreover, a benefit of a HMA is that it represents a crucial stepping stone to a more comprehensive Bayesian calibration of the GSM. A Bayesian model calibration generates confidence intervals of model output. While a HMA of a model provides minimum and maximum bounds on the system based on ruling out simulations that are unequivocally inconsistent with the available observational constraints.

Once the Antarctic configuration of the GSM was established, physical reasoning, literature, and previous experimentation established preliminary bounds on the prior distribution of the model ensemble parameters. The prior parameter ranges were expanded rather than use marginally truncated ranges to avoid excluding any pertinent portions of the parameter space. To minimize the number of assumptions made about the structure of the ensemble parameters, uniform or quadratic distributions are initially applied. Firstly, to explore the Antarctic GSM configuration, a Latin hypercube (LHC) sampling of the parameter space is conducted, then simulated using the GSM. This represents the opening exploration of the 38 ensemble parameter phase-space of the GSM which entailed thousands of simulations to initially populate the operational space of the model. The LHC sampling of uniform distributions included marginally justifiable and unlikely end-member parameter choices. The ice sheet modelling literature and previous modelling experiments

propose more likely parameter values and ranges which should be sampled more extensively. This motivates an initial perturbation of the prior uniform distributions of the ensemble parameters to ones that crudely favour the lower, upper, or middle quartile range. Another LHC sampling of the updated prior distributions is conducted to populate more relevant portions of the parameter space.

An ensemble of several thousand members was generated and evaluated to assess model performance. It is critical to verify that the ensemble of model simulations bracket the observational constraints. The goal of the model calibration is not to replicate reality but to effectively bracket the past evolution of the actual system. The aim is to have reality fall within model ensemble output given uncertainties. If large swaths of the data are not bracketed by a random exploration of the parameter space, then this suggests the model will be unable to capture the observations regardless of parameter choices. This would imply that any resulting model ensemble output would not encapsulate “reality”, directly limiting the usefulness of any model calibration results. In such instances, one should revise their model configuration, conduct model development, and/or broaden degrees of freedom in the appropriate components. During the development of the Antarctic GSM configuration, several iterations of model development were conducted to rectify this issue. Some of the model development conducted over the course of this research included revising the sediment till distribution, pinning point scheme, basal drag scheme, calving scheme, ocean forcing scheme, and updating/broadening a variety of initial and boundary conditions (see Section 1.7). After each major model development iteration, a new wave of LHC sampling was conducted to evaluate the new configuration given the previous ensembles are rendered disassociated from the latest model configuration.

When the model ensembles sufficiently bracket the observations, each simulation in the ensemble is reduced to key metrics and scores. The data-model scores are used to evaluate the performance of individual simulations. The cumulative ensemble metrics and scores are sieved for given thresholds to identify the best performing simulations. Initially the thresholds are adjusted so that the best-performing sub-ensemble consists of approximately the same number of simulations as model parameters to guarantee meaningful statistics. The parameter selections of the best-performing sub-ensemble are then applied to fit beta distribution parameters for each ensemble parameter. Beta distributions are chosen since they can accommodate a wide variety of distribution shapes. The resulting beta distributions for each ensemble parameter are then sampled to generate another large ensemble of simulations which populate more performative parameter choices. Each new ensemble is reduced to metrics and scores and appended to the full cumulative ensemble dataset. The updated cumulative ensemble is then filtered down to fit updated beta distribution parameters. This leads to the iterative process where the updated beta distributions are resampled to generate a new ensemble. The updated cumulative ensemble is then filtered down again with tightening thresholds to improve the ensemble parameter beta distributions and build density in regions of the parameter space which yield simulation results that are more consistent with the observations.

Doing this process iteratively samples promising portions of the parameter space. However, it remains a narrow exploration of the entire parameter phase-space considering the factorial exploration of each parameter five times would involve  $5^{36}$  simulations, which is computational intractable. Furthermore, this approach can lead to a local minimum in the misfit score which disregards distinct and alternate data-model misfit minima in the global

parameter phase-space. To circumvent this issue and rapidly explore broader portions of the parameter space, the full history-matching iterations were implemented with a supervised machine learning framework (Neal, 2012) and sampled via Markov Chain Monte Carlo (MCMC) sampling.

The supervised training of Bayesian Artificial Neural Networks (BANNs) with GSM output produces an GSM emulator. The BANNs aim to emulate the inherent non-linearity of the glacial system. The BANNs are akin to a pseudo non-linear multidimensional regression model, which is orders of magnitude faster than individual GSM simulations. The GSM emulators are capable of rapidly exploring the parameter space and ultimately propose regions of the parameter space worth assessing with explicit GSM simulations. To produce effective emulators, it is important to carefully explore a variety of BANN architectures. Certain BANNs can be tailored for specific targets and their architecture can be adjusted to maximize performance. The best-fitting sub-ensemble which includes metrics, scores and model parameters is divided simulation-wise into training and testing sets for cross validation. As more GSM simulations are performed, they can be used for further BANN training to improve performance. The iterative procedure between GSM simulations and artificial neural network training eventually produces a sub-ensemble of AIS chronology which exhibits consistency with the observational constraint database.

The sampling of ensemble parameters is performed through MCMC sampling. The MCMC scheme uses a truncated slice sampling algorithm. This represents a random walk through the parameter space, where each step is weighed by the nominal posterior probability of a given set of proposed ensemble parameter (parameter vector). A set of

converged MCMC chains reveal the nominal posterior probability distribution with best-fitting regions of the parameter phase-space more heavily sampled. In search of the global minimum in the data-model misfit scores and to evade potential local minima, the MCMC scheme will take chances (accept or reject) on any subsequent step even if it does not immediately lead to better scores. It is through this sampling scheme that the parameter space can be efficiently mapped. Given that the glacial system is a complex non-linear system with high dimensionality, improving the chance of identifying the global minimum is achieved by initializing many MCMC chains across dispersed parameter vectors.

The model simulations making up the full ensemble are compared to the observation constraint database. The simulations are either ruled out as being inconsistent with the constraint database given a  $4\sigma$  or  $3\sigma$  threshold or they are classified as Not-Ruled-Out-Yet (NROY) by the data. The NROY sub-ensemble constitutes a state space estimation of the system that is sufficiently consistent with the observations that it should, in its entirety, bracket the past evolution of the actual system. The resulting NROY sub-ensemble yields minimum and maximum bounds on the Antarctic LIG, MWP-1a, and LGM contributions. Moreover, the NROY sub-ensemble includes bounds on the AIS chronology and state of the PD AIS. These min/max uncertainty ranges on the PD AIS can provide more meaningful estimates when estimating PD Antarctic GIA to re-evaluate contemporary mass balance of the ice sheet or to evaluate the PD thermo-mechanical state of the AIS to investigate the response of the ice sheet to contemporary climate change.

## 1.9 Objective and thesis overview

The main goal of this research was to study and bound the evolution of the AIS using data and models. This involved developing the GSM to be suited for Antarctic simulations, with the intended aim to perform a HMA of the AIS since the last interglacial. This included compiling, curating, and recalibrating an Antarctic constraint database for state space estimation and data-model comparison. The final product of the GSM HMA of the AIS is a sub-ensemble of simulations NROY by the observational constraints. The NROY sub-ensemble yields confidence intervals, particular minimum and maximum bounds, on ice sheet evolution in response to past warm and cold periods.

The remaining chapters of the thesis are divided as follows. Chapter 2 is a publication describing the Antarctic ICE sheet database (AntICE2). This represents the second version of the Antarctic constraint database which was dramatically expanded with new data types and significantly more data (from 203 to 1023 paleo observations). Chapter 3 is the primary publication which describes the HMA of the AIS since the last interglacial. It specifically focuses on the ice sheet component and its products during key periods of interest. Chapter 4 is an accompanying publication to Chapter 3 which describes the HMA results of the Antarctic GIA component. This chapter focuses on past and present vertical land motion and sea-level change. Finally, the conclusion relates the key findings from the studies directly to the research questions discussed in Section 1.5. The thesis is concluded with an overview of future research ideas and immediate applications of Antarctic HMA.

## 1.10 References

- Ackert, R. P., Barclay, D. J., Borns, H. W., Calkin, P. E., Kurz, M. D., Fastook, J. L., and Steig, E. J.: Measurements of Past Ice Sheet Elevations in Interior West Antarctica, *Science* (1979), 286, 276–280, <https://doi.org/10.1126/science.286.5438.276>, 1999.
- Ackert, R. P., Mukhopadhyay, S., Parizek, B. R., and Borns, H. W.: Ice elevation near the West Antarctic Ice Sheet divide during the Last Glaciation, *Geophys Res Lett*, 34, 1–6, <https://doi.org/10.1029/2007GL031412>, 2007.
- Albrecht, T., Winkelmann, R., and Levermann, A.: Glacial-cycle simulations of the Antarctic Ice Sheet with the Parallel Ice Sheet Model (PISM)-Part 1: Boundary conditions and climatic forcing, *Cryosphere*, 14, 599–632, <https://doi.org/10.5194/tc-14-599-2020>, 2020a.
- Albrecht, T., Winkelmann, R., and Levermann, A.: Glacial-cycle simulations of the Antarctic Ice Sheet with the Parallel Ice Sheet Model (PISM)-Part 2: Parameter ensemble analysis, *Cryosphere*, 14, 633–656, <https://doi.org/10.5194/tc-14-633-2020>, 2020b.
- An, M., Wiens, D. A., Zhao, Y., Feng, M., Nyblade, A., Kanao, M., Li, Y., Maggi, A., and L ev eque, J. J.: Temperature, lithosphere-asthenosphere boundary, and heat flux beneath the Antarctic Plate inferred from seismic velocities, *J Geophys Res Solid Earth*, 120, 8720–8742, <https://doi.org/10.1002/2015JB011917>, 2015.
- Argus, D. F., Peltier, W. R., Drummond, R., and Moore, A. W.: The Antarctica component of postglacial rebound model ICE-6G\_C (VM5a) based on GPS positioning, exposure age dating of ice thicknesses, and relative sea level histories, *Geophys J Int*, 198, 537–563, <https://doi.org/10.1093/gji/ggu140>, 2014.
- Arif, M. H. B., Tarasov, L., Hauser, T.: The Climate Generator: Stochastic climate representation for glacial cycle integration. *Geoscientific Model Development Discussions*, 2018, 1-27, 2018.
- Austermann, J., Mitrovica, J. X., Latychev, K., and Milne, G. a.: Barbados-based estimate of ice volume at Last Glacial Maximum affected by subducted plate, *Nat Geosci*, 6, 553–557, <https://doi.org/10.1038/ngeo1859>, 2013.
- Austermann, J., Pollard, D., Mitrovica, J. X., Moucha, R., Forte, A. M., DeConto, R. M., Rowley, D. B., and Raymo, M. E.: The impact of dynamic topography change on antarctic ice sheet stability during the mid-pliocene warm period, *Geology*, 43, 927–930, <https://doi.org/10.1130/G36988.1>, 2015.

- Austermann, J., Mitrovica, J. X., Huybers, P., and Rovere, A.: Detection of a dynamic topography signal in last interglacial sea-level records, 2017.
- Bahadory, T., & Tarasov, L.: LCice 1.0—a generalized Ice Sheet System Model coupler for LOVECLIM version 1.3: description, sensitivities, and validation with the Glacial Systems Model (GSM version D2017. aug17). *Geoscientific Model Development*, 11(9), 3883-3902, 2018.
- Bamber, J. L., Griggs, J. a., Hurkmans, R. T. W. L., Dowdeswell, J. a., Gogineni, S. P., Howat, I., Mouginot, J., Paden, J., Palmer, S., Rignot, E., and Steinhage, D.: A new bed elevation dataset for Greenland, *Cryosphere*, 7, 499–510, <https://doi.org/10.5194/tc-7-499-2013>, 2013.
- Bamber, J. L., Oppenheimer, M., Kopp, R. E., Aspinall, W. P., and Cooke, R. M.: Ice sheet contributions to future sea-level rise from structured expert judgment, *Proc Natl Acad Sci U S A*, 166, 11195–11200, <https://doi.org/10.1073/pnas.1817205116>, 2019.
- Bard, E., Hamelin, B., and Fairbanks, R. G.: U-Th ages obtained by mass spectrometry in corals from Barbados: sea level during the past 130,000 years, *Nature*, 346, 456–458, <https://doi.org/10.1038/346456a0>, 1990.
- Bard, E., Hamelin, B., Arnold, M., Montaggioni, L., Cabioch, G., Faure, G., and Rougerie, F.: Deglacial sea-level record from Tahiti corals and the timing of global meltwater discharge, <https://doi.org/10.1038/382241a0>, 1996.
- Bard, E., Hamelin, B., and Delanghe-sabatier, D.: Deglacial Meltwater Pulse 1B and Younger Dryas Sea Levels Revisited with Boreholes at Tahiti, *Science* (1979), 327, 1235–1238, <https://doi.org/10.1126/science.1180557>, 2010.
- Baroni, C. and Hall, B. L.: A new Holocene relative sea-level curve for Terra Nova Bay, Victoria Land, Antarctica, *J Quat Sci*, 19, 377–396, <https://doi.org/10.1002/jqs.825>, 2004.
- Bassett, S. E., Milne, G. A., Mitrovica, J. X., and Clark, P. U.: Ice sheet and solid Earth influences on far-field sea-level histories., *Science*, 309, 925–928, <https://doi.org/10.1126/science.1111575>, 2005.
- Bassis, J. N. and Walker, C. C.: Upper and lower limits on the stability of calving glaciers from the yield strength envelope of ice, in: *Proceedings of the Royal Society A: Mathematical, Physical and Engineering Sciences*, 913–931, <https://doi.org/10.1098/rspa.2011.0422>, 2012.
- Bassis, J. N. and Jacobs, S.: Diverse calving patterns linked to glacier geometry, *Nat Geosci*, 6, 833–836, <https://doi.org/10.1038/ngeo1887>, 2013.

- Benn, D. I., Hulton, N. R. J., and Mottram, R. H.: “Calving laws”, “sliding laws” and the stability of tidewater glaciers, *Ann Glaciol*, 46, 123–130, <https://doi.org/10.3189/172756407782871161>, 2007a.
- Bentley, M. J., Ó Cofaigh, C., Anderson, J. B., Conway, H., Davies, B., Graham, A. G. C., Hillenbrand, C.-D., Hodgson, D. a., Jamieson, S. S. R., Larter, R. D., Mackintosh, A., Smith, J. a., Verleyen, E., Ackert, R. P., Bart, P. J., Berg, S., Brunstein, D., Canals, M., Colhoun, E. a., Crosta, X., Dickens, W. a., Domack, E., Dowdeswell, J. a., Dunbar, R., Ehrmann, W., Evans, J., Favier, V., Fink, D., Fogwill, C. J., Glasser, N. F., Gohl, K., Golledge, N. R., Goodwin, I., Gore, D. B., Greenwood, S. L., Hall, B. L., Hall, K., Hedding, D. W., Hein, A. S., Hocking, E. P., Jakobsson, M., Johnson, J. S., Jomelli, V., Jones, R. S., Klages, J. P., Kristoffersen, Y., Kuhn, G., Leventer, A., Licht, K., Lilly, K., Lindow, J., Livingstone, S. J., Massé, G., McGlone, M. S., McKay, R. M., Melles, M., Miura, H., Mulvaney, R., Nel, W., Nitsche, F. O., O’Brien, P. E., Post, A. L., Roberts, S. J., Saunders, K. M., Selkirk, P. M., Simms, A. R., Spiegel, C., Stollendorf, T. D., Sugden, D. E., van der Putten, N., van Ommen, T., Verfaillie, D., Vyverman, W., Wagner, B., White, D. a., Witus, A. E., and Zwartz, D.: A community-based geological reconstruction of Antarctic Ice Sheet deglaciation since the Last Glacial Maximum, *Quat Sci Rev*, 100, 1–9, <https://doi.org/10.1016/j.quascirev.2014.06.025>, 2014.
- Berger, S., Favier, L., Drews, R., Derwael, J. J., and Pattyn, F.: The control of an uncharted pinning point on the flow of an Antarctic ice shelf, *Journal of Glaciology*, 62, 37–45, <https://doi.org/10.1017/jog.2016.7>, 2016.
- Bindschadler, R., Vaughan, D. G., and Vornberger, P.: Variability of basal melt beneath the PIG ice shelf, West Antarctica, *Journal of Glaciology*, 57, 581–595, <https://doi.org/10.3189/002214311797409802>, 2011.
- Bird, M. I., Fifield, L. K., Teh, T. S., Chang, C. H., Shirlaw, N., and Lambeck, K.: An inflection in the rate of early mid-Holocene eustatic sea-level rise: A new sea-level curve from Singapore, *Estuar Coast Shelf Sci*, 71, 523–536, <https://doi.org/10.1016/j.ecss.2006.07.004>, 2007.
- Blanchon, P., Eisenhauer, A., Fietzke, J., and Liebtrau, V.: Rapid sea-level rise and reef back-stepping at the close of the last interglacial highstand., *Nature*, 458, 881–884, <https://doi.org/10.1038/nature07933>, 2009.
- Boulton, G. S., Dongelmans, P., Punkari, M., and Broadgate, M.: Palaeoglaciology of an ice sheet through a glacial cycle: The European ice sheet through the Weichselian, *Quat Sci Rev*, 20, 591–625, [https://doi.org/10.1016/S0277-3791\(00\)00160-8](https://doi.org/10.1016/S0277-3791(00)00160-8), 2001.

- Braconnot, P., Harrison, S. P., Kageyama, M., Bartlein, P. J., Masson-Delmotte, V., Abe-Ouchi, A., Otto-Bliesner, B., and Zhao, Y.: Evaluation of climate models using palaeoclimatic data, <https://doi.org/10.1038/nclimate1456>, June 2012.
- Briggs, R., Pollard, D., and Tarasov, L.: A glacial systems model configured for large ensemble analysis of Antarctic deglaciation, *Cryosphere*, 7, 1949–1970, <https://doi.org/10.5194/tc-7-1949-2013>, 2013.
- Briggs, R. D. and Tarasov, L.: How to evaluate model-derived deglaciation chronologies: A case study using Antarctica, *Quat Sci Rev*, 63, 109–127, <https://doi.org/10.1016/j.quascirev.2012.11.021>, 2013.
- Briggs, R. D., Pollard, D., and Tarasov, L.: A data-constrained large ensemble analysis of Antarctic evolution since the Eemian, *Quat Sci Rev*, 103, 91–115, <https://doi.org/10.1016/j.quascirev.2014.09.003>, 2014.
- Brondeux, J., Gagliardini, O., Gillet-Chaulet, F., and Durand, G.: Sensitivity of grounding line dynamics to the choice of the friction law, *Journal of Glaciology*, 63, 854–866, <https://doi.org/10.1017/jog.2017.51>, 2017.
- Brondeux, J., Gillet-Chaulet, F., and Gagliardini, O.: Sensitivity of centennial mass loss projections of the Amundsen basin to the friction law, *Cryosphere*, 13, 177–195, <https://doi.org/10.5194/tc-13-177-2019>, 2019.
- Brunt, K. M., Okal, E. a., and Macayeal, D. R.: Antarctic ice-shelf calving triggered by the Honshu (Japan) earthquake and tsunami, March 2011, *Journal of Glaciology*, 57, 785–788, <https://doi.org/10.3189/002214311798043681>, 2011.
- Budd, W. F., Keage, P. L., and Blundy, N. A.: Empirical Studies of Ice Sliding, *Journal of Glaciology*, 23, 157–170, <https://doi.org/10.3189/s0022143000029804>, 1979.
- Bueler, E. and Brown, J.: Shallow shelf approximation as a “sliding law” in a thermomechanically coupled ice sheet model, *J Geophys Res Solid Earth*, 114, <https://doi.org/10.1029/2008JF001179>, 2009.
- Capron, E., Govin, A., Stone, E.J., Masson-Delmotte, V., Mulitza, S., Otto-Bliesner, B., Rasmussen, T.L., Sime, L.C., Waelbroeck, C. and Wolff, E.W.: Temporal and spatial structure of multi-millennial temperature changes at high latitudes during the Last Interglacial. *Quaternary Science Reviews*, 103, 116-133, 2014.
- Capron, E., Govin, A., Feng, R., Otto-Bliesner, B. L., & Wolff, E. W.: Critical evaluation of climate syntheses to benchmark CMIP6/PMIP4 127 ka Last Interglacial simulations in the high-latitude regions. *Quaternary Science Reviews*, 168, 137-150, 2017.

- Carlson, A. E., LeGrande, A. N., Oppo, D. W., Came, R. E., Schmidt, G. a., Anslow, F. S., Licciardi, J. M., and Obbink, E. a.: Rapid early Holocene deglaciation of the Laurentide ice sheet, *Nat Geosci*, 1, 620–624, <https://doi.org/10.1038/ngeo285>, 2008.
- Carlson, a. E. and Clark, P. U.: Ice Sheet Sources of Sea Level Rise and Freshwater Discharge During the Last Deglaciation, *Reviews of Geophysics*, 50, 1–72, <https://doi.org/10.1029/2011RG000371>, 2012.
- Chang, W., Haran, M., Applegate, P., and Pollard, D.: Calibrating an Ice Sheet Model Using High-Dimensional Binary Spatial Data, *J Am Stat Assoc*, 111, 57–72, <https://doi.org/10.1080/01621459.2015.1108199>, 2016a.
- Chang, W., Haran, M., Applegate, P., and Pollard, D.: Improving ice sheet model calibration using paleoclimate and modern data, *Annals of Applied Statistics*, 10, 2274–2302, <https://doi.org/10.1214/16-AOAS979>, 2016b.
- Chang, W., Konomi, B. A., Karagiannis, G., Guan, Y., and Haran, M.: Ice Model Calibration Using Semi-continuous Spatial Data, 2019.
- Clark, J. a, Farrell, W. E., and Peltier, W. R.: Global changes in postglacial sea level: A numerical calculation, *Quat Res*, 9, 265–287, [https://doi.org/10.1016/0033-5894\(78\)90033-9](https://doi.org/10.1016/0033-5894(78)90033-9), 1978.
- Clark, P. U., Alley, R. B., Keigwin, L. D., Licciardi, J. M., Johnsen, S. J., and Wang, H.: Origin of the first global meltwater pulse following the Last Glacial Maximum, *Paleoceanography*, 11, 563, <https://doi.org/10.1029/96PA01419>, 1996.
- Clark, P. U., Mitrovica, J. X., Milne, G. a, and Tamisiea, M. E.: Sea-level fingerprinting as a direct test for the source of global meltwater pulse IA., *Science (1979)*, 295, 2438–2441, <https://doi.org/10.1126/science.1068797>, 2002.
- Clark, P., Dyke, A., Shakun, J., Carlson, A., Clark, J., Wohlfarth, B., Mitrovica, J., Hostetler, S., and McCabe, M.: The Last Glacial Maximum, *Science (1979)*, 325, 710–714, <https://doi.org/doi:10.1126/science.1172873>, 2009.
- Clark, P. U., Shakun, J. D., Baker, P. A., Bartlein, P. J., Brewer, S., Brook, E., Carlson, A. E., Cheng, H., Kaufman, D. S., Liu, Z., Marchitto, T. M., Mix, A. C., Morrill, C., Otto-Bliesner, B. L., Pahnke, K., Russell, J. M., Whitlock, C., Adkins, J. F., Blois, J. L., Clark, J., Colman, S. M., Curry, W. B., Flower, B. P., He, F., Johnson, T. C., Lynch-Stieglitz, J., Markgraf, V., McManus, J., Mitrovica, J. X., Moreno, P. I., and Williams, J. W.: Global climate evolution during the last deglaciation., *Proc Natl Acad Sci U S A*, 109, E1134-42, <https://doi.org/10.1073/pnas.1116619109>, 2012.

- Clark, P. U. and Tarasov, L.: Closing the sea level budget at the Last Glacial Maximum, <https://doi.org/10.1073/pnas.1418970111>, 11 November 2014.
- CLIP Members: Last Interglacial Arctic warmth confirms polar amplification of climate change, *Quat Sci Rev*, 25, 1383–1400, <https://doi.org/10.1016/j.quascirev.2006.01.033>, 2006.
- Colloni, F., De Santis, L., Siddoway, C. S., Bergamasco, A., Golledge, N. R., Lohmann, G., Passchier, S., and Siegert, M. J.: Spatio-temporal variability of processes across Antarctic ice-bed-ocean interfaces, *Nat Commun*, 9, <https://doi.org/10.1038/s41467-018-04583-0>, 2018.
- Conway, H., Hall, B. L., Denton, G. H., Gades, A. M., and Waddington, E. D.: Past and Future Grounding-Line Retreat of the West Antarctic Ice Sheet, *Science* (1979), 286, 280–283, <https://doi.org/10.1126/science.286.5438.280>, 1999.
- Conway, H., Waddington, E. D., and Price, S. F.: Evidence for late Pleistocene thinning of Siple Dome, West Antarctica, *J Geophys Res*, 112, F03021, <https://doi.org/10.1029/2006JF000725>, 2007.
- Cornford, S. L., Martin, D. F., Graves, D. T., Ranken, D. F., Le Brocq, A. M., Gladstone, R. M., Payne, A. J., Ng, E. G., and Lipscomb, W. H.: Adaptive mesh, finite volume modeling of marine ice sheets, *J Comput Phys*, 232, 529–549, <https://doi.org/10.1016/j.jcp.2012.08.037>, 2013.
- Cronin, T. M., Vogt, P. R., Willard, D. a., Thunell, R., Halka, J., Berke, M., and Pohlman, J.: Rapid sea level rise and ice sheet response to 8,200-year climate event, *Geophys Res Lett*, 34, 1–6, <https://doi.org/10.1029/2007GL031318>, 2007.
- Cuffey, K. M. and Paterson, W. S. B.: *The Physics of Glaciers Fourth Edition*, 2010.
- Cuffey, K. M. and Paterson, W. S. B.: *The physics of glaciers*, [https://doi.org/10.1016/0016-7185\(71\)90086-8](https://doi.org/10.1016/0016-7185(71)90086-8), 2013.
- Dahl-Jensen, D., Albert, M. R., Aldahan, a., Azuma, N., Balslev-Clausen, D., Baumgartner, M., Berggren, a.-M., Bigler, M., Binder, T., Blunier, T., Bourgeois, J. C., Brook, E. J., Buchardt, S. L., Buizert, C., Capron, E., Chappellaz, J., Chung, J., Clausen, H. B., Cvijanovic, I., Davies, S. M., Ditlevsen, P., Eicher, O., Fischer, H., Fisher, D. a., Fleet, L. G., Gfeller, G., Gkinis, V., Gogineni, S., Goto-Azuma, K., Grinsted, a., Gudlaugsdottir, H., Guillevic, M., Hansen, S. B., Hansson, M., Hirabayashi, M., Hong, S., Hur, S. D., Huybrechts, P., Hvidberg, C. S., Iizuka, Y., Jenk, T., Johnsen, S. J., Jones, T. R., Jouzel, J., Karlsson, N. B., Kawamura, K., Keegan, K., Kettner, E., Kipfstuhl, S., Kjær, H. a., Koutnik, M., Kuramoto, T., Köhler, P., Laepple, T., Landais, a., Langen, P. L., Larsen, L. B., Leuenberger, D., Leuenberger, M., Leuschen, C., Li, J., Lipenkov, V., Martinerie, P., Maselli, O. J., Masson-Delmotte,

- V., McConnell, J. R., Miller, H., Mini, O., Miyamoto, a., Montagnat-Rentier, M., Mulvaney, R., Muscheler, R., Orsi, a. J., Paden, J., Panton, C., Pattyn, F., Petit, J.-R., Pol, K., Popp, T., Possnert, G., Prié, F., Prokopiou, M., Quiquet, a., Rasmussen, S. O., Raynaud, D., Ren, J., Reutenauer, C., Ritz, C., Röckmann, T., Rosen, J. L., Rubino, M., Rybak, O., Samyn, D., Sapart, C. J., Schilt, a., Schmidt, a. M. Z., Schwander, J., Schüpbach, S., Seierstad, I., et al.: Eemian interglacial reconstructed from a Greenland folded ice core, *Nature*, 493, 489–494, <https://doi.org/10.1038/nature11789>, 2013.
- DeConto, R. M. and Pollard, D.: Contribution of Antarctica to past and future sea-level rise, *Nature*, 531, 591–597, <https://doi.org/10.1038/nature17145>, 2016.
- Denton, G. H. and Hughes, T. J.: Reconstructing the Antarctic Ice Sheet at the Last Glacial Maximum, *Quat Sci Rev*, 21, 193–202, [https://doi.org/10.1016/S0277-3791\(01\)00090-7](https://doi.org/10.1016/S0277-3791(01)00090-7), 2002.
- Denton, G. H., Anderson, R. F., Toggweiler, J. R., Edwards, R. L., Schaefer, J. M., and Putnam, E.: The last glacial termination., *Science*, 328, 1652–1656, <https://doi.org/10.1126/science.1184119>, 2010.
- Denton, G. H., Toucanne, S., Putnam, A. E., Barrell, D. J., & Russell, J. L.: Heinrich summers. *Quaternary Science Reviews*, 295, 107750, <https://doi.org/10.1016/j.quascirev.2022.107750>, 2022.
- Depoorter, M. A., Bamber, J. L., Griggs, J. A., Lenaerts, J. T. M., Ligtenberg, S. R. M., Van Den Broeke, M. R., and Moholdt, G.: Calving fluxes and basal melt rates of Antarctic ice shelves, *Nature*, 502, 89–92, <https://doi.org/10.1038/nature12567>, 2013.
- Deschamps, P., Durand, N., Bard, E., Hamelin, B., Camoin, G., Thomas, A. L., Henderson, G. M., Okuno, J., and Yokoyama, Y.: Ice-sheet collapse and sea-level rise at the Bølling warming 14,600 years ago, *Nature*, 483, 559–564, <https://doi.org/10.1038/nature10902>, 2012.
- Drouet, a. S., Docquier, D., Durand, G., Hindmarsh, R., Pattyn, F., Gagliardini, O., and Zwinger, T.: Grounding line transient response in marine ice sheet models, *The Cryosphere Discussions*, 6, 3903–3935, <https://doi.org/10.5194/tc-7-395-2013>, 2012.
- Dutton, a. and Lambeck, K.: Ice Volume and Sea Level During the Last Interglacial, *Science* (1979), 337, 216–219, <https://doi.org/10.1126/science.1205749>, 2012.
- Dutton, a, Carlson, A., Long, A., Milne, G., Clark, P., DeConto, R., Horton, B., Rahmstorf, S., and Raymo, M.: Sea-level rise due to polar ice-sheet mass loss during past warm

periods, *Science* (1979), 349, 153 aaa4019–1, <https://doi.org/10.1126/science.aaa4019>, 2015.

Dyke, A. S.: An outline of North American deglaciation with emphasis on central and northern Canada, *Developments in Quaternary Science*, 2, 373–424, [https://doi.org/10.1016/S1571-0866\(04\)80209-4](https://doi.org/10.1016/S1571-0866(04)80209-4), 2004.

Dziewonski, A. M. and Anderson, D. L.: Preliminary reference Earth model, *Physics of the Earth and Planetary Interiors*, 25, 297–356, [https://doi.org/10.1016/0031-9201\(81\)90046-7](https://doi.org/10.1016/0031-9201(81)90046-7), 1981.

Edwards, R. L., Beck, J. W., Burr, G. S., Donahue, D. J., Chappell, J. M., Bloom, a L., Druffel, E. R., and Taylor, F. W.: A Large Drop in Atmospheric  $^{14}\text{C}/^{12}\text{C}$  and Reduced Melting in the Younger Dryas, Documented with  $^{230}\text{Th}$  Ages of Corals., *Science*, 260, 962–968, <https://doi.org/10.1126/science.260.5110.962>, 1993.

Edwards, T. L., Brandon, M. A., Durand, G., Edwards, N. R., Golledge, N. R., Holden, P. B., Nias, I. J., Payne, A. J., Ritz, C., and Wernecke, A.: Revisiting Antarctic ice loss due to marine ice-cliff instability, *Nature*, 566, 58–64, <https://doi.org/10.1038/s41586-019-0901-4>, 2019.

EPICA Members: Eight glacial cycles from an Antarctic ice core, *Nature*, 429, 623–628, 2004.

Fairbanks, R. G.: A 17,000-year glacio-eustatic sea level record: influence of glacial melting rates on the Younger Dryas event and deep-ocean circulation, <https://doi.org/10.1038/342637a0>, 1989.

Fairbanks, R. G., Mortlock, R. a., Chiu, T.-C., Cao, L., Kaplan, A., Guilderson, T. P., Fairbanks, T. W., Bloom, A. L., Grootes, P. M., and Nadeau, M.-J.: Radiocarbon calibration curve spanning 0 to 50,000 years BP based on paired  $^{230}\text{Th}/^{234}\text{U}/^{238}\text{U}$  and  $^{14}\text{C}$  dates on pristine corals, *Quat Sci Rev*, 24, 1781–1796, <https://doi.org/10.1016/j.quascirev.2005.04.007>, 2005.

Favier, L., Gagliardini, O., Durand, G., and Zwinger, T.: A three-dimensional full Stokes model of the grounding line dynamics: Effect of a pinning point beneath the ice shelf, *Cryosphere*, 6, 101–112, <https://doi.org/10.5194/tc-6-101-2012>, 2012.

Favier, L., Pattyn, F., Berger, S., and Drews, R.: Dynamic influence of pinning points on marine ice-sheet stability: A numerical study in Dronning Maud Land, East Antarctica, *Cryosphere*, 10, 2623–2635, <https://doi.org/10.5194/tc-10-2623-2016>, 2016.

- Fischer, H.: Ice Core Records of Atmospheric CO<sub>2</sub> Around the Last Three Glacial Terminations, *Science* (1979), 283, 1712–1714, <https://doi.org/10.1126/science.283.5408.1712>, 1999.
- Fischer, H., Meissner, K. J., Mix, A. C., Abram, N. J., Austermann, J., Brovkin, V., Capron, E., Colombaroli, D., Daniau, A. L., Dyez, K. A., Felis, T., Finkelstein, S. A., Jaccard, S. L., McClymont, E. L., Rovere, A., Sutter, J., Wolff, E. W., Affolter, S., Bakker, P., Ballesteros-Cánovas, J. A., Barbante, C., Caley, T., Carlson, A. E., Churakova, O., Cortese, G., Cumming, B. F., Davis, B. A. S., De Vernal, A., Emile-Geay, J., Fritz, S. C., Gierz, P., Gottschalk, J., Holloway, M. D., Joos, F., Kucera, M., Loutre, M. F., Lunt, D. J., Marcisz, K., Marlon, J. R., Martinez, P., Masson-Delmotte, V., Nehrbass-Ahles, C., Otto-Bliesner, B. L., Raible, C. C., Risebrobakken, B., Sánchez Goñi, M. F., Arrigo, J. S., Sarinthein, M., Sjolte, J., Stocker, T. F., Velasquez Álvarez, P. A., Tinner, W., Valdes, P. J., Vogel, H., Wanner, H., Yan, Q., Yu, Z., Ziegler, M., and Zhou, L.: Palaeoclimate constraints on the impact of 2 °C anthropogenic warming and beyond, <https://doi.org/10.1038/s41561-018-0146-0>, 1 July 2018.
- Fleming, K. and Lambeck, K.: Constraints on the Greenland Ice Sheet since the Last Glacial Maximum from sea-level observations and glacial-rebound models, *Quat Sci Rev*, 23, 1053–1077, <https://doi.org/10.1016/j.quascirev.2003.11.001>, 2004.
- Fretwell, P., Pritchard, H. D., Vaughan, D. G., Bamber, J. L., Barrand, N. E., Bell, R., Bianchi, C., Bingham, R. G., Blankenship, D. D., Casassa, G., Catania, G., Callens, D., Conway, H., Cook, a. J., Corr, H. F. J., Damaske, D., Damm, V., Ferraccioli, F., Forsberg, R., Fujita, S., Gim, Y., Gogineni, P., Griggs, J. a., Hindmarsh, R. C. a, Holmlund, P., Holt, J. W., Jacobel, R. W., Jenkins, a., Jokat, W., Jordan, T., King, E. C., Kohler, J., Krabill, W., Riger-Kusk, M., Langlely, K. a., Leitchenkov, G., Leuschen, C., Luyendyk, B. P., Matsuoka, K., Mouginot, J., Nitsche, F. O., Nogi, Y., Nost, O. a., Popov, S. V., Rignot, E., Rippin, D. M., Rivera, a., Roberts, J., Ross, N., Siegert, M. J., Smith, a. M., Steinhage, D., Studinger, M., Sun, B., Tinto, B. K., Welch, B. C., Wilson, D., Young, D. a., Xiangbin, C., and Zirizzotti, a.: Bedmap2: Improved ice bed, surface and thickness datasets for Antarctica, *Cryosphere*, 7, 375–393, <https://doi.org/10.5194/tc-7-375-2013>, 2013.
- Fricker, H. A. and Padman, L.: Thirty years of elevation change on Antarctic Peninsula ice shelves from multimission satellite radar altimetry, *J Geophys Res Oceans*, 117, 1–17, <https://doi.org/10.1029/2011JC007126>, 2012.
- Fukumori, I., Wang, O., Fenty, I., Forget, G., Heimbach, P., and Ponte, R. M.: “ECCO Version 4 Release 3,” 2017.
- Fürst, J. J., Durand, G., Gillet-Chaulet, F., Tavaré, L., Rankl, M., Braun, M., and Gagliardini, O.: The safety band of Antarctic ice shelves, *Nat Clim Chang*, 6, 479–482, <https://doi.org/10.1038/nclimate2912>, 2016.

- Gagliardini, O., Cohen, D., Råback, P., and Zwinger, T.: Finite-element modeling of subglacial cavities and related friction law, *J Geophys Res Earth Surf*, 112, <https://doi.org/10.1029/2006JF000576>, 2007.
- Gillet-Chaulet, F., Durand, G., Gagliardini, O., Mosbeux, C., Mouginot, J., Rémy, F., and Ritz, C.: Assimilation of surface velocities acquired between 1996 and 2010 to constrain the form of the basal friction law under Pine Island Glacier, *Geophys Res Lett*, 43, 10,311–10,321, <https://doi.org/10.1002/2016GL069937>, 2016.
- Gladstone, R., Schäfer, M., Zwinger, T., Gong, Y., Strozzi, T., Mottram, R., Boberg, F., and Moore, J. C.: Importance of basal processes in simulations of a surging Svalbard outlet glacier, *Cryosphere*, 8, 1393–1405, <https://doi.org/10.5194/tc-8-1393-2014>, 2014.
- Golledge, N. R., Fogwill, C. J., Mackintosh, A. N., and Buckley, K. M.: Dynamics of the last glacial maximum Antarctic ice-sheet and its response to ocean forcing, *PNAS*, 109, 16052–16056, <https://doi.org/10.1073/pnas.1205385109/-/DCSupplemental>, 2012.
- Golledge, N. R., Menviel, L., Carter, L., Fogwill, C. J., England, M. H., Cortese, G., and Levy, R. H.: Antarctic contribution to meltwater pulse 1A from reduced Southern Ocean overturning., *Nat Commun*, 5, 5107, <https://doi.org/10.1038/ncomms6107>, 2014.
- Golledge, N. R., Kowalewski, D. E., Naish, T. R., Levy, R. H., Fogwill, C. J., and Gasson, E. G. W.: The multi-millennial Antarctic commitment to future sea-level rise, *Nature*, 526, 421–425, <https://doi.org/10.1038/nature15706>, 2015.
- Gomez, N., Pollard, D., and Mitrovica, J. X.: A 3-D coupled ice sheet - sea level model applied to Antarctica through the last 40 ky, *Earth Planet Sci Lett*, 384, 88–99, <https://doi.org/10.1016/j.epsl.2013.09.042>, 2013.
- Gomez, N., Latychev, K., and Pollard, D.: A Coupled Ice Sheet-Sea Level Model Incorporating 3D Earth Structure: Variations in Antarctica during the Last Deglacial Retreat, *J Clim*, 31, 4041–4054, <https://doi.org/10.1175/JCLI-D-17>, 2018.
- Gomez, N., Weber, M. E., Clark, P. U., Mitrovica, J. X., and Han, H. K.: Antarctic ice dynamics amplified by Northern Hemisphere sea-level forcing, *Nature*, 587, 600–604, <https://doi.org/10.1038/s41586-020-2916-2>, 2020.
- Graham, A. G. C., Wåhlin, A., Hogan, K. A., Nitsche, F. O., Heywood, K. J., Totten, R. L., Smith, J. A., Hillenbrand, C. D., Simkins, L. M., Anderson, J. B., Wellner, J. S., and Larter, R. D.: Rapid retreat of Thwaites Glacier in the pre-satellite era, *Nat Geosci*, 15, 706–713, <https://doi.org/10.1038/s41561-022-01019-9>, 2022.

- Gregoire, L. J., Payne, A. J., and Valdes, P. J.: Deglacial rapid sea level rises caused by ice-sheet saddle collapses, *Nature*, 487, 219–222, <https://doi.org/10.1038/nature11257>, 2012.
- Gudmundsson, G. H., Krug, J., Durand, G., Favier, L., and Gagliardini, O.: The stability of grounding lines on retrograde slopes, *Cryosphere*, 6, 1497–1505, <https://doi.org/10.5194/tc-6-1497-2012>, 2012.
- Hanebuth, T. J. J., Stategger, K., and Bojanowski, a.: Termination of the Last Glacial Maximum sea-level lowstand: The Sunda-Shelf data revisited, *Glob Planet Change*, 66, 76–84, <https://doi.org/10.1016/j.gloplacha.2008.03.011>, 2009.
- Harris, P. T. and Beaman, R. J.: Processes controlling the formation of the Mertz Drift, George Vth continental shelf, East Antarctica: Evidence from 3.5 kHz sub-bottom profiling and sediment cores, *Deep Sea Res 2 Top Stud Oceanogr*, 50, 1463–1480, [https://doi.org/10.1016/S0967-0645\(03\)00070-5](https://doi.org/10.1016/S0967-0645(03)00070-5), 2003.
- Hauser, T., Keats, A., and Tarasov, L.: Artificial neural network assisted Bayesian calibration of climate models, *Clim Dyn*, 39, 137–154, <https://doi.org/10.1007/s00382-011-1168-0>, 2012.
- He, F.: Simulating transient climate evolution of the last deglaciation with CCSM3, Doctoral dissertation, University of Wisconsin, Madison, 2011.
- Hearty, P. J., Hollin, J. T., Neumann, a. C., O’Leary, M. J., and McCulloch, M.: Global sea-level fluctuations during the Last Interglaciation (MIS 5e), *Quat Sci Rev*, 26, 2090–2112, <https://doi.org/10.1016/j.quascirev.2007.06.019>, 2007.
- Helm, V., Humbert, a., and Miller, H.: Elevation and elevation change of Greenland and Antarctica derived from CryoSat-2, *Cryosphere*, 8, 1539–1559, <https://doi.org/10.5194/tc-8-1539-2014>, 2014.
- Heroy, D. C. and Anderson, J. B.: Radiocarbon constraints on Antarctic Peninsula Ice Sheet retreat following the Last Glacial Maximum (LGM), *Quat Sci Rev*, 26, 3286–3297, <https://doi.org/10.1016/j.quascirev.2007.07.012>, 2007.
- Holland, D. M. and Jenkins, A.: Modeling Thermodynamic Ice–Ocean Interactions at the Base of an Ice Shelf, *J Phys Oceanogr*, 29, 1787–1800, [https://doi.org/10.1175/1520-0485\(1999\)029<1787:MTIOIA>2.0.CO;2](https://doi.org/10.1175/1520-0485(1999)029<1787:MTIOIA>2.0.CO;2), 1999.
- Holland, P. R., Jenkins, A., and Holland, D. M.: The Response of Ice Shelf Basal Melting to Variations in Ocean Temperature, *J Clim*, 21, 2558–2572, <https://doi.org/10.1175/2007JCLI1909.1>, 2008.

- Horton, B. P., Gibbard, P. L., Mine, G. M., Morley, R. J., Purintavaragul, C., Stargardt, J. M., Road, S., Dhi, D., Indah, V., Science, F., and Yai, H.: Holocene sea levels and, *Holocene*, 8, 1199–1213, 2005.
- Hulbe, C. L., Scambos, T. a., Youngberg, T., and Lamb, A. K.: Patterns of glacier response to disintegration of the Larsen B ice shelf, Antarctic Peninsula, *Glob Planet Change*, 63, 1–8, <https://doi.org/10.1016/j.gloplacha.2008.04.001>, 2008.
- Huybrechts, P.: Sea-level changes at the LGM from ice-dynamic reconstructions of the Greenland and Antarctic ice sheets during the glacial cycles, *Quat Sci Rev*, 21, 203–231, [https://doi.org/10.1016/S0277-3791\(01\)00082-8](https://doi.org/10.1016/S0277-3791(01)00082-8), 2002.
- Jacobs, S. S., Jenkins, A., Giulivi, C. F., and Dutrieux, P.: Stronger ocean circulation and increased melting under Pine Island Glacier ice shelf, *Nat Geosci*, 4, 519–523, <https://doi.org/10.1038/ngeo1188>, 2011.
- James, T. D., Murray, T., Selmes, N., Scharrer, K., and O’Leary, M.: Buoyant flexure and basal crevassing in dynamic mass loss at Helheim Glacier, *Nat Geosci*, 7, 593–596, <https://doi.org/10.1038/ngeo2204>, 2014.
- Jenkins, a. and Doake, C. S. M.: Ice-ocean interaction on Ronne Ice Shelf, *Antarctica, J Geophys Res*, 96, 791, <https://doi.org/10.1029/90JC01952>, 1991.
- Jenkins, A., Dutrieux, P., Jacobs, S. S., McPhail, S. D., Perrett, J. R., Webb, A. T., and White, D.: Observations beneath Pine Island Glacier in West Antarctica and implications for its retreat, *Nat Geosci*, 3, 468–472, <https://doi.org/10.1038/ngeo890>, 2010.
- Johnsen, S. J., Dahl-Jensen, D., Gundestrup, N., Steffensen, J. P., Clausen, H. B., Miller, H., Masson-Delmotte, V., Sveinbjrnsdottir, A. E., and White, J.: Oxygen isotope and palaeotemperature records from six Greenland ice-core stations: Camp Century, Dye-3, GRIP, GISP2, Renland and NorthGRIP, *J Quat Sci*, 16, 299–307, <https://doi.org/10.1002/jqs.622>, 2001.
- Johnson, J. S., Bentley, M. J., and Gohl, K.: First exposure ages from the Amundsen Sea Embayment, West Antarctica: The Late quaternary context for recent thinning of Pine Island, Smith, and Pope Glaciers, *Geology*, 36, 223–226, <https://doi.org/10.1130/G24207A.1>, 2008.
- Joughin, I. and Alley, R. B.: Stability of the West Antarctic ice sheet in a warming world, *Nat Geosci*, 4, 506–513, <https://doi.org/10.1038/ngeo1194>, 2011.
- Joughin, I., Smith, B. E., Howat, I. M., Scambos, T., and Moon, T.: Greenland flow variability from ice-sheet-wide velocity mapping, *Journal of Glaciology*, 56, 415–430, <https://doi.org/10.3189/002214310792447734>, 2010a.

- Joughin, I., Smith, B. E., and Holland, D. M.: Sensitivity of 21st century sea level to ocean-induced thinning of Pine Island Glacier, Antarctica, *Geophys Res Lett*, 37, <https://doi.org/10.1029/2010GL044819>, 2010b.
- Joughin, I., Smith, B. E., and Medley, B.: Marine Ice Sheet Collapse Potentially Under Way for the Thwaites Glacier Basic, *Science* (1979), 344, 735–738, <https://doi.org/10.1126/science.1249055>, 2014.
- Joughin, I., Smith, B. E., and Schoof, C. G.: Regularized Coulomb Friction Laws for Ice Sheet Sliding: Application to Pine Island Glacier, Antarctica, *Geophys Res Lett*, 46, 4764–4771, <https://doi.org/10.1029/2019GL082526>, 2019.
- Jouzel, J., Masson-Delmotte, V., Cattani, O., Dreyfus, G., Falourd, S., Hoffmann, G., Minster, B., Nouet, J., Barnola, J. M., Chappellaz, J., Fischer, H., Gallet, J. C., Johnsen, S., Leuenberger, M., Loulergue, L., Luethi, D., Oerter, H., Parrenin, F., Raisbeck, G., Raynaud, D., Schilt, a, Schwander, J., Selmo, E., Souchez, R., Spahni, R., Stauffer, B., Steffensen, J. P., Stenni, B., Stocker, T. F., Tison, J. L., Werner, M., and Wolff, E. W.: Orbital and millennial Antarctic climate variability over the past 800,000 years., *Science*, 317, 793–796, <https://doi.org/10.1126/science.1141038>, 2007.
- King, M. a., Bingham, R. J., Moore, P., Whitehouse, P. L., Bentley, M. J., and Milne, G. a.: Lower satellite-gravimetry estimates of Antarctic sea-level contribution, *Nature*, 491, 586–589, <https://doi.org/10.1038/nature11621>, 2012.
- Kopp, R. E., Simons, F. J., Mitrovica, J. X., Maloof, A. C., and Oppenheimer, M.: Probabilistic assessment of sea level during the last interglacial stage, *Nature*, 462, 863–867, <https://doi.org/10.1038/nature08686>, 2009.
- Lambeck, K. and Chappell, J.: Sea level change through the last glacial cycle., *Science* (1979), 292, 679–686, <https://doi.org/10.1126/science.1059549>, 2001.
- Lambeck, K., Purcell, A., Zhao, J., and Svensson, N.-O. O.: The Scandinavian Ice Sheet: from MIS 4 to the end of the Last Glacial Maximum, *Boreas*, 39, 410–435, <https://doi.org/10.1111/j.1502-3885.2010.00140.x>, 2010.
- Lambeck, K., Rouby, H., Purcell, A., Sun, Y., and Sambridge, M.: Sea level and global ice volumes from the Last Glacial Maximum to the Holocene, *Proc Natl Acad Sci U S A*, 111, 15296–15303, <https://doi.org/10.1073/pnas.1411762111>, 2014a.
- Larour, E., Morlighem, M., Seroussi, H., Schiermeier, J., and Rignot, E.: Ice flow sensitivity to geothermal heat flux of Pine Island Glacier, Antarctica, *J Geophys Res Earth Surf*, 117, <https://doi.org/10.1029/2012JF002371>, 2012.

- Larter, R. D., Anderson, J. B., Graham, a. G. C., Gohl, K., Hillenbrand, C. D., Jakobsson, M., Johnson, J. S., Kuhn, G., Nitsche, F. O., Smith, J. a., Witus, a. E., Bentley, M. J., Dowdeswell, J. a., Ehrmann, W., Klages, J. P., Lindow, J., Cofaigh, C. Ó., and Spiegel, C.: Reconstruction of changes in the Amundsen Sea and Bellingshausen Sea sector of the West Antarctic Ice Sheet since the Last Glacial Maximum, *Quat Sci Rev*, 100, 55–86, <https://doi.org/10.1016/j.quascirev.2013.10.016>, 2014.
- Lauderdale, J. M., Garabato, A. C. N., Oliver, K. I. C., Follows, M. J., and Williams, R. G.: Wind-driven changes in Southern Ocean residual circulation, ocean carbon reservoirs and atmospheric CO<sub>2</sub>, *Clim Dyn*, 41, 2145–2164, <https://doi.org/10.1007/s00382-012-1650-3>, 2013.
- Lazeroms, W. M., Jenkins, A., Rienstra, S. W., & Van De Wal, R. S.: An analytical derivation of ice-shelf basal melt based on the dynamics of meltwater plumes. *Journal of Physical Oceanography*, 49(4), 917-939, 2019.
- Lecavalier, B. S., Milne, G. a, Simpson, M. J. R., Wake, L., Huybrechts, P., Tarasov, L., Kjeldsen, K. K., Funder, S., Long, A. J., Woodroffe, S., Dyke, A. S., and Larsen, N. K.: A model of Greenland ice sheet deglaciation constrained by observations of relative sea level and ice extent, *Quat Sci Rev*, 102, 54–84, <https://doi.org/10.1016/j.quascirev.2014.07.018>, 2014.
- Lecavalier, B. S., Tarasov, L., Balco, G., Spector, P., Hillenbrand, C. D., Buizert, C., Ritz, C., Leduc-Leballeur, M., Mulvaney, R., Whitehouse, P. L., Bentley, M. J., and Bamber, J.: Antarctic Ice Sheet paleo-constraint database, *Earth Syst Sci Data*, 15, 3573–3596, <https://doi.org/10.5194/essd-15-3573-2023>, 2023.
- Lecavalier, B. S., & Tarasov, L. (2024). A history-matching analysis of the Antarctic Ice Sheet since the last interglacial—Part 1: Ice sheet evolution. *EGUsphere* [preprint], 1-38, <https://doi.org/10.5194/egusphere-2024-1291>, 2024.
- Lemieux-Dudon, B., Blayo, E., Petit, J.-R., Waelbroeck, C., Svensson, A., Ritz, C., Barnola, J.-M., Narcisi, B. M., and Parrenin, F.: Consistent dating for Antarctic and Greenland ice cores, *Quat Sci Rev*, 29, 8–20, <https://doi.org/10.1016/j.quascirev.2009.11.010>, 2010.
- Levermann, A., Albrecht, T., Winkelmann, R., Martin, M. A., Haseloff, M., and Joughin, I.: Kinematic first-order calving law implies potential for abrupt ice-shelf retreat, *Cryosphere*, 6, 273–286, <https://doi.org/10.5194/tc-6-273-2012>, 2012.
- Levermann, A., Winkelmann, R., Nowicki, S., Fastook, J. L., Frieler, K., Greve, R., Hellmer, H. H., Martin, M. A., Meinshausen, M., Mengel, M., Payne, A. J., Pollard, D., Sato, T., Timmermann, R., Wang, W. L., and Bindshadler, R. A.: Projecting Antarctic ice discharge using response functions from SeaRISE ice-sheet models,

- Earth System Dynamics, 5, 271–293, <https://doi.org/10.5194/esd-5-271-2014>, 2014.
- Li, X., Rignot, E., Morlighem, M., Mouginot, J., and Scheuchl, B.: Grounding line retreat of Totten Glacier, East Antarctica, 1996 to 2013, *Geophys Res Lett*, 42, 1–8, <https://doi.org/10.1002/2015GL065701.1>, 2015.
- Licciardi, J. M., Clark, P. U., Jenson, J. W., and Macayeal, D. R.: Deglaciation of a soft-bedded Laurentide Ice Sheet, *Quat Sci Rev*, 17, 427–448, [https://doi.org/10.1016/S0277-3791\(97\)00044-9](https://doi.org/10.1016/S0277-3791(97)00044-9), 1998.
- Licht, K. J.: The Ross Sea’s contribution to eustatic sea level during meltwater pulse 1A, *Sediment Geol*, 165, 343–353, <https://doi.org/10.1016/j.sedgeo.2003.11.020>, 2004.
- Lin, Y., Hibbert, F. D., Whitehouse, P. L., Woodroffe, S. A., Purcell, A., Shennan, I., and Bradley, S. L.: A reconciled solution of Meltwater Pulse 1A sources using sea-level fingerprinting, *Nat Commun*, 12, <https://doi.org/10.1038/s41467-021-21990-y>, 2021.
- Lisiecki, L. E. and Raymo, M. E.: A Pliocene-Pleistocene stack of 57 globally distributed benthic  $\delta^{18}\text{O}$  records, *Paleoceanography*, 20, 1–17, <https://doi.org/10.1029/2004PA001071>, 2005.
- Little, C. M., Oppenheimer, M., and Urban, N. M.: Upper bounds on twenty-first-century Antarctic ice loss assessed using a probabilistic framework, *Nat Clim Chang*, <https://doi.org/10.1038/nclimate1845>, 2013.
- Liu, J., Milne, G. A., Kopp, R. E., Clark, P. U., and Shennan, I.: Sea-level constraints on the amplitude and source distribution of Meltwater Pulse 1A, *Nat Geosci*, 9, 130–134, <https://doi.org/10.1038/ngeo2616>, 2016.
- Liu, Y., Moore, J. C., Cheng, X., Gladstone, R. M., Bassis, J. N., Liu, H., Wen, J., and Hui, F.: Ocean-driven thinning enhances iceberg calving and retreat of Antarctic ice shelves, *Proceedings of the National Academy of Sciences*, 112, 3263–3268, <https://doi.org/10.1073/pnas.1415137112>, 2015.
- Livingstone, S. J., Ó Cofaigh, C., Stokes, C. R., Hillenbrand, C.-D., Vieli, A., and Jamieson, S. S. R.: Antarctic palaeo-ice streams, *Earth Sci Rev*, 111, 90–128, <https://doi.org/10.1016/j.earscirev.2011.10.003>, 2012.
- Mackintosh, A., Gollledge, N., Domack, E., Dunbar, R., Leventer, A., White, D., Pollard, D., DeConto, R., Fink, D., Zwart, D., Gore, D., and Lavoie, C.: Retreat of the East Antarctic ice sheet during the last glacial termination, *Nat Geosci*, 4, 195–202, <https://doi.org/10.1038/ngeo1061>, 2011.

- Martin, M. A., Winkelmann, R., Haseloff, M., Albrecht, T., Bueler, E., Khroulev, C., and Levermann, A.: The Potsdam Parallel Ice Sheet Model (PISM-PIK) - Part 2: Dynamic equilibrium simulation of the Antarctic ice sheet, *Cryosphere*, 5, 727–740, <https://doi.org/10.5194/tc-5-727-2011>, 2011.
- Martín-Español, A., King, M. A., Zammit-Mangion, A., Andrews, S. B., Moore, P., and Bamber, J. L.: An assessment of forward and inverse GIA solutions for Antarctica, *J Geophys Res Solid Earth*, 121, 6947–6965, <https://doi.org/10.1002/2016JB013154>, 2016.
- Martos, Y. M., Catalán, M., Jordan, T. A., Golynsky, A., Golynsky, D., Eagles, G., and Vaughan, D. G.: Heat Flux Distribution of Antarctica Unveiled, *Geophys Res Lett*, 44, 11,417–11,426, <https://doi.org/10.1002/2017GL075609>, 2017.
- Masson-Delmotte, V., Zhai, P., Chen, Y., Goldfarb, L., Gomis, M. I., Matthews, J. B. R., Berger, S., Huang, M., Yelekçi, O., Yu, R., Zhou, B., Lonnoy, E., Maycock, T. K., Waterfield, T., Leitzell, K., and Caud, N.: Working Group I Contribution to the Sixth Assessment Report of the Intergovernmental Panel on Climate Change Edited by, <https://doi.org/10.1017/9781009157896>, 2021.
- Matsuoka, K., Skoglund, A., Roth, G., De Pomereu, J., Griffiths, H., Headland, R., Herried, B., Katsumata, K., Le Brocq, A., Licht, K., Morgan, F., Neff, P. D., Ritz, C., Scheinert, M., Tamura, T., Van De Putte, A., Van Den Broeke, M., Von Deschwanden, A., Deschamps-Berger, C., Liefferinge, B. Van, Tronstad, S., and Melvaer, Y.: Quantarctica, an integrated mapping environment for Antarctica, the Southern Ocean, and sub-Antarctic islands, <https://doi.org/10.21334/npolar.2018.8516e961>, 2021.
- Melchior Van Wessem, J., Jan Van De Berg, W., Noël, B. P. Y., Van Meijgaard, E., Amory, C., Birnbaum, G., Jakobs, C. L., Krüger, K., Lenaerts, J. T. M., Lhermitte, S., Ligtenberg, S. R. M., Medley, B., Reijmer, C. H., Van Tricht, K., Trusel, L. D., Van Uft, L. H., Wouters, B., Wuite, J., and Van Den Broeke, M. R.: Modelling the climate and surface mass balance of polar ice sheets using RACMO2 - Part 2: Antarctica (1979-2016), *Cryosphere*, 12, 1479–1498, <https://doi.org/10.5194/tc-12-1479-2018>, 2018.
- Menviel, L., Spence, P., and England, M. H.: Contribution of enhanced Antarctic Bottom Water formation to Antarctic warm events and millennial-scale atmospheric CO<sub>2</sub> increase, *Earth Planet Sci Lett*, 413, 37–50, <https://doi.org/10.1016/j.epsl.2014.12.050>, 2015.
- Meredith, M., Sommerkorn, M., Cassotta, S., Derksen, C., Ekaykin, A., Hollowed, A., Kofinas, G., Mackintosh, A., Melbourne-Thomas, J., Muelbert, M. M. C., Ottersen, G., Pritchard, H., and Schuur, E. A. G.: Polar Regions. In: IPCC Special Report on the Ocean and Cryosphere in a Changing Climate, IPCC, 2019.

- Milne, G. a, Mitrovica, J. X., and Schrag, D. P.: Estimating past continental ice volume from sea-level data, *Quat Sci Rev*, 21, 361–376, [https://doi.org/10.1016/S0277-3791\(01\)00108-1](https://doi.org/10.1016/S0277-3791(01)00108-1), 2002.
- Milne, G. and Shennan, I.: Sea Level Studies: Isostasy, *Encyclopedia of Quaternary Science*, 3043–3051, 2007.
- Milne, G. a. and Mitrovica, J. X.: Searching for eustasy in deglacial sea-level histories, *Quat Sci Rev*, 27, 2292–2302, <https://doi.org/10.1016/j.quascirev.2008.08.018>, 2008.
- Milne, G. A., Latychev, K., Schaeffer, A., Crowley, J. W., Lecavalier, B. S., and Audette, A.: The influence of lateral Earth structure on glacial isostatic adjustment in Greenland, *Geophys J Int*, 214, 1252–1266, <https://doi.org/10.1093/GJI/GGY189>, 2018.
- Mitrovica, J. X., Gomez, N., and Clark, P. U.: The sea-level fingerprint of West Antarctic collapse, *Science* (1979), 323, 753, <https://doi.org/10.1126/science.1166510>, 2009.
- Morlighem, M., Rignot, E., Binder, T., Blankenship, D., Drews, R., Eagles, G., Eisen, O., Ferraccioli, F., Forsberg, R., Fretwell, P., Goel, V., Greenbaum, J. S., Gudmundsson, H., Guo, J., Helm, V., Hofstede, C., Howat, I., Humbert, A., Jokat, W., Karlsson, N. B., Lee, W. S., Matsuoka, K., Millan, R., Mouginit, J., Paden, J., Pattyn, F., Roberts, J., Rosier, S., Ruppel, A., Seroussi, H., Smith, E. C., Steinhage, D., Sun, B., Broeke, M. R. van den, Ommen, T. D. van, Wessem, M. van, and Young, D. A.: Deep glacial troughs and stabilizing ridges unveiled beneath the margins of the Antarctic ice sheet, *Nat Geosci*, 13, 132–137, <https://doi.org/10.1038/s41561-019-0510-8>, 2020.
- Motyka, R. J., Hunter, L., Echelmeyer, K. a., and Connor, C.: Submarine melting at the terminus of a temperate tidewater glacier, LeConte Glacier, Alaska, U.S.A, *Ann Glaciol*, 36, 57–65, <https://doi.org/10.3189/172756403781816374>, 2003.
- Mouginit, J., Rignot, E., and Scheuchl, B.: Continent-Wide, Interferometric SAR Phase, Mapping of Antarctic Ice Velocity, *Geophys. Res. Lett.*, 46, 9710–9718, <https://doi.org/10.1029/2019GL083826>, 2019.
- Mulvaney, R., Abram, N. J., Hindmarsh, R. C. a., Arrowsmith, C., Fleet, L., Triest, J., Sime, L., Alemany, O., and Foord, S.: Recent Antarctic Peninsula warming relative to Holocene climate and ice shelf history, *Nature*, 488, 141–144, <https://doi.org/10.1038/nature11391>, 2012.

- Nias, I. J., Cornford, S. L., and Payne, A. J.: New Mass-Conserving Bedrock Topography for Pine Island Glacier Impacts Simulated Decadal Rates of Mass Loss, *Geophys Res Lett*, 45, 3173–3181, <https://doi.org/10.1002/2017GL076493>, 2018.
- Nick, F. M., Van Der Veen, C. J., Vieli, a., and Benn, D. I.: A physically based calving model applied to marine outlet glaciers and implications for the glacier dynamics, *Journal of Glaciology*, 56, 781–794, <https://doi.org/10.3189/002214310794457344>, 2010.
- Nick, F. M., Vieli, A., Andersen, M. L., Joughin, I., Payne, A., Edwards, T. L., Pattyn, F., and Van De Wal, R. S. W.: Future sea-level rise from Greenland’s main outlet glaciers in a warming climate, *Nature*, 497, 235–238, <https://doi.org/10.1038/nature12068>, 2013.
- Nowicki, S., Bindschadler, R. A., Abe-Ouchi, A., Aschwanden, A., Bueller, E., Choi, H., Fastook, J., Granzow, G., Greve, R., Gutowski, G., Herzfeld, U., Jackson, C., Johnson, J., Khroulev, C., Larour, E., Levermann, A., Lipscomb, W. H., Martin, M. A., Morlighem, M., Parizek, B. R., Pollard, D., Price, S. F., Ren, D., Rignot, E., Saito, F., Sato, T., Seddik, H., Seroussi, H., Takahashi, K., Walker, R., and Wang, W. L.: Insights into spatial sensitivities of ice mass response to environmental change from the SeaRISE ice sheet modeling project I: Antarctica, *J Geophys Res Earth Surf*, 118, 1002–1024, <https://doi.org/10.1002/jgrf.20081>, 2013.
- Otosaka, I. N., Shepherd, A., Ivins, E. R., Schlegel, N.-J., Amory, C., van den Broeke, M. R., Horwath, M., Joughin, I., King, M. D., Krinner, G., Payne, A. J., Rignot, E., Scambos, T., Simon, K. M., Smith, B. E., Sørensen, L. S., Velicogna, I., Whitehouse, P. L., Agosta, C., Ahlstrøm, A. P., Blazquez, A., Colgan, W., Engdhal, M. E., Fettweis, X., Forsberg, R., Gallée, H., Gardner, A., Gilbert, L., Gourmelen, N., Groh, A., Gunter, B. C., Harig, C., Helm, V., Abbas Khan, S., Konrad, H., Lecavalier, B. S., Liang, C.-C., Loomis, B. D., McMillan, M., Melini, D., Mernild, S. H., Mottram, R., Mouginot, J., Nilsson, J., Noël, B., Pattle, M. E., Peltier, W. R., Pie, N., Sasgen, I., Save, H. V., Seo, K.-W., Scheuchl, B., Schrama, E. J., Schröder, L., Simonsen, S. B., Slater, T., Spada, G., Sutterley, T. C., Dutt Vishwakarma, B., van, M., Wiese, D., van der Wal, W., and Wouters, B.: Mass Balance of the Greenland and Antarctic Ice Sheets from 1992 to 2020, *Earth Syst Sci Data*, 1–33, <https://doi.org/10.5194/essd-2022-261>, 2023.
- Otto-Bliesner, B. L., Rosenbloom, N., Stone, E. J., Mckay, N. P., Lunt, D. J., Brady, E. C., and Overpeck, J. T.: How warm was the last interglacial? new model-data comparisons, *Philosophical Transactions of the Royal Society A: Mathematical, Physical and Engineering Sciences*, 371, <https://doi.org/10.1098/rsta.2013.0097>, 2013.
- Pan, L., Milne, G. A., Latychev, K., Goldberg, S. L., Austermann, J., Hoggard, M. J., and Mitrovica, J. X.: The influence of lateral Earth structure on inferences of global ice

volume during the Last Glacial Maximum,  
<https://doi.org/10.1016/j.quascirev.2022.107644>, 15 August 2022.

- Paolo, F. S., Fricker, H. a, and Padman, L.: Volume loss from Antarctic ice shelves is accelerating, *Science* (1979), 348, 327–332, <https://doi.org/10.1126/science.aaa0940>, 2015.
- Pattyn, F.: Antarctic subglacial conditions inferred from a hybrid ice sheet/ice stream model, *Earth Planet Sci Lett*, 295, 451–461, <https://doi.org/10.1016/j.epsl.2010.04.025>, 2010.
- Pattyn, F., Schoof, C., Perichon, L., Hindmarsh, R. C. a., Bueler, E., de Fleurian, B., Durand, G., Gagliardini, O., Gladstone, R., Goldberg, D., Gudmundsson, G. H., Huybrechts, P., Lee, V., Nick, F. M., Payne, a. J., Pollard, D., Rybak, O., Saito, F., and Vieli, a.: Results of the Marine Ice Sheet Model Intercomparison Project, MISMIP, *Cryosphere*, 6, 573–588, <https://doi.org/10.5194/tc-6-573-2012>, 2012.
- Pattyn, F.: Sea-level response to melting of Antarctic ice shelves on multi-centennial timescales with the fast Elementary Thermomechanical Ice Sheet model (f.ETISh v1.0), *Cryosphere*, 11, 1851–1878, <https://doi.org/10.5194/tc-11-1851-2017>, 2017.
- Pattyn, F. and Morlighem, M.: The uncertain future of the Antarctic Ice Sheet, *Science* (1979), 367, 1331–1335, <https://doi.org/10.1126/science.aaz5487>, 2020.
- Peltier, W. R.: Ice age paleotopography., <https://doi.org/10.1126/science.265.5169.195>, 1994.
- Peltier, W. R.: Global Glacial Isostasy and the Surface of the Iace-Age Earth: The ICE-5G (VM2) Model and GRACE, *Annu Rev Earth Planet Sci*, 32, 111–149, <https://doi.org/10.1146/annurev.earth.32.082503.144359>, 2004.
- Peltier, W. R.: On the hemispheric origins of meltwater pulse 1a, *Quat Sci Rev*, 24, 1655–1671, <https://doi.org/10.1016/j.quascirev.2004.06.023>, 2005.
- Peltier, W. R. and Fairbanks, R. G.: Global glacial ice volume and Last Glacial Maximum duration from an extended Barbados sea level record, *Quat Sci Rev*, 25, 3322–3337, <https://doi.org/10.1016/j.quascirev.2006.04.010>, 2006.
- Petit, R. J., Raynaud, D., Basile, I., Chappellaz, J., Ritz, C., Delmotte, M., Legrand, M., Lorius, C., and Pe, L.: Climate and atmospheric history of the past 420,000 years from the Vostok ice core, Antarctica, *Nature*, 399, 429–413, <https://doi.org/10.1038/20859>, 1999.
- Philippon, G., Ramstein, G., Charbit, S., Kageyama, M., Ritz, C., and Dumas, C.: Evolution of the Antarctic ice sheet throughout the last deglaciation: A study with a new

- coupled climate-north and south hemisphere ice sheet model, *Earth Planet Sci Lett*, 248, 750–758, <https://doi.org/10.1016/j.epsl.2006.06.017>, 2006.
- Pittard, M. L., Whitehouse, P. L., Bentley, M. J., and Small, D.: An ensemble of Antarctic deglacial simulations constrained by geological observations, *Quat Sci Rev*, 298, <https://doi.org/10.1016/j.quascirev.2022.107800>, 2022.
- Pollard, D. and DeConto, R. M. R. M.: A Coupled Ice-Sheet/Ice-Shelf/Sediment Model Applied to a Marine-Margin Flowline: Forced and Unforced Variations, *Glacial sedimentary processes and products*, 37–52, <https://doi.org/10.1002/9781444304435.ch4>, 2007.
- Pollard, D. and DeConto, R. M.: Modelling West Antarctic ice sheet growth and collapse through the past five million years, *Nature*, 458, 329–332, <https://doi.org/10.1038/nature07809>, 2009.
- Pollard, D. and DeConto, R. M.: A simple inverse method for the distribution of basal sliding coefficients under ice sheets, applied to Antarctica, *Cryosphere*, 6, 953–971, <https://doi.org/10.5194/tc-6-953-2012>, 2012a.
- Pollard, D. and DeConto, R. M.: Description of a hybrid ice sheet-shelf model, and application to Antarctica, *Geosci Model Dev*, 5, 1273–1295, <https://doi.org/10.5194/gmd-5-1273-2012>, 2012b.
- Pollard, D., DeConto, R. M., and Alley, R. B.: Potential Antarctic Ice Sheet retreat driven by hydrofracturing and ice cliff failure, *Earth Planet Sci Lett*, 412, 112–121, <https://doi.org/10.1016/j.epsl.2014.12.035>, 2015.
- Pollard, D., Chang, W., Haran, M., Applegate, P., and DeConto, R.: Large ensemble modeling of the last deglacial retreat of the West Antarctic Ice Sheet: Comparison of simple and advanced statistical techniques, *Geosci Model Dev*, 9, 1697–1723, <https://doi.org/10.5194/gmd-9-1697-2016>, 2016.
- Pollard, D., and DeConto, R. M.: Improvements in one-dimensional grounding-line parameterizations in an ice-sheet model with lateral variations (PSUICE3D v2.1), *Geoscientific Model Development*, 13(12), 6481–6500, 2020.
- Pritchard, H. D., Arthern, R. J., Vaughan, D. G., and Edwards, L. a: Extensive dynamic thinning on the margins of the Greenland and Antarctic ice sheets., *Nature*, 461, 971–975, <https://doi.org/10.1038/nature08471>, 2009.
- Pritchard, H. D., Ligtenberg, S. R. M., Fricker, H. a., Vaughan, D. G., van den Broeke, M. R., and Padman, L.: Antarctic ice-sheet loss driven by basal melting of ice shelves, *Nature*, 484, 502–505, <https://doi.org/10.1038/nature10968>, 2012.

- Quiquet, A., Dumas, C., Ritz, C., Peyaud, V., and Roche, D. M.: The GRISLI ice sheet model (version 2.0): Calibration and validation for multi-millennial changes of the Antarctic ice sheet, *Geosci Model Dev*, 11, 5003–5025, <https://doi.org/10.5194/gmd-11-5003-2018>, 2018.
- Rasmussen, S. O., Andersen, K. K., Svensson, a. M., Steffensen, J. P., Vinther, B. M., Clausen, H. B., Siggaard-Andersen, M. L., Johnsen, S. J., Larsen, L. B., Dahl-Jensen, D., Bigler, M., Röthlisberger, R., Fischer, H., Goto-Azuma, K., Hansson, M. E., and Ruth, U.: A new Greenland ice core chronology for the last glacial termination, *Journal of Geophysical Research: Atmospheres*, 111, 1–16, <https://doi.org/10.1029/2005JD006079>, 2006.
- Rasmussen, S. O., Bigler, M., Blockley, S. P., Blunier, T., Buchardt, S. L., Clausen, H. B., Cvijanovic, I., Dahl-Jensen, D., Johnsen, S. J., Fischer, H., Gkinis, V., Guillevic, M., Hoek, W. Z., Lowe, J. J., Pedro, J. B., Popp, T., Seierstad, I. K., Steffensen, J. P., Svensson, A. M., Vallenga, P., Vinther, B. M., Walker, M. J. C., Wheatley, J. J., and Winstrup, M.: A stratigraphic framework for abrupt climatic changes during the Last Glacial period based on three synchronized Greenland ice-core records: refining and extending the INTIMATE event stratigraphy, *Quat Sci Rev*, 106, 14–28, <https://doi.org/10.1016/j.quascirev.2014.09.007>, 2014.
- Reese, R., Winkelmann, R., and Gudmundsson, G. H.: Grounding-line flux formula applied as a flux condition in numerical simulations fails for buttressed Antarctic ice streams, *The Cryosphere*, 12(10), 3229–3242, 2018.
- Rignot, E., Casassa, G., Gogineni, P., Krabill, W., Rivera, a., and Thomas, R.: Accelerated ice discharge from the Antarctic Peninsula following the collapse of Larsen B ice shelf, *Geophys Res Lett*, 31, 2–5, <https://doi.org/10.1029/2004GL020697>, 2004.
- Rignot, E.: Changes in West Antarctic ice stream dynamics observed with ALOS PALSAR data, *Geophys Res Lett*, 35, L12505, <https://doi.org/10.1029/2008GL033365>, 2008.
- Rignot, E., Jacobs, S., Mouginot, J., and Scheuchl, B.: Ice-shelf melting around Antarctica., *Science (1979)*, 341, 266–70, <https://doi.org/10.1126/science.1235798>, 2013.
- Rignot, E., Mouginot, J., Morlighem, M., Seroussi, H., and Scheuchl, B.: Widespread, rapid grounding line retreat of Pine Island, Thwaites, Smith, and Kohler glaciers, West Antarctica, from 1992 to 2011, *Geophys Res Lett*, 41, 3502–3509, <https://doi.org/10.1002/2014GL060140>, 2014.
- Rignot, E., Mouginot, J., Scheuchl, B., Van Den Broeke, M., Van Wessem, M. J., and Morlighem, M.: Four decades of Antarctic ice sheet mass balance from 1979–2017, *Proc Natl Acad Sci U S A*, 116, 1095–1103, <https://doi.org/10.1073/pnas.1812883116>, 2019.

- Ritz, C., Edwards, T. L., Durand, G., Payne, A. J., Peyaud, V., and Hindmarsh, R. C. A.: Potential sea-level rise from Antarctic ice-sheet instability constrained by observations, *Nature*, 528, 115–118, <https://doi.org/10.1038/nature16147>, 2015.
- Riva, R. E. M., Gunter, B. C., Urban, T. J., Vermeersen, B. L. a, Lindenbergh, R. C., Helsen, M. M., Bamber, J. L., van de Wal, R. S. W., van den Broeke, M. R., and Schutz, B. E.: Glacial Isostatic Adjustment over Antarctica from combined ICESat and GRACE satellite data, *Earth Planet Sci Lett*, 288, 516–523, <https://doi.org/10.1016/j.epsl.2009.10.013>, 2009.
- Ross, N., Bingham, R. G., Corr, H. F. J., Ferraccioli, F., Jordan, T. a., Le Brocq, A., Rippin, D. M., Young, D., Blankenship, D. D., and Siegert, M. J.: Steep reverse bed slope at the grounding line of the Weddell Sea sector in West Antarctica, *Nat Geosci*, 5, 393–396, <https://doi.org/10.1038/ngeo1468>, 2012.
- Rott, H., Müller, F., Nagler, T., and Floricioiu, D.: The imbalance of glaciers after disintegration of Larsen-B ice shelf, Antarctic Peninsula, *Cryosphere*, 5, 125–134, <https://doi.org/10.5194/tc-5-125-2011>, 2011.
- Rovere, A., Raymo, M. E., Mitrovica, J. X., Hearty, P. J., O’Leary, M. J., and Inglis, J. D.: The Mid-Pliocene sea-level conundrum: Glacial isostasy, eustasy and dynamic topography, *Earth Planet Sci Lett*, 387, 27–33, <https://doi.org/10.1016/j.epsl.2013.10.030>, 2014.
- Rowley, D. B., Forte, A. M., Moucha, R., Mitrovica, J. X., Simmons, N. A., and Grand, S. P.: Dynamic topography change of the Eastern United States since 3 million years ago, *Science* (1979), 340, 1560–1563, <https://doi.org/10.1126/science.1229180>, 2013.
- Ruckert, K. L., Shaffer, G., Pollard, D., Guan, Y., Wong, T. E., Forest, C. E., and Keller, K.: Assessing the impact of retreat mechanisms in a simple Antarctic ice sheet model using Bayesian calibration, *PLoS One*, 12, 1–15, <https://doi.org/10.1371/journal.pone.0170052>, 2017.
- Rutt, I. C., Hagdorn, M., Hulton, N. R. J., and Payne, a. J.: The glimmer community ice sheet model, *J Geophys Res Earth Surf*, 114, 1–22, <https://doi.org/10.1029/2008JF001015>, 2009.
- Sasgen, I., Martín-Español, A., Horvath, A., Klemann, V., Petrie, E. J., Wouters, B., Horvath, M., Pail, R., Bamber, J. L., Clarke, P. J., Konrad, H., and Drinkwater, M. R.: Joint inversion estimate of regional glacial isostatic adjustment in Antarctica considering a lateral varying Earth structure (ESA STSE Project REGINA), *Geophys J Int*, 211, 1534–1553, <https://doi.org/10.1093/gji/ggx368>, 2017.

- Scambos, T. A., Hulbe, C., Fahnestock, M., and Bohlander, J.: The link between climate warming and break-up of ice shelves in the Antarctic Peninsula, *Journal of Glaciology*, 46, 516–530, <https://doi.org/doi:10.3189/172756500781833043>, 2000.
- Scambos, T. a., Bohlander, J. a., Shuman, C. a., and Skvarca, P.: Glacier acceleration and thinning after ice shelf collapse in the Larsen B embayment, Antarctica, *Geophys Res Lett*, 31, 2001–2004, <https://doi.org/10.1029/2004GL020670>, 2004.
- Schoof, C.: The effect of cavitation on glacier sliding, *Proceedings of the Royal Society A: Mathematical, Physical and Engineering Sciences*, 461, 609–627, <https://doi.org/10.1098/rspa.2004.1350>, 2005.
- Schoof, C.: Variational methods for glacier flow over plastic till, *J Fluid Mech*, 555, 299–320, <https://doi.org/10.1017/S0022112006009104>, 2006.
- Schoof, C.: Ice sheet grounding line dynamics: Steady states, stability, and hysteresis, *J Geophys Res*, 112, F03S28, <https://doi.org/10.1029/2006JF000664>, 2007.
- Schoof, C.: Ice-sheet acceleration driven by melt supply variability., *Nature*, 468, 803–806, <https://doi.org/10.1038/nature09618>, 2010.
- Seroussi, H., Nowicki, S., Simon, E., Abe-Ouchi, A., Albrecht, T., Brondex, J., Cornford, S., Dumas, C., Gillet-Chaulet, F., Goelzer, H., Gолledge, N. R., Gregory, J. M., Greve, R., Hoffman, M. J., Humbert, A., Huybrechts, P., Kleiner, T., Larour, E., Leguy, G., Lipscomb, W. H., Lowry, D., Mengel, M., Morlighem, M., Pattyn, F., Payne, A. J., Pollard, D., Price, S. F., Quiquet, A., Reerink, T. J., Reese, R., Rodehacke, C. B., Schlegel, N. J., Shepherd, A., Sun, S., Sutter, J., Van Breedam, J., Van De Wal, R. S. W., Winkelmann, R., and Zhang, T.: InitMIP-Antarctica: An ice sheet model initialization experiment of ISMIP6, *Cryosphere*, 13, 1441–1471, <https://doi.org/10.5194/tc-13-1441-2019>, 2019.
- Shackleton, S., Baggenstos, D., Menking, J. A., Dyonisius, M. N., Bereiter, B., Bauska, T. K., Rhodes, R. H., Brook, E. J., Petrenko, V. V., McConnell, J. R., Kellerhals, T., Häberli, M., Schmitt, J., Fischer, H., and Severinghaus, J. P.: Global ocean heat content in the Last Interglacial, *Nat Geosci*, 13, 77–81, <https://doi.org/10.1038/s41561-019-0498-0>, 2020.
- Shakun, J. D., Clark, P. U., He, F., Marcott, S. A., Mix, A. C., Liu, Z., Otto-Bliesner, B., Schmittner, A., and Bard, E.: Global warming preceded by increasing carbon dioxide concentrations during the last deglaciation, *Nature*, 484, 49–54, <https://doi.org/10.1038/nature10915>, 2012.
- Shannon, S. R., Payne, A. J., Bartholomew, I. D., van den Broeke, M. R., Edwards, T. L., Fettweis, X., Gagliardini, O., Gillet-Chaulet, F., Goelzer, H., Hoffman, M. J., Huybrechts, P., Mair, D. W. F., Nienow, P. W., Perego, M., Price, S. F., Smeets, C.

- J. P. P., Sole, A. J., van de Wal, R. S. W., and Zwinger, T.: Enhanced basal lubrication and the contribution of the Greenland ice sheet to future sea-level rise., *Proc Natl Acad Sci U S A*, 110, 14156–61, <https://doi.org/10.1073/pnas.1212647110>, 2013.
- Shepherd, A., Wingham, D., Wallis, D., Giles, K., Laxon, S., and Sundal, A. V.: Recent loss of floating ice and the consequent sea level contribution, *Geophys Res Lett*, 37, 1–5, <https://doi.org/10.1029/2010GL042496>, 2010.
- Shepherd, A., Ivins, E. R., and IMBIE members: A Reconciled Estimate of Ice-Sheet Mass Balance, *Science* (1979), 338, 1183–1189, 2012.
- Shepherd, A., Ivins, E., Rignot, E., Smith, B., Van Den Broeke, M., Velicogna, I., Whitehouse, P., Briggs, K., Joughin, I., Krinner, G., Nowicki, S., Payne, T., Scambos, T., Schlegel, N., Geruo, A., Agosta, C., Ahlstrøm, A., Babonis, G., Barletta, V., Blazquez, A., Bonin, J., Csatho, B., Cullather, R., Felikson, D., Fettweis, X., Forsberg, R., Gallee, H., Gardner, A., Gilbert, L., Groh, A., Gunter, B., Hanna, E., Harig, C., Helm, V., Horvath, A., Horwath, M., Khan, S., Kjeldsen, K. K., Konrad, H., Langen, P., Lecavalier, B., Loomis, B., Luthcke, S., McMillan, M., Melini, D., Mernild, S., Mohajerani, Y., Moore, P., Mouginot, J., Moyano, G., Muir, A., Nagler, T., Nield, G., Nilsson, J., Noel, B., Otosaka, I., Pattle, M. E., Peltier, W. R., Pie, N., Rietbroek, R., Rott, H., Sandberg-Sørensen, L., Sasgen, I., Save, H., Scheuchl, B., Schrama, E., Schröder, L., Seo, K. W., Simonsen, S., Slater, T., Spada, G., Sutterley, T., Talpe, M., Tarasov, L., Van De Berg, W. J., Van Der Wal, W., Van Wessem, M., Vishwakarma, B. D., Wiese, D., and Wouters, B.: Mass balance of the Antarctic Ice Sheet from 1992 to 2017, *Nature*, 558, 219–222, <https://doi.org/10.1038/s41586-018-0179-y>, 2018.
- Siegert, M. J. and Dowdeswell, J. a.: Numerical reconstructions of the Eurasian Ice Sheet and climate during the Late Weichselian, *Quat Sci Rev*, 23, 1273–1283, <https://doi.org/10.1016/j.quascirev.2003.12.010>, 2004.
- Simms, A. R., Lisiecki, L., Gebbie, G., Whitehouse, P. L., and Clark, J. F.: Balancing the last glacial maximum (LGM) sea-level budget, *Quat Sci Rev*, 205, 143–153, <https://doi.org/10.1016/j.quascirev.2018.12.018>, 2019.
- Small, D., Bentley, M. J., Selwyn Jones, R., Pittard, M. L., and Whitehouse, P. L.: Antarctic ice sheet palaeo-thinning rates from vertical transects of 2 cosmogenic exposure ages, *Quaternary Science Review*, 206, 65–80, <https://doi.org/https://doi.org/10.1016/j.quascirev.2018.12.024>, 2019.
- Smith, J. a., Hillenbrand, C. D., Kuhn, G., Larter, R. D., Graham, A. G. C., Ehrmann, W., Moreton, S. G., and Forwick, M.: Deglacial history of the West Antarctic Ice Sheet in the western Amundsen Sea Embayment, *Quat Sci Rev*, 30, 488–505, <https://doi.org/10.1016/j.quascirev.2010.11.020>, 2011.

- Stanford, J. D., Hemingway, R., Rohling, E. J., Challenor, P. G., Medina-Elizalde, M., and Lester, a. J.: Sea-level probability for the last deglaciation: A statistical analysis of far-field records, *Glob Planet Change*, 79, 193–203, <https://doi.org/10.1016/j.gloplacha.2010.11.002>, 2011.
- Steig, E. J., Ding, Q., Battisti, D. S., and Jenkins, a.: Tropical forcing of Circumpolar Deep Water Inflow and outlet glacier thinning in the Amundsen Sea Embayment, West Antarctica, *Ann Glaciol*, 53, 19–28, <https://doi.org/10.3189/2012AoG60A110>, 2012.
- Stirling, C. H., Esat, T. M., Lambeck, K., and McCulloch, M. T.: Timing and duration of the Last Interglacial: Evidence for a restricted interval of widespread coral reef growth, *Earth Planet Sci Lett*, 160, 745–762, [https://doi.org/10.1016/S0012-821X\(98\)00125-3](https://doi.org/10.1016/S0012-821X(98)00125-3), 1998.
- Studinger, M., Bell, R. E., Blankenship, D. D., Finn, C. A., Arko, R. A., Morse, D. L., and Joughin, I.: Subglacial sediments: A regional geological template for iceflow in West Antarctica, *Geophys Res Lett*, 28, 3493–3496, <https://doi.org/10.1029/2000GL011788>, 2001.
- Sundal, A. V., Shepherd, A., Nienow, P., Hanna, E., Palmer, S., and Huybrechts, P.: Melt-induced speed-up of Greenland ice sheet offset by efficient subglacial drainage, *Nature*, 469, 521–524, <https://doi.org/10.1038/nature09740>, 2011.
- Tarantola, A.: Popper, Bayes and the inverse problem, *Nat Phys*, 2, 492–494, <https://doi.org/10.1038/nphys375>, 2006.
- Tarasov, L., & Peltier, W. R.: Impact of thermomechanical ice sheet coupling on a model of the 100 kyr ice age cycle. *Journal of Geophysical Research: Atmospheres*, 104(D8), 9517–9545, 1999.
- Tarasov, L. and Peltier, W. R.: A geophysically constrained large ensemble analysis of the deglacial history of the North American ice-sheet complex, *Quat Sci Rev*, 23, 359–388, <https://doi.org/10.1016/j.quascirev.2003.08.004>, 2004.
- Tarasov, L. and Peltier, W. R.: Arctic freshwater forcing of the Younger Dryas cold reversal, *Nature*, 435, 662–665, <https://doi.org/10.1038/nature03617>, 2005.
- Tarasov, L., Dyke, A. S., Neal, R. M., and Peltier, W. R.: A data-calibrated distribution of deglacial chronologies for the North American ice complex from glaciological modeling, *Earth Planet Sci Lett*, 315, 30–40, <https://doi.org/10.1016/j.epsl.2011.09.010>, 2012.

- Tarasov, L. and Goldstein, M.: Assessing uncertainty in past ice and climate evolution: overview, stepping-stones, and challenges, *Climate of the Past Discussion*, 1–54, <https://doi.org/10.5194/cp-2021-145>, 2021.
- Tarasov, L., Hank, K., Lecavalier, B. S., and Pollard, D.: The glacial systems model (GSM), [in preparation] 2024.
- Thompson, W. G., Allen Curran, H., Wilson, M. a., and White, B.: Sea-level oscillations during the last interglacial highstand recorded by Bahamas corals - Supplement, *Nat Geosci*, 4, 684–687, <https://doi.org/10.1038/ngeo1253>, 2011.
- Tsai, V. C., Stewart, A. L., and Thompson, A. F.: Marine ice-sheet profiles and stability under Coulomb basal conditions, *Journal of Glaciology*, 61, 205–215, <https://doi.org/10.3189/2015JoG14J221>, 2015.
- Tulaczyk, S., Kamb, W. B., and Engelhardt, H. F.: Basal mechanics of Ice Stream B, West Antarctica 2. Undrained plastic bed model, *J Geophys Res Solid Earth*, 105, 483–494, <https://doi.org/10.1029/1999jb900328>, 2000.
- Tulaczyk, S.: Scale independence of till rheology, *Journal of Glaciology*, 52, 377–380, <https://doi.org/10.3189/172756506781828601>, 2006.
- Turney, C. S. M., Jones, R. T., McKay, N. P., Van Sebille, E., Thomas, Z. A., Hillenbrand, C. D., and Fogwill, C. J.: A global mean sea surface temperature dataset for the Last Interglacial (129-116&thinsp;ka) and contribution of thermal expansion to sea level change, *Earth Syst Sci Data*, 12, 3341–3356, <https://doi.org/10.5194/essd-12-3341-2020>, 2020.
- Vaughan, D. G., Comiso, J. C., Allison, I., Carrasco, J., Kaser, G., Kwok, R., Mote, P., Murray, T., Paul, F., Ren, J., Rignot, E., Solomina, O., Steffen, K., and Zhang, T.: Observations: Cryosphere, *Climate Change 2013: The Physical Science Basis. Contribution of Working Group I to the Fifth Assessment Report of the Intergovernmental Panel on Climate Change*, 317–382, <https://doi.org/10.1017/CBO9781107415324.012>, 2013.
- Velicogna, I.: Increasing rates of ice mass loss from the Greenland and Antarctic ice sheets revealed by GRACE, *Geophys Res Lett*, 36, L19503, <https://doi.org/10.1029/2009GL040222>, 2009.
- Velicogna, I., Sutterley, T. C., and Broeke, M. R. Van Den: Regional acceleration in ice mass loss from Greenland and Antarctica using GRACE time-variable gravity data, *Geophys Res Lett*, 41, 8130–8137, <https://doi.org/10.1002/2014GL061052>.Received, 2014.

- Völker, C. and Köhler, P.: Responses of ocean circulation and carbon cycle to changes in the position of the Southern Hemisphere westerlies at Last Glacial Maximum, *Paleoceanography*, 28, 726–739, <https://doi.org/10.1002/2013PA002556>, 2013.
- Watanabe, O., Jouzel, J., Johnsen, S., Parrenin, F., Shoji, H., and Yoshida, N.: Homogeneous climate variability across East Antarctica over the past three glacial cycles., *Nature*, 422, 509–512, <https://doi.org/10.1038/nature01525>, 2003.
- Weber, M. E., Clark, P. U., Ricken, W., Mitrovica, J. X., Hostetler, S. W., and Kuhn, G.: Interhemispheric Ice-Sheet Synchronicity During the Last Glacial Maximum, *Science* (1979), 334, 1265–1269, <https://doi.org/10.1126/science.1209299>, 2011.
- Weber, M. E., Clark, P. U., Kuhn, G., Timmermann, a., Sprenk, D., Gladstone, R., Zhang, X., Lohmann, G., Menviel, L., Chikamoto, M. O., Friedrich, T., and Ohlwein, C.: Millennial-scale variability in Antarctic ice-sheet discharge during the last deglaciation, *Nature*, 510, 134–138, <https://doi.org/10.1038/nature13397>, 2014.
- Weertman, J.: On the Sliding of Glaciers, *Journal of Glaciology*, 3, 33–38, <https://doi.org/10.3189/s0022143000024709>, 1957.
- Weertman, J.: Stability of the junction of an ice sheet and an ice shelf, *Journal of Glaciology*, 13, 3–11, 1974.
- Whitehouse, P. L., Bentley, M. J., and Le Brocq, A. M.: A deglacial model for Antarctica: Geological constraints and glaciological modelling as a basis for a new model of Antarctic glacial isostatic adjustment, *Quat Sci Rev*, 32, 1–24, <https://doi.org/10.1016/j.quascirev.2011.11.016>, 2012.
- Whitehouse, P. L.: Glacial isostatic adjustment modelling: Historical perspectives, recent advances, and future directions, *Earth Surface Dynamics*, 6, 401–429, <https://doi.org/10.5194/esurf-6-401-2018>, 2018.
- Whitehouse, P. L., Gomez, N., King, M. A., and Wiens, D. A.: Solid Earth change and the evolution of the Antarctic Ice Sheet, <https://doi.org/10.1038/s41467-018-08068-y>, 1 December 2019.
- Wingham, D. J., Wallis, D. W., and Shepherd, a.: Spatial and temporal evolution of Pine Island Glacier thinning, 1995–2006, *Geophys Res Lett*, 36, L17501, <https://doi.org/10.1029/2009GL039126>, 2009.
- Winkelmann, R., Martin, M. A., Haseloff, M., Albrecht, T., Bueler, E., Khroulev, C., and Levermann, A.: The Potsdam Parallel Ice Sheet Model (PISM-PIK) - Part 1: Model description, *Cryosphere*, 5, 715–726, <https://doi.org/10.5194/tc-5-715-2011>, 2011.

- Yokoyama, Y., Lambeck, K., De Deckker P, Johnston, P., and Fifield, L.: Timing of the Last Glacial Maximum from observed sea-level minima, *Nature*, 406, 713–6, <https://doi.org/10.1038/35021035>, 2000.
- Yokoyama, Y., Esat, T. M., and Lambeck, K.: Coupled climate and sea-level changes deduced from Huon Peninsula coral terraces of the last ice age, *Earth Planet Sci Lett*, 193, 579–587, [https://doi.org/10.1016/S0012-821X\(01\)00515-5](https://doi.org/10.1016/S0012-821X(01)00515-5), 2001.
- Yokoyama, Y., Esat, T. M., Thompson, W. G., Thomas, A. L., Webster, J. M., Miyairi, Y., Sawada, C., Aze, T., Matsuzaki, H., Okuno, J., Fallon, S., Braga, J. C., Humblet, M., Iryu, Y., Potts, D. C., Fujita, K., Suzuki, A., and Kan, H.: Rapid glaciation and a two-step sea level plunge into the Last Glacial Maximum, <https://doi.org/10.1038/s41586-018-0335-4>, 26 July 2018.
- Young, D. a., Wright, A. P., Roberts, J. L., Warner, R. C., Young, N. W., Greenbaum, J. S., Schroeder, D. M., Holt, J. W., Sugden, D. E., Blankenship, D. D., van Ommen, T. D., and Siegert, M. J.: A dynamic early East Antarctic Ice Sheet suggested by ice-covered fjord landscapes, *Nature*, 474, 72–75, <https://doi.org/10.1038/nature10114>, 2011.
- Yu, H., Rignot, E., Morlighem, M., and Seroussi, H.: Iceberg calving of Thwaites Glacier, West Antarctica: Full-Stokes modeling combined with linear elastic fracture mechanics, *Cryosphere*, 11, 1283–1296, <https://doi.org/10.5194/tc-11-1283-2017>, 2017.
- Yu, S.-Y., Berglund, B. E., Sandgren, P., and Lambeck, K.: Evidence for a rapid sea-level rise 7600 yr ago, *Geology*, 35, 891, <https://doi.org/10.1130/G23859A.1>, 2007.
- Zwally, H. J., Abdalati, W., Herring, T., Larson, K., Saba, J., and Steffen, K.: Surface melt-induced acceleration of Greenland ice-sheet flow., *Science*, 297, 218–222, <https://doi.org/10.1126/science.1072708>, 2002.

## Preface to Chapter 2, 3, and 4

Chapter 2 consists of a one-to-one copy of the manuscript titled “Antarctic Ice Sheet paleo-constraint database” which was published the Earth System Science Data journal. Chapter 3 consists of a one-to-one copy of the manuscript titled “A history-matching analysis of the Antarctic Ice Sheet since the last interglacial – Part 1: Ice sheet evolution” which was submitted to The Cryosphere journal. Finally, Chapter 4 consists of a one-to-one copy of the manuscript titled “A history-matching analysis of the Antarctic Ice Sheet since the last interglacial – Part 2: Glacial isostatic adjustment” intended for submission to The Cryosphere journal. Each chapter has a section detailing the various authors’ contributions.

# Chapter 2: Antarctic Ice Sheet paleo-constraint database

## Abstract

We present a database of observational constraints on past Antarctic Ice Sheet changes during the last glacial cycle intended to consolidate the observations that represent our understanding of past Antarctic changes and for state-space estimation and paleo-model calibrations. The database is a major expansion of the initial work of Briggs and Tarasov (2013). It includes new data types and multi-tier data quality assessment. The updated constraint database, AntICE2 (<https://thegithub.org/resources/4884>, Lecavalier et al., 2022), consists of observations of past grounded- and floating-ice-sheet extent, past ice thickness, past relative sea level, borehole temperature profiles, and present-day bedrock displacement rates. In addition to paleo-observations, the present-day ice sheet geometry and surface ice velocities are incorporated to constrain the present-day ice sheet configuration. The method by which the data are curated using explicitly defined criteria is detailed. Moreover, the observational uncertainties are specified. The methodology by which the constraint database can be applied to evaluate a given ice sheet reconstruction is discussed. The implementation of the AntICE2 database for Antarctic Ice Sheet model calibrations will improve Antarctic Ice Sheet predictions during past warm and cold periods and yield more robust paleo-model spin ups for forecasting future ice sheet changes.

## 2.1 Introduction

Numerical ice sheet models have been applied to reconstruct past continental-scale ice sheet changes in Antarctica for decades (Whitehouse et al., 2012a; Golledge et al., 2014; Briggs et al., 2014; Huybrechts, 2002; Pollard and DeConto, 2009). However, given the host of uncertainties in such modelling, assessment of the correspondence between model results and past Antarctic Ice Sheet (AIS) evolution requires (among other things) a quality-controlled constraint database with carefully assessed observational uncertainties. To date, only one database is publicly available (Briggs and Tarasov, 2013), and it suffers from some key limitations. Specifically, many regions, such as in the ice sheet interior, lack any observational constraints, and the data quality was not explicitly evaluated and specified through standardized criteria. Paleo-ice-sheet modelling has a host of uncertainties associated with initial and boundary conditions, physical processes, and their numerical representation. As such, inferences of ice sheet evolution must be meaningfully constrained against paleo- and present-day (PD) data. This requires an accessible database with well-defined observational uncertainties and a clear understanding of model limitations.

The AIS has consistently been identified as a dominant source of uncertainty in predicting past and future global sea level change (Meredith et al., 2019; Fox-Kemper et al., 2023). Previous studies have generated a wide range of future AIS projections (Little et al., 2013; Levermann et al., 2014; Ritz et al., 2015; Ruckert et al., 2017; Golledge et al., 2015; DeConto and Pollard, 2016) and paleo-retrodictions (Whitehouse et al., 2012a; Golledge et al., 2014; Briggs et al., 2014; Argus et al., 2014; DeConto and Pollard, 2016; Huybrechts, 2002; Simms et al., 2019; Albrecht et al., 2020), often with poorly defined

confidence intervals. Most often, these issues are dealt with via parametric tuning to generate reasonable predictions and upper- or lower-bound estimates (e.g. Golledge et al., 2014; DeConto and Pollard, 2016). The integration of a constraint database would help quantify what is deemed a reasonable result. Additionally, most previous studies inadequately explored parametric uncertainties, did not account for structural uncertainties of the model, and only applied a small set of observational constraints. An incomplete uncertainty assessment for model results largely nullifies the utility of the model predictions in the context of understanding the actual physical system under consideration (Tarasov and Goldstein, 2021).

In this study, we provide an overview of a data-quality curated Antarctic constraint database intended to characterize the past evolution of the AIS and to evaluate and calibrate ice sheet models. Key features are a quality classification and careful specification of data uncertainties. The variety of data types is presented along with spatial and temporal information. A general overview is provided that discusses the data–system relationship and observational uncertainties. In addition, we discuss the future inclusion of additional data types, such as the age structure of the ice, and highlight outstanding issues and community challenges.

Antarctic ice sheet observational constraint database  
AntICE2

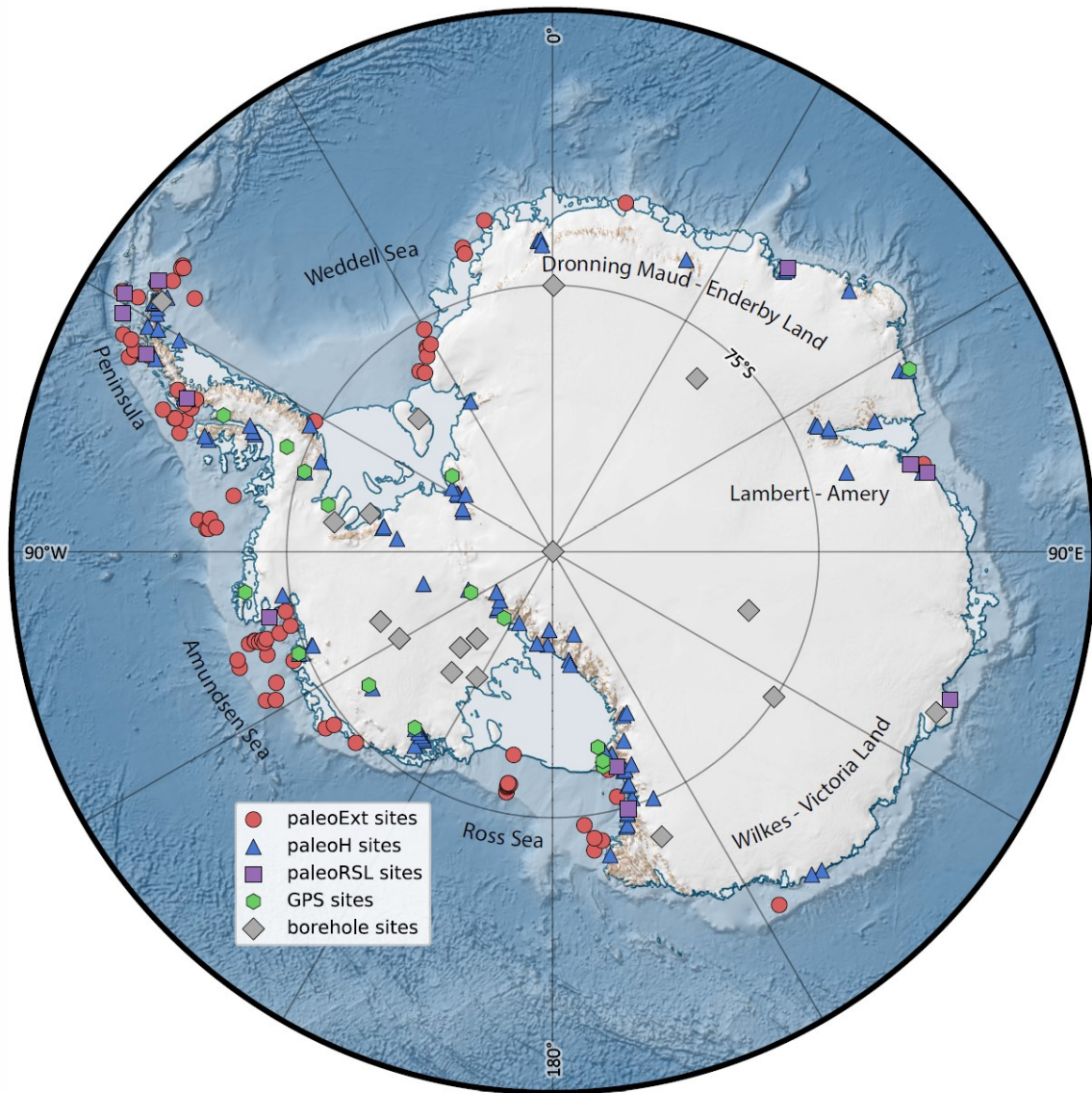


Figure 2.1: Antarctic Ice Sheet Evolution database version 2 (AntICE2) summary plot. The Antarctic basemap was generated using Quantarctica (Matsuoka et al., 2021).

## 2.2 AntICE2 constraints

The updated community Antarctic Ice Sheet Evolution observational constraint database version 2 (henceforth referred to as AntICE2) builds on the initial work of Briggs

and Tarasov (2013) by integrating additional data since the original publication, including new data types. The updated database comprises observations of (1) past grounded-ice and ice shelf extent (paleoEXT), (2) past ice sheet thickness (paleoH), (3) past relative sea level (paleoRSL), (4) borehole temperature profiles (boreTemp), and (5) Global Positioning System (GPS) observations of PD uplift rates (rdotGPS). Figure 2.1 shows a summary of the data types in the AntICE2 database and their spatial coverage. In addition to these observations, the PD ice sheet geometry (surface elevation, ice thickness, and basal topography; <https://nsidc.org/data/nsidc-0756/versions/3>, last access: 6 July 2023) and surface ice velocities (<https://nsidc.org/data/nsidc-0484/versions/2>, last access: 6 July 2023) are considered. This major revision of the AntICE database more than quintuples the direct observational constraints from 203 to 1023 (excluding the PD AIS geometry and surface velocity field). The database is open source (<https://thegithub.com/resources/4884>, last access: 6 July 2023) and available in the Supplement. The curation of data within the AntICE2 database was based on design criteria that excluded low-quality, inconsistent, and superfluous data. If the inference of past ice sheet changes is not increased when a data point is considered, then it is excluded to prevent database bloating. The curation criteria were established by the collective authorship of this study.

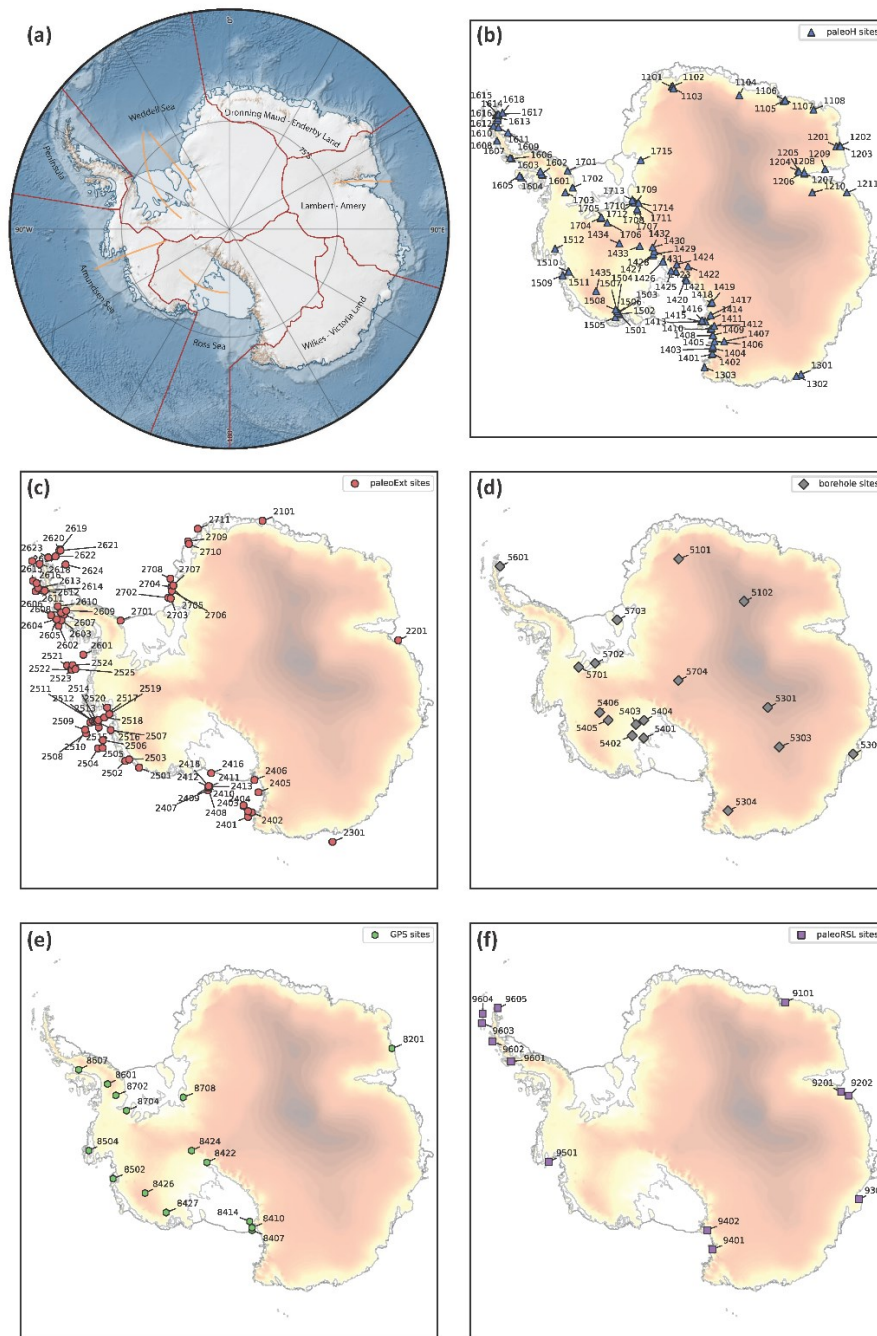


Figure 2.2: (a) Clustered IMBIE2 ice drainage basins (boundaries between clusters marked by red lines), key cross-section profiles (orange lines), and place names mentioned in the text; (b–f) are the sites with past ice thickness data (paleoH), past ice extent data (paleoExt), ice core borehole temperature profiles (boreTemp), present-day uplift rates (rdotGPS), and past relative sea level data (paleoRSL), respectively. The basemap shown in (a) was generated using Quantarctica (Matsuoka et al., 2021). The surface elevation shown in (b–f) is based on the BedMachine Antarctica version 2 dataset (Morlighem et al., 2020).

To calibrate or history match a model (Tarasov and Goldstein, 2021), it is necessary to compare model simulations to observations. For such comparison to have meaning, it logically follows that the relationship between each data point and the actual physical system must be specified. The selection of data with a high ratio of signal (measured quantity) to data uncertainty can strongly facilitate the inference process. To calculate a data–model misfit score for a given observation, the observation must include location data (latitude, longitude) and age data determined with a well-established dating technique, and it must quantify the relationship between the proxy observation and the characteristic (i.e. the recorded change in the ice sheet) it constrains. There are many sophisticated approaches to perform a meaningful data–model comparison (Tarasov and Goldstein, 2021), and there are tools that can assist those wanting an initial, albeit limited, data–model comparison implementation (e.g. Ely et al., 2019). For example, past ice thickness inferred from the elevation of an erratic boulder with an age determined by  $^{10}\text{Be}$  cosmogenic-nuclide exposure dating constrains the time when ice sheet thinning caused the ice surface to fall below the altitude of the sample. The paleo-data are categorized by site, where data from nearby samples (typically within <10 km distance) are clustered together, thereby yielding a time series at a given site (paleoRSL, paleoH). The exact spatial coordinates of the data are taken from the source publication and transcribed into the database. The sites of the paleodata in Figs. 2.1 and 2.2 show the average location of all the data clusters near a given site.

Each site has a unique four-digit identifier (Fig. 2.2). The first digit represents the data type (paleoH=1, paleoEXT=2, paleoRSL=9, boreTemp=5, and rdotGPS=8), the second digit designates the drainage basin sector (Dronning Maud Land–Enderby Land =

1, Lambert–Amery = 2, Wilkes–Victoria Land = 3, Ross Sea = 4, Amundsen Sea and Bellingshausen Sea = 5, Antarctic Peninsula = 6, and Weddell Sea = 7; sector boundaries are shown in Fig. 2.2), and the last two digits identify the site within each sector (westernmost site = 1, increasing by 1 eastward following the coast). The types of paleo-data along with full references are found in Excel tables (.xlsx) in the Supplement, and the latest version is in the online repository <https://thegithub.org/resources/4884> (Lecavalier et al., 2022). The method by which the data is processed and interpreted is described below.

## 2.2.1 Paleo-ice-sheet thickness

When an ice sheet recedes and thins, entrained terrigenous detritus in the ice is deposited on newly exposed land. The geographic coordinates, elevation, and exposure age of the bedrock or erratic sample provide a point estimate of the location of the ice surface or margin at the time of exposure. Note that, while the measured elevation is relative to PD sea level, the elevation at the time of initial exposure is unknown without knowledge of the glacial isostatic adjustment (GIA) history. However, the GIA estimate is not needed if the measurement is treated as a direct constraint on past ice thickness rather than ice surface elevation. In Antarctica, these measurements are mostly conducted along the slope of ice-free mountains or nunataks piercing through the ice sheet surface (e.g. Balco et al., 2016; Small et al., 2019). When many samples along a transect across a topographical slope are analysed, one can reconstruct a chronology of paleo-ice sheet thinning since the last ice thickness maximum in the region (Stone et al., 2003; Ackert et al., 2007). This is illustrated in Fig. 2.3, showing sample elevation histories from different sites during the deglaciation

following the Last Glacial Maximum (LGM: ca. 19–23 ka) and in Figs. S2.1 in the Supplement, showing the entire AntICE2 paleoH dataset.

Cosmogenic-nuclide exposure dating on bedrock and erratics is the primary method used to establish the timing of deglaciation of terrestrial sites (Bentley et al., 2006; Johnson et al., 2017; Nichols et al., 2019). The method entails the measurement of radioactive- and stable-nuclide isotopic concentrations ( $^{10}\text{Be}$ ,  $^{26}\text{Al}$ ,  $^3\text{He}$ ,  $^{21}\text{Ne}$ ,  $^{36}\text{Cl}$ , and  $^{14}\text{C}$ ) which accumulate in rock surfaces exposed to the atmosphere and therefore to the cosmic-ray flux. In the case of these isotopes, the nuclide concentration builds up when a rock exposed to the atmosphere is bombarded by cosmic rays (Ackert et al., 1999, 2007; Stone et al., 2003). Using the nuclide concentration and its radioactive half-life, the time when a rock was first exposed to cosmic rays, i.e. its exposure age, and thus the deglaciation age of its location can be calculated.

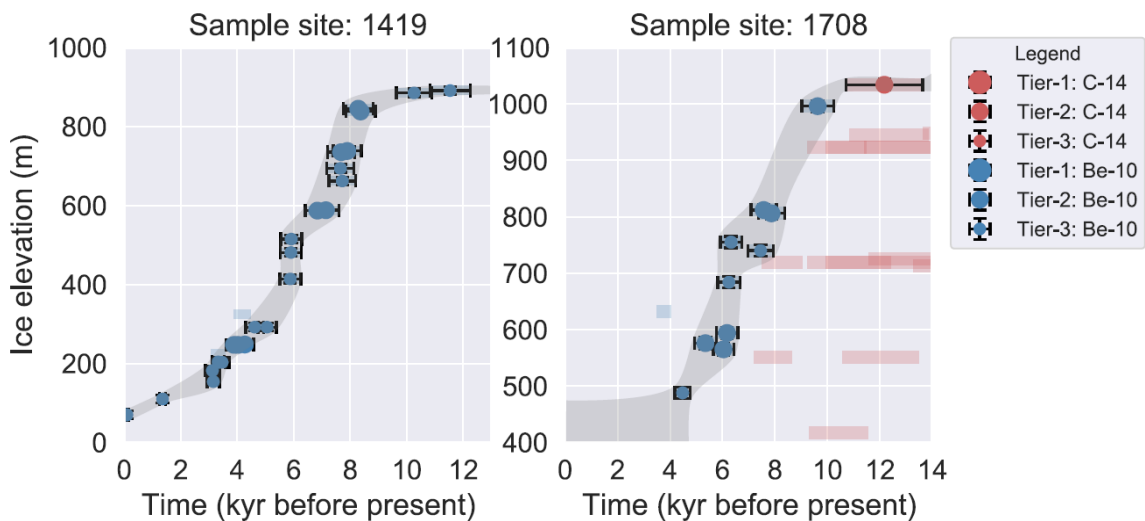


Figure 2.3: Sample past ice thickness (paleoH) data to illustrate the data quality and tier assignment. The elevation data are converted to ice thickness data using the BedMachine basal topography data. The grey band illustrates the expert-assessed  $2\sigma$  bounds on history at the given site. The blue and red transparent bands represent other C-14 and Be-10 data not assigned to a quality tier.

The interpretation of the deglaciation age can be complicated when erratics are absent or were redeposited (e.g. down a mountain slope); when the dated bedrock surface has been sufficiently eroded to remove cosmogenic nuclides accumulated during prior exposure periods; and/or when the site has subsequently been reburied by ice, snow, or sediment or shielded by topography. In a case where the cosmogenic nuclide clock was not sufficiently reset and thus where past nuclide concentrations persist, the sample would suffer from significant inheritance of pre-ice-cover exposure to cosmic rays. Given the limited number of areas in Antarctica where bedrock or erratics are exposed today, the total resulting number of collected samples is relatively low. This makes it difficult to identify when inheritance is an issue unless significant sample numbers are collected or paired  $^{10}\text{Be}$ – $^{26}\text{Al}$  dating is performed. For a complete description of the cosmogenic-nuclide-exposure-dating methodology and its challenges, we refer the reader to previous studies (Ackert et al., 1999; Stone et al., 2003; Bentley et al., 2006; Mackintosh et al., 2007; Balco et al., 2016; Johnson et al., 2017).

An informal cosmogenic-nuclide exposure age database (ICE-D) already exists and facilitates accessibility to raw data and derived exposure ages. The ICE-D database (<https://www.ice-d.org/>, last access: 6 July 2023) is inclusive and illustrates the conflicting and complex exposure histories in many regions. Quality control and processing of the data are required since many samples suffer from inheritance, and some regions provide an inconsistent record of past ice surface lowering (younger samples being higher than older samples). The deglaciation age is often inferred by the highest and youngest erratic sample (Bentley et al., 2006), with older bedrock samples at a similar elevation being discounted.

Alternatively, a mean age of several samples for a site may be calculated (Todd et al., 2010). In the original AntICE database (Briggs and Tarasov, 2013), the exposure ages and uncertainties were taken directly from the literature rather than recalibrating the ages for overall consistency, in part because the raw data were often inaccessible. The ICE-D database addresses this issue by using a single, up-to-date method to calculate all cosmogenic-nuclide exposure ages. Exposure ages used in this compilation were calculated using the LSDn scaling method of Lifton et al. (2014), as implemented in version 3 of the online exposure age calculator described by Balco et al. (2008) and subsequently updated by Balco (2020). Production rate calibration for  $^3\text{He}$  in pyroxene and olivine,  $^{10}\text{Be}$  in quartz, and  $^{26}\text{Al}$  in quartz uses the primary calibration datasets of Borchers et al. (2016). Production rate calibration for in situ  $^{14}\text{C}$  is based on measurements of the CRONUS-A quartz standard and the assumption that the concentration in this sample is at production–decay saturation, as described in Nichols et al. (2019). An altitude uncertainty value of  $\pm 10\text{m}$  is imposed when source publications do not include elevation uncertainty estimates. Whenever information on uncertainties is lacking in the source publication, uncertainty estimates are judged conservatively by relevant expert members of the author team or are derived from other studies using the same data type. The past ice thickness site IDs and locations are shown in Fig. 2.2 and visualized on a site-by-site basis in Figs. S2.1 in the Supplement.

Samples dated using in-situ-produced radiocarbon were previously not incorporated in the paleo-AIS thickness database. Because of the short half-life of  $^{14}\text{C}$ , this method is largely insensitive to inheritance on the deglacial timescales of interest and can therefore help identify cosmogenic nuclide exposure ages unbiased by inheritance. Consequently, in

situ  $^{14}\text{C}$  dating has resolved inconsistencies in AIS reconstructions for the Weddell Sea drainage sector (e.g. 1701, 1713, and 1715), where prior cosmogenic-nuclide exposure dating suggested hundreds of metres of thinning since the LGM, with neighbouring sites indicating no elevation changes relative to present during the same time period (Nichols et al., 2019). The inclusion of in situ radiocarbon data from the Shackleton Range, Lassiter Coast, and Schmidt Hills has increased consistency among paleo-ice-thickness data. Since the LGM, the revised data indicate that the Weddell Sea sector experienced a lowering of the ice sheet surface of  $\sim 300$  to  $600$  m, with a few sites exceeding  $800\text{m}$  of lowering (Balco et al., 2016; Hein et al., 2016; Bentley et al., 2010, 2017; Johnson et al., 2019; Nichols et al., 2019); this largely reconciles contradictory reconstructions of the regional post-LGM glacial history based on marine and terrestrial records (Hillenbrand et al., 2014).

New exposure data from the Transantarctic Mountains along the Ross Sea embayment tell a more complete, albeit only local, post-LGM ice-sheet-thinning history for the mountain chain. During the LGM, the surfaces of outlet glaciers presently draining directly into the Ross Sea reached an elevation of  $260$  to  $550\text{m}$  above today (e.g. Jones et al., 2015; Balco et al., 2019). Of the other outlet glaciers feeding the LGM Ross Ice Shelf and Sheet system, several had an elevation of  $\sim 1000\text{m}$  above today during the LGM (Spector et al., 2017). Paleo-ice-thickness data adjacent to the Siple Coast and Ross Island, as originally compiled in the AntICE database, showed that the ice sheet surface elevation at the onset of the post-LGM deglaciation ranged from  $\sim 1000$  to  $2000\text{m}$  above present. This illustrates the regional variability along the Transantarctic Mountains, with greater potential LGM elevation changes recorded further south and with significant variance

among the sites likely being related to local topographical features of specific valleys (Stone et al., 2003; Todd et al., 2010; King et al., 2020).

The Amundsen Sea drainage sector in West Antarctica has limited outcrops suitable for exposure dating; therefore, the region's past ice thickness is poorly constrained. The original database had a total of five data points constraining the elevation of the ice sheet surface at the LGM and at the start of the Holocene (11.7 ka) in the hinterland of the Amundsen Sea embayment to be between 45 and 300m above present (Ackert et al., 1999; Johnson et al., 2008). New cosmogenic exposure ages, totalling 25 quality exposure ages, suggest a pre-Holocene ice elevation upwards of at least 330–560m above present (Johnson et al., 2017, 2020). In the original version of the AntICE database, the Antarctic Peninsula lacked any paleo-ice-thickness data. Three new histories are included in our new iteration, and they all consistently report an ice elevation of ~350m above present early in the last deglaciation (Johnson et al., 2019; Bentley et al., 2011; Balco and Schaefer, 2013; Glasser et al., 2014). Finally, a new thinning history from the Sør Rondane Mountains in Dronning Maud Land proposes an ice surface lowering of less than 50m during the last deglaciation (Suganuma et al., 2014).

In our study here, we also include previously unpublished exposure data constraining AIS thinning since the last glacial period (Figs. S2.1 site ID 1419, 1422, 1425, and 1506). This includes some newer data of high quality (e.g. 1419, 1422, 1425, and 1506) that are not yet published in peer-reviewed articles but are included in the ICE-D database due to public access requirements of funding agencies.

## 2.2.2 Paleo-ice-sheet extent

The stratigraphy of marine sediment cores from the Antarctic continental shelf can preserve some of the complex history of glacial advance and retreat (Smith et al., 2019). The retreat of the grounding line (GL) can be inferred from the stratigraphic succession from subglacial to GL-proximal glacimarine sediments and that of the calving line can be inferred from the transition of GL-distal glacimarine to seasonal open-marine deposits (Smith et al., 2011; Anderson et al., 2014; Arndt et al., 2017; Bart et al., 2017; Heroy and Anderson, 2007).

Dating the transition from subglacial to glacimarine facies provides the age of the GL retreat across a core site, but usually, this approach has to rely on  $^{14}\text{C}$  dating of biogenic material.  $^{14}\text{C}$  dates obtained from calcareous (micro-)fossils provide the most robust age constraints for Antarctic marine sediments (e.g., Domack et al., 2005). However, there is a paucity of biogenic carbonate in Antarctic shelf sediments in general and in the GL-proximal facies directly overlying the subglacial till in particular. As such, either calcareous fossils (if present) from the open-marine facies or organic matter from the GL-proximal facies have to be dated (Bart et al., 2017). While the former dates only provide an absolute minimum age for GL retreat from a core site, the latter dating approach is hampered by the fact that the organic matter content in GL-proximal facies is typically very low and that this organic material often comprises large amounts of subglacially reworked fossil organic carbon. This can result in  $^{14}\text{C}$  ages much older than the time of sediment deposition and, thus, the time of GL retreat (Licht et al., 1998; Domack et al., 1999; Pudsey et al., 2006; Heroy and Anderson, 2007). Over the past 2 decades, some progress has been made in (i)

assessing the reliability of organic-matter-based  $^{14}\text{C}$  ages in constraining GL retreat (Hillenbrand et al., 2010a; Smith et al., 2014); (ii) compound-specific  $^{14}\text{C}$  dating of only the young, fresh fraction of the organic material (Ohkouchi and Eglinton, 2008; Rosenheim et al., 2008; Yokoyama et al., 2016; Subt et al., 2017); (iii) obtaining reliable  $^{14}\text{C}$  ages from even very small amounts of biogenic carbonate (Klages et al., 2014; Arndt et al., 2017, 2020); and (iv) utilizing paleomagnetic methods for dating Antarctic sediment cores (Hillenbrand et al., 2010b; Smith et al., 2021).

Retreat of the calving line of an ice shelf is usually reflected in a sediment core from the Antarctic shelf by means of the transition from a fine-grained terrigenous facies deposited distally from the GL into a biogenic-bearing, often diatom-rich facies deposited under open-marine conditions (Livingstone et al., 2012; Yokoyama et al., 2016; Bart et al., 2017). However, research on modern sub-ice shelf environments has shown that ocean currents can advect biogenic material from open-ocean settings far under ice shelves, where they can sustain benthic fauna assemblages and potentially result in deposition of sediments resembling open-marine facies (Hemer and Harris, 2003; Hemer et al., 2007; Post et al., 2007; Riddle et al., 2007). Measurements of the cosmogenic-nuclide  $^{10}\text{Be}$  in marine shelf sediments has shown promise that this ambiguity can be avoided in future studies (Yokoyama et al., 2016). Thus, despite all the aforementioned improvements, the dating of Antarctic shelf sediments and constraint of the time of GL and calving-line retreat still remain a challenge.

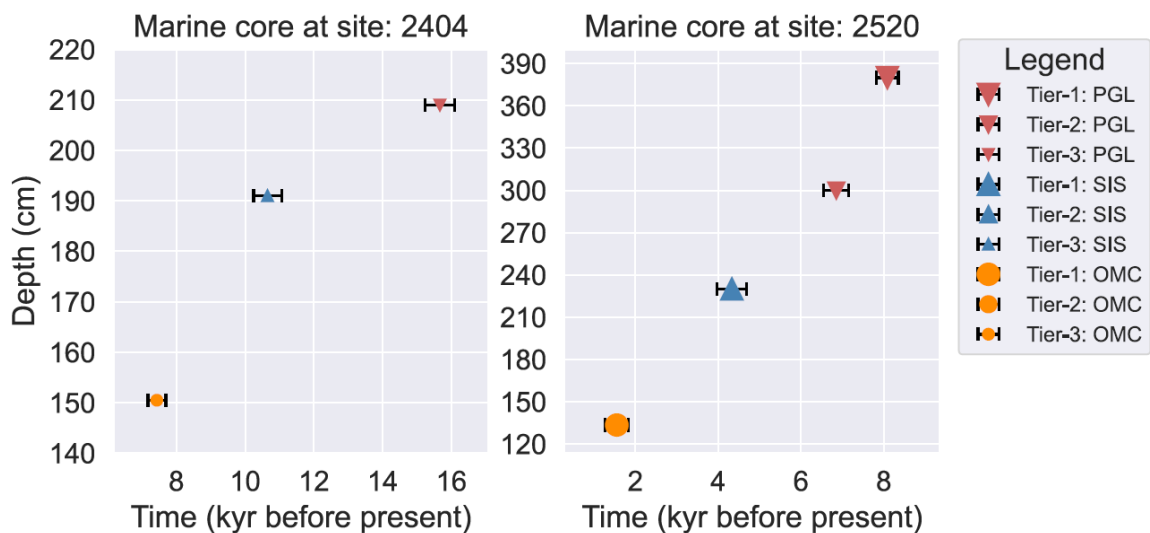


Figure 2.4: Sample past ice extent (paleoExt – proximal to the grounding line, PGL; sub-ice-shelf, SIS; open-marine conditions, OMC) data from a marine sediment core to illustrate the data quality and tier assignment.

The combination of the complex stratigraphy of sediment cores from the Antarctic continental shelf and the lack of reliable age control for key facies renders the interpretation of the proxy record in most cores non-trivial. For this reason, only those marine sediment records that clearly document a position below grounded ice, under an ice shelf, or in (seasonal) open water at a particular time are added to the AntICE2 database (Figs. 2.4 and S2.2-2.3 in the Supplement).

The paleoEXT database was originally a curated version of the GL retreat ages compiled by Livingstone et al. (2012). Our new iteration has been updated to include the RAISED consortium compilation (Bentley et al., 2014; Hillenbrand et al., 2014; Anderson et al., 2014; Mackintosh et al., 2014; Ó Cofaigh et al., 2014; Larter et al., 2014), and it has also been supplemented by a number of more recent studies (Bart et al., 2018). For each marine sediment core, obvious  $^{14}\text{C}$  age outliers or down-core age reversals, if present, were removed in accordance with the source literature. Converting measured radiocarbon

activities to calendar age requires corrections for the variable atmospheric radiocarbon history and for the reservoir age of the ocean. All the past ice extent ages were recalibrated using a consistent marine reservoir correction of  $1144 \pm 120$  yr (Hall et al., 2010) with CALIB v8.1 (CALIB rev. 8; Stuiver and Reimer, 1993) using the Marine20 calibration curve (Heaton et al., 2020). The full information for the marine cores, including expedition ID, sample depth, etc., is given in the ICE-D marine database (<http://marine.antarctica.ice-d.org/>, last access: 21 December 2023).

Since the original AntICE database, numerous cruises have collected marine sediment cores along transects from near the modern ice shelf front to the continental-shelf edge. The biggest addition of data occurred in the Amundsen Sea sector, where LGM grounded-ice extent and deglacial GL retreat have been reconstructed across Pine Island–Thwaites Trough (Smith et al., 2014; Hillenbrand et al., 2013; Kirshner et al., 2012), Dotson-Getz Trough (Smith et al., 2011; Hillenbrand et al., 2010b), Abbot–Cosgrove Trough (Klages et al., 2017), and Hobbs Trough (Klages et al., 2014). In Pine Island–Thwaites Trough, the initial GL retreat from the outer continental shelf occurred at 20 ka, reaching the middle shelf by 13.6 ka and the inner shelf by 10.6 ka (Larter et al., 2014; Smith et al., 2014). In the Ross Sea sector, marine sediment cores indicate an initial retreat from the continental shelf edge prior to the Holocene. The Holocene retreat across large sections of the eastern and western Ross Sea continental shelf was asynchronous (Anderson et al., 2014; Bart et al., 2018) but occurred during the early to middle Holocene (McKay et al., 2008, 2016; McGlannan et al., 2017; Bart et al., 2018). The calving line of the Ross Ice Shelf retreated throughout the middle to late Holocene, reaching its present extent by  $\sim 1.5$  ka (Yokoyama et al., 2016). In the Weddell Sea, cores from the outer Filchner Trough

suggest that the GL advanced and retreated prior to the LGM and readvanced again in the early Holocene before retreating by 8.7 ka (Stolldorf et al., 2012; Arndt et al., 2017). These additional paleo-ice-extent data portray a regionally complex deglacial history (Arndt et al., 2017, 2020; Hodgson et al., 2018).

### 2.2.3 Paleo relative sea level

Reconstructions of past sea level are based on a variety of indicators: isolation basins; raised beaches and deltas; marine shells; driftwood; whale, seal, and penguin fossils; bedrock exposure dating; and lower elevational limits of perched boulders (Verleyen et al., 2005, 2017; Shennan et al., 2015; Hodgson et al., 2016). The dated relative-sea-level (RSL) proxy data infer an upper bound, a lower bound, or a two-way bounded estimate on past sea level given the height of the datum relative to present sea level. Geographically proximal data form a local RSL history which constrains sea level change through time. Only 0.44% of Antarctica is ice-free land, which limits the regions where past sea level records can be investigated, and many of these outcrops are nunataks at high altitudes (Hodgson et al., 2016; Verleyen et al., 2017). For the Antarctic domain, the most common RSL data are based on records of raised beaches, isolation basins, molluscs, and penguin remains.

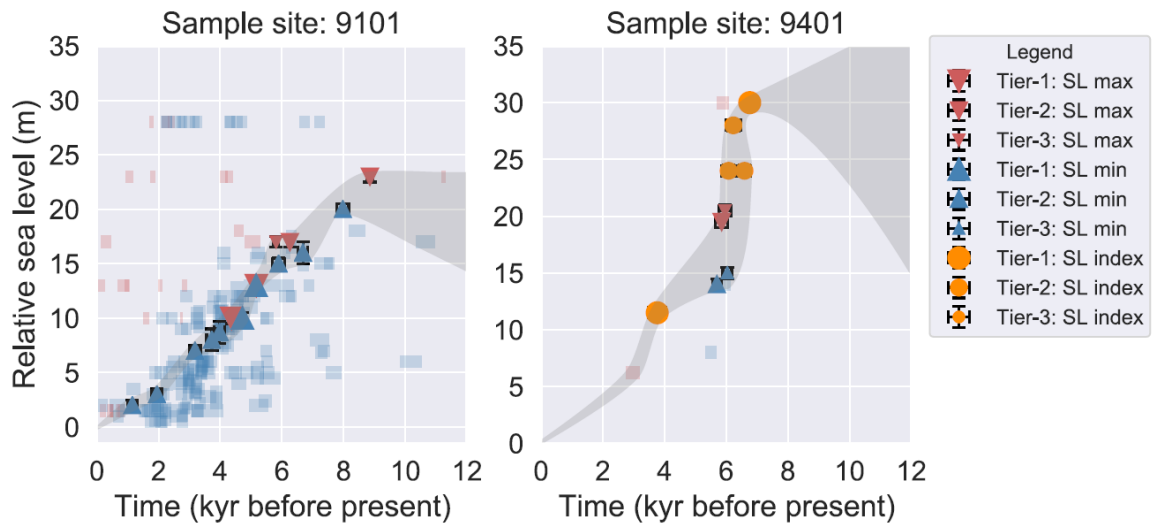


Figure 2.5: Sample past relative sea level (paleoRSL) data to illustrate the data quality and tier assignment. The grey band illustrates the expert-assessed  $2\sigma$  bounds on history at the given site. The transparent blue and red bands represent other limiting ages not assigned to a quality tier.

The sea level proxy data with the highest accuracy are those from isolation basins, which originally formed as marine basins but became subsequently isolated from the ocean through sea level fall and/or glacial isostatic rebound of the bedrock (NB: an isolation basin can later be reconnected to the ocean by subsidence and/or sea level rise). The sill height that controls drainage from the basin is the RSL elevation proxy. Dating the microfossil remains at the marine–lacustrine or lacustrine–marine transition of a sediment core extracted from an isolation basin determines the age of isolation from or reconnection to the ocean. Together, this establishes a precise RSL elevation and age for a given site (Zwartz et al., 1998; Verleyen et al., 2005; Roberts et al., 2011). Past RSL observations of lesser quality that simply constrain a maximum or minimum elevation of past sea level come from  $^{14}\text{C}$  ages on biogenic material buried in raised beaches. Dates on mollusc shells or penguin fossils provide an age for the paleo-beach (Hall and Denton, 1999; Shennan et

al., 2015). Similarly, burial ages of raised beaches can be derived from optically stimulated luminescence (OSL) dating of beach cobbles (Simkins et al., 2013). Additional details on the RSL proxy data are discussed in Briggs and Tarasov (2013).

The AntICE2 past RSL sites and their IDs are shown in Fig. 2.2 and visualized in Figs. 2.5 and S2.4 in the Supplement. When uncertainties were provided in the source publications, they were incorporated in the database. When they were lacking, a  $\pm 1\text{m}$  elevation uncertainty was assumed. Moreover, as in Briggs and Tarasov (2013), another  $\pm 1\text{m}$  uncertainty is added to allow for present and paleo tidal variations (Sun et al., 2022) when measured uncertainties are less than 2 m. The radiocarbon ages in the database were recalibrated using the CALIB v8.1 with the IntCal20 (SHCal20), Marine20, or the mixed marine Southern Hemisphere radiocarbon calibration curve depending on the sample type and content of marine material (Reimer et al., 2009; Heaton et al., 2020). The source publications use different marine reservoir corrections depending on the dated material, while our database standardizes the marine reservoir correction to  $1144 \pm 120$  yr (Hall et al., 2010) for simplicity and consistency. By providing the uncorrected  $^{14}\text{C}$  ages, uncertainties, and marine reservoir corrections, the relative sea level dataset can easily be recalibrated. Moreover, this enables the data to be incorporated within an online database (e.g. ICE-D RSL repository) so that ages can be dynamically recalibrated upon request.

The additional RSL data in the AntICE2 database have significantly increased the geographic coverage when compared to the original iteration (Simms et al., 2011; Simkins et al., 2013; Hodgson et al., 2016; Verleyen et al., 2017). In Dronning Maud Land, new isolation basin data from Lützow-Holm Bay more robustly constrain past RSL, which is estimated to have fallen by 20m over the Holocene (Verleyen et al., 2017). These sea level

index points are generally consistent with the previously published limiting dates (Miura et al., 1998). The Lambert–Amery sector around Prydz Bay contains exposed coastal land, where isolation basin contacts, shells, and penguin fossils from raised beaches were dated (Hodgson et al., 2016). This has boosted the reconstructed sea level history of the region, suggesting an early Holocene sea level rise from a -4 to +8m highstand at ~8 ka, subsequently followed by a gradual fall to PD levels starting at ~8 ka (Zwartz et al., 1998; Berg et al., 2010; Hodgson et al., 2016). In the Amundsen Sea sector, there is one  $^{10}\text{Be}$  exposure date potentially constraining sea level change from a sample that is suspected to have experienced isostatic emergence from the ocean at 2.2 ka (Johnson et al., 2008). Alternatively, this exposure date with a modern elevation of 8m above sea level could simply reflect ice margin retreat, but it generally appears to be consistent with more recent local RSL proxy data (Braddock et al., 2022). The Antarctic Peninsula is constrained by six RSL time series. Marguerite Bay provides limiting dates and a few isolation basin ages that indicate a ~20m sea level fall from 7 ka, reaching PD sea levels by 1.5 ka (Emslie and McDaniel, 2002; Bentley et al., 2005; Simkins et al., 2013). The South Shetland Islands contain some of the largest ice-free sections of land in Antarctica, providing upper and lower bounds on past sea level and, more importantly, isolation basin index data which imply a sea level fall from a 16m highstand at ~8 ka (Watcham et al., 2011; Simms et al., 2011). Near and on James Ross Island, isolation basin index data indicate a gradual Holocene sea level fall, with the earliest constraint indicating that sea level was 11m above present at 6 ka (Hjort et al., 1997; Roberts et al., 2011).

## 2.2.4 Ice core borehole temperatures

The original AntICE database lacked constraints in the interior of the ice sheet. To partly remedy this major issue, we incorporate a new powerful data type – the temperature profiles of major Antarctic ice core boreholes (Fig. 2.6). The temperature structure of the ice can be measured by running a temperature logger down the borehole of an ice core (Cuffey et al., 2016). Past changes in temperature, ice velocity, and ice thickness will affect the thermal structure of the ice sheet. Therefore, the resulting observations of temperatures through the ice constrain the present and past thermal forcing and ice dynamics.

Borehole temperature profiles generally have one of two structures characterized by the depth of the englacial thermal minimum. In the first case, a borehole temperature profile is characterized by minimum temperatures near the ice surface which progressively increase towards the bed (Engelhardt, 2004a, c; Motoyama, 2007; Lukin and Vasiliev, 2014; Weikusat et al., 2017; Mulvaney et al., 2021; Buizert et al., 2021); this case is typical of low-accumulation sites dominated by heat diffusion. In the second case, ice temperatures remain cold at depth and reach a deeper englacial thermal minimum, which is marginally cooler than the surface ice, before they warm again towards the base, such as at the sites of the West Antarctic Ice Sheet Divide ice core (WDC) and Byrd ice core (Gow et al., 1968; Van Ommen et al., 1999; Cuffey et al., 2016); this case is typical of high-accumulation sites dominated by the downward advection of cold surface ice. The ice thickness, geothermal heat flux, horizontal ice advection, and surface accumulation are the main controls on whether or not the base is at the pressure-melting point, with serious ramifications for basal hydrology and ice dynamics.

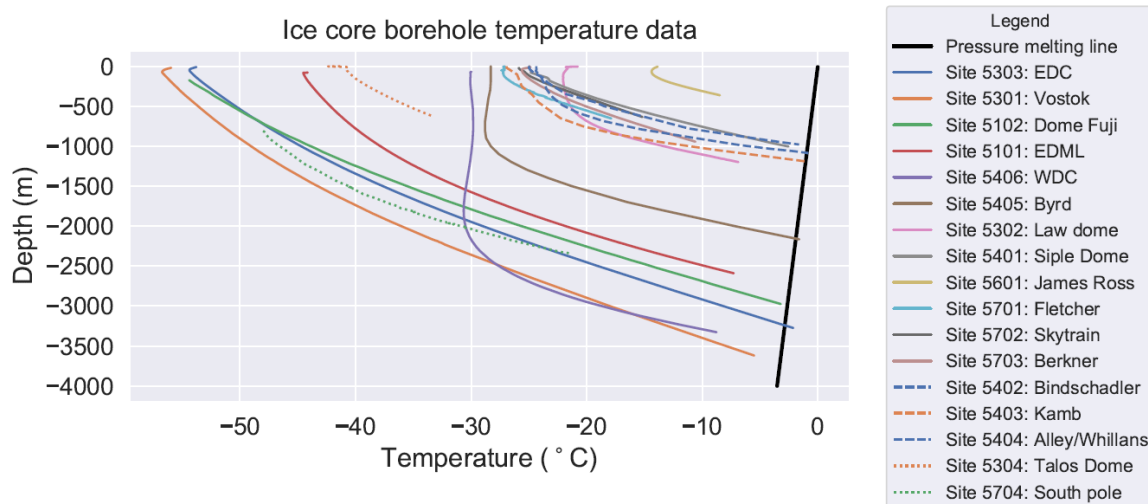


Figure 2.6: Ice core borehole temperature (boreTemp) data to illustrate the data quality and tier assignment. The dashed lines represent the sites in the Siple Coast which are tier-2 data, and the dotted lines represent the most limited borehole temperature data which do not cover the majority of the ice column (tier-3 data).

The various borehole temperature profiles were measured using different instruments, and some were measured at a time considerably after the ice core had been drilled (Motoyama, 2007; Lukin and Vasiliev, 2014). With the precision of the used temperature logger rarely reported in a source publication, an uncertainty value of  $\pm 0.1^{\circ}\text{C}$  is assumed. The Talos Dome and South Pole borehole temperature profiles do not cover the majority of the entire ice column, minimizing their overall constraint effectiveness capability. Several borehole temperature profiles have been measured along the Siple Coast in the Ross Sea sector (Engelhardt, 2004a). Although they all share a high degree of correlation, a total of four Siple Coast boreholes were included in the database to maximize both the spatial distribution and the number of prominent ice sheet features sampled. The temperature profiles are from the Siple Dome, Bindschadler, Kamb, and Alley–Whillans ice stream boreholes (Engelhardt, 2004a, b).

## 2.2.5 Present-day uplift vertical land motion

Across Antarctica, a Global Positioning System (GPS) network measures the displacement of the solid Earth. GPS measurements, although relatively scarce, can supplement the even-sparser RSL dataset in constraining the isostatic response of the solid Earth to past and present changes in surface AIS load. The vertical deformation rates derived from GPS measurements represent the integrated signal of several processes operating on various timescales. The two primary contributing factors to vertical land motion are the remaining slow viscous response to past ice and water load changes and the near-instantaneous elastic response due to contemporary ice load changes (Martín-Español et al., 2016; Sasgen et al., 2017).

GPS observations have previously been implemented to evaluate Antarctic GIA and ice sheet models (Argus et al., 2014; Gomez et al., 2018; Whitehouse et al., 2012b; Ivins et al., 2013). The resulting Antarctic GIA estimates are used in conjunction with satellite-derived remote gravimetry or altimetry data to infer contemporary mass balance changes of the AIS (Shepherd et al., 2018).

GPS deformation rates first have to be corrected for the elastic response to contemporary ice mass change before they can be inferred to reflect the background viscous response to past ice mass change (Martín-Español et al., 2016; Sasgen et al., 2017). For our database, a key criterion for GPS data evaluation is the constraint value for Antarctic GIA. We therefore divide the dataset into stations that are not influenced significantly by modern ice mass change and stations with a significant contemporary elastic signal (for details, see the discussion section below). A total of 67 GPS stations constrain the isostatic adjustment

of the land bedrock for the period 2009 to 2014, with a total of 15 GPS stations being assigned to a high-quality tier (as discussed in Sect. 2.3.1.5).

Alongside the GPS uplift rates, we provide the elastic response-corrected vertical rates from Martín-Español et al. (2016). Both the GPS and elastic-corrected datasets come associated with their own explicit and implicit uncertainties. In compiling the AntICE2 GPS dataset, we selected sites that are hardly impacted by contemporary mass balance changes (negligible elastic signal). The accuracy of the elastic-corrected high-quality subset of GPS data is dependent on the validity of the inferred contemporary ice load changes and the resulting elastic signal.

## 2.2.6 Present-day geometry and surface ice velocity

The AIS geometry from BedMachine Antarctica version 2 provides the primary PD constraint and initialization conditions (BCs) (Morlighem et al., 2020). This directly constrains several key PD metrics by comparing the modelled ice sheet to contemporary observations, namely ice thickness mean-squared errors (MSEs) for East Antarctica, West Antarctica, and all ice shelves; squared errors of latitudinal and longitudinal grounding-line positions along five key transects shown in Fig. 2.2a (Ross, Amundsen, Ronne, Filchner, and Amery transects); squared errors of grounded and total ice area; squared errors for the ice shelf area across five sectors (Ross, Amundsen–Bellingshausen, Weddell, Lambert–Amery, and all other remaining sectors combined). These PD observations provide powerful spatial constraints but limited temporal constraints that only extend back into the late Holocene. The grounding-line transects and sector margins are shown in Fig. 2.2a. The specific locations of these metrics, particularly the transects, were chosen to investigate

areas sensitive to past and present ice sheet changes. The data provided by BedMachine have a horizontal resolution of 500m by 500m and include  $2\sigma$  uncertainties on ice thickness inferences (Fig. 2.7a–d). The topographic fields must be upscaled to the appropriate resolution for a given ice sheet model grid; the metrics discussed above are then calculated at this resolution for consistency. As part of the NASA-funded Making Earth System Data Records for Use in Research Environments (MEaSUREs) programme, surface velocities of the AIS have been made available for the period from 2005 to 2017 (Mouginot et al., 2019) (Fig. 2.7e–f). The surface velocity dataset is remotely derived from satellite data provided at a horizontal resolution of 450m by 450 m, which is similarly upscaled to the ice sheet model grid resolution for data–model comparison and inversion.

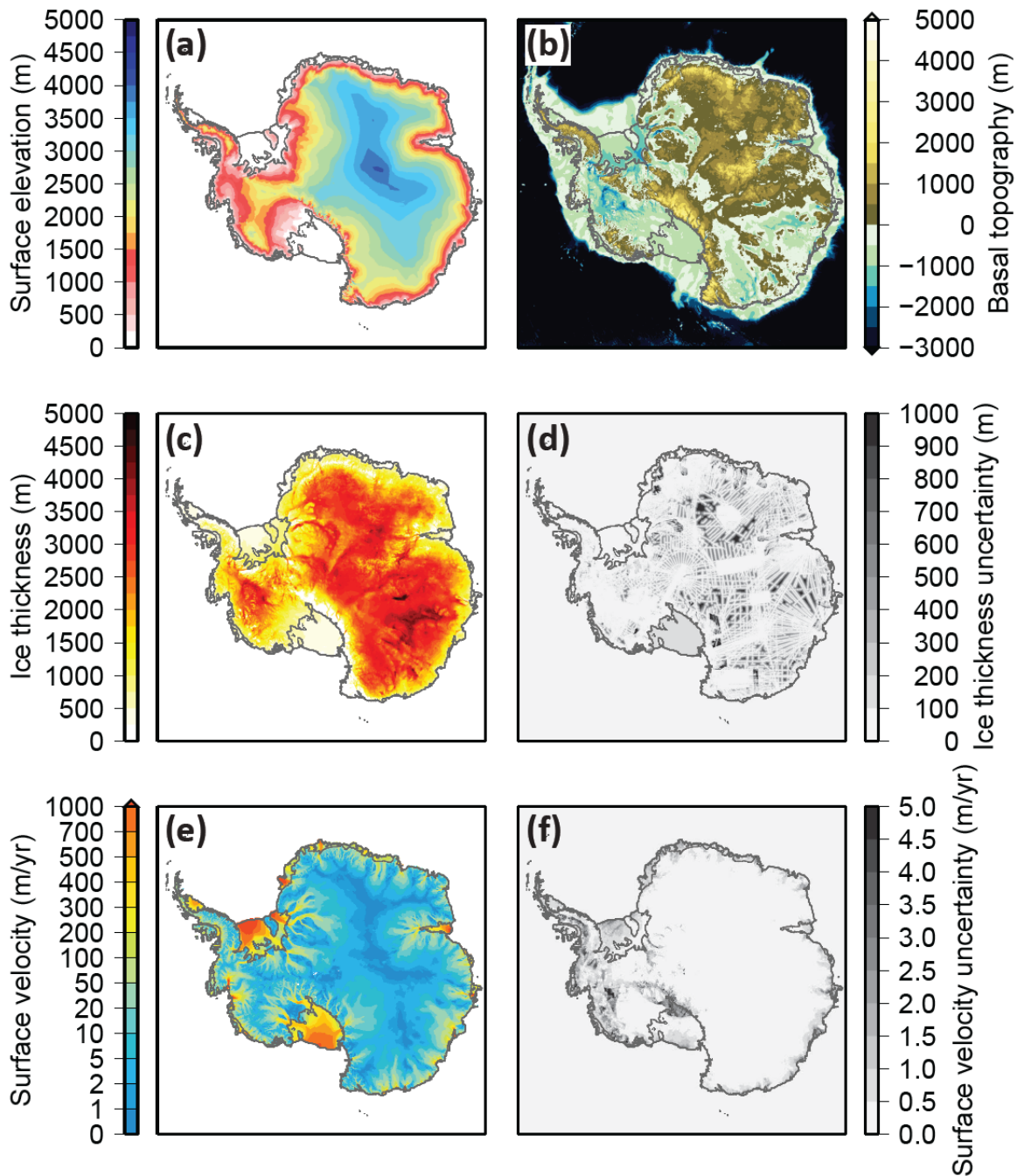


Figure 2.7: (a–d) Present-day Antarctic Ice Sheet geometry based on the BedMachine version 2 PD data (Morlighem et al., 2020) and (e–f) MEaSUREs ice surface velocity over 2005–2017 and its associated uncertainties (Mouginot et al., 2019).

## 2.2.7 Data uncertainty structure

The uncertainties in the database are explicitly stated as  $1\sigma$  and  $2\sigma$  intervals. Some of the observational data in the database exhibit two-way or one-way bounds. It follows that some proxy data and their uncertainties represent just an upper- or lower-bound constraint (one-way bounds). Two-way Gaussian uncertainties are affiliated with the PD observations (ice sheet geometry and surface velocities), the GPS observations, and borehole temperature measurements. The paleoH and paleoExt data are also represented by two-way symmetric uncertainties around the mean. Some of the paleoExt data constrain exclusively the onset of open-marine conditions, rendering them a one-way constraint. There are several one-way constraints in the RSL database as well, such as those that are limiting minimum or maximum RSL inferences (molluscs, penguin remains). The details are specified in the database itself and were previously discussed in greater detail in Briggs and Tarasov (2013). These observations are converted to nominal two-way non-symmetric constraints by assigning an exceedingly small or large uncertainty bound to the unspecified region of the probability distribution. This adoption of a Gaussian observational error model facilitates ice history scoring. However, the validity of a Gaussian error model for all the types of data in our database awaits future testing.

## 2.3 Discussion

The implementation of a database for geophysical model calibration has a number of requirements to ensure utility. In large part this boils down to clear specification of the relationship between the data and the real-world system under consideration. As such, the

database curation process and all data uncertainties need to be clearly specified. From the perspective of modellers, a careful evaluation of internal and external model limitations is necessary to produce meaningful data–model comparisons. In this discussion, some considerations are explicitly stated when it comes to the aforementioned challenges.

For much of the last glacial cycle, there are very few to no paleo-observations that directly constrain the configuration of the ice sheet (Fig. 2.8). The paleo-data (paleoEXT, paleoH, paleoRSL) have a mean age of 9.5 ka and a nonuniform distribution with a long tail of older ages beyond the LGM. A total of 81% of the paleo-data have a Holocene age (<11.7 ka). However, some data points integrate ice sheet behaviour over a period and so have constraining power far exceeding their measured age (e.g. PD borehole temperature data – Ackert, 2003).

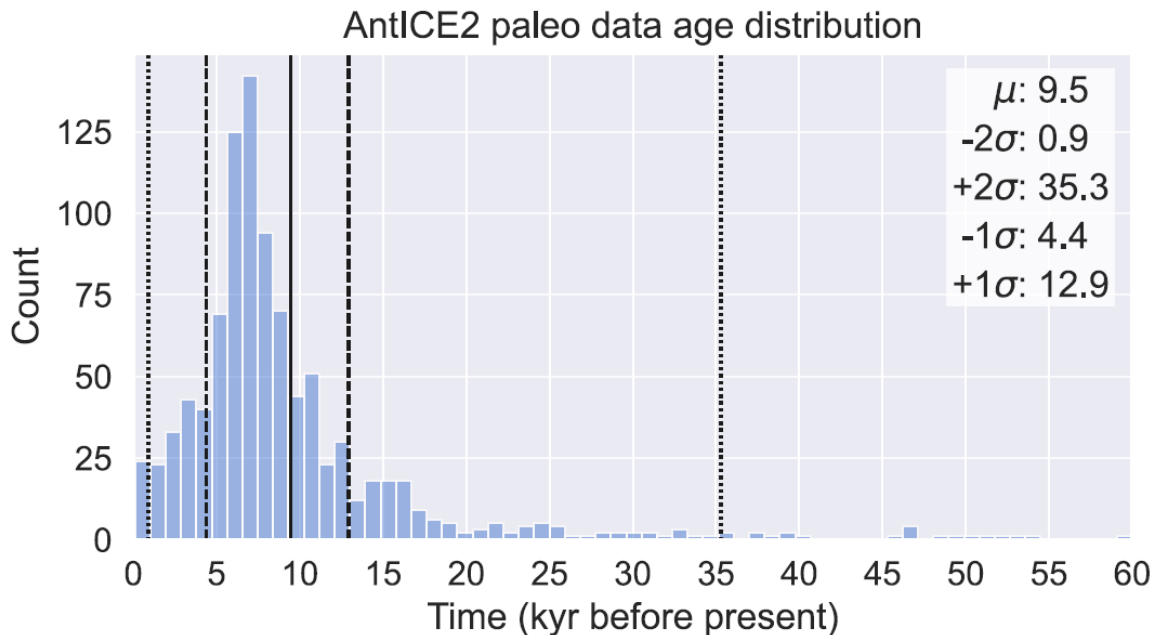


Figure 2.8: Age distribution of AntICE2 paleo-data (paleoExt, paleoH, paleoRSL), with the vertical solid line, dashed lines, and dotted lines representing the mean,  $\pm 1\sigma$ , and  $\pm 2\sigma$  ranges, respectively. The  $1\sigma$  and  $2\sigma$  bounds correspond to the nominal 68% and 95% confidence intervals. The skewed distribution has a median value of 7.4 ka.

The heterogeneity in the spatial distribution of the data is illustrated in Fig. 2.2. Data of a given type constrain the surrounding region based on the data type and data quality. This is due to the spatial correlation of certain ice sheet system changes such as margin retreat or GIA. For instance, past ice thickness data might constrain localized ice elevation changes for a particular glacier only. In contrast, past RSL data document changes in the bedrock and geoid elevation, which is a spatially smooth signal. Each data point has a specific spatio-temporal sphere of influence, which defines its ability to constrain the model. Figures 2.2 and 2.8 illustrate areas in space and time with clear data gaps and densely sampled areas. Thus, this heterogeneity highlights the importance of never equally weighing all the data when scoring since it would introduce major biases in an ice sheet model calibration. An inverse-areal weighing of the data can be used to avoid overfitting the model to a particular region with high data density if the correlation between data-model residuals is not otherwise accounted for (Tarasov and Goldstein, 2021).

Field observations are often collected in Antarctic regions with a complex and highly variable topography that is inadequately resolved in typical Antarctic-wide ice sheet simulations. Thus, the more a datum embodies broader characteristics of the glacial system as opposed to reflecting subgrid characteristics, the higher its potential constraint value. For data containing a significant subgrid signal, some combination of upscaling of the data and/or downscaling (potentially including subgrid modelling) of the model results will be required but may not always be physically justifiable. The RSL change, borehole temperatures, and GPS rates represent spatially and temporally smooth proxies and require no upscaling corrections. The marine paleoExt data capture rather broad nonlinear changes

in the GL, sub-ice-shelf, or open-marine characteristics. However, for GL sites near the continental shelf break, the gridded topography could potentially designate areas at the shelf break as immediately off the continental shelf, for which the model would never produce grounded ice. Some terrestrial data, such as nunatak indicators, may also predominantly reflect subgrid high-frequency features that will therefore not be resolved by the model. Given fundamental model limitations, such as grid resolution, for most if not all data, the physical signal represented by the data (i.e. after accounting for observational uncertainties) will only be incompletely resolvable by the model even after appropriate upscaling and/or downscaling. The resultant fundamentally irreducible discrepancy between the model results and geophysical system will then need to be accounted for in the error model describing the relationship between the model and physical system (see Sect. 3.1.8).

The uncertainties associated with the indicative meaning of various proxy data must be considered when estimating observational uncertainties. This is particularly relevant for the paleoExt data because ocean currents can advect particles from open water beneath an ice shelf so that the resulting deposits resemble open-marine facies. This can be up to 6 and 100 km from the calving front for small and large ice shelves, respectively (Riddle et al., 2007; Post et al., 2014; Hemer and Harris, 2003; Hemer et al., 2007). Similarly, facies characterizing sediments deposited proximal to the GL (PGL) can form up to 10 km seaward from the GL at the time of formation (Smith et al., 2019). When it comes to paleoRSL data, considerations should be made for the fact that storm surges can impact the in situ deposition of certain proxy data. This has previously been handled by applying a storm beach adjustment factor of up to 1m for proxy data from, but not limited to, mollusc

fragments and penguin bones (Briggs and Tarasov, 2013). This information is not integrated within the AntICE2 database, and we defer with regard to the incorporation of such uncertainties within a data–model-scoring implementation.

### 2.3.1 Data curation and tiered data quality assessment

To facilitate data–model comparison, the paleo ice extent, ice thickness, relative sea level, borehole temperatures, and PD uplift rates are all curated, and individual data points are categorized into quality tiers (Table 2.1). Tier 1 is the highest quality tier, while tier 3 is the lowest accepted tier (for example, see Fig. 2.3). Tier-1 data have the greatest power to constrain the ice sheet and GIA history. For example, in the case of cosmogenic-exposure dating, key exposure ages capturing both the LGM ice thickness and timing of deglaciation prove to be most valuable since they constrain the most prominent deglacial changes. Tier-2 data typically represent data with less constraining power that primarily supplement tier-1 data. Returning to the previous exposure data example, tier-1 data represent a minimal set of crucial tie points for the LGM ice thickness and timing of deglaciation, while tier-2 data provide finer detail for the deglacial ice-sheet-thinning history, with minimal correlation to other data. Finally, tier-3 data include lower-quality observations that exhibit a high degree of correlation with tier-1 and tier-2 data and for which data uncertainty specifications are less confident. The tier assignment depends on data type, data availability, and data density. This particularly becomes an issue at sites with limited observations. When mentioning lower-quality data, we refer to data with larger measurement or analytical uncertainties or limitations due to a proxy’s indicative strength (i.e. whether its interpretation is ambiguous or not). Data that are not assigned to a quality

tier typically represent redundant data, data with very large uncertainties, data which do not accurately represent the local environmental history, or where original publications note potential analytical problems. In the case of cosmogenic-nuclide data, exposure ages that clearly suffer from inheritance are not assigned to a quality tier. Moreover, some data are excluded from tier assignment based on physical impossibility – e.g. exposure age data require that younger ages must be at a lower elevation than older ages for a given site. In the following subsections, we describe the tier assignment process which involves evaluating the datasets with respect to strict criteria that assign the datasets to their respective tiers. Further refinements are conducted based on expert assessment and outlier identification. This is performed on a data type basis with the aim of minimizing subjectivity in quality assessment and data selection. There are a few criteria which are consistent across data types: prioritizing data with a high signal-to-noise ratio beyond a chosen data type threshold; valuing data in data-sparse regions; outlier identification and exclusion when substantiated by broadly consistent, dense data clusters (cluster density assessments are data type dependent); and superfluous data exclusion. Some data are assigned to a tier of -1, which signifies that the observation should be entirely excluded for data–model comparison since it failed one or several quality criteria. This tier equal to -1 is solely for the purpose of logging the data and identifying it as not trustworthy to ensure exclusion from analyses.

#### 2.3.1.1 PaleoH data curation

The past ice thickness dataset requires additional considerations when assessing data tiers. Some paleoH sites have few exposure ages that constrain the elevation history.

In these instances, we rely on the discretion of the original study to assess the quality of the data point which is available through ICE-D. At a given site, an assessment is conducted that identifies the highest-quality exposure ages (e.g.  $^{10}\text{Be}$ ,  $^{26}\text{Al}$ ,  $^3\text{He}$ , and  $^{14}\text{C}$ ) bracketing the elevation history and sorts the data into tiers (Figs. S2.1 in the Supplement). A high data density cluster of young exposure ages that form the expert-assessed  $2\sigma$  bounds on elevation history is identified (Fig. 2.3). This assessment considers the occurrence of inheritance and post-deglacial shielding. By evaluating paired isotope exposure ages and applying first principles (along a sample transect, older ages should always be obtained from samples collected at higher altitudes), many data points can be excluded, and an expert-assessed  $2\sigma$  elevation history based on data density can be identified. Tier-1 data are the data constraining the magnitude, timing, and rate of elevation change over the deglaciation. Tier-2 data further constrain the specific structure of the elevation history. Tier-3 data include the remaining pertinent data, which fully populate much of the expert-assessed  $2\sigma$  bounds on elevation history. The primary reason for tier-3 data to be relegated to their own tier rather than being included in the tier-2 data is the limited constraining power that they introduce to past ice thickness changes given how they correlate significantly with tier-1 and tier-2 data, which renders them nearly superfluous in many instances. When evaluating a cluster of neighbouring sites, a certain degree of consistency should be expected if the exposure data are truly representative of a broader region rather than extremely local ice elevation changes. Therefore, an additional iteration on the tiers is performed based on upstream or downstream consistency with neighbouring paleoH sites to identify potential outliers. The source literature of Antarctic exposure ages does not always report the sample position relative to the mean flow of the surrounding ice. This

proves to be an issue when comparing ice-thinning histories reconstructed by continental-scale ice sheet models with histories based on paleoH data because the exposure ages can be heavily biased depending on the nunatak flank, where the samples were collected (Mas E Braga et al., 2021). This information is not broadly accessible in the source literature, causing a limitation which propagates into the AntICE2 database, and this must be considered within the error model when scoring a reconstruction against paleoH data.

#### 2.3.1.2 PaleoExt data curation

The past-ice-extent dataset is also divided into tiers based on specific data type criteria. Firstly, the interpretation of the facies is extracted from the source literature and assigned one of the following classes (Figs. 2.4 and S2.2-2.3 in the Supplement): proximal to the GL (PGL), sub-ice-shelf (SIS), or open-marine conditions (OMC). Each core is then sorted according to the  $^{14}\text{C}$  dating method, i.e. whether the  $^{14}\text{C}$  age is obtained from biogenic carbonate or organic matter, with the latter dates typically considered to be less reliable (see Sect. 2.2). Down-core  $^{14}\text{C}$  ages obtained from organic matter in sediment cores from the Antarctic continental shelf are often corrected by subtracting the core top age rather than the marine reservoir effect only (e.g. Domack et al., 1999; Pudsey et al., 2006). This approach assumes that the degree of contamination of young organic carbon with reworked fossil organic matter has remained constant throughout the record; however, this is often not the case (e.g. Heroy and Anderson, 2007). For these reasons,  $^{14}\text{C}$  ages on calcareous microfossils, if present, are typically favoured over organic matter  $^{14}\text{C}$  ages, and the former are typically assigned to a high-quality tier. Additional criteria for sorting the paleoExt data into tiers are based on the overall quality of the marine sedimentary record

and facies interpretation, specifically whether the stratigraphy of the core is affected by reworking (e.g. due to iceberg turbation). Moreover, if in a given core multiple dates were obtained from different facies that indicate the same environmental conditions, the maximum and minimum dates bracketing the age cluster are assigned to a high-quality tier, whereas the remaining dates are excluded to avoid redundancy. These criteria are enforced when assigning tiers to the marine paleoExt data and when deciding whether to exclude ages from direct data–model scoring.

#### 2.3.1.3 PaleoRSL data curation

Compared to other data types, there are limited past RSL observations. For this reason, the quality assessment of the paleoRSL data is performed on a site-by-site basis. For a given site, we define the expert-assessed  $2\sigma$  bounds on RSL history as being constrained by sea level index points and minimum and maximum bounds (Figs. 2.5 and S2.4 in the Supplement). This approach inherently identifies potential outlier data for exclusion. Tier-1 data for a site comprise the highest-quality proxy data that constrain the highstand and the form of the deglacial sea level fall. Data that constrain the RSL history with minimal redundancy and supplement tier-1 data are assigned to a tier-2 status. The classification of tier-2 data is based on data density along the expert-assessed  $2\sigma$  bounds on theoretical RSL history (Fig. 2.5). Tier-3 RSL data further populate the most likely RSL history already defined by the tier-1 and tier-2 data and provide lower-quality constraints that correlate to tier-1 tier-2 data without being completely superfluous.

#### 2.3.1.4 Borehole temperature data curation

The ice-core borehole temperature profiles consist of a significant amount of data along a single profile, much of which is highly correlated with depth. Therefore, a subset of the profile data is chosen and assigned to a tier-1 quality for data–model scoring. The tier-1 data consist of the coolest near surface ice temperature, the nearest basal ice temperature, and the ice column midpoint englacial temperature. These data alone can effectively constrain the structure of the simulated temperature profile given the smoothness of the signal. South Pole and Talos Dome borehole temperature profiles were the only profiles that did not cover the majority of the ice column (Fig. 2.6). Therefore, they provide less constraining power on a model and are assigned a tier-3 status. The Siple Coast borehole profiles from the Siple Dome, Bindschadler, Kamb, and Alley–Whillans ice streams are relatively proximal and correlate with each other, so they are assigned a tier-2 status except for the Siple Dome profile which remains the regional tier-1 representative. The other ice core borehole temperature profiles (solid-coloured lines in Fig. 2.6) are all part of the tier-1 subset because of the quality and location of the data (Fig. 2.2d). Each respective borehole temperature profile is reduced to three data points (surface, englacial, and basal ice temperature) that most meaningfully represent the entire profile (Table 2.1).

#### 2.3.1.5 Uplift rate data curation

PD uplift rates inferred from GPS observations constrain several integrated processes. Prior to sorting the GPS uplift rates into tiers, the GPS data must be evaluated to identify a subset which is most suitable to constraining the GIA signal and hence past

ice load changes. First and foremost, contemporary ice sheet change triggers an elastic response that contributes to the PD observed uplift rates and hence masks the signal associated with past ice sheet change. GPS data from sites where significant PD elastic contributions were inferred (Fig. S2.5 in the Supplement) are considered to be low-quality constraints on the contemporary GIA signal and hence on the past ice load changes. Several criteria, such as a low elastic correction ( $< 0.55 \text{ mm yr}^{-1}$ ) and a small uplift rate standard deviation ( $< 1 \text{ mm yr}^{-1}$ ) or high signal-to-noise ratio ( $> 1.45$ ), determine which GPS data are considered for data–model evaluation and tier classification. Additionally, GPS sites that are in the vicinity of the coast ( $< 250 \text{ km}$ ) or in areas where significant mass loss has evidently occurred over the last millennium are excluded from being classified into a tier. The GPS data that pass these criteria are assigned a preliminary tier-2 status. A final criterion considers a common model limitation, which pertains to the spherically symmetric viscosity profile of many GIA models and excludes the presence of lateral viscosity structure. This criterion can be disregarded if dealing with a 3D Earth viscosity model. In several regions of West Antarctica, the continental crust is underlain by a mantle with anomalously low viscosities in the top 250 km (Whitehouse et al., 2019). GPS sites near anomalous viscosity features are more capable than others of biasing the model calibration given the structural uncertainty associated with the GIA model. Therefore, certain sites are identified along parts of the Antarctic Peninsula and in the Amundsen–Bellingshausen Sea sector and the Ross Sea sector, where the inferred viscosity at depth is below  $10^{20} \text{ Pa s}$  (Whitehouse et al., 2019). These criteria filter the GPS uplift rate data based on their quality and ability to constrain the GIA signal and past ice load changes. One persisting issue is the robustness of the elastic corrections, which are likely to have underrepresented

uncertainties (Martín-Español et al., 2016). Uncertainties in the elastic corrections can be increased by the root sum square, with the elastic correction boosting confidence that the elastic-corrected uplift rates accurately constrain the viscous GIA response. Of the tier-2 GPS sites, those which are not located in regions with anomalously low mantle viscosity are promoted to tier-1 quality status (six sites). The exact thresholds for the various criteria are based on the need to identify a higher-quality data subset while simultaneously accounting for unquantified uncertainties associated with the elastic corrections. The criteria-defined higher-quality subset size is chosen to represent the top third of tiered GPS data (tier-1 and tier-2 data), offering sites that are especially sparsely distributed. Refinements to the criteria thresholds will be required as the size of the GPS network evolves and as more robust approaches to interpreting GPS time series are developed.

Table 2.1: Summary of Antarctic Ice Sheet Evolution database version 2 (AntICE2) and quality tier subsets.

Data type	All data	Tier-1 data	Tier-2 data	Tier-3 data
Past ice extent (paleoExt)	249	63	15	30
Past ice thickness (paleoH)	2710	108	348	270
Past relative sea level (paleoRSL)	425	23	48	52
Ice core borehole temperature (boreTemp)	36740	36	9	6
Present-day GPS uplift rates (rdotGPS)	67	6	9	-
AntICE2	40191	236	429	358

### 2.3.1.6 Present-day AIS geometry data curation

The PD AIS geometry and surface velocities are crucial constraints that provide nearly complete spatial coverage, rendering them tier-1 data. Regions with large uncertainties in the PD AIS bed geometry and surface velocities could be classified as tier-

2 data points; however, given that these regions typically have no other data constraints, they remain top-tier data. For scoring ice sheet model simulations against them, it is important to account for the uncertainties in these inferences when calculating a root-mean-square-error score. It has been shown that spectral noise models, which introduce spatially correlated noise, can be used to produce an ensemble of boundary conditions that are self-consistent with the underlying field and uncertainty estimates (Sun et al., 2014; Gasson et al., 2015). This provides a method that allows for a proper quantification of uncertainties affiliated with these boundary conditions.

#### 2.3.1.7 Data standards and expert assessment

Fundamental and recurring issues, which exacerbate the challenges of evaluating data quality, remain across many studies and data types. They relate to the data availability. For example, some studies make the entirety of uncorrected, corrected, and calibrated  $^{14}\text{C}$  ages available (Heroy and Anderson, 2007; Bentley et al., 2014b), while others provide only those with robust interpretations. This makes it challenging to assess the entirety of a broad dataset by the same standards since some data rely on the implicit assessments made by their respective study. Ideally, all associated data should be made available, and the data should be categorized into quality tiers based on explicitly specified criteria. The expert quality control by the principal investigators who collected the samples and analysed and evaluated the data is exceedingly valuable and should be included with the data. This enables a broader consensus on quality control as various experts converge towards specific quality criteria. Moreover, when new proxy data of various qualities are introduced in the future, including potential novel constraints, it will be possible to re-assess the categorical

quality tiers if their criteria are clearly specified. The data made available should contain all the necessary information to recalibrate the data with clearly specified uncertainties. This will facilitate future data calibration, standardization, and quality assessment once integrated properly within an online repository, such as the ICE-D repository (Balco, 2020).

#### 2.3.1.8 Data–system and system–model uncertainties

The data presented in the AntICE2 database include data–system uncertainty, typically referred to as observational uncertainty, which consists of measurement uncertainty and indicative meaning uncertainty. The former represents uncertainties affiliated with inherent instrumental uncertainties when taking measurements, such as the elevation at which a sample for exposure dating is collected. The latter represent uncertainties relating to the interpretation of data and how these data represent a proxy observation for physical characteristics of the system, for instance a fossil mollusc fragment and how it relates to past sea level. In the AntICE2 database, we include the indicative meaning uncertainty from the source literature when available and otherwise do not attempt to specify it. On the other hand, we do specify a baseline measurement uncertainty when this is absent in the source publication or when it is clearly understated.

As the observational uncertainty specifies the data–system relationship, meaningful data–model comparison also requires specification of the relationship between the model and the physical system. However, appropriate specification of the structural error model is a major challenge. The source of this challenge is that we cannot have complete knowledge of the current and especially of the past state of the Earth system or any significant sub-component thereof. As such, we cannot easily identify and quantify model

deficiencies with respect to the system of interest. There are many approaches for dealing with these challenges, and we point the reader to Tarasov and Goldstein (2021) for a broader discussion.

### 2.3.2 Potential future and rejected data types

Radiostratigraphy of the Greenland Ice Sheet has been used to infer the age structure of the ice sheet (MacGregor et al., 2015). Proof-of-concept age-tracking simulations of a 3D slice through the Greenland summit have demonstrated the potential constraint value of such data (Born, 2017). The age structure of the ice is inferred from internal radar reflectors (reflective isochrones) visible in the radiostratigraphic profiles, which are dated at major ice core sites (Cavitte et al., 2021). The AntICE2 database does not include any direct age structure constraints for the Antarctic Ice Sheet. It would be extremely valuable to have an age structure for the entire AIS because this would provide constraints for many regions that are lacking any paleo-constraints. However, the presently available radiostratigraphy coverage for the AIS is spatially limited, and as such, no such AIS-wide reconstruction currently exists. The depth–age data from ice cores can directly constrain the age structure. Moreover, there are some regional age reconstructions for well-studied regions and transects (Ashmore et al., 2020; Winter et al., 2019; Delf et al., 2020; Cavitte et al., 2021). A compilation of age reconstructions has been started under the AntArchitecture initiative within the Scientific Committee on Antarctic Research (SCAR) (<https://www.scar.org/science/antarchitecture/antarch-news/>, last access: 6 July 2023). Sutter et al. (2021) demonstrate a data–model comparison of various age isochrones in Antarctica and illustrate the utility of this new data type. As accurate ice-age-tracing

modules become available for ice sheet models, radiostratigraphic age constraints will provide a powerful new constraint on past AIS evolution.

Ice cores have previously been used to infer past AIS elevation changes relative to PD. Originally this was done by analysing the gas content trapped in the ice (Lorius et al., 1984; Delmotte et al., 1999), relating the total gas content to the ambient atmospheric pressure at bubble close-off. This traditional method produces a high noise-to-signal ratio, especially because other processes affect the volume of open pore space in the ice, such as insolation (Raynaud et al., 2007) and climate (Eicher et al., 2016). We therefore do not include air content observations in the AntICE2 database. An alternative method to determine past elevation changes at ice core sites is through model inferences, where model simulations are locally constrained by ice core data (Barbante et al., 2006; Neumann et al., 2008; Steig et al., 2001; Waddington et al., 2005; Parrenin et al., 2007). The issue with using model inferences to constrain a model is that they integrate all the assumptions involved in making those inferences, and these are often not explicitly specified. Moreover, the uncertainties in the ice core site elevation model inferences are often inadequately explored and hence underestimated and would benefit from a greater exploration of the range of uncertainties (Steig et al., 2001). If included in a calibration, this would propagate ill-defined uncertainties and could invalidate the calibration. Therefore, we opt to exclude this dataset since it is too far removed from direct field observations and comes associated with significant and ill-defined model uncertainties.

As previously mentioned, when discussing the GPS data, geodetic observations have been used to constrain the GIA response signal associated with past ice sheet changes (Martín-Español et al., 2016; Sasgen et al., 2017). The justification for excluding the

inversion-based Antarctic GIA reconstructions as a constraint lies in the assumptions behind the elastic corrections associated with contemporary mass loss. Like the ice-core-inferred elevation changes, the elastic corrections come associated with ill-defined model uncertainties which could invalidate the calibration if implemented without expanded uncertainties. Moreover, if the intention is to calibrate an ice sheet and GIA model to infer contemporary mass balance by correcting geodetic data, it would be circular reasoning to apply a constraint that makes a priori assumptions about the form of the GIA signal.

Several ice cores have been drilled to the bed across the Siple Coast, and the retrieved basal till frequently contains organic material yielding  $^{14}\text{C}$  ages significantly younger than 40 ka but older than 20 ka (Kingslake et al., 2018). This poses the question of whether the GL retreated landward from the core sites during the most recent deglaciation. The presence of organic matter with a last-glacial-period age at the base of the modern AIS is hard to reconcile because all major continental ice sheets, including the AIS, are believed to have reached their maximum extent and size during this time. Subglacial sediments contain mixtures of eroded and reworked detritus initially deposited at different times. Therefore, a  $^{14}\text{C}$  date obtained from the organic matter of such subglacial sediments typically provides an integrated age, derived from the mixing of relatively young with old and even  $^{14}\text{C}$ -dead material, which increases the uncertainty of how to interpret such a date. Kingslake et al. (2018) opted to use the  $^{14}\text{C}$  dates as evidence of an early Holocene GL retreat upstream of its PD position, thereby arguing that the  $^{14}\text{C}$  dates do not represent true ages for sediment deposition ages. Given these uncertainties and notwithstanding further studies (Neuhaus et al., 2021) on the  $^{14}\text{C}$  dates from the till samples along the Siple Coast, these observations have not been included in the AntICE2 database

as paleoExt GL retreat constraints because they do not yet represent a firm and reliable age constraint on GL position.

The main outstanding issues with the AntICE2 database are the temporal and spatial data gaps. As shown in Figs. 2.1, 2.2, and 2.8, only a small number of dates extend beyond 20 ka, and the spatial distribution of the data leaves many regions, particularly in East Antarctica, completely devoid of observational constraints. The ramification of the data deserts is that calibrated models will likely have large uncertainties in regions with limited observational constraints. A few new data types, discussed above, could ameliorate the situation, with the most promising being the wide-scale age structure of the AIS, inferred from airborne and on-ice radar mapping of internal layering connected to sites of dated ice cores. This data type could constrain changes in the AIS far beyond 30 ka and even cover regions with little or no data due to a lack of rock outcrops and boreholes.

Future work should focus on using calibrated model results to establish an Antarctic treasure map, similar to that produced for ice cores by Bradley et al. (2012), which identifies high-priority targets for the collection of observational data (Tarasov and Goldstein, 2021). Such a map would highlight the constraining power of various hypothetical observational constraints, for example, those taken from unsampled nunataks or paleo-grounding-zone wedges preserved on the continental shelf. Finally, this future progress crucially depends on the growth of well-maintained online data repositories (e.g. ICE-D, Ghub), the careful curation of data, the standardization of the curation criteria, and the proper methodological approaches toward data–model comparison.

## 2.4 Data availability

The Supplement contains plots of the entire tiered AntICE2 database. Summary plots provide concise representations of various data types when possible. The AntICE2 database can be downloaded as Excel tables (.xlsx) from the Supplement, and the latest version is in the online repository <https://thehub.org/resources/4884> (Lecavalier et al., 2022).

## 2.5 Summary

In this study, we provide the second major iteration of the Antarctic Ice Sheet Evolution observational constraint (AntICE2) database. The AntICE2 database is a curated observational constraint database intended for the calibration of models of the Antarctic Ice Sheet and Antarctic glacial isostatic adjustment over the last glacial cycle. It can also be used to constrain a paleo-model spin up of the AIS to initialize PD simulations. This will lead to a more accurate understanding of contemporary and future changes of the AIS. The AntICE2 database includes a large variety of observational constraints necessary for model calibration. The data types included are as follows: PD geometry and surface velocity, PD uplift rates, borehole temperature profiles, past ice extent, past ice surface elevation, and past relative sea level. All the  $^{14}\text{C}$  ages in the database are recalibrated and share a consistent reservoir age correction wherever appropriate. The AntICE2 database represents a curated dataset with specified quality tiers. This was achieved by establishing and applying criteria for the different data types. Future efforts should be geared toward refining the criteria for the quality tier assignment since a community consensus would benefit data–model

integration. An ongoing effort involves automating the selection and curation process from a raw database (ICE-D) to a recalibrated curated subset (i.e. AntICE2). This would render the AntICE2 database more manageable and updatable when more data are being collected in the future. To contribute to the AntICE2 database, one can contact the corresponding author with data or publications, contribute data to the ICE-D databases, or offer data type criteria modifications to help revise the data curation process. The AntICE2 database represents the most comprehensive observational constraint dataset of high-quality data relating to the past evolution of the Antarctic Ice Sheet. The dataset facilitates data integration with AIS and GIA simulations. This dataset compilation also facilitates data–model scoring by processing and curating large raw and disparate datasets from online repositories (e.g. ICE-D) and source publications. Finally, a call to the community is made to make raw data with complete and clearly specified uncertainties publicly available and to make efforts towards establishing data quality criteria in order to facilitate data curation and hence produce meaningful data–model comparisons.

## 2.6 Author contributions.

Authorship: Benoit S. Lecavalier, Lev Tarasov, Greg Balco, Perry Spector, Claus-Dieter Hillenbrand, Christo Buizert, Catherine Ritz, Marion Leduc-Leballeur, Robert Mulvaney, Pippa L. Whitehouse, Michael J. Bentley, Jonathan Bamber

B.S.L. and L.T. led and designed the study. B.S.L. compiled and recalibrated the datasets. B.S.L. wrote the paper and generated all the figures. G.B. and P.S. contributed past-ice-thickness and past-ice-extent data via ICE-D. C.D.H. contributed some past-ice-extent datasets and assisted in its interpretation. C.B., C.R., M.L.L., and R.M. contributed some

ice core borehole datasets. P.L.W. and M.J.B. contributed some relative-sea-level datasets. J.B. provided the GPS datasets. All authors participated in establishing the data quality criteria to curate the database and provided feedback on the paper.

## 2.7 References

- Ackert, R. P.: An ice sheet remembers, *Science*, 299, 57–58, <https://doi.org/10.1126/science.1079568>, 2003.
- Ackert, R. P., Barclay, D. J., Borns, H. W., Calkin, P. E., Kurz, M. D., Fastook, J. L., and Steig, E. J.: Measurements of Past Ice Sheet Elevations in Interior West Antarctica, *Science*, 286, 276–280, <https://doi.org/10.1126/science.286.5438.276>, 1999.
- Ackert, R. P., Mukhopadhyay, S., Parizek, B. R., and Borns, H. W.: Ice elevation near the West Antarctic Ice Sheet divide during the Last Glaciation, *Geophys. Res. Lett.*, 34, 1–6, <https://doi.org/10.1029/2007GL031412>, 2007.
- Albrecht, T., Winkelmann, R., and Levermann, A.: Glacial-cycle simulations of the Antarctic Ice Sheet with the Parallel Ice Sheet Model (PISM) – Part 1: Boundary conditions and climatic forcing, *The Cryosphere*, 14, 599–632, <https://doi.org/10.5194/tc-14-599-2020>, 2020.
- Anderson, J. B., Conway, H., Bart, P. J., Witus, A. E., Greenwood, S. L., McKay, R. M., Hall, B. L., Ackert, R. P., Licht, K., Jakobsson, M., and Stone, J. O.: Ross Sea paleo-ice sheet drainage and deglacial history during and since the LGM, *Quaternary Sci. Rev.*, 100, 31–54, <https://doi.org/10.1016/j.quascirev.2013.08.020>, 2014.
- Argus, D. F., Peltier, W. R., Drummond, R., and Moore, A. W.: The Antarctica component of postglacial rebound model ICE-6G\_C (VM5a) based on GPS positioning, exposure age dating of ice thicknesses, and relative sea level histories, *Geophys. J. Int.*, 198, 537–563, <https://doi.org/10.1093/gji/ggu140>, 2014.
- Arndt, J. E., Hillenbrand, C. D., Grobe, H., Kuhn, G., and Wacker, L.: Evidence for a dynamic grounding line in outer Filchner Trough, Antarctica, until the early Holocene, *Geology*, 45, 1035–1038, <https://doi.org/10.1130/G39398.1>, 2017.
- Arndt, J. E., Larter, R. D., Hillenbrand, C.-D., Sørli, S. H., Forwick, M., Smith, J. A., and Wacker, L.: Past ice sheet–seabed interactions in the northeastern Weddell Sea embayment, Antarctica, *The Cryosphere*, 14, 2115–2135, <https://doi.org/10.5194/tc-14-2115-2020>, 2020.

- Ashmore, D. W., Bingham, R. G., Ross, N., Siegert, M. J., Jordan, T. A., and Mair, D. W. F.: Englacial Architecture and Age-Depth Constraints Across the West Antarctic Ice Sheet, *Geophys. Res. Lett.*, 47, e2019GL086663, <https://doi.org/10.1029/2019GL086663>, 2020.
- Balco, G., Stone, J. O., Lifton, N. A., and Dunai, T. J.: A complete and easily accessible means of calculating surface exposure ages or erosion rates from  $^{10}\text{Be}$  and  $^{26}\text{Al}$  measurements, *Quat. Geochronol.*, 3, 174–195, <https://doi.org/10.1016/j.quageo.2007.12.001>, 2008.
- Balco, G. and Schaefer, J. M.: Exposure-age record of Holocene ice sheet and ice shelf change in the northeast Antarctic Peninsula, *Quaternary Sci. Rev.*, 59, 101–111, <https://doi.org/10.1016/j.quascirev.2012.10.022>, 2013.
- Balco, G., Todd, C., Huybers, K., Campbell, S., Vermeulen, M., Hegland, M., Goehring, B. M., and Hillebrand, T. R.: Cosmogenic-nuclide exposure ages from the Pensacola Mountains adjacent to the foundation ice stream, Antarctica, *Am. J. Sci.*, 316, 542–577, <https://doi.org/10.2475/06.2016.02>, 2016.
- Balco, G., Todd, C., Goehring, B. M., Moening-Swanson, I., and Nichols, K.: Glacial geology and cosmogenic-nuclide exposure ages from the Tucker glacier – Whitehall glacier confluence, northern Victoria Land, Antarctica, *Am. J. Sci.*, 319, 255–286, <https://doi.org/10.2475/04.2019.01>, 2019.
- Balco, G.: Technical note: A prototype transparent-middle layer data management and analysis infrastructure for cosmogenic-nuclide exposure dating, *Geochronology*, 2, 169–175, <https://doi.org/10.5194/gchron-2-169-2020>, 2020.
- Barbante, C., Barnola, J. M., Becagli, S., Beer, J., Bigler, M., Boutron, C., Blunier, T., Castellano, E., Cattani, O., Chappellaz, J., Dahl-Jensen, D., Debret, M., Delmonte, B., Dick, D., Falourd, S., Faria, S., Federer, U., Fischer, H., Freitag, J., Frenzel, A., Fritzsche, D., Fundel, F., Gabrielli, P., Gaspari, V., Gersonde, R., Graf, W., Grigoriev, D., Hamann, I., Hansson, M., Hoffmann, G., Hutterli, M. A., Huybrechts, P., Isaksson, E., Johnsen, S., Jouzel, J., Kaczmarek, M., Karlin, T., Kaufmann, P., Kipfstuhl, S., Kohno, M., Lambert, F., Lambrecht, A., Landais, A., Lawer, G., Leuenberger, M., Littot, G., Loulergue, L., Lüthi, D., Maggi, V., Marino, F., Masson-Delmotte, V., Meyer, H., Miller, H., Mulvaney, R., Narcisi, B., Oerlemans, J., Oerter, H., Parrenin, F., Petit, J. R., Raisbeck, G., Raynaud, D., Röthlisberger, R., Ruth, U., Rybak, O., Severi, M., Schmitt, J., Schwander, J., Siegenthaler, U., Siggaard-Andersen, M. L., Spahni, R., Steffensen, J. P., Stenni, B., Stocker, T. F., Tison, J. L., Traversi, R., Udisti, R., Valero-Delgado, F., Van Den Broeke, M. R., Van DeWal, R. S.W., Wagenbach, D., Wegner, A., Weiler, K., Wilhelms, F., Winther, J. G., and Wolff, E.: One-to-one coupling of glacial climate variability in Greenland and Antarctica, *Nature*, 444, 195–198, <https://doi.org/10.1038/nature05301>, 2006.

- Bart, P. J., Krogmeier, B. J., Bart, M. P., and Tulaczyk, S.: The paradox of a long grounding during West Antarctic Ice Sheet retreat in Ross Sea, *Sci. Rep.*, 7, 1262, <https://doi.org/10.1038/s41598-017-01329-8>, 2017.
- Bart, P. J., DeCesare, M., Rosenheim, B. E., Majewski, W., and McGlannan, A.: A centuries-long delay between a paleo-ice-shelf collapse and grounding-line retreat in the Whales Deep Basin, eastern Ross Sea, Antarctica, *Sci. Rep.*, 8, 1–9, <https://doi.org/10.1038/s41598-018-29911-8>, 2018.
- Bentley, M. J., Hodgson, D. A., Smith, J. A., and Cox, N. J.: Relative sea level curves for the South Shetland Islands and Marguerite Bay, Antarctic Peninsula, *Quaternary Sci. Rev.*, 24, 1203–1216, <https://doi.org/10.1016/j.quascirev.2004.10.004>, 2005.
- Bentley, M. J., Fogwill, C. J., Kubik, P. W., and Sugden, D. E.: Geomorphological evidence and cosmogenic  $^{10}\text{Be}/^{26}\text{Al}$  exposure ages for the Last Glacial Maximum and deglaciation of the Antarctic Peninsula Ice Sheet, *Bull. Geol. Soc. Am.*, 118, 1149–1159, <https://doi.org/10.1130/B25735.1>, 2006.
- Bentley, M. J., Fogwill, C. J., Le Brocq, A. M., Hubbard, A. L., Sugden, D. E., Dunai, T. J., and Freeman, S. P. H. T.: Deglacial history of the West Antarctic Ice Sheet in the Weddell Sea embayment: Constraints on past Ice volume change, *Geology*, 38, 411–414, <https://doi.org/10.1130/G30754.1>, 2010.
- Bentley, M. J., Johnson, J. S., Hodgson, D. A., Dunai, T., Freeman, S. P. H. T., and O’Cofaigh, C.: Rapid deglaciation of Marguerite Bay, western Antarctic Peninsula in the Early Holocene, *Quaternary Sci. Rev.*, 30, 3338–3349, <https://doi.org/10.1016/j.quascirev.2011.09.002>, 2011.
- Bentley, M. J., Ó Cofaigh, C., Anderson, J. B., Conway, H., Davies, B., Graham, A. G. C., Hillenbrand, C.-D., Hodgson, D. A., Jamieson, S. S. R., Larter, R. D., Mackintosh, A., Smith, J. A., Verleyen, E., Ackert, R. P., Bart, P. J., Berg, S., Brunstein, D., Canals, M., Colhoun, E. a., Crosta, X., Dickens, W. a., Domack, E., Dowdeswell, J. A., Dunbar, R., Ehrmann, W., Evans, J., Favier, V., Fink, D., Fogwill, C. J., Glasser, N. F., Gohl, K., Golledge, N. R., Goodwin, I., Gore, D. B., Greenwood, S. L., Hall, B. L., Hall, K., Hedding, D. W., Hein, A. S., Hocking, E. P., Jakobsson, M., Johnson, J. S., Jomelli, V., Jones, R. S., Klages, J. P., Kristoffersen, Y., Kuhn, G., Leventer, A., Licht, K., Lilly, K., Lindow, J., Livingstone, S. J., Massé, G., McGlone, M. S., McKay, R. M., Melles, M., Miura, H., Mulvaney, R., Nel, W., Nitsche, F. O., O’Brien, P. E., Post, A. L., Roberts, S. J., Saunders, K. M., Selkirk, P. M., Simms, A. R., Spiegel, C., Stollendorf, T. D., Sugden, D. E., van der Putten, N., van Ommen, T., Verfaillie, D., Vyverman, W., Wagner, B., White, D. A., Witus, A. E., and Zwartz, D.: A community-based geological reconstruction of Antarctic Ice Sheet deglaciation since the Last Glacial Maximum, *Quaternary Sci. Rev.*, 100, 1–9, <https://doi.org/10.1016/j.quascirev.2014.06.025>, 2014.

- Bentley, M. J., Hein, A. S., Sugden, D. E., Whitehouse, P. L., Shanks, R., Xu, S., and Freeman, S. P. H. T.: Deglacial history of the Pensacola Mountains, Antarctica from glacial geomorphology and cosmogenic nuclide surface exposure dating, *Quaternary Sci. Rev.*, 158, 58–76, <https://doi.org/10.1016/j.quascirev.2016.09.028>, 2017.
- Berg, S., Wagner, B., White, D. A., and Melles, M.: No significant ice-sheet expansion beyond present ice margins during the past 4500 yr at Rauer Group, East Antarctica, *Quaternary Res.*, 74, 23–25, <https://doi.org/10.1016/j.yqres.2010.04.004>, 2010.
- Borchers, B., Marrero, S., Balco, G., Caffee, M., Goehring, B., Lifton, N., Nishiizumi, K., Phillips, F., Schaefer, J., and Stone, J.: Geological calibration of spallation production rates in the CRONUS-Earth project, *Quat. Geochronol.*, 31, 188–198, <https://doi.org/10.1016/j.quageo.2015.01.009>, 2016.
- Born, A.: Tracer transport in an isochronal ice-sheet model, *J. Glaciol.*, 63, 22–38, <https://doi.org/10.1017/jog.2016.111>, 2017.
- Bradley, S. L., Siddall, M., Milne, G. A., Masson-Delmotte, V., and Wolff, E.: Where might we find evidence of a Last Interglacial West Antarctic Ice Sheet collapse in Antarctic ice core records? *Global Planet. Change*, 88–89, 64–75, <https://doi.org/10.1016/j.gloplacha.2012.03.004>, 2012.
- Braddock, S., Hall, B. L., Johnson, J. S., Balco, G., Spoth, M., Whitehouse, P. L., Campbell, S., Goehring, B. M., Rood, D. H., and Woodward, J.: Relative sea-level data preclude major late Holocene ice-mass change in Pine Island Bay, *Nat Geosci*, 15, 568–572, <https://doi.org/10.1038/s41561-022-00961-y>, 2022.
- Briggs, R. D. and Tarasov, L.: How to evaluate model derived deglaciation chronologies: A case study using Antarctica, *Quaternary Sci. Rev.*, 63, 109–127, <https://doi.org/10.1016/j.quascirev.2012.11.021>, 2013.
- Briggs, R. D., Pollard, D., and Tarasov, L.: A data-constrained large ensemble analysis of Antarctic evolution since the Eemian, *Quaternary Sci. Rev.*, 103, 91–115, <https://doi.org/10.1016/j.quascirev.2014.09.003>, 2014.
- Buizert, C., Fudge, T. J., Roberts, W. H., Steig, E. J., Sherriff-Tadano, S., Ritz, C., Lefebvre, E., Edwards, J., Kawamura, K., Oyabu, I., and Motoyama, H.: Antarctic surface temperature and elevation during the Last Glacial Maximum, *Science*, 372, 1097–1101, 2021.
- Cavitte, M. G. P., Young, D. A., Mulvaney, R., Ritz, C., Greenbaum, J. S., Ng, G., Kempf, S. D., Quartini, E., Muldoon, G. R., Paden, J., Frezzotti, M., Roberts, J. L., Tozer, C. R., Schroeder, D. M., and Blankenship, D. D.: A detailed radiostratigraphic data

- set for the central East Antarctic Plateau spanning from the Holocene to the mid-Pleistocene, *Earth Syst. Sci. Data*, 13, 4759–4777, <https://doi.org/10.5194/essd-13-4759-2021>, 2021.
- Cuffey, K. M., Clow, G. D., Steig, E. J., Buizert, C., Fudge, T. J., Koutnik, M., Waddington, E. D., Alley, R. B., and Severinghaus, J. P.: Deglacial temperature history of West Antarctica, *P. Natl. Acad. Sci. USA*, 113, 14249–14254, <https://doi.org/10.1073/pnas.1609132113>, 2016.
- DeConto, R. M. and Pollard, D.: Contribution of Antarctica to past and future sea-level rise, *Nature*, 531, 591–597, <https://doi.org/10.1038/nature17145>, 2016.
- Delf, R., Schroeder, D. M., Curtis, A., Giannopoulos, A., and Bingham, R. G.: A comparison of automated approaches to extracting englacial-layer geometry from radar data across ice sheets, *Ann. Glaciol.*, 61, 234–241, <https://doi.org/10.1017/aog.2020.42>, 2020.
- Delmotte, M., Raynaud, D., Morgan, V., and Jouzel, J.: Climatic and glaciological information inferred from air-content measurements of a Law Dome (East Antarctica) ice core, *J. Glaciol.*, 45, 255–263, <https://doi.org/10.3189/s0022143000001751>, 1999.
- Domack, E. W., Jacobson, E. A., Shipp, S., and Anderson, J. B.: Late Pleistocene–Holocene retreat of the West Antarctic Sheet system in the Ross Sea: Part 2 – sedimentologic and stratigraphic signature, *Geol. Soc. Am. Bull.*, 111, 1517–1536, 1999.
- Domack, E., Duran, D., Leventer, A., Ishman, S., Doane, S., McCallum, S., Amblas, D., Ring, J., Gilbert, R., and Prentice, M.: Stability of the Larsen B ice shelf on the Antarctic Peninsula during the Holocene epoch, *Nature*, 436, 681–685, <https://doi.org/10.1038/nature03908>, 2005.
- Eicher, O., Baumgartner, M., Schilt, A., Schmitt, J., Schwander, J., Stocker, T. F., and Fischer, H.: Climatic and insolation control on the high-resolution total air content in the NGRIP ice core, *Clim. Past*, 12, 1979–1993, <https://doi.org/10.5194/cp-12-1979-2016>, 2016.
- Ely, J. C., Clark, C. D., Small, D., and Hindmarsh, R. C. A.: ATAT 1.1, the Automated Timing Accordance Tool for comparing ice-sheet model output with geochronological data, *Geosci. Model Dev.*, 12, 933–953, <https://doi.org/10.5194/gmd-12-933-2019>, 2019.
- Emslie, S. D. and McDaniel, J. D.: Adelie penguin diet and climate change during the middle to late Holocene in northern Marguerite Bay, Antarctic Peninsula, *Polar Biol.*, 25, 222–229, <https://doi.org/10.1007/s00300-001-0334-y>, 2002.

- Engelhardt, H.: Ice temperature and high geothermal flux at Siple Dome, West Antarctica, from borehole measurements, *J. Glaciol.*, 50, 251–256, <https://doi.org/10.3189/172756504781830105>, 2004a.
- Engelhardt, H.: Thermal regime and dynamics of the West Antarctic ice sheet, *Ann. Glaciol.*, 39, 85–92, <https://doi.org/10.3189/172756404781814203>, 2004b.
- Fox-Kemper, B., Hewitt, H. T., Xiao, C., Aðalgeirsdóttir, G., Drijfhout, S. S., Edwards, T. L., Golledge, N. R., Hemer, M., Kopp, R. E., Krinner, G., Mix, A., Notz, D., Nowicki, S., Nurhati, I. S., Ruiz, L., Sallée, J.-B., Slangen, A. B. A., and Yu, Y.: Intergovernmental Panel on Climate Change. Ocean, Cryosphere and Sea Level Change, in: *Climate Change 2021 – The Physical Science Basis: Working Group I Contribution to the Sixth Assessment Report of the Intergovernmental Panel on Climate Change*, Cambridge University Press, Cambridge, 1211–1362, <https://doi.org/10.1017/9781009157896.011>, 2023.
- Gasson, E., Deconto, R., and Pollard, D.: Antarctic bedrock topography uncertainty and ice sheet stability, *Geophys. Res. Lett.*, 42, 5372–5377, <https://doi.org/10.1002/2015GL064322>, 2015.
- Glasser, N. F., Davies, B. J., Carrivick, J. L., Rodés, A., Hambrey, M. J., Smellie, J. L., and Domack, E.: Ice-stream initiation, duration and thinning on James Ross Island, northern Antarctic Peninsula, *Quaternary Sci. Rev.*, 86, 78–88, <https://doi.org/10.1016/j.quascirev.2013.11.012>, 2014.
- Golledge, N. R., Menviel, L., Carter, L., Fogwill, C. J., England, M. H., Cortese, G., and Levy, R. H.: Antarctic contribution to meltwater pulse 1A from reduced Southern Ocean overturning, *Nat. Commun.*, 5, 5107, <https://doi.org/10.1038/ncomms6107>, 2014.
- Golledge, N. R., Kowalewski, D. E., Naish, T. R., Levy, R. H., Fogwill, C. J., and Gasson, E. G. W.: The multi-millennial Antarctic commitment to future sea-level rise, *Nature*, 526, 421–425, <https://doi.org/10.1038/nature15706>, 2015.
- Gomez, N., Latychev, K., and Pollard, D.: A coupled ice sheet sea level model incorporating 3D earth structure: Variations in Antarctica during the Last Deglacial Retreat, *J. Climate*, 31, 4041–4054, <https://doi.org/10.1175/JCLI-D-17-0352.1>, 2018.
- Gow, A. J., Ueda, H. T., and Garfield, D. E.: Antarctic ice sheet: Preliminary results of first core hole to bedrock, *Science*, 161, 1011–1013, <https://doi.org/10.1126/science.161.3845.1011>, 1968.
- Hall, B. L. and Denton, G. H.: New relative sea-level curves for the southern Scott Coast, Antarctica: Evidence for Holocene deglaciation of the western Ross Sea, *J.*

- Quaternary Sci., 14, 641–650, [https://doi.org/10.1002/\(SICI\)1099-1417\(199912\)14:7<641::AID-JQS466>3.0.CO;2-B](https://doi.org/10.1002/(SICI)1099-1417(199912)14:7<641::AID-JQS466>3.0.CO;2-B), 1999.
- Hall, B. L., Henderson, G. M., Baroni, C., and Kellogg, T. B.: Constant Holocene Southern-Ocean <sup>14</sup>C reservoir ages and ice-shelf flow rates, *Earth Planet. Sc. Lett.*, 296, 115–123, <https://doi.org/10.1016/j.epsl.2010.04.054>, 2010.
- Heaton, T. J., Köhler, P., Butzin, M., Bard, E., Reimer, R. W., Austin, W. E. N., Bronk Ramsey, C., Grootes, P. M., Hughen, K. A., Kromer, B., Reimer, P. J., Adkins, J., Burke, A., Cook, M. S., Olsen, J., and Skinner, L. C.: Marine20 – The Marine Radiocarbon Age Calibration Curve (0–55 000 cal BP), *Radiocarbon*, 62, 779–820, <https://doi.org/10.1017/RDC.2020.68>, 2020.
- Hein, A. S., Woodward, J., Marrero, S. M., Dunning, S. A., Steig, E. J., Freeman, S. P. H. T., Stuart, F. M., Winter, K., Westoby, M. J., and Sugden, D. E.: Evidence for the stability of the West Antarctic Ice Sheet divide for 1.4 million years, *Nat. Commun.*, 7, 10325, <https://doi.org/10.1038/ncomms10325>, 2016.
- Hemer, M. A. and Harris, P. T.: Sediment core from beneath the Amery Ice shelf, East Antarctica, suggests mid-Holocene ice-shelf retreat, *Geology*, 31, 127–130, [https://doi.org/10.1130/0091-7613\(2003\)031<0127:SCFBTA>2.0.CO;2](https://doi.org/10.1130/0091-7613(2003)031<0127:SCFBTA>2.0.CO;2), 2003.
- Hemer, M. A., Post, A. L., O'Brien, P. E., Craven, M., Truswell, E. M., Roberts, D., and Harris, P. T.: Sedimentological signatures of the sub-Amery Ice Shelf circulation, *Antarct. Sci.*, 19, 497–506, <https://doi.org/10.1017/S0954102007000697>, 2007.
- Heroy, D. C. and Anderson, J. B.: Radiocarbon constraints on Antarctic Peninsula Ice Sheet retreat following the Last Glacial Maximum (LGM), *Quaternary Sci. Rev.*, 26, 3286–3297, <https://doi.org/10.1016/j.quascirev.2007.07.012>, 2007.
- Hillenbrand, C. D., Larter, R. D., Dowdeswell, J. A., Ehrmann, W., Ó Cofaigh, C., Benetti, S., Graham, A. G. C., and Grobe, H.: The sedimentary legacy of a palaeo-ice stream on the shelf of the southern Bellingshausen Sea: Clues to West Antarctic glacial history during the Late Quaternary, *Quaternary Sci. Rev.*, 29, 2741–2763, <https://doi.org/10.1016/j.quascirev.2010.06.028>, 2010a.
- Hillenbrand, C.-D., Smith, J. A., Kuhn, G., Esper, O., Gersonde, R., Larter, R. D., Maher, B., Moreton, S. G., Shimmield, T. M., and Korte, M.: Age assignment of a diatomaceous ooze deposited in the western Amundsen Sea Embayment after the Last Glacial Maximum, *J. Quaternary Sci.*, 25, 280–295, 2010b.
- Hillenbrand, C.-D., Kuhn, G., Smith, J. A., Gohl, K., Graham, A. G. C., Larter, R. D., Klages, J. P., Downey, R., Moreton, S. G., Forwick, M., and Vaughan, D. G.: Grounding-line retreat of the west Antarctic ice sheet from inner Pine island Bay, *Geology*, 41, 35–38, 2013.

- Hillenbrand, C. D., Bentley, M. J., Stollendorf, T. D., Hein, A. S., Kuhn, G., Graham, A. G. C., Fogwill, C. J., Kristoffersen, Y., Smith, J. A., Anderson, J. B., Larter, R. D., Melles, M., Hodgson, D. A., Mulvaney, R., and Sugden, D. E.: Reconstruction of changes in the Weddell Sea sector of the Antarctic Ice Sheet since the Last Glacial Maximum, *Quaternary Sci. Rev.*, 100, 111–136, <https://doi.org/10.1016/j.quascirev.2013.07.020>, 2014.
- Hjort, C., Ingólfsson, Ó., Möller, P., and Lirio, J. M.: Holocene glacial history and sea-level changes on James Ross Island, Antarctic Peninsula, *J. Quaternary Sci.*, 12, 259–273, [https://doi.org/10.1002/\(sici\)1099-1417\(199707/08\)12:4<259::aid-jqs307>3.0.co;2-6](https://doi.org/10.1002/(sici)1099-1417(199707/08)12:4<259::aid-jqs307>3.0.co;2-6), 1997.
- Hodgson, D. A., Whitehouse, P. L., De Cort, G., Berg, S., Verleyen, E., Tavernier, I., Roberts, S. J., Vyverman, W., Sabbe, K., and O'Brien, P.: Rapid early Holocene sea-level rise in Prydz Bay, East Antarctica, *Global Planet. Change*, 139, 128–140, <https://doi.org/10.1016/j.gloplacha.2015.12.020>, 2016.
- Hodgson, D. A., Hogan, K., Smith, J. M., Smith, J. A., Hillenbrand, C.-D., Graham, A. G. C., Fretwell, P., Allen, C., Peck, V., Arndt, J.-E., Dorschel, B., Hübscher, C., Smith, A. M., and Larter, R.: Deglaciation and future stability of the Coats Land ice margin, Antarctica, *The Cryosphere*, 12, 2383–2399, <https://doi.org/10.5194/tc-12-2383-2018>, 2018.
- Huybrechts, P.: Sea-level changes at the LGM from ice-dynamic reconstructions of the Greenland and Antarctic ice sheets during the glacial cycles, *Quaternary Sci. Rev.*, 21, 203–231, [https://doi.org/10.1016/S0277-3791\(01\)00082-8](https://doi.org/10.1016/S0277-3791(01)00082-8), 2002.
- Ivins, E. R., James, T. S., Wahr, J., Ernst, E. J., Landerer, F. W., and Simon, K. M.: Antarctic contribution to sea level rise observed by GRACE with improved GIA correction, *J. Geophys. Res.-Sol. Ea.*, 118, 3126–3141, <https://doi.org/10.1002/jgrb.50208>, 2013.
- Johnson, J. S., Bentley, M. J., and Gohl, K.: First exposure ages from the Amundsen Sea Embayment, West Antarctica: The Late quaternary context for recent thinning of Pine Island, Smith, and Pope Glaciers, *Geology*, 36, 223–226, <https://doi.org/10.1130/G24207A.1>, 2008.
- Johnson, J. S., Smith, J. A., Schaefer, J. M., Young, N. E., Goehring, B. M., Hillenbrand, C. D., Lamp, J. L., Finkel, R. C., and Gohl, K.: The last glaciation of Bear Peninsula, central Amundsen Sea Embayment of Antarctica: Constraints on timing and duration revealed by in situ cosmogenic  $^{14}\text{C}$  and  $^{10}\text{Be}$  dating, *Quaternary Sci. Rev.*, 178, 77–88, <https://doi.org/10.1016/j.quascirev.2017.11.003>, 2017.

- Johnson, J. S., Nichols, K. A., Goehring, B. M., Balco, G., and Schaefer, J. M.: Abrupt mid-Holocene ice loss in the western Weddell Sea Embayment of Antarctica, *Earth Planet. Sc. Lett.*, 518, 127–135, <https://doi.org/10.1016/j.epsl.2019.05.002>, 2019.
- Johnson, J. S., Roberts, S. J., Rood, D. H., Pollard, D., Schaefer, J. M., Whitehouse, P. L., Ireland, L. C., Lamp, J. L., Goehring, B. M., Rand, C., and Smith, J. A.: Deglaciation of Pope Glacier implies widespread early Holocene ice sheet thinning in the Amundsen Sea sector of Antarctica, *Earth Planet. Sc. Lett.*, 548, 116501, <https://doi.org/10.1016/j.epsl.2020.116501>, 2020.
- Jones, R. S., Mackintosh, A. N., Norton, K. P., Golledge, N. R., Fogwill, C. J., Kubik, P. W., Christl, M., and Greenwood, S. L.: Rapid Holocene thinning of an East Antarctic outlet glacier driven by marine ice sheet instability, *Nat. Commun.*, 6, 8910, <https://doi.org/10.1038/ncomms9910>, 2015.
- King, C., Hall, B., Hillebrand, T., & Stone, J.: Delayed maximum and recession of an East Antarctic outlet glacier. *Geology*, 48(6), 630-634, <https://doi.org/10.1130/G47297.1> 2020.
- Kingslake, J., Scherer, R. P., Albrecht, T., Coenen, J., Powell, R. D., Reese, R., Stansell, N. D., Tulaczyk, S., Wearing, M. G., and Whitehouse, P. L.: Extensive retreat and re-advance of the West Antarctic Ice Sheet during the Holocene, *Nature*, 558, 430–434, <https://doi.org/10.1038/s41586-018-0208-x>, 2018.
- Kirshner, A. E., Anderson, J. B., Jakobsson, M., O'Regan, M., Majewski, W., and Nitsche, F. O.: Post-LGM deglaciation in Pine Island Bay, West Antarctica, *Quaternary Sci. Rev.*, 38, 11–26, <https://doi.org/10.1016/j.quascirev.2012.01.017>, 2012.
- Klages, J. P., Kuhn, G., Hillenbrand, C.-D., Graham, A. G. C., Smith, J. A., Larter, R. D., Gohl, K., and Wacker, L.: Retreat of the West Antarctic Ice Sheet from the western Amundsen Sea shelf at a pre-or early LGM stage, *Quaternary Sci. Rev.*, 91, 1–15, 2014.
- Klages, J. P., Kuhn, G., Hillenbrand, C. D., Smith, J. A., Graham, A. G. C., Nitsche, F. O., Frederichs, T., Jernas, P. E., Gohl, K., and Wacker, L.: Limited grounding-line advance onto the West Antarctic continental shelf in the easternmost Amundsen Sea Embayment during the last glacial period, *PLoS One*, 12, e0181593, <https://doi.org/10.1371/journal.pone.0181593>, 2017.
- Larter, R. D., Anderson, J. B., Graham, A. G. C., Gohl, K., Hillenbrand, C. D., Jakobsson, M., Johnson, J. S., Kuhn, G., Nitsche, F. O., Smith, J. A., Witus, A. E., Bentley, M. J., Dowdeswell, J. A., Ehrmann, W., Klages, J. P., Lindow, J., Cofaigh, C. O., and Spiegel, C.: Reconstruction of changes in the Amundsen Sea and Bellingshausen Sea sector of the West Antarctic Ice Sheet since the Last Glacial Maximum,

- Quaternary Sci. Rev., 100, 55–86, <https://doi.org/10.1016/j.quascirev.2013.10.016>, 2014.
- Lecavalier, B., Tarasov, L., Balco, G., Spector, P., Hillenbrand, C.-D., Buizert, C., Ritz, C., Leduc-Leballeur, M., Mulvaney, R., Whitehouse, P. L., Bentley, M. J., and Bamber, J.: Antarctic ice sheet paleo-constraint database, Ghub [dataset], <https://thehub.org/resources/4884>, 2022.
- Levermann, A., Winkelmann, R., Nowicki, S., Fastook, J. L., Frieler, K., Greve, R., Hellmer, H. H., Martin, M. A., Meinshausen, M., Mengel, M., Payne, A. J., Pollard, D., Sato, T., Timmermann, R., Wang, W. L., and Bindshadler, R. A.: Projecting Antarctic ice discharge using response functions from SeaRISE ice-sheet models, *Earth Syst. Dynam.*, 5, 271–293, <https://doi.org/10.5194/esd-5-271-2014>, 2014.
- Licht, K. J., Cunningham, W. L., Andrews, J. T., Domack, E. W., and Jennings, A. E.: Establishing chronologies from acid insoluble organic  $^{14}\text{C}$  dates on antarctic (Ross Sea) and arctic (North Atlantic) marine sediments, *Polar Res.*, 17, 203–216, <https://doi.org/10.3402/polar.v17i2.6619>, 1998.
- Lifton, N., Sato, T., and Dunai, T. J.: Scaling in situ cosmogenic nuclide production rates using analytical approximations to atmospheric cosmic-ray fluxes, *Earth Planet. Sc. Lett.*, <https://doi.org/10.1016/j.epsl.2013.10.052>, 2014.
- Little, C. M., Oppenheimer, M., and Urban, N. M.: Upper bounds on twenty-first-century Antarctic ice loss assessed using a probabilistic framework, *Nat. Clim. Change*, 3, 654–659, <https://doi.org/10.1038/nclimate1845>, 2013.
- Livingstone, S. J., Ó Cofaigh, C., Stokes, C. R., Hillenbrand, C.-D., Vieli, A., and Jamieson, S. S. R.: Antarctic palaeo-ice streams, *Earth Sci. Rev.*, 111, 90–128, <https://doi.org/10.1016/j.earscirev.2011.10.003>, 2012.
- Lorius, C., Raynaud, D., Petit, J. R., Jouzel, J., and Merlivat, L.: Late-glacial maximum-Holocene atmospheric and ice-thickness changes from Antarctic ice-core studies, *Ann. Glaciol.*, 5, 88–94, <https://doi.org/10.3189/1984aog5-1-88-94>, 1984.
- Lukin, V. V. and Vasiliev, N. I.: Technological aspects of the final phase of drilling borehole 5G and unsealing Vostok Subglacial Lake, East Antarctica, *Ann. Glaciol.*, 55, 83–89, <https://doi.org/10.3189/2014AoG65A002>, 2014.
- MacGregor, J. A., Fahnestock, M. A., Catania, G. A., Paden, J. D., Prasad Gogineni, S., Young, S. K., Rybarski, S. C., Mabrey, A. N., Wagman, B. M., and Morlighem, M.: Radiostratigraphy and age structure of the Greenland Ice Sheet, *J. Geophys. Res.-Earth*, 120, 212–241, <https://doi.org/10.1002/2014JF003215>, 2015.

- Mackintosh, A., White, D., Fink, D., Gore, D. B., Pickard, J., and Fanning, P. C.: Exposure ages from mountain dipsticks in Mac. Robertson Land, East Antarctica, indicate little change in ice sheet thickness since the Last Glacial Maximum, *Geology*, 35, 551–554, <https://doi.org/10.1130/G23503A.1>, 2007.
- Mackintosh, A. N., Verleyen, E., O'Brien, P. E., White, D. A., Jones, R. S., McKay, R., Dunbar, R., Gore, D. B., Fink, D., Post, A. L., and Miura, H.: Retreat history of the East Antarctic Ice Sheet since the last glacial maximum, *Quaternary Sci. Rev.*, 100, 10–30, 2014.
- Martín-Español, A., Zammit-Mangion, A., Clarke, P. J., Flament, T., Helm, V., King, M. A., Luthcke, S. B., Petrie, E., Rémy, F., Schön, N., Wouters, B., and Bamber, J. L.: Spatial and temporal Antarctic Ice Sheet mass trends, glacio-isostatic adjustment, and surface processes from a joint inversion of satellite altimeter, gravity, and GPS data, *J. Geophys. Res.-Earth*, 121, 182–200, <https://doi.org/10.1002/2015JF003550>, 2016.
- Mas e Braga, M., Selwyn Jones, R., Newall, J. C. H., Rogozhina, I., Andersen, J. L., Lifton, N. A., and Stroeven, A. P.: Nunataks as barriers to ice flow: implications for palaeo ice sheet reconstructions, *The Cryosphere*, 15, 4929–4947, <https://doi.org/10.5194/tc-15-4929-2021>, 2021.
- Matsuoka, K., Skoglund, A., Roth, G., de Pomereu, J., Griffiths, H., Headland, R., Herried, B., Katsumata, K., le Brocq, A., Licht, K., Morgan, F., Neff, P. D., Ritz, C., Scheinert, M., Tamura, T., van de Putte, A., van den Broeke, M., von Deschanden, A., Deschamps-Berger, C., Liefferinge, B. van, Tronstad, S., and Melvaer, Y.: Quantarctica, an integrated mapping environment for Antarctica, the Southern Ocean, and sub-Antarctic islands, *Environ. Modell. Softw.*, 140, 105015, <https://doi.org/10.21334/npolar.2018.8516e961>, 2021.
- McGlannan, A. J., Bart, P. J., Chow, J. M., and DeCesare, M.: On the influence of post-LGM ice shelf loss and grounding zone sedimentation on West Antarctic ice sheet stability, *Mar. Geol.*, 392, 151–169, <https://doi.org/10.1016/j.margeo.2017.08.005>, 2017.
- McKay, R. M., Dunbar, G. B., Naish, T. R., Barrett, P. J., Carter, L., and Harper, M.: Retreat history of the Ross Ice Sheet (Shelf) since the Last Glacial Maximum from deep-basin sediment cores around Ross Island, *Palaeogeogr. Palaeoclimatol.*, 260, 245–261, <https://doi.org/10.1016/j.palaeo.2007.08.015>, 2008.
- McKay, R., Golledge, N. R., Maas, S., Naish, T., Levy, R., Dunbar, G., and Kuhn, G.: Antarctic marine ice-sheet retreat in the Ross Sea during the early Holocene, *Geology*, 44, 7–10, 2016.

- Meredith, M., Sommerkorn, M., Cassotta, S., Derksen, C., Ekaykin, A., Hollowed, A., Kofinas, G., Mackintosh, A., Melbourne-Thomas, J., Muelbert, M. M. C., Ottersen, G., Pritchard, H., and Schuur, E. A. G.: Polar Regions, in: IPCC Special Report on the Ocean and Cryosphere in a Changing Climate, IPCC, <https://doi.org/10.1017/9781009157964.005>, 2019.
- Miura, H., Moriwaki, K., Maemoku, H., and Hirakawa, K.: Fluctuations of the East Antarctic ice-sheet margin since the last glaciation from the stratigraphy of raised beach deposits along the Soya Coast, *Ann. Glaciol.*, 27, 297–301, 1998.
- Morlighem, M., Rignot, E., Binder, T., Blankenship, D., Drews, R., Eagles, G., Eisen, O., Ferraccioli, F., Forsberg, R., Fretwell, P., Goel, V., Greenbaum, J. S., Gudmundsson, H., Guo, J., Helm, V., Hofstede, C., Howat, I., Humbert, A., Jokat, W., Karlsson, N. B., Lee, W. S., Matsuoka, K., Millan, R., Mouginot, J., Paden, J., Pattyn, F., Roberts, J., Rosier, S., Ruppel, A., Seroussi, H., Smith, E. C., Steinhage, D., Sun, B., van den Broeke, M. R., van Ommen, T. D., van Wessem, M., and Young, D. A.: Deep glacial troughs and stabilizing ridges unveiled beneath the margins of the Antarctic ice sheet, *Nat. Geosci.*, 13, 132–137, <https://doi.org/10.1038/s41561-019-0510-8>, 2020.
- Motoyama, H.: The Second Deep Ice Coring Project at Dome Fuji, Antarctica, *Sci. Dril.*, 5, 41–43, <https://doi.org/10.2204/iodp.sd.5.05.2007>, 2007.
- Mouginot, J., Rignot, E., and Scheuchl, B.: Continent-Wide, Interferometric SAR Phase, Mapping of Antarctic Ice Velocity, *Geophys. Res. Lett.*, 46, 9710–9718, <https://doi.org/10.1029/2019GL083826>, 2019.
- Mulvaney, R., Rix, J., Polfrey, S., Grieman, M., Martin, C., Nehrbass-Ahles, C., Rowell, I., Tuckwell, R., and Wolff, E.: Ice drilling on Skytrain Ice Rise and Sherman Island, Antarctica, *Ann. Glaciol.*, 62, 311–323, <https://doi.org/10.1017/aog.2021.7>, 2021.
- Neuhaus, S. U., Tulaczyk, S. M., Stansell, N. D., Coenen, J. J., Scherer, R. P., Mikucki, J. A., and Powell, R. D.: Did Holocene climate changes drive West Antarctic grounding line retreat and readvance?, *The Cryosphere*, 15, 4655–4673, <https://doi.org/10.5194/tc-15-4655-2021>, 2021.
- Neumann, T. A., Conways, H., Price, S. F., Waddington, E. D., Catania, G. A., and Morse, D. L.: Holocene accumulation and ice sheet dynamics in central West Antarctica, *J. Geophys. Res.-Earth*, 113, 1–9, <https://doi.org/10.1029/2007JF000764>, 2008.
- Nichols, K. A., Goehring, B. M., Balco, G., Johnson, J. S., Hein, A. S., and Todd, C.: New Last Glacial Maximum ice thickness constraints for the Weddell Sea Embayment, Antarctica, *The Cryosphere*, 13, 2935–2951, <https://doi.org/10.5194/tc-13-2935-2019>, 2019.

- Ó Cofaigh, C., Davies, B. J., Livingstone, S. J., Smith, J. A., Johnson, J. S., Hocking, E. P., Hodgson, D. A., Anderson, J. B., Bentley, M. J., Canals, M., Domack, E., Dowdeswell, J. A., Evans, J., Glasser, N. F., Hillenbrand, C.-D., Larter, R. D., Roberts, S. J., and Simms, A. R.: Reconstruction of ice-sheet changes in the Antarctic Peninsula since the Last Glacial Maximum, *Quaternary Sci. Rev.*, 100, 87–110, <https://doi.org/10.1016/j.quascirev.2014.06.023>, 2014.
- Ohkouchi, N. and Eglinton, T. I.: Compound-specific radiocarbon dating of Ross Sea sediments: A prospect for constructing chronologies in high-latitude oceanic sediments, *Quat. Geochronol.*, 3, 235–243, <https://doi.org/10.1016/j.quageo.2007.11.001>, 2008.
- Parrenin, F., Barnola, J.-M., Beer, J., Blunier, T., Castellano, E., Chappellaz, J., Dreyfus, G., Fischer, H., Fujita, S., Jouzel, J., Kawamura, K., Lemieux-Dudon, B., Loulergue, L., Masson-Delmotte, V., Narcisi, B., Petit, J.-R., Raisbeck, G., Raynaud, D., Ruth, U., Schwander, J., Severi, M., Spahni, R., Steffensen, J. P., Svensson, A., Udisti, R., Waelbroeck, C., and Wolff, E.: The EDC3 chronology for the EPICA Dome C ice core, *Clim. Past*, 3, 485–497, <https://doi.org/10.5194/cp-3-485-2007>, 2007.
- Pollard, D. and DeConto, R. M.: Modelling West Antarctic ice sheet growth and collapse through the past five million years, *Nature*, 458, 329–332, <https://doi.org/10.1038/nature07809>, 2009.
- Post, A. L., Hemer, M. A., O'Brien, P. E., Roberts, D., and Craven, M.: History of benthic colonisation beneath the Amery Ice Shelf, East Antarctica, *Mar. Ecol. Prog. Ser.*, 344, 29–37, <https://doi.org/10.3354/meps06966>, 2007.
- Post, A. L., Galton-Fenzi, B. K., Riddle, M. J., Herraiz-Borreguero, L., O'Brien, P. E., Hemer, M. A., McMinn, A., Rasch, D., and Craven, M.: Modern sedimentation, circulation and life beneath the Amery Ice Shelf, East Antarctica, *Cont. Shelf Res.*, 74, 77–87, <https://doi.org/10.1016/j.csr.2013.10.010>, 2014.
- Pudsey, C. J., Murray, J. W., Appleby, P., and Evans, J.: Ice shelf history from petrographic and foraminiferal evidence, Northeast Antarctic Peninsula, *Quaternary Sci. Rev.*, 25, 2357–2379, <https://doi.org/10.1016/j.quascirev.2006.01.029>, 2006.
- Raynaud, D., Lipenkov, V., Lemieux-Dudon, B., Duval, P., Loutre, M. F., and Lhomme, N.: The local insolation signature of air content in Antarctic ice. A new step toward an absolute dating of ice records, *Earth Planet. Sc. Lett.*, 261, 337–349, <https://doi.org/10.1016/j.epsl.2007.06.025>, 2007.
- Reimer, P. J., Baillie, M. G. L., Bard, E., Bayliss, A., Beck, J. W., Blackwell, P. G., Bronk Ramsey, C., Buck, C. E., Burr, G. S., Edwards, R. L., Friedrich, M., Grootes, P. M., Guilderson, T. P., Hajdas, I., Heaton, T. J., Hogg, A. G., Hughen, K. A., Kaiser, K.

- F., Kromer, B., McCormac, F. G., Manning, S. W., Reimer, R. W., Richards, D. A., Southon, J. R., Talamo, S., Turney, C. S. M., van der Plicht, J., and Weyhenmeyer, C. E.: INTCAL 09 and MARINE09 radiocarbon age calibration curves, 0–50 000 years Cal BP, *Radiocarbon*, 51, 1111–1150, [https://doi.org/10.2458/azu\\_js\\_rc.51.3569](https://doi.org/10.2458/azu_js_rc.51.3569), 2009.
- Riddle, M. J., Craven, M., Goldsworthy, P. M., and Carsey, F.: A diverse benthic assemblage 100 km from open water under the Amery Ice Shelf, Antarctica, *Paleoceanography*, 22, PA1204, <https://doi.org/10.1029/2006PA001327>, 2007.
- Ritz, C., Edwards, T. L., Durand, G., Payne, A. J., Peyaud, V., and Hindmarsh, R. C. A.: Potential sea-level rise from Antarctic ice sheet instability constrained by observations, *Nature*, 528, 115–118, <https://doi.org/10.1038/nature16147>, 2015.
- Roberts, S. J., Hodgson, D. A., Sterken, M., Whitehouse, P. L., Verleyen, E., Vyverman, W., Sabbe, K., Balbo, A., Bentley, M. J., and Moreton, S. G.: Geological constraints on glacio-isostatic adjustment models of relative sea level change during deglaciation of Prince Gustav Channel, Antarctic Peninsula, *Quaternary Sci. Rev.*, 30, 3603–3617, <https://doi.org/10.1016/j.quascirev.2011.09.009>, 2011.
- Rosenheim, B. E., Day, M. B., Domack, E., Schrum, H., Benthien, A., and Hayes, J. M.: Antarctic sediment chronology by programmed-temperature pyrolysis: Methodology and data treatment, *Geochem. Geophys. Geosy.*, 9, Q04005, <https://doi.org/10.1029/2007GC001816>, 2008.
- Ruckert, K. L., Shaffer, G., Pollard, D., Guan, Y., Wong, T. E., Forest, C. E., and Keller, K.: Assessing the impact of retreat mechanisms in a simple antarctic ice sheet model using Bayesian calibration, *PLoS One*, 12, 1–15, <https://doi.org/10.1371/journal.pone.0170052>, 2017.
- Sasgen, I., Martín-Español, A., Horvath, A., Klemann, V., Petrie, E. J., Wouters, B., Horvath, M., Pail, R., Bamber, J. L., Clarke, P. J., Konrad, H., and Drinkwater, M. R.: Joint inversion estimate of regional glacial isostatic adjustment in Antarctica considering a lateral varying Earth structure (ESA STSE Project REGINA), *Geophys. J. Int.*, 211, 1534–1553, <https://doi.org/10.1093/gji/ggx368>, 2017.
- Shennan, I., Long, A. J., and Horton, B. P.: *Handbook of Sea-Level Research*, John Wiley & Sons Ltd., <https://doi.org/10.1002/9781118452547>, 2015.
- Shepherd, A., Ivins, E., Rignot, E., Smith, B., Van Den Broeke, M., Velicogna, I., Whitehouse, P., Briggs, K., Joughin, I., Krinner, G., Nowicki, S., Payne, T., Scambos, T., Schlegel, N., Geruo, A., Agosta, C., Ahlstrøm, A., Babonis, G., Barletta, V., Blazquez, A., Bonin, J., Csatho, B., Cullather, R., Felikson, D., Fettweis, X., Forsberg, R., Gallee, H., Gardner, A., Gilbert, L., Groh, A., Gunter, B., Hanna, E., Harig, C., Helm, V., Horvath, A., Horvath, M., Khan, S., Kjeldsen,

K. K., Konrad, H., Langen, P., Lecavalier, B., Loomis, B., Luthcke, S., McMillan, M., Melini, D., Mernild, S., Mohajerani, Y., Moore, P., Mouginot, J., Moyano, G., Muir, A., Nagler, T., Nield, G., Nilsson, J., Noel, B., Otsuka, I., Pattle, M. E., Peltier, W. R., Pie, N., Rietbroek, R., Rott, H., Sandberg-Sørensen, L., Sasgen, I., Save, H., Scheuchl, B., Schrama, E., Schröder, L., Seo, K. W., Simonsen, S., Slater, T., Spada, G., Sutterley, T., Talpe, M., Tarasov, L., Van De Berg, W. J., Van Der Wal, W., Van Wessel, M., Vishwakarma, B. D., Wiese, D., and Wouters, B.: Mass balance of the Antarctic Ice Sheet from 1992 to 2017, *Nature*, 558, 219–222, <https://doi.org/10.1038/s41586-018-0179-y>, 2018.

Simkins, L. M., Simms, A. R., and DeWitt, R.: Relative sea-level history of Marguerite Bay, Antarctic Peninsula derived from optically stimulated luminescence dated beach cobbles, *Quaternary Sci. Rev.*, 77, 141–155, <https://doi.org/10.1016/j.quascirev.2013.07.027>, 2013.

Simms, A. R., Milliken, K. T., Anderson, J. B., and Wellner, J. S.: The marine record of deglaciation of the South Shetland Islands, Antarctica since the Last Glacial Maximum, *Quaternary Sci. Rev.*, 30, 1583–1601, 2011.

Simms, A. R., Lisiecki, L., Gebbie, G., Whitehouse, P. L., and Clark, J. F.: Balancing the last glacial maximum (LGM) sea-level budget, *Quaternary Sci. Rev.*, 205, 143–153, <https://doi.org/10.1016/j.quascirev.2018.12.018>, 2019.

Small, D., Bentley, M. J., Jones, R. S., Pittard, M. L., and Whitehouse, P. L.: Antarctic ice sheet palaeo-thinning rates from vertical transects of cosmogenic exposure ages, *Quaternary Sci. Rev.*, 206, 65–80, <https://doi.org/10.1016/j.quascirev.2018.12.024>, 2019.

Smith, J. A., Hillenbrand, C. D., Kuhn, G., Larter, R. D., Graham, A. G. C., Ehrmann, W., Moreton, S. G., and Forwick, M.: Deglacial history of the West Antarctic Ice Sheet in the western Amundsen Sea Embayment, *Quaternary Sci. Rev.*, 30, 488–505, <https://doi.org/10.1016/j.quascirev.2010.11.020>, 2011.

Smith, J. A., Hillenbrand, C. D., Kuhn, G., Klages, J. P., Graham, A. G. C., Larter, R. D., Ehrmann, W., Moreton, S. G., Wiers, S., and Frederichs, T.: New constraints on the timing of West Antarctic Ice Sheet retreat in the eastern Amundsen Sea since the Last Glacial Maximum, *Global Planet. Change*, 122, 224–237, <https://doi.org/10.1016/j.gloplacha.2014.07.015>, 2014.

Smith, J. A., Graham, A. G. C., Post, A. L., Hillenbrand, C. D., Bart, P. J., and Powell, R. D.: The marine geological imprint of Antarctic ice shelves, *Nat. Commun.*, 10, 5635, <https://doi.org/10.1038/s41467-019-13496-5>, 2019.

Smith, J. A., Hillenbrand, C. D., Subt, C., Rosenheim, B. E., Frederichs, T., Ehrmann, W., Andersen, T. J., Wacker, L., Makinson, K., Anker, P., Venables, E. J., and Nicholls,

- K. W.: History of the Larsen C Ice Shelf reconstructed from sub-ice shelf and offshore sediments, *Geology*, 49, 978–982, <https://doi.org/10.1130/G48503.1>, 2021.
- Spector, P., Stone, J., Cowdery, S. G., Hall, B., Conway, H., and Bromley, G.: Rapid early-Holocene deglaciation in the Ross Sea, Antarctica, *Geophys. Res. Lett.*, 44, 7817–7825, <https://doi.org/10.1002/2017GL074216>, 2017.
- Steig, E., Fastook, J., Zweck, C., Goodwin, I., Licht, K., White, J., and Ackert Jr., R. P.: West Antarctic ice sheet elevation changes, *The West Antarctic Ice Sheet: Behaviour and Environment*, *Antar. Res. S.*, 77, 75–90, 2001.
- Stolldorf, T., Schenke, H.-W., and Anderson, J. B.: LGM ice sheet extent in the Weddell Sea: evidence for diachronous behavior of Antarctic Ice Sheets, *Quaternary Sci. Rev.*, 48, 20–31, 2012.
- Stone, J. O. H., Balco, G. A., Sugden, D. E., Caffee, M. W., Sass, L. C., Cowdery, S. G., and Siddoway, C.: Holocene deglaciation of Marie Byrd Land, West Antarctica, *Science*, 299, 99–102, <https://doi.org/10.1126/science.1077998>, 2003.
- Stuiver, M. and Reimer, P. J.: Extended  $^{14}\text{C}$  data base and revised CALIB 3.0  $^{14}\text{C}$  age calibration program, *Radiocarbon*, 35, 215–230, <https://doi.org/10.1017/S0033822200013904>, 1993.
- Subt, C., Yoon, H. I., Yoo, K. C., Lee, J. I., Leventer, A., Domack, E. W., and Rosenheim, B. E.: Sub-ice shelf sediment geochronology utilizing novel radiocarbon methodology for highly detrital sediments, *Geochem. Geophys. Geosy.*, 18, 1404–1418, <https://doi.org/10.1002/2016GC006578>, 2017.
- Suganuma, Y., Miura, H., Zondervan, A., and Okuno, J.: East Antarctic deglaciation and the link to global cooling during the Quaternary: Evidence from glacial geomorphology and  $^{10}\text{Be}$  surface exposure dating of the Sør Rondane Mountains, Dronning Maud Land, *Quaternary Sci. Rev.*, 97, 102–120, <https://doi.org/10.1016/j.quascirev.2014.05.007>, 2014.
- Sun, S., Cornford, S. L., Liu, Y., and Moore, J. C.: Dynamic response of Antarctic ice shelves to bedrock uncertainty, *The Cryosphere*, 8, 1561–1576, <https://doi.org/10.5194/tc-8-1561-2014>, 2014.
- Sun, W., Zhou, X., Zhou, D., and Sun, Y.: Advances and Accuracy Assessment of Ocean Tide Models in the Antarctic Ocean, *Front. Earth Sci.*, 10, 757821, <https://doi.org/10.3389/feart.2022.757821>, 2022.

- Sutter, J., Fischer, H., and Eisen, O.: Investigating the internal structure of the Antarctic ice sheet: the utility of isochrones for spatiotemporal ice-sheet model calibration, *The Cryosphere*, 15, 3839–3860, <https://doi.org/10.5194/tc-15-3839-2021>, 2021.
- Tarasov, L. and Goldstein, M.: Assessing uncertainty in past ice and climate evolution: overview, stepping-stones, and challenges, *Clim. Past Discuss.* [preprint], <https://doi.org/10.5194/cp-2021-145>, 2021.
- Todd, C., Stone, J., Conway, H., Hall, B., and Bromley, G.: Late Quaternary evolution of Reedy Glacier, Antarctica, *Quaternary Sci. Rev.*, 29, 1328–1341, <https://doi.org/10.1016/j.quascirev.2010.02.001>, 2010.
- Van Ommen, T. D., Morgan, V. I., Jacka, T. H., Woon, S., and Elcheikh, A.: Near-surface temperatures in the Dome Summit South (Law Dome, East Antarctica) borehole, *Ann. Glaciol.*, 29, 141–144, <https://doi.org/10.3189/172756499781821382>, 1999.
- Verleyen, E., Hodgson, D. A., Milne, G. A., Sabbe, K., and Vyverman, W.: Relative sea-level history from the Lambert Glacier region, East Antarctica, and its relation to deglaciation and Holocene glacier readvance, *Quaternary Res.*, 63, 45–52, <https://doi.org/10.1016/j.yqres.2004.09.005>, 2005.
- Verleyen, E., Tavernier, I., Hodgson, D. A., Whitehouse, P. L., Kudoh, S., Imura, S., Heirman, K., Bentley, M. J., Roberts, S. J., De Batist, M., Sabbe, K., and Vyverman, W.: Ice sheet retreat and glacio-isostatic adjustment in Lützow-Holm Bay, East Antarctica, *Quaternary Sci. Rev.*, 169, 85–98, <https://doi.org/10.1016/j.quascirev.2017.06.003>, 2017.
- Waddington, E. D., Conway, H., Steig, E. J., Alley, R. B., Brook, E. J., Taylor, K. C., and White, J. W. C.: Decoding the dipstick: Thickness of Siple Dome, West Antarctica, at the Last Glacial Maximum, *Geology*, 33, 281–284, <https://doi.org/10.1130/G21165.1>, 2005.
- Watcham, E. P., Bentley, M. J., Hodgson, D. A., Roberts, S. J., Fretwell, P. T., Lloyd, J. M., Larter, R. D., Whitehouse, P. L., Leng, M. J., Monien, P., and Moreton, S. G.: A new Holocene relative sea level curve for the South Shetland Islands, Antarctica, *Quaternary Sci. Rev.*, 30, 3152–3170, <https://doi.org/10.1016/j.quascirev.2011.07.021>, 2011.
- Weikusat, I., Jansen, D., Binder, T., Eichler, J., Faria, S. H., Wilhelms, F., Kipfstuhl, S., Sheldon, S., Miller, H., Dahl-Jensen, D., and Kleiner, T.: Physical analysis of an Antarctic ice core-towards an integration of micro-and macrodynamics of polar ice, *Philos. T. R. Soc. A*, 375, 20150347, <https://doi.org/10.1098/rsta.2015.0347>, 2017.
- Whitehouse, P. L., Bentley, M. J., and Le Brocq, A. M.: A deglacial model for Antarctica: Geological constraints and glaciological modelling as a basis for a new model of

- Antarctic glacial isostatic adjustment, *Quaternary Sci. Rev.*, 32, 1–24, <https://doi.org/10.1016/j.quascirev.2011.11.016>, 2012a.
- Whitehouse, P. L., Bentley, M. J., Milne, G. A., King, M. A., and Thomas, I. D.: A new glacial isostatic adjustment model for Antarctica: calibrated and tested using observations of relative sea-level change and present-day uplift rates, *Geophys. J. Int.*, 190, 1464–1482, <https://doi.org/10.1111/j.1365-246X.2012.05557.x>, 2012b.
- Whitehouse, P. L., Gomez, N., King, M. A., and Wiens, D. A.: Solid Earth change and the evolution of the Antarctic Ice Sheet, *Nat. Commun.*, 10, 1–14, <https://doi.org/10.1038/s41467-018-08068-y>, 2019.
- Winter, A., Steinhage, D., Creyts, T. T., Kleiner, T., and Eisen, O.: Age stratigraphy in the East Antarctic Ice Sheet inferred from radio-echo sounding horizons, *Earth Syst. Sci. Data*, 11, 1069–1081, <https://doi.org/10.5194/essd-11-1069-2019>, 2019.
- Yokoyama, Y., Anderson, J. B., Yamane, M., Simkins, L. M., Miyairi, Y., Yamazaki, T., Koizumi, M., Suga, H., Kusahara, K., Prothro, L., Hasumi, H., Southon, J. R., and Ohkouchi, N.: Widespread collapse of the Ross Ice Shelf during the late Holocene, *P. Natl. Acad. Sci. USA*, 113, 2354–2359, <https://doi.org/10.1073/pnas.1516908113>, 2016.
- Zwartz, D., Bird, M., Stone, J., and Lambeck, K.: Holocene sea-level change and ice-sheet history in the Vestfold Hills, East Antarctica, *Earth Planet. Sc. Lett.*, 155, 131–145, [https://doi.org/10.1016/S0012-821X\(97\)00204-5](https://doi.org/10.1016/S0012-821X(97)00204-5), 1998.

# Chapter 3: A history-matching analysis of the Antarctic Ice Sheet since the last interglacial – Part 1: Ice sheet evolution

## Abstract

In this study we present the evolution of the Antarctic Ice Sheet (AIS) since the last interglacial. This is achieved by means of a history-matching analysis where a newly updated observational database (AntICE2, Lecavalier et al., 2023) was used to constrain a large ensemble of 9,293 model simulations. The Glacial Systems Model (GSM) configured with 38 ensemble parameters was history matched against observations of past ice extent, past ice thickness, past sea level, ice core borehole temperature profiles, present-day uplift rates, and present-day ice sheet geometry and surface velocity. Successive ensembles were used to train Bayesian Artificial Neural Network emulators. The parameter space was efficiently explored to identify the most relevant portions of the parameter space through Markov Chain Monte Carlo sampling with the emulators. The history-matching ruled out model simulations which were inconsistent with the observational constraint database.

During the last interglacial (LIG), the AIS yielded several meters equivalent sea-level (mESL) grounded ice volume deficit relative to present with subsurface ocean warming during this period being the key uncertainty. At the global Last Glacial Maximum

(LGM), the best-fitting sub-ensemble of AIS simulations reached an excess grounded ice volume relative to present of 9.2 to 26.5 mESL. Considering the data does not rule out simulations with an LGM grounded ice volume  $> 20$  mESL with respect to present, the AIS volume at the LGM can partly explain the missing ice problem and help close the LGM sea-level budget. Moreover, during the deglaciation, the state space estimation of the AIS based on the GSM and near-field observational constraints allow only a negligible Antarctic Melt Water Pulse 1a contribution (-0.2 to 0.3 mESL).

### 3.1 Introduction

The Antarctic Ice Sheet (AIS) has been identified as a major source of uncertainty to future sea level change (Meredith et al., 2019; Masson-Delmotte et al., 2021). It is one of the slowest components of the climate system given that its interior responds on 100 kyr timescales. Therefore, studying the past evolution of the AIS can quantify the sensitivity of the ice sheet to past warm and cold periods, and facilitate the interpretation and projection of contemporary and future ice sheet changes and corresponding sea level rise. This is primarily achieved using model simulations that aim to reconstruct past changes of the AIS (Golledge et al., 2012; DeConto and Pollard, 2016; Albrecht et al., 2020b). However, relevant modelling studies to date are generally characterized by limited parameter sampling, reliance on hand-tuning, incomplete validation against observational constraints, and the absence of meaningful uncertainty analysis. As such, the relationship of the resultant simulations to the actual past ice sheet evolution is unclear. This is particularly relevant given ice sheet instabilities could potentially contribute metres to sea-level rise over the next two centuries (Rignot et al., 2014; DeConto and Pollard, 2016; Pattyn and

Morlighem, 2020; Edwards et al., 2019). Although these studies provide insights on the AIS, there remains a critical need to incorporate a broader variety of data to constrain past and future AIS evolution. For reference, an Antarctic map with places named in the paper and the data used in the history-matching analysis is given in Figure 3.1.

Our understanding of the AIS has dramatically increased over the past several decades through remote sensing and field campaigns. A large portion of AIS research and resources evaluate the present-day (PD) state, and the processes and drivers of contemporary changes. Too often, past and future AIS simulations solely rely on the PD ice sheet geometry and surface velocity to constrain and initialize their models (Martin et al., 2019). This fails to recognize that the contemporary AIS is not in a steady state and disregards the past trajectory of the ice sheet. To address the latter, it is important to incorporate valuable albeit limited paleo observations to constrain and initialize AIS simulations. Nonetheless, our knowledge of the PD AIS state represents our most powerful constraints and well-defined boundary conditions. Understanding both the present and past AIS dynamics is crucial given its potential impact on future sea-level rise.

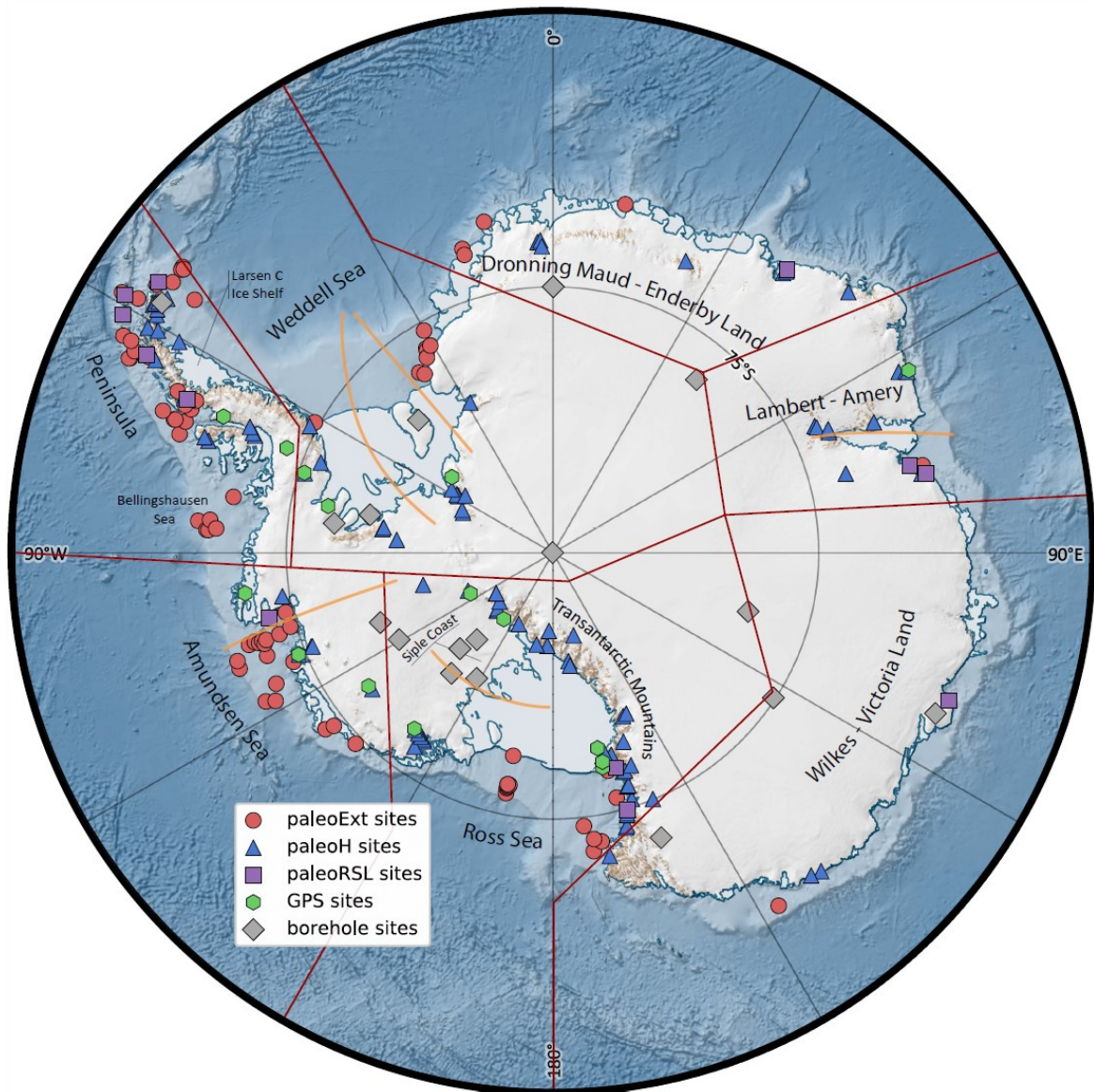


Figure 3.1: a) Antarctic continent and names of locations mentioned in the study are shown alongside the Antarctic Ice sheet Evolution database version 2 (AntICE2) database (symbols), the main Antarctic sectors delineated by the dark red outlines, and key cross section profiles (orange lines). The data ID numbers and ice core names are labelled in Figure S3.1. The Antarctic basemap was generated using Quantarctica (Matsuoka et al., 2021).

Large sections of the AIS are marine-based (Fig. 3.1) and are susceptible to marine ice sheet instabilities (MISI) and potentially marine ice cliff instabilities (MICI) that could contribute ~1 meter equivalent sea-level (mESL) by the end of the century (Golledge et al.,

2015a; DeConto and Pollard, 2016; Edwards et al., 2019). The PD mass balance of the AIS has been inferred using a variety of methods which have in turn identified the Amundsen Sea sector of the West Antarctic Ice Sheet (WAIS) as a major contributor to the negative mass balance of the AIS (Shepherd et al., 2018). However, a common requirement across geodetic mass balance inferences of the AIS is the background viscous glacial isostatic adjustment (GIA) signal which represents a major source of uncertainty (Whitehouse et al., 2019). The AIS mass balance from 1992 to 2017 was  $-109 \pm 56$  Gt/yr ( $7.6 \pm 3.9$  mm of sea level rise) (Shepherd et al., 2018). These estimates use poorly constrained GIA estimates that are based on a limited exploration of uncertainties against observational constraints (Otosaka et al., 2023). To address the uncertainties in PD AIS mass balance estimates and future projections, it is essential to refine our understanding of the sensitivity of the AIS to past climate change by integrating data with comprehensive modelling methodologies.

There remain several outstanding research questions regarding the past evolution of the AIS that revolve around the sensitivity and susceptibility of the AIS to past and future climate change. In this study we primarily focus on those pertaining to the grounded ice volume of the AIS since the Last Interglaciation (LIG). A history-matching analysis requires observational data to initialize, force, constrain, and score model simulations. Moreover, this needs clearly defined observational uncertainties, quantified internal model discrepancies, and reasonable external discrepancy estimations. The robustness of the history-matching analysis results are contingent on the completeness of the error model and an adequate exploration of the parameter phase-space. Given the system nonlinearities, as well as data and model uncertainties, it is highly unlikely that any single model simulation will actually closely replicate past ice sheet evolution. As such, a much more reasonable

objective is to produce an envelope of model reconstructions that convincingly bracket the true evolution, thus confidently bounding the trajectory of the actual system. The history-matching analysis produces bounds of the AIS evolution which improve our understanding of the sea-level budget during key periods of interest: LIG, Last Glacial Maximum (LGM), and Meltwater Pulses (MWP) (Fig. 3.2). Another product of the history-matching analysis is an ensemble of AIS reconstructions consistent with observational constraints which can be applied as orographic boundary conditions and/or freshwater forcing in general circulation models to better understand atmosphere-ocean circulation and CO<sub>2</sub> outgassing in the past.

To address these research objectives, proxy data are required to force and constrain paleo ice sheet and climate simulations. These efforts have increased our understanding of processes, triggers, and feedbacks of past climate change (Lemieux-Dudon et al., 2010; Shakun et al., 2012; Rasmussen et al., 2014). In this study an unprecedented quantity of data and computational resources are used to reconstruct the evolution of the AIS. The observational constraint data is from the new Antarctic Ice sheet Evolution database version 2 (AntICE2, Lecavalier et al., 2023). Moreover, the model uses a variety of ice core data including the EPICA Dome C (EDC) ice core water isotope record, a proxy for Antarctic air temperature (EPICA, 2004; Jouzel et al., 2007). Key periods of interest referred in the text are labeled alongside the EDC record in Fig. 3.2 to show the last interglacial and last glacial cycle.

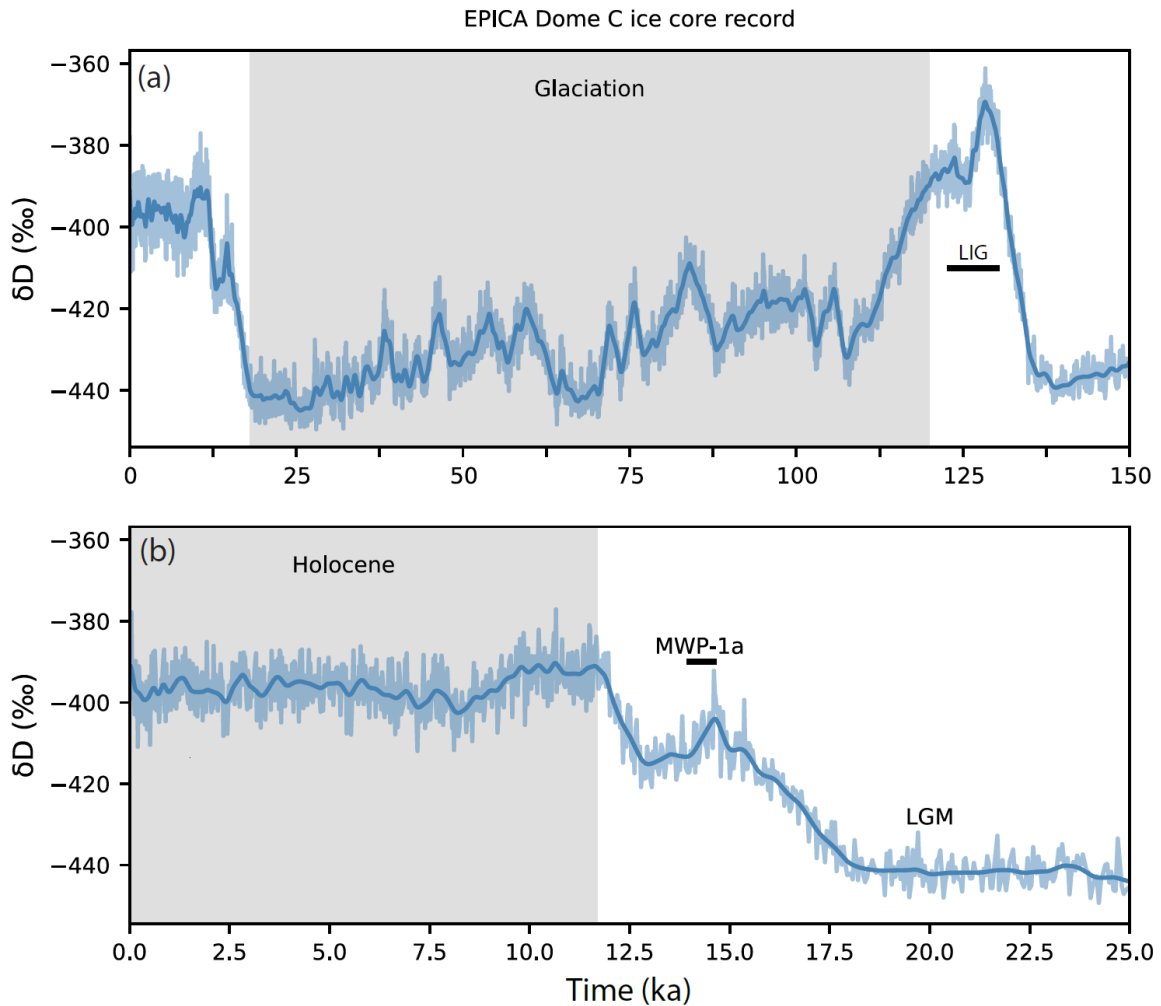


Figure 3.2: The EPICA Dome C deuterium record spanning (a) the time since the last interglacial (LIG), and b) the Last Glacial Maximum (LGM), post-LGM deglaciation (including Meltwater Pulse 1a, MWP1a) and the Holocene.

The LIG is a warm period (129-116 ka; MIS 5e) with global mean temperatures inferred to be 0.5 to 1.0 °C warmer than preindustrial (Turney et al., 2020; Fischer et al., 2018; Hoffman et al., 2017), with even warmer amplified polar temperatures (Otto-Bliesner et al., 2021; Yau et al., 2016). Moreover, inferred peak global mean ocean temperatures during the LIG were ~1 to 1.5 °C above preindustrial values (Shackleton et al., 2020). Given that the LIG interval offers a constraint on the sensitivity of glacial systems to past natural warm periods, this constraint can improve our ability to forecast

future projections considering various climate scenarios. The LIG had a higher orbital obliquity (tilt angle of Earth's axis) relative to the current interglacial which leads to a positive annual insolation anomaly at high latitudes. During this period of warm climate, global mean sea level (GMSL) was 6 to 9 m above present (Dutton and Lambeck, 2012; Kopp et al., 2009a; Dutton et al., 2015). There are several relative sea level (RSL) reconstructions during the LIG which exhibit variable spatio-temporal structure, with some suggesting multiple sea-level highstands (Stirling et al., 1998; Hearty et al., 2007; Blanchon et al., 2009; Thompson et al., 2011; Dutton et al., 2015). Moreover, a relatively minor thermosteric sea-level contribution of less than 1 mESL tapers down into MIS 5e (McKay et al., 2011; Vaughan et al., 2013; Shackleton et al., 2020a). This suggests significant sea-level contributions from various sectors of the Greenland Ice Sheet and AIS. Simulations of the Greenland Ice Sheet during the LIG have proposed a mass loss of 0.6 to 4.5 mESL (Tarasov and Peltier, 2003; Quiquet et al., 2013; Dahl-Jensen et al., 2013; Helsen et al., 2013; Stone et al., 2013). The sea-level budget suggests an AIS contribution between 1.5 and 7.4 mESL during the LIG (Dutton et al., 2015), commonly attributed to the collapse of the WAIS.

Unfortunately, high quality constraints on the forcing and configuration of the AIS during the LIG are lacking. Additionally, previous modelling studies insufficiently explored parametric uncertainties and uncertainties in boundary conditions to robustly constrain the Antarctic contribution to the LIG sea-level highstand (Albrecht et al., 2020b; DeConto and Pollard, 2016). There are little data constraining the chronology of AIS changes during the LIG. A recent study using octopus genome sequences suggested WAIS collapse during the LIG (Lau et al., 2023) but, so far, any direct evidence from proximal to

the WAIS is ambiguous or under debate. Furthermore, the susceptibility of the various AIS sectors to significant regional ice volume change is effectively set by sub ice-shelf marine temperatures and circulation, both of which are very poorly represented in glaciological models especially in paleo contexts. While the LIG offers insights into the sensitivity of the AIS to warmer conditions, the LGM provides a contrasting sensitivity to cold conditions.

The LGM is the period of maximum global grounded ice volume, approximately 26 to 19 ka BP (Clark et al., 2009). However, the major continental ice sheets reached their respective local maximum grounded glacial volumes at different times, termed the local LGM (Clark et al., 2009). The local LGM of the AIS is poorly constrained and model reconstructions propose a range of values, while few AIS glacial simulations consider the available paleo observational data (Albrecht et al., 2020b; Briggs et al., 2013). Observational constraints on the past geometry of the AIS suggest a maximal but regionally variable LGM configuration around 20 ka (Livingstone et al., 2012; The RAISED Consortium, 2014). During the global LGM, GMSL was 120 - 134 metres below PD primarily due to the growth of large northern hemisphere ice sheets (Milne et al., 2002; Peltier and Fairbanks, 2006; Clark et al., 2012; Austermann et al., 2013; Lambeck et al., 2014).

An outstanding issue regarding the LGM revolves around the question of missing ice to account for the GMSL low stand (Lambeck et al., 2014; Clark and Tarasov, 2014; Simms et al., 2019). Studies reconstructing LGM ice sheet volumes during the LGM demonstrate a large variance. Near-field geological and geomorphological constraints on past ice sheet geometry apparently conflict with the far-field RSL, as the former tend to favour smaller ice sheet volumes (Lambeck et al., 2014a; Clark and Tarasov, 2014; Simms

et al., 2019). This could reflect potential issues in the interpretation of the living depth ranges of ancient corals since they might not be analogous to their present-day counter parts (Hibbert et al., 2016). Additionally, there remain uncertainties in dynamic topography and GIA corrections (Austermann et al., 2013; Pan et al., 2022). More recently, in-situ radiocarbon ages from nunataks around the Ronne-Filchner ice-shelves have rejected a scenario that the LGM ice surface to the East of the Weddell Sea Embayment remained the same as present (Hillenbrand et al., 2014) but rather had thickened at the LGM by several hundreds of meters (Nichols et al., 2019), more consistent with an alternative LGM scenario of widespread grounded ice advance across the Weddell Sea shelf (Hillenbrand et al., 2014). The latest data on LGM ice surface height in the Weddell Sea sector could constrain numerical simulations and enable larger AIS LGM volume than previously thought. By performing a large-ensemble history matching of the AIS since the LIG, inferential bounds for the LGM volume of the AIS will quantify the viability of larger Antarctic ice volumes and potentially diminish the sea-level budget shortfall or emphasize outstanding issues in the interpretation of the far-field RSL records.

During the subsequent deglaciation, GMSL rose with several distinct and abrupt accelerations in sea-level rise. The most pronounced event is Melt Water Pulse 1a (MWP-1a) at ~14.6 ka (Bard et al., 1990). The far-field RSL records exhibit a 15.7 to 20.2 m sea-level change over 500 years for MWP-1a (Carlson and Clark, 2012; Lambeck et al., 2014; Lin et al., 2021). The Tahiti RSL record best constrains the magnitude and timing of MWP-1a and specifically suggests that it lasted for 300 years (14.6 to 14.3 ka) (Hanebuth et al., 2009; Deschamps et al., 2012). Models have often estimated MWP-1a sea-level contributions over a 500-year period rather than the shorter 300-year interval inferred by

the Tahiti RSL record (Deschamps et al., 2012). This implies that simulated MWP-1a sea-level contributions from individual ice sheets are likely overestimated. Historically, the MWP-1a budget shortfall had typically been attributed to an Antarctic contribution since it remains the least constrained of all the continental ice sheet volumes (Clark et al., 1996; Heroy and Anderson, 2007; Conway et al., 2007; Carlson and Clark, 2012). This was originally supported by geophysical GIA inversions of far-field RSL data which identified a significant Antarctic MWP-1a contribution (Bassett et al., 2005; Clark et al., 2002). More complete subsequent sea-level fingerprinting analyses indicate only a marginal contribution is required from the AIS to MWP-1a (Lin et al., 2021; Liu et al., 2016). This is more consistent with the observational record (The RAISED Consortium, 2014). A few AIS modelling studies that were constrained by near-field observations found that the AIS had contributed a relatively small volume to MWP-1a (Albrecht et al., 2020b), although these studies performed a limited exploration of parametric uncertainties using 4 ensemble parameters. Through a large-ensemble history-matching methodology, we aim to quantify the AIS contribution to MWP-1a given near-field observational constraints to better interpret past abrupt sea-level change.

To accurately quantify past AIS evolution, it is essential to address existing model limitations and uncertainties as part of a history-matching analysis. Model deficiencies are broadly categorized as follows: approximations of the relevant dynamical equations, missing physics, unresolved subgrid processes, limited model resolution, and boundary and initial condition uncertainties. The variation of model parameters is generally the primary (and to date usually the only) method to represent the bulk of the uncertainties associated with these model limitations. The model ensemble parameters form a potentially high-

dimensional parameter space from which a sample of each individual ensemble parameter, termed a parameter vector, represents one simulation. Previous modelling studies have generally conducted a limited exploration of the parameter space, generally using less than six ensemble parameters (Denton and Hughes, 2002; Huybrechts, 2002; Pollard and DeConto, 2009a; Golledge et al., 2014a; Pollard et al., 2016; DeConto and Pollard, 2016b), and even fewer studies have incorporated the available field observations to constrain their models (Golledge et al., 2012; Whitehouse et al., 2012a; Albrecht et al., 2020a, b). A large ensemble analysis exceeding thousands of simulations and supplemented by machine learning emulation has been effectively conducted to explore North American Quaternary ice sheets (Tarasov et al., 2012) but has yet to be applied to the AIS.

In this study, an approximate history matching of the glacial system model (GSM) is performed against the updated observational AntICE2 database. We present a large ensemble of simulations of the AIS evolution since the LIG with a high degree of confidence that it approximately brackets the true AIS history (subject to some explicit caveats presented in the conclusions). The resultant approximate history-matching analysis explores several fundamental questions about the AIS. The main research questions answered in this study are: the AIS sea-level contribution during the LIG at ca. 125 ka and MWP-1a around 14.6 ka; the temporal and volume changes of the AIS around the LGM (ca. 19-26 ka); and the influence of past uncertainties on the PD AIS. Moreover, bounds on the AIS geometry through time are presented. Antarctic GIA evolution and relative sea-level change are examined in an accompanying paper (Lecavalier et al., 2024).

## 3.2 Observational constraints – AntICEdat 2.0

The Antarctic Ice sheet Evolution observational constraint (AntICE) database version 2 (henceforth referred to as the AntICE2 database) is used to evaluate Antarctic model reconstructions. The AntICE2 database is the most extensive collection of Antarctic paleo-data available (Fig. S3.1). It was recently expanded, recalibrated, curated, and discussed in detail in Lecavalier et al. (2023). The updated database partially built on the work of Briggs and Tarasov (2013). AntICE2 contains PD and paleo ice sheet constraints. The PD ice sheet configuration is constrained by BedMachine version 2 (Morlighem et al., 2020a) and surface ice velocities (Mouginot et al., 2019). Additionally, there are PD observations which constrain contemporary and past AIS changes. These are ice core borehole temperature profiles and GPS uplift rate measurements. The remaining data consists of paleo-proxy observations of past AIS extent and thickness, and relative sea-level change. In addition to the PD state of the ice sheet, the AntICE2 database consists of 1023 high-quality observational data points that constrain past AIS evolution (Lecavalier et al., 2023). Fig. 3.1 and S3.1 illustrates the spatial distribution of the various data types and data identifiers. The first digit of a site ID or datapoint ID is associated to the data type (past ice thickness (paleoH) = 1, past ice extent (paleoExt) = 2, borehole temperature profile = 5, GPS uplift rate = 8, past RSL = 9), while the second digit is associated to the sector (Dronning Maud-Enderby Land = 1, Lambert-Amery = 2, Wilkes-Victoria Land = 3, Ross Sea = 4, Amundsen Sea and Bellingshausen Sea = 5, Antarctic Peninsula = 6, Weddell Sea = 7; sector boundaries are shown in Fig. 3.1). The available observational data enable the identification of a sub-ensemble of simulations that are not-ruled-out-yet (NROY) by the

data (which is not equivalent to “best-fitting simulations” typically presented in other studies, cf Tarasov and Goldstein, 2023).

The GSM history-matching analysis against the AntICE2 database is divided in two parts. Even though this study employs a joint/coupled ice sheet and GIA model, only data-model comparisons pertaining predominantly to ice sheet evolution are shown (past ice extent, past ice thickness, ice core borehole temperature, present-day geometry and velocity). Data-model comparisons to the GPS and RSL data are relegated to part 2, where the GIA relevant model results are presented in detail (Lecavalier et al., 2024).

### 3.3 Model description

The GSM has progressively undergone significant development to be suited for efficient millennial-scale AIS simulations. In this Section we present a short summary of the GSM and its various systems and components. The model descriptions, developments, verification and validation experiments are discussed in greater detail in Tarasov et al. (submitted). The more recent model developments incorporated in the calibration include: 1) hybrid ice physics; 2) subgrid grounding line parameterization; 3) revision to the basal drag scheme; 4) ice shelf hydro-fracturing and ice cliff failure; 4) ocean temperature dependent sub ice-shelf melt parameterization; 5) subgrid ice shelf pinning point scheme; 6) expanded climate forcing scenarios; 7) expanded Earth rheology models for GIA. A diagram summarizing the major components of the Glacial Systems Model is shown in Fig. S3.2.

The ice dynamics in the GSM is based on the dynamical core of the Penn State University ice sheet model (PSU-ISM; Pollard and DeConto, 2007, 2009). The PSU-ISM

dynamical core was extracted, rendered modular, and coupled into the GSM. It consists of hybrid ice physics representing shallow ice and shallow shelf/stream regimes (SIA-SSA). The non-linear viscous flow of the ice is represented by Glen's flow law with a temperature-dependent Arrhenius coefficient (Cuffey and Paterson, 2013). To capture transient or steady-state grounding line (GL) migration involves resolving the GL (<200m resolution) or employing an analytical constraint on ice flux through the GL (Pattyn et al., 2012a; Drouet et al., 2012). The GSM employs a subgrid GL flux parameterization based on boundary layer theory (Schoof, 2007). The parameterization relates the GL ice flux to longitudinal stress, sliding coefficient, and ice thickness. The subgrid interpolated depth-averaged ice velocity is imposed in the shelf flow equations.

The GL flux parameterization is defined for power law basal (Schoof, 2007) and Coulomb plastic rheologies (Tsai et al., 2015). The GSM is configured to work with either a power law or Coulomb plastic basal drag parameterization. The underlying uncertainties of the ice-bed interface are incorporated in the basal drag coefficient which depends on basal temperature, hydrology, basal roughness, and subglacial substrate, i.e., whether the ice is resting atop hard bedrock or unconsolidated sediment. The power law exponent is determined based on the substrate type since these basal environmental conditions yield different basal deformation. Alternatively, the basal drag over subglacial till can be represented using Coulomb plastic deformation (Tsai et al., 2015). The GSM basal drag component is broadly based on Pollard et al. (2015) and effective basal roughness derived from the basal topography subgrid standard deviation.

The basal drag coefficients can drastically impact ice sheet dynamics since they characterize ice deformation across the uncertain and poorly accessible basal environment.

The GSM contains a dual basal drag scheme where ice deforming across a hard bedrock is described with a quartic power-law that jointly represents regelation and enhanced creep flow. To facilitate both basal deformation and rugosity of the soft till, basal drag schemes that characterize the various regimes are used (Schoof, 2005; Gagliardini et al., 2007; Tsai et al., 2015; Brondex et al., 2017, 2019). It has been shown that a power-law with sufficiently high basal drag exponent can effectively represent a Coulomb-plastic scheme (Tulaczyk et al., 2000; Nowicki et al., 2013; Gillet-Chaulet et al., 2016; Joughin et al., 2019). Furthermore, Antarctic surface velocity assimilation studies concluded that till basal drag exponent exceeding five yields better agreement with observations (Joughin et al., 2019; Gillet-Chaulet et al., 2016). To represent all the compounding uncertainties affiliated with the till basal drag schemes, the till basal drag exponent in the GSM is chosen to be an ensemble parameter ranging between one and seven, which allows for a wide variety of till flow (Gillet-Chaulet et al., 2016; Nias et al., 2018; Brondex et al., 2019; Joughin et al., 2019). Moreover, the GSM includes a Coulomb plastic till deformation-based derivation of the subgrid GL flux scheme (Tsai et al., 2015; Brondex et al., 2017, 2019).

The PD AIS loses a considerable amount of ice via iceberg calving (Depoorter et al., 2013; Rignot et al., 2013). This is represented in the GSM using three calving components. The first component is based on crevasse propagation due to horizontal strain rate divergence and yields a calving rate (Winkelmann et al., 2011; Pollard and Deconto, 2012; Pattyn, 2017; Levermann et al., 2012). An additional parameterization contributes to the calving rate based on hydrofracturing, where surface meltwater or rain drains into crevasses. This additionally contributes to the strain rate divergence of the ice and helps propagate crevasses; thereby it increases the calving rate and can lead to potential ice shelf

collapse (Nick et al., 2010). The third form of calving in the GSM is a tidewater ice cliff failure scheme (Pollard et al., 2015), this arises wherever high ice cliffs experience an unbalanced horizontal stress gradient. Iceberg calving occurs when the overburden weight of the ice surpasses its yield strength, causing the ice cliff to collapse (Bassis and Walker, 2012; Bassis and Jacobs, 2013; Pollard et al., 2015). The GSM applies a conservative approach to the ice cliff failure which prevents a cascading failure across an entire basin in only one model time step. This provides an allowance for the ice dynamics to adjust the geometry which can stabilize and buttress ice. The latter two calving components represent the Marine Ice Cliff Instability (MICI) where the hydrofracturing collapses an ice shelf which produces an unstable ice cliff (Pollard et al., 2015).

The most poorly constrained components of the glacial system are the surface climate and ocean forcing since the LIG. Most commonly, the climate forcing in ice sheet simulations is based on a single source, whether parameterized in the model or obtained from a single climate model (Golledge et al., 2014b; Albrecht et al., 2020a; Pittard et al., 2022). This neglects spatial variability and climate uncertainties which should be represented by an envelope of viable climate scenarios based on various climate reconstructions and inferences. In these instances, the resultant ice sheet simulations generate an envelope of outcomes which are predominantly constrained by the chosen forcing. Therefore, three climate forcing schemes are blended in the GSM to best represent an envelope of viable climate realizations. The three sets of climate fields are merged using ensemble parameter weights that blend the temperature and precipitation fields. The glacial index scheme uses a glacial index derived from the EPICA Deuterium record ( $\delta D = \delta^2H$ ) (EPICA, 2004; Jouzel et al., 2007). The glacial index provides temporal evolution to

spatial reconstructions. The glacial index is effectively a temperature anomaly relative to present which is normalized such that the LGM is equal to one (e.g. Tarasov and Peltier, 2004; Niu et al., 2019). The first scheme simply perturbs the PD monthly climatology (RACMO 2.3p2; Melchior Van Wessem et al., 2018) by lapse rate for elevation and scale contributions from the glacial index value and atmospheric pCO<sub>2</sub>. The second scheme uses PD monthly climatology fields (Melchior Van Wessem et al., 2018) and Paleo-Modelling Intercomparison Project 3 (PMIP3) glacial climatology fields (Braconnot et al., 2012). The chosen LGM temperature and precipitation fields are the PMIP3 ensemble mean (excluding data-model misfit outlier) where temperature and precipitation empirical orthogonal functions (EOFs) are included to broaden the LGM degrees of freedom by capturing inter-model variance. The climate forcing is weighed back in time using the glacial index. The third scheme is based on a coupled geographically-resolved energy balance climate model driven by orbital forcing and greenhouse gases. The surface mass balance is then estimated using a positive degree day and positive temperature insolation surface melt scheme.

Table 3.1: Ensemble parameters in the Antarctic configuration of the Glacial Systems Model.

<b>Interface</b>	<b>Component</b>	<b>Parm #</b>	<b>Parm name</b>	<b>Definition</b>
Ice dynamic	Basal env	1	r <sub>mu</sub>	Soft bed basal sliding coef.
Ice dynamic	Basal env	2	f <sub>slid</sub>	Hard bed basal sliding coef.
Ice dynamic	Ice deformation	3	f <sub>nflow</sub>	Glenn flow law enhancement factor
Ice - ocean	Calving	4	F <sub>fc<sub>calvin</sub></sub>	Calving coef.
Ice - atmosphere	Calving	5	p <sub>factdwCrack</sub>	Geometric surface melt factor for hydrofracturing
Ice - ocean	Calving	6	C <sub>faceMelt</sub>	Ice shelf face melt coef.
Ice dynamic	Basal env	7	w <sub>GF1</sub>	Deep geothermal heat flux blending weight
Ice - atmosphere	Climate forcing	8	f <sub>nT<sub>dexp</sub></sub>	Phase exponent of temperature
Ice - atmosphere	Climate forcing	9	f <sub>npre</sub>	Glacial index scaling coef. for precipitation
Ice - ocean	SSM	10	f <sub>SSMdeep</sub>	Sub-shelf melt parameter
Ice - atmosphere	Climate forcing	11	f <sub>hPRE</sub>	Exponent for precipitation dependence on surface temperature change

Ice - atmosphere	Climate forcing	12	fnPdexp	Phase exponent of precipitation
Ice - atmosphere	Climate forcing	13	fnTdfscale	LGM scaling coefficient for glacial index
Ice - atmosphere	Climate forcing	14	rlapselgm	LGM temperature lapse rate
Ice - atmosphere	Climate forcing	15	fTweightPMIP	Mean PMIP3 temperature blending weight
Ice - atmosphere	Climate forcing	16	fPRE-weightPMIP	Mean PMIP3 precipitation blending weight
Ice - atmosphere	Climate forcing	17	fPEOF1	LGM precipitation EOF field
Ice - atmosphere	Climate forcing	18	fTEOF1	LGM temperature EOF field
Ice - atmosphere	Climate forcing	19	fTEOF2	LGM temperature EOF field
Ice - atmosphere	Climate forcing	20	fnTEBMscale	Energy balance model scaling
Ice - atmosphere	Climate forcing	21	fTweightEBM	Energy balance model temperature blending weight
Ice dynamic	Basal env	22	Fbedpow	Till fraction exponent for bed classification and basal drag adjustment due to fractional till
Ice - ocean	SSM	23	TregSSMCut0	Default ocean temperature bias corr.
Ice - ocean	SSM	24	TregSSMCut1	Ross sector ocean temperature bias corr.
Ice - ocean	SSM	25	TregSSMCut2	Amundsen sector ocean temperature bias corr.
Ice - ocean	SSM	26	TregSSMCut3	Ronne sector ocean temperature bias corr.
Ice - ocean	SSM	27	TregSSMCut4	Filchner sector ocean temperature bias corr.
Ice - ocean	SSM	28	TregSSMCut5	Amery sector ocean temperature bias corr.
Ice dynamic	Basal env	29	POWbtill	Soft bed power law exponent
Ice dynamic	Basal env	30	fSTDtill	Sub-grid roughness dependency parameter for soft bed sliding
Ice dynamic	Basal env	31	fSTDslid	Sub-grid roughness dependency parameter for hard bed sliding
Ice - ocean	SSM	32	rToceanPhase	Glacial index exponential phase factor for Tocean
Ice - ocean	SSM	33	rToceanWrm	Scaling factor for negative glacial index
Ice dynamic	Basal env	34	wtBedTill1	Basal till fraction blending weight
Ice dynamic	Basal env	35	rHhp0	Grounding line parametrization selection
Ice - solid Earth	GIA	36	earthLT	Lithosphere thickness
Ice - solid Earth	GIA	37	earthUV	Upper mantle viscosity
Ice - solid Earth	GIA	38	earthLV	Lower mantle viscosity

The other dominant method by which the PD AIS undergoes negative mass balance is through sub-ice-shelf melt (SSM) (Rignot et al., 2013; Depoorter et al., 2013; Liu et al., 2015). The GSM calculates sub-ice-shelf mass balance via an ocean temperature dependent

parameterization at the ice-ocean interface (Tarasov et al., submitted). This calculates mass balance at the ice front, beneath the ice shelves, and at the grounding line. The ocean temperature forcing is based on transient TraCE-21ka simulations (He, 2011) which are PD bias corrected by the Estimating the Circulation and Climate of the Ocean (ECCO) reanalysis ocean temperatures (Fukumori et al., 2018). For ocean forcing temperatures going back beyond 21 ka, the glacial index scheme is applied to the PD bias corrected TraCE-21ka predictions. The ocean temperature field is extrapolated beneath the ice shelves with a cut off defined by the minimum sill height when dealing with deeper continental shelves. As the changes in sub-ice shelf ocean temperature during the LIG have a critical impact on the resulting LIG sea-level high-stand and to avoid extrapolating TraCE ocean temperatures for warmer conditions, a separate ensemble parameter is introduced. Given the relationship between Antarctic  $\delta^2\text{H}$  and mean ocean temperature (Shackleton et al., 2021), this parameter ( $r\text{ToceanWrm}$ ) simply scales the glacial index derived atmospheric warming and adds it to the PD ocean temperature climatology. The deep-sea benthic foraminifera stack represents a proxy for deep ocean temperatures and global grounded ice sheet volume during the past (Lisiecki and Raymo, 2005). Within the GSM, the benthic stack and RSL observations drive the far-field global sea-level forcing (Lambeck et al., 2014) when performing joint ice sheet and GIA calculations. After a transient AIS simulation finishes, the AIS chronology is amalgamated into the GLAC3 global ice chronology to perform fully gravitationally self-consistent sea-level calculations.

One of the primary initialization conditions is the PD AIS geometry - bedrock topography, ice thickness, and ice surface elevation. The Antarctic GSM configuration uses the Antarctic BedMachine version 2 (Morlighem et al., 2020b). The poorly observed basal

environment remains a major source of uncertainty to ice sheet evolution. There are several key basal boundary conditions: the basal topography, geothermal heat flux, and subglacial substrate type (i.e. sediment distribution). The ice sheet is externally forced at its base by the geothermal heat flux. There are sparse measurements and inferences made at ice core sites that reached the bed (Pattyn, 2010). To partially account for uncertainties in the geothermal heat flux, an envelope of realizations is produced by blending two inferred geothermal heat flux fields with an ensemble parameter controlling the relative weighting ( $GHF = \text{weight} \cdot GHF1 + (1 - \text{weight}) \cdot GHF2$ ). The first geothermal heat flux field is based on the spectral analysis of airborne magnetic data (Martos et al., 2017), while the other complementary field is based on the thermoelastic properties of seismic data in the crust and upper mantle (An et al., 2015).

With respect to the substrate type distribution beneath the AIS, an elevation-based approach is used to infer the till fraction which effectively controls the basal drag. An elevation-based approach generally postulates that unconsolidated material, i.e. subglacial till and/or fossil marine sediments, prevails in areas below sea level, whereas hard bedrock dominates in areas above sea level (Studinger et al., 2001; Pollard and DeConto, 2009; Martin et al., 2011). The most probable regions with infill of marine sediments are those below sea level prior to large scale glaciation across Antarctica with a glacial isostatic equilibrated topography (e.g., Studinger et al., 2001). Over the course of many glacial cycles, the ice sheet transported detritus eroded from elevated bedrock down to submarine sectors. However, at present there are many features beneath the ice sheet that have survived successive glaciations, thus some features below sea level are presumed to be composed of hard bedrock, too (e.g., Bingham et al., 2017; Alley et al., 2021). The GSM

is geared to avoid potential overfitting issues to the PD geometry since our aim is to confidently bracket past and present transient changes. Hence, we avoid a basal drag inversion scheme to infer basal drag coefficients since many processes are integrated in these coefficients. Therefore, to maximize long term retrodictive capabilities, the GSM uses a fully unloaded glacial isostatic equilibrium sea-level threshold scheme. Additional considerations must be made to account for dynamic topography (Austermann et al., 2015, 2017). Uncertainties in dynamic topography on a 35 Myr timescale can significantly impact the range of viable sea-level elevation thresholds for determining probable subglacial sediment distributions. Regional elevation thresholds ranging between -300 to -100 m are justified given the spatial variability in dynamic topography and its uncertainties. The regional thresholds are selected based on first principles where deep subglacial basins/troughs, and regions of fast-flowing ice exceeding 400m/yr are properly delineated as being underlain by soft till. To properly classify crucial pinning points and local maxima in basal topography as highly consolidated sediment and hard bedrock, respectively, the thresholds are refined to properly delineate key pinning features. After the first few large ensemble results, persistent outstanding PD ice thickness misfits were related to the misattribution of the subglacial substrate type distribution. These persistent PD misfits were used to perform an update to the substrate distribution.

Pinning points that often manifest as ice rises and ice rumples can significantly affect GL dynamics (Favier et al., 2012, 2016; Berger et al., 2016; Wild et al., 2022). Ice shelves are buttressed by various topographical features; however, many crucial pinning points are inadequately resolved in model simulations due to horizontal resolution limitations. This is particularly relevant because small ice shelf pinning points can

significantly influence transient ice dynamics and grounding line migration (Favier et al., 2012, 2016). The GSM uses a subgrid statistical pinning point parametrization scheme to rectify these limitations. Unresolved subgrid features must be represented since they produce characteristic features at the PD AIS surface, such as ice ridges, rumples, and rises, that buttress the ice by generating substantial basal stresses that impact upstream flow. Since subgrid pinning points have been preserved through many consecutive glaciations, they must consist of hard bedrock. Therefore, to enhance the subgrid pinning points and prescribe their hard bed geomorphology, the till sediment fraction is exponentiated. Originally, the till fraction is upscaled from the Antarctic BedMachine native resolution of 500x500 m to 40x40 km. The upscaling emphasizes or de-emphasizes certain subgrid pinning point features depending on their scale, geometry, and how they are distributed against the model grid. An additional preprocessing step involves applying a subgrid pinning point enhancement exponent, that is varied regionally between 1 and 12 to enhance the till fraction value of subgrid features that are currently pinning ice across the present-day ice sheet.

The GSM is coupled to a glacial isostatic adjustment model of sea-level change. The GIA component is based on a spherically-symmetric viscoelastic gravitationally self-consistent Earth model which calculates GIA due to the redistribution of surface ice and ocean loads (Tarasov and Peltier, 2004). The Earth model rheology has a density structure based on the preliminary reference Earth model (PREM) (Dziewonski and Anderson, 1981) and an ensemble parameter controlled three-shell viscosity structure. The viscosity structure is defined by the depth of the lithosphere, upper and lower mantle viscosity. The GIA component shares many similarities to that used in Whitehouse et al., (2012b) for post-

process glaciological model runs. However, our GIA component is fully coupled to the ice sheet model and includes broader parametric uncertainties. The GIA calculations are computed every 100 simulation years. To minimize the considerable computational cost of solving for a complete gravitationally self-consistency solution coupled with an ice sheet model (Gomez et al., 2013), a linear geoidal approximation is used to account for the gravitational deflection of the sea surface. However, upon completing the full transient simulation, a gravitationally self-consistent solution is computed for determining RSL and vertical land motion.

The Antarctic GSM domain is polar stereographic with a horizontal model resolution of 40 by 40 km. The vertical model resolution has 10 layers unevenly spaced when dealing with ice dynamics, while the thermodynamic component uses 65 vertical layers. The ice dynamics temporal resolution is annual to subannual, it is adaptively reduced whenever ice dynamic calculations fail to converge. The Antarctic simulations were initialized at 205 ka using the PD AIS geometry. The englacial temperature was initialized using an analytical approximation of the EDC ice core borehole temperature profile. The basal ice is scaled to a temperature below the pressure melting point to stabilize the initial ice dynamics. The initial ice velocities are computed using a shallow ice approximation solution over a 1.5 kyr period to achieve a partial thermal equilibrated initialization prior to transient hybrid ice physics calculations. The model is spun up to the penultimate glacial maximum at ~140 ka to minimize any dependencies on the initialization. The Antarctic configuration of the GSM consists of 38 ensemble parameters which is the most comprehensive representation of uncertainties in the Antarctic glacial system of any study to date. A given simulation is defined by the chosen values of the ensemble

parameters, referred to as a parameter vector. Model parameters which exhibited no significant impact on a set of critical simulation output metrics for a diverse set of reference parameter vectors were dropped from being included as ensemble parameters. The ensemble parameters define the uncertainties in the climate forcing, mass balance, ice dynamics, and GIA (Table 3.1). The ensemble parameter history-matched distributions are shown in Figure S3.3 to S3.7.

## 3.4 Methodology

### 3.4.1 Scoring a reconstruction

For a given full transient simulation, the resulting AIS reconstruction is compared to the present-day ice sheet geometry on the simulated grid and several scores are produced. Using the Antarctic BedMachine version 2 dataset (Morlighem et al., 2020b), a thickness root-mean-square-error (RMSE) for the WAIS (which includes the Antarctic Peninsula Ice Sheet for simplicity), the East Antarctic Ice Sheet (EAIS), and floating ice are separately calculated considering uncertainties in the BedMachine inferences. Moreover, an RMSE is calculated for the PD ice shelf area and PD GL position score along 5 transects (shown in Fig. 3.1). Using the MeaSURES PD surface velocity dataset (Mouginot et al., 2019), a RMSE is calculated for surface velocities in the interior and margin of the ice sheet as defined by a 2500 m surface elevation threshold. The ice sheet simulation is then scored against the data described in AntICE2, with a predominant focus on tier-1 and 2 data. Tier-1 data is the highest quality data which has the greatest power to constrain the ice sheet and GIA model (e.g. exposure age data constraining LGM ice thickness), while tier-2 data

supplements tier-1 by providing more granular detail on past changes (e.g. exposure age data constraining the deglacial timing and thinning rate). Tier-3 data is excluded from the history-matching analysis since it correlates highly with the higher quality tier-1/2 data and is mostly used for visual comparison (Lecavalier et al., 2023).

The ice core borehole temperature profiles are scored by extracting a PD temperature profile from the reconstruction at each borehole site. A given borehole temperature can be broadly described by five observations: 1) depth of profile; 2) ice thickness at the borehole site; 3) near surface temperature, 4) englacial temperature, and 5) basal borehole temperature. Typically, there are ice thickness mismatches with the observed PD ice thickness, therefore, the simulated borehole temperature profile depth must be rescaled to match the observed borehole depths. The englacial temperature comparison was performed at the englacial temperature minima which aligned most closely with the GSM vertical grid ice temperature output. Subsequently, the RMSE from the near surface, englacial, and basal temperature is calculated to infer a score for a given borehole temperature profile. The square root of the sum of the squared residuals is calculated for all of the borehole temperature profiles to obtain a borehole temperature profile score for a given simulation.

Using the Antarctic BedMachine basal topography and the AntICE2 cosmogenic exposure ages, the paleoH data can be directly compared to an AIS simulation. The model produces a chronology for ice thickness changes across the entire Antarctic continent, and changes in ice thickness are extracted at each respective paleoH data site. For a given paleoH observation, the nearest simulated ice thickness value is identified in space and time. Considering model resolution limitations, the neighbouring spatial grid cells ( $\pm 40$

km) and time steps ( $\pm 500$  yrs) are accounted for in the paleoH scoring error model. The quadrature of all residuals based on the simulated and observed past ice thickness given uncertainties is calculated to generate a paleoH score. The paleoExt score is similarly calculated as in paleoH score, except it considers the timing that a grid cell is covered by ice, when that ice becomes ungrounded, and when the grid cell is deglaciated. This enables a broader comparison to the paleoExt database which includes proxy data for proximal to GL (PGL), sub-ice-shelf (SIS), and open marine conditions (OMC).

When a joint AIS and GIA simulation is completed, a full gravitationally self-consistent GIA simulation of sea-level change is performed over the last glacial cycle. This provides RSL and PD bedrock deformation rates which can be compared to the AntICE2 paleoRSL and GPS database. These results have consequences on AIS evolution and are integrated in the results presented in this study. Comprehensive data-model scoring details can be found in Tarasov et al. (in prep).

### 3.4.2 History-matching analysis

This study involves a history-matching analysis of a complex system against observational constraints of various data types to rule out simulations which are inconsistent with the data (Tarasov and Goldstein, 2021). History matching requires a full accounting of uncertainties, though the error models for quantifying these uncertainties can be specified much more freely than required for a full Bayesian Inference. A history-matching analysis and initial model calibration consist of ruling out model reconstructions which are unequivocally inconsistent with the observational constraints to produce a state-space estimation of the AIS which brackets the true ice sheet history. This yields a sub-ensemble

of model simulations that are not inconsistent with the data within a threshold, and thereby provide approximate bounds on the probable evolution of the AIS since the LIG.

Table 3.2: The full ensemble and sub-ensemble descriptions.

<b>Ensemble name</b>	<b># of members</b>	<b>Description</b>
ANtot	27,500	All previous AIS waves of ensembles leading up to final waves
AN	9,293	Full ensemble – final wave of ensembles
AN4sig	973	Sub-ensemble of AN sieved to be $4\sigma$ of AntICE2
AN3sig	82	Sub-ensemble of AN sieved to be $3\sigma$ of AntICE2, except $3.5\sigma$ of paleoExt data and floating ice RMSE, and $4\sigma$ of paleoRSL data

As part of this study, several large-ensemble data-constrained analyses were iteratively performed to evaluate the model’s ability to bracket AntICE2. A series of large-ensemble model simulations were performed iteratively, where a given iteration constitutes a wave of simulations consisting of anywhere between 500 to 2000+ simulations. GSM simulation output was applied towards supervised machine learning of Bayesian Artificial Neural Networks (BANNs) for Markov Chain Monte Carlo (MCMC) sampling to efficiently explore relevant portions of the parameter space. A flow chart is shown in Figure S3.8 that illustrates the history-matching algorithm and the waves of large-ensemble simulations conducted in this study. The appearance of significant data-model discrepancies that persist after converged history-matching waves is generally indicative of insufficient sampling of the model parameter space and/or underestimated uncertainties in data and/or model. Given our sampling approach and care in constraint database specification, this problem was indicative of insufficiently specified model structural uncertainty. When structural uncertainties were so large that they were deemed unacceptable, the model degrees of freedom were expanded, and refinements were made

to model components and inputs. This included revising the subglacial substrate type distribution, pinning point, and basal drag schemes, as well as broadening the geothermal heat flux ranges and defining distinct marine basins to parametrize regional ocean forcing. This necessitated a series of repeated history-matching cycles, culminating in ~40,000 AIS simulations over the last two glacial cycles. The methodological details of this work are specified in Tarasov et al. (in prep). In this study we present the most relevant final waves of ensembles which consist of 9,293 simulations. We will refer to these as the “full ensemble” (Table 3.2).

Our initial understanding of the glacial system is encapsulated within the ensemble parameter prior probability distribution ranges. The distributions are based on previous studies and expert judgement, and are initially kept wide as not to miss any potentially viable ensemble parameter combinations. The data-model comparison is characterized by the error model which combines all the errors from the observational and structural uncertainties. Observational data include data-system uncertainties that are composed of measured uncertainties and uncertainties affiliated with the indicative meaning of the proxy. Structural uncertainties are irreducible (in that they cannot be reduced by a more appropriate choice of model ensemble parameters) and are non-trivial to specify because they represent the model deficiencies with respect to reality. The structural uncertainty must be carefully defined and not underestimated since underestimated uncertainty will invalidate inferential bounds (Tarasov and Goldstein, 2021). Structural uncertainty will remain a major community challenge going forward but can be partially quantified using an internal and external discrepancy analysis.

Internal discrepancy is the component of structural uncertainty that can be quantified by numerical experiments. The internal discrepancy analysis conducted on the GSM involved assessing the impact of uncertainties from basal topography, geothermal heat flux, climate forcing, sea-level forcing, and initialization. This is evaluated by experimenting on a high variance set of reference parameter vectors using a wide variety of boundary conditions with noise super imposed to bound the response of the GSM to the uncertainties in these input boundary conditions and forcings. This defines a variance or covariance matrix of the internal discrepancy multivariate distribution. The internal discrepancy analysis yields an uncertainty contribution and bias contribution for each of the data type scores. The external discrepancy of the model cannot be inferred directly through model experimentation and is particularly challenging to define. The main structural uncertainties associated with the GSM are model approximations (e.g. hybrid physics, parameterizations), grid resolution and subgrid processes. As an initial estimate, the external discrepancy bias and uncertainties are assigned a large value so as to not underestimate structural error. The value is consequently refined/narrowed over successive ensemble iterations. The structural error assessment will be described in detail in a future publication.

The observational error model has a Gaussian distribution which assumes minimal spatiotemporal error correlation between observations. The AntICE2 observational dataset was curated for quality over quantity with the objective of also minimizing the multivariate structure of the error correlation. Some of the more significant error correlation is associated with the age calibration and corrections of the data (e.g.  $C^{14}$  and  $Be^{10}$  dating, reservoir corrections). Moreover, the data-model comparison needs to account for the

uncertainties affiliated with transposing the exact location of the data, i.e., the geographical location of a sample, onto the coarse model grid, such that a meaningful comparison can be made. This involves evaluating model output from neighbouring grid cells of the data's transposed location to ascertain whether any deficiency is a result of structural errors associated with resolution dependencies.

We address the fact that parameter space cannot be exhaustively evaluated (because it is computationally intractable) by performing a MCMC sampling of the parameter space to evaluate the most relevant portions of the parameter space which performs well against the AntICE2 database. Hundreds of nominally converged MCMC chains initiated from dispersed regions of the prior distribution were performed since the GSM is a non-linear system with high dimensionality, and a single chain could potentially only evaluate a local high scoring region in the parameter phase-space.

### 3.4.3 Ensembles and not-ruled-out-yet (NROY) sub-ensembles

Several large ensembles of simulations were conducted (~40,000 members), and their output was compared against observational constraints. The full ensemble of simulations is iteratively expanded through successive waves of new simulation ensembles. The latest ensemble waves are used to progressively rule out unlikely parameter vectors that significantly misfit the observations beyond chosen multiples of the total uncertainty (internal discrepancy, external discrepancy, and data uncertainty). This involves defining thresholds for each implausibility component. In the case of the Antarctic GSM configuration, the metrics of interest were chosen to be: present-day ice thickness root-

mean-square-error for WAIS, EAIS, and ice shelves; present-day ice shelf area score; present-day GL position score along 5 transects; ice core borehole temperature profile score; GPS uplift rate score; past ice thickness score; past ice extent score; and past relative sea level score. The data type implausibility thresholds are based on the Pukelsheim  $3\sigma$  rule which states that 89% of the probability density for any continuous distribution is within  $3\sigma$  of the mean. Directly applying a  $3\sigma$  cut-off yielded just a few plausible runs, therefore, a broadening to a  $4\sigma$  of the total uncertainty threshold for all data type scores was applied (AN4sig: N=973). A  $3\sigma$  of the total uncertainty threshold was then applied on all data type scores when sieving for best-fitting sub-ensembles but allowing past ice extent ( $3.5\sigma$ ), ice shelf RMSE ( $3.5\sigma$ ), and relative sea-level scores ( $4\sigma$ ) a less restricted threshold (AN3sig: N=82). This larger allowance with these three scores was justified given the model struggles to bracket a few observations in these data types, which previously resulted in ruling out nearly all simulations. Simulations beyond the implausibility thresholds for any data type (Table S3.1) were then ruled out as part of the history-matching analysis. The sub-ensemble not ruled out consists of simulations and parameter vectors which define the basis for BANN training and GSM emulation. MCMC sampling of the BANNs is used to propose new parameter vectors that make up subsequent waves of ensembles for history matching. Each successive wave of ensembles refines the regions of the parameter space that reasonably fit the observations. These ensembles are further used to revise the emulators for MCMC sampling. The iterative process of incorporating additional ensembles and subsequent history matching, defines and expands the NROY ensemble parameter space.

Initially the prior distributions for the ensemble parameters were chosen to be uniform, or quadratic functions favouring the top, bottom, or middle values of the parameter range. Wide prior distributions were determined with ranges physically motivated or taken from the literature. Secondary narrow prior distributions were defined to sample regions which are more commonly assigned in the literature. A dispersed random sampling of the ensemble parameters based on Latin Hypercube sampling was initially conducted using both wide and narrow prior distributions. The majority of these initial simulations performed quite poorly, with a limited few approaching the PD geometry. From these initial ensembles, few selected runs were chosen as initial reference simulations and parameter vectors. A sensitivity analysis was performed across the GSM ensemble parameters using this set of reference parameter vectors to evaluate the relative impact of various ensemble parameters.

The ensemble thus far was then sieved to isolate the best ~10% of simulations. The initial best fitting sub-ensemble was then used to fit beta distribution parameters for each ensemble parameter. From these beta distributions a series of parameter vectors was generated that ideally produced better performing AIS reconstructions. The full ensemble was carefully evaluated against the AntICE2 database and PD observations to verify that the observations are adequately bracketed within uncertainty. This initially led to a revision of ensemble parameters, model developments, and revisions to certain boundary conditions. Considering all the simulations leading up to the final waves of ensembles, all previous experimentation, sensitivity analyses, Latin Hypercube and beta fit sampling consisted of ~30,000 model simulations (total ensemble AN<sub>tot</sub> minus full ensemble AN). Unfortunately, when a model undergoes significant model development, much of the

previous model results lose relevance because they are based on a different model configuration which exhibits different behaviour than the latest version. Beyond those efforts, additional Latin Hypercube and beta distribution sampling was carried out before training BANNs and MCMC sampling. In Section 3.5 and 3.6, we present the latest waves of ensemble results based on the history-matching large-ensemble data-constrained analysis (full ensemble AN with  $N=9,293$ ; see Table 3.2).

### 3.5 NROY fits to data constraints

In this study we conducted  $\sim 40,000$  AIS reconstructions since the LIG and present the results from the final ensembles consisting of 9,293 reconstructions. The full ensemble is sieved such that runs must perform beyond a specified  $4\sigma/3\sigma$  threshold across all data type scores. The full ensemble is reduced to a sub-ensemble representing the best-fitting reconstructions when compared to the AntICE2 observational constraint database (termed the NROY AN3sig sub-ensemble consisting of 82 reconstructions). The NROY bounds presented in this study are those defined by the entire AntICE2 database, alternate bounds can be produced which target a subset of the AntICE2 database to explicitly focus on specific research objectives (e.g. targeting PD observations or jointly targeting paleoRSL and GPS data).

Here we present the data-model comparison of the full ensemble, NROY AN3sig sub-ensemble, and a high variance subset (HVSS) selection from AN3sig sub-ensemble, with the latter being integrated within the GLAC3 global ice sheet chronology for future analysis. A HVSS of 18 simulations was extracted from the NROY AN3sig sub-ensemble to showcase some glaciologically self-consistent simulation results. The HVSS simulations

are shown against the LIG and LGM metrics of interest in Figure S3.9. Three simulations are showcased from a HVSS from the NROY sub-ensemble, they collectively represent the nominally best-fitting simulations with varied LGM and LIG grounded ice volume anomalies. (RefSim1, RefSim2, RefSim3 being the reference simulations with run identification number nn61639, nn60138, nn61896, respectively). Summary of key data-model comparisons are shown in Fig. 3.3-3.8, while the remaining comparisons are found in Lecavalier et al., (2024). Data-model comparisons shown in this Section can illustrate instances where the full ensemble or NROY sub-ensemble fail to bracket the observations, however this does not necessarily imply the simulations are entirely inconsistent with the data given that these visual comparisons do not account for the structural uncertainties.

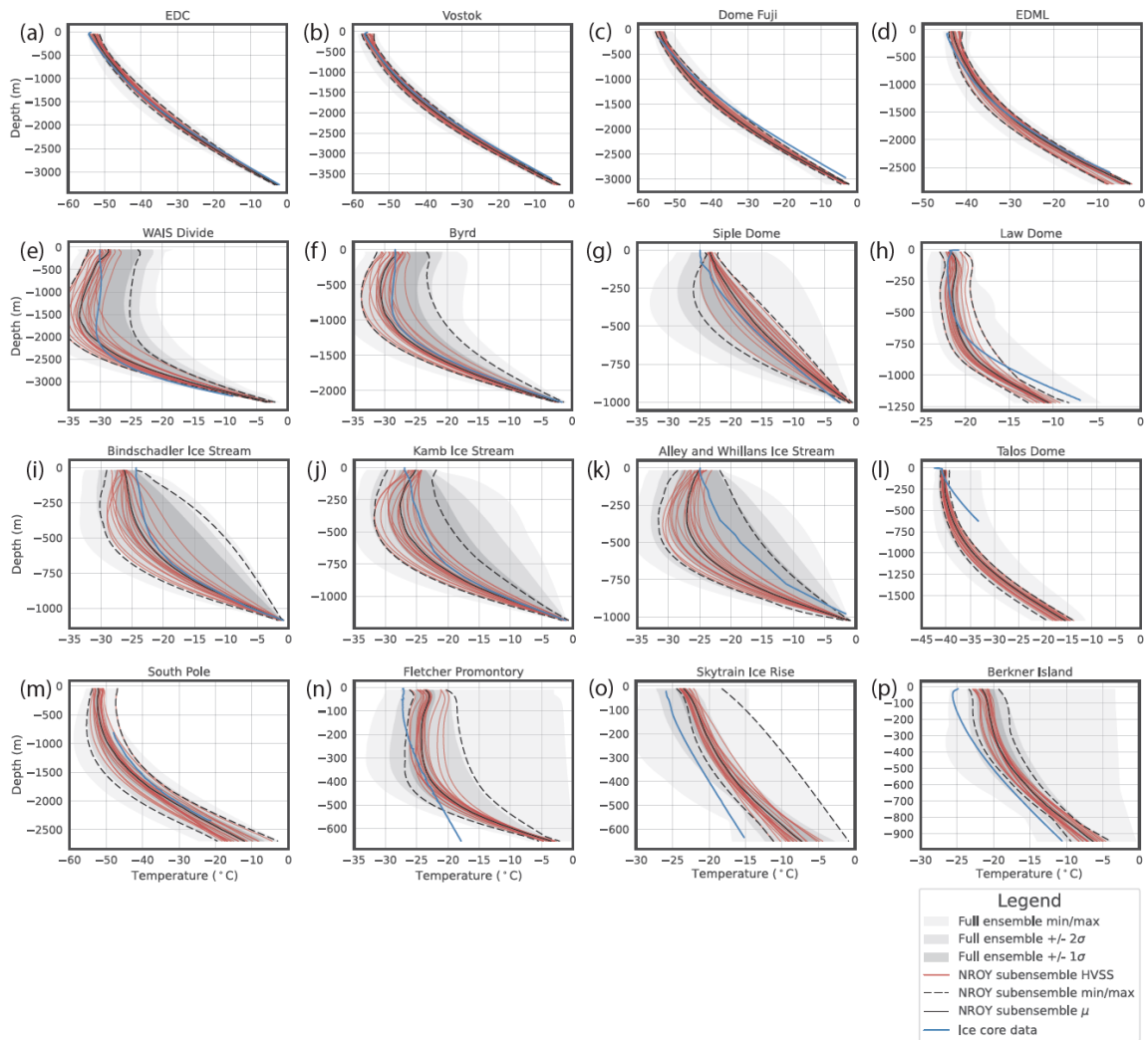


Figure 3.3: Ice core borehole temperature profile data-model comparison where the grey shading are the full ensemble statistics. The solid and dashed black lines are the mean and min/max ranges for the not-ruled-out-yet (NROY) best fitting AN3sig sub-ensemble. Simulations consisting of a high variance subset (HVSS) of the NROY AN3sig sub-ensemble are shown in red. Site a-h) and n-p) are high quality tier-1 temperature profiles; i-k) are tier-2 profiles since they correlate significantly with the Siple Dome profile; and l-m) are lower quality tier-3 profiles which only partially span the ice column. The  $2\sigma$  and  $1\sigma$  ranges are the nominal 95% and 68% ensemble intervals based on the equivalent Gaussian quantiles, respectively.

### 3.5.1 Ice core borehole temperature profiles

Many processes impact the temperature of Antarctic ice through time. Even though the temperature profiles were acquired in the late 20<sup>th</sup> and early 21<sup>st</sup> century, the temperature profiles contain a substantial amount of integrated information about past ice sheet changes, atmospheric forcings, the geothermal heat flux, and basal conditions, since temperatures propagate through the ice slowly (Cuffey and Paterson, 2010). Generally, the borehole temperature profiles can be categorized into two groups, 1) those whose near surface temperatures are clearly the coldest across the entire profile (e.g. EPICA Dome C), and 2) those whose englacial temperature remain as cold as near surface ice temperatures (e.g. WAIS Divide); generally, these two categories reflect low and high rates of snow accumulation, respectively, and corresponding rates of downward advection of cold surface ice. Broadly speaking, the full ensemble brackets the ice core borehole temperature profiles with NROY sub-ensemble simulations effectively capturing the observed data (Fig. 3.3). The model reproduces both categories of temperature profiles. The ensemble results can explain these types of profiles by identifying the dominant forcings and processes which impact the temperature profiles. Firstly, the geothermal heat flux warms from the base, a primary energy flux impacting basal ice temperatures and whether basal ice reaches the pressure melting point. Places with a warm bed tend to experience higher ice velocities, which draws in surrounding ice. Atmospheric temperatures and incoming radiation directly force the surface of the ice sheet where the firn layer buffers temperatures before conducting temperatures directly into the surface ice. Ice dynamics will advect ice which will perturb the temperature profile, this can displace colder ice from the surface deeper

into the ice column. When evaluating the best-fitting NROY sub-ensemble, the temperatures of type 1 profiles tend to remain clustered relatively close to the observations. Conversely, the NROY sub-ensemble results at type 2 profiles show significant variance. Simulations that produce cold englacial temperatures, achieve this because colder ice from higher in adjacent ice columns is advected in.

The simulated temperature profiles are scaled to the observed ice thickness at each borehole site to properly compare the simulation results to the observations. Notable outstanding misfits with respect to the full ensemble and NROY sub-ensemble remain. The interior of the EAIS has four high quality borehole temperature records (EDC, Vostok, Dome Fuji, and EPICA Dronning Maud Land; tier-1 sites Fig. 3.3a-d) and one lower quality partial borehole record at the South Pole (tier-3 site Fig. 3.3m). The NROY AN3sig sub-ensemble simulations capture the observations in the EAIS interior with a few exceptions. The AN3sig simulations in this region tend to favor warmer temperatures near the surface and cooler temperatures at depth with respect to the observations, suggesting issues with the implemented PD reanalysis climatology and/or PD elevation mismatches. The simulated temperatures near the bed narrowly capture the observed temperatures or are insufficiently warm, such as at Dome Fuji, where neither the full ensemble nor the NROY ensemble get warm enough at depth. These deficiencies are likely a product of the surface and basal thermal forcing. In previous ensemble waves attempts were made to address the cold basal ice issue with limited success. The geothermal heat flux is based on a magnetic (Martos et al., 2017) and seismic inferences (An et al., 2015), and a weight ranging between 0 and 1 is used to blend the fields. The degrees of freedom in the geothermal heat flux (GHF) boundary condition were expanded by allowing for a weight marginally greater than

1 to enable a broader range of GHF values. Albeit the extrapolated GHF fields remained bounded by their inferred uncertainties to prevent entirely unphysical values (An et al., 2015; Martos et al., 2017). Ultimately, this partially addressed basal misfits but at some sites the proposed range of GHF values between the magnetic and seismic inferences were too similar to sample a sufficiently wide range of potentially viable GHF (e.g. Dome Fuji). This points to the need for more complete inferences of the GHF field especially on the uncertainty side. Especially troubling are the lack of uncertainty range overlap for key GHF inference for some regions.

The borehole temperature profiles in the WAIS interior are clearly type-2 profiles with cold englacial temperatures (WAIS Divide, Byrd; tier-1 sites Fig. 3.3e-f). The full ensemble AN and NROY AN3sig sub-ensemble are capable of producing cold temperatures at depth, however, with a large variance of simulation outcomes with limited simulations reproducing the observed profile. At the WAIS Divide borehole site, the simulations tend to favor warmer basal temperatures with respect to the observations and again highlight potential limitations in simply blending two GHF inferences with similar inferences at a given site. This results in a narrowed exploration of GHF values at certain sites. Several borehole temperature profiles have been obtained from ice streams along the Siple Coast and from Siple Dome. These profiles correlate with each other. The Siple Dome borehole profile is the local high-quality tier-1 representative for the region (Fig. 3.3g), while the temperature profiles from the ice streams are relegated to tier-2 status (Fig. 3.3i-k). The full ensemble and NROY sub-ensemble both capture the ice stream temperature profiles. The full ensemble manages to bracket the Siple Dome temperature profile, however the NROY sub-ensemble remains too warm at the surface and base. This is likely

due to the misrepresentation of the local ice dome due to horizontal resolution limitations, deep geothermal heat flux uncertainties, or basal drag representation, where the model has the ability to better resolve the ice streams on the Siple Coast. Thus, the modelled ice thickness in this region is generally less than the PD ice thickness, which in turn leads to warmer surface temperatures overall.

There are several other temperature profiles near the PD GL, Law Dome, Talos Dome, Fletcher Promontory, Skytrain Ice Rise, and Berkner Island (Fig. 3.3h,l,n-p). These are all high-quality temperature profiles (tier-1), with the exception of the partial temperature profile at Talos Dome (tier-3). The borehole sites are located near or around topographic and basal features which are poorly resolved in the GSM. The full ensemble brackets the observed profiles at the Law Dome, Talos Dome, Skytrain Ice Rise, and Berkner Island, albeit not by the  $2\sigma$  range. The NROY sub-ensemble fails to bracket the observations at these borehole sites. Additionally, at the Fletcher Promontory, the simulated temperatures are far too warm at the base. Considering these borehole sites are surrounded by complex basal topography that is poorly resolved, the analysis prioritized to capture the temperature profiles in the interior of the ice sheet.

The GHF boundary condition inferences are spatial fields and a chosen weight parameter might improve the fit at one site but directly decrease the fit at another. Therefore, future work will focus on broadening the degrees of freedom in the GHF boundary conditions to enable some additional spatial variability beyond the GHF inferences to explore a broader range of potentially viable GHF values across borehole sites that are too warm or too cold with respect to the observations. Additionally, due to mismatches in PD ice thickness between observed and simulated at the borehole sites, this

directly leads to misfits in surface ice temperature which should be factored into the scoring calculations. Otherwise, one is double counting misfits across multiple data types (borehole temperatures and PD ice thickness).

### 3.5.2 Past ice extent

The full ensemble of simulations is compared to observations of past ice extent that are in the AntICE2 database. The data-model comparison is performed against tier-1 and 2 observations which includes proximal to the GL (PGL), sub-ice-shelf (SIS), open marine conditions (OMC) (ages shown in in Fig. S103 of Lecavalier et al., 2023). However, this discussion will focus on the data-model comparison with the highest quality data only (tier-1 data-model comparison; Fig. 3.4). Most past ice extent data are bracketed by the full ensemble and NROY sub-ensemble, with a few noted exceptions.

Additionally, the GSM simulations are compared to the reconstructions by The RAISED Consortium (2014), which was a large community effort with expert interpretations of a variety of data types. Even though there has been more observational data collected in the decade since the initial RAISED Consortium effort, the NROY AN3sig sub-ensemble ice extent statistics are compared to the reconstructions published in The RAISED Consortium (2014) in Fig. 3.5. The RAISED Consortium (2014) binned their ice extent contours to the nearest 20, 15, 10, or 5 ka intervals, which makes their speculated and inferred ice extent contours somewhat poorly defined from the raw observations.

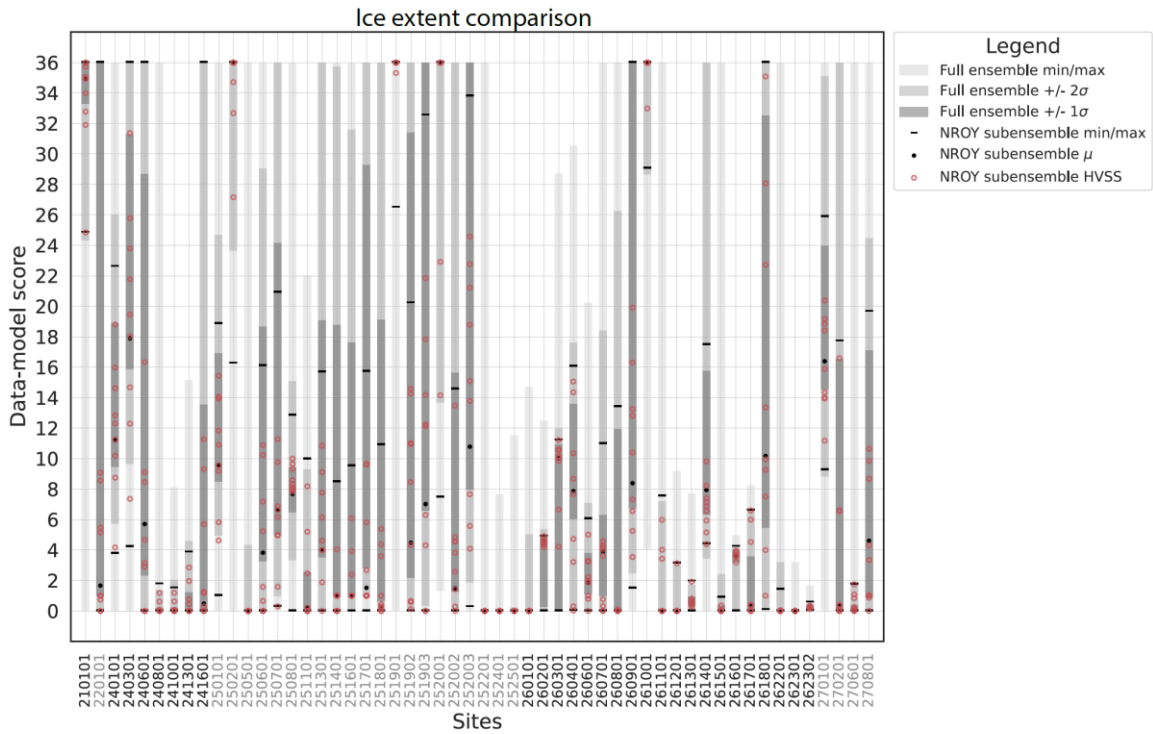


Figure 3.4: Past ice extent data-model comparison misfit scores for the highest quality tier-1 data in AntICE2. The grey shading represents the min/max,  $1\sigma$  and  $2\sigma$  ranges of the full ensemble. The solid black circles and lines are the mean and min/max ranges for the not-ruled-out-yet (NROY) AN3sig sub-ensemble. Simulations consisting of a high variance subset (HVSS) of the NROY AN3sig sub-ensemble are shown as red circles. The  $2\sigma$  and  $1\sigma$  ranges are the nominal 95% and 68% ensemble intervals based on the equivalent Gaussian quantiles, respectively. The AntICE2 paleoExt data ID are shown in Figure S3.1.

East Antarctica has limited ice extent observations with only three constraints for all of Dronning Maud – Enderby Land, Lambert – Amery, and Wilkes – Victoria Land sectors combined. In the Dronning Maud – Enderby Land sector, OMC near the PD ice shelf edge is dated at the turn of the Holocene (site 2101; 11.6 ka). The ice shelf in this area is buttressed by prominent pinning points which are poorly resolved by the GSM. The subgrid pinning point parametrization in the GSM attempts to represent these features using a statistical scheme but mismatches with the PD ice shelf extent remain a challenge as discussed in other modelling studies (e.g. Albrecht et al., 2020b). Moreover, the coarseness

of the model grid results in the marine core site being binned with the PD ice shelf grid cell. Without a proper accounting of structural error, model predictions at the marine core site might falsely never deglaciate since the site is so proximal to a relatively stable ice shelf. Figure 3.5 shows the data-model score for paleoExt tier-1 data in AntICE2. Regardless, the full ensemble is able to capture the OMC in the region but the NROY simulations struggle to deglaciate the site. The ranges of the NROY sub-ensemble  $2\sigma$  ice extent bracket the RAISED Consortium (2014) contours across East Antarctica (Fig. 3.5). This is unsurprising given how few marine core observations exist across the East Antarctic continental shelf.

In the Ross Sea sector, NROY simulations confidently bracket the paleoExt observations with the exception of two marine cores, which are closest to the continental shelf edge (2401, 2403). These PGL observations suggest an early retreat from the shelf edge, with the GL retreating over these sites around 27.5 to 23.9 ka. NROY simulations deglaciate later to remain consistent with the rest of the Ross Sea sector ice extent observations. The degrees of freedom in the ocean forcing can produce an initial partial retreat from the shelf edge since the full ensemble is able to capture these observations. However, a trade-off occurs between capturing these continental shelf edge observations versus the remaining Ross Sea deglacial ice extent observations. When comparing the ranges of the NROY sub-ensemble ice extent to ice extent reconstructed by the RAISED Consortium in the Ross Sea sector, the ice margin contours overlap broadly. The only exception is the western Ross GL at 15 ka where the simulated GL remains extended on the continental shelf for another few thousand years relative to the RAISED contours.

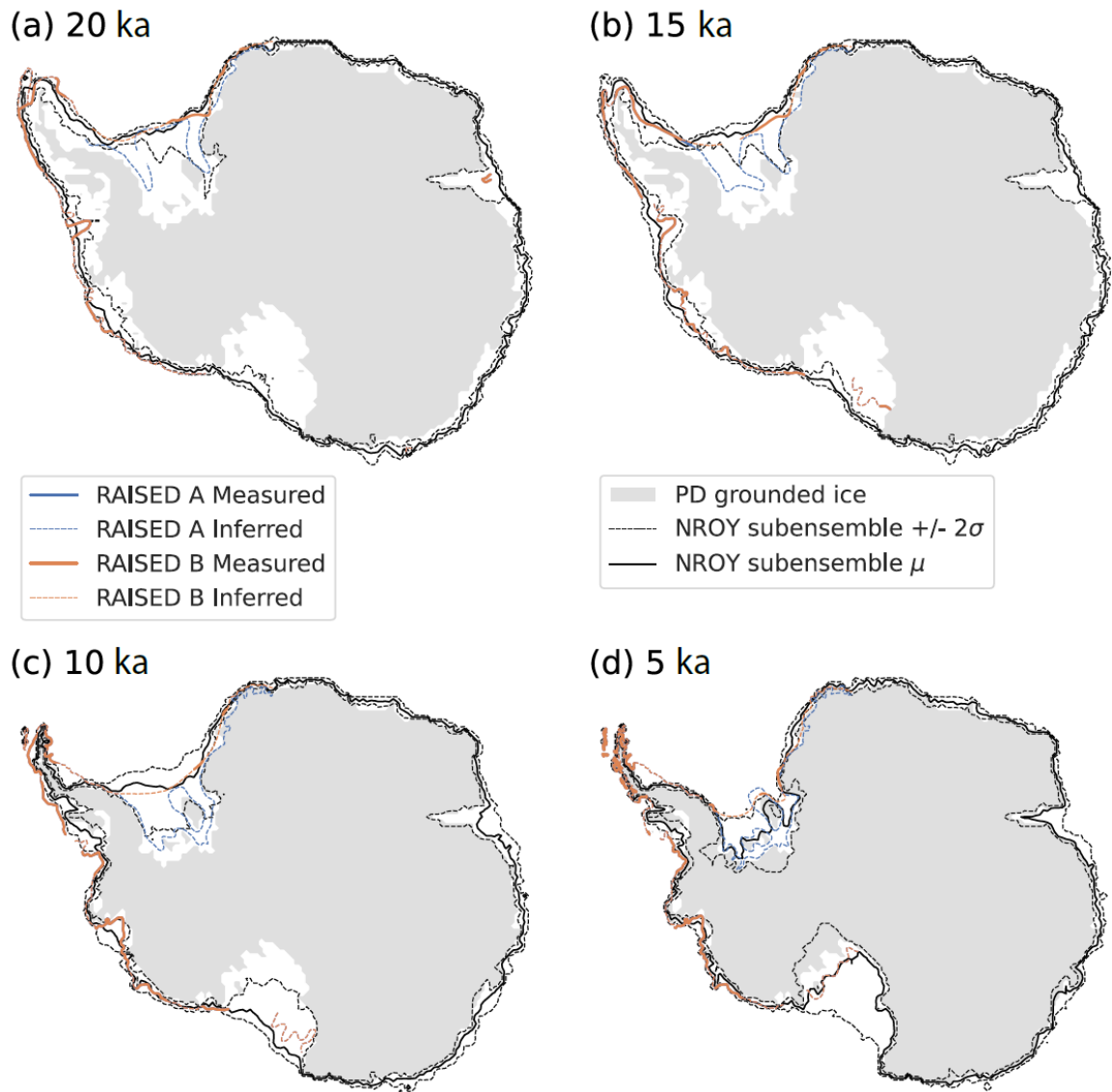


Figure 3.5: The mean and  $2\sigma$  range grounded ice extent for the not-ruled-out-yet (NROY) AN3sig sub-ensemble is shown by the black and dashed black line, respectively. It is compared against the RAISED consortium scenario A and B measured and inferred contours at a) 20 ka, b) 15 ka, c) 10 ka, and d) 5 ka. The  $2\sigma$  ranges are the nominal 95% ensemble intervals based on the equivalent Gaussian quantiles.

In the Amundsen Sea sector, the full ensemble and NROY sub-ensemble bracket the data quite well. However, areas with complex topography, small islands, and subgrid pinning points lead to misfits at core site 2502 for the NROY sub-ensemble. A series of marine sediment cores was taken along transects in several paleo-ice stream troughs,

starting at the continental shelf edge and heading toward the coast. OMC were first recorded at the shelf edge as early as 19 ka (2508). However, other marine sediment cores from the outer to inner continental shelf, document a persistent early Holocene GL retreat starting at 12.5 ka until 7.9 ka (2511, 2513, 2514, 2516-2520). The full ensemble manages to bracket all but one OMC observation at 2520. The NROY ensemble manages to fit the past GL extent data along the Pine Island-Thwaites paleo-ice stream trough. However, NROY simulations struggle with the OMC data (251901 and 252001). In the Amundsen Sea sector, a persistent issue was the simulated PD ice shelf extent which would remain marginally too advanced, and which included smaller ice shelves coalescing to larger ice shelves as a result of the coarseness of the model resolution. This is attributed to resolution limitations of the ice sheet grid and ocean forcing, as well as the presence of subgrid pinning points that buttress the ice in the region. When comparing the ranges of the NROY sub-ensemble ice extent to the reconstructions by the RAISED Consortium (2014), the best-fitting sub-ensemble brackets the measured and inferred contours confidently. This includes observations that place the GL near the PD GL at Pine Island Bay at ~10 ka (Hillenbrand et al., 2013).

The Antarctic Peninsula and Bellingshausen Sea sector is a topographically complex region with many features below the GSM resolution. During post-LGM deglaciation the GL retreated from 18.2 to 7.5 ka, albeit with significant regional variability. The full and NROY ensemble perform well in this sector given the aforementioned challenges, with a few exceptions. For example, there are two sites which are quite close to the coast which report a GL retreat at 9.2 ka (2609, 2610). While NROY simulations narrowly misfit 2609, not even the full ensemble brackets 2610. These sites are

close to the coast and the basal topography was unfavourably upscaled to produce a shallow marine environment and above sea-level topography, which resists deglaciation for the lack of direct ocean forcing. It is crucial to verify how the upscaling impacts the basal topography since some data-model comparison will be challenging without a proper accounting of such structural errors. The remaining reconstructions of post-LGM deglaciation based on marine sediment cores are captured by the full ensemble and NROY sub-ensemble, except site 2614 which is PGL at 11.8 ka. This core site is located near subgrid islands, potential pinning points, and PD grounded ice. These common challenges occur frequently with the ice extent observations and explain the remaining misfits. With regards to the RAISED Consortium (2014) ice extent reconstructions, the GL ranges of the NROY ensemble bracket the geologically-inferred GL in the Antarctic Peninsula-Bellingshausen Sea sector, except for the 10 ka measured contour. The AntICE2 data suggests the GL approached the PD coastline by 10 ka at many locations along the western Antarctic Peninsula shelf, as discussed above. This, however, conflicts directly with the RAISED Consortium (2014) inference at this time. Given the GSM is data-constrained by the AntICE2 database, a mismatch to the RAISED contour is expected.

The Weddell Sea sector has few observations of past ice extent. The only marine core site for the shelf in front of the Ronne Ice Shelf (2701) consists of observations of OMC as early as 5.5 ka. The site is relatively close to the intersection of the bedrock above sea-level and the PD Ronne Ice Shelf margin. Therefore, it is unsurprising that the NROY simulations struggle at the site since overly extended ice shelves are a persistent challenge across the full ensemble. The remaining tier-1 observations near the Filchner Ice Shelf front at core sites 2702, 2706, and 2708 document a PGL at 8.8, 1.9, and 12.9 ka BP, respectively

and are bracketed by the NROY sub-ensemble. The RAISED Consortium (2014) proposed two distinct scenarios in the Weddell Sea sector, with scenario B being more compatible with recently published exposure ages from around the Weddell Sea embayment that propose much thicker ice upstream of the Ronne-Filchner ice shelf (Nichols et al., 2019). The NROY sub-ensemble ice extent contours bracket the RAISED Consortium (2014) scenarios, particularly scenario B, for the Weddell Sea sector.

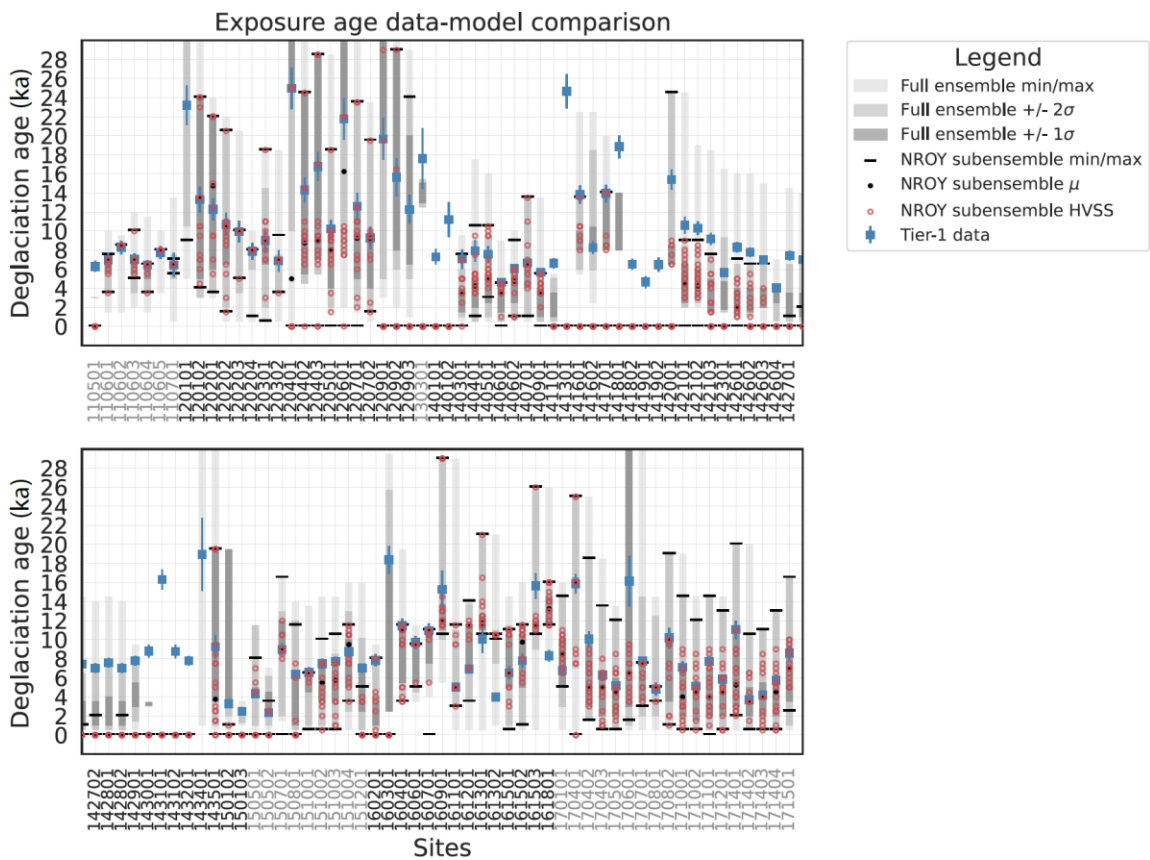


Figure 3.6: Past ice thickness data-model comparison for the highest quality tier-1 exposure data in AntICE2 at its respective elevation. The grey shading represents the min/max, 1 and 2 $\sigma$  ranges of the full ensemble. The solid black circles and lines are the mean and min/max ranges for the not-ruled-out-yet (NROY) AN3sig sub-ensemble. Simulations consisting of a high variance subset (HVSS) of the NROY AN3sig sub-ensemble are shown as red circles. The 2 $\sigma$  and 1 $\sigma$  ranges are the nominal 95% and 68% ensemble intervals based on the equivalent Gaussian quantiles, respectively. The AntICE2 paleoH data ID are shown in Figure S3.1.

At sites where the NROY sub-ensemble struggles to bracket the paleoExt observations (i.e. data-model score  $\neq 0$ ), the mismatch is usually caused by horizontal resolution limitations. There, poorly-resolved complex topography leads to mismatches between observed and simulated ice extent. This is particularly a challenge where subgrid pinning points can stabilize ice shelves or, similarly, where basal topography can stabilize the GL. This can impact the transient evolution of the ice margin which can yield persistent misfits that cannot be simply reconciled within the error model.

### 3.5.3 Past ice thickness

There are cosmogenic exposure ages taken from PD ice free regions scattered across Antarctica that constrain past ice thickness. The deglaciation age at its respective elevation (paleoH tier-1 data; Lecavalier et al., 2023), full ensemble (AN) statistics and NROY AN3sig sub-ensemble model prediction are shown in Fig. 3.6. The full ensemble and NROY sub-ensemble broadly bracket the paleoH observations with the exception of the Transantarctic Mountains. Instances, where the NROY simulations fail to capture the observations are discussed in the following.

Across East Antarctica, there are only two sites where the NROY sub-ensemble does not bracket the paleoH observations. A simulated deglaciation age of zero in Fig. 3.6 represents instances, where the site either never glaciated or never deglaciated. At both 1105 and 1303, the full ensemble manages to deglaciate the site but the NROY simulations fail to deglaciate those regions. This is a much broader issue in the Transantarctic Mountains, where 17 paleoH sites (e.g. 1401, 1402) are not bracketed by the NROY sub-ensemble. At some of these sites, the full ensemble does manage to capture the exposure

age constraints (e.g. 1416). However, the NROY simulations struggle to predict sufficient thinning in the Ross Sea sector. While in the Amundsen Sea, Antarctic Peninsula and Bellingshausen Sea, and Weddell Sea sectors, the NROY sub-ensemble brackets the paleoH data with the exception of five sites (1501, 1512, 1603, 1613, 1618). At these five sites, the full ensemble brackets the deglaciation ages, although the simulations responsible for this are ruled out, when considering the entire AntICE2 database.

Once more the NROY data-model misfits are attributed to horizontal resolution limitations. The 40 km by 40 km horizontal grid is based on upscaling the BedMachine version 2 subglacial topography, which effectively converts features such as nunataks and valleys that fall within a single grid cell into a uniform plateau. The fact that deep subglacial valleys are not resolved in topographically complex terrain has a considerable impact on ice dynamics. This manifests itself in entire regions excessively covered by thick ice because a region is simulated as a plateau and ice drainage is underestimated. This results in glaciated areas where ice is not sufficiently thinning, and these misfits persist until the end of the simulation period (Fig. 3.7). The best examples of these regions are the Transantarctic Mountains, the Antarctic Peninsula, and Bellingshausen Sea sector. Moreover, by improperly resolving deep subglacial valleys, misattributions of the basal environment are possible (i.e. ice atop soft sedimentary substrate instead of hard bedrock). The implementation of basal topography subgrid statistics in the basal drag scheme led to warm basal conditions in subgrid valley glaciers, thinning ice in regions that tended to be too thick with respect to PD. Although it did not fully rectify the excessive ice bias entirely, it improved the paleoH data-model misfits in certain regions. At some paleoH sites with excessive PD ice in the model, the AIS thins in accordance with data constraints during the

simulated post-LGM deglaciation. Thus, data-model misfits of PD ice thickness do not necessarily imply an equivalent bias in the past.

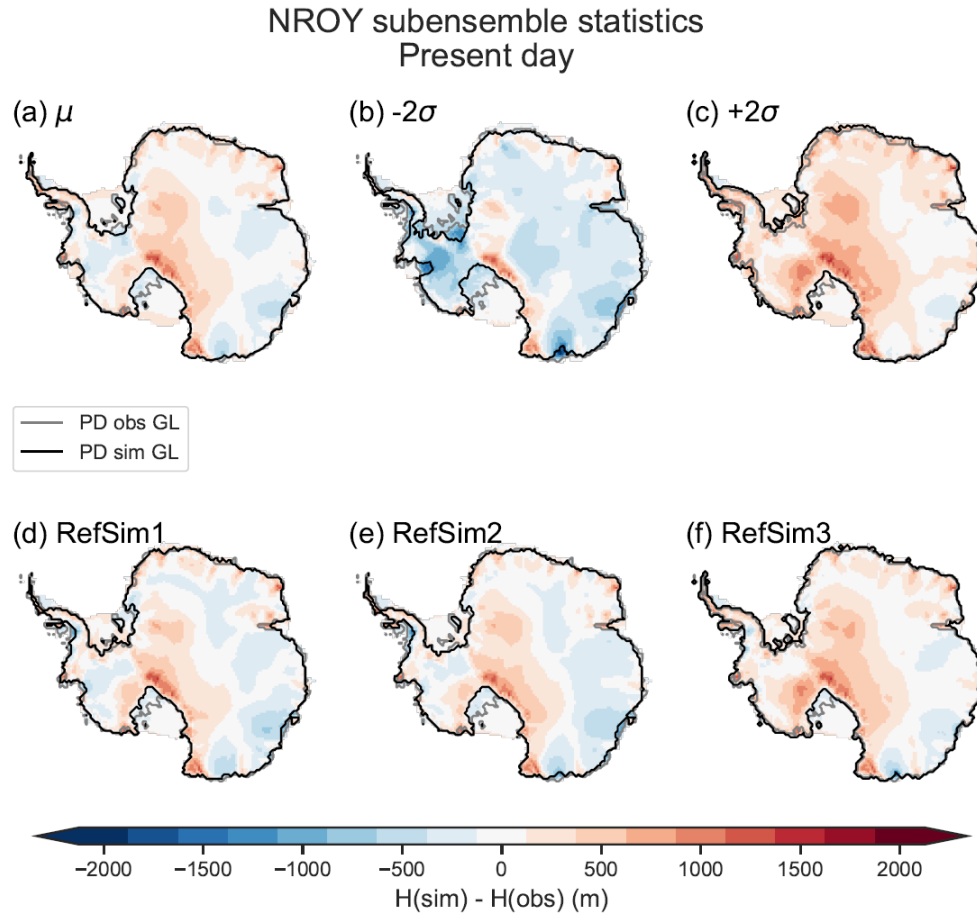


Figure 3.7: Present-day ice thickness data-model comparison for the not-ruled-out-yet (NROY) AN3sig sub-ensemble a) mean, b-c) minus and plus  $2\sigma$ , d-e) minus and plus  $2\sigma$ . Three glaciology self-consistent simulations chosen from a NROY high variance subset (HVSS): d) RefSim1; e) RefSim2; f) RefSim3. The  $2\sigma$  ranges are the nominal 95% ensemble intervals based on the equivalent Gaussian quantiles.

Mas E Braga et al. (2021) emphasized that the sampling position relative to the direction of ice flow can bias an exposure age. This can result in significant paleoH data-model misfits when dealing with continental-scale ice sheet models since they do not resolve a nunatak flank. The inability to resolve key features below the model horizontal grid size is a recurring theme to explain patterns of data-model misfits in this analysis.

However, resolving the nunatak flank is not within the scope of continental ice sheet models, even of those operating at a computationally costly high spatial resolution with a 10 km by 10 km grid. Only models that nest a domain around a nunatak or leverage adaptive grids may be capable of simulating the age offset caused by the sampling location relative to mean flow. However, continental-scale AIS models with a constant horizontal grid resolution can only hope to address this exposure age bias by broadening the error model and incorporating the mean flow direction relative to the sample position. It has also to be taken into account that the mean flow direction is generally not reported alongside exposure ages in the paleoH source studies.

### 3.5.4 Present day geometry

The PD geometry of the AIS is an essential boundary condition and a powerful constraint to evaluate model performance. Since we are dealing with imperfect models operating at a relatively coarse model resolution, one would naturally expect misfits with the PD observed geometry (Fig. 3.7). This constitutes the context by which to evaluate the performance of the GSM against PD observations, particularly when comparing the PD misfits reported in this section to those of other studies (Seroussi et al., 2019a), which solely focus on minimizing misfits to only the PD geometry using inverse approaches. As previously discussed, the aim is to avoid overfitting to the PD geometry by using an inversion scheme as to maximize the transient predictive capabilities of the model output.

The PD ice thickness misfit for the NROY AN3sig sub-ensemble is shown in Fig. 3.7. The NROY sub-ensemble mean is mostly  $\pm 250$  m of the observations (Fig. 3.7a), which is reasonable given the model resolution and the uncertainties attributed to PD

observed ice thickness across much of the ice sheet. The NROY simulations bracket the PD geometry observations as shown by the  $2\sigma$  range of the NROY sub-ensemble (Fig. 3.7b-c). The NROY sub-ensemble minimum should exclusively demonstrate negative values while the maximum should demonstrate the converse. This is mostly the case across the AIS with some prominent exceptions. There are a few sites where the ice is too thin across the entire NROY sub-ensemble (blue areas shown in Fig. 3.7g), such as the Larsen C Ice Shelf, parts of East Antarctica, and ice in the Siple Coast region near the Ross Ice Shelf GL. In the case of the latter, the transient behaviour of the GL in the Ross Sea sector requires that it captures past ice extent/thickness observations and the PD GL position and geometry. This trade-off results in NROY simulations with a retreated GL in the Ross Sea sector and yields floating ice near the Siple Coast and, in turn, thinner grounded ice in the region.

The most prominent ice thickness misfits are found in the Transantarctic Mountains (Fig. 3.7b). As discussed in Section 5.3, the model resolution produces a flat bedrock plateau beneath the ice over much of the region rather than peaks with deep valley trough. This impedes ice flow and promotes the formation of a broad ice dome. Moreover, the subglacial substrate type is based on subgrid information from the BedMachine subglacial topography but ultimately, a threshold designates the ice in the grid cell as being underlain by either being unconsolidated sediment/till or hard bed. This favours hard bedrock basal conditions across much of the Transantarctic Mountains which again impedes ice discharge. Both characteristics are static in time, which suggests that the excessive PD ice thickness in the Transantarctic Mountains likely persist throughout the simulations.

When considering for the relative size of an ice shelf, the most impactful mismatches with the PD ice shelf extent affect small ice shelves which are at or marginally below the model grid resolution. Given the resolution of the model, some poorly resolved simulated ice shelves, such as those in the Amundsen Sea embayment and along the Bellingshausen Sea coast, manage to persist and buttress grounded ice. This can manifest in PD GL mismatches which can in turn lead to ice thickness misfits for the ice shelves and upstream of the GL. This also can affect larger ice shelves, for which discrepancies between the simulated and observed PD GL can produce considerable ice thickness misfits.

### 3.5.5 Present day surface velocities

The ice flow velocity measurements for the AIS surface are based on observations taken from 2005 to 2017 (Mouginot et al., 2019). Slow-moving ice is usually present at inland locations while ice streams and ice shelves contain fast surface ice velocities. For this reason, the RMSEs are calculated for two regions delineated by a 2500 m elevation threshold. At locations in the AIS where the PD surface elevation is greater than the threshold usually slow-moving interior ice is present. Conversely, faster-moving marginal ice is expected for areas below the surface elevation threshold, which includes the aforementioned ice streams and ice shelves. The two regions exhibit different sensitivities to parameter changes (basal ice deformation ensemble parameters), and, therefore, the scores were divided in two. For example, the interior surface ice velocity score is more sensitive to hard bed parameter choices when compared to the margin surface ice velocity score, which is very sensitive to the ice-shelf front and grounding line locations.

NROY subensemble statistics  
Present day

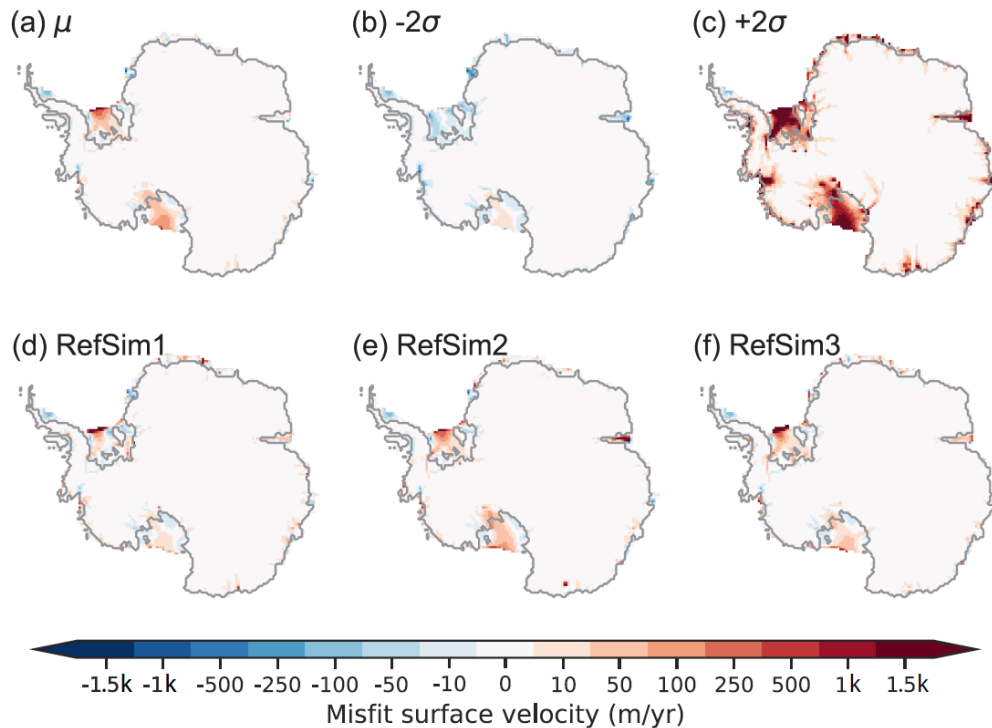


Figure 3.8: Present-day surface velocity model-data comparison for the not-ruled-out-yet (NROY) AN3sig sub-ensemble a) mean, b-c) minus and plus  $2\sigma$ , d-e) minus and plus  $2\sigma$ . Three glaciology self-consistent simulations chosen from a NROY high variance subset (HVSS): d) RefSim1; e) RefSim2; f) RefSim3. The  $2\sigma$  ranges are the nominal 95% ensemble intervals based on the equivalent Gaussian quantiles.

The spatial misfit with the PD surface ice velocities is shown in Fig. 3.8. The largest data-model misfits are observed at ice shelves and their tributaries. Any mismatch in PD ice shelf extent leads to large surface ice velocity discrepancies, such as in the Ross, Amundsen, and Weddell Sea sectors. If one excludes regions with mismatches in ice-shelf extent, the NROY simulations broadly bracket the observations within  $2\sigma$ , especially when considering uncertainties affiliated with the observations (upwards of 5 m/yr). The NROY sub-ensemble  $2\sigma$  surface velocities generally bracket the PD surface velocities of grounded ice (Fig. 3.8b-c). Any exceptions to this are associated with the ice shelves, specifically the

Larsen C Ice Shelf and the Ross Ice Shelf, where modeled surface flow speed is either too slow or too fast. This can likely be attributed to the tributary glaciers or ice streams feeding these ice shelves and the potential misattribution of subglacial substrate type at crucial grid cells.

## 3.6 Results

The AIS grounded ice volume for the full ensemble and progressively more data-constrained sub-ensembles are shown in Fig. 3.9. The full ensemble grounded ice volume demonstrates significant variance since the LIG. By history matching the ensemble, the grounded ice volume variance progressively decreases as the sieve becomes stricter from AN4sig to AN3sig. The  $2\sigma$  and  $1\sigma$  ensemble ranges shown across several figures (e.g. Fig. 3.9, Fig. 3.10, Table 3.3) are the nominal 95% and 68% ensemble intervals based on the equivalent Gaussian quantiles (2.275 - 97.725%, Gaussian  $2\sigma$  quantiles and 15.866 - 84.134% Gaussian  $1\sigma$  quantiles).

### 3.6.1 Last interglacial

The LIG changes in grounded ice volume for the full ensemble and NROY sub-ensemble are displayed in Figure 3.9. At the termination of the penultimate glacial period (starting at ~135 ka) the AIS retreated rapidly, with its GL reaching a position upstream of its PD position in several AIS sectors during the LIG and thus contributing significantly to the LIG sea-level highstand (Fig. 3.10). Relative to PD, the AIS had a minimum grounded ice volume between -2.9 to -13.8 mESL as per the NROY sub-ensemble (Table 3.3). The AN3sig sub-ensemble presents a variety of LIG grounded ice deficit scenarios with

ungrounding of marine-based sectors in the WAIS and/or EAIS. It should be noted that if marine-based grounded ice retreats, ocean water will flood the vacated submarine region. Therefore, only the ice above the point of flotation is initially responsible for sea-level rise as observed in far-field RSL records. In all instances, the AIS recovers relatively quickly after the LIG (~119 to 105 ka). Depending on the duration of the AIS LIG minima (Fig. 3.10d-f) and the Earth viscosity used in the GIA determination, it takes GIA rebound up to 10 kyr to raise the bed and displace ocean water away from Antarctic marine sectors. The viscous relaxation of the seafloor in formerly marine-based AIS sectors throughout the LIG therefore gradually increases the AIS contribution to far-field sea-level rise by displacing ocean water.

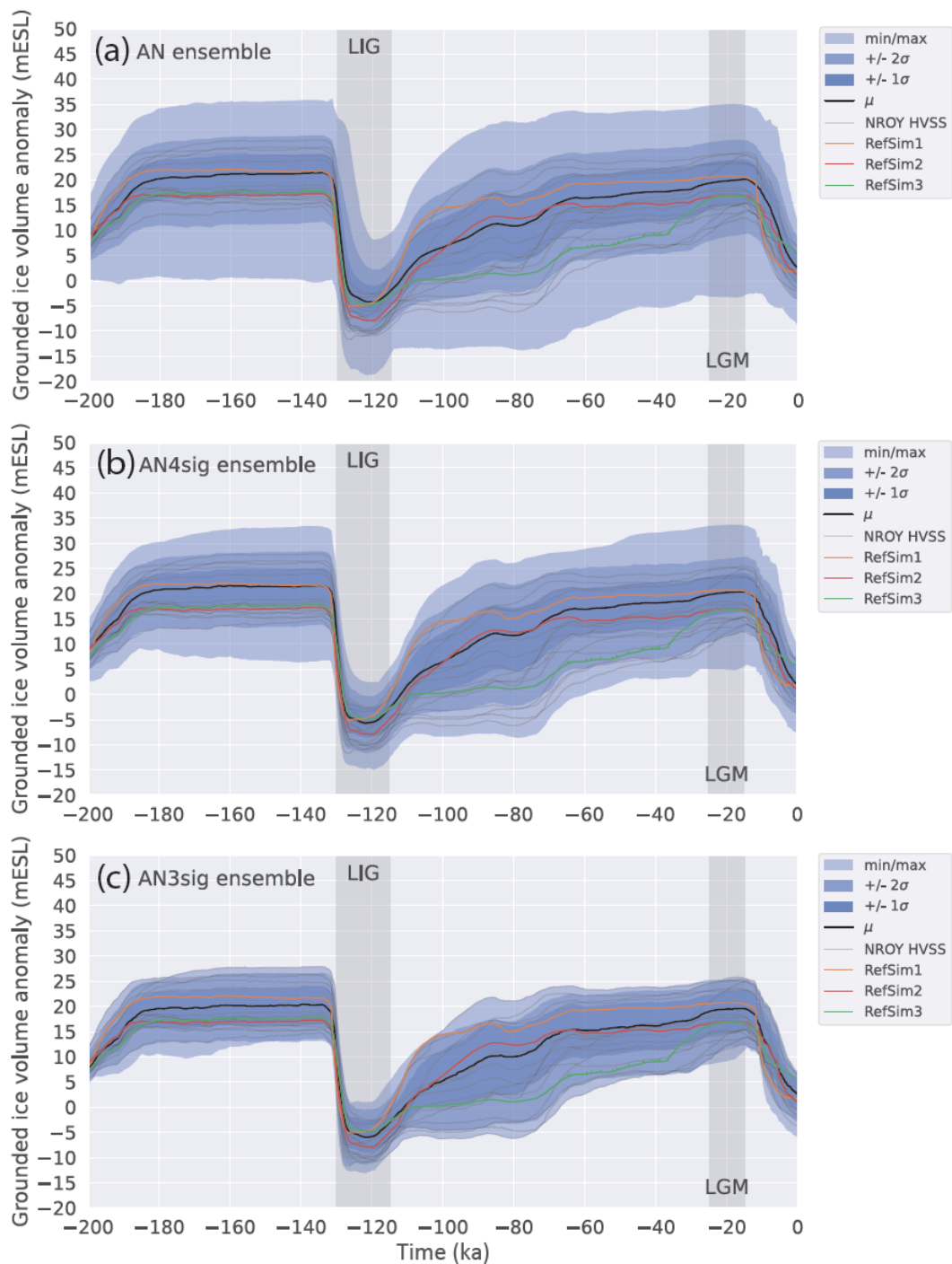


Figure 3.9: Antarctic grounded ice volume anomaly through time for the a) full ensemble AN; b) AN4sig sub-ensemble; and c) not-ruled-out-yet (NROY) AN3sig sub-ensemble. A high variance subset (HVSS) of the NROY AN3sig sub-ensemble is shown in grey which also includes three reference simulations (RefSim1, RefSim2, RefSim3) to illustrate glaciologically self-consistent simulation results. The  $2\sigma$  and  $1\sigma$  ranges are the nominal 95% and 68% ensemble intervals based on the equivalent Gaussian quantiles, respectively.

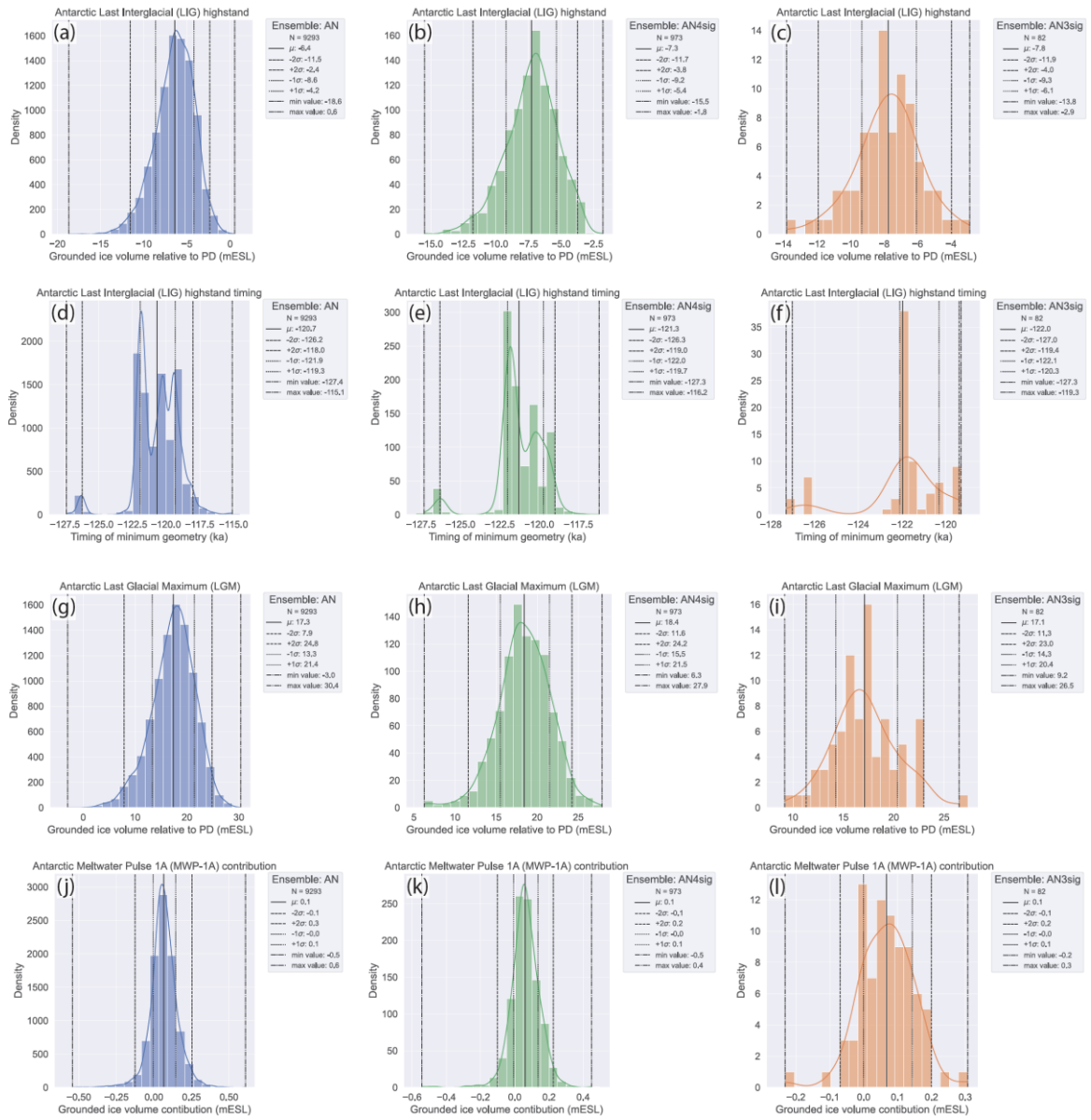


Figure 3.10: The histograms of key metrics are shown for the full ensemble (leftmost column), AN4sig sub-ensemble (middle column), and not-ruled-out-yet (NROY) AN3sig sub-ensemble (rightmost column). The key metrics of interest being a-c) the LIG Antarctic Ice Sheet (AIS) grounded ice volume deficit relative to present day (PD); d-f) the timing of the LIG grounded volume minimum; g-i) the LGM grounded volume excess relative to PD; and j-l) the AIS contribution to MWP-1a. The  $2\sigma$  and  $1\sigma$  ranges are the nominal 95% and 68% ensemble intervals based on the equivalent Gaussian quantiles, respectively.

Table 3.3: The contribution of the AIS to the LIG (deficit relative to present) and LGM (excess relative to present) for the full ensemble, AN4sig sub-ensemble, and not-ruled-out-yet (NROY) AN3sig sub-ensembles.

Last interglacial Antarctic Deficit (mESL)				
Ensemble name	Mean	1 $\sigma$ range	2 $\sigma$ range	Min to max
AN	6.4	4.2 to 8.6	2.4 to 11.5	0.6 to 18.6
AN4sig	7.3	5.4 to 9.2	3.8 to 11.7	1.8 to 15.5
AN3sig	7.8	6.1 to 9.3	4.0 to 11.9	2.9 to 13.8
Last Glacial Maximum Antarctic Excess (mESL)				
Ensemble name	Mean	1 $\sigma$ range	2 $\sigma$ range	Min to max
AN	17.3	13.3 to 21.4	7.9 to 24.8	-3.0 to 30.4
AN4sig	18.4	15.5 to 21.5	11.6 to 24.2	6.3 to 27.9
AN3sig	17.1	14.3 to 20.4	11.3 to 23.0	9.2 to 26.5

During the LIG sea-level highstand, GMSL has been inferred to be 1.2 to 11.3 meters above present-day (Kopp et al., 2009b; Dutton et al., 2015; Düsterhus et al., 2016; Rohling et al., 2019; Dyer et al., 2021). For this period, the steric contribution was estimated at 0.8 m (Shackleton et al., 2020b; Turney et al., 2020), the glaciers and ice caps contribution was  $0.32 \pm 0.08$  mESL (Marzeion et al., 2020). The Greenland Ice Sheet contribution to sea-level change during this period was constrained to 0.9 to 5.2 mESL (Tarasov et al., 2003; Dahl-Jensen et al., 2013; Goelzer et al., 2016; Yau et al., 2016; Bradley et al., 2018; Clark et al., 2020). A LIG sea-level highstand budget suggests a broad range of AIS contribution of -5.2 to 9.4 mESL. Therefore, the NROY AN3sig sub-ensemble AIS LIG ice deficit relative to present overlaps significantly with the LIG sea-level highstand budget. However, considering that only ice loss from above floatation immediately contributes to GMSL rise, the AIS LIG sea-level contribution is less than the value stated in Table 3.3. The max LIG AIS volume deficit from AN3sig is 13.8 mESL

(Fig. 3.10). Fig. 3.11 illustrates the source regions which underwent the greatest amount of ice loss during the LIG in the NROY AN3sig sub-ensemble. The bulk of the mass loss is across the West Antarctica, with a retreated GL with respect to PD in the Ross, Amundsen, Bellingshausen and Weddell Sea sectors. Many regions across the WAIS experience ice-sheet thinning in excess of 1000 m. The NROY sub-ensemble suggests that in limited areas the EAIS was a few hundred meters thinner relative to PD, particularly, in the Wilkes–Victoria Land sectors. With George V Land being the only EAIS sector with a GL significantly landward of the PD position. Three simulations from the HVSS are shown in Fig. 3.11d-f to illustrate the variety of configurations that yield distinct LIG configurations. Fig. 3.11d illustrates a partially collapsed WAIS (mainly ungrounding of the Thwaites Glacier and Siple Coast ice stream drainage basins) with a seaway connecting the Amundsen and Ross Sea sectors, while Fig. 3.11e shows a nearly full WAIS collapse with seaways connecting the Weddell, Bellingshausen, Amundsen, and Ross Sea sectors. Fig. 3.11f demonstrates a fully collapsed WAIS and a more pronounced retreated grounded ice margin in Victoria Land.

The main caveat to the LIG AIS simulation results remains the lack of observational constraints during the LIG. This translates to a large variance across the NROY sub-ensemble. Due to the lack of constraining records during this key period of interest, the model parameters (e.g.  $r_{\text{OceanWrm}}$ ) which induce the greatest sensitivity for the AIS LIG sea-level contribution ( $\text{volgLIGdiff}$ ) remain poorly constrained (Fig. S3.3 to S3.7, S3.10). Therefore, it is difficult to rule out either a low-end or a high-end AIS LIG sea-level contribution from the NROY sub-ensemble, given the considerable impact of poorly constrained parametric uncertainties and very limited data-constraints. Moreover, the

extent and strength of sub-surface ocean warming at the ice sheet margin during the LIG remains highly uncertain. This implies that no definitive statements can be made regarding the closure of the sea-level budget.

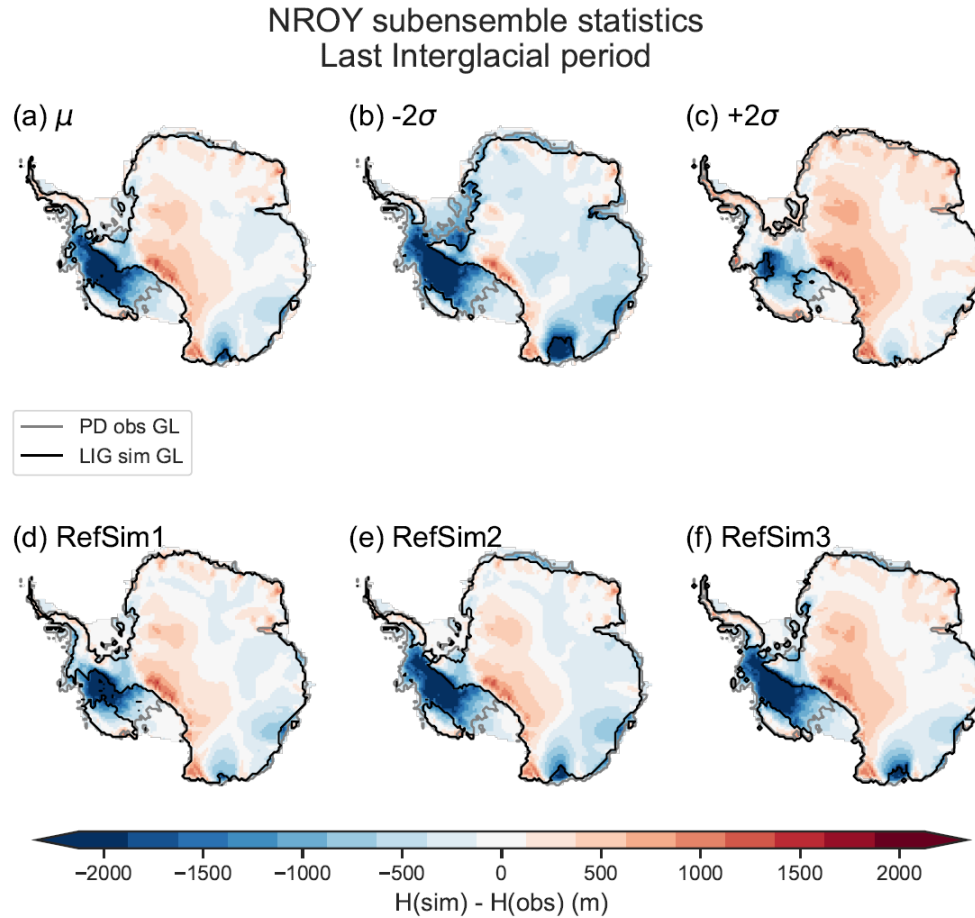


Figure 3.11: The not-ruled-out-yet (NROY) AN3sig sub-ensemble a) mean and b-c)  $2\sigma$  range are shown during the LIG. Three glaciology self-consistent simulations chosen from a NROY high variance subset (HVSS) are showcased: d) RefSim1; e) RefSim2; f) RefSim3. The  $2\sigma$  ranges are the nominal 95% ensemble intervals based on the equivalent Gaussian quantiles.

### 3.6.2 Last Glacial Maximum

During the LGM the NROY AN3sig sub-ensemble has min/max grounded ice volumes of 9.2 to 26.5 mESL excess relative to PD (Table 3.3). The AntICE2 database

mostly consists of data spanning the post-LGM deglaciation, and as the observations were more strictly imposed on the full ensemble during the history-matching analysis from  $4\sigma$  to  $3\sigma$  thresholds (Fig. 3.10 and Table S3.1), the overall variance decreased, and smaller LGM ice volumes were sieved out. In the AN4sig sub-ensemble, there remained AIS simulations with an LGM excess volume of 6.3 mESL; by imposing a  $3\sigma$  sieve threshold, the AN3sig sub-ensemble ruled out these smaller LGM excess volumes (Table 3.3).

Fig. 3.12 shows the NROY AN3sig sub-ensemble mean and  $2\sigma$  range LGM ice thickness difference relative to PD and LGM GL position which illustrates where more ice than at PD was stored during the LGM. Previous studies typically yielded smaller AIS LGM volumes between 5.9 to 14.1 mESL (e.g. Whitehouse et al., 2012a; Argus et al., 2014; Briggs et al., 2014; Albrecht et al., 2020b). But critically, none of these studies explicitly showed that their model had the degrees of freedom to produce larger AIS configurations that could then be tested for inconsistency with data constraints. The LGM GL advanced to the continental shelf edge in most sectors. Towards the interior of the EAIS, certain regions were thinner during the LGM relative to present due to reduced precipitation, which agrees with earlier modelling studies (Golledge et al., 2012). This is particularly illustrated when evaluating a single glaciologically self-consistent simulation (Fig. 3.12d-f). The sectors most responsible for the LGM ice excess are shown in Fig. 3.13. In these sectors the PD GL is very far away from the continental shelf edge but had advanced to near the shelf edge at the LGM. Thus, significantly more ice could be stored on the shelf there, hence the larger LGM contributions from the Ross and Weddell Sea sectors.

The main differentiating factors between the largest versus smallest LGM reconstructions in the NROY sub-ensemble (26.5 vs 9.2 mESL) are the GL extent on the

continental shelf, and the ice surface slope towards the interior. The latter can be attributed to parameter choices yielding a till basal drag and climate forcing conducive to thicker ice to build up and persist (fnpre, r1ps, POWbtill, rHhp0, earthUV in Fig. S3.10). Moreover, it requires basal conditions with basal stresses and drag that are capable of supporting thicker ice. The ice thickness on the shelf impedes the ability of the ice sheet interior from easily displacing ice to the margin where it is more susceptible to negative mass balance over the course of the glacial cycle.

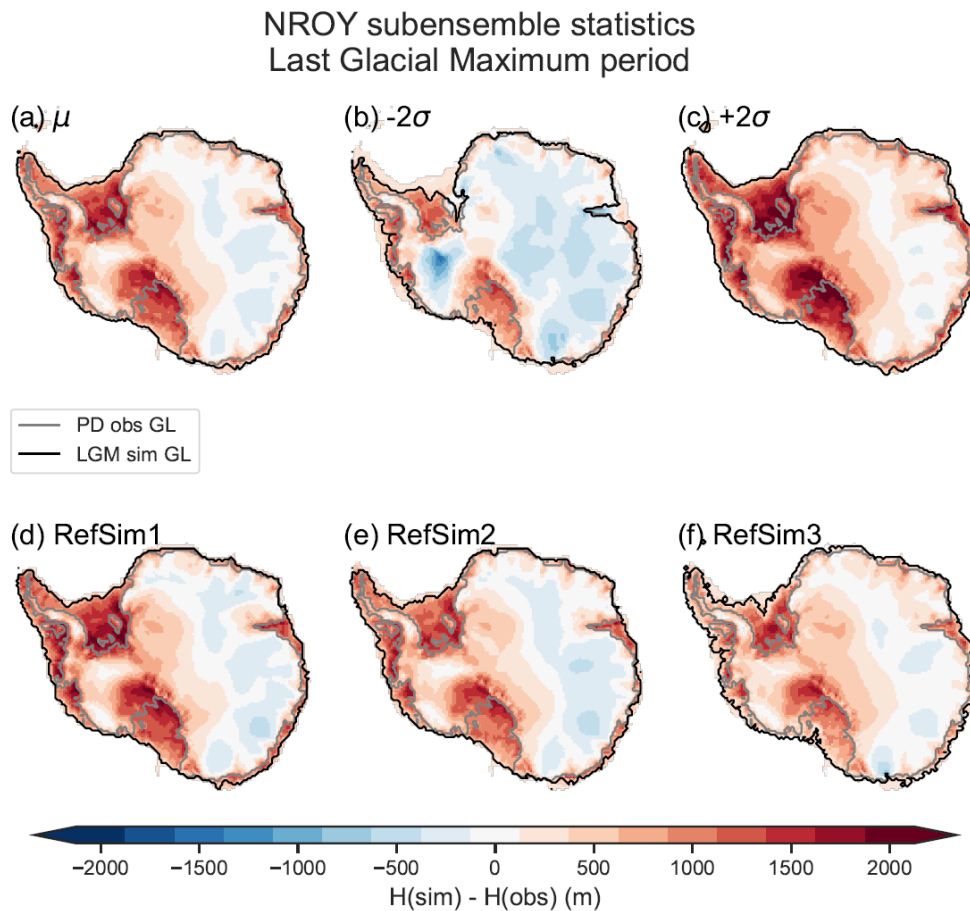


Figure 3.12: The not-ruled-out-yet (NROY) AN3sig sub-ensemble a) mean and b-c)  $2\sigma$  range are shown during the LGM. Three glaciology self-consistent simulations chosen from a NROY high variance subset (HVSS) are showcased: d) RefSim1; e) RefSim2; f) RefSim3. The  $2\sigma$  ranges are the nominal 95% ensemble intervals based on the equivalent Gaussian quantiles.

When the AIS reaches its LGM extent, it decreases the total area of the Earth's ocean by  $3.5 \times 10^{12} \text{ m}^2$  (1% decrease). This represents a relatively modest decrease in the global ocean area. However, for a present-day ocean area of  $3.618 \times 10^{14} \text{ m}^2$ , it marginally decreases the water equivalent ice volume needed to produce a 1 m GMSL change. When discussing ice sheet sea-level contributions, it is important to explicitly state whether it is in relation to a dynamically changing ocean area or entirely referenced to the PD ocean area. The GIA model accounts for migrating shorelines within the ice sheet grid but the mESL estimates presented in this study are derived on the PD ocean surface area.

The larger AIS geometries in the NROY sub-ensemble can considerably contribute towards closing the sea-level budget and resolving the missing ice problem. Albeit some of the LGM excess ice is grounded below sea-level which partially negates the Antarctic contribution to a sea-level lowstand during the LGM. Moreover, to conclusively quantify the contribution of the AIS to the missing ice problem based on far-field RSL observations, additional GIA simulations are required using a variety of global ice chronologies and Earth models. The accompanying paper, Lecavalier et al., (In prep), discusses these research objectives and future modelling is planned to quantify the AIS sea-level contribution to past global sea-level change.

### 3.6.3 Deglaciation

The post-LGM deglaciation represents the period during which the model is heavily data-constrained by AntICE2. The NROY AN3sig sub-ensemble simulations illustrate the timing of the local LGM at 15.7 ka (Fig. 3.13). The deglaciation begins gradually and peak rates of mass loss are not simulated until 10.7 ka. In all instances, the full ensemble and

NROY AN3sig sub-ensemble simulations all provide a very minor AIS contribution to MWP1a from -0.5 to 0.6 mESL and -0.2 to 0.3 mESL, respectively (minimum and maximum contributions). The history matched NROY simulations provide a considerable constraint on the AIS contribution to MWP1a. When compared to the source region contributions as inferred by far-field RSL observations (0 to 5.9 mESL from the AIS; Lin et al. (2021)), it illustrates that near-field observations rule out a significant MWP1a sea-level contribution from Antarctica. Moreover, the rate of mass loss from the AIS over the MWP1a interval is not anomalous to the background rate of mass loss during the deglaciation. This implies the AIS did not contribute towards an acceleration in sea-level rise during the MWP1a period. GIA model simulations focused on far-field RSL observations and AIS simulations data-constrained by near-field observations (AntICE2) provide a consistent and conclusive result that MWP1a was clearly not sourced from the AIS.

Over the course of the deglaciation, the AIS retreated most dramatically from 12 to 4 ka (Fig. 3.13, S3.11 and S3.12). This includes major grounding line retreat across the continental shelf occurring during the early to middle Holocene. Many sectors reach their present-day extents around ~4 ka. In particular based on the NROY AN3sig sub-ensemble mean, the GL in the the Ross Sea sector had retreated upstream of the PD ice-shelf front by 6 ka to reach the PD GL by 4 ka. In the Amundsen sector, the GL retreated in a series of steps across the continental shelf over the course of the Holocene with the most prominent retreats occurring between 12-10 ka and 6-4 ka. Around the Antarctic Peninsula and on the Bellingshausen Sea shelf, the majority of marine-based ice retreat occurred from 16-10 ka, when the PD ice margin is reached at many locations. In the Weddell Sea embayment,

grounded ice reached the PD Ronne-Filchner ice shelf fronts around 10 ka, and the PD GL position was reached by 4 ka. The Dronning Maud Land and Victoria Land sectors are characterized today by narrow continental shelves where grounded ice reached the PD GL between 6-4 ka. In Prydz Bay (= Amery Ice Shelf sector) grounded ice was present at the continental shelf edge until 12 ka, when it started to retreat to reach the PD GL by 6-4 ka. The timeline described above is based on the NROY AN3sig sub-ensemble mean chronology, and a wide variety of chronologies are described within the NROY sub-ensemble, enabling a multitude of distinct timing and regional retreat scenarios from a more modest LGM extent.

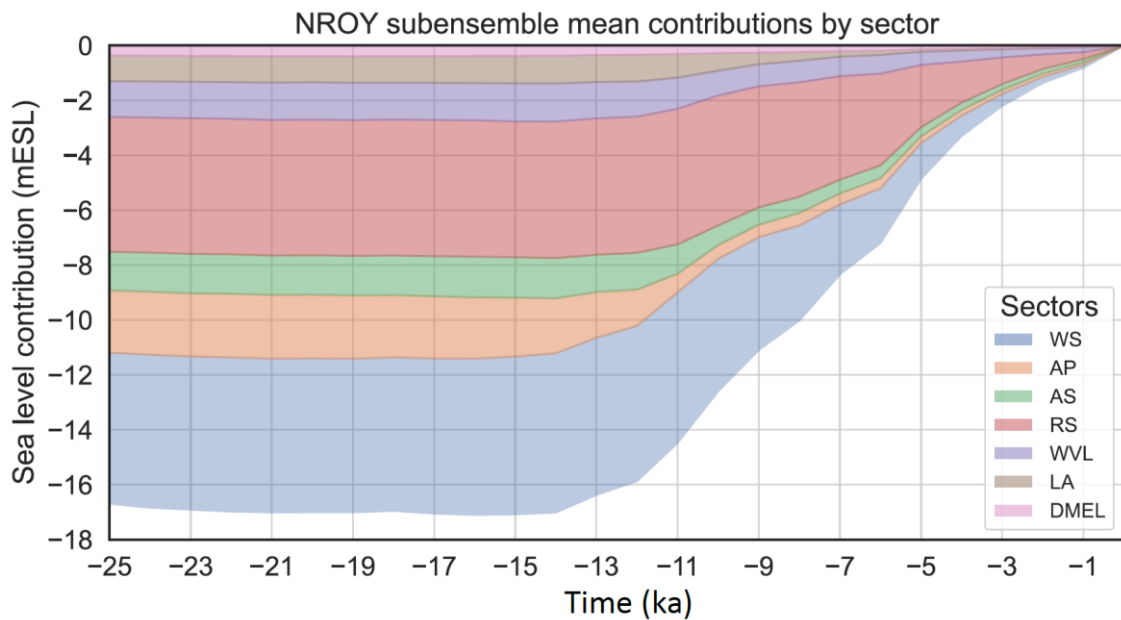


Figure 3.13: AIS grounded ice volume equivalent sea-level contributions since the LGM for the Weddell Sea (WS), Antarctic Peninsula (AP), Amundsen Sea (AS), Ross Sea (RS), Wilkes – Victoria Land (WVL), Lambert – Amery (LA), Dronning Maud-Enderby Land (DMEL) as defined in Fig. 3.1 during the deglaciation based on the NROY AN3sig sub-ensemble mean.

Over the Holocene, a few studies have discussed the viability of a GL retreat landward of its PD position. This was reported in the eastern Ross Sea, where

subglacial sediment cores taken across the Siple Coast retrieved sediments which had carbon ages dating back to approximately the LGM (>20 ka), implying a retreated GL during the early Holocene, as the inferred ages were discounted as the actual timing of GL retreat (Kingslake et al., 2018). Other studies have indicated that these ages are inconsistent with other observations and offered alternative interpretations, suggesting maximum GL retreat during the middle or late Holocene (Neuhaus et al., 2021; Venturelli et al., 2023). Due to their ambiguous interpretation, these data were not included in the AntICE2 database as constraints. Some of the best-fitting AN3sig sub-ensemble simulations tend to yield a retreated GL position with respect to PD in the Ross Sea sector during the late Holocene, but these simulations do not reconstruct GL re-advance in time to match the PD GL position. The climate forcing and its degrees of freedom were unable to yield a sufficient GL retreat in the Ross Sea sector during the last deglaciation followed by a re-advance towards the PD position. It is possible, however, that the climate forcing envelope in the model inadequately represents the appropriate regional forcing to enable a re-advance. Alternately, the radiocarbon ages of the subglacial sediments from the Siple Coast sector may need to be reinterpreted (cf. Neuhaus et al., 2021; Venturelli et al., 2023).

### 3.6.4 Present-day AIS

At PD the AIS is in a non-steady state. The transient evolution of the AIS implies that our ability to understand the present and future state of the AIS is contingent on its past trajectory. Model simulations that investigate the transient evolution of the AIS at present and in the future tend to spin up their ice sheet models (e.g. Golledge et al., 2015b; DeConto and Pollard, 2016; Albrecht et al., 2020b). Alternatively, some studies initialize models

using data-assimilation approaches which presume the PD observations as an accurate steady-state representation of the AIS (Cornford et al., 2015; Fürst et al., 2016; Pattyn, 2017). The latter approach achieves simulations with the smallest RMSE to the PD geometry (Seroussi et al., 2019a), but offer limited predictive capabilities given the risk posed by overfitting to PD observations (Schannwell et al., 2020). Therefore, paleo spin-up approaches are much better suited to evaluate the transient evolution of the AIS and the full breadth of systemic sensitivities.

The aim of a transient model spin up is to retrace the thermo-mechanical trajectory of the ice sheet over time to properly initialize the thermal memory of the system and basal environment in preparation for exploratory experiments (e.g. paleo simulations or future projections). By prioritizing the transient behaviour of the system, paleo spin-up initializations usually lead to larger PD misfits as compared to data assimilated initializations (Seroussi et al., 2019b). The resulting PD bias can be used to correct model predictions and subsume their bias into error model. In future projections, a paleo spin-up preserves the sensitivity of the ice sheet due to past warm and cold periods. The paleo model calibration and spin-up conveniently constrain the parameter space and encapsulate all past uncertainties into the PD boundary conditions for potential AIS projections. Our best-fitting NROY AN3sig sub-ensemble results represent a series of paleo spin-up boundary conditions which can be employed as initialization conditions to evaluate PD and future AIS changes. Moreover, they can be used as a basis to propagate uncertainty bounds forward in time to help quantify projection uncertainties.

## 3.7 Conclusion

This study presents a history-matching analysis of AIS evolution since the last interglacial. This was achieved through a history-matching analysis, where a large ensemble of simulations ( $N=9,293$ ) was constrained by a comprehensive observational database (AntICE2; Lecavalier et al., 2023). Simulations were considered NROY by the data if the simulations were within  $3\sigma$  of the highest quality data in the AntICE2 database (tier-1 and 2 data). This yielded a NROY sub-ensemble termed AN3sig, which comprises 82 simulations. The NROY sub-ensemble exhibits a wide range of viable reconstructions and represents bounds on the evolution of the AIS during past warm and cold periods.

The configuration of the AIS during the LIG lacks near-field observational constraints and its modeled reconstruction depends on an uncertain oceanic forcing. The NROY sub-ensemble yields a grounded ice volume deficit relative to present of 2.9 to 13.8 mESL. These wide bounds are predominantly the product of parametric uncertainties associated with sub-surface ocean temperatures for the LIG. Conversely, the configuration of the AIS during the LGM and the post-LGM deglaciation is better constrained by the AntICE2 database. During the LGM, the AIS had an excess grounded ice volume of 9.2 to 26.5 mESL relative to present. This raises the possibility that the LGM AIS was significantly larger than previously thought. The regions with the largest  $2\sigma$  range in Figure 11, 12, S11, and S12 illustrate areas that are poorly constrained by the data given the uncertainties in the entire glacial system. The history-matching analysis over the last glacial cycle yields a variety of viable AIS changes that enable a more meaningful evaluation of the atmospheric/oceanic circulation and sea-level budget during the LIG and LGM. Future

research will focus on addressing remaining data-model misfits that are not bracketed by the full ensemble and NROY sub-ensemble, improving the representation of structural uncertainties in the error model, and achieving probabilistically robust model predictions as outlined in Tarasov and Goldstein (2021).

## 3.8 Author Contributions

B.S.L. and L.T. led and designed the study. B.S.L. wrote the manuscript with editorial input from co-author. B.S.L. and L.T. ran the model simulations, processed the dataset and simulation output. B.S.L. and L.T. performed the data-model analysis. L.T. conducted the BANN training and MCMC sampling. B.S.L. visualized the model results.

## 3.9 References

- Ackert, R. P.: An ice sheet remembers, *Science*, 299, 57–58, <https://doi.org/10.1126/science.1079568>, 2003.
- Albrecht, T., Winkelmann, R., and Levermann, A.: Glacial-cycle simulations of the Antarctic Ice Sheet with the Parallel Ice Sheet Model (PISM)-Part 1: Boundary conditions and climatic forcing, *Cryosphere*, 14, 599–632, <https://doi.org/10.5194/tc-199-2020>, 2020a.
- Albrecht, T., Winkelmann, R., and Levermann, A.: Glacial-cycle simulations of the Antarctic Ice Sheet with the Parallel Ice Sheet Model (PISM)-Part 2: Parameter ensemble analysis, *Cryosphere*, 14, 633–656, <https://doi.org/10.5194/tc-14-633-2020>, 2020b.
- Alley, R. B., Holschuh, N., MacAyeal, D. R., Parizek, B. R., Zoet, L., Riverman, K., Muto, A., Christianson, K., Clyne, E., Anandakrishnan, S., Stevens, N., Smith, A., Arthern, R., Bingham, R., Brisbourne, A., Eisen, O., Hofstede, C., Kulesa, B., Sterns, L., Winberry, P., Bodart, J., Borthwick, L., Case, E., Gustafson, C., Kingslake, J., Ockenden, H., Schoonman, C., and Schwans, E.: Bedforms of Thwaites Glacier, West Antarctica: Character and Origin, *J Geophys Res Earth Surf*, 126, <https://doi.org/10.1029/2021JF006339>, 2021.
- An, M., Wiens, D. A., Zhao, Y., Feng, M., Nyblade, A., Kanao, M., Li, Y., Maggi, A., and L ev eque, J. J.: Temperature, lithosphere-asthenosphere boundary, and heat flux beneath the Antarctic Plate inferred from seismic velocities, *J Geophys Res Solid Earth*, 120, 8720–8742, <https://doi.org/10.1002/2015JB011917>, 2015.
- Argus, D. F., Peltier, W. R., Drummond, R., and Moore, A. W.: The Antarctica component of postglacial rebound model ICE-6G\_C (VM5a) based on GPS positioning, exposure age dating of ice thicknesses, and relative sea level histories, *Geophys J Int*, 198, 537–563, <https://doi.org/10.1093/gji/ggu140>, 2014.
- Austermann, J., Mitrovica, J. X., Latychev, K., and Milne, G. a.: Barbados-based estimate of ice volume at Last Glacial Maximum affected by subducted plate, *Nat Geosci*, 6, 553–557, <https://doi.org/10.1038/ngeo1859>, 2013.
- Austermann, J., Pollard, D., Mitrovica, J. X., Moucha, R., Forte, A. M., DeConto, R. M., Rowley, D. B., and Raymo, M. E.: The impact of dynamic topography change on antarctic ice sheet stability during the mid-pliocene warm period, *Geology*, 43, 927–930, <https://doi.org/10.1130/G36988.1>, 2015.

- Austermann, J., Mitrovica, J. X., Huybers, P., and Rovere, A.: Detection of a dynamic topography signal in last interglacial sea-level records, 2017.
- Bamber, J. L., Alley, R. B., and Joughin, I.: Rapid response of modern day ice sheets to external forcing, *Earth Planet Sci Lett*, 257, 1–13, <https://doi.org/10.1016/j.epsl.2007.03.005>, 2007.
- Bard, E., Hamelin, B., and Fairbanks, R. G.: U-Th ages obtained by mass spectrometry in corals from Barbados: sea level during the past 130,000 years, *Nature*, 346, 456–458, <https://doi.org/10.1038/346456a0>, 1990.
- Bassett, S. E., Milne, G. A., Mitrovica, J. X., and Clark, P. U.: Ice sheet and solid Earth influences on far-field sea-level histories., *Science*, 309, 925–928, <https://doi.org/10.1126/science.1111575>, 2005.
- Bassis, J. N. and Walker, C. C.: Upper and lower limits on the stability of calving glaciers from the yield strength envelope of ice, in: *Proceedings of the Royal Society A: Mathematical, Physical and Engineering Sciences*, 913–931, <https://doi.org/10.1098/rspa.2011.0422>, 2012.
- Bassis, J. N. and Jacobs, S.: Diverse calving patterns linked to glacier geometry, *Nat Geosci*, 6, 833–836, <https://doi.org/10.1038/ngeo1887>, 2013.
- Bentley, M. J., Ó Cofaigh, C., Anderson, J. B., Conway, H., Davies, B., Graham, A. G. C., Hillenbrand, C.-D., Hodgson, D. a., Jamieson, S. S. R., Larter, R. D., Mackintosh, A., Smith, J. a., Verleyen, E., Ackert, R. P., Bart, P. J., Berg, S., Brunstein, D., Canals, M., Colhoun, E. a., Crosta, X., Dickens, W. a., Domack, E., Dowdeswell, J. a., Dunbar, R., Ehrmann, W., Evans, J., Favier, V., Fink, D., Fogwill, C. J., Glasser, N. F., Gohl, K., Gollidge, N. R., Goodwin, I., Gore, D. B., Greenwood, S. L., Hall, B. L., Hall, K., Hedding, D. W., Hein, A. S., Hocking, E. P., Jakobsson, M., Johnson, J. S., Jomelli, V., Jones, R. S., Klages, J. P., Kristoffersen, Y., Kuhn, G., Leventer, A., Licht, K., Lilly, K., Lindow, J., Livingstone, S. J., Massé, G., McGlone, M. S., McKay, R. M., Melles, M., Miura, H., Mulvaney, R., Nel, W., Nitsche, F. O., O'Brien, P. E., Post, A. L., Roberts, S. J., Saunders, K. M., Selkirk, P. M., Simms, A. R., Spiegel, C., Stollendorf, T. D., Sugden, D. E., van der Putten, N., van Ommen, T., Verfaillie, D., Vyverman, W., Wagner, B., White, D. a., Witus, A. E., and Zwartz, D.: A community-based geological reconstruction of Antarctic Ice Sheet deglaciation since the Last Glacial Maximum, *Quat Sci Rev*, 100, 1–9, <https://doi.org/10.1016/j.quascirev.2014.06.025>, 2014.
- Berger, S., Favier, L., Drews, R., Derwael, J. J., and Pattyn, F.: The control of an uncharted pinning point on the flow of an Antarctic ice shelf, *Journal of Glaciology*, 62, 37–45, <https://doi.org/10.1017/jog.2016.7>, 2016.

- Bingham, R. G., Vaughan, D. G., King, E. C., Davies, D., Cornford, S. L., Smith, A. M., Arthern, R. J., Brisbourne, A. M., De Rydt, J., Graham, A. G. C., Spagnolo, M., Marsh, O. J., and Shean, D. E.: Diverse landscapes beneath Pine Island Glacier influence ice flow, *Nat Commun*, 8, <https://doi.org/10.1038/s41467-017-01597-y>, 2017.
- Blanchon, P., Eisenhauer, A., Fietzke, J., and Liebetrau, V.: Rapid sea-level rise and reef back-stepping at the close of the last interglacial highstand., *Nature*, 458, 881–884, <https://doi.org/10.1038/nature07933>, 2009.
- Braconnot, P., Harrison, S. P., Kageyama, M., Bartlein, P. J., Masson-Delmotte, V., Abe-Ouchi, A., Otto-Bliesner, B., and Zhao, Y.: Evaluation of climate models using palaeoclimatic data, <https://doi.org/10.1038/nclimate1456>, June 2012.
- Bradley, S. L., Reerink, T. J., Van De Wal, R. S. W., and Helsen, M. M.: Simulation of the Greenland Ice Sheet over two glacial-interglacial cycles: investigating a sub-ice-shelf melt parameterization and relative sea level forcing in an ice-sheet-ice-shelf model, *Climate of the Past*, 14, 619–635, <https://doi.org/10.5194/cp-14-619-2018>, 2018.
- Briggs, R., Pollard, D., and Tarasov, L.: A glacial systems model configured for large ensemble analysis of Antarctic deglaciation, *Cryosphere*, 7, 1949–1970, <https://doi.org/10.5194/tc-7-1949-2013>, 2013.
- Briggs, R. D. and Tarasov, L.: How to evaluate model-derived deglaciation chronologies: A case study using Antarctica, *Quat Sci Rev*, 63, 109–127, <https://doi.org/10.1016/j.quascirev.2012.11.021>, 2013.
- Briggs, R. D., Pollard, D., and Tarasov, L.: A data-constrained large ensemble analysis of Antarctic evolution since the Eemian, *Quat Sci Rev*, 103, 91–115, <https://doi.org/10.1016/j.quascirev.2014.09.003>, 2014.
- Brondex, J., Gagliardini, O., Gillet-Chaulet, F., and Durand, G.: Sensitivity of grounding line dynamics to the choice of the friction law, *Journal of Glaciology*, 63, 854–866, <https://doi.org/10.1017/jog.2017.51>, 2017.
- Brondex, J., Gillet-Chaulet, F., and Gagliardini, O.: Sensitivity of centennial mass loss projections of the Amundsen basin to the friction law, *Cryosphere*, 13, 177–195, <https://doi.org/10.5194/tc-13-177-2019>, 2019.
- Budd, W. F., Keage, P. L., and Blundy, N. A.: Empirical Studies of Ice Sliding, *Journal of Glaciology*, 23, 157–170, <https://doi.org/10.3189/s0022143000029804>, 1979.

- Bueler, E. and Brown, J.: Shallow shelf approximation as a “sliding law” in a thermomechanically coupled ice sheet model, *J Geophys Res Solid Earth*, 114, <https://doi.org/10.1029/2008JF001179>, 2009.
- Carlson, a. E. and Clark, P. U.: Ice Sheet Sources of Sea Level Rise and Freshwater Discharge During the Last Deglaciation, *Reviews of Geophysics*, 50, 1–72, <https://doi.org/10.1029/2011RG000371>, 2012.
- Clark, P. U., Alley, R. B., Keigwin, L. D., Licciardi, J. M., Johnsen, S. J., and Wang, H.: Origin of the first global meltwater pulse following the Last Glacial Maximum, *Paleoceanography*, 11, 563, <https://doi.org/10.1029/96PA01419>, 1996.
- Clark, P. U., Mitrovica, J. X., Milne, G. a, and Tamisiea, M. E.: Sea-level fingerprinting as a direct test for the source of global meltwater pulse IA., *Science (1979)*, 295, 2438–2441, <https://doi.org/10.1126/science.1068797>, 2002.
- Clark, P., Dyke, A., Shakun, J., Carlson, A., Clark, J., Wohlfarth, B., Mitrovica, J., Hostetler, S., and McCabe, M.: The Last Glacial Maximum, *Science (1979)*, 325, 710–714, <https://doi.org/doi:10.1126/science.1172873>, 2009.
- Clark, P. U., Shakun, J. D., Baker, P. A., Bartlein, P. J., Brewer, S., Brook, E., Carlson, A. E., Cheng, H., Kaufman, D. S., Liu, Z., Marchitto, T. M., Mix, A. C., Morrill, C., Otto-Bliesner, B. L., Pahnke, K., Russell, J. M., Whitlock, C., Adkins, J. F., Blois, J. L., Clark, J., Colman, S. M., Curry, W. B., Flower, B. P., He, F., Johnson, T. C., Lynch-Stieglitz, J., Markgraf, V., McManus, J., Mitrovica, J. X., Moreno, P. I., and Williams, J. W.: Global climate evolution during the last deglaciation., *Proc Natl Acad Sci U S A*, 109, E1134-42, <https://doi.org/10.1073/pnas.1116619109>, 2012.
- Clark, P. U. and Tarasov, L.: Closing the sea level budget at the Last Glacial Maximum, *Proceedings of the National Academy of Sciences*, 111, 15861–15862, <https://doi.org/10.1073/pnas.1418970111>, 2014.
- Clark, P. U., He, F., Golledge, N. R., Mitrovica, J. X., Dutton, A., Hoffman, J. S., and Dendy, S.: Oceanic forcing of penultimate deglacial and last interglacial sea-level rise, *Nature*, 577, 660–664, <https://doi.org/10.1038/s41586-020-1931-7>, 2020.
- Conway, H., Waddington, E. D., and Price, S. F.: Evidence for late Pleistocene thinning of Siple Dome, West Antarctica, *J Geophys Res*, 112, F03021, <https://doi.org/10.1029/2006JF000725>, 2007.
- Cornford, S. L., Martin, D. F., Graves, D. T., Ranken, D. F., Le Brocq, A. M., Gladstone, R. M., Payne, A. J., Ng, E. G., and Lipscomb, W. H.: Adaptive mesh, finite volume modeling of marine ice sheets, *J Comput Phys*, 232, 529–549, <https://doi.org/10.1016/j.jcp.2012.08.037>, 2013.

- Cornford, S. L., Martin, D. F., Payne, A. J., Ng, E. G., Le Brocq, A. M., Gladstone, R. M., Edwards, T. L., Shannon, S. R., Agosta, C., Van Den Broeke, M. R., Hellmer, H. H., Krinner, G., Ligtenberg, S. R. M., Timmermann, R., and Vaughan, D. G.: Century-scale simulations of the response of the West Antarctic Ice Sheet to a warming climate, *Cryosphere*, 9, 1579–1600, <https://doi.org/10.5194/tc-9-1579-2015>, 2015.
- Cuffey, K. M. and Paterson, W. S. B.: *The Physics of Glaciers Fourth Edition*, [https://doi.org/10.1016/0016-7185\(71\)90086-8](https://doi.org/10.1016/0016-7185(71)90086-8), 2010.
- Dahl-Jensen, D., Albert, M. R., Aldahan, a., Azuma, N., Balslev-Clausen, D., Baumgartner, M., Berggren, a.-M., Bigler, M., Binder, T., Blunier, T., Bourgeois, J. C., Brook, E. J., Buchardt, S. L., Buizert, C., Capron, E., Chappellaz, J., Chung, J., Clausen, H. B., Cvijanovic, I., Davies, S. M., Ditlevsen, P., Eicher, O., Fischer, H., Fisher, D. a., Fleet, L. G., Gfeller, G., Gkinis, V., Gogineni, S., Goto-Azuma, K., Grinsted, a., Gudlaugsdottir, H., Guillevic, M., Hansen, S. B., Hansson, M., Hirabayashi, M., Hong, S., Hur, S. D., Huybrechts, P., Hvidberg, C. S., Iizuka, Y., Jenk, T., Johnsen, S. J., Jones, T. R., Jouzel, J., Karlsson, N. B., Kawamura, K., Keegan, K., Kettner, E., Kipfstuhl, S., Kjær, H. a., Koutnik, M., Kuramoto, T., Köhler, P., Laepple, T., Landais, a., Langen, P. L., Larsen, L. B., Leuenberger, D., Leuenberger, M., Leuschen, C., Li, J., Lipenkov, V., Martinerie, P., Maselli, O. J., Masson-Delmotte, V., McConnell, J. R., Miller, H., Mini, O., Miyamoto, a., Montagnat-Rentier, M., Mulvaney, R., Muscheler, R., Orsi, a. J., Paden, J., Panton, C., Pattyn, F., Petit, J.-R., Pol, K., Popp, T., Possnert, G., Prié, F., Prokopiou, M., Quiquet, a., Rasmussen, S. O., Raynaud, D., Ren, J., Reutenauer, C., Ritz, C., Röckmann, T., Rosen, J. L., Rubino, M., Rybak, O., Samyn, D., Sapart, C. J., Schilt, a., Schmidt, a. M. Z., Schwander, J., Schüpbach, S., Seierstad, I., et al.: Eemian interglacial reconstructed from a Greenland folded ice core, *Nature*, 493, 489–494, <https://doi.org/10.1038/nature11789>, 2013.
- DeConto, R. M. and Pollard, D.: Contribution of Antarctica to past and future sea-level rise, *Nature*, 531, 591–597, <https://doi.org/10.1038/nature17145>, 2016.
- Denton, G. H. and Hughes, T. J.: Reconstructing the Antarctic Ice Sheet at the Last Glacial Maximum, *Quat Sci Rev*, 21, 193–202, [https://doi.org/10.1016/S0277-3791\(01\)00090-7](https://doi.org/10.1016/S0277-3791(01)00090-7), 2002.
- Depoorter, M. A., Bamber, J. L., Griggs, J. A., Lenaerts, J. T. M., Ligtenberg, S. R. M., van den Broeke, M. R., and Moholdt, G.: Calving fluxes and basal melt rates of Antarctic ice shelves, *Nature*, 502, 89–92, <https://doi.org/10.1038/nature12567>, 2013.
- Deschamps, P., Durand, N., Bard, E., Hamelin, B., Camoin, G., Thomas, A. L., Henderson, G. M., Okuno, J., and Yokoyama, Y.: Ice-sheet collapse and sea-level rise at the

- Bølling warming 14,600 years ago, *Nature*, 483, 559–564, <https://doi.org/10.1038/nature10902>, 2012.
- Drouet, a. S., Docquier, D., Durand, G., Hindmarsh, R., Pattyn, F., Gagliardini, O., and Zwinger, T.: Grounding line transient response in marine ice sheet models, *The Cryosphere Discussions*, 6, 3903–3935, <https://doi.org/10.5194/tc-7-395-2013>, 2012.
- Düsterhus, A., Tamisiea, M. E., Jevrejeva, S.: Estimating the sea level highstand during the last interglacial: a probabilistic massive ensemble approach. *Geophysical Journal International*, 206(2), 900–920, <https://doi.org/10.1093/gji/ggw174>, 2016.
- Dutton, a. and Lambeck, K.: Ice Volume and Sea Level During the Last Interglacial, *Science* (1979), 337, 216–219, <https://doi.org/10.1126/science.1205749>, 2012.
- Dutton, A., Carlson, A. E., Long, A. J., Milne, G. A., Clark, P. U., DeConto, R., Horton, B. P., Rahmstorf, S., and Raymo, M. E.: Sea-level rise due to polar ice-sheet mass loss during past warm periods, <https://doi.org/10.1126/science.aaa4019>, 10 July 2015.
- Dyer, B., Austermann, J., D’Andrea, W.J., Creel, R.C., Sandstrom, M.R., Cashman, M., Rovere, A. and Raymo, M.E.: Sea-level trends across The Bahamas constrain peak last interglacial ice melt, *Proceedings of the National Academy of Sciences*, 118(33), e2026839118, <https://doi.org/10.1073/pnas.2026839118>, 2021.
- Dziewonski, A. M. and Anderson, D. L.: Preliminary reference Earth model, *Physics of the Earth and Planetary Interiors*, 25, 297–356, [https://doi.org/10.1016/0031-9201\(81\)90046-7](https://doi.org/10.1016/0031-9201(81)90046-7), 1981.
- Edwards, T. L., Brandon, M. A., Durand, G., Edwards, N. R., Golledge, N. R., Holden, P. B., Nias, I. J., Payne, A. J., Ritz, C., and Wernecke, A.: Revisiting Antarctic ice loss due to marine ice-cliff instability, *Nature*, 566, 58–64, <https://doi.org/10.1038/s41586-019-0901-4>, 2019.
- EPICA Members: Eight glacial cycles from an Antarctic ice core, *Nature*, 429, 623–628, 2004.
- Favier, L., Gagliardini, O., Durand, G., and Zwinger, T.: A three-dimensional full Stokes model of the grounding line dynamics: Effect of a pinning point beneath the ice shelf, *Cryosphere*, 6, 101–112, <https://doi.org/10.5194/tc-6-101-2012>, 2012.
- Favier, L., Pattyn, F., Berger, S., and Drews, R.: Dynamic influence of pinning points on marine ice-sheet stability: A numerical study in Dronning Maud Land, East Antarctica, *Cryosphere*, 10, 2623–2635, <https://doi.org/10.5194/tc-10-2623-2016>, 2016.

- Fischer, H., Meissner, K. J., Mix, A. C., Abram, N. J., Austermann, J., Brovkin, V., Capron, E., Colombaroli, D., Daniau, A. L., Dyez, K. A., Felis, T., Finkelstein, S. A., Jaccard, S. L., McClymont, E. L., Rovere, A., Sutter, J., Wolff, E. W., Affolter, S., Bakker, P., Ballesteros-Cánovas, J. A., Barbante, C., Caley, T., Carlson, A. E., Churakova, O., Cortese, G., Cumming, B. F., Davis, B. A. S., De Vernal, A., Emile-Geay, J., Fritz, S. C., Gierz, P., Gottschalk, J., Holloway, M. D., Joos, F., Kucera, M., Loutre, M. F., Lunt, D. J., Marcisz, K., Marlon, J. R., Martinez, P., Masson-Delmotte, V., Nehrbass-Ahles, C., Otto-Bliesner, B. L., Raible, C. C., Risebrobakken, B., Sánchez Goñi, M. F., Arrigo, J. S., Sarinthein, M., Sjolte, J., Stocker, T. F., Velasquez Álvarez, P. A., Tinner, W., Valdes, P. J., Vogel, H., Wanner, H., Yan, Q., Yu, Z., Ziegler, M., and Zhou, L.: Palaeoclimate constraints on the impact of 2 °c anthropogenic warming and beyond, <https://doi.org/10.1038/s41561-018-0146-0>, 1 July 2018.
- Fukumori, I., Heimbach, P., Ponte, R. M., and Wunsch, C.: A dynamically consistent, multivariable ocean climatology, *Bull Am Meteorol Soc*, 99, 2107–2127, <https://doi.org/10.1175/BAMS-D-17-0213.1>, 2018.
- Fürst, J. J., Durand, G., Gillet-Chaulet, F., Tavard, L., Rankl, M., Braun, M., and Gagliardini, O.: The safety band of Antarctic ice shelves, *Nat Clim Chang*, 6, 479–482, <https://doi.org/10.1038/nclimate2912>, 2016.
- Gagliardini, O., Cohen, D., Råback, P., and Zwinger, T.: Finite-element modeling of subglacial cavities and related friction law, *J Geophys Res Earth Surf*, 112, <https://doi.org/10.1029/2006JF000576>, 2007.
- Gillet-Chaulet, F., Durand, G., Gagliardini, O., Mosbeux, C., Mougintot, J., Rémy, F., and Ritz, C.: Assimilation of surface velocities acquired between 1996 and 2010 to constrain the form of the basal friction law under Pine Island Glacier, *Geophys Res Lett*, 43, 10,311–10,321, <https://doi.org/10.1002/2016GL069937>, 2016.
- Goelzer, H., Huybrechts, P., Marie-France, L., and Fichet, T.: Last Interglacial climate and sea-level evolution from a coupled ice sheet-climate model, *Climate of the Past*, 12, 2195–2213, <https://doi.org/10.5194/cp-12-2195-2016>, 2016.
- Golledge, N. R., Fogwill, C. J., Mackintosh, A. N., and Buckley, K. M.: Dynamics of the last glacial maximum Antarctic ice-sheet and its response to ocean forcing, *PNAS*, 109, 16052–16056, <https://doi.org/10.1073/pnas.1205385109/-/DCSupplemental>, 2012.
- Golledge, N. R., Menviel, L., Carter, L., Fogwill, C. J., England, M. H., Cortese, G., and Levy, R. H.: Antarctic contribution to meltwater pulse 1A from reduced Southern Ocean overturning., *Nat Commun*, 5, 5107, <https://doi.org/10.1038/ncomms6107>, 2014.

- Golledge, N. R., Kowalewski, D. E., Naish, T. R., Levy, R. H., Fogwill, C. J., and Gasson, E. G. W.: The multi-millennial Antarctic commitment to future sea-level rise, *Nature*, 526, 421–425, <https://doi.org/10.1038/nature15706>, 2015.
- Gomez, N., Pollard, D., and Mitrovica, J. X.: A 3-D coupled ice sheet - sea level model applied to Antarctica through the last 40 ky, *Earth Planet Sci Lett*, 384, 88–99, <https://doi.org/10.1016/j.epsl.2013.09.042>, 2013.
- Gudmundsson, G. H., Krug, J., Durand, G., Favier, L., and Gagliardini, O.: The stability of grounding lines on retrograde slopes, *Cryosphere*, 6, 1497–1505, <https://doi.org/10.5194/tc-6-1497-2012>, 2012.
- Hanebuth, T. J. J., Stattegger, K., and Bojanowski, a.: Termination of the Last Glacial Maximum sea-level lowstand: The Sunda-Shelf data revisited, *Glob Planet Change*, 66, 76–84, <https://doi.org/10.1016/j.gloplacha.2008.03.011>, 2009.
- He, F.: Simulating transient climate evolution of the last deglaciation with CCSM3, Doctoral dissertation, University of Wisconsin, Madison, 2011.
- Hearty, P. J., Hollin, J. T., Neumann, a. C., O’Leary, M. J., and McCulloch, M.: Global sea-level fluctuations during the Last Interglaciation (MIS 5e), *Quat Sci Rev*, 26, 2090–2112, <https://doi.org/10.1016/j.quascirev.2007.06.019>, 2007.
- Helsen, M. M., Van De Berg, W. J., Van De Wal, R. S. W., Van Den Broeke, M. R., and Oerlemans, J.: Coupled regional climate-ice-sheet simulation shows limited Greenland ice loss during the Eemian, *Climate of the Past*, 9, 1773–1788, <https://doi.org/10.5194/cp-9-1773-2013>, 2013.
- Heroy, D. C. and Anderson, J. B.: Radiocarbon constraints on Antarctic Peninsula Ice Sheet retreat following the Last Glacial Maximum (LGM), *Quat Sci Rev*, 26, 3286–3297, <https://doi.org/10.1016/j.quascirev.2007.07.012>, 2007.
- Hibbert, F. D., Rohling, E. J., Dutton, A., Williams, F. H., Zhao, C., and Tamisiea, M. E.: Coral indicators of past sea-level change: a global repository of U-series dated benchmarks, *Quat Sci Rev*, 145, 1–56, <https://doi.org/https://doi.org/10.1016/j.quascirev.2016.04.019>, 2016.
- Hillenbrand, C. D., Kuhn, G., Smith, J. A., Gohl, K., Graham, A. G. C., Larter, R. D., Klages, J. P., Downey, R., Moreton, S. G., Forwick, M., and Vaughan, D. G.: Grounding-line retreat of the West Antarctic Ice Sheet from inner Pine Island Bay, *Geology*, 41, 35–38, <https://doi.org/10.1130/G33469.1>, 2013.
- Hillenbrand, C. D., Bentley, M. J., Stollendorf, T. D., Hein, A. S., Kuhn, G., Graham, A. G. C., Fogwill, C. J., Kristoffersen, Y., Smith, J. A., Anderson, J. B., Larter, R. D.,

- Melles, M., Hodgson, D. A., Mulvaney, R., and Sugden, D. E.: Reconstruction of changes in the Weddell Sea sector of the Antarctic Ice Sheet since the Last Glacial Maximum, *Quat Sci Rev*, 100, 111–136, <https://doi.org/10.1016/j.quascirev.2013.07.020>, 2014.
- Hoffman, J. S., Peter, †, Clark, U., Parnell, A. C., and He, F.: Regional and global sea-surface temperatures during the last interglaciation, *Science* (1979), 355, 276–279, 2017.
- Huybrechts, P.: Sea-level changes at the LGM from ice-dynamic reconstructions of the Greenland and Antarctic ice sheets during the glacial cycles, *Quat Sci Rev*, 21, 203–231, [https://doi.org/10.1016/S0277-3791\(01\)00082-8](https://doi.org/10.1016/S0277-3791(01)00082-8), 2002.
- Joughin, I., Smith, B. E., and Holland, D. M.: Sensitivity of 21st century sea level to ocean-induced thinning of Pine Island Glacier, Antarctica, *Geophys Res Lett*, 37, <https://doi.org/10.1029/2010GL044819>, 2010.
- Joughin, I., Smith, B. E., and Schoof, C. G.: Regularized Coulomb Friction Laws for Ice Sheet Sliding: Application to Pine Island Glacier, Antarctica, *Geophys Res Lett*, 46, 4764–4771, <https://doi.org/10.1029/2019GL082526>, 2019.
- Jouzel, J., Masson-Delmotte, V., Cattani, O., Dreyfus, G., Falourd, S., Hoffmann, G., Minster, B., Nouet, J., Barnola, J. M., Chappellaz, J., Fischer, H., Gallet, J. C., Johnsen, S., Leuenberger, M., Loulergue, L., Luethi, D., Oerter, H., Parrenin, F., Raisbeck, G., Raynaud, D., Schilt, a, Schwander, J., Selmo, E., Souchez, R., Spahni, R., Stauffer, B., Steffensen, J. P., Stenni, B., Stocker, T. F., Tison, J. L., Werner, M., and Wolff, E. W.: Orbital and millennial Antarctic climate variability over the past 800,000 years., *Science*, 317, 793–796, <https://doi.org/10.1126/science.1141038>, 2007.
- Kingslake, J., Scherer, R. P., Albrecht, T., Coenen, J., Powell, R. D., Reese, R., Stansell, N. D., Tulaczyk, S., Wearing, M. G., and Whitehouse, P. L.: Extensive retreat and re-advance of the West Antarctic Ice Sheet during the Holocene, *Nature*, 558, 430–434, <https://doi.org/10.1038/s41586-018-0208-x>, 2018.
- Kopp, R. E., Simons, F. J., Mitrovica, J. X., Maloof, A. C., and Oppenheimer, M.: Probabilistic assessment of sea level during the last interglacial stage, *Nature*, 462, 863–867, <https://doi.org/10.1038/nature08686>, 2009.
- Lambeck, K., Rouby, H., Purcell, a., Sun, Y., and Sambridge, M.: Sea level and global ice volumes from the Last Glacial Maximum to the Holocene, *Proceedings of the National Academy of Sciences*, 111, 15296–15303, <https://doi.org/10.1073/pnas.1411762111>, 2014.

- Larour, E., Morlighem, M., Seroussi, H., Schiermeier, J., and Rignot, E.: Ice flow sensitivity to geothermal heat flux of Pine Island Glacier, Antarctica, *J Geophys Res Earth Surf*, 117, <https://doi.org/10.1029/2012JF002371>, 2012.
- Lecavalier, B. S., Tarasov, L., Balco, G., Spector, P., Hillenbrand, C. D., Buizert, C., Ritz, C., Leduc-Leballeur, M., Mulvaney, R., Whitehouse, P. L., Bentley, M. J., and Bamber, J.: Antarctic Ice Sheet paleo-constraint database, *Earth Syst Sci Data*, 15, 3573–3596, <https://doi.org/10.5194/essd-15-3573-2023>, 2023.
- Lecavalier, B. S., Tarasov, L.: A history-matching analysis of the Antarctic Ice Sheet since the last interglacial – Part 2: Glacial isostatic adjustment, [in preparation] 2024.
- Lemieux-Dudon, B., Blayo, E., Petit, J.-R., Waelbroeck, C., Svensson, A., Ritz, C., Barnola, J.-M., Narcisi, B. M., and Parrenin, F.: Consistent dating for Antarctic and Greenland ice cores, *Quat Sci Rev*, 29, 8–20, <https://doi.org/10.1016/j.quascirev.2009.11.010>, 2010.
- Levermann, A., Albrecht, T., Winkelmann, R., Martin, M. A., Haseloff, M., and Joughin, I.: Kinematic first-order calving law implies potential for abrupt ice-shelf retreat, *Cryosphere*, 6, 273–286, <https://doi.org/10.5194/tc-6-273-2012>, 2012.
- Lin, Y., Hibbert, F. D., Whitehouse, P. L., Woodroffe, S. A., Purcell, A., Shennan, I., and Bradley, S. L.: A reconciled solution of Meltwater Pulse 1A sources using sea-level fingerprinting, *Nat Commun*, 12, <https://doi.org/10.1038/s41467-021-21990-y>, 2021.
- Lisiecki, L. E. and Raymo, M. E.: A Pliocene-Pleistocene stack of 57 globally distributed benthic  $\delta^{18}\text{O}$  records, *Paleoceanography*, 20, 1–17, <https://doi.org/10.1029/2004PA001071>, 2005.
- Liu, J., Milne, G. A., Kopp, R. E., Clark, P. U., and Shennan, I.: Sea-level constraints on the amplitude and source distribution of Meltwater Pulse 1A, *Nat Geosci*, 9, 130–134, <https://doi.org/10.1038/ngeo2616>, 2016.
- Liu, Y., Moore, J. C., Cheng, X., Gladstone, R. M., Bassis, J. N., Liu, H., Wen, J., and Hui, F.: Ocean-driven thinning enhances iceberg calving and retreat of Antarctic ice shelves, *Proceedings of the National Academy of Sciences*, 112, 3263–3268, <https://doi.org/10.1073/pnas.1415137112>, 2015.
- Livingstone, S. J., Ó Cofaigh, C., Stokes, C. R., Hillenbrand, C.-D., Vieli, A., and Jamieson, S. S. R.: Antarctic palaeo-ice streams, *Earth Sci Rev*, 111, 90–128, <https://doi.org/10.1016/j.earscirev.2011.10.003>, 2012.

- Martin, D. F., Cornford, S. L., and Payne, A. J.: Millennial-Scale Vulnerability of the Antarctic Ice Sheet to Regional Ice Shelf Collapse, *Geophys Res Lett*, 46, 1467–1475, <https://doi.org/10.1029/2018GL081229>, 2019.
- Martin, M. A., Winkelmann, R., Haseloff, M., Albrecht, T., Bueller, E., Khroulev, C., and Levermann, A.: The Potsdam Parallel Ice Sheet Model (PISM-PIK) - Part 2: Dynamic equilibrium simulation of the Antarctic ice sheet, *Cryosphere*, 5, 727–740, <https://doi.org/10.5194/tc-5-727-2011>, 2011.
- Martos, Y. M., Catalán, M., Jordan, T. A., Golynsky, A., Golynsky, D., Eagles, G., and Vaughan, D. G.: Heat Flux Distribution of Antarctica Unveiled, *Geophys Res Lett*, 44, 11,417–11,426, <https://doi.org/10.1002/2017GL075609>, 2017.
- Marzeion, B., Hock, R., Anderson, B., Bliss, A., Champollion, N., Fujita, K., Huss, M., Immerzeel, W. W., Kraaijenbrink, P., Malles, J. H., Maussion, F., Radić, V., Rounce, D. R., Sakai, A., Shannon, S., van de Wal, R., and Zekollari, H.: Partitioning the Uncertainty of Ensemble Projections of Global Glacier Mass Change, *Earths Future*, 8, <https://doi.org/10.1029/2019EF001470>, 2020.
- Mas E Braga, M., Selwyn Jones, R., Newall, J. C. H., Rogozhina, I., Andersen, J. L., Lifton, N. A., and Stroeven, A. P.: Nunataks as barriers to ice flow: Implications for palaeo ice sheet reconstructions, *Cryosphere*, 15, 4929–4947, <https://doi.org/10.5194/tc-15-4929-2021>, 2021.
- Masson-Delmotte, V., Zhai, P., Chen, Y., Goldfarb, L., Gomis, M. I., Matthews, J. B. R., Berger, S., Huang, M., Yelekçi, O., Yu, R., Zhou, B., Lonnoy, E., Maycock, T. K., Waterfield, T., Leitzell, K., and Caud, N.: Working Group I Contribution to the Sixth Assessment Report of the Intergovernmental Panel on Climate Change Edited by, <https://doi.org/10.1017/9781009157896>, 2021.
- Matsuoka, K., Skoglund, A., Roth, G., de Pomereu, J., Griffiths, H., Headland, R., Herried, B., Katsumata, K., le Brocq, A., Licht, K., Morgan, F., Neff, P. D., Ritz, C., Scheinert, M., Tamura, T., van de Putte, A., van den Broeke, M., von Deschanden, A., Deschamps-Berger, C., Liefferinge, B. van, Tronstad, S., and Melvaer, Y.: Quantarctica, an integrated mapping environment for Antarctica, the Southern Ocean, and sub-Antarctic islands, <https://doi.org/10.21334/npolar.2018.8516e961>, 2021.
- McKay, N. P., Overpeck, J. T., and Otto-Bliesner, B. L.: The role of ocean thermal expansion in Last Interglacial sea level rise, *Geophys Res Lett*, 38, n/a-n/a, <https://doi.org/10.1029/2011GL048280>, 2011.
- Melchior Van Wessem, J., Jan Van De Berg, W., Noël, B. P. Y., Van Meijgaard, E., Amory, C., Birnbaum, G., Jakobs, C. L., Krüger, K., Lenaerts, J. T. M., Lhermitte, S., Ligtenberg, S. R. M., Medley, B., Reijmer, C. H., Van Tricht, K., Trusel, L. D., Van

- Ulf, L. H., Wouters, B., Wuite, J., and Van Den Broeke, M. R.: Modelling the climate and surface mass balance of polar ice sheets using RACMO2 - Part 2: Antarctica (1979-2016), *Cryosphere*, 12, 1479–1498, <https://doi.org/10.5194/tc-12-1479-2018>, 2018.
- Meredith, M., Sommerkorn, M., Cassotta, S., Derksen, C., Ekaykin, A., Hollowed, A., Kofinas, G., Mackintosh, A., Melbourne-Thomas, J., Muelbert, M. M. C., Ottersen, G., Pritchard, H., and Schuur, E. A. G.: Polar Regions. In: IPCC Special Report on the Ocean and Cryosphere in a Changing Climate, IPCC, 2019.
- Milne, G. a, Mitrovica, J. X., and Schrag, D. P.: Estimating past continental ice volume from sea-level data, *Quat Sci Rev*, 21, 361–376, [https://doi.org/10.1016/S0277-3791\(01\)00108-1](https://doi.org/10.1016/S0277-3791(01)00108-1), 2002.
- Morlighem, M., Rignot, E., Binder, T., Blankenship, D., Drews, R., Eagles, G., Eisen, O., Ferraccioli, F., Forsberg, R., Fretwell, P., Goel, V., Greenbaum, J. S., Gudmundsson, H., Guo, J., Helm, V., Hofstede, C., Howat, I., Humbert, A., Jokat, W., Karlsson, N. B., Lee, W. S., Matsuoka, K., Millan, R., Mouginit, J., Paden, J., Pattyn, F., Roberts, J., Rosier, S., Ruppel, A., Seroussi, H., Smith, E. C., Steinhage, D., Sun, B., Broeke, M. R. van den, Ommen, T. D. van, Wessem, M. van, and Young, D. A.: Deep glacial troughs and stabilizing ridges unveiled beneath the margins of the Antarctic ice sheet, *Nat Geosci*, 13, 132–137, <https://doi.org/10.1038/s41561-019-0510-8>, 2020.
- Mouginit, J., Rignot, E., and Scheuchl, B.: Continent-Wide, Interferometric SAR Phase, Mapping of Antarctic Ice Velocity, *Geophys Res Lett*, 46, 9710–9718, <https://doi.org/10.1029/2019GL083826>, 2019.
- Neal, R.M.: Bayesian learning for neural networks. Vol. 118. Springer Science & Business Media, 2012.
- Neuhaus, S. U., Tulaczyk, S. M., Stansell, N. D., Coenen, J. J., Scherer, R. P., Mikucki, J. A., and Powell, R. D.: Did Holocene climate changes drive West Antarctic grounding line retreat and readvance?, *Cryosphere*, 15, 4655–4673, <https://doi.org/10.5194/tc-15-4655-2021>, 2021.
- Nias, I. J., Cornford, S. L., and Payne, A. J.: New Mass-Conserving Bedrock Topography for Pine Island Glacier Impacts Simulated Decadal Rates of Mass Loss, *Geophys Res Lett*, 45, 3173–3181, <https://doi.org/10.1002/2017GL076493>, 2018.
- Nichols, K. A., Goehring, B. M., Balco, G., Johnson, J. S., Hein, A. S., and Todd, C.: New Last Glacial Maximum ice thickness constraints for the Weddell Sea Embayment, Antarctica, *Cryosphere*, 13, 2935–2951, <https://doi.org/10.5194/tc-13-2935-2019>, 2019.

- Nick, F. M., van der Veen, C. J., Vieli, A., and Benn, D. I.: A physically based calving model applied to marine outlet glaciers and implications for the glacier dynamics, *Journal of Glaciology*, 56, 781–794, <https://doi.org/10.3189/002214310794457344>, 2010.
- Niu, L. U., Lohmann, G., Hinck, S., Gowan, E. J., & Krebs-Kanzow, U. T. A.: The sensitivity of Northern Hemisphere ice sheets to atmospheric forcing during the last glacial cycle using PMIP3 models. *Journal of Glaciology*, 65(252), 645–661. doi:10.1017/jog.2019.42, 2019.
- Nowicki, S., Bindschadler, R. A., Abe-Ouchi, A., Aschwanden, A., Bueller, E., Choi, H., Fastook, J., Granzow, G., Greve, R., Gutowski, G., Herzfeld, U., Jackson, C., Johnson, J., Khroulev, C., Larour, E., Levermann, A., Lipscomb, W. H., Martin, M. A., Morlighem, M., Parizek, B. R., Pollard, D., Price, S. F., Ren, D., Rignot, E., Saito, F., Sato, T., Seddik, H., Seroussi, H., Takahashi, K., Walker, R., and Wang, W. L.: Insights into spatial sensitivities of ice mass response to environmental change from the SeaRISE ice sheet modeling project I: Antarctica, *J Geophys Res Earth Surf*, 118, 1002–1024, <https://doi.org/10.1002/jgrf.20081>, 2013.
- Otosaka, I. N., Shepherd, A., Ivins, E. R., Schlegel, N.-J., Amory, C., van den Broeke, M. R., Horwath, M., Joughin, I., King, M. D., Krinner, G., Nowicki, S., Payne, A. J., Rignot, E., Scambos, T., Simon, K. M., Smith, B. E., Sørensen, L. S., Velicogna, I., Whitehouse, P. L., A. G., Agosta, C., Ahlstrøm, A. P., Blazquez, A., Colgan, W., Engdahl, M. E., Fettweis, X., Forsberg, R., Gallée, H., Gardner, A., Gilbert, L., Gourmelen, N., Groh, A., Gunter, B. C., Harig, C., Helm, V., Khan, S. A., Kittel, C., Konrad, H., Langen, P. L., Lecavalier, B. S., Liang, C.-C., Loomis, B. D., McMillan, M., Melini, D., Mernild, S. H., Mottram, R., Mouginot, J., Nilsson, J., Noël, B., Pattle, M. E., Peltier, W. R., Pie, N., Roca, M., Sasgen, I., Save, H. V., Seo, K.-W., Scheuchl, B., Schrama, E. J. O., Schröder, L., Simonsen, S. B., Slater, T., Spada, G., Sutterley, T. C., Vishwakarma, B. D., van Wessem, J. M., Wiese, D., van der Wal, W., and Wouters, B.: Mass balance of the Greenland and Antarctic ice sheets from 1992 to 2020. *Earth Syst. Sci. Data*, 15, 1597–1616, <https://doi.org/10.5194/essd-15-1597-2023>, 2023.
- Otto-Bliesner, B. L., Brady, E. C., Zhao, A., Brierley, C. M., Axford, Y., Capron, E., Govin, A., Hoffman, J. S., Isaacs, E., Kageyama, M., Scussolini, P., Tzedakis, P. C., Williams, C. J. R., Wolff, E., Abe-Ouchi, A., Braconnot, P., Ramos Buarque, S., Cao, J., De Vernal, A., Vittoria Guarino, M., Guo, C., Legrande, A. N., Lohmann, G., Meissner, K. J., Menviel, L., Morozova, P. A., Nisancioglu, K. H., O’Ishi, R., Méliá, D. S. Y., Shi, X., Sicard, M., Sime, L., Stepanek, C., Tomas, R., Volodin, E., Yeung, N. K. H., Zhang, Q., Zhang, Z., and Zheng, W.: Large-scale features of Last Interglacial climate: Results from evaluating the lig127k simulations for the Coupled Model Intercomparison Project (CMIP6)-Paleoclimate Modeling Intercomparison Project (PMIP4), *Climate of the Past*, 17, 63–94, <https://doi.org/10.5194/cp-17-63-2021>, 2021.

- Pan, L., Milne, G. A., Latychev, K., Goldberg, S. L., Austermann, J., Hoggard, M. J., and Mitrovica, J. X.: The influence of lateral Earth structure on inferences of global ice volume during the Last Glacial Maximum, <https://doi.org/10.1016/j.quascirev.2022.107644>, 2022.
- Pattyn, F.: Antarctic subglacial conditions inferred from a hybrid ice sheet/ice stream model, *Earth Planet Sci Lett*, 295, 451–461, <https://doi.org/10.1016/j.epsl.2010.04.025>, 2010.
- Pattyn, F., Schoof, C., Perichon, L., Hindmarsh, R. C. a., Bueler, E., de Fleurian, B., Durand, G., Gagliardini, O., Gladstone, R., Goldberg, D., Gudmundsson, G. H., Huybrechts, P., Lee, V., Nick, F. M., Payne, a. J., Pollard, D., Rybak, O., Saito, F., and Vieli, a.: Results of the Marine Ice Sheet Model Intercomparison Project, MISMIP, *Cryosphere*, 6, 573–588, <https://doi.org/10.5194/tc-6-573-2012>, 2012.
- Pattyn, F.: Sea-level response to melting of Antarctic ice shelves on multi-centennial timescales with the fast Elementary Thermomechanical Ice Sheet model (f.ETISh v1.0), *Cryosphere*, 11, 1851–1878, <https://doi.org/10.5194/tc-11-1851-2017>, 2017.
- Pattyn, F. and Morlighem, M.: The uncertain future of the Antarctic Ice Sheet, *Science* (1979), 367, 1331–1335, <https://doi.org/10.1126/science.aaz5487>, 2020.
- Peltier, W. R. and Fairbanks, R. G.: Global glacial ice volume and Last Glacial Maximum duration from an extended Barbados sea level record, *Quat Sci Rev*, 25, 3322–3337, <https://doi.org/10.1016/j.quascirev.2006.04.010>, 2006.
- Pittard, M. L., Whitehouse, P. L., Bentley, M. J., and Small, D.: An ensemble of Antarctic deglacial simulations constrained by geological observations, *Quat Sci Rev*, 298, <https://doi.org/10.1016/j.quascirev.2022.107800>, 2022.
- Pollard, D. and DeConto, R. M. R. M.: A Coupled Ice-Sheet/Ice-Shelf/Sediment Model Applied to a Marine-Margin Flowline: Forced and Unforced Variations, *Glacial sedimentary processes and products*, 37–52, <https://doi.org/10.1002/9781444304435.ch4>, 2007.
- Pollard, D. and DeConto, R. M.: Modelling West Antarctic ice sheet growth and collapse through the past five million years, *Nature*, 458, 329–332, <https://doi.org/10.1038/nature07809>, 2009.
- Pollard, D. and DeConto, R. M.: Description of a hybrid ice sheet-shelf model, and application to Antarctica, *Geosci Model Dev*, 5, 1273–1295, <https://doi.org/10.5194/gmd-5-1273-2012>, 2012.

- Pollard, D., DeConto, R. M., and Alley, R. B.: Potential Antarctic Ice Sheet retreat driven by hydrofracturing and ice cliff failure, *Earth Planet Sci Lett*, 412, 112–121, <https://doi.org/10.1016/j.epsl.2014.12.035>, 2015.
- Pollard, D., Chang, W., Haran, M., Applegate, P., and DeConto, R.: Large ensemble modeling of the last deglacial retreat of the West Antarctic Ice Sheet: Comparison of simple and advanced statistical techniques, *Geosci Model Dev*, 9, 1697–1723, <https://doi.org/10.5194/gmd-9-1697-2016>, 2016.
- Quiquet, a., Ritz, C., Punge, H. J., and Salas y Méliá, D.: Greenland ice sheet contribution to sea level rise during the last interglacial period: a modelling study driven and constrained by ice core data, *Climate of the Past*, 9, 353–366, <https://doi.org/10.5194/cp-9-353-2013>, 2013.
- Rasmussen, S. O., Bigler, M., Blockley, S. P., Blunier, T., Buchardt, S. L., Clausen, H. B., Cvijanovic, I., Dahl-Jensen, D., Johnsen, S. J., Fischer, H., Gkinis, V., Guillevic, M., Hoek, W. Z., Lowe, J. J., Pedro, J. B., Popp, T., Seierstad, I. K., Steffensen, J. P., Svensson, A. M., Vallelonga, P., Vinther, B. M., Walker, M. J. C., Wheatley, J. J., and Winstrup, M.: A stratigraphic framework for abrupt climatic changes during the Last Glacial period based on three synchronized Greenland ice-core records: refining and extending the INTIMATE event stratigraphy, *Quat Sci Rev*, 106, 14–28, <https://doi.org/10.1016/j.quascirev.2014.09.007>, 2014.
- Rignot, E., Jacobs, S., Mouginot, J., and Scheuchl, B.: Ice-shelf melting around Antarctica., *Science* (1979), 341, 266–70, <https://doi.org/10.1126/science.1235798>, 2013.
- Rignot, E., Mouginot, J., Morlighem, M., Seroussi, H., and Scheuchl, B.: Widespread, rapid grounding line retreat of Pine Island, Thwaites, Smith, and Kohler glaciers, West Antarctica, from 1992 to 2011, *Geophys Res Lett*, 41, 3502–3509, <https://doi.org/10.1002/2014GL060140>, 2014.
- Rohling, E. J., Hibbert, F. D., Grant, K. M., Galaasen, E. V., Irvall, N., Kleiven, H. F., Marino, G., Ninnemann, U., Roberts, A. P., Rosenthal, Y., Schulz, H., Williams, F. H., and Yu, J.: Asynchronous Antarctic and Greenland ice-volume contributions to the last interglacial sea-level highstand, *Nat Commun*, 10, <https://doi.org/10.1038/s41467-019-12874-3>, 2019.
- Schäfer, M., Gillet-Chaulet, F., Gladstone, R., Pettersson, R., Pohjola, V. A., Strozzi, T., and Zwinger, T.: Assessment of heat sources on the control of fast flow of Vestfonna ice cap, Svalbard, *Cryosphere*, 8, 1951–1973, <https://doi.org/10.5194/tc-8-1951-2014>, 2014.
- Schannwell, C., Drews, R., Ehlers, T., Eisen, O., Mayer, C., Malinen, M., Smith, E., and Eisermann, H.: Quantifying the effect of ocean bed properties on ice sheet geometry

over 40,000 years with a full-Stokes model, *The Cryosphere Discussions*, <https://doi.org/10.5194/tc-2020-98>, 2020.

Schoof, C.: The effect of cavitation on glacier sliding, *Proceedings of the Royal Society A: Mathematical, Physical and Engineering Sciences*, 461, 609–627, <https://doi.org/10.1098/rspa.2004.1350>, 2005.

Schoof, C.: Variational methods for glacier flow over plastic till, *J Fluid Mech*, 555, 299–320, <https://doi.org/10.1017/S0022112006009104>, 2006.

Schoof, C.: Ice sheet grounding line dynamics: Steady states, stability, and hysteresis, *J Geophys Res*, 112, F03S28, <https://doi.org/10.1029/2006JF000664>, 2007.

Seroussi, H., Nowicki, S., Simon, E., Abe-Ouchi, A., Albrecht, T., Brondex, J., Cornford, S., Dumas, C., Gillet-Chaulet, F., Goelzer, H., Golledge, N. R., Gregory, J. M., Greve, R., Hoffman, M. J., Humbert, A., Huybrechts, P., Kleiner, T., Larour, E., Leguy, G., Lipscomb, W. H., Lowry, D., Mengel, M., Morlighem, M., Pattyn, F., Payne, A. J., Pollard, D., Price, S. F., Quiquet, A., Reerink, T. J., Reese, R., Rodehacke, C. B., Schlegel, N. J., Shepherd, A., Sun, S., Sutter, J., Van Breedam, J., Van De Wal, R. S. W., Winkelmann, R., and Zhang, T.: InitMIP-Antarctica: An ice sheet model initialization experiment of ISMIP6, *Cryosphere*, 13, 1441–1471, <https://doi.org/10.5194/tc-13-1441-2019>, 2019.

Shackleton, S., Baggenstos, D., Menking, J. A., Dyonisius, M. N., Bereiter, B., Bauska, T. K., Rhodes, R. H., Brook, E. J., Petrenko, V. V., McConnell, J. R., Kellerhals, T., Häberli, M., Schmitt, J., Fischer, H., and Severinghaus, J. P.: Global ocean heat content in the Last Interglacial, *Nat Geosci*, 13, 77–81, <https://doi.org/10.1038/s41561-019-0498-0>, 2020.

Shackleton, S., Menking, J. A., Brook, E., Buizert, C., Dyonisius, M. N., Petrenko, V. V., Baggenstos, D., and Severinghaus, J. P.: Evolution of mean ocean temperature in Marine Isotope Stage 4, *Climate of the Past*, 17, 2273–2289, <https://doi.org/10.5194/cp-17-2273-2021>, 2021.

Shakun, J. D., Clark, P. U., He, F., Marcott, S. a., Mix, A. C., Liu, Z., Otto-Bliesner, B., Schmittner, A., and Bard, E.: Global warming preceded by increasing carbon dioxide concentrations during the last deglaciation, *Nature*, 484, 49–54, <https://doi.org/10.1038/nature10915>, 2012.

Shepherd, A., Ivins, E., Rignot, E., Smith, B., Van Den Broeke, M., Velicogna, I., Whitehouse, P., Briggs, K., Joughin, I., Krinner, G., Nowicki, S., Payne, T., Scambos, T., Schlegel, N., Geruo, A., Agosta, C., Ahlstrøm, A., Babonis, G., Barletta, V., Blazquez, A., Bonin, J., Csatho, B., Cullather, R., Felikson, D., Fettweis, X., Forsberg, R., Gallee, H., Gardner, A., Gilbert, L., Groh, A., Gunter, B., Hanna, E., Harig, C., Helm, V., Horvath, A., Horvath, M., Khan, S., Kjeldsen,

- K. K., Konrad, H., Langen, P., Lecavalier, B., Loomis, B., Luthcke, S., McMillan, M., Melini, D., Mernild, S., Mohajerani, Y., Moore, P., Mouginit, J., Moyano, G., Muir, A., Nagler, T., Nield, G., Nilsson, J., Noel, B., Otsuka, I., Pattle, M. E., Peltier, W. R., Pie, N., Rietbroek, R., Rott, H., Sandberg-Sørensen, L., Sasgen, I., Save, H., Scheuchl, B., Schrama, E., Schröder, L., Seo, K. W., Simonsen, S., Slater, T., Spada, G., Sutterley, T., Talpe, M., Tarasov, L., Van De Berg, W. J., Van Der Wal, W., Van Wessel, M., Vishwakarma, B. D., Wiese, D., and Wouters, B.: Mass balance of the Antarctic Ice Sheet from 1992 to 2017, *Nature*, 558, 219–222, <https://doi.org/10.1038/s41586-018-0179-y>, 2018.
- Simms, A. R., Lisiecki, L., Gebbie, G., Whitehouse, P. L., and Clark, J. F.: Balancing the last glacial maximum (LGM) sea-level budget, *Quat Sci Rev*, 205, 143–153, <https://doi.org/10.1016/j.quascirev.2018.12.018>, 2019.
- Stirling, C. H., Esat, T. M., Lambeck, K., and McCulloch, M. T.: Timing and duration of the Last Interglacial: Evidence for a restricted interval of widespread coral reef growth, *Earth Planet Sci Lett*, 160, 745–762, [https://doi.org/10.1016/S0012-821X\(98\)00125-3](https://doi.org/10.1016/S0012-821X(98)00125-3), 1998.
- Stone, E. J., Lunt, D. J., Annan, J. D., and Hargreaves, J. C.: Quantification of the Greenland ice sheet contribution to Last Interglacial sea level rise, *Climate of the Past*, 9, 621–639, <https://doi.org/10.5194/cp-9-621-2013>, 2013.
- Studinger, M., Bell, R. E., Blankenship, D. D., Finn, C. A., Arko, R. A., Morse, D. L., and Joughin, I.: Subglacial sediments: A regional geological template for iceflow in West Antarctica, *Geophys Res Lett*, 28, 3493–3496, <https://doi.org/10.1029/2000GL011788>, 2001.
- Tarasov, L., and Peltier, W. R.: Greenland glacial history, borehole constraints, and Eemian extent. *Journal of Geophysical Research: Solid Earth*, 108(B3), 2003.
- Tarasov, L. and Peltier, W. R.: A geophysically constrained large ensemble analysis of the deglacial history of the North American ice-sheet complex, *Quat Sci Rev*, 23, 359–388, <https://doi.org/10.1016/j.quascirev.2003.08.004>, 2004.
- Tarasov, L., Dyke, A. S., Neal, R. M., and Peltier, W. R.: A data-calibrated distribution of deglacial chronologies for the North American ice complex from glaciological modeling, *Earth Planet Sci Lett*, 315, 30–40, <https://doi.org/10.1016/j.epsl.2011.09.010>, 2012.
- Tarasov, L. and Goldstein, M.: Assessing uncertainty in past ice and climate evolution: overview, stepping-stones, and challenges, *Climate of the Past Discussion*, 1–54, <https://doi.org/10.5194/cp-2021-145>, 2021.

- Tarasov, L., Hank, K., Lecavalier, B. S., and Pollard, D.: The glacial systems model (GSM), [in preparation] 2024.
- Thompson, W. G., Allen Curran, H., Wilson, M. a., and White, B.: Sea-level oscillations during the last interglacial highstand recorded by Bahamas corals - Supplement, *Nat Geosci*, 4, 684–687, <https://doi.org/10.1038/ngeo1253>, 2011.
- Tsai, V. C., Stewart, A. L., and Thompson, A. F.: Marine ice-sheet profiles and stability under Coulomb basal conditions, *Journal of Glaciology*, 61, 205–215, <https://doi.org/10.3189/2015JoG14J221>, 2015.
- Tulaczyk, S., Kamb, W. B., and Engelhardt, H. F.: Basal mechanics of Ice Stream B, West Antarctica 2. Undrained plastic bed model, *J Geophys Res Solid Earth*, 105, 483–494, <https://doi.org/10.1029/1999jb900328>, 2000.
- Turney, C. S. M., Jones, R. T., McKay, N. P., Van Sebille, E., Thomas, Z. A., Hillenbrand, C. D., and Fogwill, C. J.: A global mean sea surface temperature dataset for the Last Interglacial (129-116&thinsp;ka) and contribution of thermal expansion to sea level change, *Earth Syst Sci Data*, 12, 3341–3356, <https://doi.org/10.5194/essd-12-3341-2020>, 2020.
- Venturelli, R. A., Boehman, B., Davis, C., Hawkings, J. R., Johnston, S. E., Gustafson, C. D., Michaud, A. B., Mosbeux, C., Siegfried, M. R., Vick-Majors, T. J., Galy, V., Spencer, R. G. M., Warny, S., Christner, B. C., Fricker, H. A., Harwood, D. M., Leventer, A., Priscu, J. C., and Rosenheim, B. E.: Constraints on the Timing and Extent of Deglacial Grounding Line Retreat in West Antarctica, *AGU Advances*, 4, <https://doi.org/10.1029/2022AV000846>, 2023.
- Vaughan, D. G., Comiso, J. C., Allison, I., Carrasco, J., Kaser, G., Kwok, R., Mote, P., Murray, T., Paul, F., Ren, J., Rignot, E., Solomina, O., Steffen, K., and Zhang, T.: Observations: Cryosphere, *Climate Change 2013: The Physical Science Basis. Contribution of Working Group I to the Fifth Assessment Report of the Intergovernmental Panel on Climate Change*, 317–382, <https://doi.org/10.1017/CBO9781107415324.012>, 2013.
- Weertman, J.: On the Sliding of Glaciers, *Journal of Glaciology*, 3, 33–38, <https://doi.org/10.3189/s0022143000024709>, 1957.
- Whitehouse, P. L., Bentley, M. J., and Le Brocq, A. M.: A deglacial model for Antarctica: Geological constraints and glaciological modelling as a basis for a new model of Antarctic glacial isostatic adjustment, *Quat Sci Rev*, 32, 1–24, <https://doi.org/10.1016/j.quascirev.2011.11.016>, 2012a.
- Whitehouse, P. L., Bentley, M. J., Milne, G. A., King, M. A., and Thomas, I. D.: A new glacial isostatic adjustment model for Antarctica: Calibrated and tested using

observations of relative sea-level change and present-day uplift rates, *Geophys J Int*, 190, 1464–1482, <https://doi.org/10.1111/j.1365-246X.2012.05557.x>, 2012b.

Wild, C. T., Alley, K. E., Muto, A., Truffer, M., Scambos, T. A., and Pettit, E. C.: Weakening of the pinning point buttressing Thwaites Glacier, West Antarctica, *Cryosphere*, 16, 397–417, <https://doi.org/10.5194/tc-16-397-2022>, 2022.

Winkelmann, R., Martin, M. A., Haseloff, M., Albrecht, T., Bueller, E., Khroulev, C., and Levermann, A.: The Potsdam Parallel Ice Sheet Model (PISM-PIK) - Part 1: Model description, *Cryosphere*, 5, 715–726, <https://doi.org/10.5194/tc-5-715-2011>, 2011.

Yau, A. M., Bender, M. L., Robinson, A., and Brook, E. J.: Reconstructing the last interglacial at Summit, Greenland: Insights from GISP2, *Proc Natl Acad Sci U S A*, 113, 9710–9715, <https://doi.org/10.1073/pnas.1524766113>, 2016.

Yu, H., Rignot, E., Morlighem, M., and Seroussi, H.: Iceberg calving of Thwaites Glacier, West Antarctica: Full-Stokes modeling combined with linear elastic fracture mechanics, *Cryosphere*, 11, 1283–1296, <https://doi.org/10.5194/tc-11-1283-2017>, 2017.

# Chapter 4: A history-matching analysis of the Antarctic Ice Sheet since the last interglacial – Part 2: Glacial isostatic adjustment

## Abstract

We present a glacial isostatic adjustment (GIA) analysis for a joint ice and GIA history matching of the Antarctic Ice Sheet (AIS) since the last interglacial. This was achieved using the Glacial Systems Model (GSM) – which includes a glaciological ice sheet model asynchronously coupled to a viscoelastic earth model. A large ensemble of 9,293 simulations was conducted using the GSM. The history matching was against the AntICE2 database, which includes observations of past relative sea level, present-day (PD) vertical land motion, past ice extent, past ice thickness, borehole temperature profiles, PD geometry and surface velocity (Lecavalier et al., 2023). The 38 ensemble parameters of the GSM were history matched using Markov Chain Monte Carlo sampling that in turn employed Bayesian Artificial Neural Network emulators. The implications on the evolution of the AIS are detailed in a companion paper which predominantly focuses on the ice sheet component (Lecavalier et al. 2024). The history-matching analysis identified simulations

from the full ensemble that are Not-Ruled-Out-Yet (NROY) by the data. This yielded a NROY sub-ensemble of simulations consisting of 82-members that approximately bound past and present GIA and sea-level change given uncertainties across the entire glacial system. The NROY Antarctic ice sheet and GIA results represent the Antarctic component of the “GLAC3” global ice sheet chronology which acts as a primary input to GIA models of sea-level change.

Data-model comparisons are shown against a subset of the AntICE2 database which directly constrains relative sea-level (RSL) change and GIA. A large variety of ice loading histories and Earth rheologies are evaluated against the available data. Significant spatial variability in Antarctic RSL and GIA are presented. The uncertainties affiliated with these inferences are large given the limited number of observational constraints which results in inferred RSL bounds with max/min ranges up to 150 m during the Holocene. Finally, estimates of PD rates of bedrock displacement with tolerance intervals are presented and compared against reference Antarctic GIA studies. These previous Antarctic GIA studies are key inputs for geodetic studies of the contemporary AIS mass balance. We demonstrate that by adequately exploring glacial and rheological uncertainties against a comprehensive database, past studies have underestimated Antarctic GIA uncertainties across vast regions, while other sectors are now more narrowly constrained. This history matching presents meaningful Antarctic GIA bounds of the rate of PD bedrock displacement with direct implications on mass balance estimates of the PD AIS.

## 4.1 Introduction

Large sectors of the Antarctic Ice Sheet (AIS) are undergoing accelerated mass loss (Seroussi et al., 2020; Masson-Delmotte et al., 2021). Of particular concern is that positive feedbacks can destabilize sectors of marine-based ice sheet, which raises concerns about the future evolution of the AIS (Pattyn and Morlighem, 2020; McKay et al., 2022). Even though the atmosphere and ocean directly influence AIS evolution, processes at the ice-bed interface can also dramatically impact ice dynamics. This is dictated by the basal environment which is characterized by several boundary conditions from basal topography, geothermal heat flux, and sediment distribution (Whitehouse et al., 2019). Moreover, the ice-bed interface is dynamic on a wide range of time-scales due to tectonic and volcanic activity, erosion and sedimentation, and glacial isostatic adjustment (GIA). GIA represents one of the key interactions between ice sheets and the solid Earth, which includes how the gravitational field and solid Earth respond to changes in ice and water load distribution. The GIA signal encompasses the continuous response of the solid Earth, gravity field, and relative sea-level to present and past ice sheet changes. Therefore, a robust understanding of GIA has implications on our understanding of AIS changes.

GIA can function as feedback that slows a potential unstable retreat of a marine-based ice sheet (Gomez et al., 2010, 2012, 2015; Konrad et al., 2015; Larour et al., 2019). The GIA component included in ice sheet models vary significantly in terms of complexity (de Boer et al., 2017; Whitehouse, 2018). AIS simulations have historically relied on a: simplified elastic lithosphere relaxed asthenosphere models GIA models (e.g. Huybrechts, 2002; DeConto and Pollard, 2016; Pattyn, 2017); 1D GIA models based on a depth varying

self-gravitating viscoelastic solid-Earth model (Whitehouse et al., 2012; Gomez et al., 2012; Briggs et al., 2013; Han et al., 2022) and 3D GIA models that account for lateral Earth structure (A et al., 2012; van derWal et al., 2015; Nield et al., 2018; Powell et al., 2021; Blank et al., 2021; Van Calcar et al., 2023).

To evaluate Antarctic GIA, one approach is to prescribe a predefined ice load history, although this neglects solid-ice sheet feedbacks on ice dynamics. A GIA model can be applied in series with ice sheet model output to produce higher fidelity GIA estimates than those computed exclusively within the ice sheet model (Whitehouse et al., 2012; Lecavalier et al., 2014). Finally, self-consistent Antarctic GIA predictions are based on a fully coupled GIA component with an ice sheet model (Gomez et al., 2013; Briggs et al., 2014; Konrad et al., 2015; Pollard et al., 2017; Gomez et al., 2018; Han et al., 2022; Van Calcar et al., 2023). Although the fully coupled approach is effective at evaluating ice sheet and solid Earth processes and their feedbacks, the computational cost associated with these simulations typically prevents an adequate exploration of uncertainties across the glacial system. This remains a challenge when dealing with coupled ice sheet and 3D Earth models since the computational resources required prohibits a large-ensemble data-constrained analysis to infer the actual Antarctic GIA history rather than simply studying model behaviour from a small sample of simulations. Moreover, past studies generally relied on the use of a few observational constraints to evaluate model performance (Gomez et al., 2013, 2018; Pollard et al., 2017; Konrad et al., 2015) and/or conducted a limited exploration of system-wide parametric uncertainties (Ivins and James, 2005; Whitehouse et al., 2012; Peltier et al., 2015). This directly limits the precise degree by which GIA or climate feedbacks might have actually impacted ice sheet instabilities in the actual past. Therefore,

it is important to evaluate models against an observational constraint database that jointly consider coupled feedbacks between ice sheets and GIA.

The interaction between the solid Earth and the AIS through GIA is dictated by the rate and magnitude of ice sheet changes, and Earth's rheological properties. However, beneath the Antarctic continent there are large variations in rheological properties of the mantle (Ritzwoller et al., 2001; Schaeffer and Lebedev, 2013; Heeszel et al., 2016; Shen et al., 2018; Lloyd et al., 2020). These rheological variations define the viscosity of the mantle and the subsequent relaxation timescales from a surface loading or unloading event. There are regions of apparently anomalously low upper mantle viscosities in the Antarctic Peninsula and Amundsen Sectors that experience a more rapid GIA response to mass loss relative to other Antarctic sectors (Nield et al., 2014; Barletta et al., 2018). This implies that the present-day (PD) viscous GIA signal in certain regions is possibly more dominated by ice sheet changes over the last several millennia rather than early deglacial ice sheet mass loss. As such, any approach to past inference of AIS evolution should account for this lateral variation in effective earth viscosity.

The contemporary mass balance of the Antarctic ice sheet is inferred using a variety of geodetic methods. Ice sheet changes can be monitored using satellite altimetry, radar imagery, optical imagery, and gravimetry (e.g. Mouginot et al., 2017; Gardner et al., 2018; Smith et al., 2020; Tapley et al., 2019; Velicogna et al., 2020; Sasgen et al., 2020). However, to infer the mass balance of the AIS using these methods, GIA estimates with meaningful uncertainty estimates are required (Shepherd et al., 2018; Otosaka et al., 2023). The Ice Sheet Mass Balance Inter-comparison Exercise (IMBIE) initially reconciled these various satellite methods (Shepherd et al., 2012, 2018) and has continued to provide mass

balance estimates extending to 2020 (Otosaka et al., 2023). By combining these different mass balance inference methodologies, uncertainties for both contemporary mass balance and contributions to sea-level rise are reduced. Uncertainties in Antarctic GIA dominate the contemporary mass balance confidence intervals. As of now, all these methods rely on Antarctic GIA models with limited attention to full system and observational uncertainties (Ivins and James, 2005; Whitehouse et al., 2012; Peltier et al., 2015). This limitation will propagate to the inferred magnitude of PD mass balance. These past reference GIA studies did not adequately consider system-model uncertainties when quantifying data-model scores. At best, a limited exploration of parametric uncertainties on a very narrow set of ice sheet and GIA model ensemble parameters was performed and no effort was done to quantify the considerable impact of model structural uncertainties. A data-constrained AIS and GIA model which accounts for complete uncertainties in the glacial system and Earth rheology is necessary to provide accurate bounds on contemporary mass balance of the AIS.

## 4.2 Model description

The GSM consists of comprehensive ice dynamic, climate forcing, and glacial isostatic components which are described in Tarasov et al. (submitted) and Lecavalier and Tarasov (2024). To summarize the GSM includes: Hybrid SIA-SSA ice physics; subgrid grounding line ice flux parameterization; dual power basal drag for hard bed and till sliding; ice shelf hydrofracturing and ice cliff failure; ocean temperature dependent sub ice shelf melt parameterization; subgrid ice shelf pinning point scheme; expanded climate forcing

scenarios. An illustration showing the key components of the GSM is found in Figure S1 of Lecavalier and Tarasov (2024).

The GSM is coupled to a glacial isostatic adjustment model of sea-level change based on a self-gravitating viscoelastic solid-Earth model which calculates GIA due to the redistribution of surface ice and ocean loads (Tarasov and Peltier, 1997). The Earth model rheology has a PREM density structure (Dziewonski and Anderson, 1981) and an ensemble parameter controlled three shell viscosity structure defined by the depth of the lithosphere, upper and lower mantle viscosity. The GIA component shares many similarities to that used in Whitehouse et al. (2012) for post-processing modelled ice sheet chronologies, however, our GIA component is asynchronously coupled to the ice sheet component and includes broader parametric uncertainties. Considering GIA operates on longer timescales, the GIA calculations are computed every 100 simulation years. To minimize the considerable computational cost of solving for a complete gravitationally self-consistent solution coupled with an ice sheet model (Gomez et al., 2010, 2013), a zeroth order geoidal approximation is used to account for the gravitational deflection of the sea surface. However, upon completing the full transient simulation, a gravitationally self-consistent solution is computed. The complete solutions are those that are compared against the GPS and RSL observations in Section 4.4. The continental scale transient Antarctic simulations over 205 ka have a 40 by 40 km horizontal resolution with the full sea-level solution having a spherical harmonic degree and order of 512.

As detailed in the accompanying study (Lecavalier and Tarasov, 2024), the Antarctic configuration of the GSM consists of 38 ensemble parameters. This represents the most comprehensive exploration of uncertainties across the entire Antarctic glacial

system of any study to date. A given simulation is defined by a parameter vector which consists of chosen values for each ensemble parameter. The ensemble parameters define the uncertainties in the climate forcing, mass balance, ice dynamics, and solid earth rheology. A total of three ensemble parameters defines the uncertainties in the viscosity profile of the solid Earth which directly impact GIA. Specifically, the lithospheric thickness, upper mantle viscosity, and lower mantle viscosity can respectively vary between 46 to 146 km,  $0.1 \cdot 10^{21}$  to  $5 \cdot 10^{21}$  Pa·s, and  $1 \cdot 10^{21}$  to  $90 \cdot 10^{21}$  Pa·s. GIA models simulate the response of the solid Earth due to present and past changes in surface loading from the redistribution of ice, water, and mantle material. The two primary inputs to a GIA model are a global ice chronology and the Earth rheology. In this study, the GSM simulates AIS changes over the last 2 glacial cycles to minimize initialization uncertainties propagating into the last interglacial start of our history-matching interval. The GSM relies on several eustatic global sea-level forcing time series (e.g. Lambeck et al., 2014; Lisiecki and Raymo, 2005) when performing joint ice sheet and GIA calculations.

## 4.3 Methodology

As part of the history-matching analysis conducted in this study, simulations are ruled out given their inconsistency with observational constraints. This involves a data-model comparison that accounts for both data-system and system-model uncertainties to accurately evaluate the performance of a simulation (Tarasov and Goldstein, 2021). The observational constraint database applied in this research is the Antarctic ICE sheet Evolution observational constraint database version 2 (AntICE2 database; Lecavalier et al., 2023). The AntICE2 database is to date the largest quality-curated database of Antarctic

paleo-data based on a variety of data types that can be leveraged to constrain various facets of the Antarctic glacial system. The AntICE2 database (Fig. 4.1) consists of observations of past RSL, ice sheet thickness, ice sheet extent and PD observations of land motion from GPS measurements, ice core borehole temperature profiles, ice sheet geometry (Bedmachine version 2 Morlighem et al., 2020) and surface velocity (Mouginot et al., 2019). The GSM simulations are scored against the highest quality data in the AntICE2 database, with a predominant focus on tier-1 and 2 data. Tier-1 data has the greatest power to constrain the ice sheet and GIA model and is deemed the highest quality data. Generally, tier-2 data provides more granular detail on past changes supplements tier-1 data. Tier-3 data correlates highly with the higher quality tier-1/2 data, therefore, it is excluded from the history-matching analysis and only used for visual comparison. In this study, the data-model comparison focuses on the RSL and GPS data given its relevance to GIA processes. All other data-model comparisons and discussions can be found in the accompanying study (Lecavalier and Tarasov, 2024) which specifically focuses on the glaciological evolution of the AIS.

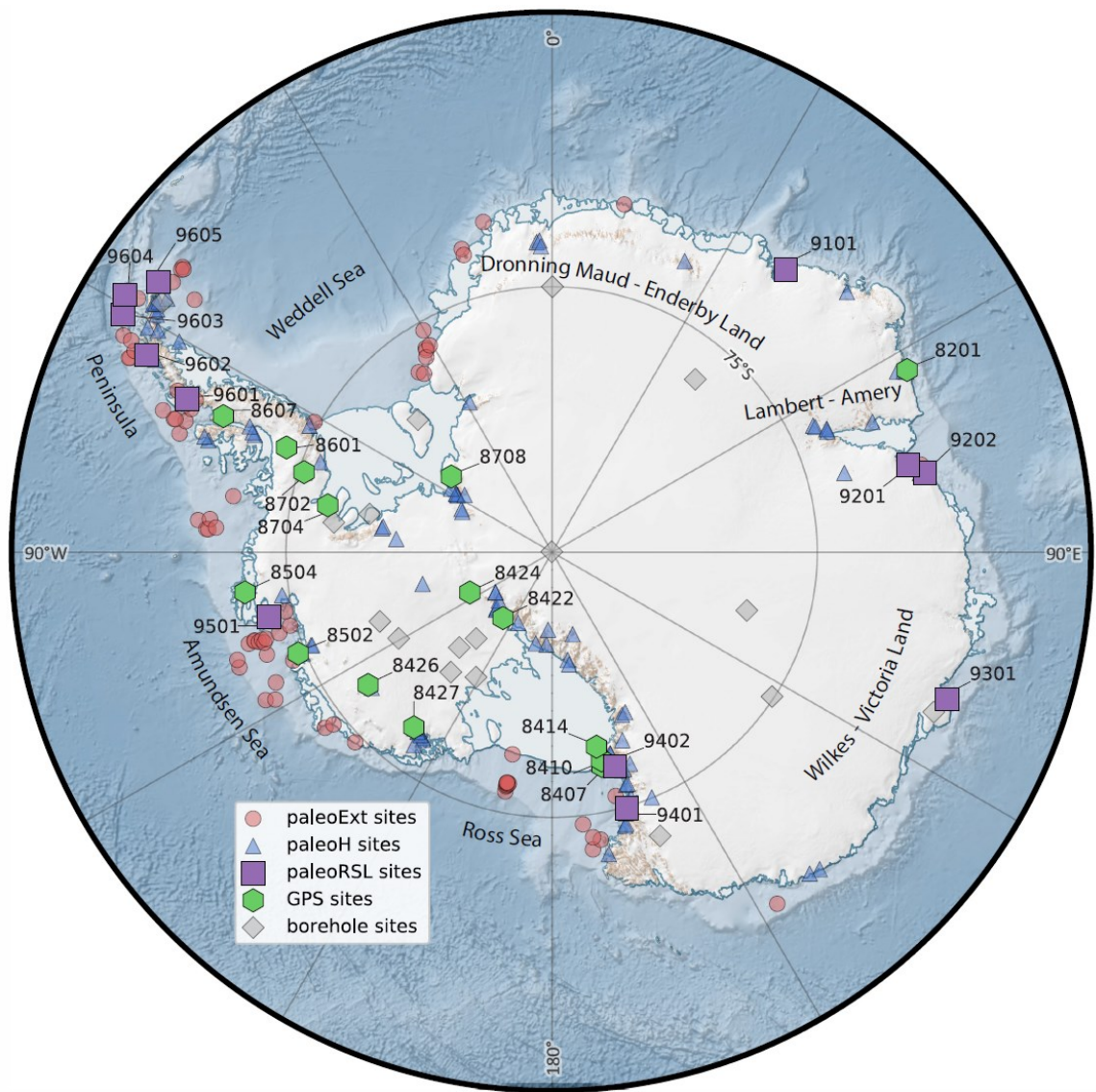


Figure 4.1: Antarctic continent and sector names mentioned in the study are shown alongside the Antarctic Ice sheet Evolution database version 2 (AntICE2) database (symbols). The data ID numbers for the paleoRSL and GPS data are shown. The remaining data ID information can be found in Figure 2 of Lecavalier et al. (2023). The Antarctic basemap was generated using Quantarctica (Matsuoka et al., 2021).

The paleoRSL and GPS data are inhomogeneously distributed across Antarctic in both space and time. The majority of the paleoRSL data spans the mid to late Holocene ages. The PD GPS measurements of bedrock displacement integrate the signal from several

processes that operate on various time scales. The integrated time scale of the viscous relaxation due to ice and ocean unloading or loading depends on the viscosity of mantle material underlying the GPS station. Therefore, the paleoRSL and GPS bedrock displacement data most meaningfully constrain the Holocene Antarctic GIA. There are few places in Antarctica that are deglaciated and preserved RSL proxy data. Similarly, there are a limited number of GPS observations which have a significant signal-to-noise ratio with a minimal elastic correction due to contemporary mass loss.

In this study we only provide a cursory overview of history matching, for a comprehensive description we point the reader to Tarasov and Goldstein, 2021 (a future submission will detail the exact methodology used here). This analysis yields a sub-ensemble of model simulations that are not-ruled-out-yet (NROY) by the data. The NROY sub-ensemble provides initial confidence intervals, minimum and maximum bounds on the probable evolution of the AIS and GIA since the last interglacial.

As part of this study, several large-ensemble data-constrained analyses were iteratively performed to evaluate the model's ability to bracket the AntICE2 observational constraint database (Lecavalier and Tarasov, 2024). GSM simulations were applied to supervised machine learning of Bayesian Artificial Neural Networks (BANNs) to create an emulator of the GSM to efficiently explore the parameter space. The history-matching methodology is diagrammatically illustrated in Figure S4 in Lecavalier and Tarasov, 2024. The ensemble parameter prior ranges are based on experimentation, previous studies, expert judgement, and are initially kept wide as to not pre-emptively neglect any potentially relevant regions of the parameter space. When comparing a simulation to data, we carefully characterize the error model which combines all the errors attributed to data-system

(measurement and indicative meaning uncertainties) and system-model (structural) uncertainties to produce a meaningful implausibility score (Tarasov and Goldstein, 2021; Lecavalier and Tarasov, 2024; Tarasov et al., in prep). This includes a 5% structural bias error for RSL and a 1 mm/yr to 0.5 mm/yr bias error for PD vertical uplift due to the use of a global 1D earth rheology instead of a 3D Earth rheology based on the discrepancies between corresponding results for regional 1D and 3D Earth modelling of Fennoscandia (Whitehouse et al., 2006; Whitehouse, 2009). However, a similar analysis for Antarctica is lacking.

As the robustness of history matching is predicated on complete sampling of the model parameter space, we use Markov Chain Monte Carlo (MCMC) to sample for the parameter vectors that are most likely to be consistent with the constraint data. To computationally enable the required multi-million-point MCMC sampling, GSM ensemble output is used for supervised training and validation of BANNs to establish computationally efficient emulators of the GSM. Many BANNs were trained to predict specific targets (e.g. grounded ice volume and area, past ice extent, ice thickness, RSL, GPS uplift rates) given parameter vectors as input and site coordinates. The BANN architectures that proved to be effective for these targets are detailed in Tarasov et al. (in prep). The BANN targets are key model metrics and/or specific predictions intended for data-model comparison. A sub-sample of parameter vectors from an order 100 set of MCMC converged sampling chains is in turn used to create an ensemble of GSM simulations. This combined MCMC and GSM ensemble iteration constitutes a “wave” of simulations that get added to the full ensemble.

The history-matching criteria rules out simulations with respect to the observations. As detailed in Tarasov and Goldstein (2021), a  $3\sigma$  of total uncertainty threshold is the minimum generally used in history matching (and can go as high as  $5\sigma$ ). This is achieved by comparing key metrics of interest and model output against observational constraints and ruling out simulations which are inconsistent with the constraint data. Our implausibility threshold for inconsistency is a simulation-data misfit score component value of between  $3\text{-}\sigma$  and  $4\text{-}\sigma$  of the total uncertainty (internal discrepancy, external discrepancy, and data uncertainty; see Table S1 in Lecavalier and Tarasov, 2024). In the case of the Antarctic GSM configuration, the primary metrics of interest were chosen to be: PD ice thickness root-mean-square-error for WAIS, EAIS, and floating ice; PD ice shelf area score; PD grounding-line position score along 5 transects; ice core borehole temperature profile score; GPS uplift rate score; past ice thickness score; past ice extent score; and past relative sea level score. To ensure an adequately sized NROY sub-ensemble,  $3\sigma$  of the total uncertainty threshold was applied on all data type scores except for the following: past ice extent ( $3.5\sigma$ ), floating ice RMSE ( $3.5\sigma$ ), and relative sea-level scores ( $4\sigma$ ). This gives an NROY set of 82 simulations (and corresponding parameter vectors). This larger allowance with these three scores was justified given the model struggles to bracket a few observations in these data types, which resulted in ruling out nearly all simulations if imposing a  $3\sigma$  threshold across all data types.

Previous ensembles of simulations were evaluated against the AntICE2 database and PD observations to verify that the observations are adequately bracketed by the GSM given uncertainties. This initially led to a revision of ensemble parameters, model developments, and revisions to certain BCs. Leading up to the final waves of ensembles,

over 30,000 model simulations were performed as part of previous experimentation, sensitivity analyses, Latin Hypercube, and beta fit sampling of ensemble parameters. In the results section, we present the latest iterations of large-ensemble results based on the history-matching analysis which consists of the final 9,293 simulations.

In addition to the history-matching analysis, an initial exploration on the potential impact of lateral Earth structure was conducted through a sensitivity analysis. Past studies have found that the spatially averaged upper mantle viscosity to be on the order of  $10^{20}$  to  $10^{21}$  Pa·s (Ivins and James, 2005; Whitehouse et al., 2012) which is within the range evaluated as part of the history-matching analysis. However, there are more recent estimates of an anomalously low upper mantle viscosity for the Antarctic Peninsula, Amundsen sector, and part of the Weddell and Ross Sea sector on the order of  $10^{18}$  to  $10^{19}$  Pas (Wolstencroft et al., 2015; Zhao et al., 2017; Barletta et al., 2018; Nield et al., 2018; Whitehouse et al., 2019). A high variance 17 member subset (HVSS) of simulations were selected from the NROY sub-ensemble according to key metrics of interest, such as the AIS grounded ice volume during the Last Glacial Maximum (LGM) (Figure S7 in Lecavalier and Tarasov, 2024). This also included selecting simulations with minimum scores to certain data types. The ice load chronologies from the 17 members of the NROY sub-ensemble HVSS were subject to repeated GIA post-processing over a range of Earth models. Specifically, the lithospheric thickness and upper mantle viscosity was progressively decreased to 46 km and  $5 \cdot 10^{18}$  Pa·s, respectively, to evaluate the impact of an anomalously low upper mantle viscosity on isostasy (Fig. S4.1 and S4.2). This experimental design isolates the Earth model sensitivity at the cost of lost dynamical self-consistency between the ice history and earth model.

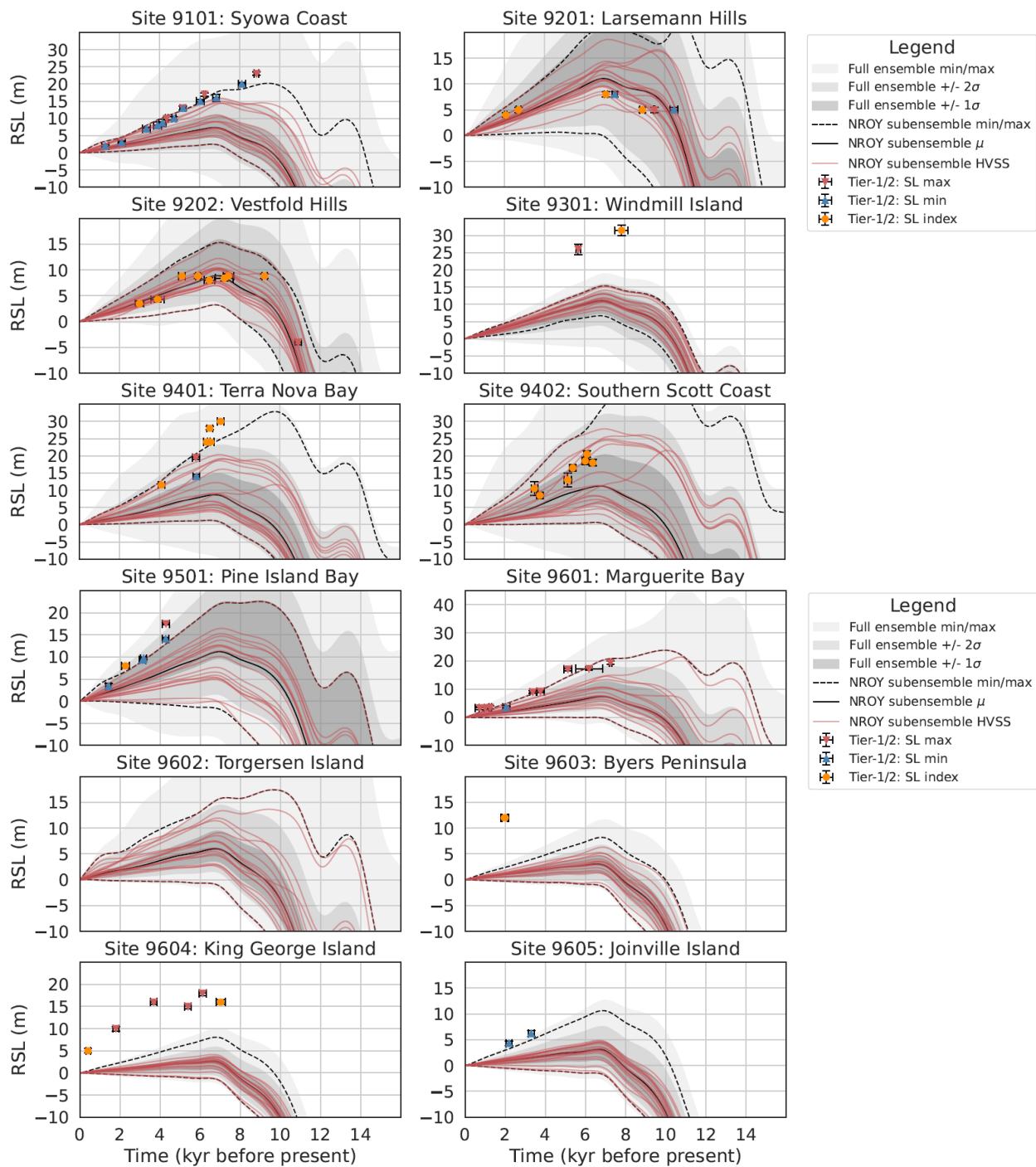


Figure 4.2: Paleo relative sea level data-model comparison where the grey shading are the full ensemble statistics. The solid and dashed black lines are the mean and min/max ranges for the not-ruled-out-yet (NROY) best fitting sub-ensemble. Simulations consisting of a high variance subset (HVSS) of the NROY sub-ensemble are shown in red. The  $2\sigma$  and  $1\sigma$  ranges are the nominal 95% and 68% ensemble intervals based on the equivalent Gaussian quantiles, respectively.

## 4.4 Results and Discussion

Below we present the full ensemble and NROY sub-ensemble against the AntICE2 observational constraints of most relevance to GIA: past RSL and elastic-corrected GPS measured rates of vertical land motion. Data-model comparison to the other constraints in AntICE2 are shown in Lecavalier and Tarasov (2024). The  $2\sigma$  and  $1\sigma$  ensemble ranges shown across several figures (e.g. Fig. 4.2-4.7) are the nominal 95% and 68% ensemble intervals based on the equivalent Gaussian quantiles (2.275 - 97.725%, Gaussian  $2\sigma$  quantiles and 15.866 - 84.134% Gaussian  $1\sigma$  quantiles).

There are a limited number of sites that record past RSL history across Antarctic and few sites with GPS measurements which are minimally contaminated by the elastic signal. There are considerably more observations that constrain the ice sheet evolution, thereby constraining the ice load history which acts as a primary input to GIA modelling. The other primary input is the Earth rheology which remains challenging to constrain given the limited observational constraints across a large spatial scale with inherent variation in lateral Earth structure. Data-model discrepancies are then due to some combination of the following: ice load history or Earth rheology, system-model uncertainties (e.g. lateral Earth structure), and data-system uncertainties (e.g. incorrect proxy indicative interpretation, underestimated elastic correction).

### 4.4.1 Data-model comparisons

There are a total of 12 sites across Antarctica that record past RSL change based on the quality curated data (Tier-1/2 quality data; Lecavalier et al., 2023). Figure 4.2 shows

the full ensemble and NROY sub-ensemble against tier-1 and tier-2 paleo RSL data. There is a direct trade-off between improving the fit to one data type versus another in the database. This results in simulations which perform very well against just a single data type (e.g. paleo RSL data) to be ruled out if it performs poorly against any other ( $>3\sigma$  threshold).

The full ensemble brackets the RSL site in Dronning Maud-Enderby Land (site 9101) within observational uncertainty. The NROY sub-ensemble is also able to bracket the majority of the RSL observations at the Syowa Coast except for the two limiting dates between 8 and 9 ka, which constrain the sea-level highstand in the region. The amplitude of the NROY sub-ensemble mean RSL at Syowa Coast is quite low as compared to the data. Only simulations in the NROY sub-ensemble with the highest amplitude fit the data. The NROY RSL simulations demonstrate a high level of correlation between simulations, albeit with a different amplitude. A change in Earth structure in the region does considerably impact the amplitude of RSL change and time of decay (Fig. S4.1). Therefore, lateral Earth structure that corresponds to a lower upper mantle viscosity can produce a RSL fall consistent with the data. Although, there is limited evidence of lateral structure in this region. This suggests the unloading history and magnitude of ice loss could be responsible for the discrepancy with the sea-level highstand data in this area. The exposure age data constraining the paleo ice thickness (paleoH) history in the region (i.e. site 1105:7 in Lecavalier and Tarasov, 2024) are all dated to the early to mid Holocene (9 to 6 ka). The NROY sub-ensemble bracket 6 of the 7 paleoH observations in the region. This highlights a potential issue in the climate forcing leading into the Holocene. For example, the ocean forcing drastically impacts the regional timing of unloading which leads to a RSL highstand of 15 meters above sea level (masl) at 7 ka instead of 20 masl at 8.5 ka. This combined with

poorly resolve subgrid features (subgrid till basal trough or pinning points) off the coast of Syowa could impact the timing and magnitude of RSL highstand in the region.

In the Lambert-Amery sector, there are two RSL sites east of the Amery ice shelf that are both bracketed by the full ensemble and NROY sub-ensemble which demonstrate a RSL highstand of 7 to 9 masl around 7 ka (site 9201 and 9202; Fig. 4.2). With only the oldest lower limiting date in Larsemann Hills (site 9201) being inconsistent with the NROY predictions. The area surrounding these two RSL sites is also constrained by a proximal to grounding line constraint with an age of 10.5 ka (site 2201) which are bracketed by the NROY sub-ensemble. Among the NROY RSL predictions, there are some simulations that demonstrate RSL oscillations, with one highstand peak at 9 ka and another at 7 ka, which mirror the RSL data at Larsemann Hills except at the wrong amplitude. Simulations that produce such RSL oscillations in the region using an alternate Earth rheology can dampen the RSL amplitude in line with observations based on the Earth model sensitivity analysis (Fig. S4.1).

The Wilkes-Victoria Land represents the region with the fewest observational constraints along the margin of the PD ice sheet. At Windmill Island (site 9301), a limiting sea-level date and index point suggests a sea-level highstand of ~30 meters at 8 ka which is not bracketed by either the full ensemble or NROY sub-ensemble. The NROY sub-ensemble produces a sea-level highstand at 7 ka between 7 to 16 masl which is half of the amplitude necessary to be consistent with the few observations in the region. Given the full ensemble does not achieve the necessary amplitude needed to capture the observations at Windmill Island regardless of the range of Earth rheology considered in the history-matching analysis and Earth model sensitivity analysis, the discrepancy can be attributed

to the ice load chronology. The region is poorly constrained with only the Law Dome borehole temperature profile which provides a minimal constraint on isostasy and ice unloading across the continental shelf. A broadening of viable ice reconstructions in the Windmill Island region is necessary to produce a larger ice unloading event over the deglaciation to match the observed sea-level amplitude. This suggests the climate forcing or basal conditions may lack the proper degrees of freedom to produce a sufficiently larger ice load in the region, and subsequent deglaciation timing to reach the observed sea-level highstand in the paleo RSL data.

Along the Transantarctic Mountains, there are two RSL records (site 9401 and 9402) which are bracketed by the full ensemble of RSL simulations. The NROY sub-ensemble brackets the sites except for the highest sea-level observations at Terra Nova Bay (9401). The region is topographically complex with subgrid valley glaciers that are poorly resolved in the GSM. This is a recurring challenge performing a data-model comparison to paleoH data in the region which can manifest in an inaccurate ice unloading history. Moreover, this region of the Transantarctic Mountains has an anomalous low viscosity zone in the upper mantle which has consequences on the viscous response to past load changes (Whitehouse et al., 2019). The NROY HVSS Earth model sensitivity analysis demonstrates that by lowering the upper mantle viscosity in this region, a more rapid viscous response to ice unloading can reach the peak observed RSL at Terra Nova Bay.

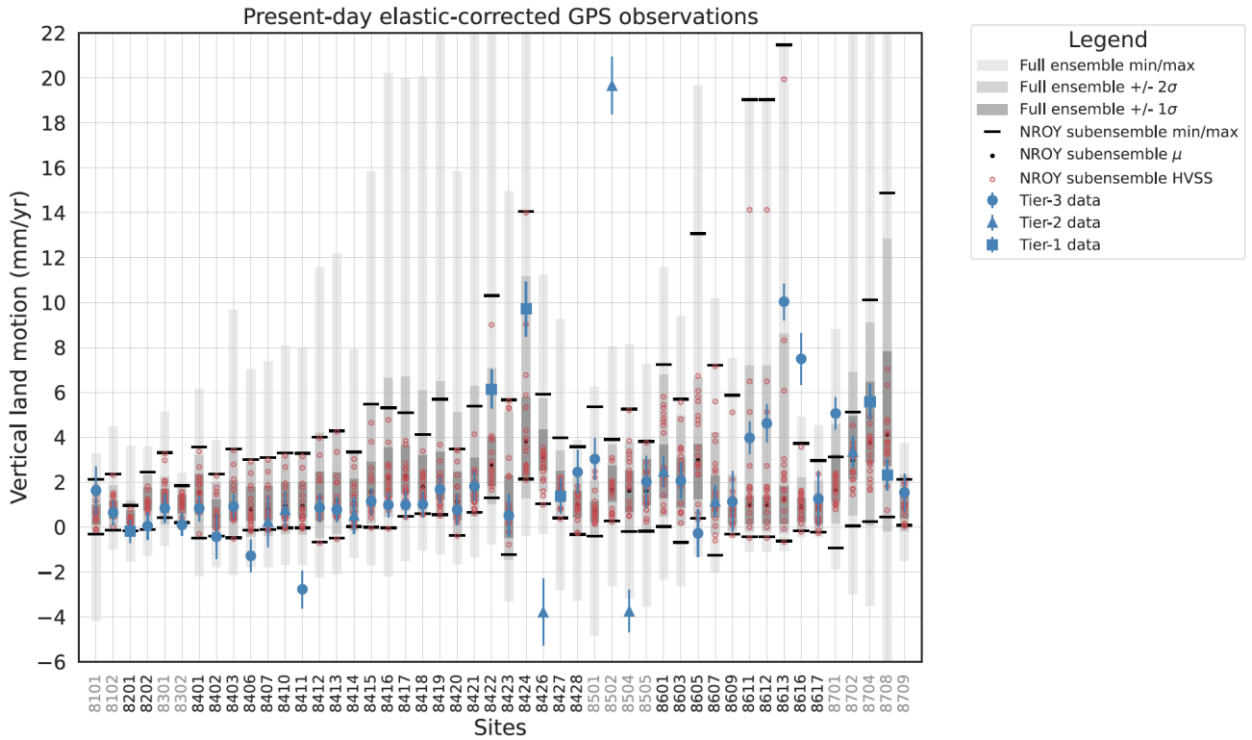


Figure 4.3: Global Positioning System elastic-corrected rate of bedrock displacement data-model comparison for tier-1/2/3 data in AntICE2. The grey shading represents the min/max,  $1\sigma$  and  $2\sigma$  ranges of the full ensemble. The solid black circles and lines are the mean and min/max ranges for the not-ruled-out-yet (NROY) sub-ensemble. Simulations consisting of a high variance subset (HVSS) of the NROY sub-ensemble are shown as red circles. The  $2\sigma$  and  $1\sigma$  ranges are the nominal 95% and 68% ensemble intervals based on the equivalent Gaussian quantiles, respectively.

In the Amundsen sector there is a RSL record which demonstrates rapid RSL fall of  $\sim 15$  m over 4 ka (Fig. 4.2). The NROY sub-ensemble narrowly fails to bracket the sea-level observations by the upper bound RSL predictions at Pine Island Bay by  $\sim 1$  m. The full ensemble does manage to bracket the RSL observations. As such, simulations that produce the appropriate amplitude of RSL fall at Pine Island Bay are ruled out when compared against the entirety of the AntICE2 database. The region has extensive paleoH/Ext observations, which points to issues with the Earth rheology in the region. Considering the region has lateral Earth structure with a lower viscosity with respect to the

interior of the WAIS, the amplitude and rate of RSL fall could be considerably impacted since the GSM operates with a spherically symmetric Earth model. A single viscosity profile is applied across Antarctica which biases regions that are data rich. The data rich sections in the AntICE2 database, particular with regards to RSL and GPS data, are in West Antarctica, Antarctic Peninsula, and Transantarctic mountains, which are coincidentally regions that have anomalous lateral viscosity structures (Whitehouse et al., 2019). Therefore, evaluating a coupled ice sheet and 3D GIA Earth model could delineate the potential GIA feedbacks impacting ice dynamics and ice mass loss in Pine Island Bay. However, the HVSS Earth model sensitivity analysis does not improve the fits at Pine Island Bay which suggests limitations with the NROY loading histories.

The remaining RSL data is in the Antarctic Peninsula (site 9601 to 9605) document a RSL fall of ~20m from the mid Holocene to present. Generally, the full ensemble and NROY sub-ensemble struggles to bracket some notable observations. The NROY sub-ensemble struggles to produce a rapid late Holocene RSL fall as reported at Byers Peninsula (9603), King George Island (9604), and Joinville Island (9605). The model does not appear to produce the necessary magnitude of mass loss sufficiently late to result in the GIA required to capture these late Holocene observations, regardless of the chosen viscosity structure (Fig. 4.2 and S4.1). This is particularly the case at Byers Peninsula and King George Island where there is a misfit of over 10 m at 2 ka and 8 m at 7 ka, respectively. This suggests the climate forcing enabling thick ice in the region also fails to appropriately deglaciate the local region late enough. Additionally, the regional topography consists of a poorly resolved subgrid archipelago. The data at site 9602 is not shown considering it is a singular low quality tier-3 data point. It is a max limiting age at ~7 m with large temporal

uncertainties ranging between 1.25 to 2.75 ka. This data suggests a similar, albeit poorly constrained rapid late Holocene RSL fall, like other RSL data in the region. However, the HVSS Earth model sensitivity analysis demonstrates that a dramatic late Holocene RSL fall exceeding 7 m can be produced using lower upper mantle viscosities (Fig. S4.1). This highlights that with a late Holocene unloading event, a rapid RSL fall of considerable amplitude is achievable in this region. Unfortunately, the necessary unloading events at the northern tip of the Antarctic Peninsula are not represented in the NROY sub-ensemble to the extent needed to address the outstanding discrepancies at site 9603, 9604, and 9605.

With respect to the elastic-corrected GPS observations of vertical land motion, the full ensemble and NROY sub-ensemble broadly bracket the observations (Fig. 4.3). Although there are a few exceptions, our focus will remain on the highest quality tier-1 and tier-2 data. The quality GPS data are predominantly located in the Ross Sea, Amundsen, Antarctic Peninsula, and Weddell Sea sectors, with a lone site in the Lambert-Amery sector. Tier-1 and tier-2 GPS observations that are not bracketed by the simulations tend to misfit both the full ensemble and NROY sub-ensemble at 3 distinct sites 8426, 8504, and 8502 in or near the Amundsen Sea sector. The Amundsen Sea sector has an anomalous low viscosity zone in the upper mantle which is not differentiated in the spherically symmetric GIA model. The HVSS Earth model sensitivity analysis does demonstrate that by considering a low upper mantle viscosity, elastic-corrected GPS predictions are captured at site 8406, 8411, 8504, 8616, and 8701 (Fig. S4.2) which are regions with inferred anomalously low viscosity structure. As the upper mantle viscosity is decreased by several orders of magnitude, this can significantly increase or decrease the amplitude of the GIA response depending on the temporal proximity of the unloading event. None of the HVSS

Earth model sensitivity simulations capture the GPS bedrock trends (-4 mm/yr at site 8426, and 19 mm/yr at site 8502; Fig. S4.2), even though such amplitudes are attainable at other sites. Alternatively, the elastic corrections applied to the GPS data could be underestimated, particularly given their full uncertainties are ill-defined with its limited reliance on the input contemporary mass balance estimates (Martín-Español et al., 2016; Sasgen et al., 2017). Negative vertical land motion at 8426 suggests regional loading not represented by the elastic correction and/or GSM simulations. Conversely, 8502 with its exceedingly high elastic-corrected uplift rate suggests significant mass loss in the late Holocene. This suggests that the GSM might have insufficient degrees of freedom in the regional climate forcing and basal environment to produce a sufficiently late ice load scenario to reconcile these remaining discrepancies.

## 4.4.2 Glacial isostatic adjustment model predictions

The history-matching result being the NROY sub-ensemble is a product of ruling out simulations that were inconsistent (within 3 to  $4\sigma$ ) with all the data types in the AntICE2 database. A given data type in the database constrains the Antarctic GIA ensemble results to various degrees since some data types are direct constraints on GIA (e.g. bedrock displacement) while others are indirect (e.g. load history). The NROY sub-ensemble brackets the majority of the AntICE2 database with some limited outstanding exceptions discussed above and in Lecavalier et al., (2024). The full ensemble is sieved on a data type basis which avoids the need for any inter data type weighing. History matching on its own does not produce a probabilistic distribution of chronologies. Throughout this study, we present the NROY sub-ensemble nominal  $2\sigma$  range since studies that apply GIA corrections

are typically interested in accounting for nominal  $2\sigma$  uncertainties. Moreover, by visualizing  $2\sigma$  ranges one avoid any one outlier simulation from dominating the visualization. However, these nominal ranges should not be confused with traditional Gaussian confidence intervals and the reader is encouraged to also consider the complete NROY sub-ensemble min and max GIA and RSL ranges shown in Figure S3-S6.

The NROY sub-ensemble spatial RSL bounds during the deglaciation are shown in Figure 4.4. The figure demonstrates the spatial variability in Antarctic RSL during the deglaciation. The NROY sub-ensemble RSL ranges (centre and rightmost columns of Fig. 4.4) can be quite wide considering how data-poor the Antarctic continent is in comparison to other currently or previously glaciated regions. Based on the NROY sub-ensemble mean, the range in RSL change surrounding the AIS during the local LGM ( $\sim 15$  ka) is -90 m off the continental shelf to 20 m near the Ronne-Filchner ice shelf grounding line (Fig. 4.4a). Similarly, spatial RSL variability during the Holocene for the NROY sub-ensemble mean range between -25 to 63 m (Fig. 4.4d). When comparing the  $2\sigma$  range surrounding the AIS, there are RSL differences of 200, 150, and 50 m at 15, 10, and 5 ka, respectively (Fig. 4.4). This emphasizes the large regional RSL uncertainties in the entire glacial system. The RSL mean and ranges of the NROY sub-ensemble reflects the regional AntICE2 data density which constrains the range of viable ice load histories and Earth rheologies. Some regions can only load so much ice during the LGM because of a limited continental shelf. This directly limits the maximum possible ice load in certain regions which impacts the subsequent deglacial GIA response.

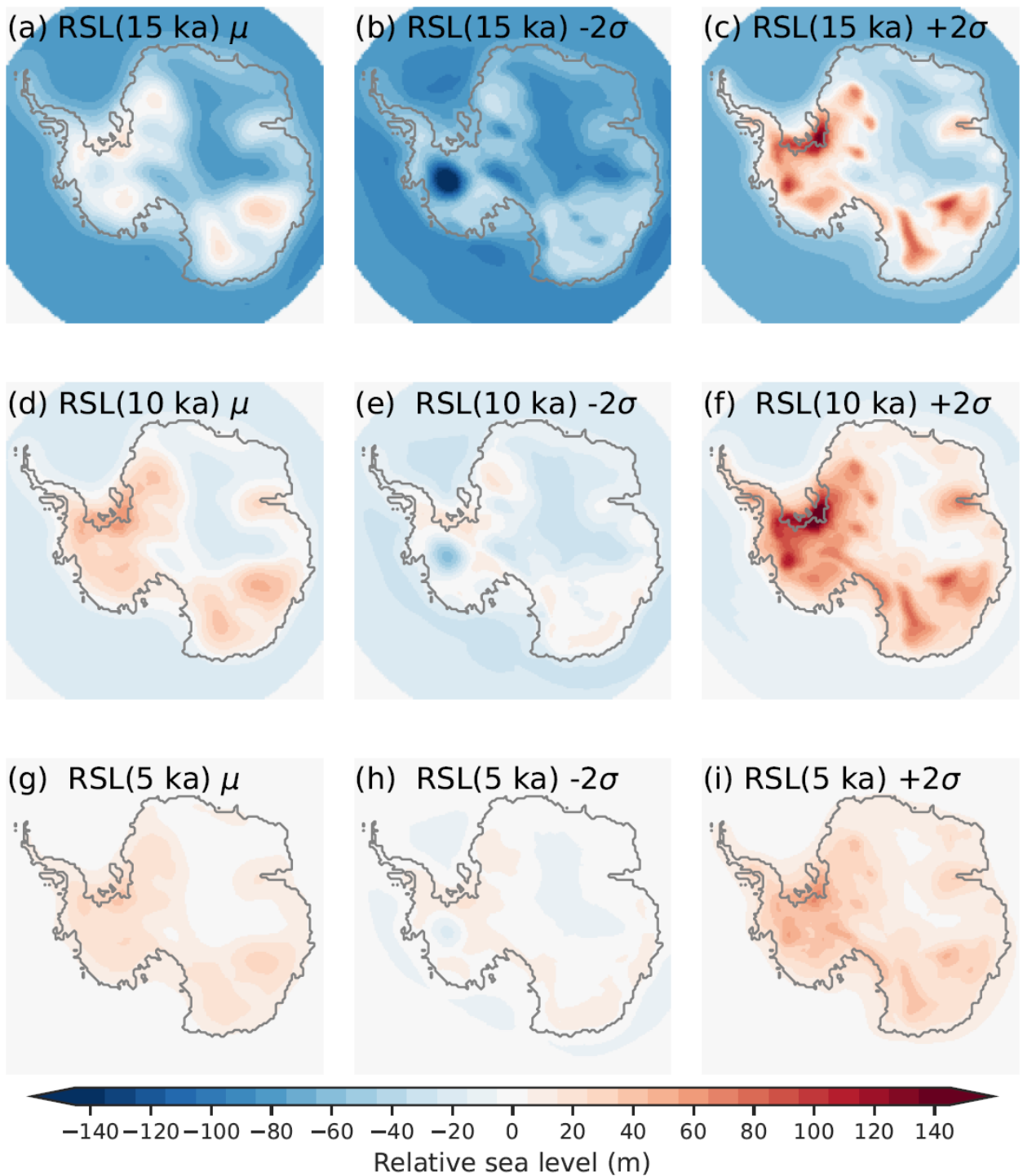


Figure 4.4: The not-ruled-out-yet (NROY) sub-ensemble mean (left), minus  $2\sigma$  (middle), and plus  $2\sigma$  (right) regional Antarctic RSL during the deglaciation at 15 ka (top), 10 ka (middle), and 5 ka (lower). The  $2\sigma$  ranges are the nominal 95% ensemble intervals based on the equivalent Gaussian quantiles.

The PD rate of vertical land and geoid displacement due to past changes in ice load demonstrate the background viscous GIA signal (Fig. 4.5 and Fig. 4.6). The range presented by the NROY sub-ensemble can be down to -3 mm/yr for wide regions in the interior of the EAIS or WAIS; conversely, they can be beyond 10 mm/yr across the WAIS. A few reference simulations (RefSim1 = nn61639, RefSim4 = nn63807, RefSim5 = nn64802) are shown in Figure 4.5 and Figure 4.6 to convey GIA estimates at PD based on individual simulations rather than solely presenting sub-ensemble statistics. The reference simulations are all in the NROY sub-ensemble, where RefSim1 has the minimum score across all the data types in AntICE2, RefSim4 has the minimum GPS score, and RefSim5 has the joint minimum score across all the paleo data types in AntICE2.

The NROY sub-ensemble demonstrates the wide range of viable PD GIA uplift rate estimates when one accounts for uncertainties across the entire glacial system and data-constrain a model against a comprehensive observational constraint database. There are three primary GIA reference models (IJ05\_R2 - Ivins and James, 2005; W12a - Whitehouse et al., 2012; ICE-6G\_D - Peltier et al., 2015) applied across the IMBIE studies (Shepherd et al., 2018; Otosaka et al., 2023). These three reference GIA models have been used to produce a minimum and maximum range that represent nominal  $2\sigma$  bounds on the PD GIA corrections when inferring contemporary AIS mass balance (Fig. 4.7). Comparison of these bounds with those from our history matching (Fig. 4.7) arguably provides an indication of where IMBIE GIA uncertainties are over and under estimated. The most prominent area where the reference GIA models have underestimated PD uplift rate uncertainties are in the Amundsen sector (Fig. 4.7d). This area suggests that uplift rates can exceed 10 mm/yr (Fig. 4.5c) which is not captured by the three reference GIA models (Fig. 4.7b). This corresponds

to a negative geoid trend of -2.5 mm/yr across the Amundsen sector due to continued late Holocene mass loss (Fig. 4.6b). This is expected given the three reference GIA models were not designed to assess predictive uncertainties. Moreover, significantly more observational constraints have been collected in the Amundsen sector since the three reference GIA models were originally published. This includes past ice extent data along the Pine Island-Thwaites paleo-ice stream trough, and past ice thickness data near the Pine Island and Thwaites glacier (Fig. 4.1). Elastic-corrected GPS observations in the Amundsen sector indicate an uplift rate of  $\sim 20$  mm/yr (site 8502). Finally, the latest RSL observations near Pine Island Bay propose a late and significant sea-level fall over the mid to late Holocene (site 9501 - Braddock et al., 2022) with implications on PD GIA estimates. Considering that at present, the Amundsen sector is undergoing by far the most mass loss across Antarctica (Shepherd et al., 2018; Otosaka et al., 2023), our revised PD GIA estimates and uncertainty range has significant consequences on the inference of the magnitude of mass loss across the West Antarctica and its corresponding confidence intervals.

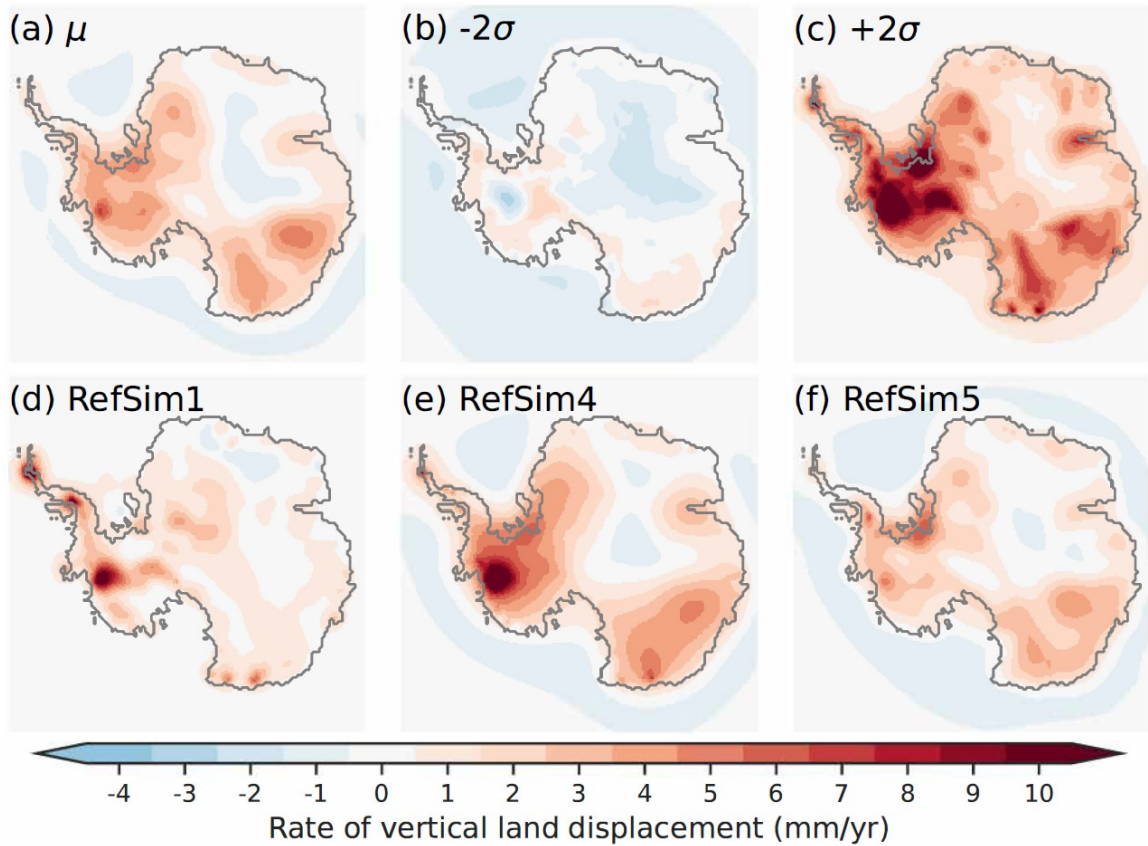


Figure 4.5: Present-day rate of bedrock displacement for the not-ruled-out-yet (NROY) sub-ensemble a) mean, b-c) minus and plus  $2\sigma$ . Three glaciology self-consistent simulations chosen from a NROY high variance subset (HVSS): d) RefSim1 (NROY member with minimum score across all the data types in AntICE2); e) RefSim4 (NROY member with minimum GPS score); f) RefSim5 (NROY member with joint minimum score across all the paleo data types in AntICE2). The  $2\sigma$  ranges are the nominal 95% ensemble intervals based on the equivalent Gaussian quantiles.

The NROY sub-ensemble HVSS Earth model sensitivity analysis resulted in 153 simulations that were compared to the RSL and elastic corrected GPS observations to assess whether heterogeneity in Earth structure can potentially explain any outstanding discrepancies. This HVSS Earth model sensitivity analysis reveals that some of the previous RSL and GPS data not bracketed by the NROY sub-ensemble are captured if one considers an alternate regional Earth rheology (Fig. S4.1 and S4.2). The potentially rectification of some data-model discrepancies by an anomalously low upper mantle

viscosity does not mean that the NROY sub-ensemble suddenly brackets this data. It simply demonstrates the plausibility that lateral Earth structure could reconcile some of these data-model discrepancies. Based on the Earth model sensitivity analysis, a more appropriate structural error is needed to study Antarctica GIA when using a 1D Earth model since the current specification is based on the discrepancies between 1D and 3D Earth models for Fennoscandia which appear to be significantly smaller than for Antarctica. To better address this question will require a more involved specification of the structural uncertainty attributed to lateral Earth structure or a history-matching analysis with a coupled 3D GIA Earth model. Moreover, the upper mantle viscosity sensitivity analysis shows that regions with a low viscosity zone can exhibit significant sensitivity to recent loading or unloading. Thus, the NROY sub-ensemble GIA predictions likely underestimate the uplift and geoid rate bounds in specific regions with anomalous viscosity structure. Addressing these issues in future research is critical since GIA corrections and their uncertainties are used to infer contemporary AIS mass balance.

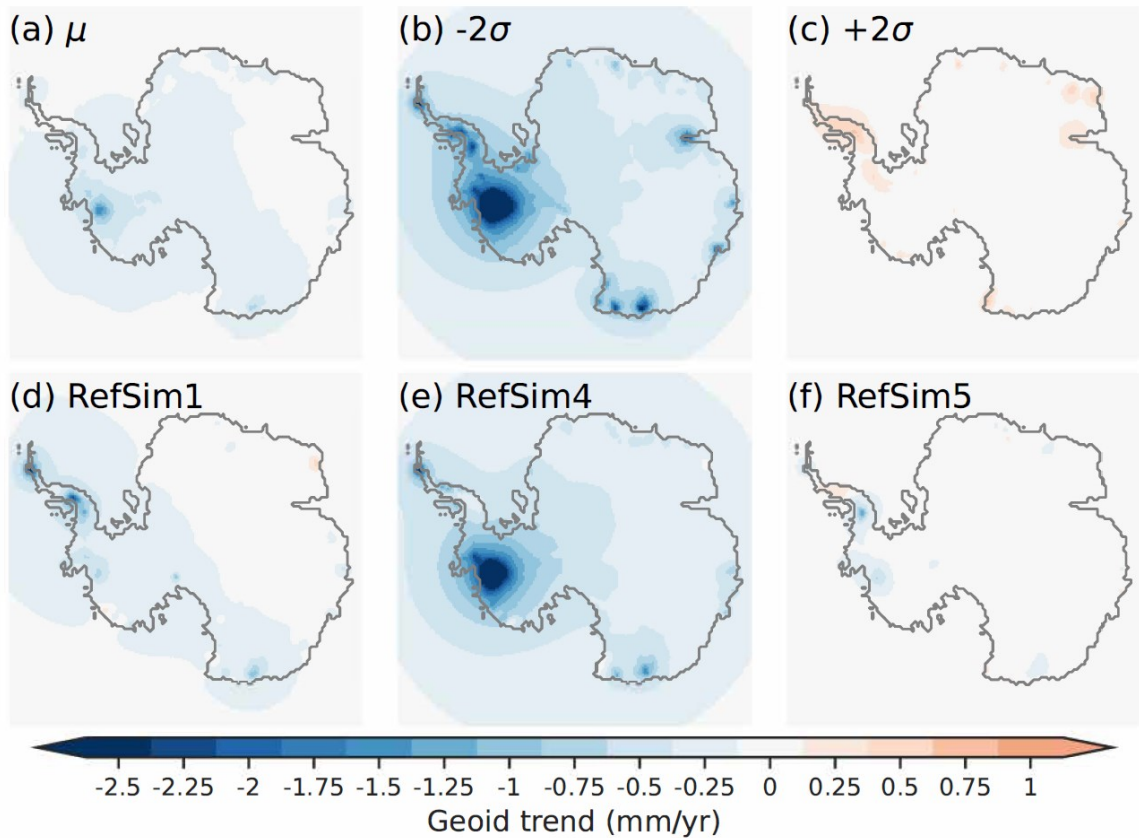


Figure 4.6: Present-day Antarctic rate of geoid displacement for the not-ruled-out-yet (NROY) sub-ensemble a) mean, b-c) minus and plus  $2\sigma$ . The geoid trend presented above only includes the Antarctic contribution to geoid perturbations and does not include global eustatic contributions. Three glaciology self-consistent simulations chosen from a NROY high variance subset (HVSS): d) RefSim1 (NROY member with minimum score across all the data types in AntICE2); e) RefSim4 (NROY member with minimum GPS score); f) RefSim5 (NROY member with joint minimum score across all the paleo data types in AntICE2). The  $2\sigma$  ranges are the nominal 95% ensemble intervals based on the equivalent Gaussian quantiles.

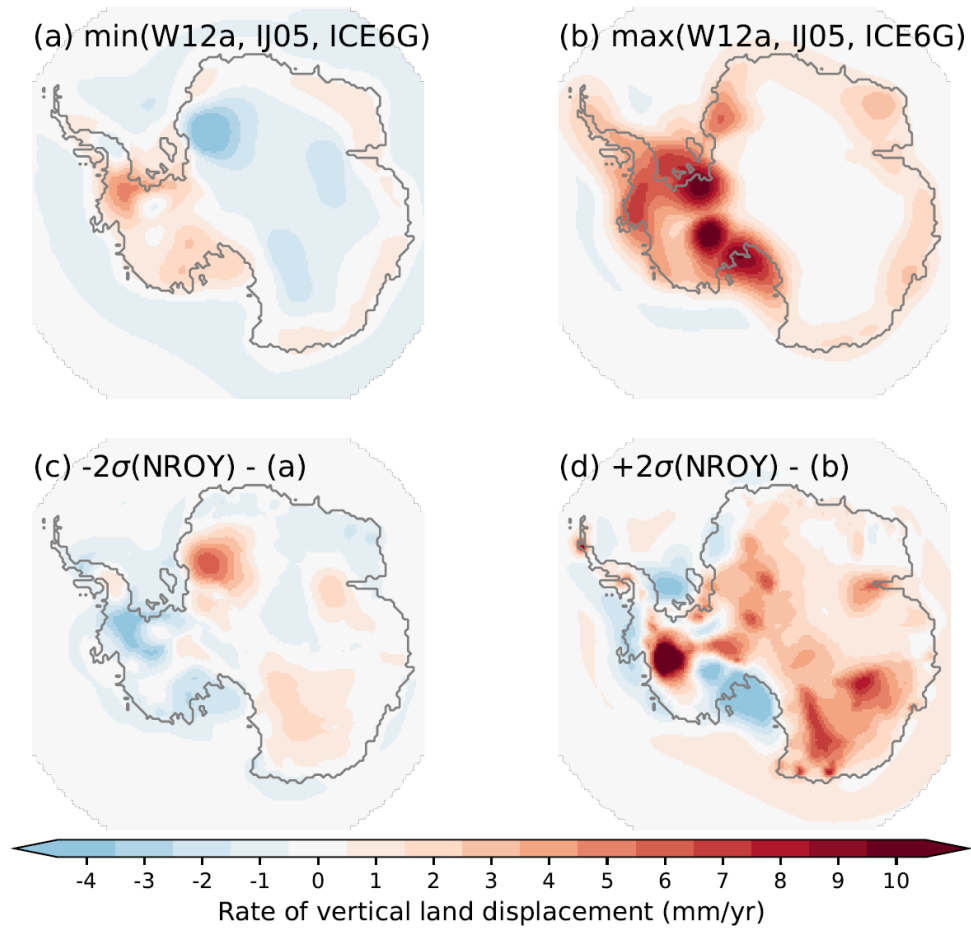


Figure 4.7: The (a) minimum and (b) maximum bounds for the PD rate of bedrock displacement for the three reference Antarctic GIA models (IJ05\_R2 - Ivins and James, 2005; W12a - Whitehouse et al., 2012; ICE-6G\_D - Peltier et al., 2015). These three GIA models represent nominal  $2\sigma$  bounds on the PD GIA corrections applied in the IMBIE studies to infer contemporary mass balance of the AIS. (Shepherd et al., 2018; Ootosaka et al., 2023). The not-ruled-out-yet (NROY) sub-ensemble  $2\sigma$  (c) lower and (d) upper bounds minus the respective bounds of the three reference GIA models. The differences shown in (c) and (d) demonstrate regions where the three reference GIA models underestimate PD GIA uncertainties or where the NROY sub-ensemble better constrain the regional GIA response relative to the three reference GIA models.

## 4.5 Conclusion

In this study an Antarctic GIA model is presented based on a history-matching analysis of the GSM against the AntICE2 database. The fully coupled glaciological and

GIA model was used to generate a full ensemble consisting of 9,292 Antarctic simulations spanning the last 2 glacial cycles. BANNs were trained to emulate the GSM for rapid exploration of the parameter space via MCMC sampling. Simulation results were scored against past relative sea level, PD vertical land motion, past ice extent, past ice thickness, borehole temperature profiles, PD geometry and surface velocity. The scores were used in the history-matching analysis to rule out simulations that were inconsistent with the data given observational and structural uncertainties, thereby a NROY sub-ensemble (N=82) that bound past and present GIA and sea-level change was generated. The NROY sub-ensemble of AIS results represent a collection of not-ruled-out-yet Antarctic components for the global GLAC3 ice sheet chronology.

The NROY sub-ensemble AIS chronologies represent the Antarctic component in the GLAC global ice sheet chronology. This research enables the upcoming evaluation of global RSL predictions and the Antarctic far-field sea-level contributions during the last interglacial, LGM, and deglacial melt water pulses. The AIS NROY sub-ensemble chronologies are constrained by near-field observations. Evaluating the updated global ice sheet chronology against far-field RSL observations would in turn constrain the AIS NROY sub-ensemble by said far-field data, potentially ruling out additional AIS simulations that are currently in the NROY sub-ensemble. This future work could leverage 3D Earth GIA models to formally evaluate lateral Earth structure and its impact on far-field and near-field RSL predictions.

Given that our history matching accounts for data-system and system-model uncertainties to a much deeper extent than any previous AIS study, the NROY sub-ensemble provides the most credible bounds to date on actual Antarctic GIA. As such, our

analysis demonstrates that previous Antarctic GIA studies have underestimated PD uplift rates across several key regions. This is particularly the case in the Amundsen sector, an area currently undergoing significant mass loss, which has a large range of viable PD GIA estimates. Our NROY set of chronologies will therefore facilitate more accurate inference of the PD mass balance of the AIS, including for vulnerable marine-based regions.

## 4.6 Author Contributions

B.S.L. and L.T. led and designed the study. B.S.L. wrote the manuscript with editorial input from L.T., B.S.L. and L.T. ran the model simulations, processed the dataset and simulation output. B.S.L. and L.T. performed the data-model analysis. L.T. conducted the BANN training and MCMC sampling. B.S.L. visualized the model results.

## 4.7 References

- Barletta, V. R., Bevis, M., Smith, B. E., Wilson, T., Brown, A., Bordoni, A., Willis, M., Abbas Khan, S., Rovira-Navarro, M., Dalziel, I., Smalley, R., Kendrick, E., Konfal, S., Caccamise II, D. J., Aster, R. C., Nyblade, A., and Wiens, D. A.: Observed rapid bedrock uplift in Amundsen Sea Embayment promotes ice-sheet stability, *Science* (1979), 360, 1335–1339, 2018.
- de Boer, B., Stocchi, P., Whitehouse, P. L., and van de Wal, R. S. W.: Current state and future perspectives on coupled ice-sheet – sea-level modelling, <https://doi.org/10.1016/j.quascirev.2017.05.013>, 1 August 2017.
- Braddock, S., Hall, B. L., Johnson, J. S., Balco, G., Spoth, M., Whitehouse, P. L., Campbell, S., Goehring, B. M., Rood, D. H., and Woodward, J.: Relative sea-level data preclude major late Holocene ice-mass change in Pine Island Bay, *Nat Geosci*, 15, 568–572, <https://doi.org/10.1038/s41561-022-00961-y>, 2022.
- Briggs, R., Pollard, D., & Tarasov, L.: A glacial systems model configured for large ensemble analysis of Antarctic deglaciation, *Cryosphere*, 7(6), 1949–1970, <https://doi.org/10.5194/tc-7-1949-2013>, 2013.

- Briggs, R. D., Pollard, D., & Tarasov, L.: A data-constrained large ensemble analysis of Antarctic evolution since the Eemian, *Quaternary Science Reviews*, 103, 91–115, <https://doi.org/10.1016/j.quascirev.2014.09.003>, 2014.
- Van Calcar, C. J., Van De Wal, R. S. W., Blank, B., De Boer, B., and Van Der Wal, W.: Simulation of a fully coupled 3D glacial isostatic adjustment - ice sheet model for the Antarctic ice sheet over a glacial cycle, *Geosci Model Dev*, 16, 5473–5492, <https://doi.org/10.5194/gmd-16-5473-2023>, 2023.
- DeConto, R. M. and Pollard, D.: Contribution of Antarctica to past and future sea-level rise, *Nature*, 531, 591–597, <https://doi.org/10.1038/nature17145>, 2016.
- Dziewonski, A. M. and Anderson, D. L.: Preliminary reference Earth model, *Physics of the Earth and Planetary Interiors*, 25, 297–356, [https://doi.org/10.1016/0031-9201\(81\)90046-7](https://doi.org/10.1016/0031-9201(81)90046-7), 1981.
- Gardner, A. S., Moholdt, G., Scambos, T., Fahnestock, M., Ligtenberg, S., Van Den Broeke, M., and Nilsson, J.: Increased West Antarctic and unchanged East Antarctic ice discharge over the last 7 years, *Cryosphere*, 12, 521–547, <https://doi.org/10.5194/tc-12-521-2018>, 2018.
- Gomez, N., Mitrovica, J. X., Huybers, P., and Clark, P. U.: Sea level as a stabilizing factor for marine-ice-sheet grounding lines, *Nat Geosci*, 3, 850–853, <https://doi.org/10.1038/ngeo1012>, 2010.
- Gomez, N., Pollard, D., Mitrovica, J. X., Huybers, P., and Clark, P. U.: Evolution of a coupled marine ice sheet-sea level model, *J Geophys Res Earth Surf*, 117, <https://doi.org/10.1029/2011JF002128>, 2012.
- Gomez, N., Pollard, D., and Mitrovica, J. X.: A 3-D coupled ice sheet - sea level model applied to Antarctica through the last 40 kyr, *Earth Planet Sci Lett*, 384, 88–99, <https://doi.org/10.1016/j.epsl.2013.09.042>, 2013.
- Gomez, N., Pollard, D., and Holland, D.: Sea-level feedback lowers projections of future Antarctic Ice-Sheet mass loss, *Nat Commun*, 6, <https://doi.org/10.1038/ncomms9798>, 2015.
- Gomez, N., Latychev, K., and Pollard, D.: A Coupled Ice Sheet-Sea Level Model Incorporating 3D Earth Structure: Variations in Antarctica during the Last Deglacial Retreat, *J Clim*, 31, 4041–4054, <https://doi.org/10.1175/JCLI-D-17>, 2018.
- Han, H. K., Gomez, N., and Wan, J. X. W.: Capturing the interactions between ice sheets, sea level and the solid Earth on a range of timescales: A new “time window” algorithm, *Geosci Model Dev*, 15, 1355–1373, <https://doi.org/10.5194/gmd-15-1355-2022>, 2022.

- Heeszel, D. S., Wiens, D. A., Anandakrishnan, S., Aster, R. C., Dalziel, I. W. D., Huerta, A. D., Nyblade, A. A., Wilson, T. J., and Winberry, J. P.: Upper mantle structure of central and West Antarctica from array analysis of Rayleigh wave phase velocities, *J Geophys Res Solid Earth*, 121, 1758–1775, <https://doi.org/10.1002/2015JB012616>, 2016.
- Huybrechts, P.: Sea-level changes at the LGM from ice-dynamic reconstructions of the Greenland and Antarctic ice sheets during the glacial cycles, *Quaternary Science Reviews*, 203–231 pp., 2002.
- Ivins, E. R. and James, T. S.: Antarctic glacial isostatic adjustment: A new assessment, <https://doi.org/10.1017/S0954102005002968>, December 2005.
- Konrad, H., Sasgen, I., Pollard, D., and Klemann, V.: Potential of the solid-Earth response for limiting long-term West Antarctic Ice Sheet retreat in a warming climate, *Earth Planet Sci Lett*, 432, 254–264, <https://doi.org/10.1016/j.epsl.2015.10.008>, 2015.
- Lambeck, K., Rouby, H., Purcell, A., Sun, Y., and Sambridge, M.: Sea level and global ice volumes from the Last Glacial Maximum to the Holocene, *Proc Natl Acad Sci U S A*, 111, 15296–15303, <https://doi.org/10.1073/pnas.1411762111>, 2014.
- Larour, E., Seroussi, H., Adhikari, S., Ivins, E., Caron, L., Morlighem, M., and Schlegel, N.: Slowdown in Antarctic mass loss from solid Earth and sea-level feedbacks, *Science* (1979), 364, <https://doi.org/10.1126/science.aav7908>, 2019.
- Lisiecki, L. E., and Raymo, M. E.: A Pliocene-Pleistocene stack of 57 globally distributed benthic  $\delta^{18}\text{O}$  records. *Paleoceanography*, 20(1), 2005.
- Lecavalier, B. S., Milne, G. A., Simpson, M. J. R., Wake, L., Huybrechts, P., Tarasov, L., Kjeldsen, K. K., Funder, S., Long, A. J., Woodroffe, S., Dyke, A. S., and Larsen, N. K.: A model of Greenland ice sheet deglaciation constrained by observations of relative sea level and ice extent, *Quat Sci Rev*, 102, 54–84, <https://doi.org/10.1016/j.quascirev.2014.07.018>, 2014.
- Lecavalier, B. S., Tarasov, L., Balco, G., Spector, P., Hillenbrand, C. D., Buizert, C., Ritz, C., Leduc-Leballeur, M., Mulvaney, R., Whitehouse, P. L., Bentley, M. J., and Bamber, J.: Antarctic Ice Sheet paleo-constraint database, *Earth Syst Sci Data*, 15, 3573–3596, <https://doi.org/10.5194/essd-15-3573-2023>, 2023.
- Lecavalier, B. S. and Tarasov, L.: A history-matching analysis of the Antarctic Ice Sheet since the last interglacial – Part 1: Ice sheet evolution, *EGUsphere* [preprint], <https://doi.org/10.5194/egusphere-2024-1291>, 2024.

- Lloyd, A. J., Wiens, D. A., Zhu, H., Tromp, J., Nyblade, A. A., Aster, R. C., Hansen, S. E., Dalziel, I. W. D., Wilson, T. J., Ivins, E. R., and O'Donnell, J. P.: Seismic Structure of the Antarctic Upper Mantle Imaged with Adjoint Tomography, *J Geophys Res Solid Earth*, 125, <https://doi.org/10.1029/2019JB017823>, 2020.
- Martín-Español, A., Zammit-Mangion, A., Clarke, P. J., Flament, T., Helm, V., King, M. A., Luthcke, S. B., Petrie, E., Rémy, F., Schön, N., Wouters, B., and Bamber, J. L.: Spatial and temporal Antarctic Ice Sheet mass trends, glacio-isostatic adjustment, and surface processes from a joint inversion of satellite altimeter, gravity, and GPS data, *J Geophys Res Earth Surf*, 121, 182–200, <https://doi.org/10.1002/2015JF003550>, 2016.
- Masson-Delmotte, V., Zhai, P., Chen, Y., Goldfarb, L., Gomis, M. I., Matthews, J. B. R., Berger, S., Huang, M., Yelekçi, O., Yu, R., Zhou, B., Lonnoy, E., Maycock, T. K., Waterfield, T., Leitzell, K., and Caud, N.: Working Group I Contribution to the Sixth Assessment Report of the Intergovernmental Panel on Climate Change Edited by, <https://doi.org/10.1017/9781009157896>, 2021.
- Matsuoka, K., Skoglund, A., Roth, G., De Pomereu, J., Griffiths, H., Headland, R., Herried, B., Katsumata, K., Le Brocq, A., Licht, K., Morgan, F., Neff, P. D., Ritz, C., Scheinert, M., Tamura, T., Van De Putte, A., Van Den Broeke, M., Von Deschwanden, A., Deschamps-Berger, C., Liefveringe, B. Van, Tronstad, S., and Melvaer, Y.: Quantarctica, an integrated mapping environment for Antarctica, the Southern Ocean, and sub-Antarctic islands, <https://doi.org/10.21334/npolar.2018.8516e961>, 2021.
- McKay, D. I. A., Staal, A., Abrams, J. F., Winkelmann, R., Sakschewski, B., Loriani, S., Fetzer, I., Cornell, S. E., Rockström, J., and Lenton, T. M.: Exceeding 1.5°C global warming could trigger multiple climate tipping points, *Science* (1979), 377, <https://doi.org/10.1126/science.abn7950>, 2022.
- Morlighem, M., Rignot, E., Binder, T., Blankenship, D., Drews, R., Eagles, G., Eisen, O., Ferraccioli, F., Forsberg, R., Fretwell, P., Goel, V., Greenbaum, J. S., Gudmundsson, H., Guo, J., Helm, V., Hofstede, C., Howat, I., Humbert, A., Jokat, W., Karlsson, N. B., Lee, W. S., Matsuoka, K., Millan, R., Mouginit, J., Paden, J., Pattyn, F., Roberts, J., Rosier, S., Ruppel, A., Seroussi, H., Smith, E. C., Steinhage, D., Sun, B., Broeke, M. R. van den, Ommen, T. D. van, Wessem, M. van, and Young, D. A.: Deep glacial troughs and stabilizing ridges unveiled beneath the margins of the Antarctic ice sheet, *Nat Geosci*, 13, 132–137, <https://doi.org/10.1038/s41561-019-0510-8>, 2020.
- Mouginit, J., Rignot, E., Scheuchl, B., and Millan, R.: Comprehensive annual ice sheet velocity mapping using Landsat-8, Sentinel-1, and RADARSAT-2 data, *Remote Sens (Basel)*, 9, <https://doi.org/10.3390/rs9040364>, 2017.

- Mouginot, J., Rignot, E., and Scheuchl, B.: Continent-Wide, Interferometric SAR Phase, Mapping of Antarctic Ice Velocity, *Geophys Res Lett*, 46, 9710–9718, <https://doi.org/10.1029/2019GL083826>, 2019.
- Nield, G. A., Barletta, V. R., Bordoni, A., King, M. A., Whitehouse, P. L., Clarke, P. J., Domack, E., Scambos, T. A., and Berthier, E.: Rapid bedrock uplift in the Antarctic Peninsula explained by viscoelastic response to recent ice unloading, *Earth Planet Sci Lett*, 397, 32–41, <https://doi.org/10.1016/j.epsl.2014.04.019>, 2014.
- Nield, G. A., Whitehouse, P. L., van der Wal, W., Blank, B., O'Donnell, J. P., and Stuart, G. W.: The impact of lateral variations in lithospheric thickness on glacial isostatic adjustment in West Antarctica, *Geophysical Journal International*, 214(2), 811–824, 2018.
- Otosaka, I. N., Shepherd, A., Ivins, E. R., Schlegel, N.-J., Amory, C., van den Broeke, M. R., Horwath, M., Joughin, I., King, M. D., Krinner, G., Payne, A. J., Rignot, E., Scambos, T., Simon, K. M., Smith, B. E., Sørensen, L. S., Velicogna, I., Whitehouse, P. L., Agosta, C., Ahlstrøm, A. P., Blazquez, A., Colgan, W., Engdhal, M. E., Fettweis, X., Forsberg, R., Gallée, H., Gardner, A., Gilbert, L., Gourmelen, N., Groh, A., Gunter, B. C., Harig, C., Helm, V., Abbas Khan, S., Konrad, H., Lecavalier, B. S., Liang, C.-C., Loomis, B. D., McMillan, M., Melini, D., Mernild, S. H., Mottram, R., Mouginot, J., Nilsson, J., Noël, B., Pattle, M. E., Peltier, W. R., Pie, N., Sasgen, I., Save, H. V., Seo, K.-W., Scheuchl, B., Schrama, E. J., Schröder, L., Simonsen, S. B., Slater, T., Spada, G., Sutterley, T. C., Dutt Vishwakarma, B., van, M., Wiese, D., van der Wal, W., and Wouters, B.: Mass Balance of the Greenland and Antarctic Ice Sheets from 1992 to 2020, *Earth Syst Sci Data*, 1–33, <https://doi.org/10.5194/essd-2022-261>, 2023.
- Pattyn, F.: Sea-level response to melting of Antarctic ice shelves on multi-centennial timescales with the fast Elementary Thermomechanical Ice Sheet model (f.ETISH v1.0), *Cryosphere*, 11, 1851–1878, <https://doi.org/10.5194/tc-11-1851-2017>, 2017.
- Pattyn, F. and Morlighem, M.: The uncertain future of the Antarctic Ice Sheet, *Science* (1979), 367, 1331–1335, 2020.
- Peltier, W. R., Argus, D. F., and Drummond, R.: Space geodesy constrains ice age terminal deglaciation: The global ICE-6G-C (VM5a) model, *J Geophys Res Solid Earth*, 120, 450–487, <https://doi.org/10.1002/2014JB011176>, 2015.
- Pollard, D., Gomez, N., and Deconto, R. M.: Variations of the Antarctic Ice Sheet in a Coupled Ice Sheet-Earth-Sea Level Model: Sensitivity to Viscoelastic Earth Properties, *J Geophys Res Earth Surf*, 122, 2124–2138, <https://doi.org/10.1002/2017JF004371>, 2017.

- Ritzwoller, M. H., Shapiro, N. M., Levshin, A. L., and Leahy, G. M.: Crustal and upper mantle structure beneath Antarctica and surrounding oceans, *J Geophys Res Solid Earth*, 106, 30645–30670, <https://doi.org/10.1029/2001jb000179>, 2001.
- Sasgen, I., Martín-Español, A., Horvath, A., Klemann, V., Petrie, E. J., Wouters, B., Horvath, M., Pail, R., Bamber, J. L., Clarke, P. J., Konrad, H., and Drinkwater, M. R.: Joint inversion estimate of regional glacial isostatic adjustment in Antarctica considering a lateral varying Earth structure (ESA STSE Project REGINA), *Geophys J Int*, 211, 1534–1553, <https://doi.org/10.1093/gji/ggx368>, 2017.
- Sasgen, I., Wouters, B., Gardner, A. S., King, M. D., Tedesco, M., Landerer, F. W., Dahle, C., Save, H., and Fettweis, X.: Return to rapid ice loss in Greenland and record loss in 2019 detected by the GRACE-FO satellites, *Commun Earth Environ*, 1, <https://doi.org/10.1038/s43247-020-0010-1>, 2020.
- Schaeffer, A. J. and Lebedev, S.: Global shear speed structure of the upper mantle and transition zone, *Geophys J Int*, 194, 417–449, <https://doi.org/10.1093/gji/ggt095>, 2013.
- Seroussi, H., Nowicki, S., Payne, A. J., Goelzer, H., Lipscomb, W. H., Abe-Ouchi, A., Agosta, C., Albrecht, T., Asay-Davis, X., Barthel, A., Calov, R., Cullather, R., Dumas, C., Galton-Fenzi, B. K., Gladstone, R., Golledge, N. R., Gregory, J. M., Greve, R., Hattermann, T., Hoffman, M. J., Humbert, A., Huybrechts, P., Jourdain, N. C., Kleiner, T., Larour, E., Leguy, G. R., Lowry, D. P., Little, C. M., Morlighem, M., Pattyn, F., Pelle, T., Price, S. F., Quiquet, A., Reese, R., Schlegel, N. J., Shepherd, A., Simon, E., Smith, R. S., Straneo, F., Sun, S., Trusel, L. D., Van Breedam, J., Van De Wal, R. S. W., Winkelmann, R., Zhao, C., Zhang, T., and Zwinger, T.: ISMIP6 Antarctica: A multi-model ensemble of the Antarctic ice sheet evolution over the 21st century, *The Cryos Discuss* 2020, 1-54, <https://doi.org/10.5194/tc-14-3033-2020>, 2020.
- Shen, W., Wiens, D. A., Anandakrishnan, S., Aster, R. C., Gerstoft, P., Bromirski, P. D., Hansen, S. E., Dalziel, I. W. D., Heeszel, D. S., Huerta, A. D., Nyblade, A. A., Stephen, R., Wilson, T. J., and Winberry, J. P.: The Crust and Upper Mantle Structure of Central and West Antarctica From Bayesian Inversion of Rayleigh Wave and Receiver Functions, *J Geophys Res Solid Earth*, 123, 7824–7849, <https://doi.org/10.1029/2017JB015346>, 2018.
- Shepherd, A., Ivins, E. R., Geruo, A., Barletta, V. R., Bentley, M. J., Bettadpur, S., Briggs, K. H., Bromwich, D. H., Forsberg, R., Galin, N., Horvath, M., Jacobs, S., Joughin, I., King, M. A., Lenaerts, J. T. M., Li, J., Ligtenberg, S. R. M., Luckman, A., Luthcke, S. B., McMillan, M., Meister, R., Milne, G., Mougintot, J., Muir, A., Nicolas, J. P., Paden, J., Payne, A. J., Pritchard, H., Rignot, E., Rott, H., Sørensen, L. S., Scambos, T. A., Scheuchl, B., Schrama, E. J. O., Smith, B., Sundal, A. V., Van Angelen, J. H., Van De Berg, W. J., Van Den Broeke, M. R., Vaughan, D. G.,

Velicogna, I., Wahr, J., Whitehouse, P. L., Wingham, D. J., Yi, D., Young, D., and Zwally, H. J.: A reconciled estimate of ice-sheet mass balance, *Science* (1979), 338, 1183–1189, <https://doi.org/10.1126/science.1228102>, 2012.

Shepherd, A., Ivins, E., Rignot, E., Smith, B., van den Broeke, M., Velicogna, I., Whitehouse, P., Briggs, K., Joughin, I., Krinner, G., Nowicki, S., Payne, T., Scambos, T., Schlegel, N. A., Geruo, A., Agosta, C., Ahlstrøm, A., Babonis, G., Barletta, V., Blazquez, A., Bonin, J., Csatho, B., Cullather, R., Felikson, D., Fettweis, X., Forsberg, R., Gallee, H., Gardner, A., Gilbert, L., Groh, A., Gunter, B., Hanna, E., Harig, C., Helm, V., Horvath, A., Horvath, M., Khan, S., Kjeldsen, K. K., Konrad, H., Langen, P., Lecavalier, B., Loomis, B., Luthcke, S., McMillan, M., Melini, D., Mernild, S., Mohajerani, Y., Moore, P., Mouginot, J., Moyano, G., Muir, A., Nagler, T., Nield, G., Nilsson, J., Noel, B., Otosaka, I., Pattle, M. E., Peltier, W. R., Pie, N., Rietbroek, R., Rott, H., Sandberg-Sørensen, L., Sasgen, I., Save, H., Scheuchl, B., Schrama, E., Schröder, L., Seo, K., Simonsen, S., Slater, T., Spada, G., Sutterley, T., Talpe, M., Tarasov, L., van de Berg, W. J., van der Wal, W., van Wessem, M., Vishwakarma, B. D., Wiese, D., and Wouters, B.: Mass balance of the Antarctic Ice Sheet from 1992 to 2017, *Nature*, 558, 219–222, <https://doi.org/10.1038/s41586>, 2018.

Smith, B., Fricker, H. A., Gardner, A. S., Medley, B., Nilsson, J., Paolo, F. S., Holschuh, N., Adusumilli, S., Brunt, K., Csatho, B., Harbeck, K., Markus, T., Neumann, T., Siegfried, M. R., and Zwally, H. J.: Pervasive ice sheet mass loss reflects competing ocean and atmosphere processes, *Science* (1979), 368, 1239–1242, 2020.

Tapley, B. D., Watkins, M. M., Flechtner, F., Reigber, C., Bettadpur, S., Rodell, M., Sasgen, I., Famiglietti, J. S., Landerer, F. W., Chambers, D. P., Reager, J. T., Gardner, A. S., Save, H., Ivins, E. R., Swenson, S. C., Boening, C., Dahle, C., Wiese, D. N., Dobslaw, H., Tamisiea, M. E., and Velicogna, I.: Contributions of GRACE to understanding climate change, <https://doi.org/10.1038/s41558-019-0456-2>, 1 May 2019.

Tarasov, L., and Peltier, W. R.: Terminating the 100 kyr ice age cycle, *Journal of Geophysical Research: Atmospheres*, 102(D18), 21665–21693, 1997.

Tarasov, L., Dyke, A. S., Neal, R. M., and Peltier, W. R.: A data-calibrated distribution of deglacial chronologies for the North American ice complex from glaciological modeling, *Earth Planet Sci Lett*, 315–316, 30–40, <https://doi.org/10.1016/j.epsl.2011.09.010>, 2012.

Tarasov, L. and Goldstein, M.: Assessing uncertainty in past ice and climate evolution: overview, stepping-stones, and challenges, *Climate of the Past Discussion*, 1–54, <https://doi.org/10.5194/cp-2021-145>, 2021.

- Tarasov, L., Hank, K., Lecavalier, B. S., and Pollard, D.: The glacial systems model (GSM), [in preparation] 2024.
- Velicogna, I., Mohajerani, Y., Geruo, A., Landerer, F., Mouginot, J., Noel, B., Rignot, E., Sutterley, T., van den Broeke, M., van Wessem, M., and Wiese, D.: Continuity of Ice Sheet Mass Loss in Greenland and Antarctica From the GRACE and GRACE Follow-On Missions, *Geophys Res Lett*, 47, <https://doi.org/10.1029/2020GL087291>, 2020.
- Whitehouse, P., Latychev, K., Milne, G. A., Mitrovica, J. X., and Kendall, R.: Impact of 3-D Earth structure on Fennoscandian glacial isostatic adjustment: Implications for space-geodetic estimates of present-day crustal deformations. *Geophysical Research Letters*, 33(13), 2006.
- Whitehouse, P.: Glacial isostatic adjustment and sea-level change, State of the art report, 2009.
- Whitehouse, P. L., Bentley, M. J., Milne, G. A., King, M. A., and Thomas, I. D.: A new glacial isostatic adjustment model for Antarctica: Calibrated and tested using observations of relative sea-level change and present-day uplift rates, *Geophys J Int*, 190, 1464–1482, <https://doi.org/10.1111/j.1365-246X.2012.05557.x>, 2012.
- Whitehouse, P. L.: Glacial isostatic adjustment modelling: Historical perspectives, recent advances, and future directions, *Earth Surface Dynamics*, 6, 401–429, <https://doi.org/10.5194/esurf-6-401-2018>, 2018.
- Whitehouse, P. L., Gomez, N., King, M. A., and Wiens, D. A.: Solid Earth change and the evolution of the Antarctic Ice Sheet, <https://doi.org/10.1038/s41467-018-08068-y>, 1 December 2019.
- Wolstencroft, M., King, M.A., Whitehouse, P.L., Bentley, M.J., Nield, G.A., King, E.C., McMillan, M., Shepherd, A., Barletta, V., Bordoni, A. and Riva, R.E.: Uplift rates from a new high-density GPS network in Palmer Land indicate significant late Holocene ice loss in the southwestern Weddell Sea, *Geophysical Journal International*, 203(1), 737-754, 2015.
- Zhao, C., King, M.A., Watson, C.S., Barletta, V.R., Bordoni, A., Dell, M., and Whitehouse, P.L.: Rapid ice unloading in the Fleming Glacier region, southern Antarctic Peninsula, and its effect on bedrock uplift rates, *Earth and Planetary Science Letters*, 473, 164-176, 2017.

## Chapter 5: Conclusion

This research provides bounds on the evolution of the AIS since the last interglacial through a HMA by combining a comprehensive database with the GSM. To meaningfully assess spatio-temporal bounds of a complex system, it is necessary to rigorously evaluate data and model uncertainties across the entire system. An extensive observational constraint database of the past AIS evolution was compiled, recalibrated, and standardized. This involved evaluating data-system uncertainties such as the indicative meaning of proxy data and measurement uncertainties. Moreover, an Antarctic configuration of the GSM was developed. This research included carefully evaluating system-model uncertainties, specifically: initial and boundary condition uncertainties, parametric uncertainties, and structural uncertainties. The resulting HMA of the AIS answers the research questions detailed in Section 1.5 and demonstrates that previous modelling studies yielded a too narrow uncertainty range for predictions due to the inadequate integration of observational constraints and insufficient accounting for glacial system uncertainties.

### 5.1 Antarctic Ice Sheet constraints

A single field observation represents a point-like proxy inference in space and time, plus or minus uncertainties, that constrains the integrated localized conditions. By compiling a wide variety of field observations that constrain the past AIS, a data-oriented state-space estimation of the AIS is created. An extensive database of observations that constrain the AIS over the last glacial cycle was compiled, termed the AntICE2 database. The AntICE2 database consists of a variety of data types from observations of past ice

extent, past ice thickness, past relative sea level, borehole temperature profiles, and present-day bedrock displacement rates. The AntICE2 consists of a total of 1023 paleo-observations that were recalibrated and standardized for consistency. A series of data type specific criteria were defined to curate and evaluate the quality of the data throughout the database. The curation criteria sorted the data into quality tiers and were designed to exclude low-quality, inconsistent, and superfluous data. Due to data scarcity, large areas of the AIS are unconstrained by field data. Therefore, by combining the AntICE2 database with the GSM and its many degrees of freedom, the model effectively produces a dynamic interpolation across the spatio-temporal domain. This approach produces bounds on the evolution of the AIS given the available data and uncertainties in the glacial system.

The AntICE2 database will directly benefit the entire AIS modelling community by reducing the challenges of integrating a large, varied, and high-quality collection of observational constraints in an AIS model. This will help improve reconstructions of the AIS over the last glacial cycle. In turn the latter will feed into more confident ice sheet model initialization for simulating contemporary or future AIS changes.

## 5.2 Antarctic Ice Sheet evolution

Simulations of the AIS over the last two glacial cycles were history matched to the AntICE2 database to generate meaningful bounds on the evolution of the AIS since the LIG. The GSM was configured for the AIS with 38 ensemble parameters. A large ensemble of 9,293 simulations were performed as part of the final wave of the history-matching analysis. This involved successive ensembles based on Markov Chain Monte Carlo sampling of Bayesian Artificial Neural Network emulators to efficiently explore the

parameter space. Each simulation in the large ensemble was scored against the high-quality tier-1 and tier-2 data in the AntICE2 database to identify simulations that are unequivocally inconsistent with the database beyond  $3\sigma$ . This yielded a NROY sub-ensemble of model simulations that represents bounds on the evolution of the actual AIS.

The LIG is an interval with considerable uncertainties with subsurface ocean warming surrounding the AIS that can potentially drive strong grounding-line retreat. Additionally, the interval lacks direct constraints on the geometry of the AIS. Therefore, the history-matching analysis NROY sub-ensemble exhibits a wide range of possible chronologies during the LIG, with a grounded ice deficit relative to present ranging between 2.9 to 13.8 mESL. The AntICE2 database predominant constrains the LGM and deglaciation. The NROY sub-ensemble bounds the LGM grounded ice excess relative to present of 9.2 to 26.5 mESL with several simulations exceeding 20 mESL. This suggests that previous studies underestimated the viability of larger Antarctic ice volumes during the LGM. This excess Antarctic ice during the LGM can partly address the missing ice problem by nearly closing the LGM sea-level budget. Finally, the NROY sub-ensemble demonstrates that the AIS only modestly contributed to the meltwater pulse 1a (MWP-1a, -0.2 to 0.3 mESL around  $\sim 14.3$  ka) since the AIS largely deglaciated after this period.

### 5.3 Antarctic glacial isostatic adjustment

The GSM includes a coupled GIA component based on a spherically symmetric viscoelastic Earth model. The history-matching analysis was jointly performed on the ice sheet as well as the Antarctic GIA Earth model since the LIG. The primary input to a GIA model of sea-level change is an: ice chronology which defines changes in the ice and ocean

load; and Earth model specified by its density and rheological structure. The GIA component in the GSM depends on three ensemble parameters that define the rheological properties of the Earth. The rheological structure of the Earth model and GIA response following an unloading event is directly constrained by past RSL and GPS observations.

The present-day rate of bedrock displacement and geoidal change is an essential input when trying to infer the contemporary mass balance of an ice sheet. These inputs can have a considerable impact on the inferred magnitude of mass loss; therefore, accurate assessment of the latter requires accurate assessment of GIA uncertainties. The NROY sub-ensemble yield bounds on past and present GIA and sea-level change. Relative to the NROY sub-ensemble bounds, past studies have significantly underestimated PD GIA predictions in key regions. This is particularly relevant for the Amundsen sector, a region undergoing the most mass loss in all of Antarctica. Thus, the NROY sub-ensemble GIA estimates will directly impact our understanding of the contemporary mass balance of the AIS, include the mass balance estimates of the most vulnerable sectors of marine-based ice in the world.

## 5.4 Future work

A logical continuation of the AntICE2 database is to include additional data types that could constrain a new facet of the AIS. Specially, the englacial age structure of the ice as inferred from reflective isochrones visible in radiostratigraphic profiles. The Scientific Committee on Antarctic Research AntArchitecture initiative is actively producing and compiling data to provide such an age structure for large sections of the AIS which would constrain many regions that are relatively data poor. Thus, including the Antarctic age

structure and processing it to a format suited for data-model comparison would be a valuable addition to the AntICE2 database.

Future modelling research should be aimed at model development to improve the GSM to rectify any remaining outstanding model-data discrepancies. Particularly, this could be achieved by broadening the degrees of freedom in the atmospheric and oceanic forcings, and basal conditions. Generally, this would be achieved by developing a climate generator for the period of interest (e.g. Arif et al., 2018; Bahadory & Tarasov, 2018). However, some data-model discrepancies are the product of structural uncertainties attributed to resolution limitations and model approximations which can be accounted for by refining the error model.

The NROY sub-ensemble simulations can be used for initialization of glaciological models examining the future response of the AIS to a variety of climate change scenarios. This would enable a wide range of exploratory research to investigate the degree by which field observations (i.e. source location of data, data types, data quality) constrain future AIS projections. Moreover, this work would provide more meaningful bounds on the future response of the AIS to climate change.

Additionally, the history matching AIS results can be leveraged as an Antarctic treasure map, specifically a tool to identify potential high-priority fieldwork targets. This treasure map would help motivate future field work since it would identify the constraining power of hypothetical observational constraint. The map would point to unsampled features (e.g. nunataks, grounding-zone wedges, potential ice core sites) and quantify the resulting impact if the hypothetical data was used in an upcoming history-matching analysis (e.g. reducing the sea-level contribution bounds for a given sector).

The GLAC3 global ice sheet chronology will be used to study global sea-level change. The NROY AIS reconstructions represent the Antarctic component of the global ice sheet chronology. By evaluating sea-level change using a GIA model with the GLAC3 global ice sheet chronology, the NROY AIS reconstructions can be used to compute the Antarctic sea-level contributions at several far-field RSL site. This work would precisely assess the deglacial sea-level budget and quantify to which extent the NROY sub-ensemble AIS simulations address the LGM missing ice problem. Moreover, the far-field RSL observations can in turn be used to constrain the global ice sheet chronology, potentially further narrowing the NROY sub-ensemble bounds.

Finally, this research would benefit from future work that leverages a 3D Earth GIA model to study Antarctic and global GIA and sea-level change. By properly resolving lateral Earth structure, higher fidelity GIA estimates could be produced to contextualize the NROY sub-ensemble Antarctica GIA predictions and more accurate far-field RSL predictions can be made. This would quantify the relative importance of resolving lateral Earth structure on the necessary GIA corrections to infer contemporary AIS mass balance. Moreover, it would help specify the structural error associated with using a simpler GIA component in the GSM.

The research detailed in this study has enhanced our understanding of the AIS by specifically providing bounds on how it responded to past warm and cold periods. This directly improves our understanding of the contemporary mass balance of the ice sheet and provides a clear path to producing more accurate bounds on future AIS changes.

# Supplement for Chapter 1

## Eismint experiment G hGSM (Hybrid)

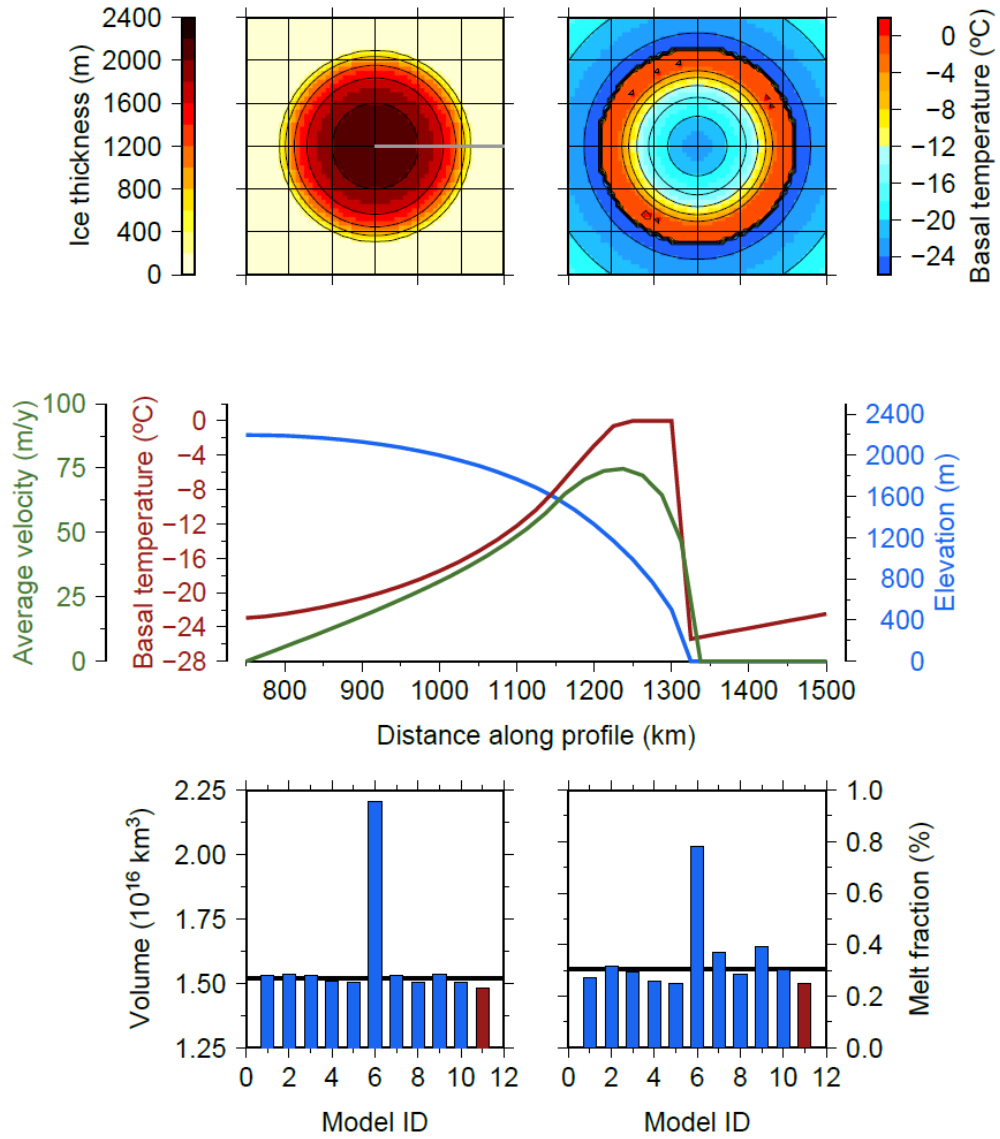


Figure S1.1: Verification & Validation EISMINT experiments conducted after integrating the hybrid ice physics into the GSM. Experiment G consists basal slip throughout the base of the ice. The top row illustrates the ice thickness (left) and basal temperature (right), the grey horizontal line depicts the cross section for the middle frames. The middle row shows the velocity, basal temperature, and elevation profile across the centre of the dome. The

bottom row shows the volume (left) and basal melt fraction (right) of the GSM (red) compared to reference ice sheet models (blue) (Payne et al., 2000).

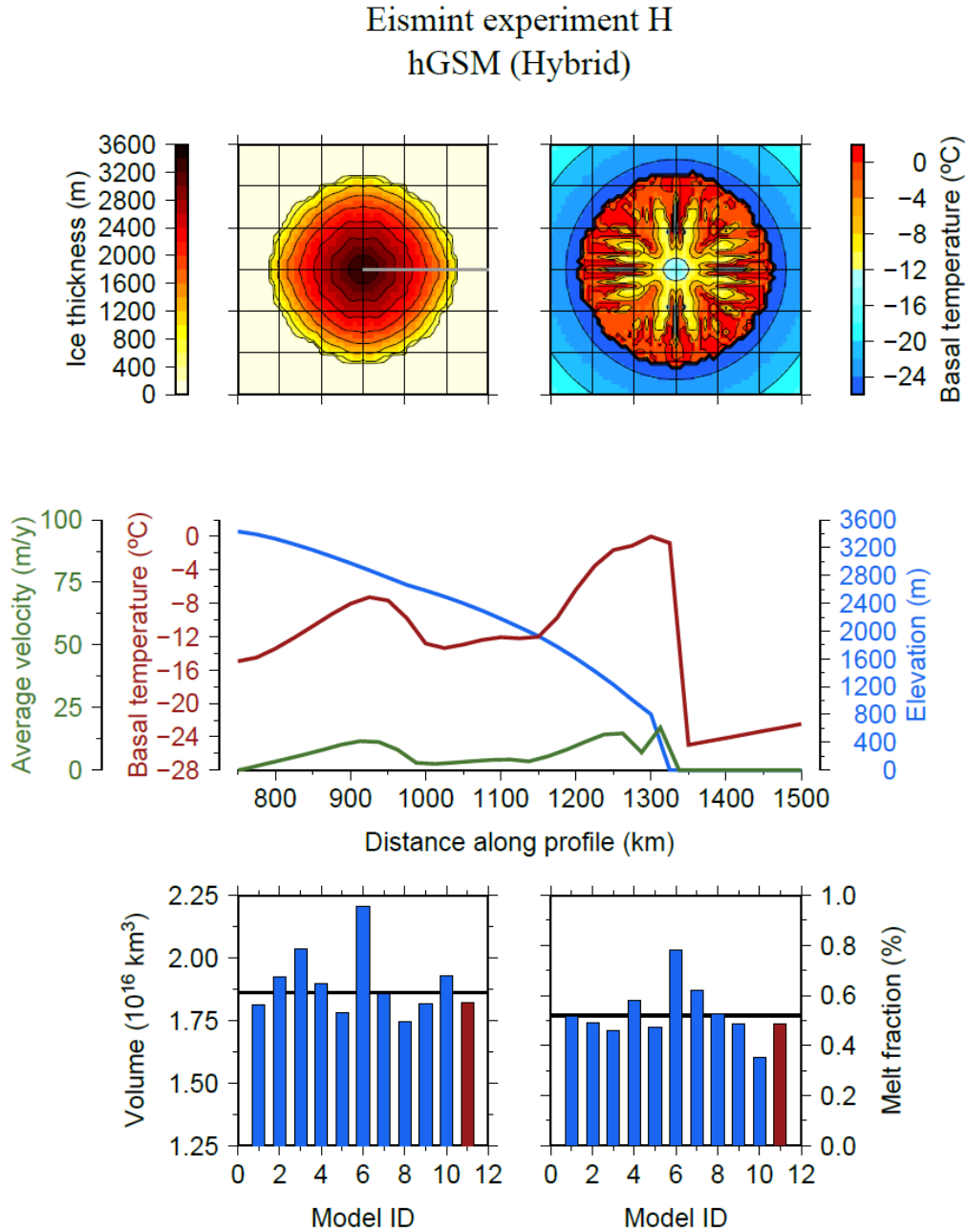


Figure S1.2: Verification & Validation EISMINT experiments conducted after integrating the hybrid ice physics into the GSM. Experiment H consists basal slip only where basal ice reaches the melting point. The top row illustrates the ice thickness (left) and basal temperature (right), the grey horizontal line depicts the cross section for the middle frames.

The middle row shows the velocity, basal temperature, and elevation profile across the centre of the dome. The bottom row shows the volume (left) and basal melt fraction (right) of the GSM (red) compared to reference ice sheet models (blue) (Payne et al., 2000).

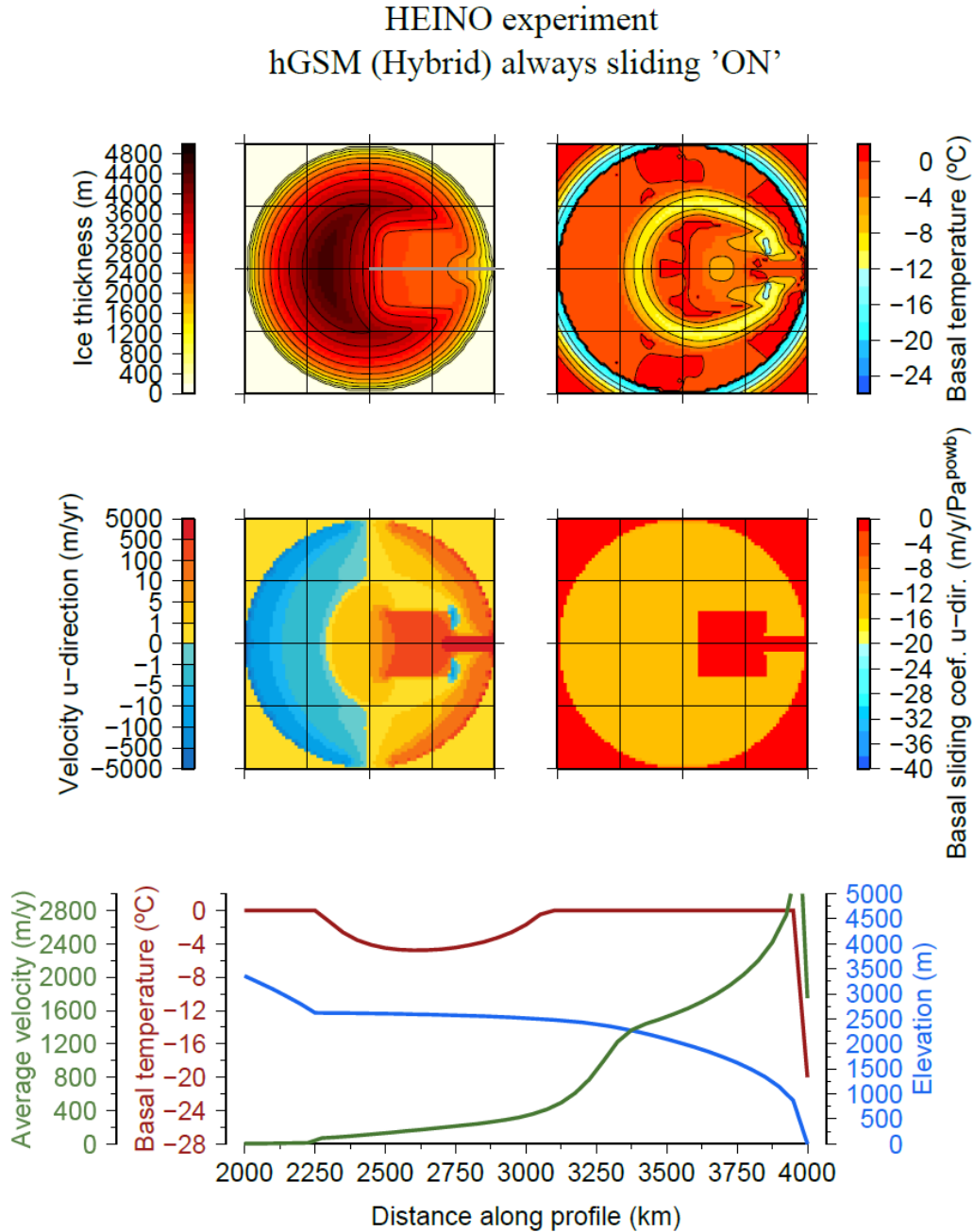


Figure S1.3: Verification & Validation HEINO experiments conducted after integrating the hybrid ice physics into the GSM. The HEINO experiment shown here consists of an idealized North America domain with a square Hudson Bay (Calov et al., 2010) with basal sliding always on. The top row illustrates the ice thickness (left) and basal temperature

(right), the grey horizontal line depicts the cross section for the bottom frames. The middle row shows the surface velocity (left) and basal drag coefficient (right) in the u-direction. The bottom row shows the average velocity, basal temperature, and elevation profile across the centre of the domain.

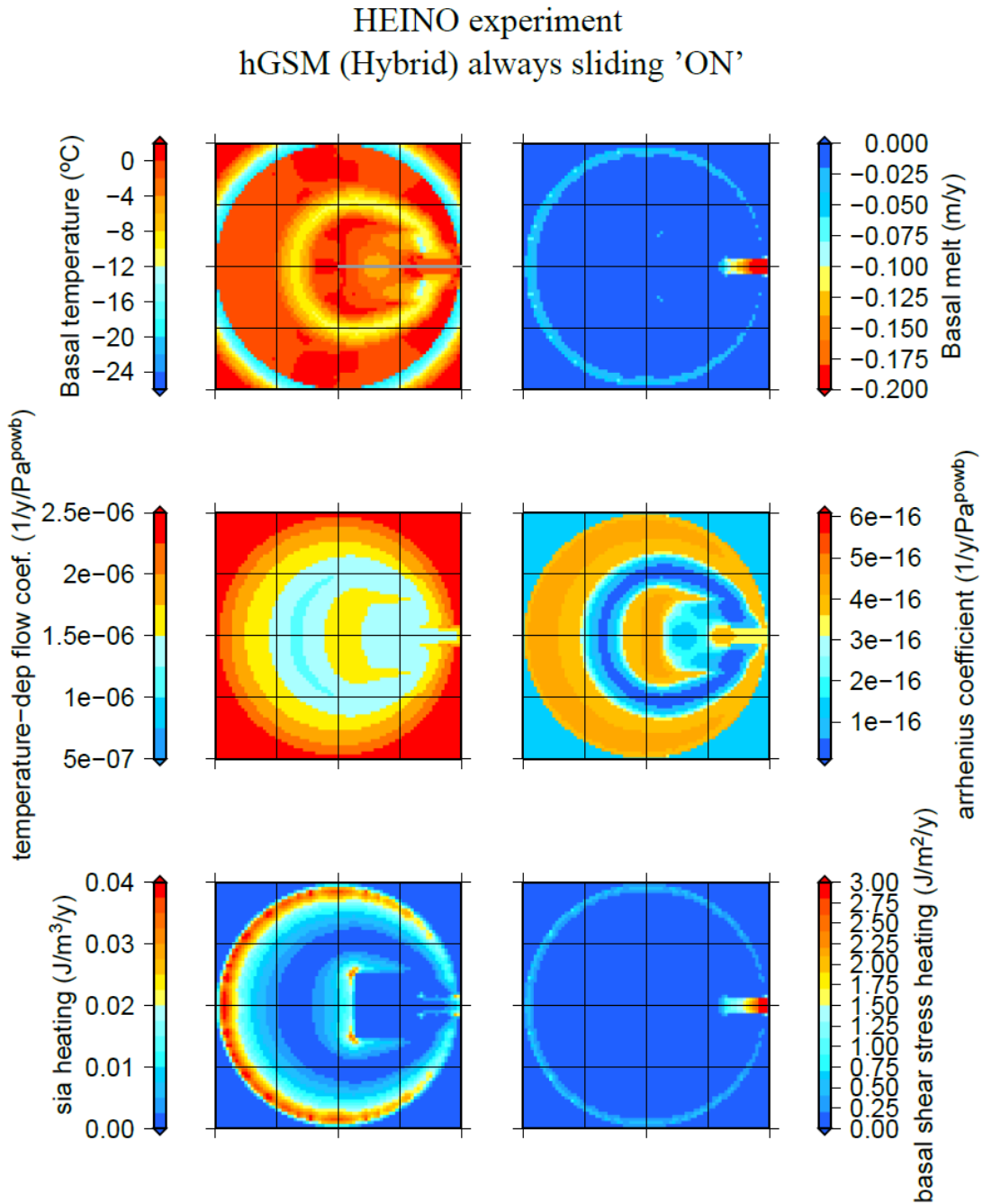


Figure S1.4: Verification & Validation HEINO experiments conducted after integrating the hybrid ice physics into the GSM. The HEINO experiment shown here consists of an

idealized North America domain with a square Hudson Bay (Calov et al., 2010) with basal sliding always on. The top row illustrates the basal temperature (left) and basal melt (right). The middle row shows the temperature-dependent flow coefficient (left) and Arrhenius coefficient (right). The bottom row shows the shallow ice approximation heating term (left) and basal shear stress heating term (right).

HEINO experiment  
hGSM (Hybrid)

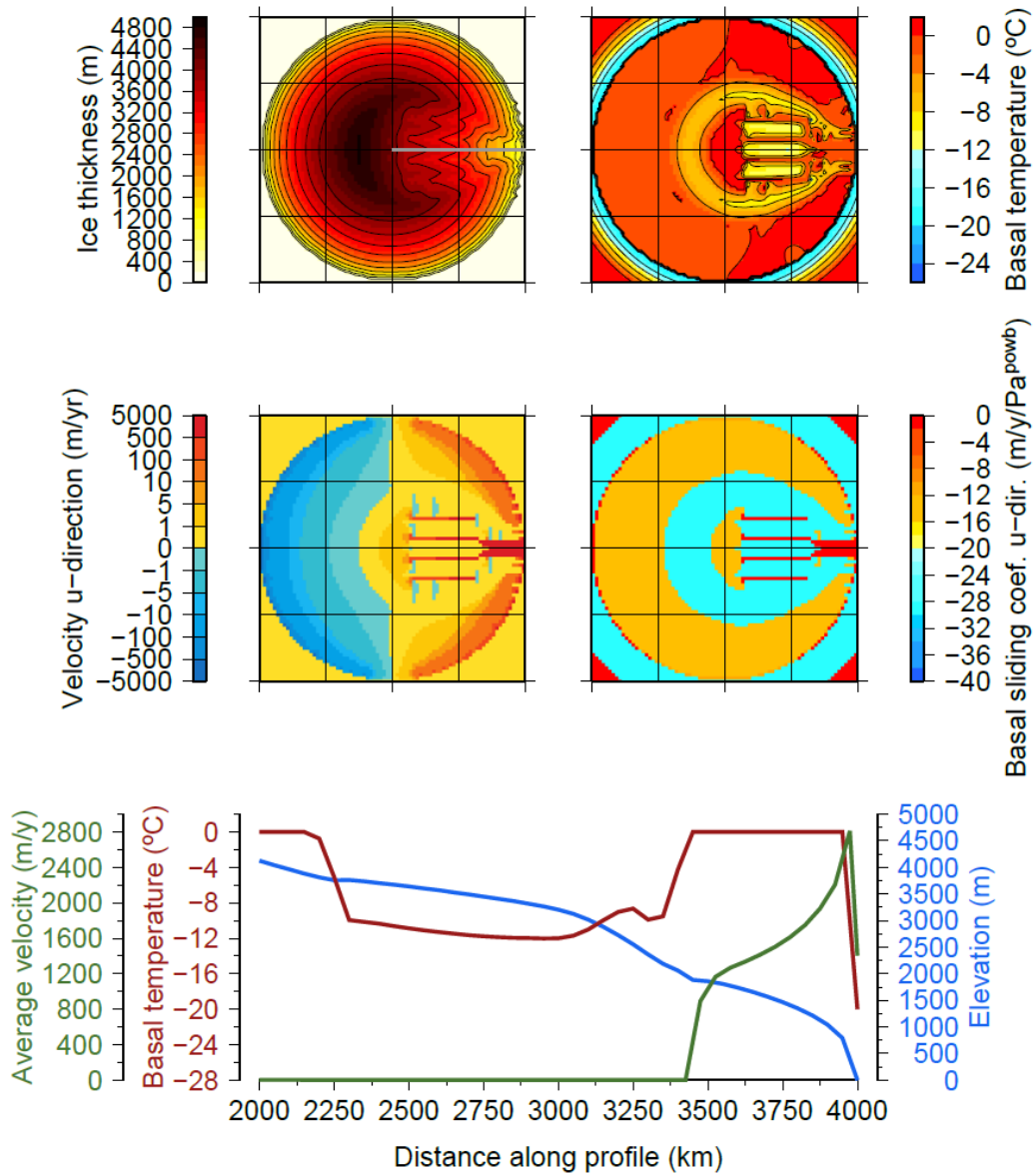


Figure S1.5: Verification & Validation HEINO experiments conducted after integrating the hybrid ice physics into the GSM. The HEINO experiment shown here consists of an

idealized North America domain with a square Hudson Bay (Calov et al., 2010) with basal sliding occurring wherever the base reaches the pressure melting point. The top row illustrates the ice thickness (left) and basal temperature (right), the grey horizontal line depicts the cross section for the bottom frames. The middle row shows the surface velocity (left) and basal drag coefficient (right) in the u-direction. The bottom row shows the average velocity, basal temperature, and elevation profile across the centre of the domain.

HEINO experiment  
hGSM (Hybrid)

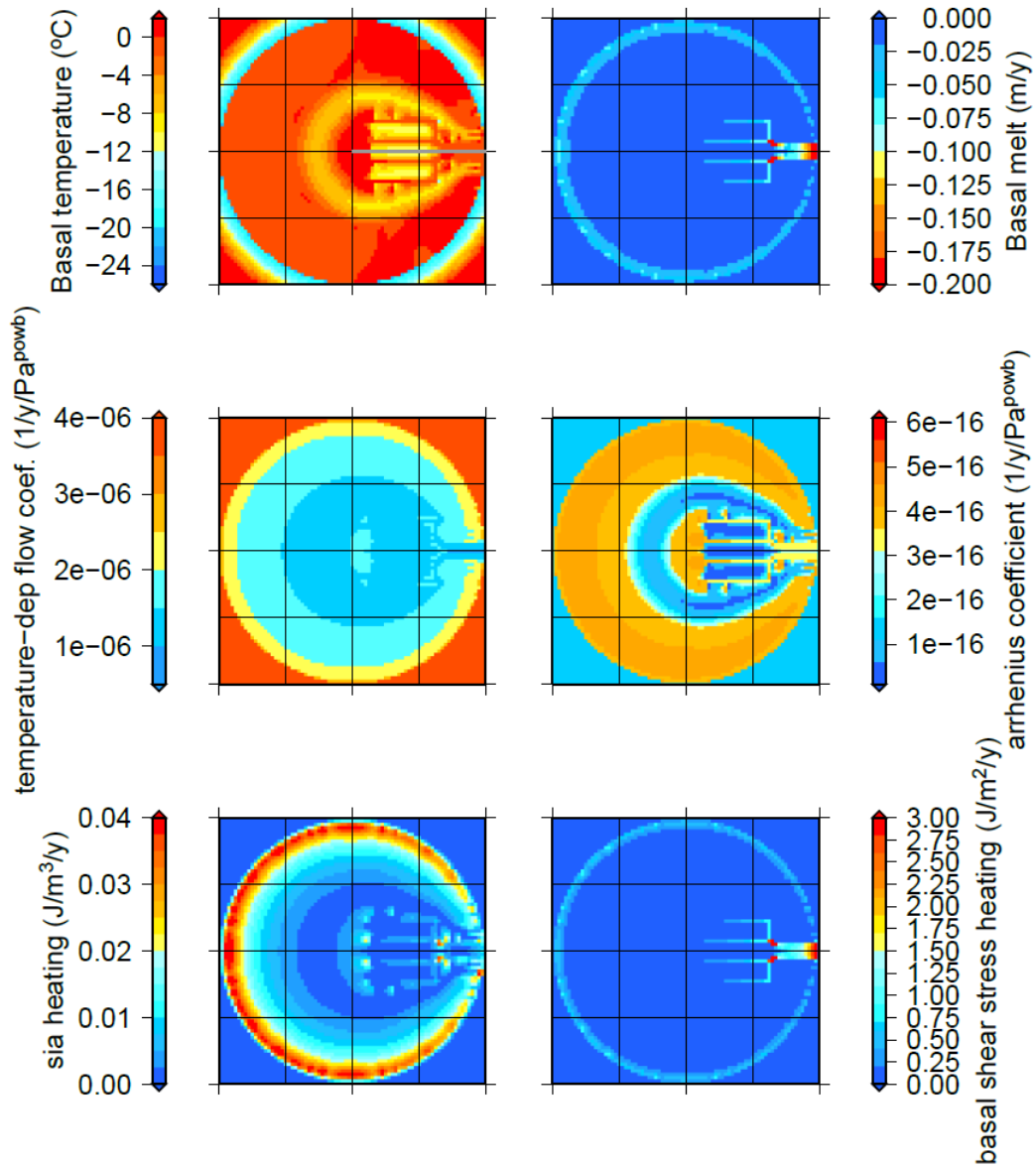


Figure S1.6: Verification & Validation HEINO experiments conducted after integrating the hybrid ice physics into the GSM. The HEINO experiment shown here consists of an idealized North America domain with a square Hudson Bay (Calov et al., 2010) with basal sliding occurring wherever the base reaches the pressure melting point. The top row illustrates the basal temperature (left) and basal melt (right). The middle row shows the temperature-dependent flow coefficient (left) and Arrhenius coefficient (right). The bottom row shows the shallow ice approximation heating term (left) and basal shear stress heating term (right).

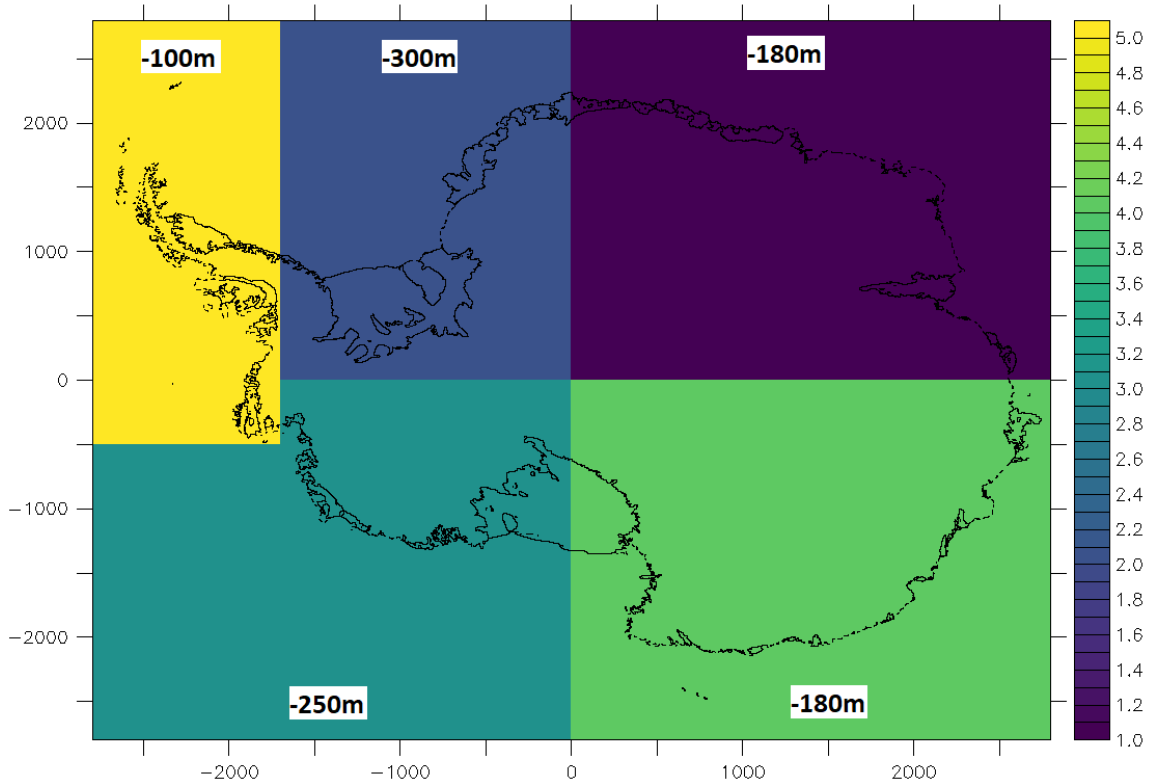


Figure S1.7: The fully unloaded glacial isostatic equilibrium sea-level thresholds range between -300 to -100 m due to significant uncertainties in dynamic topography on timescales of  $\sim 35$  Myr. These elevation thresholds are regional chosen to delineate deep subglacial troughs and regions where PD surface ice moves at  $>400$  m/yr since this indicates loose basal till.

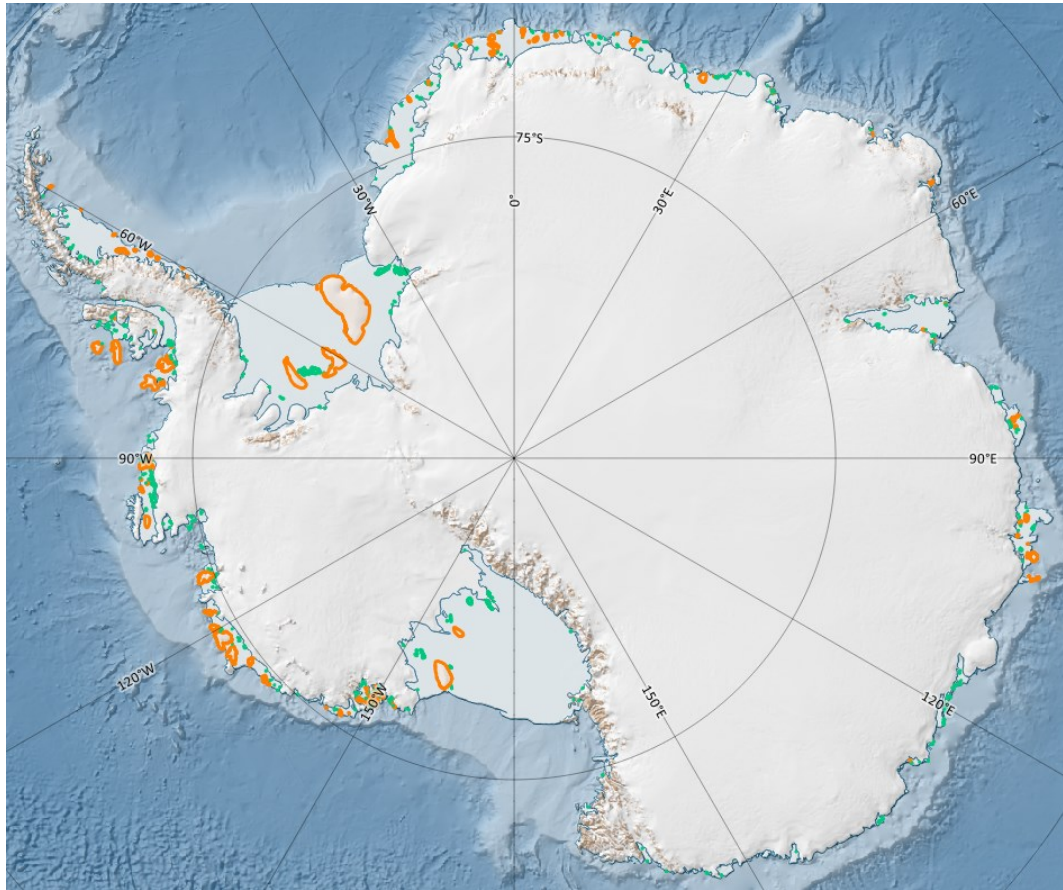


Figure S1.8: Ice rises (orange) and ice rumples (green) across the present-day Antarctic ice sheet. Ice rises and rumples are frequently below the model grid resolution and can buttress back ice. Therefore, it is important to resolve these key features that can have a significant impact on ice dynamics. The Antarctic basemap was generated using Quantarctica (Matsuoka et al., 2021).

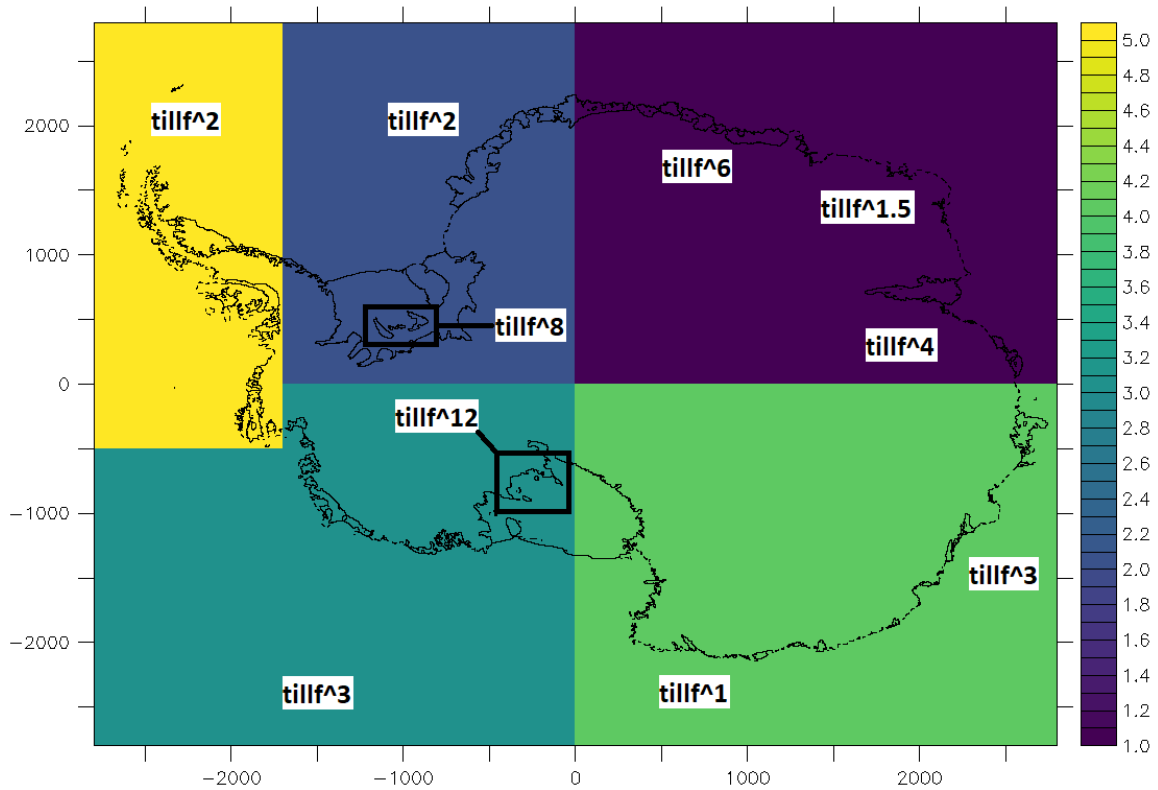
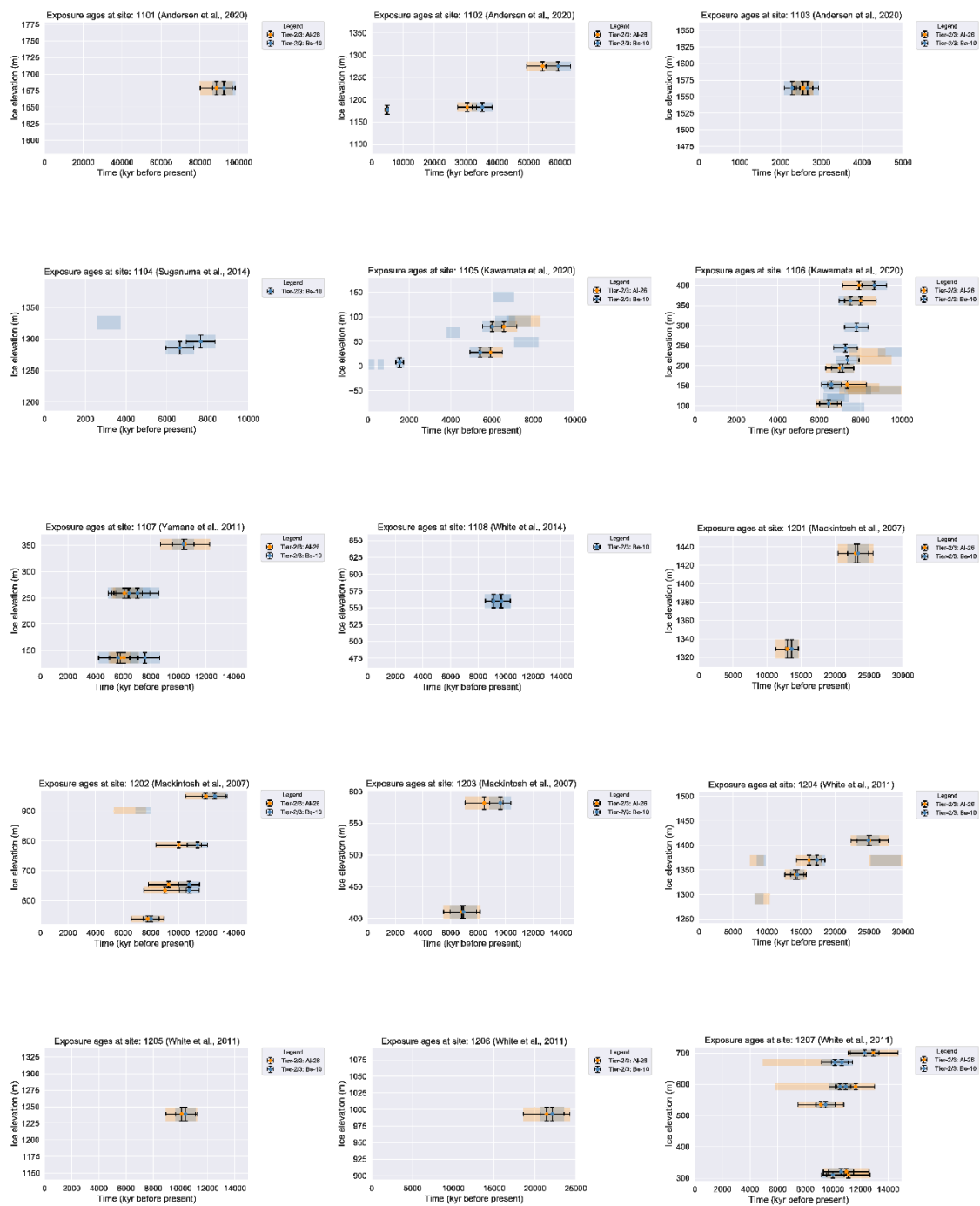


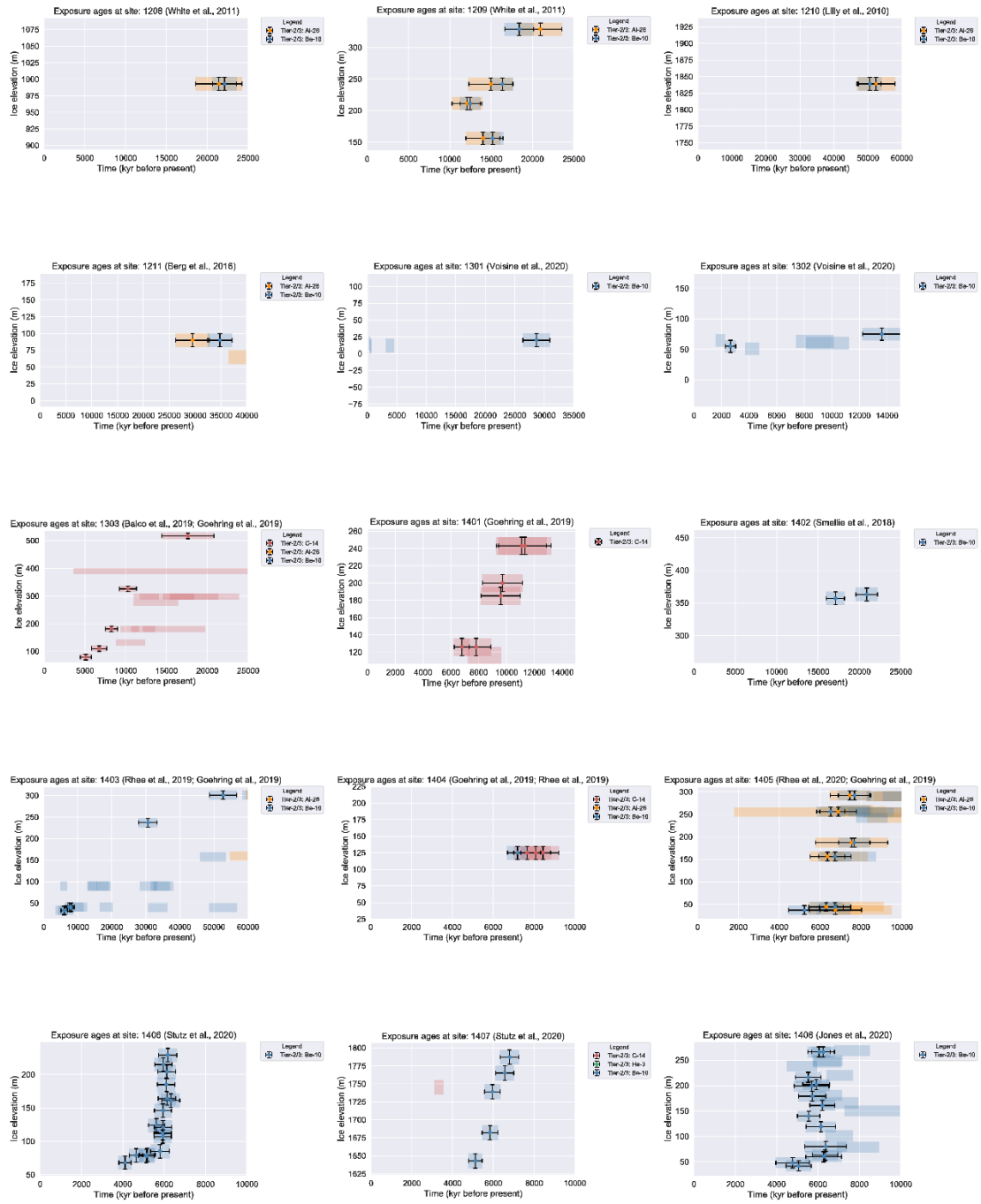
Figure S1.9: The method by which the raw basal topography is upscaled to the model grid resolution can emphasize or de-emphasize certain subgrid pinning points. This is due to the pinning point scale, geometry, relative position and orientation of the model grid. Subgrid pinning points have persisted throughout several glaciations and therefore should be represented by hard bedrock basal features. This is achieved by using a subgrid enhancement exponent ranging between 1 to 12 that is regionally varied to enhance specific key PD subgrid hard bedrock features which would otherwise be neglected by the upscaling procedure.

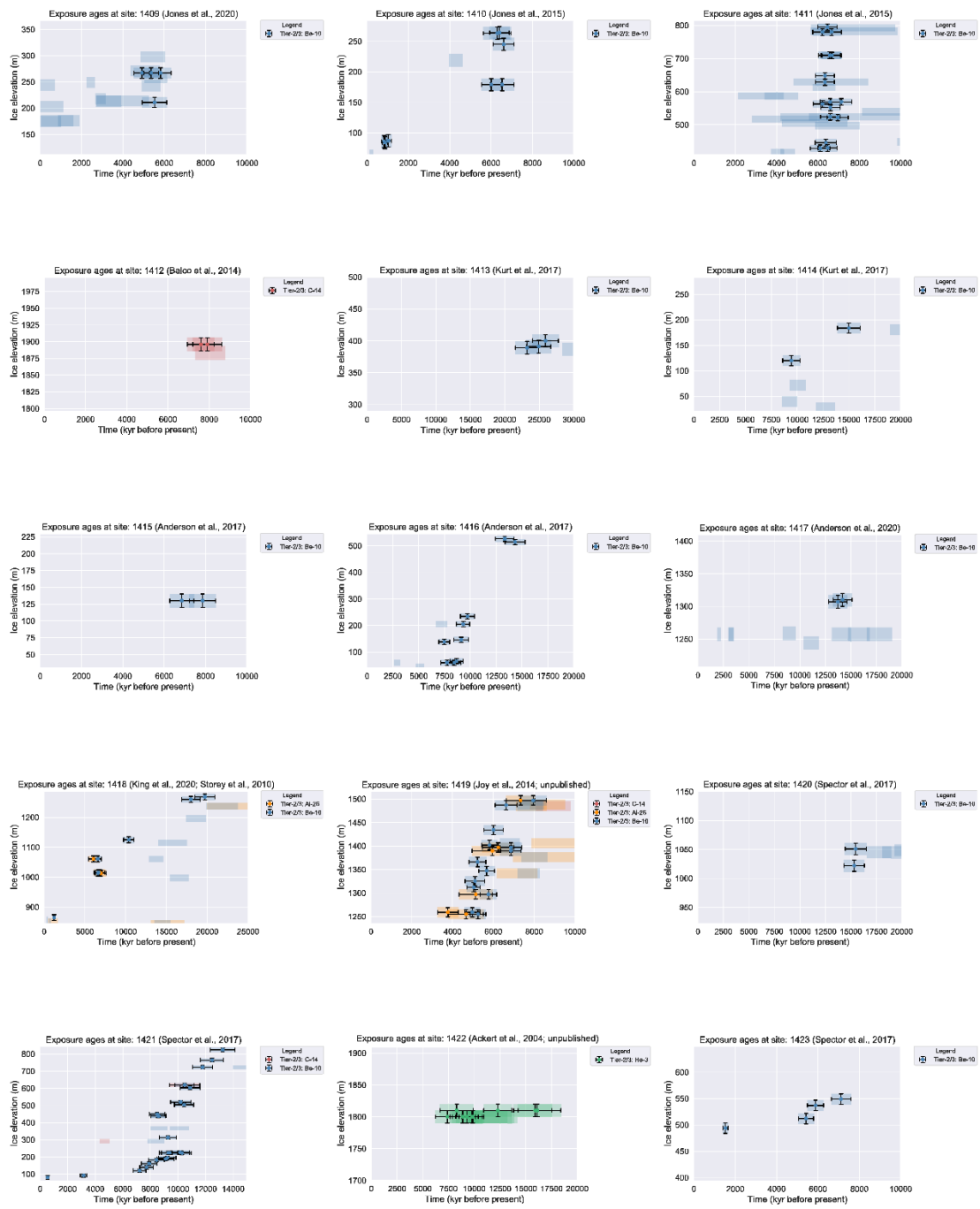
## Supplement for Chapter 2

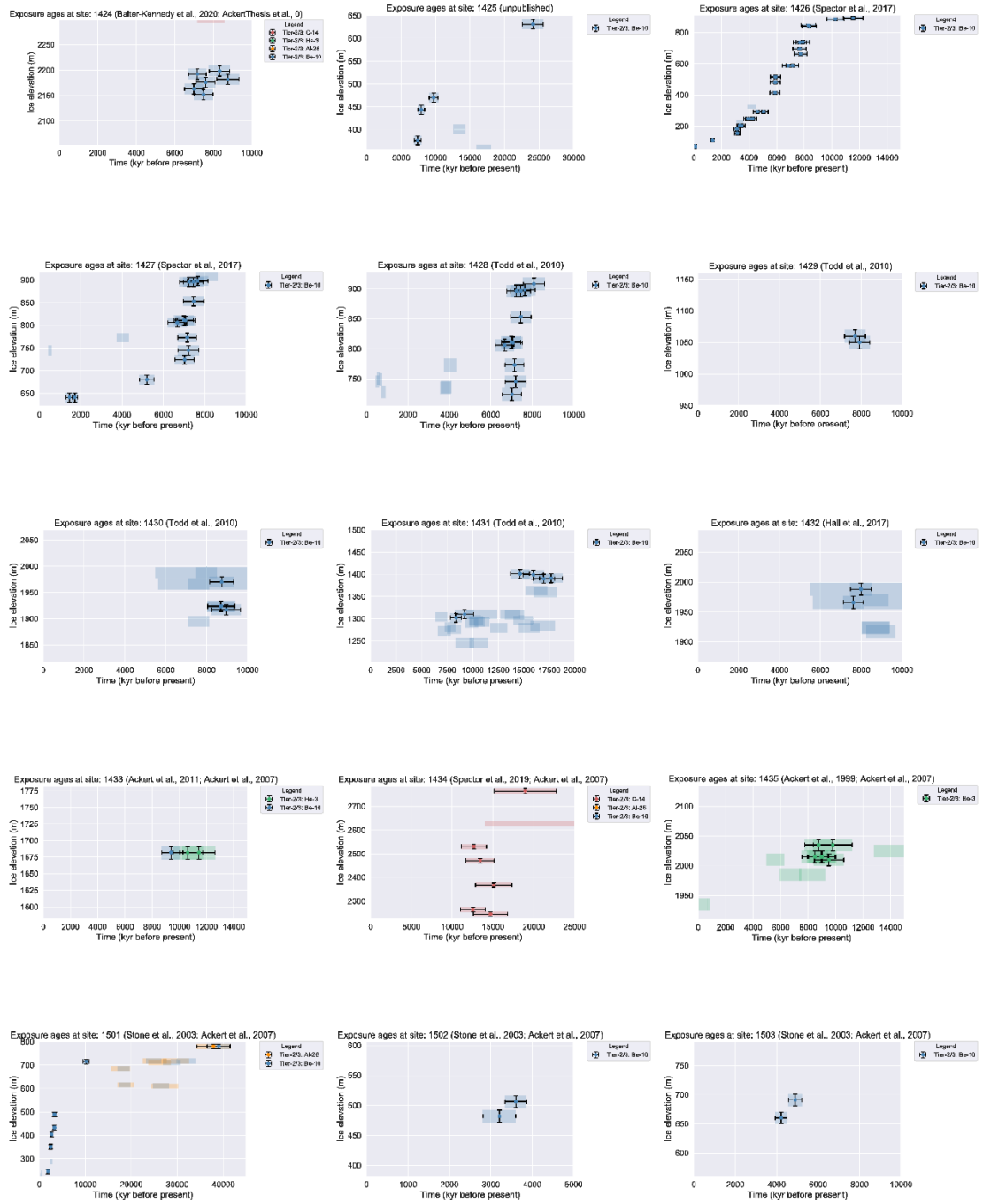
The supplement spreadsheets related to this article are available online at:

<https://doi.org/10.5194/essd-15-3573-2023-supplement>.

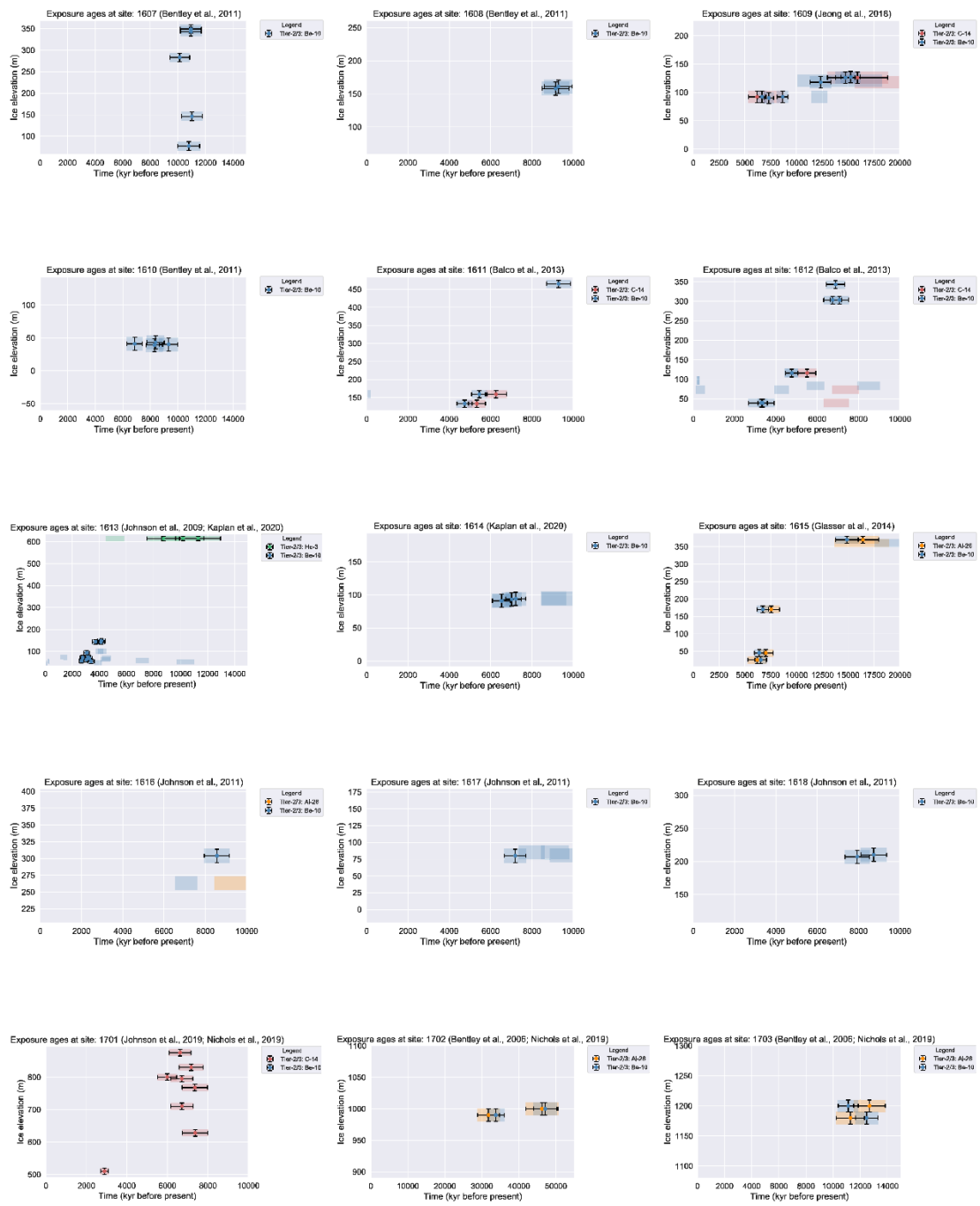












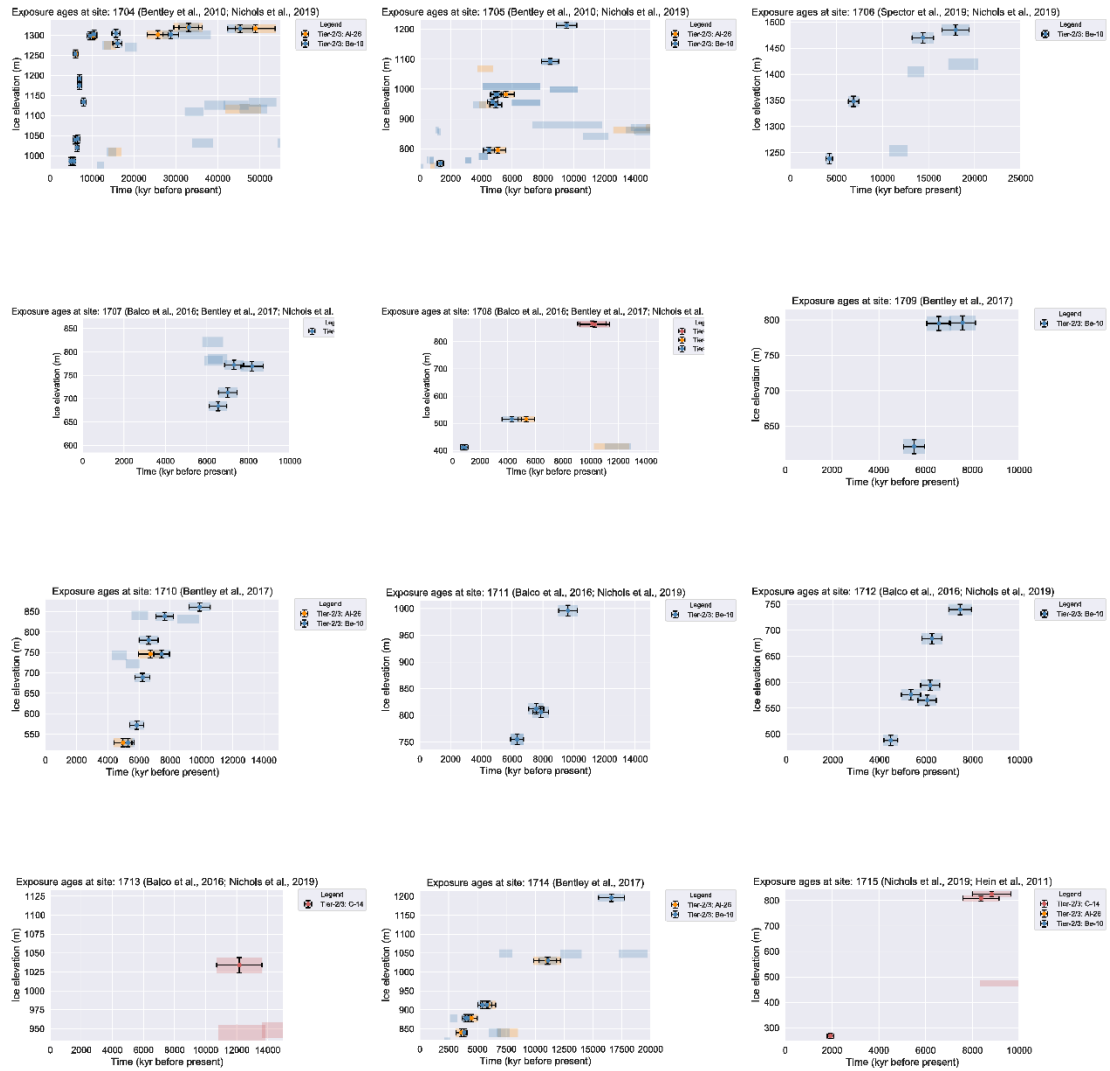


Figure S2.1: Past ice thickness (paleoH) entire tier-2/3 dataset.

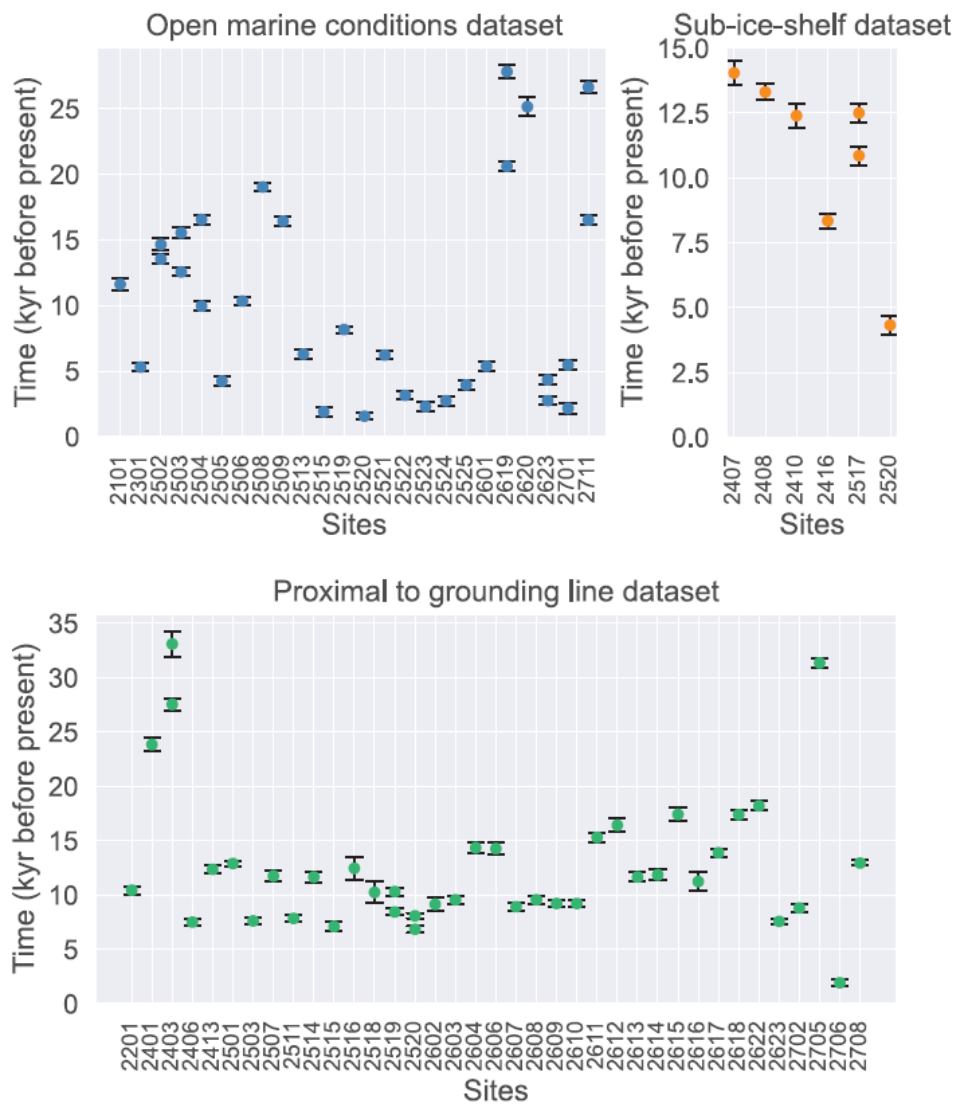
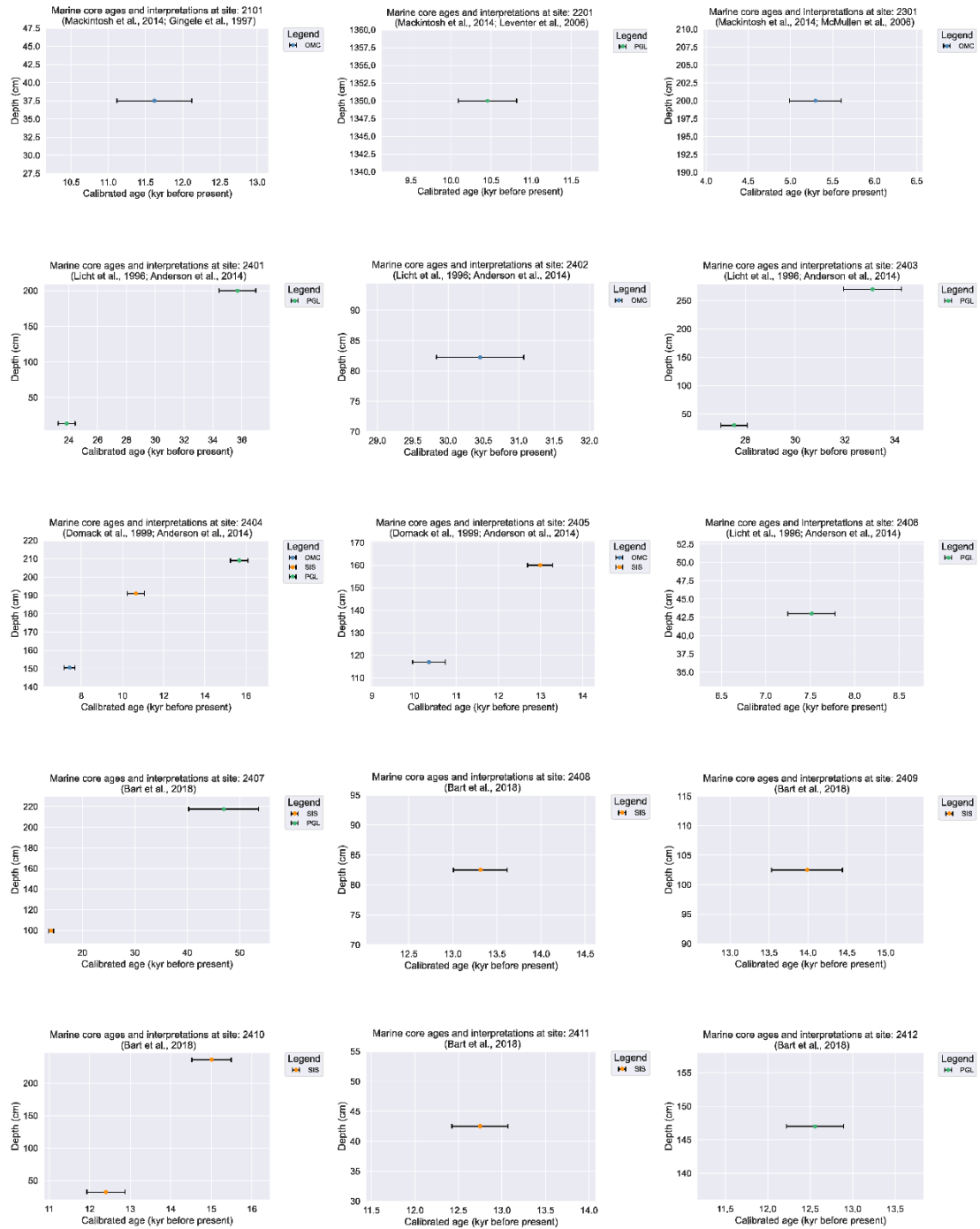
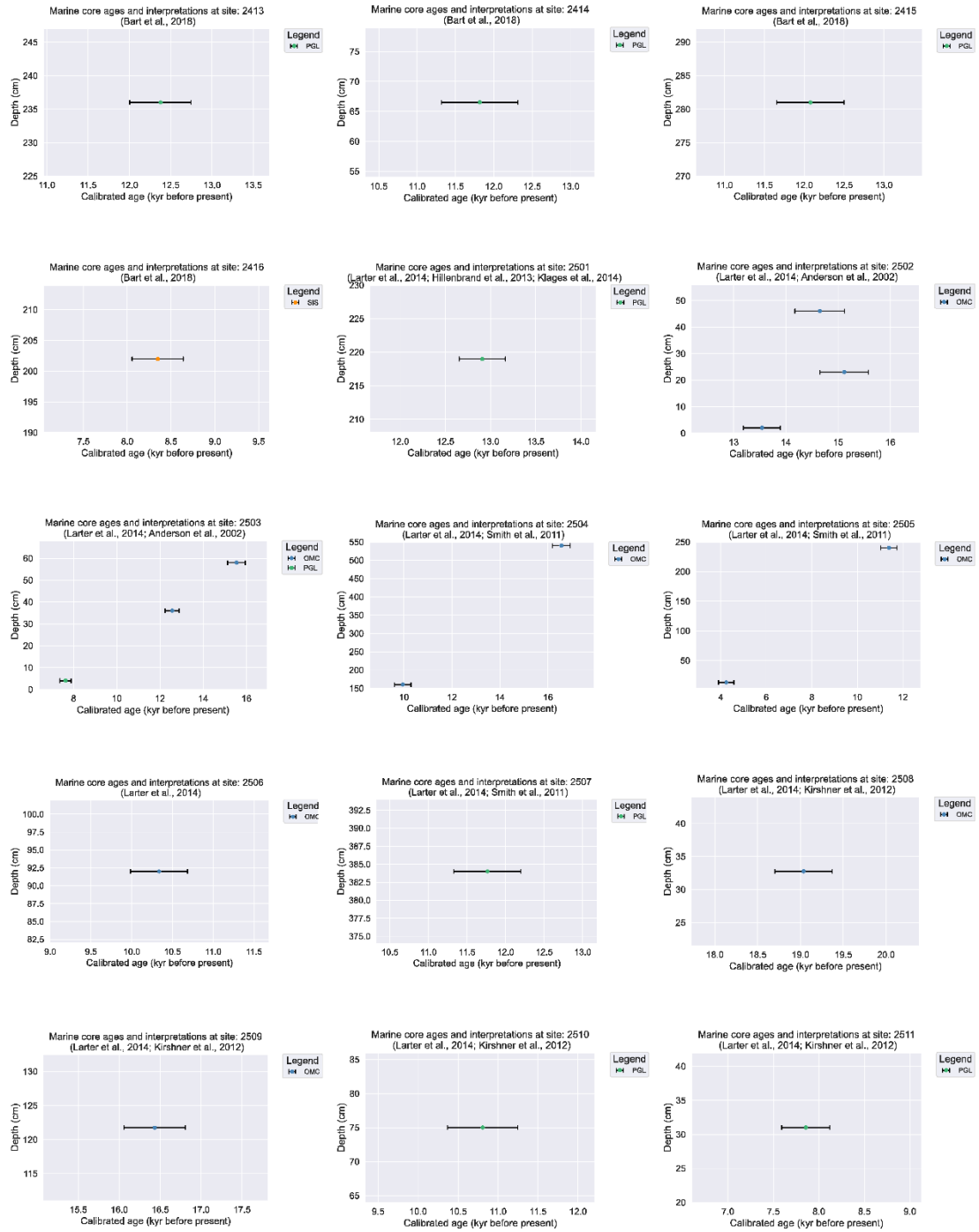
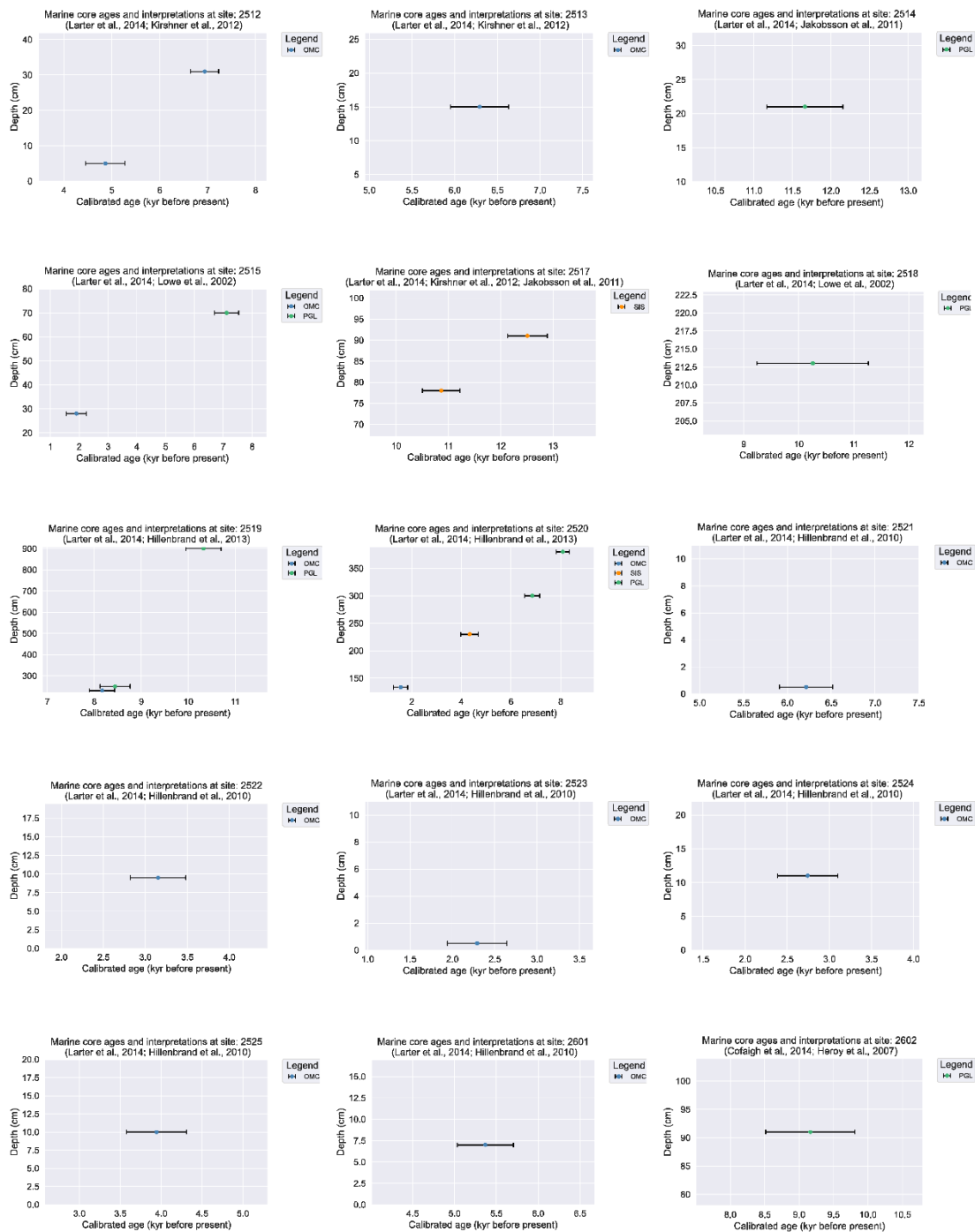
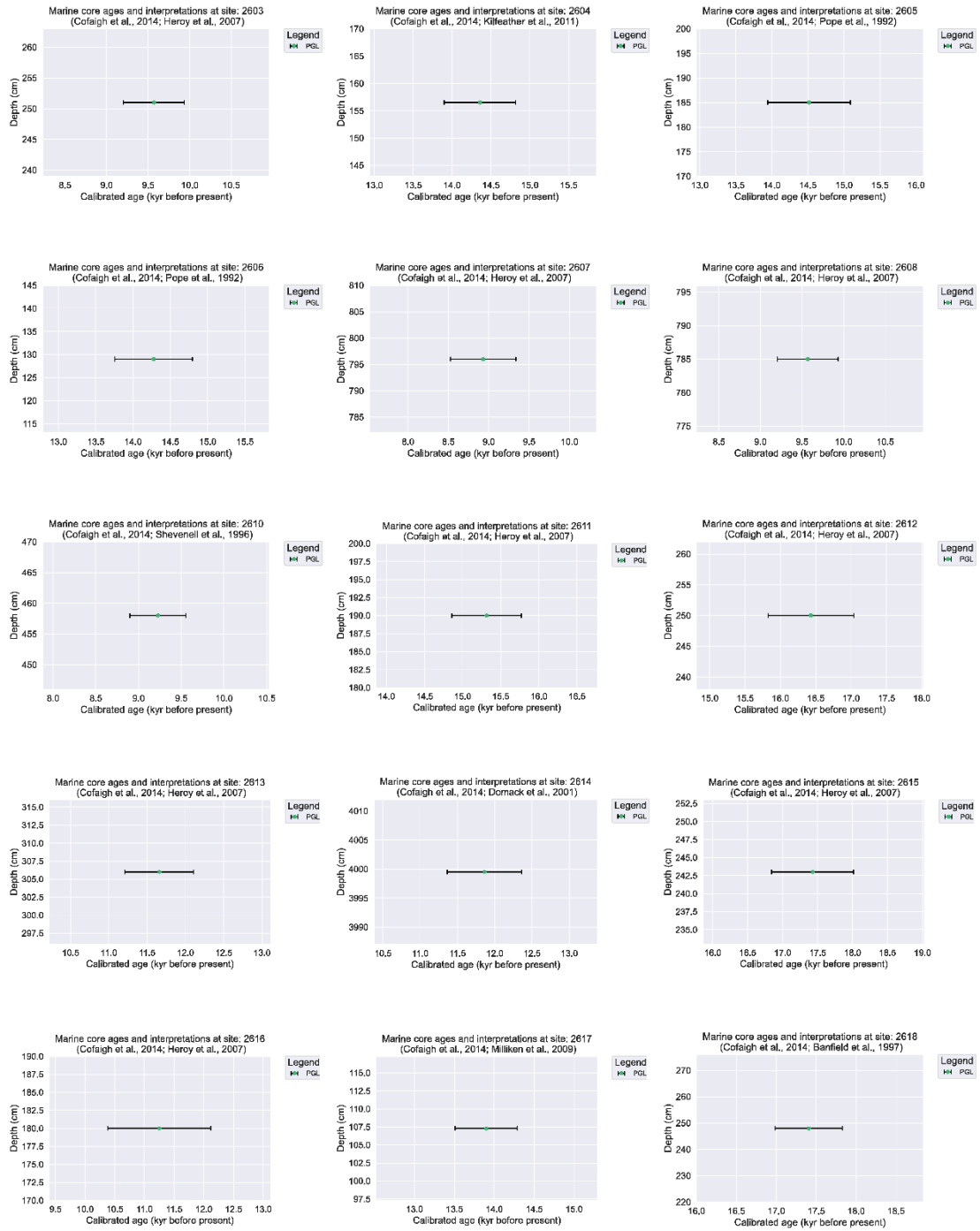


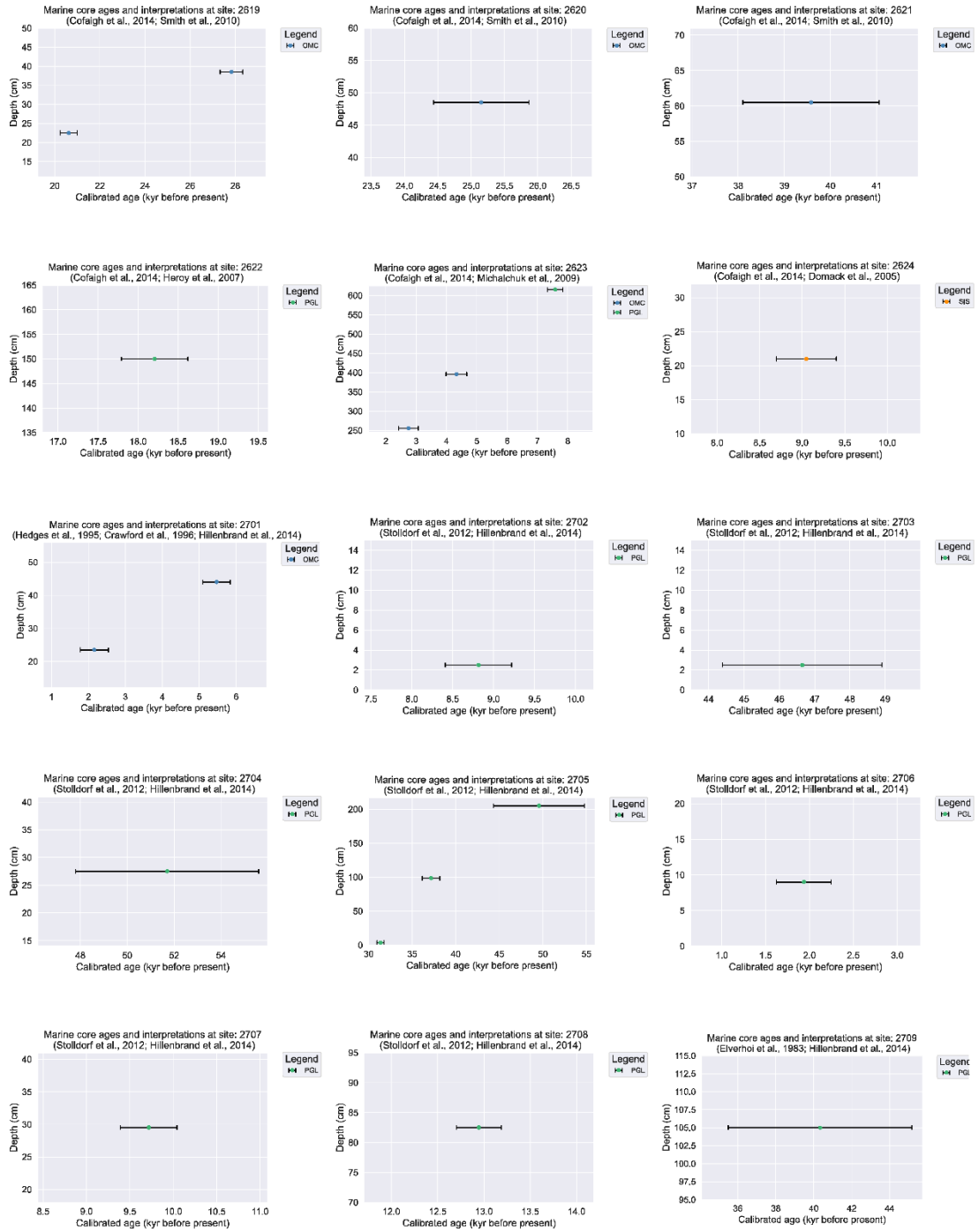
Figure S2.2: Past ice extent (paleoExt) summary tier-1/2 dataset.











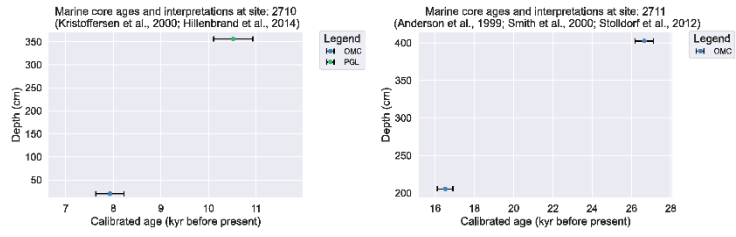


Figure S2.3: Past ice extent (paleoExt) entire tier-1/2 dataset.

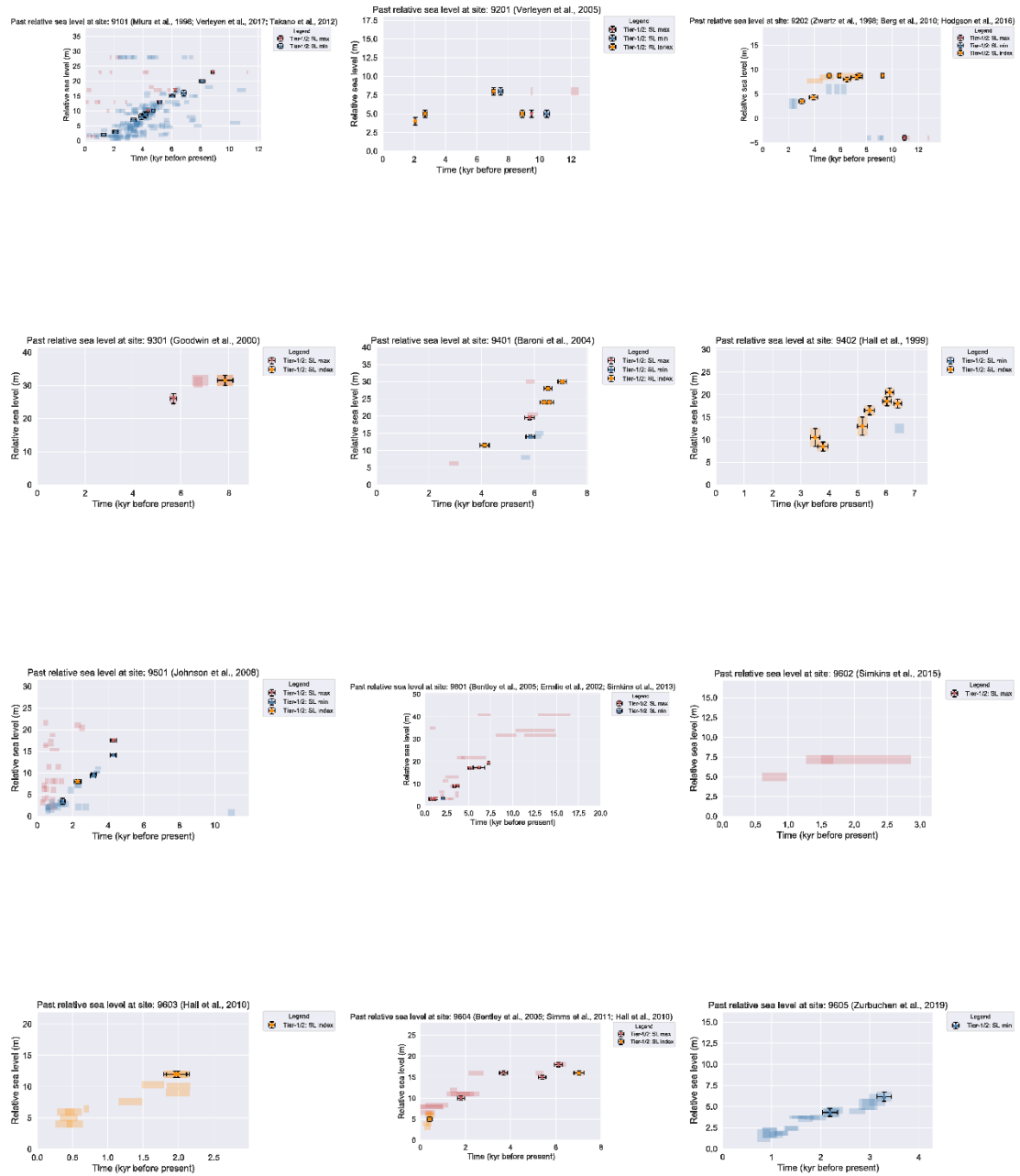


Figure S2.4: Past sea level (paleoRSL) entire tier-1/2 dataset.

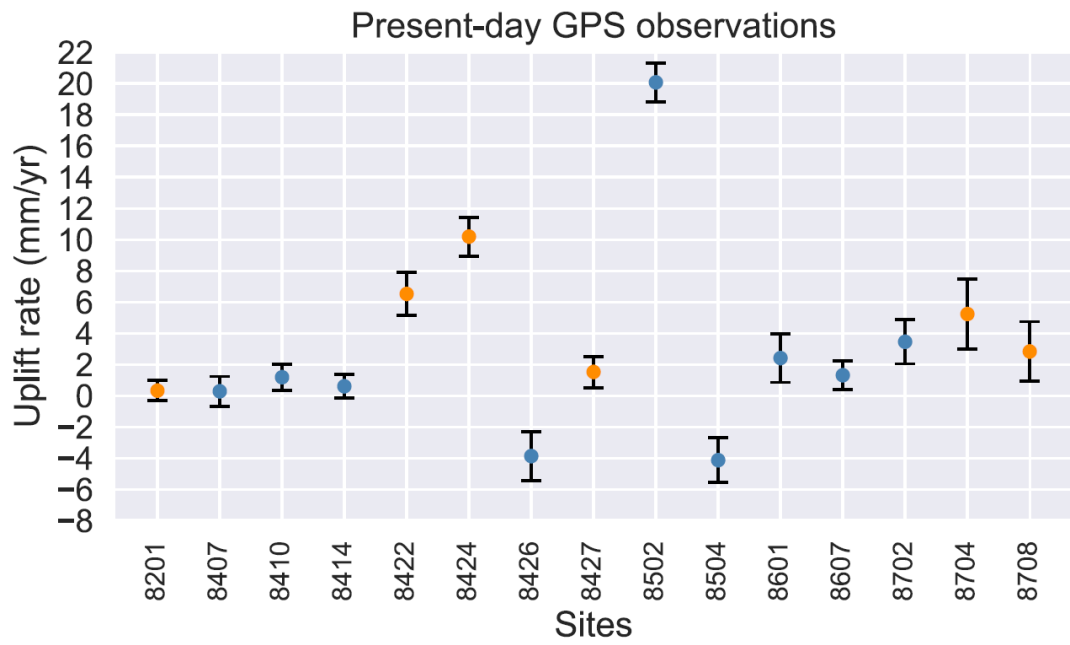


Figure S2.5: Present-day GPS uplift rate (rdotGPS) of the tier-1 (orange circle) and tier-2 (blue circles) data.

## Supplement for Chapter 3

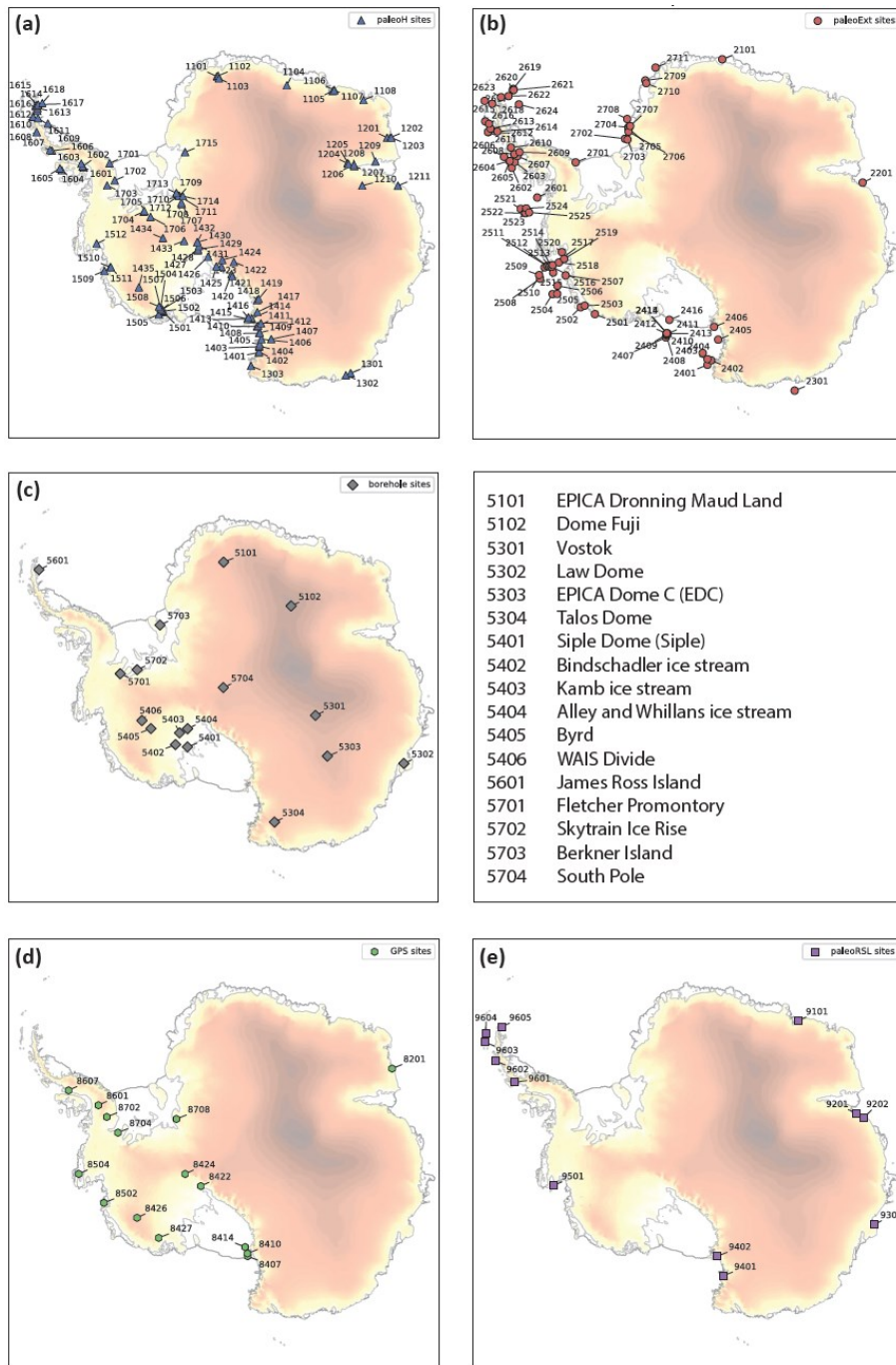


Figure S3.1: AntICE2 observational constraint database used to history match the Glacial Systems Model. a - f) are the site locations and identification numbers for past ice thickness data (paleoH), past ice extent data (paleoExt), ice core borehole temperature profiles (ICbore) and names, present-day uplift rates (rdotGPS), and past relative sea level data (paleoRSL) respectively.

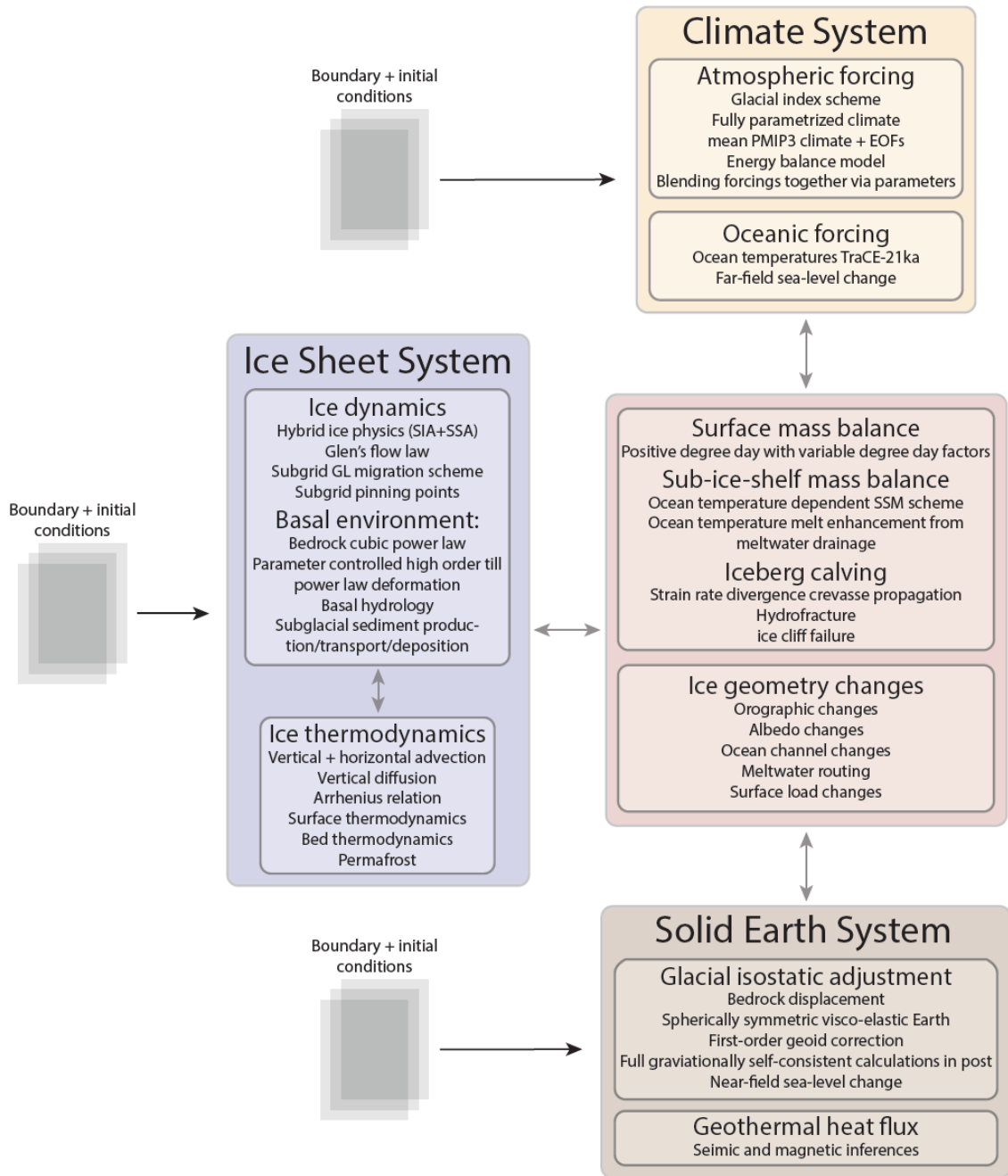


Figure S3.2: Diagram summarizing major components of the Glacial Systems Model (GSM).

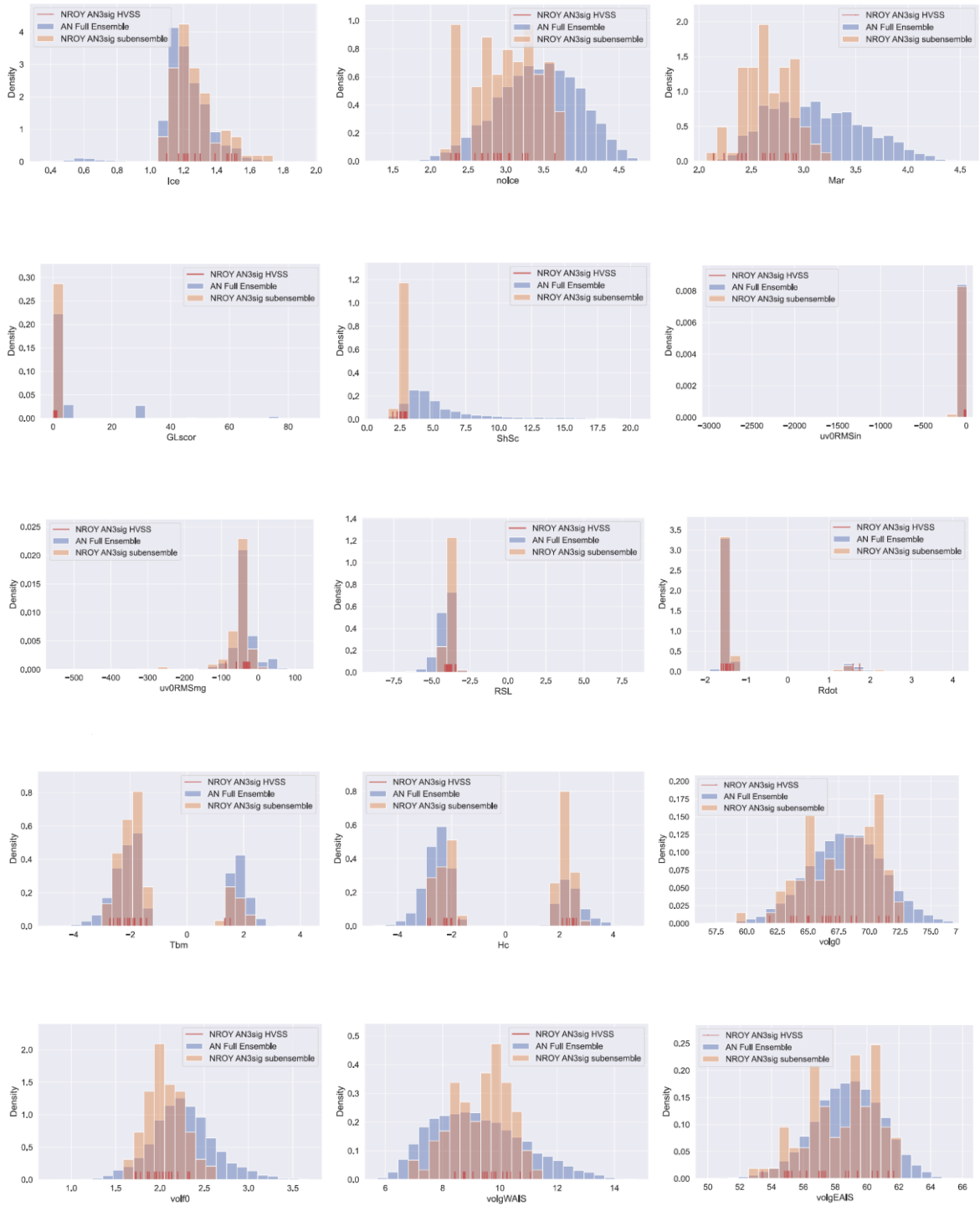


Figure S3.3: Distribution of output scores and metrics for the full ensemble (blue), not-ruled-out-yet (NROY) AN3sig sub-ensemble (orange), and NROY sub-ensemble high variance subset (red). The individual model scores are defined in Table S1. The present-day (PD) metrics shown are the PD grounded ice volume ( $volg_0$ ), PD floating ice volume

(volf0), PD West AIS grounded ice volume (volgWAIS), and PD East AIS grounded ice volume (volgEAIS).

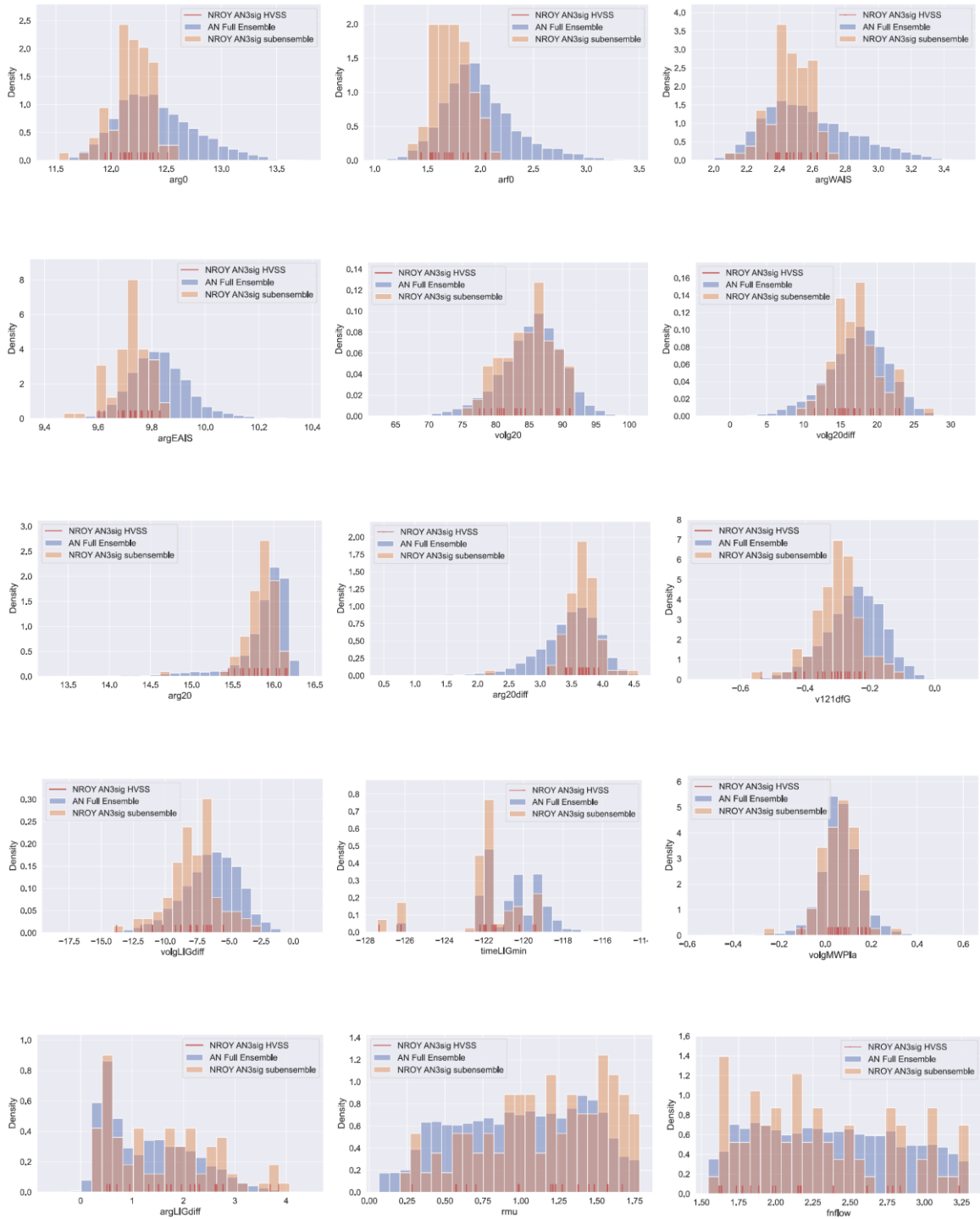
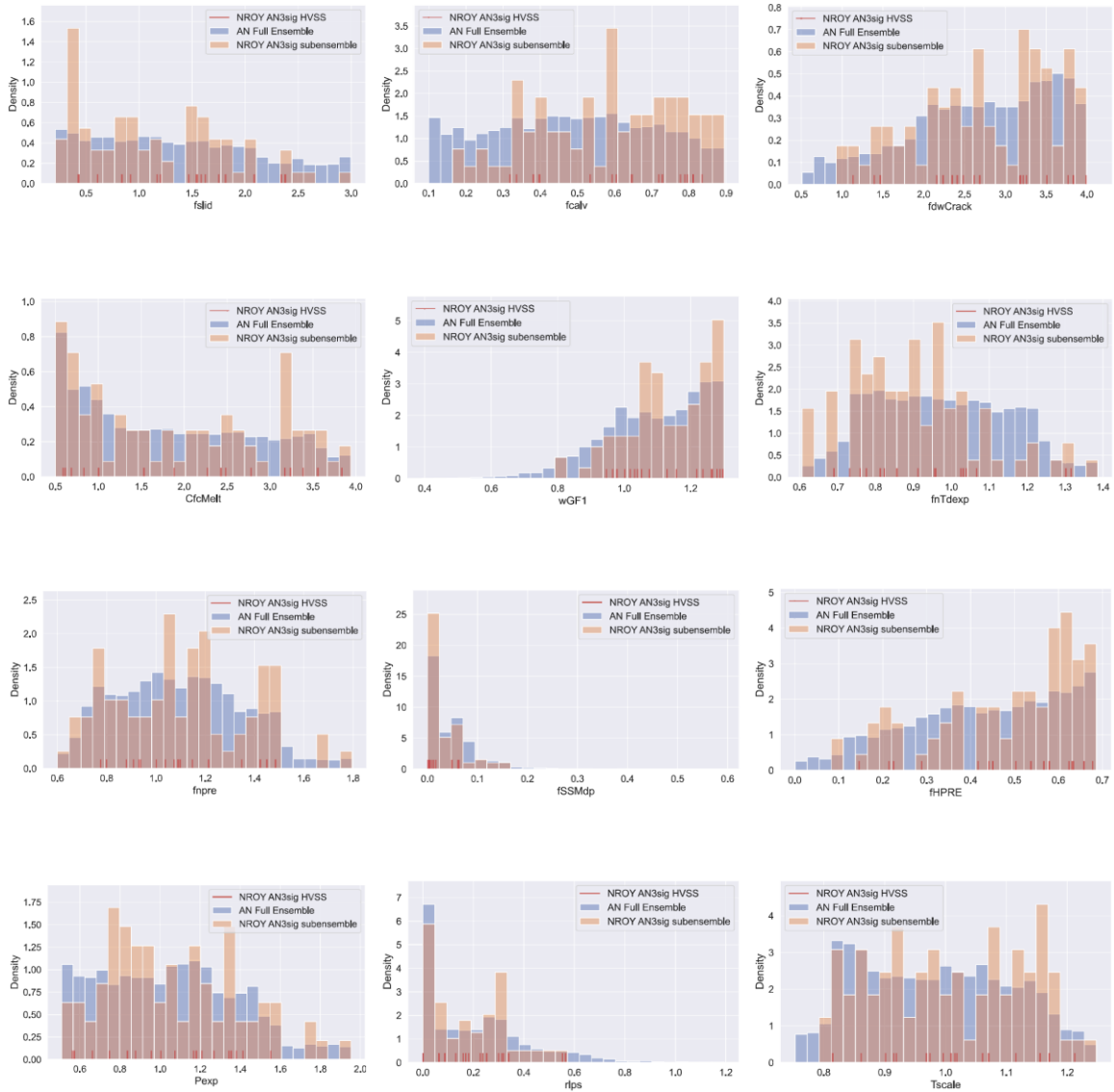


Figure S3.4: Distribution of output metrics, scores, and ensemble parameters (detailed in Table 3.1) for the full ensemble (blue), not-ruled-out-yet (NROY) AN3sig sub-ensemble

(orange), and NROY sub-ensemble high variance subset (red). The present-day (PD) metrics shown are PD grounded ice area (arg0), PD floating ice area (arf0), PD West AIS grounded ice area (argWAIS), and PD East AIS grounded ice area (argEAIS). The LGM metrics shown are the 20 ka grounded ice volume (volg20), 20 ka grounded ice volume excess relative to present (volg20diff), 20 ka grounded ice area (arg20), 20 ka grounded ice area excess relative to present (arg20diff). The Meltwater Pulse 1a (MWP1a) metric is the grounded ice volume change over the MWP1 interval (volgMWP1a). The last interglacial (LIG) metrics are the timing of the LIG AIS minimum (timeLIGmin), LIG grounded ice volume deficit relative to present (volgLIGdiff/v121dfG), and LIG grounded ice area deficit relative to present (argLIGdiff).



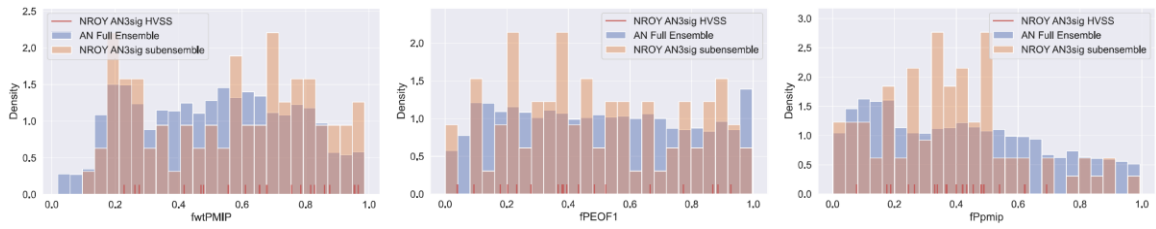
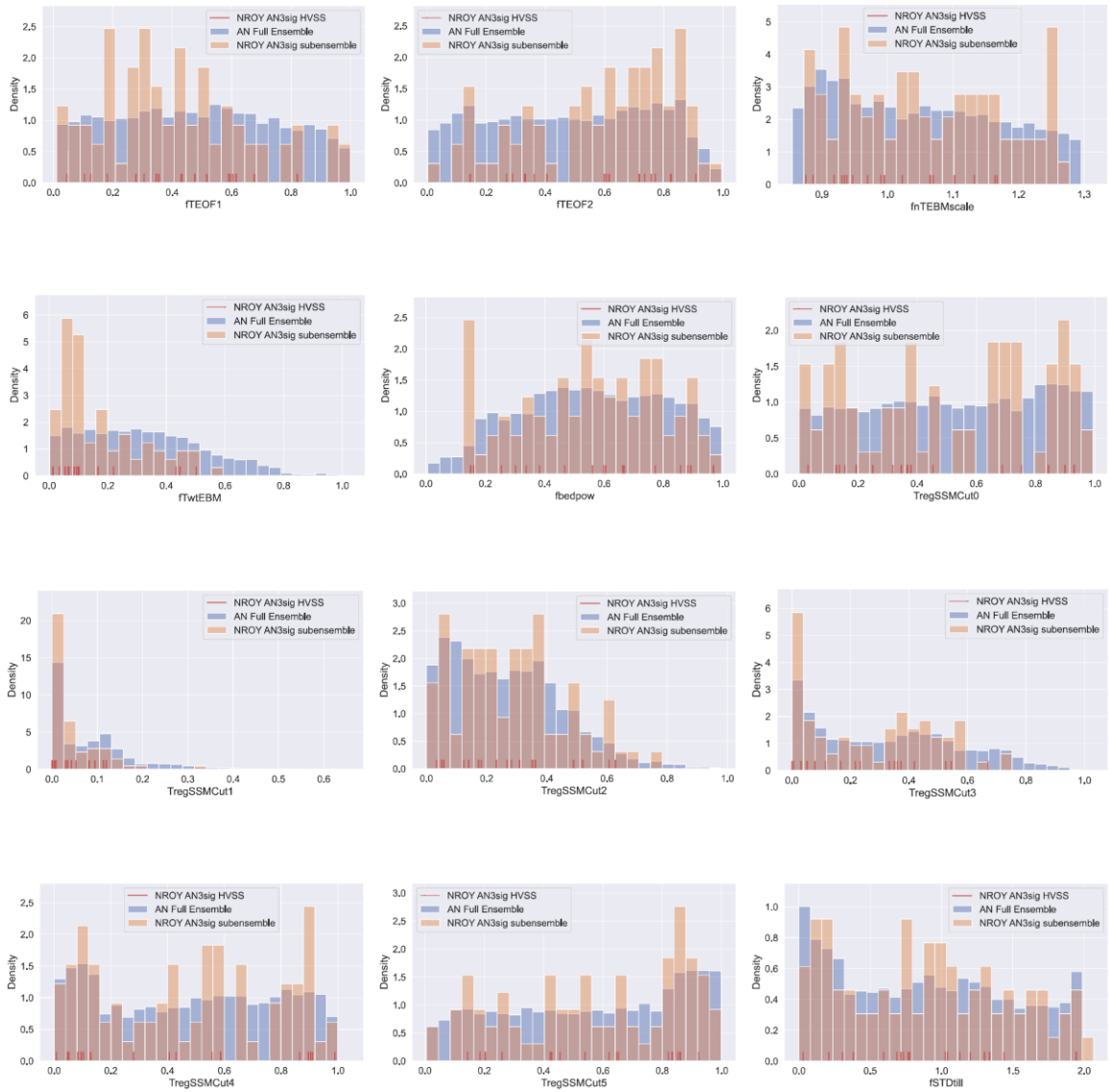


Figure S3.5: Distribution of ensemble parameters (detailed in Table 3.1) for the full ensemble (blue), not-ruled-out-yet (NROY) AN3sig sub-ensemble (orange), and NROY sub-ensemble high variance subset (red).



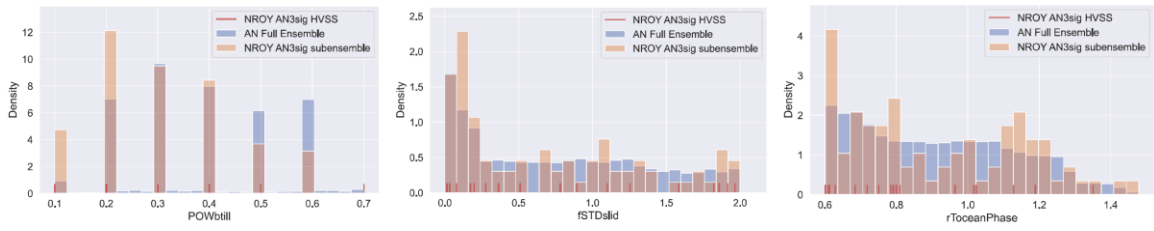


Figure S3.6: Distribution of ensemble parameters (detailed in Table 3.1) for the full ensemble (blue), not-ruled-out-yet (NROY) AN3sig sub-ensemble (orange), and NROY sub-ensemble high variance subset (red).

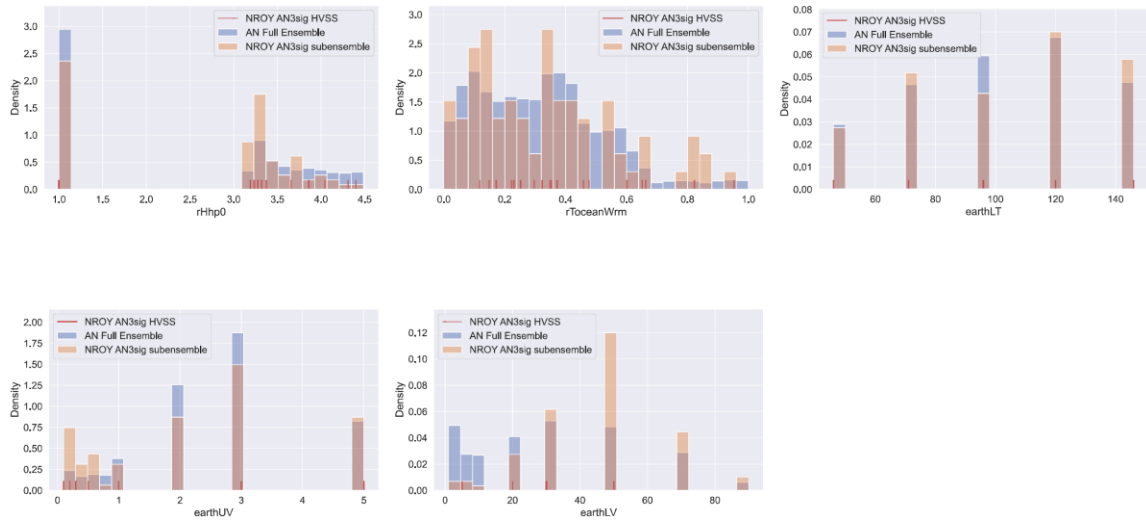


Figure S3.7: Distribution of ensemble parameters (detailed in Table 3.1) for the full ensemble (blue), not-ruled-out-yet (NROY) AN3sig sub-ensemble (orange), and NROY sub-ensemble high variance subset (red).

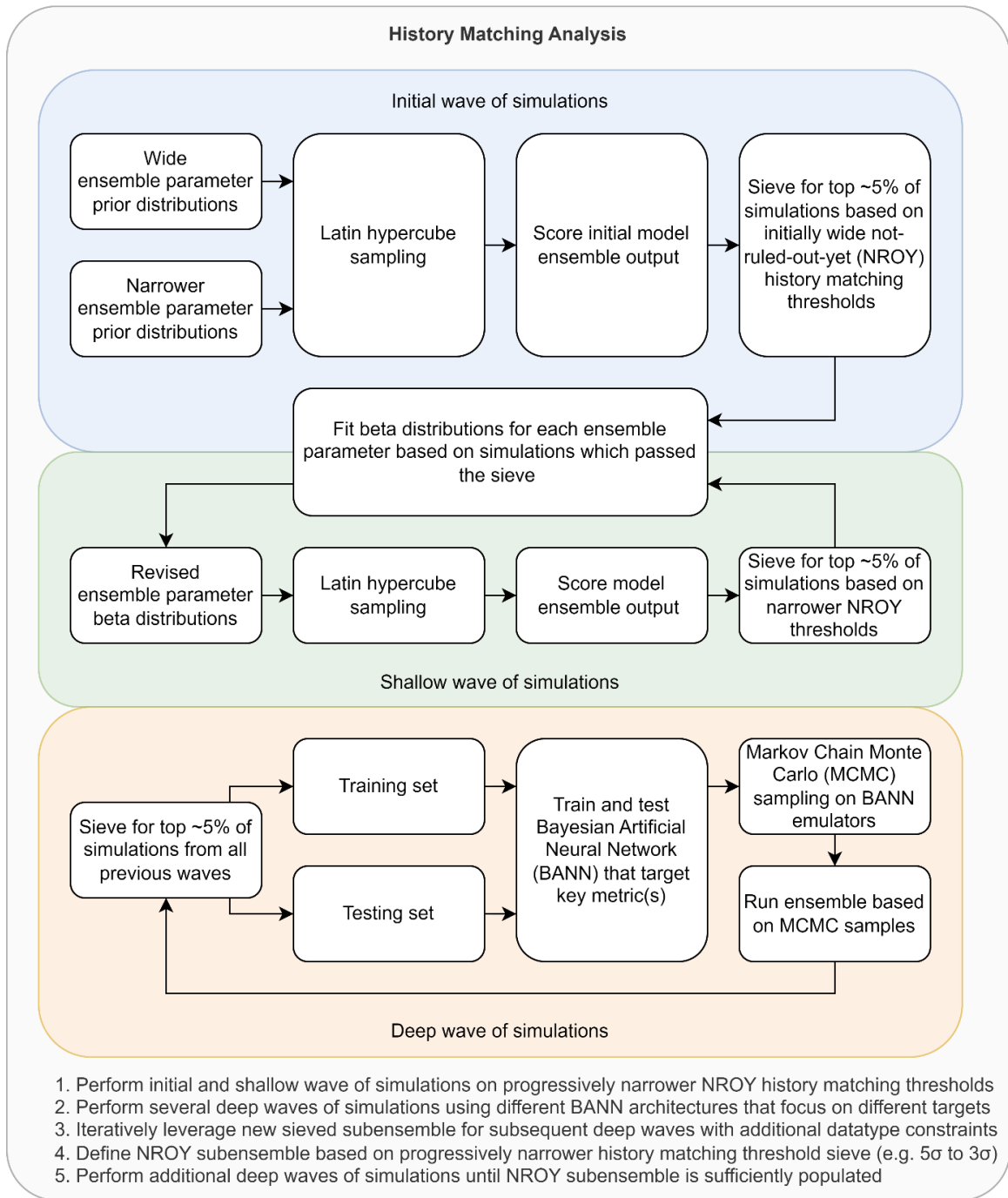


Figure S3.8: Diagram illustrating the history-matching analysis methodology.

Table S3.1: The thresholds imposed on the AntICE2 data-model scores in the history-matching analysis. The thresholds to define the AN4sig and AN3sig sub-ensembles are based on internal/external discrepancy bias corrections plus 4 or 3 multiples of the standard deviations, respectively.

<b>Constraint data type</b>	<b>Score</b>	<b>Bias</b>	<b>Standard deviation</b>
Present-day	WAIS H RMS (waisRMS)	0	161
Present-day	EAIS H RMS (eaisRMS)	16	135
Present-day	Floating ice H RMS (fltRMS)	34	65
Present-day	Ice shelf score (ShSc)	0	1
Present-day	PD grounding line score (GLscor)	0	1
Borehole temp	Borehole ice temp score (Tbm)	0	1
Borehole temp	Ice core site H diff score (Hc)	0	1
Paleo extent	Marine extent score (Mar)	0.14	1.04
Paleo ice thickness	Deglaciated no ice score (noIce)	0.22	1.02
Paleo ice thickness	Glaciation ice score (Ice)	0.15	1
Paleo RSL	RSL score (RSL)	-0.1	1.01
GPS	Uplift rate score (Rdot)	-0.02/0.06	1.06

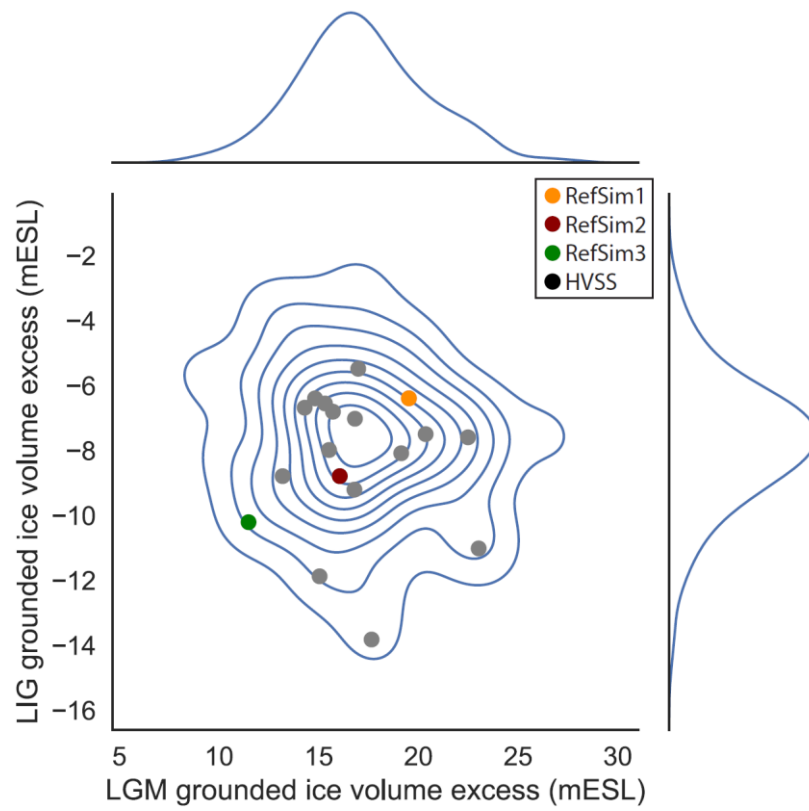


Figure S3.9: High variance subset (HVSS; N=18) of simulations in the not-ruled-out-yet (NROY) AN3sig sub-ensemble.

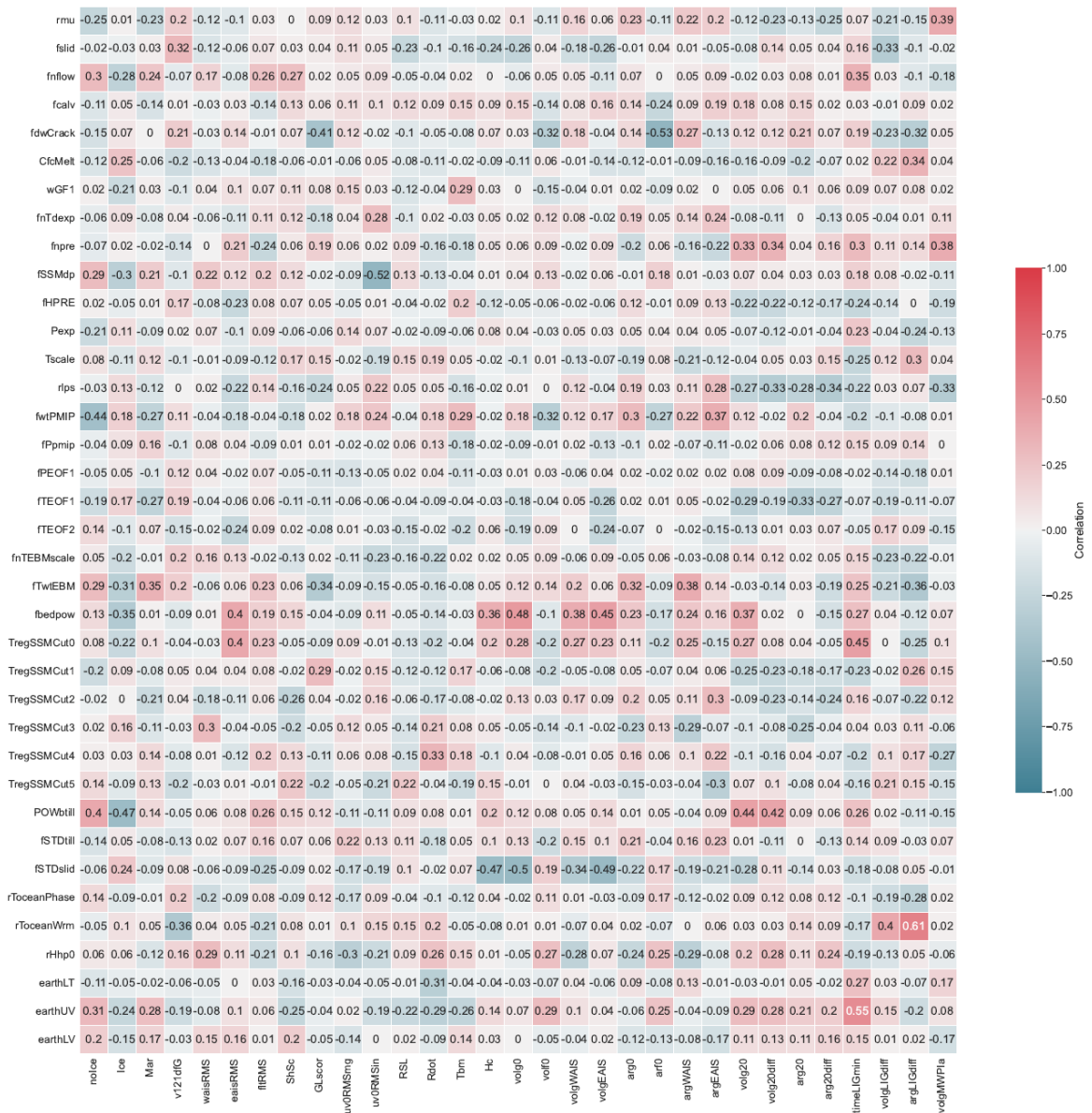


Figure S3.10: Metric/score-parameter correlation heat map of not-ruled-out-yet (NROY) AN3sig sub-ensemble. The ensemble parameters are defined in Table 3.1, the individual model scores are defined in Table S3.1. The present-day (PD) metrics shown are the PD grounded ice volume (volg0), PD floating ice volume (volf0), PD West AIS grounded ice volume (volgWAS), PD East AIS grounded ice volume (volgEAS), PD grounded ice area (arg0), PD floating ice area (arf0), PD West AIS grounded ice area (argWAS), and PD East AIS grounded ice area (argEAS). The LGM metrics shown are the 20 ka grounded ice volume (volg20), 20 ka grounded ice volume excess relative to present (volg20diff), 20 ka grounded ice area (arg20), 20 ka grounded ice area excess relative to present (arg20diff). The Meltwater Pulse 1a (MWP1a) metric is the grounded ice volume change over the MWP1 interval (volgMWP1a). The last interglacial (LIG) metrics are the timing of the LIG

AIS minimum (timeLIGmin), LIG grounded ice volume deficit relative to present (volgLIGdiff), and LIG grounded ice area deficit relative to present (argLIGdiff).

### NROY subensemble statistics

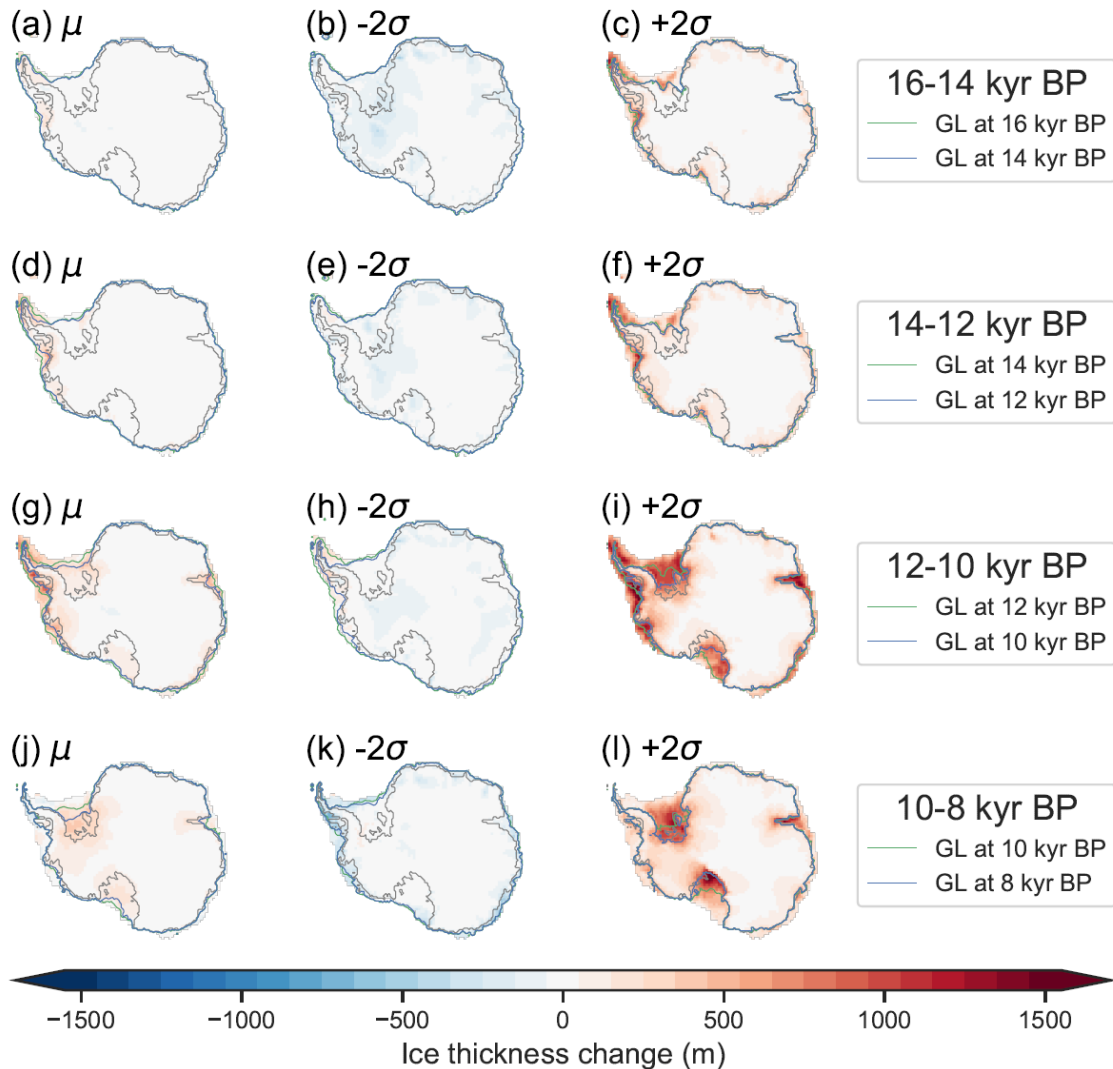


Figure S3.11: NROY AN3sig sub-ensemble deglacial ice thickness difference for the interval of a-c) 16-14 ka d-f) 14-12 ka g-i) 12-10 ka j-l) 10-8 ka and their respective grounding lines for the ensemble mean (leftmost column),  $-2\sigma$  bound (center column), and  $+2\sigma$  bound (rightmost column).

## NROY subensemble statistics

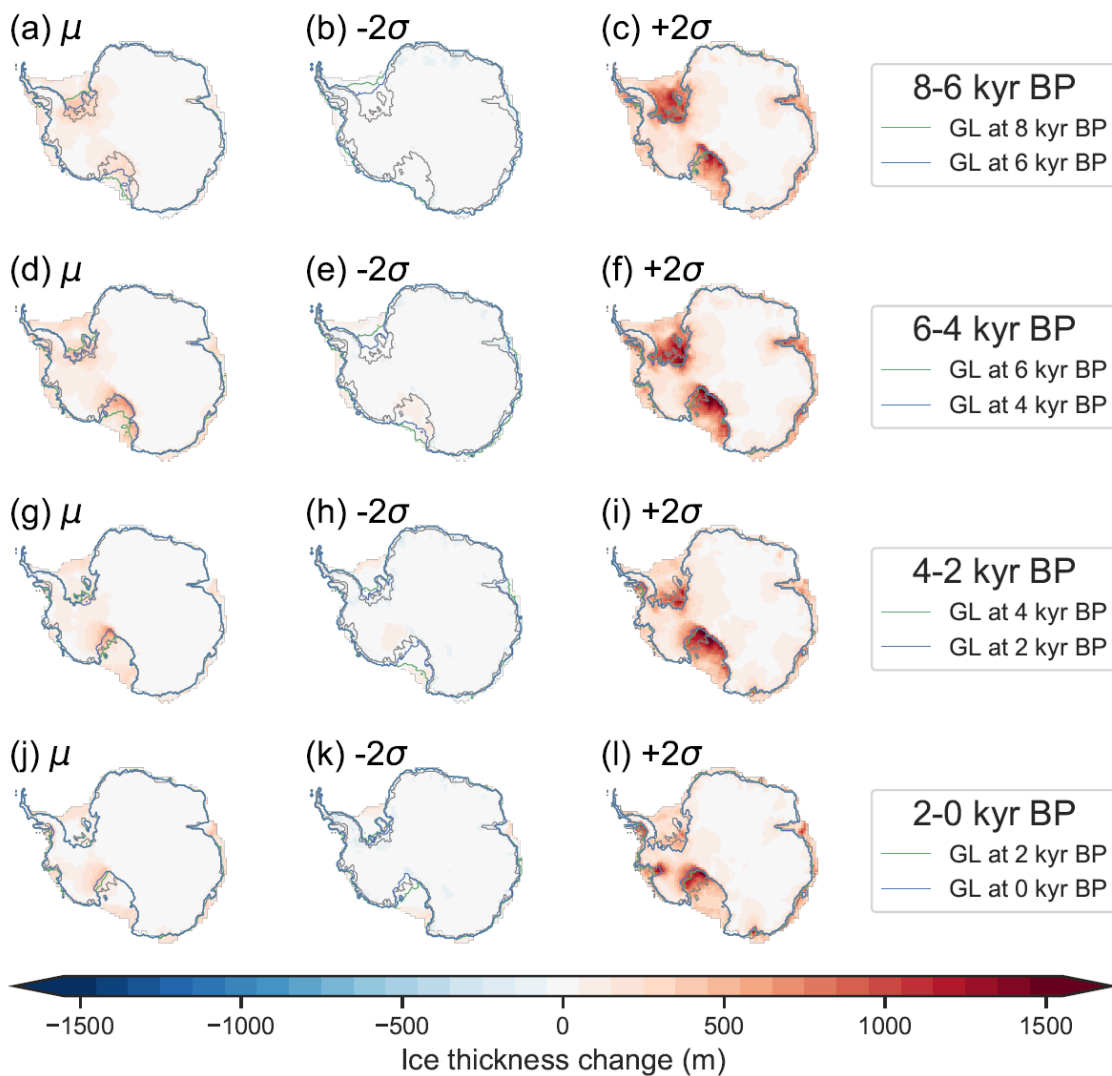


Figure S3.12: NROY AN3sig sub-ensemble deglacial ice thickness difference for the interval of a-c) 8-6 ka d-f) 6-4 ka g-i) 4-2 ka j-l) 2-0 ka and their respective grounding lines for the ensemble mean (leftmost column),  $-2\sigma$  bound (center column), and  $+2\sigma$  bound (rightmost column).

# Supplement for Chapter 4

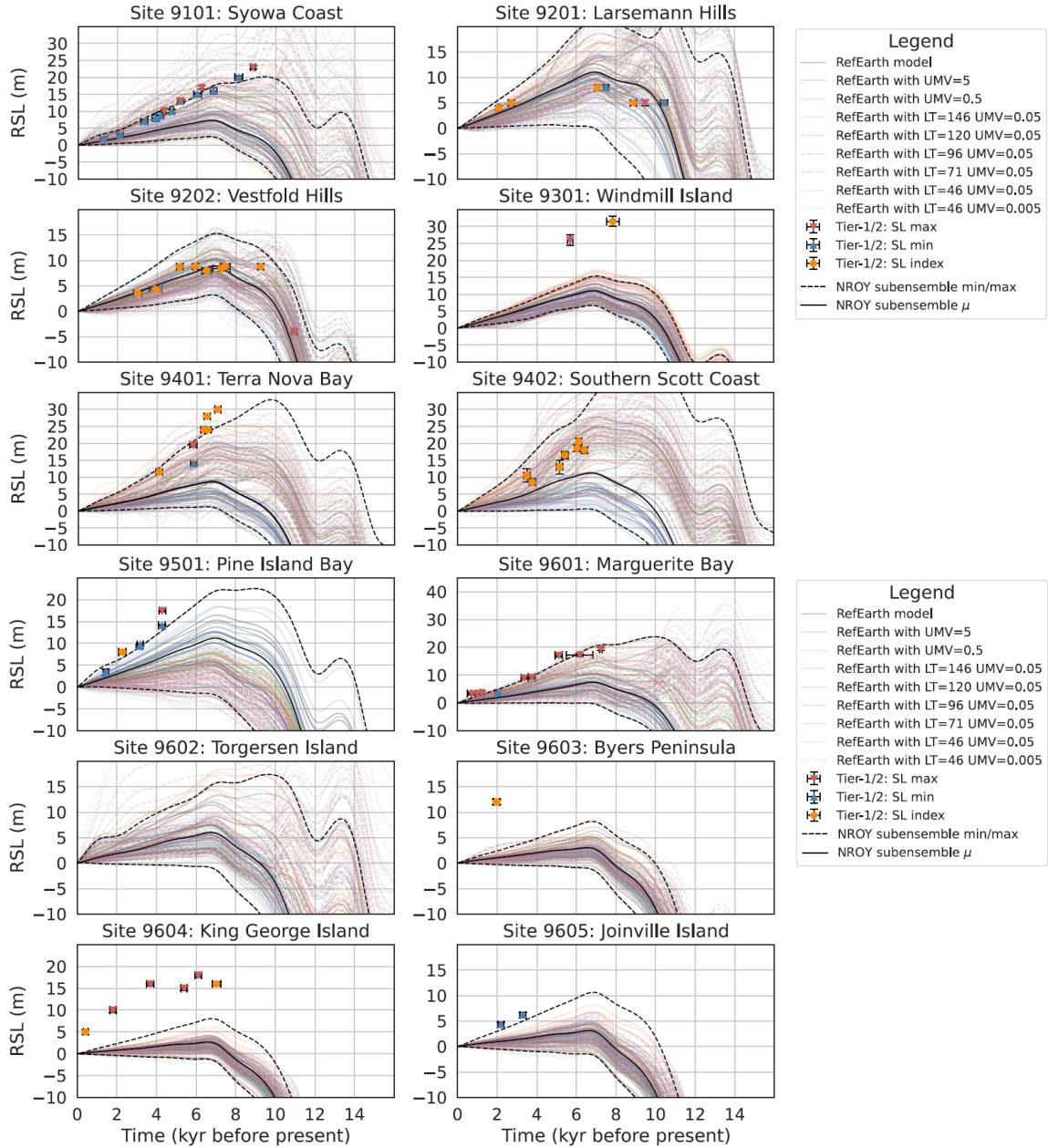


Figure S4.1: Paleo relative sea level data-model comparison of the not-ruled-out-yet (NROY) sub-ensemble high variance subset. A sensitivity analysis was performed on the NROY HVSS based on their respective reference Earth (RefEarth) model with a progressively lower upper mantle viscosity (UMV) and thinner lithospheric thickness (LT) to investigate the impact of lateral Earth structure. The LT and UMV experiments  $\mu$  range from 146 to 46 km and  $5 \cdot 10^{21}$  to  $0.005 \cdot 10^{21}$  Pa·s, respectively.

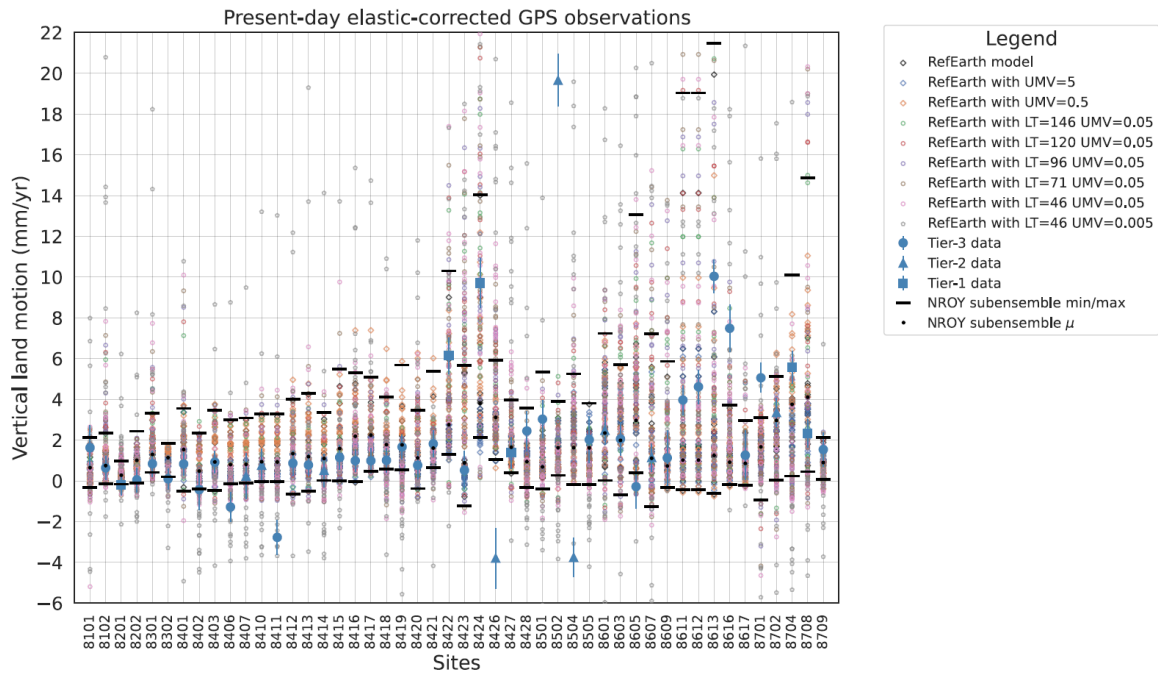


Figure S4.2: Global Positioning System elastic-corrected rate of bedrock displacement data-model comparison of the not-ruled-out-yet (NROY) sub-ensemble high variance subset. A sensitivity analysis was performed on the NROY HVSS based on their respective reference Earth (RefEarth) model with a progressively lower upper mantle viscosity (UMV) and thinner lithospheric thickness (LT) to investigate the impact of lateral Earth structure. The LT and UMV experiments range from 146 to 46 km and  $5 \cdot 10^{21}$  to  $0.005 \cdot 10^{21}$  Pa·s, respectively.

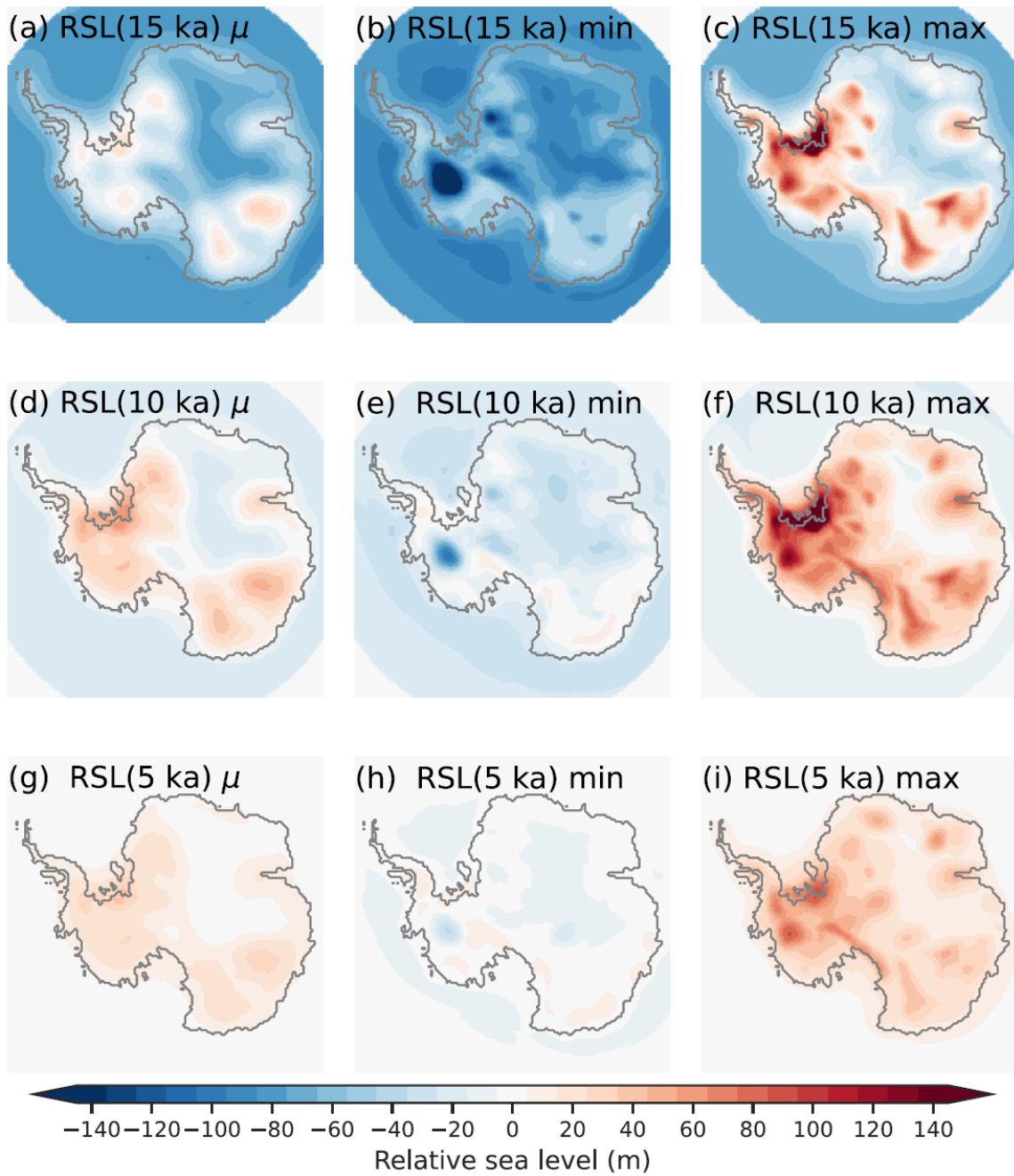


Figure S4.3: The not-ruled-out-yet (NROY) sub-ensemble mean (left), min (middle), and max (right) regional Antarctic RSL during the deglaciation at 15 ka (top), 10 ka (middle), and 5 ka (lower).

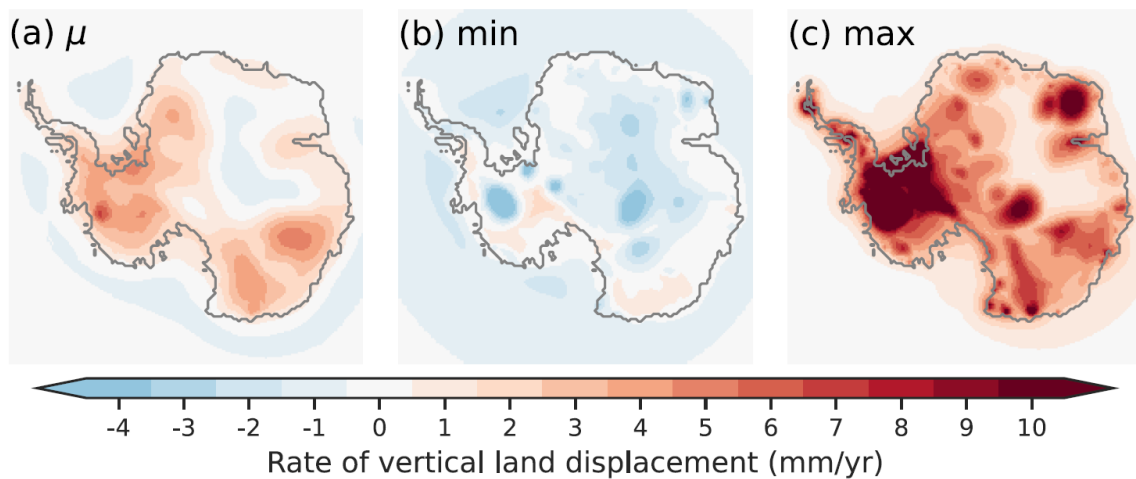


Figure S4.4: Present-day rate of bedrock displacement for the not-ruled-out-yet (NROY) sub-ensemble a) mean, b-c) minimum and maximum.

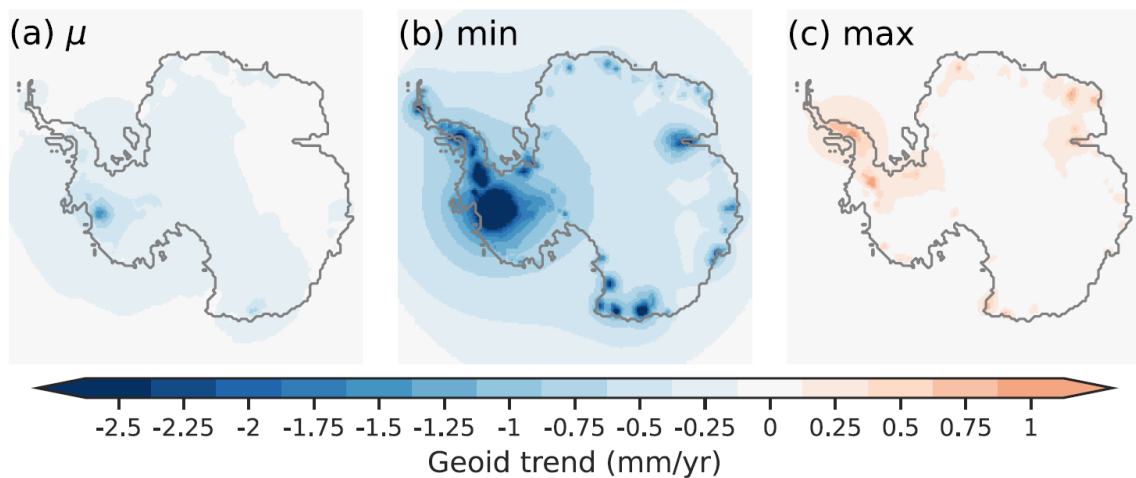


Figure S4.5: Present-day Antarctic rate of geoid displacement for the not-ruled-out-yet (NROY) sub-ensemble a) mean, b-c) minimum and maximum.

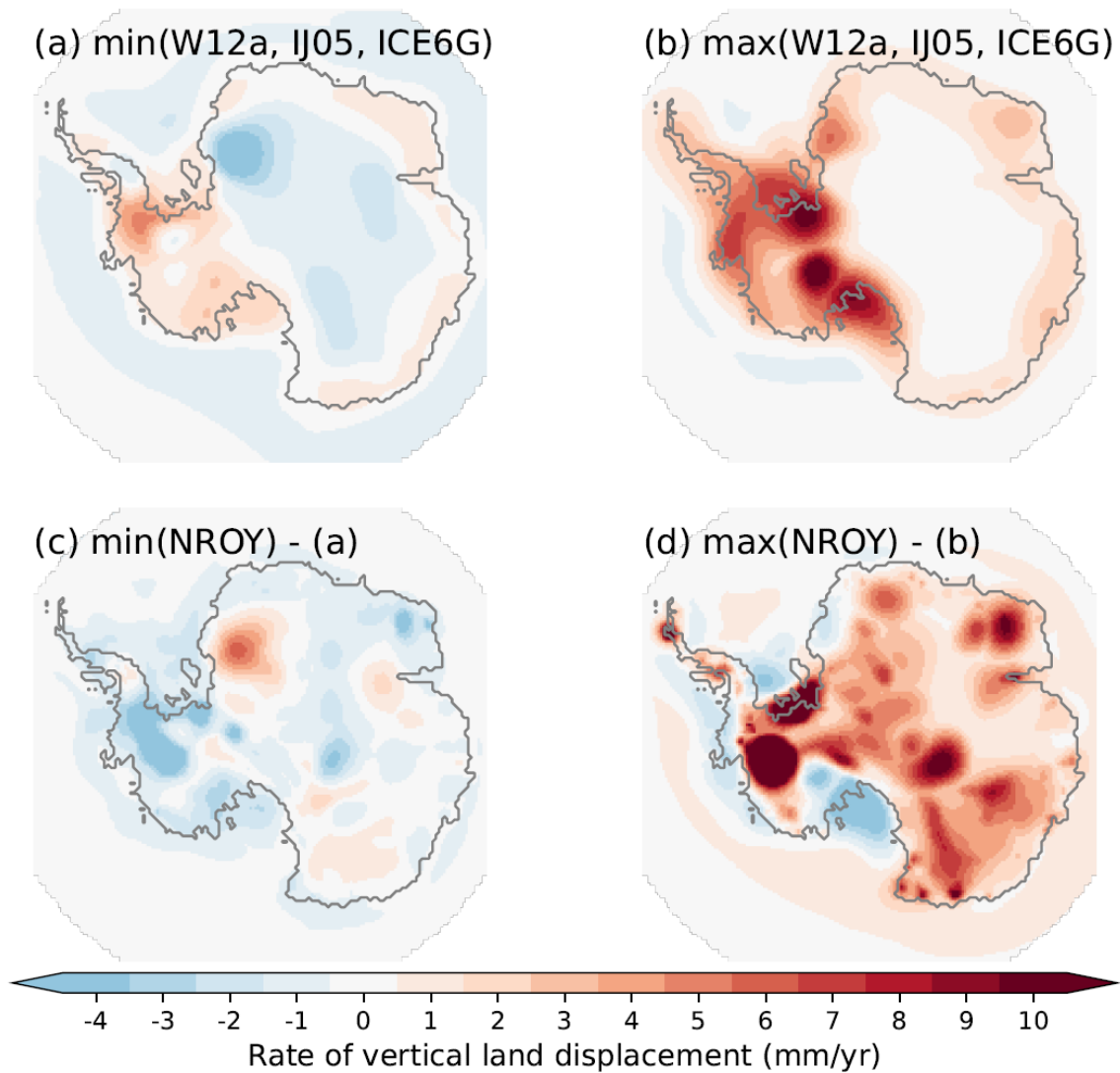


Figure S4.6: The (a) minimum and (b) maximum bounds for the PD rate of bedrock displacement for the three reference Antarctic GIA models (IJ05\_R2 - Ivins and James, 2005; W12a - Whitehouse et al., 2012; ICE-6G\_D - Peltier et al., 2015). These three GIA models represent nominal  $2\sigma$  bounds on the PD GIA corrections applied in the IMBIE studies to infer contemporary mass balance of the AIS. (Shepherd et al., 2018; Otosaka et al., 2023). The not-ruled-out-yet (NROY) sub-ensemble (c) minimum and (d) maximum minus the respective bounds of the three reference GIA models. The differences shown in (c) and (d) demonstrate regions where the three reference GIA models underestimate PD GIA uncertainties or where the NROY sub-ensemble better constrain the regional GIA response relative to the three reference GIA models.